Une brève histoire du climat, de l'importance des interactions mémoire présenté par Guillaume LE HIR Devant le jury composé de

Pr Adatte Thierry, Pr Ader Magali, Guillaume Le Hir

Habilitation à Diriger les Recherches

Une brève histoire du climat, de l'importance des interactions

---

mémoire présenté par Guillaume LE HIR

Devant le jury composé de :

Pr. ADATTE Thierry, Professeur, Université de Lausanne	Rapporteur
Pr. ADER Magali, Professeure, Institut de physique du globe	Rapporteur
Pr. BOPP Laurent, Professeur, Ecole Normale Supérieure Paris	Examinateur
Dr. CHAUSSIDON Marc, CNRS, Institut de physique du globe	Examinateur
Dr. CRASQUIN Sylvie, CNRS, Museum Nationale d'Histoire Naturelle	Examinateur
Dr. PAILLARD Didier, Ingénieur CEA, Laboratoire des Sciences du Climat	Rapporteur

Ce manuscrit n'est pas une synthèse de mes recherches, mais davantage la synthèse de mes réflexions J'ai choisi de développer 3 grands axes afin d'illustrer l'importance des processus au sein du système climatique- trop souvent le parent pauvre de l'étude des climats passés (et actuels) et de présenter plusieurs pistes prometteuses pour le futur.

L'ensemble des développements et des résultats présentés dans ce manuscrit sont le fruit d'une collaboration étroite depuis de longues années. Ces personnes, chercheurs, enseignants et amis, m'ont toujours permis de garder en tête que le système Terre est un système intégré où un mécanisme ne peut être considéré seul. C'est grâce à ces échanges et discussions fructueuses que nous avons pu avancé scientifiquement (et humainement).

Merci à Frédéric pour sa constante bienveillance et son incroyable acuité de recherche. Ces dix années ont été un plaisir grâce à toi

Merci à Yannick et à Yves, vous avez élevé la modélisation climatique et biogéochimique au premier plan en France – et au-delà !

Merci à Pierre (ah Pierre), de LMDz à l'IPSL jusque sous les panneaux de basket, tu restes l'esprit calme et posé, le point de repère lorsque les choses se brouillent.

Merci à Aude pour ton écoute et ta patience (dix années passées à me supporter, ce n'est pas rien). Merci aussi de m'avoir fait découvrir les méandres de la psychologie humaine.

Merci à Edouard pour m'avoir fait confiance ... sans oublier tes judicieux conseils.

Merci à mes parents, ils ont tout de même assurés le bon déroulement d'une bonne partie du début de cette aventure…

Enfin une énorme merci à ma chère femme, Marie-Anne, j'ai grandi grâce à toi !

Bises à Clément (mon fils)

POURQUOI ÉTUDIER LES CLIMATS ANCIENS ?

... un brin d'histoire

La climatologie est la science du climat. La définition de ce concept date de l'Antiquité où Aristote découpa la Terre en zones habitables (inhabitables) selon qu'il soit possible à l'Homme de les occuper (ou pas). Cette définition Antique du climat a laissé place à une vision plus moderne qui s'appuie sur l'analyse de la distribution statistique de variables météorologiques, comme la température ou les précipitations. Cette approche statistique du climat s'effectue sur une période de trente ans, soit une durée de vie d'Homme, c'est donc un concept qui demeure éminemment « anthropocentré ». Cette nouvelle définition révèle également les distinctions entre climat et météorologie. En effet cette période de trente ans permet de s'affranchir des variations diurnes, journalières, saisonnières ou même interannuelles, ces variations rapides étant le domaine de la météorologie.

Comment en est-on arrivé à comprendre que le climat du passé pouvait être différent de celui que nous observons de notre vivant ? Ce concept émergea avec les premières expériences effectuées par le **Comte de Buffon** *(1707-1788) dans sa forge de Montbeliard (Franche-Comté) sur le temps de refroidissement d'un boulet porté à chaud comme analogue de la Terre. Ainsi* **G. L Leclerc - comte de Buffon***, comme ses contemporains, affirmaient que le refroidissement irréversible de la Terre depuis « sa création » allait irrémédiablement conduire la Terre vers un état gelé et sans vie. Il restait aux scientifiques de cette époque d'en déterminer le moment. Cette vision théorique fût toutefois contestée par les travaux des géologues Suisses. Dans le canton helvétique du Valais, l'inondation accidentelle du Val de Bagnes survenue en 1818 questionna le géologue Suisse* **I. Venetz** *(1788-1859) sur les raisons de l'existence des importants lacs et glaciers Alpins. La somme des observations hydrologiques conduisit* **I. Venetz** *a pensé que ces lacs étaient les reliquats des glaciers qui avaient existé par le passé. Cette idée fut reprise quelques décennies plus tard par* **J. Charpentier** *puis* **L. Agassiz** *qui popularisa, lors de son discours de Neuchâtel (1837), l'idée d'âges glaciaires passés.*

Cette idée a probablement germé plus tôt chez d'autres géologues mais l'acceptation de la notion d'âge glaciaire est intiment liée au concept de catastrophisme défendu par la paléontologue **G. Cuvier**, *devenu en 1802 titulaire de la chaire d'anatomie comparée au Muséum d'histoires Naturelles de Paris. De son Jura natal,* **G. Cuvier** *avait pris conscience de l'existence de bouleversements*

paléontologiques. En marchant sur les terrains de sa jeunesse, ces ruptures - que nous appelons aujourd'hui crises de biodiversité (ou extinctions de masse) - étaient pour **G. Cuvier** *les « révolutions du globe ». En proposant une explication aux ruptures paléontologiques enregistrées dans les terrains du Jura, les âges glaciaires devenaient à leur tour un sujet d'intérêt. La fin du XIX^e^ siècle et le début du XX^e^ verront des résultats marquants sur ce thème – dont la fameuse théorie astronomique des climats élaborée par* **M. Milankovic** *(1879- 1958).*

En parallèle de la naissance de ces concepts, l'invention du thermomètre - et la standardisation des unités de mesures de la température (1702-1794) - transforma la climatologie en une science quantitative. D'abord locale la mesure de la température s'est généralisée avec la création des observatoires puis des réseaux de mesures au XIX^e^ siècle. La couverture globale de la Terre avec l'arrivée des mesures satellitaires, dans les années 1970, permis de généraliser l'enregistrement continu des données météorologiques.

La première Année Géophysique Internationale (1^er^ Juillet 1957-31 Décembre 1958) marqua le début de la climatologie physique, branche ayant pour but de prédire le climat et son évolution à partir de "lois physiques". Les moyens de calcul limités ne permettant pas de résoudre l'ensemble des processus climatiques, pendant 20 ans, co-existèrent des modèles traitant exclusivement la dynamique de l'atmosphère (c'est à dire la prédiction des mouvements de masses d'air) et d'autres uniquement la physique de l'atmosphère (calcul de la température par un équilibre radiatif-convectif). Poussée par l'essor des ordinateurs, la fin des années 70, début des années 80, vit l'émergence des modèles de climat de première génération couplant ces deux approches (dynamique et physique). Nos modèles actuels sont les versions actualisées de ces ancêtres.

Il faut bien comprendre que l'intérêt suscité par la climatologie physique à la fin des années 1950 était motivée par la rivalité entre le bloc Soviétique et le bloc de l'Ouest. Ainsi parmi les premiers résultats marquant de la modélisation climatiques, on peut noter la découverte de l'instabilité du climat par **W. Sellers** *aux Etats-Unis et* **M. Budyoko** *en Union Soviétique qui popularisèrent la notion d'«hiver nucléaire» (1969). Aujourd'hui encore, la plus grande part de l'effort de modélisation climatique concerne un besoin sociétal : savoir où nous mène le réchauffement climatique. Ces deux exemples contemporains illustrent le besoin de la société de prédire l'évolution du climat, essentiellement pour des raisons sociales et économiques. A la périphérie de ces questionnements de*

société, une branche (très) mineure a émergé dont l'objectif est de mieux comprendre l'évolution naturelle du climat tout simplement. Ce thème sera l'objet exclusif de ce manuscrit.

des questions fondamentales anciennes ….

… mais toujours d'actualité

La notion de climat ancien (ou paléoclimat) est assez floue, elle revêt un sens différent selon qu'elle soit traitée par un historien des climats comme l'académicien Emmanuel Le Roi Ladury (1929-) ou par un géologue travaillant à l'Institut de physique du globe de Paris. Une définition, très anthropocentrée, définirait un ***climat ancien comme un climat uniquement soumis aux processus naturels****, donc pré-anthropocène. L'ensemble des travaux présentés dans ce manuscrit suit cette définition, tous étudient la variabilité naturelle du climat.*

Comme le montre les différents rapports du GIEC (Groupement Intergouvernemental de l'Etude du Climat, https://www.ipcc.ch/reports), l'objectif principal de ces études paléoclimatiques est de nous éclairer sur la vitesse et l'intensité de la perturbation actuelle. Ainsi, à la lumière des connaissances accumulées sur les perturbations naturelles du Quaternaire (0-1.8Ma), *et pré-Quaternaire (>1.8Ma), le GIEC peut aujourd'hui défendre l'affirmation que la* ***perturbation actuelle est probablement un ordre de grandeur plus rapide (ΔpCO2/an ~ 1 %)*** *que toutes les perturbations naturelles jamais étudiés (hors événement catastrophique tel un impact) alors qu'à contrario la pCO_2 n'a jamais été aussi faible depuis le Précambrien (>542Ma) – (pages 27). Cette simple comparaison démontre que, plus que la température de la Terre et les niveaux de CO_2, c'est la vitesse des perturbations qui importe. Cette fragilité du climat terrestre trouve sa cause dans les gaz responsables de l'effet de serre. Aujourd'hui moins de 1% des composés atmosphériques participent à la régulation du climat terrestre, notamment l'H_2O_{vap} et le CO_2. Un déséquilibre persistant, même faible, entre les sources et les puits de carbone peut donc aisément modifier la pCO_2 atmosphérique et en cascade l'intensité de l'effet de serre et le climat terrestre.*

Cette constatation basique pose une question fondamentale: « ***comment l'habitabilité de la Terre a pu être maintenue depuis plus de 4Ga en dépit de cette fragilité*** *». Cette problématique est un sujet d'étude depuis presque deux siècles et questionne sur les mécanismes régulateurs du climat terrestre. Le chimiste* **J-J. Ebelmen***, en 1851, fût le premier à évoquer de tels mécanismes en suggérant une régulation de la composition atmosphérique via une balance entre le volcanisme et l'altération chimique.* **J. Lovelock** *(1919-) popularisa l'idée d'une auto-régulation biologique du système Terre avec la théorie de « Gaia » (1974). Néanmoins si un tel équilibre climatique existe, il reste suffisamment souple pour permettre au climat terrestre d'alterner entre i) périodes chaudes – 90% du temps, ii) période froide (présence de calotte de glaces continentales) – 9,9% du temps, et iii) périodes extrêmement froides (calotte de glace et banquise recouvrent la Terre) – 0,1% du temps.* ***Dans la première partie de ce manuscrit, je présenterai l'importance du couplage entre climat et cycle du carbone afin d'illustrer l'importance de ces rétro-actions dans la stabilité du climat terrestre et ses variations.***

L'existence de 3 états climatiques stables, entre lesquels la Terre bascule, est une singularité de notre planète au sein du système solaire. Cette propriété unique s'explique par les changements d'état de l'eau autour de l' isotherme 0°C sur Terre, qui module la réflectivité de la Terre (aussi appelé albédo planétaire) ***Le plus exceptionnel, et le moins fréquent de ces 3 états climatiques, est une Terre entièrement gelée. Devenue totalement blanche, cette Terre boule de neige*** *a un albedo est très élevé ce qui maintient la température moyenne à des valeurs extrêmement basses (-60°C en global, la température de l'équateur étant celle des pôles actuels). Les premiers indices géologiques d'une telle glaciation furent découvert en 1964 par le géologue* **B.W. Harland***. Il démontra, grâce aux premières mesures paléomagnétiques, que des formations sédimentaires glaciaires du Svalbard et du Groenland d'âge Néoprotérozoïque (1-0,54Ga) s'étaient déposées à basse latitude. Comme aucun mécanisme réaliste ne permettait d'expliquer comment sortir (cad réchauffer) une Terre devenue entièrement blanche, cette observation fût rejetée par ses contemporains. Il fallut les travaux du géochimiste* **M. Lagache** *(1965), puis de* **M. Meybeck** *et finalement de* **J.C Walker, R. Garrels** *et* **J. Kasting** *(1981) pour résoudre l'énigme de l'interaction entre climat et cycle du carbone (théorie connue depuis comme la théorie du thermostat terrestre). Depuis cette date, et les travaux successifs de* **P. Hoffman** *et collaborateurs (1998, 2017), de nombreux indices semblent confirmer l'existence de plusieurs glaciations globales à la fin du Néoprotérozoïque (0,73-0,63Ga).* ***Les occurrences de ces événements climatiques extrêmes et leur durée (10-60Ma) posent des questions fondamentales sur les limites de***

la régulation du climat. *Cette problématique sera développée dans la partie 2 de ce manuscrit, où en plus des* ***interactions climat-cycle du carbone, l'importance des interactions avec la cryosphère sera mis en avant.***

Si les scientifiques du XIX^e^ siècle, comme **J.J. Ebelmen***, étudièrent avec tant d'attention le climat terrestre, c'est qu'une question essentielle les y poussait. Les abondantes bases de données paléontologiques collectionnées dans les muséum révélaient déjà une histoire du Vivant bien agitée. Ces constations conduisirent* **G. Cuvier** *(1769-1832) à énoncer sa théorie du catastrophisme. A sa suite, son étudiant* **A.D. d'Orbigny** *(1802-1857) établit la première échelle des temps géologiques où chaque période (définie par un stratotype) était délimitée par des crises biologiques.* ***En étudiant le climat, les scientifiques du XIX^e^ siècle cherchaient simplement à élucider la cause des crises du Vivant****. Deux siècles plus tard, le développement des techniques de datation a permis de confirmer le synchronisme entre les grandes provinces magmatiques (ou trapps) et les épisodes exceptionnels de perte de biodiversité, ou extinction de masse. Depuis ces travaux impulsés par* V. Courtillot *nous ne savons toujours pas comment les trapps ont pu perturbé l'environnement au point d'initier une extinction de masse ? Cette question fera l'objet de la troisième et dernière partie du manuscrit. J'y développerai l'importance d'un troisième niveau de couplage – celui de la biosphère – et comment cette biosphère est modulée par le climat Terrestre et comment cette dernière impacte à son tour l'équilibre climatique Terrestre****. Au final ; après avoir présenté la régulation inorganique de la terre dans les deux premières parties de ce manuscrit, nous évoquerons ici l'importance de la régulation biologique – ce qui nous placera à la frontière de la fameuse théorie de Gaia développée par James Lovelock et Lynn Margulis (1974).***

Une méthode ...des outils

La modélisation climatique se heurte à la complexité du système climatique. Par exemple, la théorie de l'effet de serre est assez simple, mais paradoxalement il est difficile d'estimer précisément l'augmentation de la température liée à un doublement de la concentration atmosphérique en CO_2 car de nombreuses rétroactions interviennent, ces rétroactions masquant les effets directs. Dès lors, une question fondamentale se pose: quel degré de complexité est nécessaire pour représenter correctement l'évolution du climat? La réponse dépend fortement du problème posé. La Terre est marquée par une

succession de changements climatiques dont la périodicité s'échelonne de la décennie aux millions d'années. Un tel éventail de cycles suggère des causes et des mécanismes très variés. Cette diversité s'explique par la complexité du système climatique qui est constitué de cinq sous-systèmes: l'atmosphère, l'hydrosphère (les océans, les lacs), la cryosphère (les calottes polaires, les glaciers, et au sens large la banquise), la biosphère (terrestre et marine) et enfin la lithosphère. Chacune de ces cinq composantes du système climatique est régie par un fonctionnement et des propriétés très différents. Dès lors, un modèle climatique « parfait » devrait prendre en compte l'ensemble des mécanismes du système pour chacune des composantes. Cependant ces cinq sous-systèmes ont des temps de relaxation (temps nécessaire pour qu'un système soumis à une perturbation atteigne un nouvel équilibre) très variables; quelques secondes (cycle de l'eau); plusieurs milliers d'années (calottes de glace); un million d'années (lithosphère).

Une simulation climatique 3D ne pouvant excéder quelques milliers d'années, le système climatique modélisé doit être simplifié pour des raisons de limites de puissance de calcul et des capacités de stockage. Cela suppose la prise en compte de certains sous-systèmes uniquement et une représentation plus simple d'un certain nombre de mécanismes. Pour simuler le climat actuel, il est possible de se limiter aux sous-systèmes dont les constantes de temps sont inférieures à quelques dizaines d'années (l'atmosphère, l'océan de surface) et de fixer les autres composantes du système (océan profond, biosphère, cryosphère, lithosphère). Inversement, modéliser un climat et son évolution sur de plus longues échelles de temps nécessite de prendre en compte toutes les composantes qui interagissent avec l'atmosphère, et ayant des constantes de temps supérieures à quelques dizaines d'années (océan profond, végétation…). Autrement dit, le nombre de composantes intervenant dans le modèle climatique dépendra avant tout de l'échelle de temps considérée. ***Il n'y a donc pas de modèle climatique universel, mais une grande diversité de modèles plus ou moins adapté à la question posée.*** *Au cours de ces dix dernières années, cette contrainte m'a conduit a utiliser i) une large variété de modèles climatiques et géochimiques ii) à élaborer des couplages entre différents modèles afin d'intégrer au mieux les processus géologiques fondamentaux en fonction des échelles de temps étudiées.*

SYNOPSIS

Pour ceux qui n'auront pas le courage de tourner les pages suivantes, la suite de ce manuscrit présente les grands processus qui contrôlent l'évolution du climat terrestre, processus qui peuvent se résumer par l'interaction entre trois molécules : CO_2, H_2O et C_{org}

- ***le climat terrestre est régulé grâce à la molécule de CO_2*** *- molécule qui réagit chimiquement avec les minéraux de la surface terrestre (et notamment avec les silicates de calcium).*
- ***cette régulation n'est pas monotone dans la temps car la Terre en surface est riche en H_2O.*** *Cette molécule a, selon son état physique et donc la température de surface, des propriétés de réflexion très variable (10 à 90 %). Cette propriété (albédo) amplifie chaque modulation de la température rendant le climat instable.*
- ***le dernière molécule d'intérêt est la molécule de Carbone organique - C_{org}-*** *(constitué des 5 atomes suivants CHONP). Présente dans tous les organismes vivants (et morts), elle semble, comme la molécule d'H_2O, capable d'amplifier les modulations du climat en modifiant l'abondance de la molécule de CO_2.*

Si la biosphère semble jouer un rôle actif, ce manuscrit révèle une distinction nette avec la théorie de Gaia (Lovelock et Margulis, 1974), à savoir que la biosphère n'est jamais le moteur de la perturbation, toute perturbation débute par un événement inorganique (sauf la période actuelle…)

L''importance des couplages entre les réservoirs externes de la Terre (atmosphère, océan, biosphère, lithosphère, cryosphère) est illustrée par 10 papiers – synthèse de mes travaux sur cette question.

Enfin ces dix années de recherche n'auraient pas eu la même saveur sans les étudiants et leurs questionnements. Merci à eux.

« Ce que l'on conçoit bien s'énonce clairement,
Et les mots pour le dire arrivent aisément''

Boileau (17ème siècle)

TABLE DES MATIÈRES

page

EXPOSE SYNTHÉTIQUE DES RECHERCHES :

THÈME 1: Chaude ou Froide , 4 milliards d'années de variabilité climatiques

Le dernier siècle a été marqué par une hausse de la température de surface d'environ 0,7°C en moyenne globale. Cette hausse est déterminée par rapport à l'état climatique de référence défini sur la période 1961-1990, qui établit cette température moyenne annuelle globale à 15^0C. Ce réchauffement est très largement causé par l'augmentation de la pression partielle de CO_2 dans l'atmosphère. Celle-ci vient de dépasser la barre symbolique des 400ppmv[1], un niveau que l'on ne retrouve pas, ni dans l'enregistrement historique, ni dans l'enregistrement délivré par les carottes de glace (Lüthi et al., 2008). Il faut remonter au Pliocène, il y a quelques 3 millions d'années, pour retrouver de tels niveaux de CO_2 (Seki et al., 2010). Si la hausse de la pression partielle de CO_2 se poursuit à ce rythme, la teneur à la fin du siècle sera équivalente à celle enregistrée au cours de l'Eocène (>1000ppmv), il y a environ 50 Ma (Beerling & Royer, 2011) – cette hausse des températures sera probablement la plus rapide jamais enregistrée dans l'histoire de la Terre.

L'exemple actuel du réchauffement climatique nous rappelle que la variabilité climatique se décline sous 2 aspects : i) son amplitude tout d'abord qui se résume par la fluctuation de la température de surface autour de l'état climatique de référence (ΔT). Le second aspect tout aussi important est la vitesse de ce changement. En fonction des échelles de temps considérées, l'amplitude, la vitesse et la durée des écarts à la moyenne fluctuent considérablement. En voici un bref aperçu.

A travers les récits historiques du **dernier millénaire [ka]** nous constatons un déclin rapide des glaciers alpins d'Europe, depuis le milieu du XIX^{e} siècle. Cette fonte marque la fin du « Petit âge glaciaire », période sensiblement plus fraîche (ΔT~ -0,7°C) qui aurait débuté au XIII^{ème} siècle et ferait suite à une période légèrement plus chaude (ΔT~ -0,2°C) appelée « l'optimum climatique médiéval ». Cet optimum, au climat plus clément, fut popularisé par les récits héroïques véhiculés dans les saga islandaises relatant la colonisation du Groenland (ou Greenland) et de l'ensemble des terres du Nord par les vikings. A plus long terme, les enregistrements climatiques du **dernier million d'années [Ma]** (glaces polaires ou tests de foraminifères) montrent une variabilité plus marquée, contrôlée par des cycles de 100 ka, oscillant entre de longues périodes froides de 90 ka (ou périodes glaciaires, ΔT~ -5°C) et de courtes périodes interglaciaires 10 ka (ΔT~ -0,5 à +1°C). Si une variabilité haute fréquence caractérise les périodes glaciaires, la vitesse de ces variations est 10 à 100 fois plus lente que la perturbation anthropique actuelle. Enfin à très long terme, la présence épisodique de dépôts glaciaires continentaux nous révèle l'existence de transition climatique lente (en quelques millions d'années) d'une Terre chaude vers une Terre froide, et inversement. L'extension géographie de ces dépôts sur le **dernier milliard d'années [Ga]**, permet de définir trois états climatiques distincts et stables. 1) l'état climatique où les calottes de glaces continentales sont limitées aux régions polaires et aux régions des moyennes latitudes aussi connue sous le terme de **période ice-house**. La mieux documentée est évidemment la dernière période glaciaire qui débuta il y a 34 Ma avec l'installation des glaces sur l'Antarctique (ΔT~-2 à +2°C, cet état représente ~10% du dernier milliard d'années). 2) Un état climatique chaud, caractérisé par l'absence de calottes de

1 ppmv : unité de concentration exprimée en partie par million par volume (ex : 400ppmv ou 0.04%)

glace continentale (ΔT~ +5 à +10°C) et qui représenterait l'état climatique dominant (~90 % de la durée globale) : **période greenhouse**. Les périodes Éocène (55Ma) et Trias (250-200 Ma) en seraient les exemples types. 3) Enfin un état climatique où la Terre serait entièrement couverte de glace des pôles à l'équateur (ΔT~ -70°C), ou **snowball Earth** (Terre boule de neige). Cas extrêmement rare puisque deux ou trois événements de ce type ont été dénombrés au cours des 4,54 milliards d'années de l'histoire de la Terre, le dernier s'étant terminé il y a 630 Ma.

Comme le montre ces quelques exemples, le climat terrestre fluctue autour d'une température moyenne. Cependant aucune de ces variations ne furent suffisamment intenses pour mettre un terme à la Vie sur Terre. Dès lors on peut s'interroger sur les raisons qui expliquent:

***- le maintien de l'habitabilité** terrestre depuis 3,8 Ga*

***- les mécanismes responsables de ces variations** climatiques.*

Cette double interrogation, a été l'un de mes principaux axes de recherche. En effet de nombreuses études ont eu pour but de déterminer la température moyenne de la Terre. La température moyenne peut être définie comme la température d'équilibre (dT/dt ~ 0) si cette dernière est intégrée sur une période suffisamment longue (> siècle).

Ci-après sont présentés, à travers l'étude de l'Archéen et des conditions du maintien de habitabilité de la planète, nos avancées importantes sur la notion d'équilibre climatique et les conditions nécessaires pour maintenir cet équilibre sur de longues échelles de temps (> 100 Ma).

BILAN: Comment expliquer la stabilité du climat depuis 3,8 Ga?

I. La recherche de la température d'équilibre illustrée par le problème du Soleil Jeune

La faible luminosité solaire est la principale contrainte du climat Archéen (4 – 2,45 Ga). Le rayonnement solaire est l'unique source d'énergie reçue à la surface de la Terre, il suffit d'observer les fluctuations du cycle diurne pour s'en convaincre. Ainsi toute fluctuation du flux solaire impacte directement le climat terrestre. A. Eddington et M. Schwarzschild (1926) furent les premiers à suggérer que le Soleil produisait son énergie par un processus de fusion nucléaire. Avec les progrès de l'observation, notre connaissance sur la vie et la mort des étoiles, dont le Soleil, se sont affinées. A l'ordre un, la luminosité de notre étoile, peu massive, peut être résumée par une simple équation paramétrique (modèle de Gough, 1981). Elle permet de décrire l'évolution temporelle de la constante solaire .

$$\frac{S(t)}{S_0} = \frac{1}{1+0.4\left(t/4.6\right)}$$

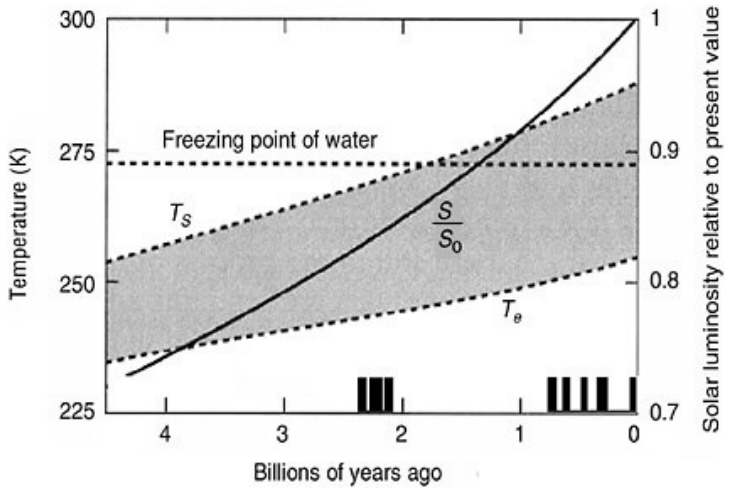

Figure 1: Diagramme illustrant le paradoxe du faible soleil jeune. La courbe « $S(t)/S_0$ » représente l'évolution de la constante solaire normalisée à la valeur actuelle (S_0) où est t le temps avant aujourd'hui exprimé en Ga (cf équation - exemple : il y a 4,56 Ga, S(t) ~30 % plus faible que S_0). T_e et T_s correspondent respectivement à la température (en Kelvin, échelle de gauche) d'équilibre radiatif et à la température effective de surface, en supposant une concentration constante en CO_2 atmosphérique de 300ppmv. Ces températures sont calculées via un RCM à une dimension (Kasting et al., 1988).

A l'équilibre radiatif, la quantité totale d'énergie absorbée par la Terre (S_{abs}) doit être égale aux termes de chaleur latente (F_{lat}), sensible (F_{sens}) et au flux d'infrarouge émis (IR).

$$S_{abs} = IR + F_{lat} + F_{sens} \qquad \text{equation (1)}$$

$$S_{abs} = (S/4)\,(1-\alpha) \qquad \text{equation (2)}$$

$$IR = \sigma T_e^4 \qquad \text{equation (3)}$$

S la constante solaire, α l'albédo planétaire, σ la constante de Stefan-Boltzmann *et* T_e la température d'équilibre

Les deux flux dominants étant S_{abs} et IR, il est donc possible de définir simplement la température respectant l'équilibre radiatif (ou température d'équilibre, T_e):

$$T_e = \sqrt[4]{[(S/4)(1-\alpha)]/[\sigma]}$$ equation (4)

$T_s = T_e + \Delta T$ où ΔT est le réchauffement induit par l'effet de serre

En considérant une atmosphère n'absorbant pas les infrarouges (T_e, Fig.1) – donc sans effet de serre – la puissance solaire actuelle ne suffirait pas à éviter à la Terre d'être entièrement gelée en surface (253K ou -19°C). Avec une concentration de CO_2 de 300ppmv (valeur en 1980) (T_s, Fig.1), la faiblesse du flux solaire durant les deux premiers milliards d'années (4.5-2Ga) n'aurait pas évité cet état glaciaire généralisé. ***Ce résultat de premier ordre révèle que le problème fondamental de l'évolution à long terme du climat terrestre est la faible luminosité solaire.***

Un englacement généralisé de la Terre durant les deux premiers milliards d'années de l'histoire de la Terre n'étant pas compatible avec les nombreux indices de traces de vie marine (3,45Ga – Buick et al., 1981; Nisbet and Sleep, 2001; Bell et al., 2015]) Sagan et Mullen (1972) ont très vite évoqué les gaz à effet serre comme solution : le NH_3 puis le CO_2 atmosphérique lorsque l'accumulation NH_3 s'est révélée impossible (la molécule étant détruite par les U.V).

A la fin des années 70 et début des années 80 (voir Kiehl and Dickinson, 1987), plusieurs études furent conduites à l'aide de modèles purement radiatifs ou radiatifs-convectifs (ou RCM pour Radiative Convective Model) pour estimer la concentration atmosphérique seuil de CO_2 nécessaire à contrebalancer la faible luminosité solaire. Jusqu'en 2010, 0,3bar de CO_2 (~ 750 fois la valeur actuelle) était la pression partielle supposée nécessaire au maintien d'une température de 15°C au début de l'Archéen (Kasting, 1984 et 2010).

Cependant ces concentrations très élevées de CO_2 furent contestées par Rye et al. (1995). Sur la base de l'absence de sidérite ($FeCO_3$) dans les paléosols datés de 2,76 à 2,2Ga, Rye et al. (1995) proposèrent pour la première fois une estimation de la pCO_2 maximale de 0,04bar (~ 100 fois la valeur actuelle), là où les RCM proposent pour la même période une pCO_2 de 0,2bar (Kasting et Catling 2003), soit 20 fois supérieure aux contraintes issues des paléosols.

Une contrainte supplémentaire arriva avec le développement des approches quantitatives pour estimer les températures de l'océan précambrien (> 0,54 Ga). La plus reproductible et abondante repose sur la mesure du rapport isotopique de l'oxygène, méthode qui révéla des températures de l'océan de l'ordre de 60° à 80°C [Knauth et Epstein, 1976; Shields et Veizer, 2002, Knauth et Lowe, 2003; Robert et Chaussidon, 2006]. Si ces résultats sont compatibles avec une vie ancienne dominée par des organismes hyperthermophiles [Gaucher et al., 2008], ces conclusions restent intensément débattues [Kasting et Howard, 2006; van den Boorn et al., 2007; Marin-Carbonne et al., 2014; Tartese et al., 2016] et nombre de mesures plus récentes suggèrent des températures plus modérées (< 40°C) bien que plus chaude qu'aujourd'hui (> 15°C) (Hren et al., 2009; Blake et al., 2010).

Cette situation paradoxale d'une Terre supposée plus chaude qu'aujourd'hui alors que l'énergie incidente arrivant du Soleil est nettement plus faible est connue depuis Sagan et Mullen (1972) sous le terme de « Paradoxe du Soleil jeune » (ou FYSP pour Faint Young Sun Paradox).

II. Les estimations des paléo-pCO_2 et de la fiabilité de leur reconstruction

- Thèse de Y. Teitler *Climat et composition de l'atmosphère au Précambrien : des paléosols aux simulations numériques*.

- Article : Teitler, Y., Philippot, P., Gérard, M., Le Hir G., Fluteau F., Ader M., *Ubiquitous occurrence of basaltic-derived paleosols in the Late Archean Fortescue Group, Western Australia*. Precambrian Research. 2015 doi:10.1016/j.precamres.2015.05.014

- Projet : ANR : eLife2 (Environnement of Early Life on Earth 2) – dirigée par P. Philippot CRPG-Nancy (B. Marty, M. Pujol), Géochimie des Isotopes Stables IPG-Paris (M. Ader, P. Cartigny), Biopshère Actuelle et Primitive IPG-Paris (M. Gérard, P. Philippot).

Problématique : *l'incompatibilité des estimations et des résultats de modélisation motiva une étude combinant modélisation et données (thèse de Y. Teitler). La première partie de cette thèse s'attacha à analyser précisément la minéralogie des paléo-sols archéens développés sur la formation basaltique de Mont Roe - Fortescue Group, (Western Australia) – sols de référence de Rye et al. (1995).*

Le modèle initial de reconstruction des paléo-CO_2 à partir de l'équilibre thermodynamique entre sidérite et greenalite reposait sur 2 hypothèses fortes :

- l'interprétation du Fe^{2+}-chlorites dans les paléosols comme le produit de la diagenèse et/ou d'un léger métamorphisme à partir d'un précurseur silicaté : la greenalite ($Fe_3Si_2O_5(OH)_4$).

- une atmosphère réductrice à 2,76Ga dépourvue d'oxygène. En absence d'O_2 on s'attend à un lessivage et la reprécipitation du fer depuis les horizons supérieurs vers les horizons inférieurs du sol. Dans ces conditions, la nature des minéraux de fer qui reprécipitent en base de sol dépend de la teneur en CO_2 du fluide altérant, en relation directe avec celle de l'atmosphère (du à l'absence de dégradation de matière organique). Sous une forte pCO_2, le fer est censé reprécipiter sous forme de carbonate (sidérite, $FeCO_3$). Sous une pCO_2 plus faible, le fer reprécipite sous forme de silicates de Fe^{2+} (les fluides sont censés être 40% plus faiblement concentrés en dioxide de carbone que l'atmosphère).

Teitler et al. (2015) réinterpréta en grande partie les conclusions défendues par Rye et al. (1995). Des reliquats de la formation pédogénique initiale furent retrouvés (fig.2) ; paléosol qui révéla que i) la greenalite n'était pas le minéral précurseur riche en fer – ce précurseur est sans doute la berthierine, comme l'avait suggéré Sheldon (2006) sur des paléosols plus récents. ii) De plus la présence de smectite ferrique (Fe-smectite) pédogénique issue de la bauxitisation des basaltes est un indicateur d'une paléo-pO_2 non nulle (et donc non négligeable). Ces résultats invalident les hypothèses initiales et rendent donc caduque le calcul de la paléo-pCO_2 de 0,04bar à 2,76Ga par équilibre thermodynamique entre greenalite et siderite en l'absence d'oxygène. *A contrario il semble possible d'estimer la paléo-pCO_2/O_2 à partir de l'équilibre thermodynamique de la Fe-smectite - faute de temps cet axe n'a pas été davantage développé.*

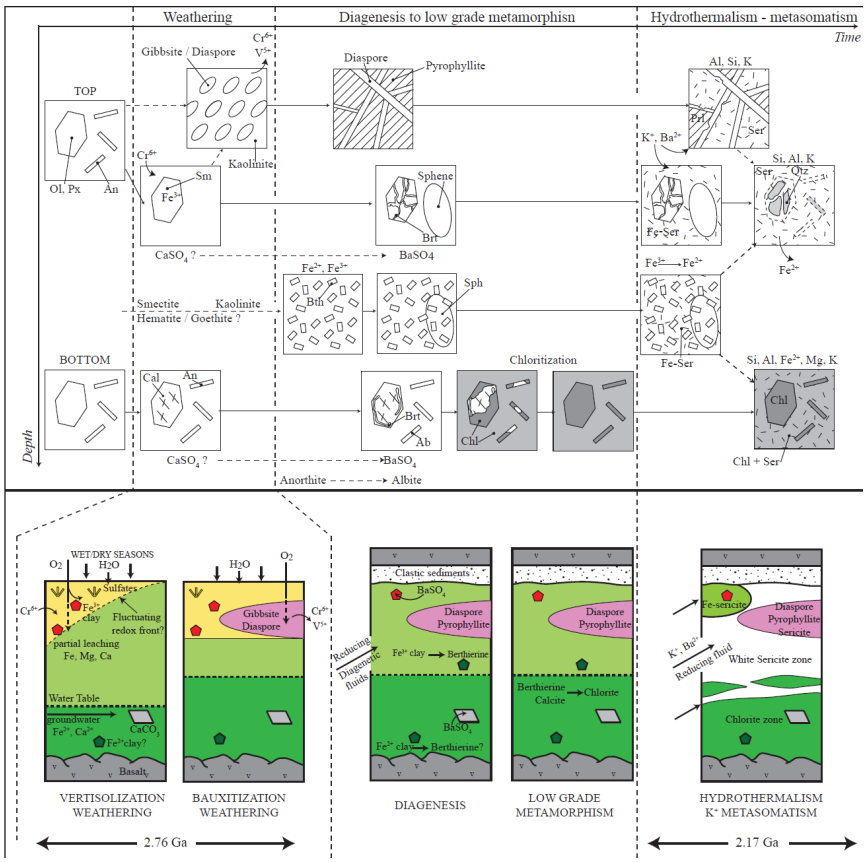

Figure 2 : modèle proposé de formation et d'évolution du paléosol de Mount Roe montrant les 3 grandes étapes successives : i) l'altération de la formation basaltique initiale, ii) la diagenèse et le métamorphisme de faible degré, et enfin iii) l'hydrothermalisme (Teitler et al. 2015).

III. Quels seuils de pCO_2 pour résoudre le paradoxe du Soleil jeune ?

- Thèse de Y. Teitler *Climat et composition de l'atmosphère au Précambrien : des paléosols aux simulations numériques*.

- Article : Le Hir, G., Teitler, Y., Fluteau, F., Donnadieu, Y., and Philippot, P. ,2014, The faint young Sun problem revisited with a 3-D climate–carbon model–Part 1,Climate of the Past,vol 10, p:697-713, doi:10.5194/cp-10-697-2014

- Projet : ANR : eLife2 (Environnement of Early Life on Earth 2) – dirigée par P. Philippot CRPG-Nancy (B. Marty, M. Pujol), Géochimie des Isotopes Stables IPG-Paris (M. Ader, P. Cartigny), Biopshère Actuelle et Primitive IPG-Paris (M. Gérard, P. Philippot).

De nombreuses études semi-quantitives sur les paléosols se sont succédées. Ainsi Sheldon (2006) par un calcul de bilan de masse proposa une paléo-pCO_2 fluctuant entre 26 et 3mbar entre 2,2 et 1,0 Ga. Puis en 2010, Rosing at al. (2010) publia, dans la revue Nature, une étude défendant l'idée d'une pCO_2 extrêmement faible dès le début de l'Archéen : ~ 0,9 mbar de CO_2 à 3,5Ga (seulement 2,25 fois la valeur actuelle) ! Bien que de multiples fois invalidés depuis sa parution (voir Dauphas et Kasting, 2011; Reinhard et Planavsky, 2011), cette étude de Rosing et al. (2010) constitua un tournant car elle fut la première à proposer une pCO_2 en s'appuyant sur des données, et à démontrer sa faisabilité à l'aide d'un modèle climatique (un RCM relativement simple).

Entre 2010 et 2013, plusieurs études furent réalisées à l'aide de modèles climatiques complexes pour tester la robustesse de l'idée de Rosing et al. (2010). Kienert et al. (2012) avec un EMIC (Earth system models of intermediate complexity) évaluèrent la pCO_2 à 0,6bar – soit 600 fois plus que Rosing et al. (2010), alors que les GCM (General Circulation Model) nécessitaient des pCO_2 plus modestes ~ 0,1bar de CO_2 et 2 mbar de CH_4 à 3,8Ga (Charney at al. 2013) ou 20 mbar de CO_2 et 1 mbar de CH_4 à 2,8Ga (Wolf et Toon, 2013).

Ainsi 40 ans après l'apparition du concept de FYSP par Sagan et Mullen (1972), aucun consensus n'est trouvé du fait de l'absence de réelles contraintes issues des données combinées au spectre très (trop) large de solutions fournies par les modèles – 0,9mbar à 0,6bar (soit 3 ordres de grandeur d'écart !).

Problématique : *La disparité des résultats proposés par les modèles climatiques nécessitait de résoudre une double interrogation : i) quels facteurs sont réellement fondamentaux à la résolution du paradoxe du Soleil jeune et ii) pourquoi les modèles RCM, EMIC et GCM proposaient-ils des paléo-pCO_2 si disparates ?*

Pour résoudre cette double problématique, nous avons utilisé un modèle de type GCM nommé FOAM (Fast Ocean Atmospheric Model). Nous avons conduit un grand nombre de simulations pour explorer les effets respectifs des i) conditions aux limites de l'Archéen (constante solaire, paléogéographies, surface de continents émergés, microphysique des nuages), ii) l'intensité de l'effet de serre en fonction des couples pCO_2 - pCH_4 iii) puis l'intensité de la rétroaction de l'albédo de la glace lorsque la vitesse de rotation de la Terre est plus élevée (16h au lieu de 24h) ou lorsque l'océan est deux fois plus salée.

3.1 Quels facteurs sont fondamentaux à la résolution du FYSP ?

<u>*La constante solaire.*</u> Un simple calcul à partir de l'équation de Gough (1981) montre que le forçage radiatif imposé par la constante solaire induit un **F_{RAD} négatif de -55W/m²** (refroidissement) entre 3,5 et 1Ga, soit le facteur climatique le plus important du système (fig.3a).

<u>*L'importance de la nébulosité.*</u> Soumis à ce F_{RAD} négatif, il devient impossible de résoudre le FYSP, la température moyenne de surface atteint les -75°C à 3,5 Ga (Terre entièrement englacée). Toutefois il suffit d'augmenter l'effet de serre, (pCO_2 de 2,4mbar au lieu de 0,9mbar), combinée à une nébulosité idéalisée (d'après le scenario de Rosing et al. 2010) pour atteindre une température de 14°C.

Si ce résultat démontre qu'un effet de serre modéré suffit à résoudre le paradoxe du Soleil jeune, cette solution est rendue possible uniquement par la présence d'une nébulosité idéalisée. En effet, une nébulosité classique induit un refroidissement de 5 à 10°C due à l'effet d'albédo des nuages (F_{RAD} négatif de -10 à -20 W/m²). En considérant une microphysique des nuages différente (faible abondance des gouttelettes d'eau mais de grosses tailles – idée de Charleston et al. 1987 repris par Rosing et al. 2010) l'effet d'albédo des nuages (I.R) disparaît quasiment (ils deviennent transparents au rayonnement solaire visible) – seul persiste l'effet de serre des nuages (**F_{RAD} positif de +20 à +40 W/m²**). Ce résultat démontre l'extrême sensibilité à la microphysique des nuages – cependant en l'absence de contraintes solide cette solution demeure très spéculative (fig.3).

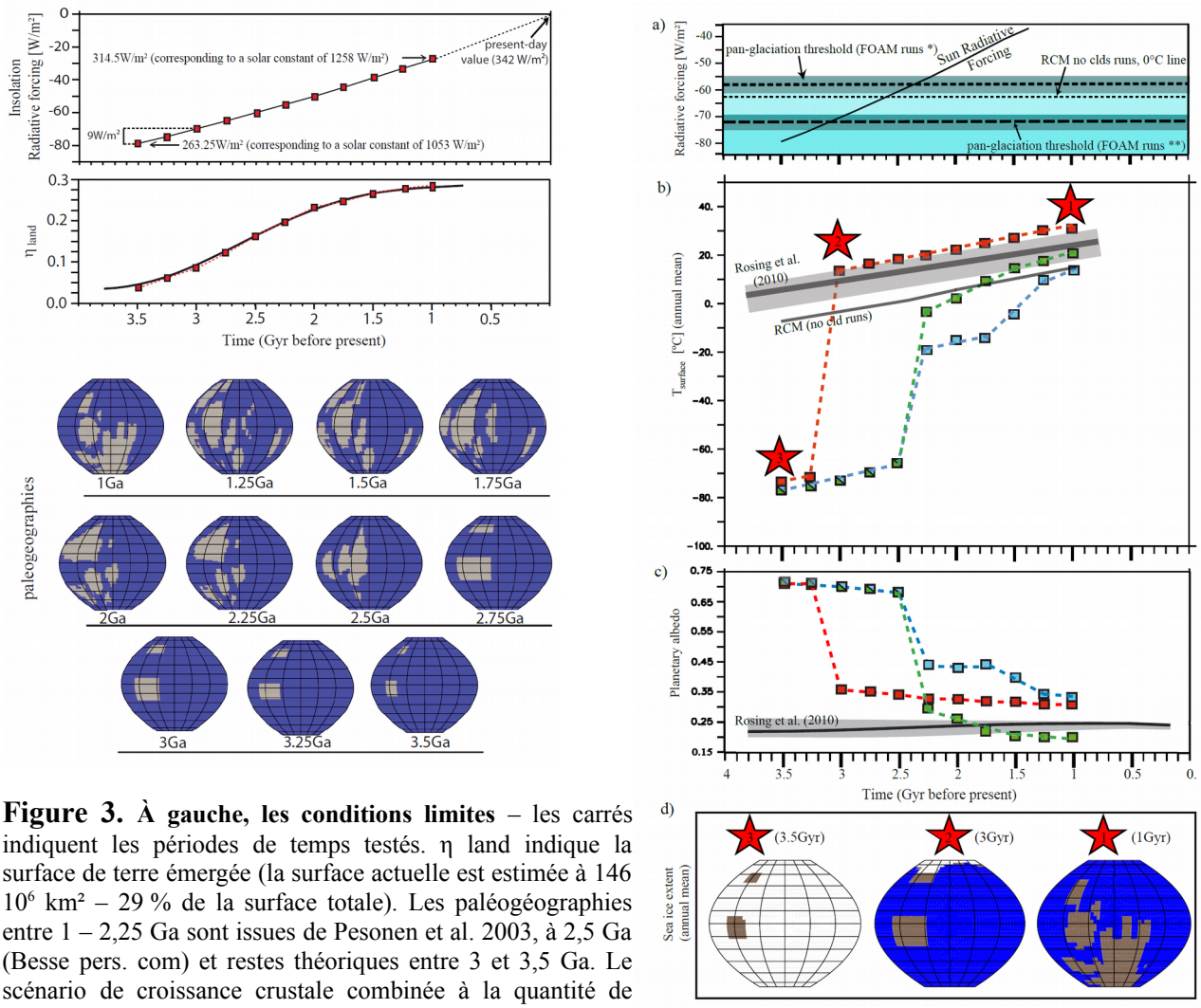

Figure 3. À gauche, les conditions limites – les carrés indiquent les périodes de temps testés. η land indique la surface de terre émergée (la surface actuelle est estimée à 146 10^6 km² – 29 % de la surface totale). Les paléogéographies entre 1 – 2,25 Ga sont issues de Pesonen et al. 2003, à 2,5 Ga (Besse pers. com) et restes théoriques entre 3 et 3,5 Ga. Le scénario de croissance crustale combinée à la quantité de surface continentale émergée est issue de Goddéris et Veizer (2000) et est basé sur le $^{87}Sr/^{86}Sr$.

À droite. Resultats des simulations climatiques 3D réalisées avec FOAM en utilisant un forçage radiatif (F_{RAD}) de +19W/m². **a)** Valeurs de F_{RAD} (négatif) permettant d'initier une englacement global de la surface terrestre en fonction de 3 scénarios de nébulosité (microphysique des nuages actuelles, absence de nuages, microphysique des nuages modifiée – taille de gouttelettes augmentée / abondance des gouttelettes réduite). **b)** température moyenne de surface en fonction de l'évolution de l'irradiance , courbe bleue – nuages actuels, courbe verte – absence de nuages, courbe rouge – nuages modifiés. **c)** évolution de l'albédo planétaire dans les 3 cas de nébulosité. **d)** étendue de la banquise dans 3 cas illustrant les 3 états climatiques.

La nature de la surface. En supposant les nuages transparents au rayonnement visible, Rosing et al. (2010) résume l'albédo terrestre à sa seule composante de surface. La Terre primitive étant dominée par les océans ($\alpha_{sol\ nu} = 0.32$, $\alpha_{océan} = 0.06$), cette Terre primitive devait, en théorie, être plus chaude. Pourtant un modèle de climat 3D montre une augmentation de l'albédo de surface ($\Delta\alpha = +0.10$ entre 2,25-1Ga) soit un **F_{RAD} négatif de -29W/m²** (refroidissement) ($F = S/4(1-\alpha)$, avec $\Delta\alpha = 0.10$ et $S = 1148 W/m^{-2}$ à 2,25Ga). Ce calcul révèle le fort impact de la rétroaction de la glace, un léger refroidissement (dû à la faible constante solaire) induit une extension de la banquise ($\alpha_{banquise} = 0,6$) qui surpasse largement le forçage radiatif positif induit par la présence des surfaces océaniques. Ainsi le contexte d'aquaplanète proposée par Rosing et al. (2010) n'apparait pas comme une solution au problème du FYSP car cette situation est très dépendante à la rétroaction de la glace de mer.

Est-il possible de réduire la formation de la banquise aux pôles et d'ainsi réduire l'influence de la rétro-action des glaces ?

La Terre archéenne, une planète à rotation rapide et à l'océan plus salé ?

Les simulations menées avec une vitesse de rotation de la Terre plus élevée (16h de durée du jour – durée estimée ~ 4Ga) montre un réchauffement des basses latitudes associé à un refroidissement des hautes latitudes pour un effet global nul. En réduisant le transport de chaleur de l'océan vers les pôles, une rotation plus rapide de la planète amplifie l'extension des surfaces couvertes de glaces-neige. Cela signifie que l'augmentation de la vitesse de la rotation rend le climat plus instable.

En abaissant le point de congélation de l'eau mer à -3,3°C pour une salinité de 60‰ (Millero et Poisson, 1981, Foriel et al. 2004), on obtient un réchauffement de ~0,8°C en réponse à une simple diminution de l'extension de la banquise. En combinant, vitesse de rotation et salinité plus élevée, le réchauffement est presque nul. Ces deux facteurs n'apparaissent donc pas essentiels à la résolution du FYSP.

3.2 Les paléo-pCO_2 déduites des modèles unidimensionnels (RCM) sont-elles robustes?

En plus de nuages transparents au rayonnement dans le spectre visible, Rosing et al. (2010) résout le FYSP avec une pCO_2 de 0,9mbar en fixant l'albédo de surface en fonction du pourcentage de la surface relative occupée par les océans/continents - donc in fine de la croissance crustale. Cette hypothèse revient donc de ne pas considérer l'effet de la température de surface (T_s) sur l'albédo de surface. Nous avons voulu savoir si cette approximation était justifiée.

Pour représenter cette dépendance, la relation suivante peut être utilisée (Pierrehumbert et al. 2011).

$$\alpha(T)= \alpha_o +(\alpha_f - \alpha_o)[(T - T_O)^2/(T_{freeze} - T_O)^2]$$

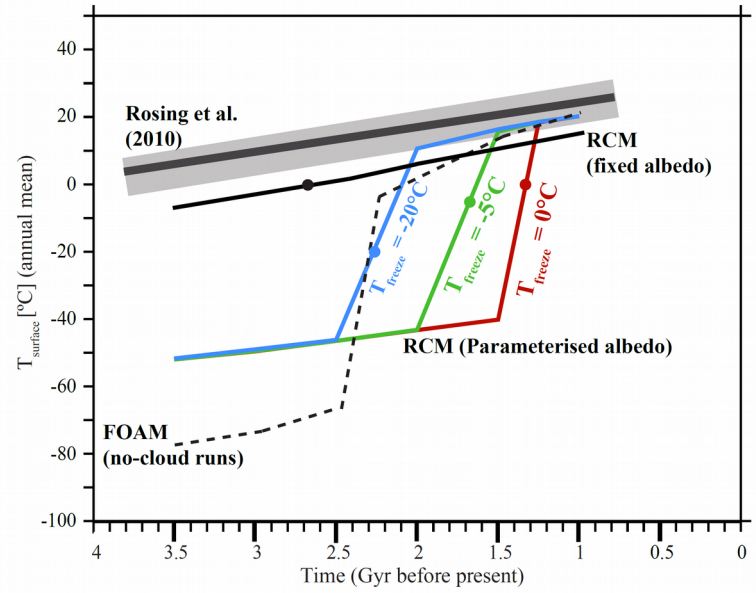

cette équation définit l'évolution de l'albedo planétaire α(T) en fonction de la température. la variation d'albédo est dépendante de la variation de température au carré

Figure 4. Simulations de sensibilités à Tfreeze effectuées avec un RCM où (α_o) = 0.2 (surface sans glace) et (α_f) = 0.6 (surface à 100% englacée), T la température de surface de la Terre, T_{freeze} la température d'englacement et To la température des basses latitudes. *$T_{freeze} - T_O$ représente donc indirectement le flux de chaleur entre l'équateur et les poles.*

En menant une série d'expériences avec différentes T_{freeze} (0°C, -5°C et -20°C, fig.4), on constate la très grande dépendance de l'albédo terrestre à la température. Pour retrouver une rétroaction climatique similaire à un modèle 3D (courbe en pointillée noir – FOAM), il faudrait supposer que la température d'englacement de la Terre se situe vers -20°C (à la place des 0°C actuellement considérée). Cet écart entre la température de formation de la banquise (0°C) et d'englacement de la planète (-20°C) est difficile justifiable. Il apparaît ici que la principale faiblesse des RCM est leur impossibilité à bien calculer T_{freeze} en l'absence de transfert latitudinal de chaleur.

3.3 Les paléo-pCO_2 déduites des modèles complexes sont - elles réalistes ?

Si l'ensemble des GCM arrivent à résoudre le FYSP ($Ts \geq 15°C$) avec des pCO_2 allant de 0,02 à 0,1 bar en fonction de la nébulosité, un EMIC (Earth system models of intermediate complexity) évalue cette pCO_2 à 0,6bar – soit 6 à 10 fois que les GCM sous les mêmes conditions (Kienert et al., 2012). Le calcul de l'albédo ne pouvant ici être responsable de tels écarts, les causes sont à chercher ailleurs.

Les EMICs sont des modèles développés pour réaliser des simulations longues (>2-5kans), durée inaccessibles aux GCM. Le calcul de la physique de l'atmosphère sur une grille fine étant très coûteuse en temps, les EMIC ont une atmosphère simplifiée (maillage large). Cette simplification s'accompagne de paramétrisations, dont celle du gradient vertical de température atmosphérique. Dans un GCM ce gradient est la conséquence de l'absorption/rémission de l'atmosphère. Dans l'EMIC de Kienert et al. (2012), ce gradient vertical (Γ) est calculé à partir d'une équation semi-empirique (Petoukhov et al. 2000):

$$\Gamma\ (K/m) = \Gamma o + \Gamma_1\ (Ts - 273.16K) * (1-a_q*Q^2) - \Gamma_2*n_{cld}$$

Γo, Γ_1, Γ_2 paramètres ($\Gamma o = 5.2\ 10^{-3} K/m$, $\Gamma_1 = 5.5\ 10^{-5}$ K/m, $\Gamma_2 = 10^{-3} K/m$, $a_q = 10^{3}\ (kg.kg)^{-2}$, Q est l'humidité spécifique ($kg.kg^{-1}$), et n_{cld} la fraction nuageuse.

La comparaison révèle un gradient de température bien plus faible chez un EMIC (adapté à l'atmosphère humide actuelle) que dans un GCM. La température de surface étant très basse dans les deux types de modèles (effet de l'albédo), la température de l'atmosphère est bien plus chaude au sommet chez un EMIC. Ce biais s'accompagne d'un flux infrarouge plus important à sommet de l'atmosphère, ce qui réduit d'autant l'effet de serre :

$$\text{Effet de serre } (W/m^2) = \sigma T_s^4 - OLR$$

OLR (Outgoing Longwave Radiation au sommet de l'atmosphère), Ts la température de surface (K), et σ la constante de Stefan-Boltzmann.

Si cette paramétrisation est correcte pour les conditions actuelles, elle sous-estime le gradient atmosphérique dans les conditions extrêmes où l'atmosphère est presque sèche, et donc sous-estime l'effet de serre de manière importante, ce qui signifie que la solution haute de pCO_2 (0,6bar) est un artefact.

Conclusion : *Cette étude montre que la disparité des paléo-pCO_2 calculés par les modèles climatiques est en partie due à des artefacts. Les pCO_2 < 20mbar ont pour cause l'absence de rétro-action entre l'albédo et la température terrestre, alors que les pCO_2 > 0,1bar sont quant à elles des artefacts dûs à un calcul incorrect de l'intensité de l'effet de serre. Le spectre de solution du FYSP (Ts ≥ 15°C) pour les modèles climatiques complexes est probablement inclus dans un intervalle plus restreint allant de 0,02 à 0,1 bar à 3,8Ga en fonction de la nébulosité, la vitesse de rotation, la chimie de l'océan n'ayant que peu d'influence sur ces valeurs.*

Malgré la qualité des données acquises et les études de modélisation conduites, aucune étude ne résout le FYSP. Car résoudre le FYSP implique non seulement d'estimer le couple pCO_2/température mais également d'expliquer quels facteurs permettent à la pCO_2/température Archéenne d'être si élevée. C'est pour contraindre ce point essentiel que l'étude suivante a été conduite (Charney et al. 2017).

IV. les interactions climat-carbone et leurs importance dans la résolution du FYSP

Problématique : *En s'affranchissent du cycle du carbone, toutes les études mentionnées dans la précédente section présupposent un cycle du carbone à l'équilibre. Avec les conditions modernes, le système climat-carbone s'équilibre pour une température de surface oscillant entre 10 et 15°C. Malheureusement le cycle du carbone de la Terre Archéenne est loin de ressembler au système actuel. Cela signifie que l'ensemble des études présentées souffrent d'un biais important. L'objet de cette partie est donc d'évaluer l'importance des interactions climat-carbone.*

Pourquoi la rétroaction climat cycle du carbone est-elle essentielle ? Principalement car la pCO_2 est également dépendante de la température de la Terre ! En 1981, J.C.C Walker et ses collaborateurs ont publié un article fondateur dans lequel ils proposèrent une relation quantitative liant climat, insolation, dégazage de CO_2 de la Terre solide (F_{vol}) et la consommation de CO_2 atmosphérique par l'altération des silicates continentaux (F_{sw}) :

$$F_{vol} = F_{sw}(T,R)$$

où l'altération continentale est une fonction des paramètres climatiques que sont la température de l'air T et le ruissellement continental R

Au premier ordre, cette relation montre que si la source de carbone du système exosphérique est insensible au climat, le puits de carbone (l'altération) est dépendante au climat. Cette dépendance de l'altération au climat peut être utilisée pour reconstituer l'histoire de la teneur en CO_2 dans l'atmosphère. Pour cela il faut que 1) l'histoire du dégazage, 2) la constante solaire (i.e l'insolation) et 3) la forme mathématique de la fonction Fsw (T,R) soient connues.

Sur ce concept, des modèles numériques à zéro-dimension couplant climat et carbone ont été développés. Le plus influent est GEOCARB, modèle développé par Robert Berner de l'Université de Yale (1982). Ce modèle intègre une dépendance logarithmique de la température du type T = Constante x ln (pCO_2) combinée à une dépendance à la constante solaire, couplée à une relation linéaire entre T et R, du type R = aT + b.

Ainsi la relation $F_{vol} = F_{sw}(T,R)$ où T est la température de l'air et R le ruissellement continental

devient $F_{vol} = k * R * pCO_2^{0.3} \exp[6.5 \ln(pCO_2)/17.7]$

$F_{vol} = k\,[1+0.038\,(6.5 \ln(pCO_2))]\,pCO_2^{0.3} \exp[6.5 \ln(pCO_2)/17.7]$

où k est une constante représentant l'altérabilité des sols (k = 0.15 avant l'apparition des plantes, 0.75 avant l'apparition des angiospermes, puis 1 ensuite)

Dès lors, seules 2 inconnues subsistent dans cette équation, F_{vol} et la pCO_2. En supposant le dégazage (F_{vol}) proportionnel au taux d'accrétion des dorsales (ou aux variations eustatiques si le taux d'accrétion n'est pas connu) il devient donc possible de simuler la teneur en CO_2 de l'atmosphère. L'avantage indéniable du modèle GEOCARB est sa simplicité qui permet d'intégrer de nombreux processus influant sur le cycle du carbone. L'inconvénient majeur est que les processus intégrés dans GEOCARB sont simplifiés à l'extrême, sous forme de facteurs correcteurs multiplicatifs.

Pour des climats très anciens, de nombreuses questions restent en suspens :

1. Que sait-on du dégazage ? Connaissons-nous son histoire au cours du temps ?
2. L'altération des silicates, bien que dépendante du climat, est probablement pilotée par d'autres facteurs (i.e. la surface des continents, la nature des roches à l'affleurement).
3. Que sait-on des relations des relations entre la croûte océanique et la teneur en CO_2 atmosphérique ?

Problématique : *Résoudre le FYSP nécessite d'intégrer un grand nombre de facteurs, dont certains sont directement dépendant de la géodynamique de la planète. Plutôt que de vouloir intégrer tous les processus du cycle du carbone au prix d'une sur simplification de ces derniers, nous avons préféré coupler un modèle de climat 3D type GCM (voir section précédente) avec un modèle du cycle du carbone incluant explicitement nombre des processus intervenant à l'Archéen. A l'aide de ce modèle, nous avons étudié les climats possibles entre 4 et 3,8Ga.*

4.1. Quelles sont les pCO_2 qui répondent à l'équilibre climat-carbone à 3.8Ga ?

- Article. Charnay B., Le Hir G., Fluteau F., Forget F., Catling D.C., *A warm or a cold early Earth? New insights from a 3-D climate-carbon model*, Volume 474, 15 September 2017, Pages 97-109. doi.org/10.1016/j.epsl.2017.06.029

- projet INSU (comité SYSTER) : *« Conséquences du grand bombardement tardif sur la Terre archéenne »* piloté par F. Fluteau (IPGP) - 2016

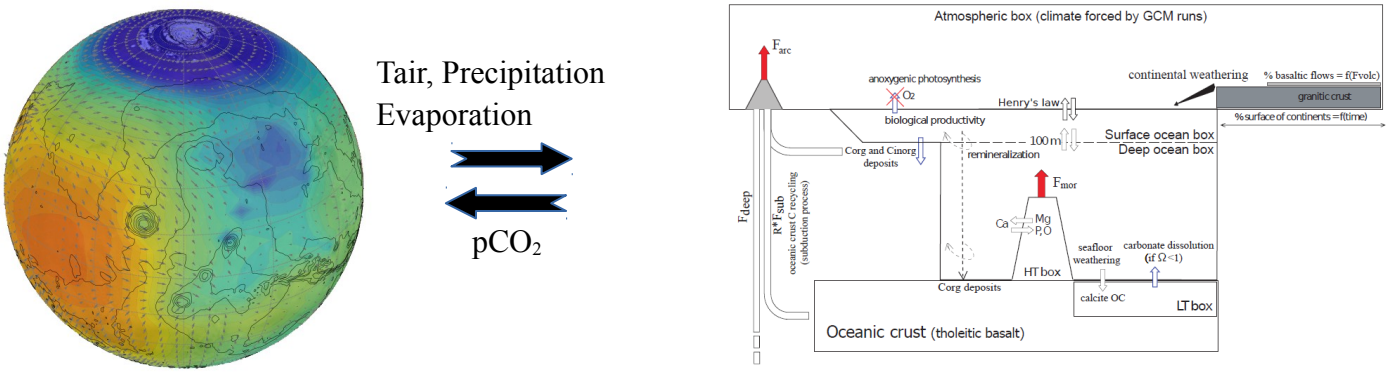

Figure 5 : couplage entre le modèle de climat 3D Hadéen (Generic LMDz) et le modèle du cycle du carbone modifié pour intégrer les contraintes de la transition Hadéen/Archéen. Les pressions testées vont de 0,01 à 1bar de CO_2 sous 2 atmosphères (CH_4=0 et 2mbar). Les 2 modèles échanges les variables afin de calculer un équilibre climat-carbone.

Plutôt que de vouloir intégrer tous les processus du cycle du carbone au prix d'une sur simplification de ces derniers, nous avons préféré coupler un modèle de climat 3D type GCM (Generic LMDz) avec un modèle du cycle du carbone incluant explicitement nombre des processus intervenant à l'Archéen. A l'aide de ce modèle (fig.5), nous avons étudié les états climatiques possibles entre 4 et 3,8Ga afin de répondre au problème du FYSP.

En plus des conditions climatiques de l'Archéen, plusieurs nouvelles conditions affectant le cycle du carbone Archéen ont été testées : i) le pourcentage de surfaces continentales émergées (0 cad une aquaplanète, 0,12 et 0,26 fois la surface continentale actuelle), ii) un taux de production de lithosphère océanique plus élevé déduit de la température potentielle du manteau, iii) un taux de recyclage du matériel subducté plus important du fait d'une lithosphère entrant en subduction à des températures plus chaudes car plus jeunes (conséquence directe d'un taux d'accrétion plus élevé). iv) Un dernier test suppose un régime différent de la géodynamique actuel basée sur la tectonique des plaques, un scénario dit heat-pipe où la chaleur est dissipée en grande partie liée au volcanisme.

Ces résultats montrent que la résolution du FYSP en incluant la rétro-action climat-carbone reste dans une gamme restreinte de pCO_2 d'équilibre, majoritairement entre 0,12 et 0,36bar de CO_2, pour des températures entre 20 et 30°C. Étrangement la surface des continents n'influencent que très peu la pCO_2 d'équilibre, l'interaction avec la croûte océanique et l'altération basse température (<110°C) des basaltes océanique étant prépondérante dans la régulation du cycle du carbone. Les plus hautes températures sont obtenues lorsqu'une lithosphère océanique épaisse (18 km au lieu de 6 km aujourd'hui) limite l'altération des basaltes aux couches superficielles et dans des atmosphères dépourvues de méthane (fig.6). De même une solution heat-pipe : un volcanisme très intense mais sans tectonique des plaques, ne favorise pas les hautes températures, l'abondance des basaltes émis augmentant l'altérabilité de la planète.

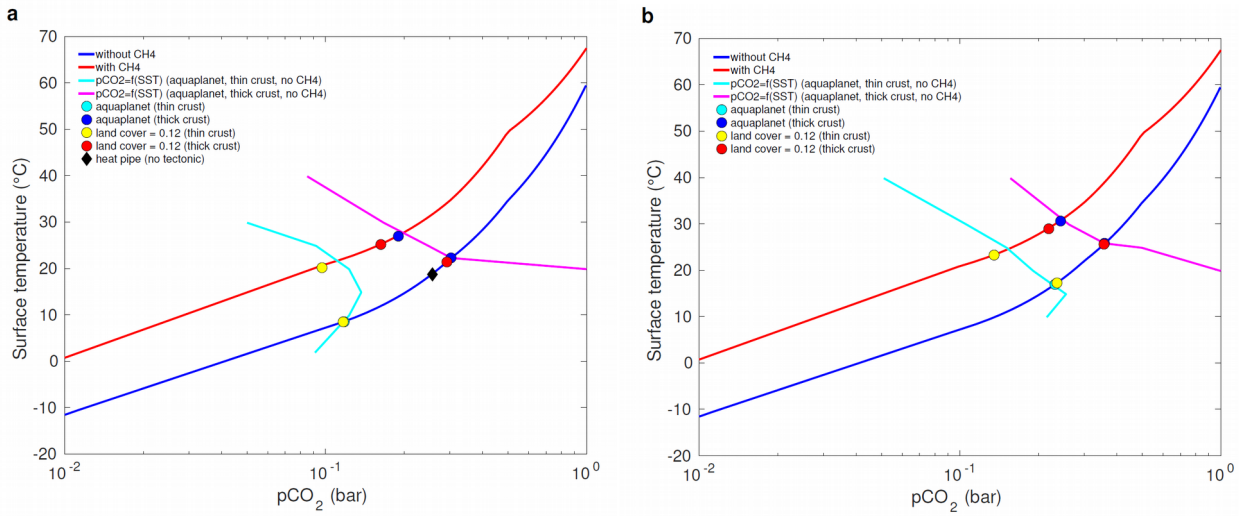

Figure 6: Température de surface moyenne respectant l'équilibre climat-carbone pour des fractions de surface continentale équivalente à 1 % (cercles bleus et bleus clair) ou 12 % (cercles jaunes et rouges) de la surface actuelle. **A gauche.** Simulée avec une tectonique des plaques aussi active qu'aujourd'hui (taux de recyclage par les subduction identique à l'actuel) pour 2 épaisseurs de croûte océanique (actuelle et 3 fois plus épaisse). Le sigle diamant noir représente le scénario heat-pipe, un scénario où la tectonique des plaques n'est pas encore présente (le flux de chaleur est uniquement dissipé sous forme d'un volcanisme très intense). **A droite,** simulée avec une tectonique des plaques 3 fois plus active qu'aujourd'hui.

Conclusion : *dans les conditions de la Terre primitive, l'évolution de la pCO_2 est essentiellement contrôlée par l'altération des basaltes océaniques, c'est ce processus qui maintient la Terre dans la zone d'habitabilité - la présence de continents importante peu si la surface émergée demeure sous la barre des 25 % actuels. Ces interactions climat-carbone doivent théoriquement maintenir un climat clément sur Terre (entre 20-30°C) avec des pCO_2 comprises entre 0,1 et 0,3 bar sans qu'il soit possible d'aller au-delà de ce seuil. En effet l'acidification des océans induit par les hautes pression de CO_2 fait croître exponentiellement la dissolution des minéraux silicatés (altération des basaltes océaniques) ce qui constitue une limite sans doute absolue à la pCO_2 terrestre. Si des valeurs plus hautes de pCO_2 étaient atteintes pour des raisons exogènes, alors le réchauffement des masses d'eau en surface limiterait la solubilité du CO_2 dans l'océan ce qui tendrait à limiter la consommation de carbone par l'altération des basaltes océaniques. Si cette situation se prolongeait, l'accumulation de CO_2 dans l'atmosphère serait une exponentielle croissante. Si cette frontière avait été franchie, l'habitabilité terrestre n'aurait peu être maintenue.*

4.2. Quelles conséquences au bombardement tardif de la Terre Archéenne ?

- Article. Charnay B., Le Hir G., Fluteau F., Forget F., Catling D.C., *A warm or a cold early Earth? New insights from a 3-D climate-carbon model*, Volume 474, 15 September 2017, Pages 97-109. doi.org/10.1016/j.epsl.2017.06.029

- projet INSU (comité SYSTER) : *« Conséquences du grand bombardement tardif sur la Terre archéenne »* piloté par F. Fluteau (IPGP) - 2016

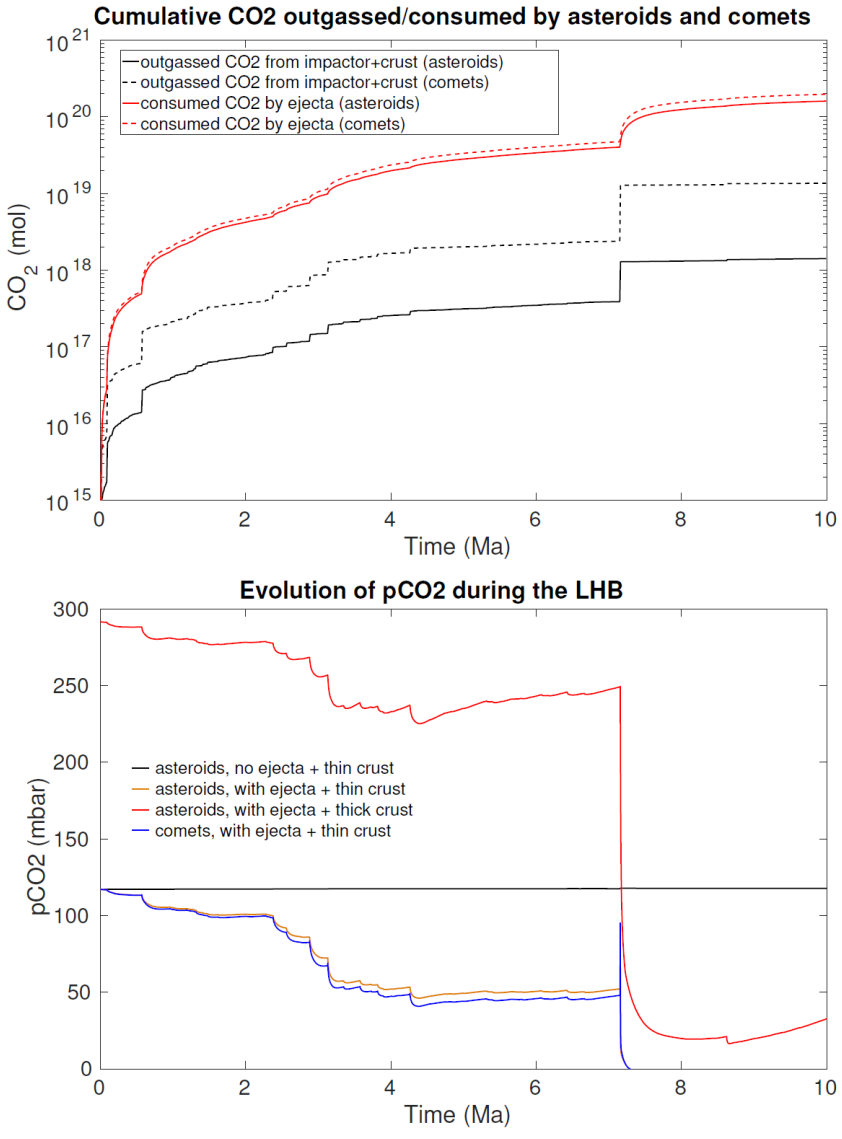

Figure 7: scenario incluant 10Ma d'impact du LHB (durée estimée 100 à 200Ma). **Haut.** Impact sur le cycle du carbone exprimé en mol de CO2 cumulées libérées lors des multiples impacts (en noir) et consommé par l'altération des éjectas (rouge) dans 2 cas. Les corps impacteurs sont des astéroïdes (ligne continue), des comètes (pointillés). **Bas.** évolution de la pCO_2 simulée (atmosphère sans méthane, tectonique des plaques standard) en supposant 2 épaisseurs de croûte océanique (standard et 3 fois plus épaisse qu'aujourd'hui).

L'équilibre climat-carbone de cette période ne fût pas uniquement influencé par ces seuls processus long-termes. En effet, la Terre a connu un intense bombardement de corps extraterrestres durant l'Hadéen. Ce bombardement planétaire décroit pendant l'Hadéen avant de connaître une phase exceptionnelle, entre 4.1 et 3,8 Ga, période dite du "grand bombardement tardif » ou Late Heavy Bombardment (i.e. LHB). Gomes et al. (2005) relie le LHB à la migration des planètes géantes Uranus et Neptune sur leurs orbites définitives, ce qui aurait conduit à la déstabilisation de la ceinture de Kuiper. Le LHB a profondément déstabilisé le cycle du carbone. Les ejectas et sphérules produits lors les collisions ont considérablement augmenté la quantité de matériaux facilement altérables, augmentant considérablement les puits de carbone malgré de fortes quantités de CO_2 émis lors des impacts.

Conclusion: *le LHB a certainement modifié le visage de la Terre Hadéenne, en induisant des climats froids – voire très froids de manière répétée sans toutefois aller jusqu'à un englacement total de la Terre.*

BILAN: comment expliquer l'existence d'une variabilité climatique?

V. *La variabilité climatique à long-terme et le forçage tectonique*

La variabilité climatique constatée sur le Phanérozoïque (542-0Ma) illustre - sans doute possible - qu'à plusieurs reprises le climat terrestre a subit des transitions de périodes froides (ice-house) vers des périodes chaudes (greenhouse) et inversement (fig.8). La dernière transition enregistrée dans le registre géologique ($\delta^{18}O$ des foraminifères benthiques, présence de diamictites, alkenones, …) se situe à la limite Eocène-Oligocène (34Ma) et se caractérise par la mise en place d'un important volume de glace en Antarctique, ~20 Ma après l'optimum thermique de l'Eocène (55Ma).

De nombreuses études ont présenté des mécanismes à l'origine de ces variations mais leur réel impact, cad leur quantification, reste à ce jour lacunaire. Une partie importante de ce travail de quantification a été réalisée par les précurseurs dans ce domaine à savoir Y. Donnadieu et Y. Goddéris, notamment par leurs travaux sur la dislocation du Rodinia (2003) et de la Pangée (2006). Dans la continuité de ces travaux je me focaliserai sur le Paléozoïque (542-252Ma), période que j'ai plus particulièrement explorée.

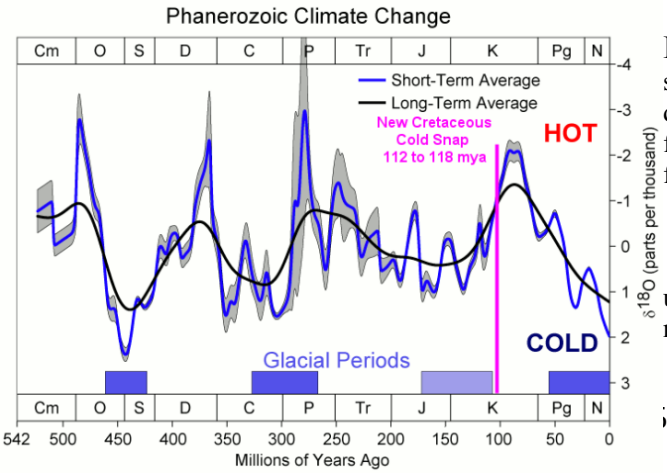

Figure 8. courbe synthétique des variations climatiques sur le Phanérozoïque. 3 périodes sont reconnues comme des périodes suffisamment froides pour permettre la formation de glaciers continentaux étendus. Le période froide du Jurassique-Crétacé Inférieur n'est pas encore établie bien que discutée. Les valeurs du $\delta^{18}O$ sont extraites de tests carbonatés d'organismes benthiques (ex : foraminifères). NB les valeurs ont subi une correction pour éviter une dérive vers les valeurs négatives au Paléozoïque

Pourquoi étudier le Paléozoïque ?

L'histoire du Paléozoïque (541 Ma–252 Ma, Cohen et al., 2013) commence avec la fragmentation du supercontinent Rodinia, et se termine par la formation d'un nouveau supercontinent, la Pangée. Le Paléozoïque forme donc, avec le Néoprotérozoïque, un cycle entier de regroupement-dislocation des continents, ou cycle de Wilson (Elmi et Babin, 2012). Le début du Paléozoïque est un monde bien différent d'aujourd'hui avec un hémisphère Nord recouvert à 80 %par les océans, la grande majorité des cratons connus étant localisée dans l'hémisphère Sud. Les continents Laurentia (actuelle Amérique du Nord), Baltica (actuelle Europe du Nord) et Siberia sont à basses latitudes (fig. 9A) tandis que le Pôle Sud est occupé par un vaste continent (Gondwana) regroupant à la fois l'Antarctique, l'Afrique, l'Arabie, l'Amérique du Sud, l'Inde et l'Australie. La dispersion des continents connaît son apogée à l'Ordovicien Moyen (fig. 9A), avant que les continents ne commencent à se regrouper de nouveau pour former la Pangée au Permien (Valentine et Moores, 1972).

En parallèle de cette évolution paléogéographique importante, 3 extinctions de masse (444, 370, et 252Ma) et 2 transitions climatiques majeures se sont produites. Le premier refroidissement intervient à la fin de l'Ordovicien (glaciation Hirnantienne, 445-444Ma) auquel est associé une extinction de masse. Il sera suivi 100 millions d'années plus tard par un second refroidissement (Carbonifère 360-300Ma), qui sera le plus intense et le plus long du Phanérozoïque.

5.1. La transition climatique au Paléozoïque inférieur où l'évolution de la paléogéographie comme cause du lent refroidissement.

- Article. Nardin, E., Goddéris, Y., Donnadieu, Y., **Le Hir, G**., Blakey, R., Pucéat, E., Aretz, M., 2011, *Modeling the early Paleozoic long-termed climatic trend,* Geological Society of America Bulletin. Vol. 123, p: 1181-1192, doi: 10.1130/B30364.1

Problématique : *comment expliquer la baisse de la pCO_2 nécessaire à l'installation des glaces sur le Gondwana ?*

Nardin et al. (2011) ont étudié l'évolution à long-terme du cycle du carbone au cours du Paléozoïque inférieur en utilisant le modèle couplé climat-carbone GEOCLIM pour quantifier les impacts respectifs de l'évolution paléogéographique. En complément de cette approche climat-carbone, une reconstruction des variations du rapport $^{87}Sr/^{86}Sr$ dans l'océan est aussi utilisée afin de déterminer l'évolution des surface des roches volcaniques/granitiques à l'affleurement entre le Cambrien terminal (Furongien, 490 Ma) et le Dévonien Inférieur (Emsien supérieur, 400 Ma).

Le modèle GEOCLIM (Donnadieu et al., 2004; Goddéris et al., 2014) est le produit du couplage entre le GCM océan-atmosphère FOAM, et un modèle « en boîtes » représentant les cycles du carbone et de l'alcalinité (COMBINE). Sa construction se fonde sur le concept de stabilité à long terme du climat global : à l'échelle des temps géologiques, les puits et les sources de CO_2 – altération continentale et volcanisme – sont à l'équilibre (Walker et al., 1981). Un ensemble d'états climatiques est tout d'abord modélisé avec FOAM, de manière à couvrir une large gamme de pCO_2 pour chacune des configurations continentales étudiées. Ces champs climatiques sont stockés dans une matrice, fournie en entrée au modèle de biogéochimie. Ce dernier détermine alors pour chaque

configuration continentale, par interpolation entre les différents champs climatiques, le climat permettant d'équilibrer le cycle du carbone. Il s'agit du climat pour lequel l'altération continentale équilibre le volcanisme. La pCO_2 associée à ce climat représente donc l'équilibre climat-carbone de la configuration continentale de l'époque considérée. L'innovation de cette étude est que calcul intègre également la surface de surface basaltique pour établir un rapport $^{87}Sr/^{86}Sr$ en accord avec les données.

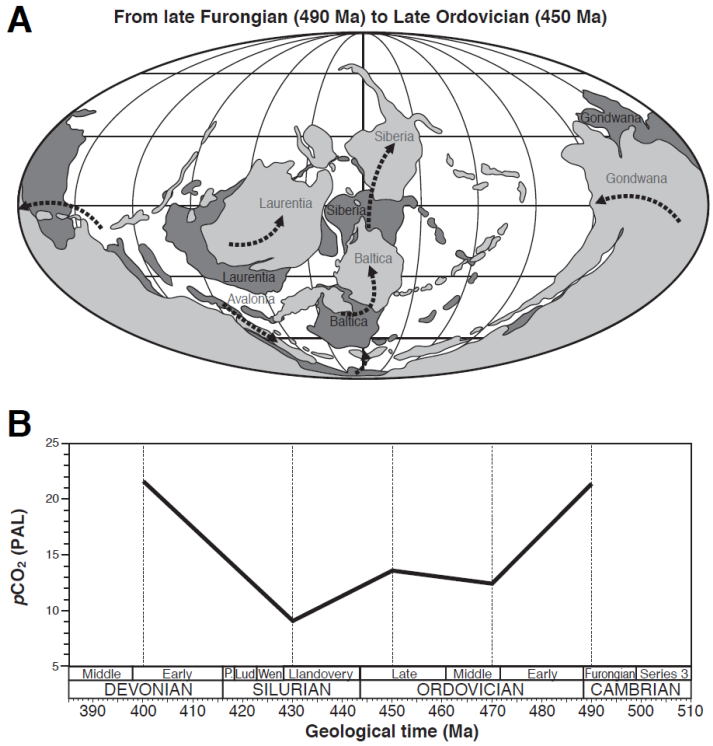

Figure 9 : Impact de l'évolution paléogéographique sur la pCO_2 au Paléozoïque inférieur. modifié d'après Nardin et al. (2011). **(A)** : Migration des continents entre le Furongien supérieur (Cambrien, 490 Ma ; gris foncé) et l'Ordovicien Supérieur (450 Ma ; gris clair). Les reconstructions continentales sont d'après Blakey (2007). Les flèches représentent les mouvements des masses continentales. **(B)** : Évolution de la $pCO2$ modélisée par Nardin et al. (2011) avec le modèle GEOCLIM. Ces résultats correspondent aux simulations *NormSr*, dans lesquelles la surface des roches volcaniques à l'affleurement a varié au cours du Paléozoïque en fonction de l'évolution du rapport $^{87}Sr/^{86}Sr$ documentée par Veizer et al. (1999).

Conclusion

L'évolution paléogéographique à l'Ordovicien est caractérisée par le détachement de blocs continentaux de la marge Nord de Gondwana, et par la migration des principaux continents en direction du Nord (fig. 9A). Nardin et al. (2011) ont montré que la migration des continents à travers la zone de convergence intertropicale, combinée à une augmentation de la surface des roches volcaniques à l'affleurement, entraîne une chute de la pCO_2 tout au long de l'Ordovicien, d'environ 21 PAL au Cambrien terminal jusqu'à 14 PAL à l'Ordovicien Supérieur (Fig. 9B). Ces résultats suggèrent que l'évolution paléogéographique serait à l'origine du refroidissement à long terme documenté par l'analyse géochimique des isotopes stables de l'oxygène par Trotter et al. (2008). En revanche, ils ne fournissent aucune explication aux variations climatiques à plus haute fréquence, telles que le refroidissement Hirnantien (Finnegan et al., 2011 ; Trotter et al., 2008).

5.2. Vers une courbe synthétique de référence de la pCO_2

- article. Goddéris Y.; Donnadieu Y.; Le Hir G.; Lefebvre V.; Nardin E. 2013. The role of paleogeography in the Phanerozoic history of atmospheric CO_2 and climate. Earth Science Reviews. 128,122-138, doi. 10.1016/j.earscirev.2013.11.004

L'étude des mécanismes expliquant les transitions climatiques a révélé l'importance des rétro-actions. Un nouveau paradigme semble apparaître où les tendances climatiques à très long terme seraient le résultat d'une expression externe de l'activité interne de notre planète. Les effets de la tectonique des plaques sur l'altération, le principal puits de CO_2, permettent de simuler deux épisodes froid au Paléozoique, une autour de l'Ordovicien, et une autre à la fin du Dévonien. Des récentes études sur le Permo-Carbonifère (Goddéris et al, 2017) et le Cénozoïque (Lefebvre, et al. 2013), combinées à de plus anciennes sur le Mésozoïque (Donnadieu et al. 2006) ont fini de compléter les lacunes du Phanérozoïque. Il est donc depuis peu possible de fournir une courbe de référence de CO_2 sur le Phanérozoïque simulée avec GEOCLIM directement comparable à celle proposée par Berner avec le modèle GEOCARB (Berner, 2006). Si Robert Berner, et de nombreux autres, ***ont démontré que le CO_2 est le principal acteur du climat sur le Phanérozoïque, cette étude montre sans équivoque que le cycle du carbone (donc le CO_2) est contrôlé par la position des continents. C'est donc au final la tectonique qui joue le rôle principal dans les transitions climatiques,*** même si parfois le forçage biologique interfère brièvement (comme au Dévonien).

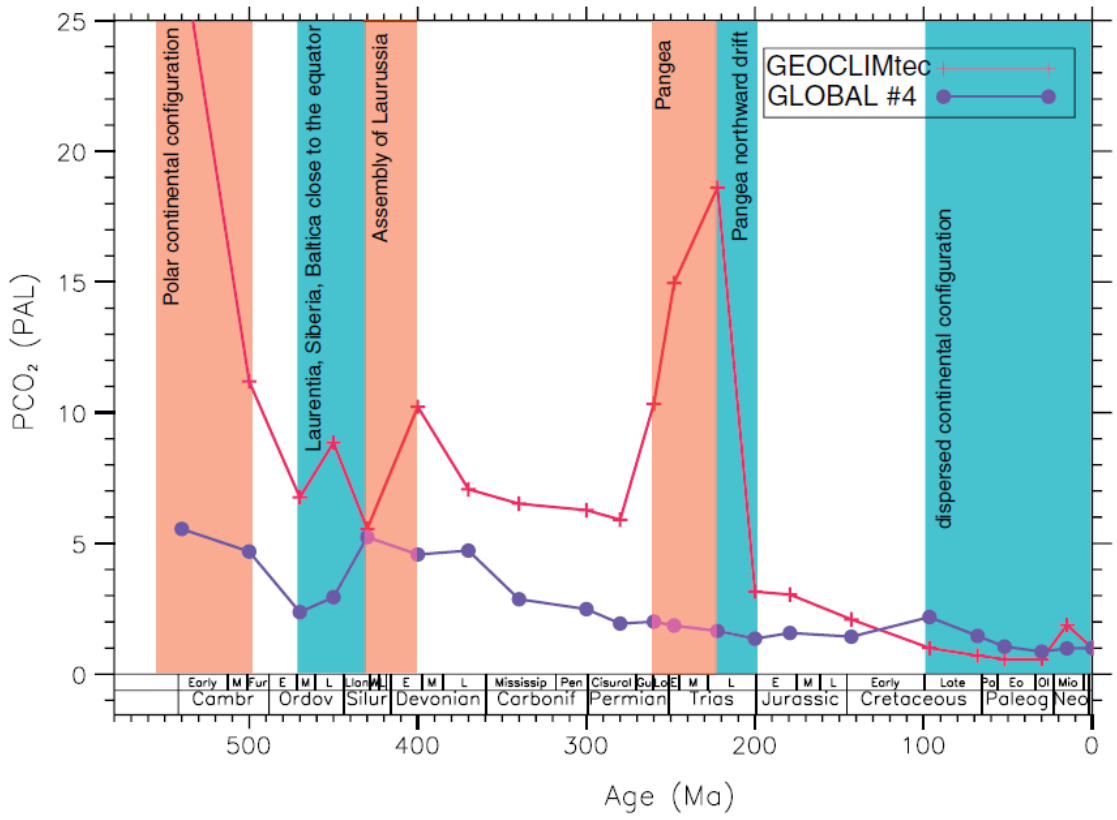

Figure 10. Évolution de la pCO_2 . La courbe Global4 est basée sur un modèle type GEOCARB où la pCO_2 dépend de la constante solaire et de la géographie. La courbe GEOCLIMtec intègre les mêmes forçages mais utilise un modèle de climat 3D pour calculer le climat (température et ruissellement) et l'altération chimique des silicates. Les zones rouges/bleues indiquent les périodes où la configuration des continents réchauffe/refroidit la surface de la Terre (les modifications paléographiques essentielles sont indiquées dans chacune des boites).

PERSPECTIVES: vers une modélisation des paléoclimats intégrant toutes les composantes

VI. la variabilité du Cénozoïque : l'exemple de la paléo-mousson asiatique

Jusqu'à présent, l'ensemble de mes travaux concernait les périodes anciennes (Paléozoïque et Précambrien). Ce choix thématique était autant lié à un centre d'interêt personnel qu'aux outils disponibles. En effet les outils dont nous disposions souffraient de plusieurs faiblesses : i) une résolution spatiale modérée (cad quelques centaines de kilomètres de résolution), ii) un couplage asynchrone entre les enveloppes (cad entre atmosphère et océan ou bien entre les enveloppes fluides et le modèle de glaces, ...). Il était donc approprié d'étudier des problèmes de premier ordre comme les transitions climatiques. Cet état de fait vient de changer.

Les prochaines années seront dévolues à des périodes plus récentes, notamment le Cénozoïque. Cette inflexion s'explique par le développement du GDR CEV *(Climat Environnement Vie: les apports du pré-Quaternaire)*. Le GDR est né en 2013 à l'initiative des modélisateurs des climats anciens en France, sous l'impulsion de Y. Donnadieu en réponse à la dispersion géographique de la communauté des modélisateurs des paléoclimats en France. Nous avons souhaité fédérer nos forces pour : i) permettre le développement d'outils toujours plus performants, et ii) augmenter notre visibilité dans la communauté en étudiant de manière poussée une période et ainsi plus facilement discuter avec "la communauté des données". L'exemple type de cet effort fut l'encadrement de la thèse d'Alexandre Pohl entre 2013 et 2016 par Y. Donnadieu et moi-même. Pendant ces 3 années nous avons pu réfléchir sur des problématiques communes et en parallèle développer des méthodes de couplages (entre modèle atmosphérique et couplé, et entre modèle couplé et modèle de calottes de glace) et/ou l'utilisation de nouveaux outils performants comme le MiTgcm. Fin 2016, les travaux réalisés par Alexandre Pohl lors de sa thèse avaient permis une net avancée dans notre compréhension de l'Ordovicien et de l'ensemble du Paléozoïque inférieur à la fois en terme de processus mais également dans l'explication de données parfois difficilement conciliables.

Le développement de nouveaux outils est une nécessité impérieuse pour permettre l'innovation dans les recherches sur les périodes de temps anciennes. Depuis quelques mois, nous testons un nouvel outil complexe mais très prometteur à savoir le modèle couplé (IPSL-CM5A2 ou paléo-IPSL), modèle issu du couplage entre les différents modèles développés au sein de l'Institut Pierre Simon Laplace (ISPL) qui sont respectivement LMDz (atmosphère), Nemo (océan), Pisces (biogéochimie marine) et Orchidées (sol-végétation). L'intégration de ces outils, couplés de manière synchrone et/ou forcé, nous permet une représentation du climat passé et de ses interactions avec les autres enveloppes nettement plus avancée que par le passé. Dès lors, étudier les périodes anciennes où les données sont trop fragmentaires et les conditions limites mal contraintes n'apparaît plus très opportun.

Afin de maximiser la potentialité de ce modèle, nous nous sommes concentrés sur des périodes plus récentes, et plus particulièrement sur des problèmes "chauds" du Cénozoïque.
Ce projet fédérateur à l'échelle du GDR est mené conjointement au projet ERC sur la mousson Asiatique (porté G. Dupont-Nivet, Université de Rennes et Postdam)

Que nous apprennent les données sur l'histoire de la mousson ? L'âge de l'apparition (ou du renforcement) de la mousson en Asie est l'objet de débat depuis les années 90. Kroon et al. (1991) interprète l'augmentation de l'abondance de foraminifères endémiques aux upwellings en mer d'Arabie vers 8 Ma comme une évidence d'un renforcement ou de l'apparition de la mousson. Au nord-est du plateau tibétain, la découverte de dépôts éoliens dans la région de Qinan au nord-est du plateau Tibétain datés de 22 à 25 Ma est interprétée comme le marqueur de la présence d'un climat semi-aride au début du Miocène qui aurait perduré jusqu'à aujourd'hui (Guo et al., 2001 ; Qiang et al., 2011). Pour Guo et al. (2002), ces dépôts éoliens seraient la preuve d'une dynamique atmosphérique analogue à la mousson d'hiver actuelle. Yan et al. (2017) y voit surtout une évidence de la surrection du plateau tibétain et de l'évolution des sources de sédiments éoliens. Caves et al. (2015) interprètent l'absence de variations de $\partial^{18}0$ des carbonates pédogéniques au nord du plateau tibétain depuis (56-50Ma) comme la preuve d'un climat uniquement contrôlé par le régime des vents d'ouest (« westerlies ») et indépendant de la mousson ou de l'effet de la surrection du plateau tibétain. Licht et al. (2014) ont montré à l'aide de la signature isotopique de l'oxygène ($\partial^{18}O$) des gastéropodes et des dents de rhinocérotidés (découverts au sein des formations sédimentaires du bloc Birman) que la mousson était présente dès la fin de l'Eocène (~38Ma) sur le sud de l'Asie. Finalement la présence d'une mousson en Inde dès 55 Ma a été proposée par Shukla et al. (2014) à partir de l'analyse de la physionomie de feuilles fossiles du Rajasthan (Inde) situées à l'époque à une latitude inférieure à 10°N.

L'objectif de ce projet en cours et qui constitue une part très importante de la thèse D. Tardif (thèse débutée le 01/10/2017) est d'utiliser un modèle climatique couplé océan-atmosphère-biosphère pour étudier les conséquences des modifications tectoniques sur la circulation atmosphérique et océanique pour 3 périodes clés du Cénozoïque (60Ma, 40Ma et 20Ma). En confrontant les expériences réalisées aux données, nous proposerons un scénario d'évolution de la mousson depuis le début du Cénozoïque. Ce scénario nous permettra de répondre aux questions suivantes: i) Existe t-il une mousson avant la collision Inde-Asie ? ii) Comment varie l'intensité de la mousson en Asie au cours du Cénozoïque en réponse aux changements paléogéographiques ? iii) Quel est l'impact de la transition climatique Eocène-Oligocène (40-34Ma) sur le climat en Asie ? Est ce que les changements paléoclimatiques au cours du Cénozoïque au nord du plateau Tibétain sont-ils un marqueur de la mousson ou bien de l'intensité du flux d'ouest des moyennes latitudes (« westerlies ») ? iv) Comment expliquer les changements de cyclicité observée dans les enregistrements sédimentaires ?

EXPOSE SYNTHÉTIQUE DES RECHERCHES
Thème 2: le couplage avec la cryosphère

La Terre est, à ce jour, l'unique planète où ***trois états climatiques distincts*** et stables sont connus. Ces 3 états climatiques sont possibles car les ***3 états physique de l'eau co-existent*** à la surface de la Terre. La transition entre ces 3 états se caractérise par la croissance, décroissance ou la disparition de la cryosphère.

On définie la cryosphère comme la glace continentale posée sur les continents (aux hautes latitudes essentiellement et marginalement en altitude). Cette définition restrictive peut être élargie à la banquise (issue de la congélation de l'eau de mer). Ainsi l'extension de la cryosphère est déterminée par l'isotherme 0°C. Pour cette raison, toute modulation de l'effet de serre (voir thème 1) ou bien de l'ensoleillement saisonnier peut induire une transition climatique si l'amplitude est suffisante. Si ce seuil est franchi alors, une fois la perturbation terminée, le système climatique ne retrouve pas son état initial. L'existence de ces points de bascule qui, une fois franchi, ne permettent pas le retour à l'état initial définissent les ***hystérésis*** du climat terrestre **(Fig. 11)**.

Ce comportement est liée à la rétro-action de l'albédo des glaces (comme l'ont montré M. Budyoko et W. Sellers à la fin des années 60) qui définit la relation cryosphère-climat comme instable sauf en *« 3 points d'équilibre»*, que l'on appelle les états climatiques. Tout refroidissement est amplifié (et inversement) par le changement d'état de l'eau, son passage à l'état solide accompagnant d'une augmentation nette d'albédo ($\alpha_{ocean} \sim 0.1 < \alpha_{glace} \sim 0.6 < \alpha_{neige} \sim 0.8$). Ainsi la simple diminution de la surface occupée par les glaces entre le Dernier Maximum Glaciaire (DMG, 21 kans : 35 10^6 km²) et l'Holocène (10 kans – 1850 après J.C : 14 10^6 km²) a généré $\Delta\alpha \sim 0.02$ (0.33-0.31), soit un réchauffement de 2°C.

$$4\Delta T_s/T_s = \Delta S/S - \Delta\alpha/(1-\alpha) + \Delta\varepsilon/(1-\varepsilon)$$
$$4\Delta T_s/T_s \sim -\Delta\alpha/(1-\alpha)$$
$$\Delta T_{s\,(\Delta\alpha)} \sim +2°C$$

On a ici intégré l'équation du bilan radiatif de la Terre (équation 4) et introduit l'effet de serre (ε)

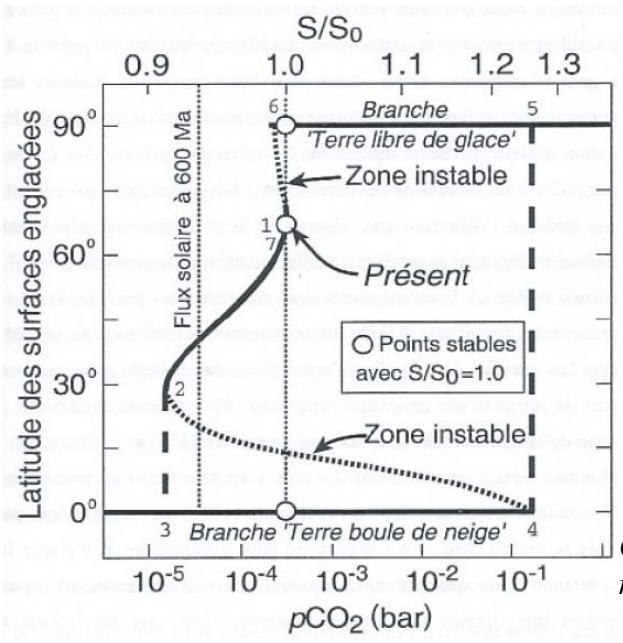

Figure 11.
Hysterésis climatique de la Terre montrant les 3 états stables du climat « libre de glace », partiellement englacé « Présent » et « Terre boule de neige », ainsi que les transitions (instables par définition). S_0 représente la constante solaire actuelle, $S/S_0=1$ est donc la période moderne.

Figure extraite et modifiée d'Hoffmann and Schrag 2002.

Cette observation simple a deux conséquences majeures :

*- la position latitudinale de **l'isotherme 0°C définira l'état climatique stable de la Terre** (greenhouse, icehouse ou bien snowball). Ainsi même si l'on calcule l'équilibre climat-carbone (thème 1), cet équilibre n'est à lui seul pas suffisant si **l'isotherme 0°C bouge significativement** (cas d'un refroidissement/réchauffement important).*

*- toute transition étant amplifiée par la rétraction de l'albédo de la glace, **la cryosphère constitue un facteur majeur d'instabilité climatique***. Bien trop souvent, la cryosphère est considérée comme invariante (car elle possède un temps caractéristique de réponse longue ~ siècle) . Nous verrons ici les limites de cette approche en proposant un couplage climat-cryosphère.

Pour illustrer l'apport de nos travaux sur ce couplage, je présenterai dans un premier temps, une étude illustrant l'importance de la cryosphère sur la sensibilité climatique. La seconde partie traitera de la Terre boule de neige.

BILAN: Limites de la régulation du système climatique

I. La sensibilité climatique : cas du refroidissement abrupt de l'Ordovicien

- Article. Pohl, A; Donnadieu, Y; Le Hir, G; Buoncristiani, J-F; Vennin, E; 2014, Effect of the Ordovician paleogeography on the (in) stability of the climate, Climate of the Past, 10, 2053-2066, doi:10.5194/cp-10- 2053-2014

- projet INSU (comité SYSTER) : Response of global marine biodiversity to a major climate change: modeling the Ordovician glaciation (445 Ma) with the MITgcm and its marine ecology model Darwin (responsable Pohl, A. 2015)

- thèse Pohl, A., (Soutenance effectuée le 16/11/2016) sujet : *Modélisation des changements climatiques et cryosphériques à l'Ordovicien.*

L'Ordovicien a longtemps été perçu comme une période globalement très chaude, caractérisée par un fort effet de serre, et donc une pCO_2 élevée (Berner, 2006 ; Goddéris et al., 2014 ; Yapp et Poths, 1992). Dans la section précédente (p17-18) les travaux de Nardin et al. (2011) ont démontré que la tectonique était la cause du refroidissement, ce qui implique une baisse lente des températures. Cependant le registre sédimentaire en Afrique du Nord et au Moyen-Orient (e.g., Ghienne et al., 2007 ; Turner et al., 2005), mais aussi en Afrique du Sud et en Amérique du Sud (e.g., Diaz-Martínez et Grahn, 2007 ; Grahn et Caputo, 1992) ont tous montré **un refroidissement brutal à l' Hirnantien (445–444 Ma)**. Une étude détaillée de la stratigraphie a par ailleurs mis en évidence plusieurs phases d'avancées et retraits des glaces au cours de l'Hirnantien (Denis et al., 2007 ; Ghienne et al., 2007), suggérant l'existence de cycles glaciaires-interglaciaires (e.g., Moreau, 2011) semblables à ceux de la glaciation Plio-Pléistocène (e.g., Jouzel et al., 2007).

***Problématique :** Si la baisse progressive du CO_2 (Nardin et al, 2011) semble favorable à la mise en place lente et régulière des calottes de glaces, les données montrent que l'englacement semble avoir été intense et abrupt. Comment expliquer ce paradoxe ?*

1.1 l'importance du couplage circulation océanique – banquise : la notion de *tipping point*

Les résultats obtenus par Poussart et al. (1999) et Herrmann et al. (2004a,b) suggèrent un rôle clé de la dynamique océanique dans les changements climatiques ordoviciens, mais cet aspect n'a jamais fait l'objet d'une étude approfondie avec un modèle de circulation générale couplé océan-atmosphère. Nous avons revisité cette question de l'importance de la dynamique océanique ordovicienne sur la chute de la température avec le GCM océan-atmosphère FOAM.

Jusqu'à présent, la majorité des simulations numériques de cette période reposait sur des modèles atmosphèriques couplés à des modèles de couche de mélange océanique (ou slab) qui prennent en compte seulement l'effet thermique d'une couche d'eau d'épaisseur avoisinant les 50 mètres. L'influence des courants marins et de la circulation océanique profonde sur le climat est alors représentée par un terme de diffusion de type Loi de Fick avec des raffinements pouvant ou non inclure un coefficient de diffusion variable en fonction de la latitude et de la longitude. Ce type d'approche permet alors de tenir compte de la réponse de l'atmosphère tout en laissant les points océaniques libres de s'ajuster thermiquement. Le coefficient de diffusion est réglé de façon à ce que le transport global par l'océan entre l'équateur et les pôles atteignent un ordre de grandeur similaire au système actuel.

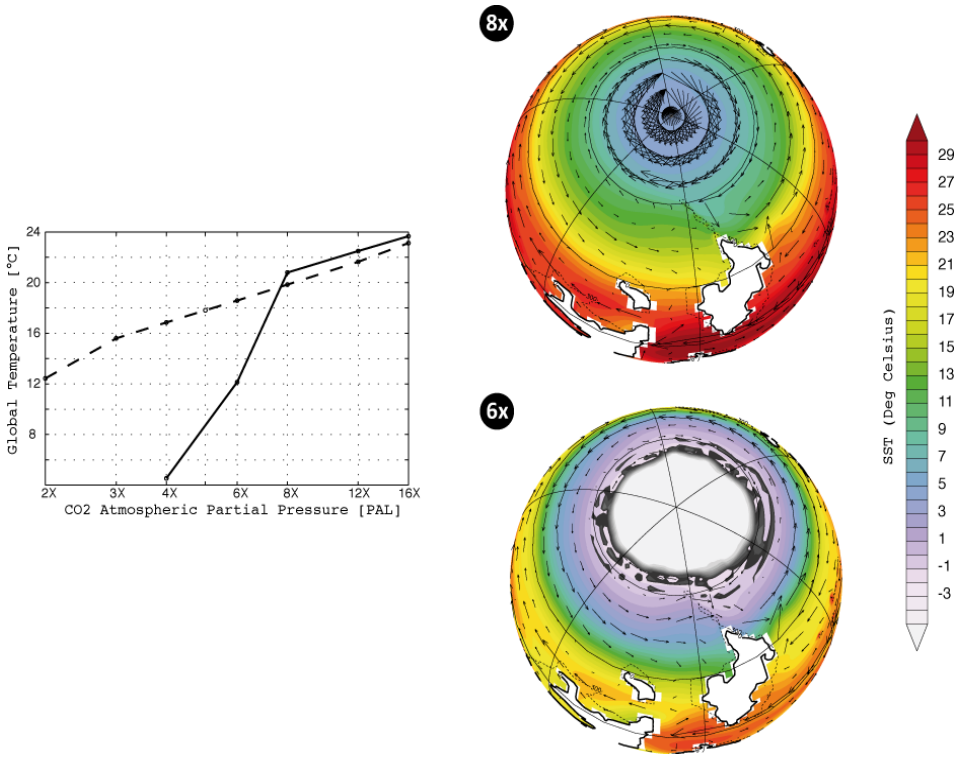

Figure 12:
Lien CO_2 –température durant l'Ordovicien établi à partir de simulations slab et couplée (thèse d'A. Pohl). A gauche, évolution de la température globale annuelle, en pointillé, simulations slab, en trait plein, simulations couplées. A droite, vue du pôle Nord, température de surface de l'océan à 8x et à 6x. En blanc, la mise en place d'une couverture de glace de mer est visible sur la figure en bas à droite. NB : la pCO_2 est exprimée ici en fonction de la pCO_2 pré-industrial (PAL), 1x (1PAL) = 280 ppmv

Les simulations réalisées avec FOAM avec un océan dynamique ou avec une couche de mélange montrent 2 comportements très différents. Lorsqu'une baisse de la teneur en CO_2 atmosphérique est imposée, les simulations réalisées avec un océan dynamique montre un rupture climatique – comportement absent si l'océan est représenté par une couche de mélange (fig. 12 – figure de gauche).

Utilisé avec une simple couche de mélange océanique, le modèle FOAM produit des résultats comparables aux études précédentes (Hermann.. (2004a,b) La température globale décroît linéairement avec la pCO_2. La relation ΔT / ΔpCO_2 ***(appelée sensibilité climatique)*** avoisine les 3°C par doublement de la pCO_2 ([2] note bas de page). **La relation entre température globale et pCO_2 est clairement non-linéaire lorsque la dynamique océanique est prise en compte.** Cette rupture se traduit par une baisse de la température globale annuelle de plus de 9°C suite à l'englacement de l'océan polaire dans l'hémisphère Nord (fig.10). On observe ainsi deux modes climatiques bien distincts : i) Pour de fortes concentrations en CO_2 (12 PAL à 470 Ma et 8 PAL à 450 Ma), le climat est chaud et il n'y a pas de glace de mer dans l'Hémisphère Nord.

ii) Lorsque la pCO_2 est abaissée à 8 PAL et 6 PAL à 470 Ma à 450 Ma respectivement, un point de bascule climatique (« *tippingpoint*») est franchi. La glace de mer s'étend soudainement jusqu'aux moyennes latitudes dans l'hémisphère nord et le climat se refroidit brutalement (– 9 ◦C à l'échelle globale à 450 Ma).

Ce refroidissement brutal et intense est causé par l'évolution du transport de chaleur océanique et non par une baisse brutale de CO_2. La circulation océanique est influencée par la géométrie des bassins océaniques (Fig. 13). Dans le cas de l'Ordovicien, un hémisphère (le Nord) est quasi-exclusivement océanique, seul le craton Siberia occupe cet hémisphère.

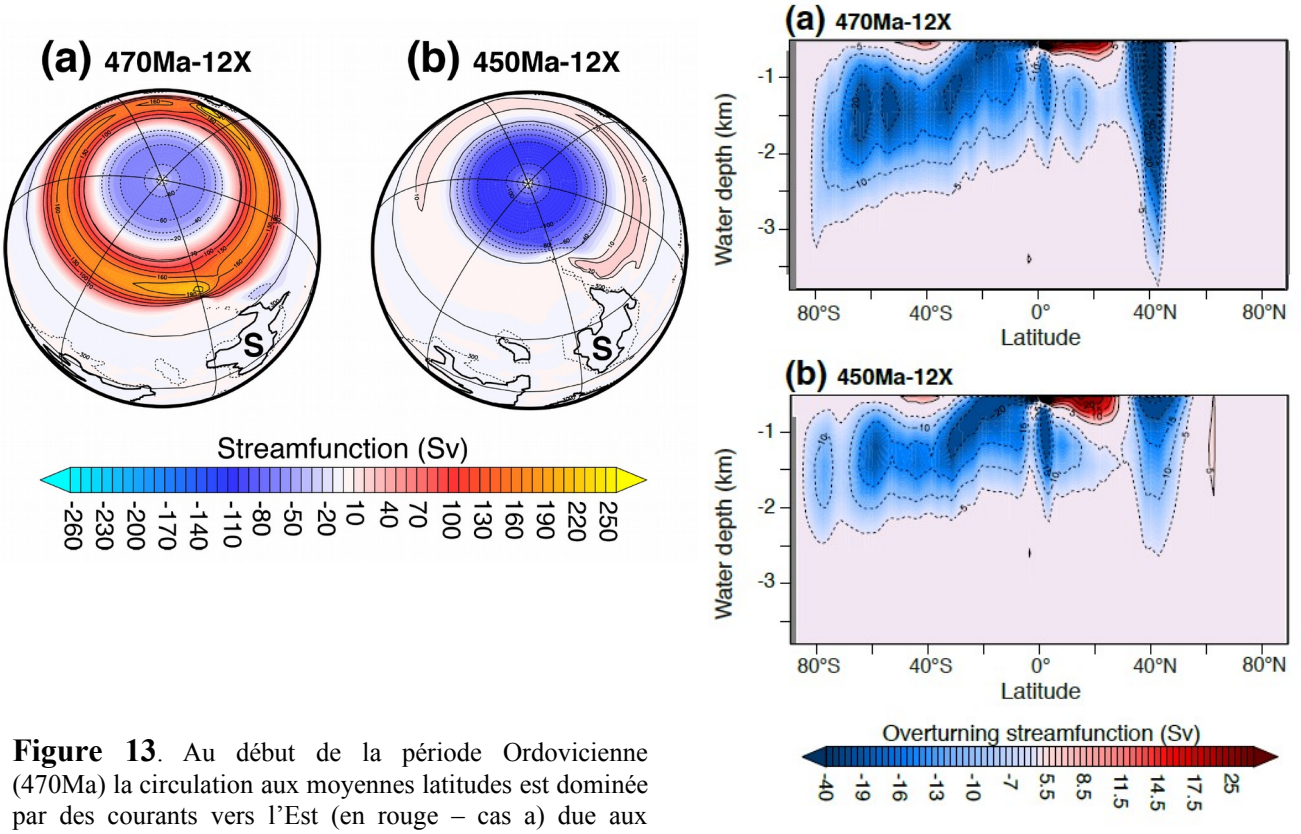

Figure 13. Au début de la période Ordovicienne (470Ma) la circulation aux moyennes latitudes est dominée par des courants vers l'Est (en rouge – cas a) due aux vents de surface dont l'intensité n'est pas limitée par la présence des continents. La force de Coriolis (déflexion d'Ekman) induit dès lors un transport des masses d'eaux froides vers les moyennes latitudes (~ 40°N, en bleu – fig. de droite) et donc un transport de chaleur négatif. Dans ces conditions particulières, l'extension de la glace de mer est facilitée. La remontée du craton Siberie vers la fin de l'Ordovicien (450Ma) réduit le courant de surface vers l'Est, le flux de masse d'eau froide est donc plus faible ce qui rend plus difficile la formation et l'extension de la banquise jusqu'aux moyennes latitudes.

2 *Dans le cinquième rapport du GIEC, chaque doublement de CO_2 s'accompagne d'un accroissement de la température ΔT_{2x} ~1.5 – 4.5°C, avec comme maximum 6.5°C.*

1.2 l'importance de la tectonique dans la sensibilité climatique

La migration vers le Nord du continent Siberie induit une réorganisation de la circulation océanique au cours de l'Ordovicien. En réduisant l'intensité des courants d'Est, et donc le transport d'eau froide vers l'équateur, il devient plus difficile d'atteindre l'instabilité climatique à la fin de l'Ordovicien (450 Ma) qu'au milieu de l'Ordovicien (470 Ma). Cette instabilité climatique est franchie entre 12 PAL et 8 PAL à 470 Ma, alors qu'elle survient entre 8 PAL et 6 PAL à 450 Ma. en raison de l'anomalie du transport de chaleur vers le Nord.

Si la configuration à 470Ma est très favorable à l'installation de glace, la pCO_2 de cette époque était sans doute trop haute pour permettre la mise en place de banquise. Avec la réduction de la pCO_2 durant l'Ordovicien, ce seuil d'englacement fût probablement atteint. Cependant la configuration étant moins favorable il fallut une baisse de CO_2 plus marquée pour atteindre ce seuil. Dès ce seuil atteint, un point de bascule est franchi – *tipping point* - la banquise s'étend alors très rapidement jusqu'à 40°N.

Les reconstructions continentales de Blakey (2016) indiquent que cette migration du continent Siberie se poursuit au Silurien. Un test de sensibilité à la présence de masses continentales aux hautes latitudes de l'Hémisphère Nord au Silurien (Wenlock, 430 Ma) confirme les résultats observés sur les configurations de 470 et 450Ma. La remontée de Siberia aux moyennes latitudes bloque complètement le courant océanique transportant les eaux froides aux moyennes latitudes. Ainsi même en baissant fortement la pCO_2 (4PAL) - *le tipping point (point de bascule) n'est pas atteint* - la Terre demeure dans un mode chaud (fig. 14).

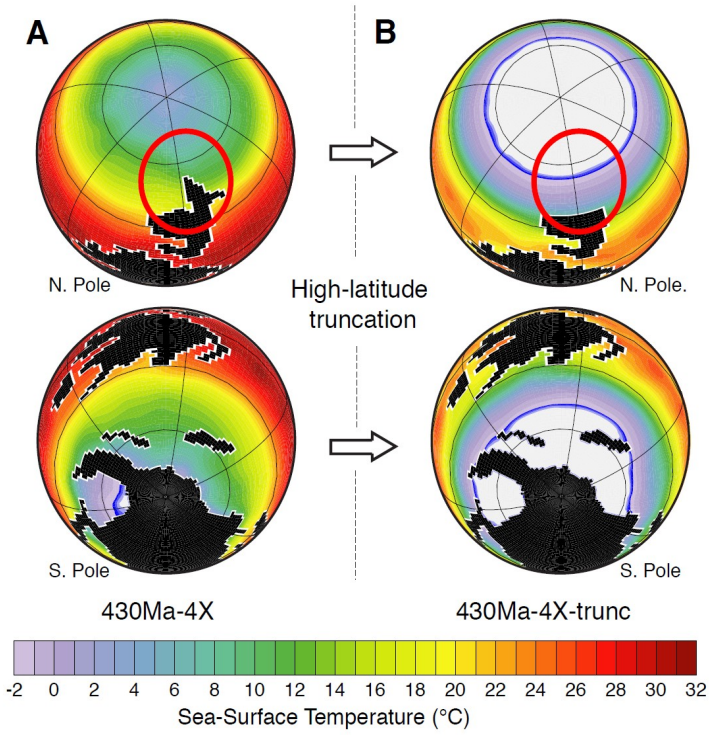

Figure 14. Projections orthographiques des températures océaniques de surface simulées en moyenne annuelle. Les résultats ont été obtenus à 4 PAL, avec (A) : la paléogéographie de Blakey (2016) ; (B) : la paléogéographie de Blakey (2016), dans laquelle les masses continentales situées au-delà de 40◦ N ont été tronquées (cercle rouge). Une palette de couleurs allant du blanc au bleu indique l'extension de la glace de mer permanente, définie comme l'ensemble des points de grille dont au moins 80 % de la surface sont occupés par la banquise au cours de l'année. Les continents sont représentés en noir.

Conclusion

Ces deux études montrent que l'évolution de la configuration continentale au Paléozoïque inférieur induit une baisse de la pCO_2. Cette baisse de CO_2 semble de prime abord insuffisante pour expliquer la glaciation. Cependant la configuration paléogéographique très singulière durant l'Ordovicien est susceptible d'induire une instabilité climatique. En effet la présence d'un hémisphère quasi-exclusivement océanique favorise la sensibilité du climat - l'absence de masses continentales induit une dynamique océanique très zonale, avec un minimum de transport de chaleur océanique aux moyennes latitudes. Le passage d'un mode climatique chaud à froid suite à une légère réduction de CO_2 est un mécanisme climatique robuste, confirmé par des expériences menées avec un GCM océanique performant : le MITgcm. En plus d'expliquer l'entrée en glaciation, cette instabilité climatique fournit une explication aux données géochimiques qui révèlent une chute des SST (Températures de Surface Océanique) tropicales de 7°C durant l'Hirnantien (445–444 Ma)

II. Une Terre entièrement couverte de glace et dynamique ... oui c'est possible !

2.1 Qu'appelle t-on une Terre entièrement englacée (Snowball Earth) ?

L'idée d'une glaciation globale n'est pas nouvelle. Dès les années 60, le géologue anglais Brian Walter Harland (1917-2004) postula l'existence d'une grande glaciation à la fin du précambrien (>542Ma). Il dénomma cet événement « the great-infra cambrian glaciation » (Harland, 1964). Si l'absence de datations radiochronologiques priva B.W Harland de reconnaître la synchronicité des dépôts glaciaires qu'il observait, ses mesures paléomagnétiques, plaçant ces sédiments glaciaires à de faibles latitudes, lui permit de découvrir leur caractère tropical.

Cependant au même moment Mikhail Budyko (1969), climatologue soviétique, travaillant sur les conséquences climatiques d'un conflit nucléaire généralisé, entre les blocs de l'Est et de l'Ouest, rendit les constations de B.W Harland inaudibles. A l'aide d'un des premiers modèles numériques de climat, M. Budyko démontra qu'un refroidissement suffisamment intense (un hiver nucléaire par exemple) qui entraînerait l'extension de la banquise (et/ou de la neige) au-delà de 30° de latitude devait, dès ce seuil franchit, enclencher un refroidissement irréversible de la Terre conduisant à un englacement total de sa surface. Le principe est simple. La zone entre les tropiques est la zone terrestre qui reçoit la plus grande part du rayonnement solaire incident. Si des surfaces blanches (banquise, neige, …) situées dans les tropiques réfléchissent la majorité du rayonnement, alors tout réchauffement de la planète devient impossible. Une fois ce seuil franchi (*tipping-point*), débute une spirale de refroidissement aboutissant à un englacement total du globe terrestre. En l'absence de scénario permettant d'expliquer la sortie de ce stade glaciaire généralisé, l'idée de B.W. Harland resta marginalisée.

Il fallu attendre la fin des années 80 pour voir ressurgir l'idée d'une glaciation globale. Cette mise au goût du jour de l'idée d'une glaciation globale est l'œuvre de J. Kirschvink, qui proposa pour la première fois un scénario vraisemblable. En 1987, J. Kirschvink expliqua l'initiation de la glaciation globale par la dislocation du super-continent Rodinia (800-750Ma). Cette fragmentation généra une situation inédite où la grande majorité des cratons issus de Rodinia se concentrèrent aux basses latitudes. Ces surfaces continentales ayant un albédo plus élevé que les océans (~0.3 et ~0.1 respectivement), cette situation singulière aurait initié un refroidissement amplifié par la rétroaction

de l'albedo des glaces. L'énigme de la sortie de glaciation fut également amenée par J. Kirschvink sur la base de l'idée de J.C.G. Walker (1981). Une fois la Terre entièrement englacée, son albédo est si élevé que les températures de l'air sont en permanence négatives (T_{air} < -50°C) rendant la présence d'eau liquide en surface impossible. Dans ces conditions le cycle du carbone est déstabilisé car l'altération des silicates devient inopérante. En l'absence de puits de carbone, la lente accumulation du CO_2 volcanique génère un puissant effet de serre qui conduit, à terme, à une fonte brutale et irréversible des glaces. Se basant sur le taux de dégazage actuel des volcans, J. Kirschvink estima que plusieurs millions d'années seraient nécessaires pour accumuler le CO_2 nécessaire à la déglaciation (~0.1bar de CO_2, soit plus de 250 fois la concentration actuelle de dioxyde de carbone atmosphérique).

Cette hypothèse radicalement innovante, présentée devant une assemblée réduite de chercheurs en 1987 (Proterozoic Paleobiology Research Group organisé par Bill Schopf – Université de Californie), cristallisa le concept de glaciation globale de la Terre sous le terme de "snowball Earth" ou Terre boule de neige. Cette hypothèse demeurait fragile car encore trop peu contrainte, mais avait l'avantage d'être facilement vérifiable tant les conséquences devaient être importantes ; à savoir (1) la présence de formations glaciaires synchrones et abondantes, (2) la déstabilisation majeure du cycle du carbone, (3) un océan à la chimie très différente car isolé de l'atmosphère (O_2) et non perturbé chimiquement par les flux continentaux.

Pour vérifier les conséquences découlant de l'hypothèse de la Terre boule de neige, P. Hoffman passa 6 ans à étudier les terrains de Namibie avec son étudiant Galen Halverson. Le choix de cette région n'est pas lié au hasard. Ex-colonie allemande puis protectorat de l'Afrique du Sud, la Namibie devint indépendant en 1990. Dans les années 90, la Namibie offrait donc à la fois des affleurements exceptionnels du fait de l'aridité du climat mais aussi une relative sécurité pour mener à bien les études de terrain.

D'observations dispersées, toutes critiquables prisent indépendamment, P. Hoffman fonda son raisonnement sur l'aspect fédérateur de l'hypothèse de la Terre boule de neige pour expliquer la singularité des enregistrements géologiques de la fin du Néoprotérozoïque (1000-542Ma) :

i) Les occurrences des dépôts glaciaires permirent de distinguer deux événements glaciaires globaux : la glaciation Sturtienne (718-660Ma) et la Marinoenne (650-636Ma). (Fig. 15)

ii) La présence de carbonates (ou cap-carbonates) surmontant les dépôts glaciaires, qui tracent la reprise de l'altération intense des continents consécutive à la déglaciation.

iii) Des valeurs de $\delta^{13}C_{carbonates}$ à 5‰ mesurées dans les dépôts post-glaciaires, soit la valeur mantellique, signe de la quasi-absence de biomasse en sortie de glaciation.

iv) Le retour des Banded Iron Formations (BIFs), preuve que l'océan était redevenu, pour un temps, anoxique suite à la formation d'une épaisse couche de banquise bloquant les échanges entre l'océan et l'atmosphère (le principal réservoir d'O_2). Selon ce scénario, les BIFs se seraient formés lors de la déglaciation, lorsque les échanges entre l'océan (anoxique) et l'atmosphère (riche en d'O_2) seraient devenus à nouveau possibles suite à la fonte de la banquise. Cependant certains niveaux de fer rubanés sont recouverts de plus de 600m de dépôts glaciaires, laissant penser que des zones libres de glaces ont très certainement existé épisodiquement pendant la glaciation.

L'ensemble des observations apportées par P. Hoffman (1998), toutes explicables par une seule et même cause, confirma l'hypothèse énoncée par J. Kirschvink. Ce long travail trouva un écho important dans la communauté scientifique mais aussi plus largement dans le grand public (documentaire de la BBC sur ce sujet en 2001, document qui déclencha mon intérêt pour ce sujet).

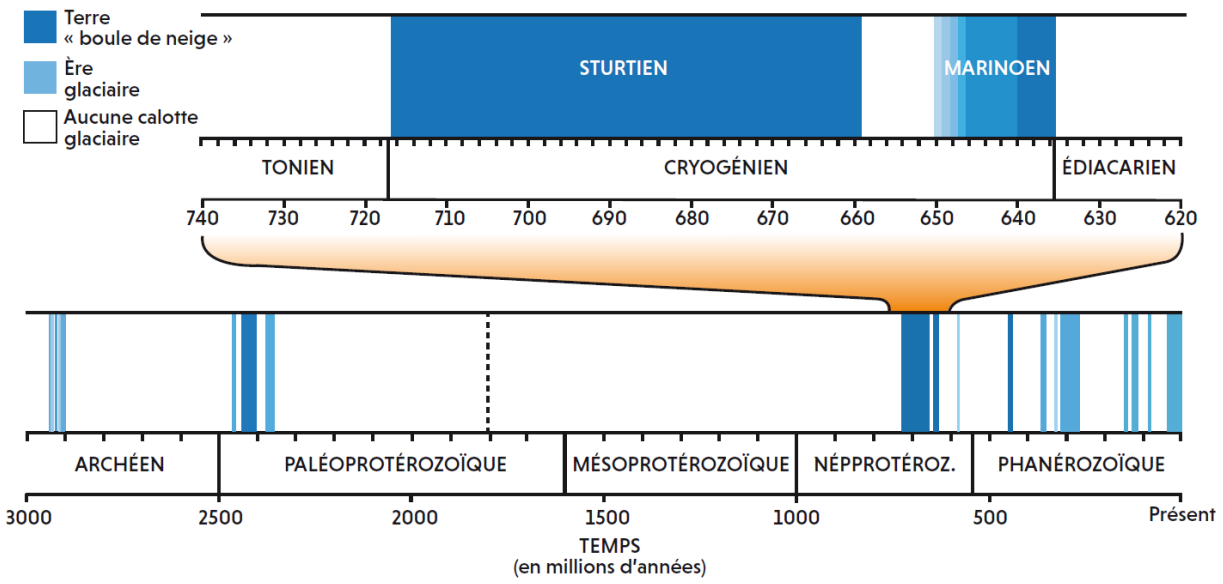

Figure 15. la période du *Cryogenien* inclue les 2 épisodes de Terre boule de neige (Sturtien et Marinoen) . A noter que l'abondance des dépôts glaciaires entre 717-636Ma a conduit à dénommer cette période le Cryogenien (cryos signifiant froid en grecque ancien)

Cependant plusieurs questions restaient sans réponse. La survie des organismes demeure la plus controversée et discutée. Les producteurs primaires des zones polaires actuelles nous montrent que la biosphère est très tolérante aux basses températures, et que la photosynthèse se maintient sous des épaisseurs modérées de banquise (<5m). Donc la question de la survie de la biosphère lors d'une glaciation globale revient à déterminer l'épaisseur de la banquise et son extension. Ce point n'est toujours pas solutionné à cette heure !

Le second point concernait l'incohérence apparente entre l'activité glaciaire et la théorie de la Terre boule de neige. Ce point fût le fer de lance de la contreverse initiée dans les années 2000 avec comme point d'orgue la conférence d'Ascona en 2006 (Suisse). 10 ans plus tard ce point fut enfin résolu (étude présentée ci-après).

2.2 De l'importance du couplage climat-calotte dans les climats froids

2.2.1 Problématique

Nos connaissances du système climatique, acquises dans les années 60 par l'étude de l'*hiver nucléaire* (guerre froide), permettent d'affirmer que la présence de glaces aux tropiques implique une glaciation globale. Dans ces conditions, le cycle hydrologique est supposé inopérant et les processus sédimentaires très limités.

Paradoxalement cette vision figée d'une Terre entièrement gelée ne correspond pas aux traces géologiques laissées par la glaciation, une sédimentation très variée, tant spatialement que temporellement. Les dépôts glaciaires montrent, sans équivoque possible, des avancées et des reculs répétés des glaciers continentaux, suggérant un cycle hydrologique actif alors que l'arrêt de l'altération chimique des silicates suppose un cycle hydrologique en sommeil.

Ainsi la formation de Wilsonbreen (Svalbard) d'âge Marinoen (650-635Ma) révèle une succession sédimentaire caractéristique d'un environnement glaciaire où s'intercalent régulièrement des niveaux typiques d'environnements lacustres et fluviatiles suggérant la présence d'eau libre associée à des épisodes de réchauffement au cours de la glaciation globale (Benn et al. 2015). Ces variations environnementales sont supposées être causées par des avancées/retraits successifs des glaces à la manière des cycles glaciaires-interglaciaires du Quaternaire. En association à ces observations sédimentologiques, des valeurs très négatives de $\Delta^{17}O$ sont également mesurées dans les carbonates. Ce proxy suggère donc une pCO_2 atmosphérique élevée et constante (entre 35 et 350 fois la valeur de CO_2 actuelle, soit entre 9 et 100mbar de pCO_2) durant la période de dépôt.

Cette inadéquation, entre théorie et observations sédimentaires, fût souvent évoquée comme preuve de l'impossible existence d'épisodes de glaciation globale.

2.2.2 Une Terre froide mais dynamique à sa surface !

- Article : Benn D. Le Hir G., Bao H., Donnadieu Y, Dumas C., Fleming E.J., Hambrey M., McMillan E., Petronis M., Ramstein G., Stevenson C., Wynn P., Fairchild I. *Orbitally forced ice sheet fluctuations during the Marinoan Snowball Earth glaciations*. Nature Geoscience, vol.8, p704-707,2015, doi:10.1038/ngeo2502

Dans cette étude, nous avons démontré que ces observations de terrain sont en réalité entièrement compatibles avec la théorie de la Terre boule de neige. Ce résultat, basé sur l'étude de la formation glaciaire de Wilsonbreen, est le résultat d'une collaboration internationale initiée par D. Benn et I. Fairchild, associant sédimentologues, géochimistes mais aussi une équipe française de modélisation du climat, dont j'étais responsable.

Comment expliquer ces observations ? La grande difficulté de cet exercice est que le climat d'une Terre *blanche* est désespérément stable. Globalement l'albédo de surface, très élevé, contrôle la température, qui ne fait que lentement s'accroître sous l'influence de la lente accumulation (>1Ma) du CO_2. Dans ces conditions, nous avons testé le seul facteur agissant à des échelles suffisamment courtes pour expliquer les traces sédimentaires, à savoir les paramètres orbitaux (temps caractéristiques : de 10 à 100 kans). A ces échelles de temps, considérer la cryosphère comme invariante n'est pas correcte. Nous avons donc développé un couplage entre un modèle de climat (LMDz, Hourdin et al. 2006) et un modèle de glace (GRISLI, Ritz et al. 2001). ***L'originalité de ce couplage est d'être synchrone,*** cad que si la glace se forme, alors le climat est recalculé en fonction de ce nouveau glacier (effets d'albédo, topographie, …). ***L'avantage de cette approche réside dans sa prise en compte de la rétroaction climat-cryosphère*** *(c'est à dire la prise en compte des effets du climat sur la cryosphère et inversement [3)].*

La modélisation en 3D des interactions climat-dynamique des glaces révèlent que, sur une Terre entièrement gelée et en présence d'une importante quantité de CO_2 dans l'atmosphère, les tropiques deviennent sensibles à une saisonnalité plus marquée causée par de faibles variations d'ensoleillement. Dans ces conditions, les températures diurnes sont proches de l'isotherme 0°C durant l'été et le cycle hydrologique devient suffisamment réactif aux basses latitudes pour que le forçage orbital induit par le couple excentricité/précession permette la fonte des glaciers dans la zone de maximum d'insolation. Ainsi à la différence de la recherche du climat global d'équilibre (approche climat-carbone – thème 1), ici nous explorons l'importance des échelles courtes (< année, cad les effets saisonniers) dans les hystérésis du climat.

3 Toute les études précédentes (même sur le Cénozoïque) ne considèrent pas ces interactions. Le plus souvent si les conditions climatiques font qu'un glacier se forme alors ce dernier n'affecte pas le climat en retour.

Dans le détail, pour l'hémisphère où l'été intervient à l'aphélie (distance Terre-Soleil la plus grande - le 4 Juillet actuellement), l'insolation estivale – minimale dans cette configuration orbitale - favorise la croissance des glaciers du fait d'une ablation moins intense (**figure 16**). A l'opposé pour l'hémisphère où l'été intervient au périhélie (le 3 janvier actuellement), l'insolation estivale - plus forte - favorise la fonte des glaciers du fait d'une ablation plus intense que l'accumulation. A noter que cet effet est très similaire au processus avancé par M. Milankovitch dans sa théorie astronomique des climats, où l'ablation estivale est le principal facteur de l'évolution à la baisse/hausse du bilan de masse des glaciers. Toutefois à l'inverse des cycles glaciaires/interglaciaires du Quaternaire, où l'isotherme 0°C se situe entre les moyennes et les hautes latitudes, ici cette limite oscille dans la zone tropicale au gré de l'insolation maximale. Notre étude démontre donc que les avancées/retraits des glaciers continentaux sont en réalité une conséquence attendue de la Terre boule de neige et non une anomalie de la théorie.

En résumé, cette étude a permis de dresser un scénario plus nuancé de la Terre boule de neige. Si la pCO_2 atmosphérique est trop faible (<35 fois la valeur de CO_2 actuelle, ~0,01bar), ses successions d'avancées/retraits des glaciers tropicaux ne peuvent pas se dérouler car la température de l'air est trop basse et l'ablation estivale demeure négligeable. A contrario lorsque la pCO_2 atmosphérique atteint de très hautes valeurs (> 170 fois la valeur de CO_2 actuelle, ~0,05bar), le faible albédo des zones déglacées empêche toute nouvelle accumulation de neige pérenne, la déglaciation de la calotte continentale devient irréversible. Entre ces deux limites, la Terre boule de se situe dans une zone transitionnelle (Goldilocks[4] zone), les zones soumises au maximum d'insolation deviennent trop chaudes pour rester gelées (recul des glaciers) mais redeviennent à nouveau froides lors du minimum d'insolation pour permettre à la glace de se former (avancée des glaciers). Les valeurs de pCO_2 nous indiquent que cette période de transition n'existe que vers la fin de la période glaciaire du fait de la lente accumulation du CO_2 volcanique.

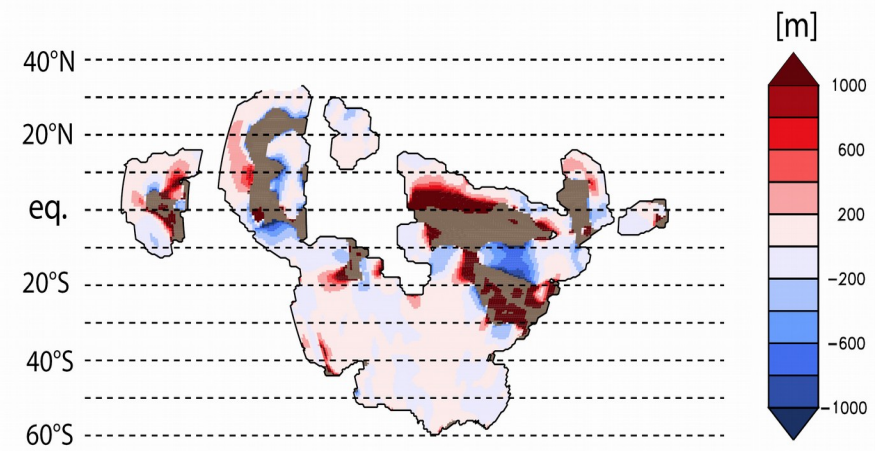

Figure 16. variation de l'épaisseur de glace continentale causée par le forçage orbital en 10kans (soit la 1/2 période de précession) pour une pCO_2 atmosphérique de 20mbars et une excentricité de 0,06. Le trait noir délimite le contour du supercontinent Rodinia. Les zones marron indiquent les zones continentales libres de glace. Les mesures paléomagnétiques placent le craton du Svalbard en zone tropicale vers ~20°S.

Ce résultat nous indique également qu'une Terre entièrement gelée n'est pas un système figé et les conditions environnementales, bien que très rudes, ne sont pas aussi extrêmes qu'envisagées. Mais surtout en dessinant un visage plus « clément » de la Terre boule de neige (du moins lors de la période chaude - cad la période où le CO_2 est déjà accumulé), cet état climatique apparaît moins singulier.

4 *en référence à l'histoire de boucle d'or et des 3 ours*

En effet, une Terre entièrement gelée est une Terre où les flux continents-océans sont coupés et où la seule régulation du cycle du carbone est l'interaction océan-lithosphère (altération des basaltes océaniques – Le Hir et al. 2009) ce qui diffère des stades climatiques standards (greenhouse et icehouse). De l'existence de ces surfaces équatoriales libres de glaces, découlent des échanges océans/continents permettant une régulation continentale du cycle du carbone – suggérant donc une régulation minimum du climat. Il devient possible d'en étudier les limites minimales et d'en extrapoler les conséquences. La section suivante présente les effets directs de la survivance des interactions climat-cycle du carbone-cryosphère.

PERSPECTIVE

III. 60Ma dans un état glaciaire généralisé, est-ce possible ?

La durée des glaciations du type terre boule de neige est un élément déterminant car seules des glaciations prolongées peuvent expliquer la réapparition des niveaux de fer rubanés après 1Ga d'absence, la présence de carbonates dans la continuité immédiate des dépôts glaciaires et l'anomalie négative de $\delta^{13}C$ de ces mêmes carbonates.

En 1998, Hoffman et collaborateurs estimèrent, sur la base d'un modèle thermique de subsidence, que l'excursion du $\delta^{13}C$ indiquait une durée de glaciation ~9Ma (Hoffman et al., 1998). En 1999, Jacobsen et Kaufman évaluèrent, sur la base du temps de résidence du $^{87}Sr/^{86}Sr$ enregistré dans les carbonates pré et post glaciaires, que les glaciations étaient très courtes - entre 0,35 et 1Ma. Cependant, ils négligèrent un processus très influent, à savoir la source de $^{87}Sr/^{86}Sr$ fournie par la possible dissolution des carbonates durant la glaciation. Entre 1999 et 2005, de nombreuses datations radiochronologiques U-Pb sur les zircons ont permis d'affiner la durée des glaciations Néoprotérozoïque. Zhou et al. (2004) et Condon et al. (2005) ont ainsi borné la durée maximale de la glaciation Marinoenne à 33Ma (entre 635 +/- 1Ma et 663+/- 5Ma). En 2005, une avancée majeure est venue de l'étude des platinoïdes extraterrestres contenus à la limite dépôts glaciaires/carbonates post-glaciaires du Craton Congolais (Bodiselitsch et al., 2005). Une forte anomalie en Iridium (Ir) y fût détectée. La répétition de ces anomalies d'Ir, en l'absence d'astroblèmes, suggéra que l'origine de cet enrichissement était la présence d'une banquise sur laquelle se serait accumulée la poussière extraterrestre pendant des millions d'années. Cet argument implique que la durée d'accumulation de l'Ir égale la durée de la glaciation. Sur la base du flux moyen des 80 derniers millions d'années, ils estimèrent la durée d'accumulation d'Ir à 12Ma +/- 4Ma. L'incertitude sur le flux cosmique élargit la barre d'erreur entre 3 et 40Ma.

Jusqu'en 2012, la durée de ces deux épisodes glaciaires demeurait donc peu contrainte ~ 10Ma avec une forte incertitude (0,35 à 30Ma). Puis, en 2013, un apport important fut donné par Rooney et collaborateurs qui, en datant les multiples niveaux glaciaires (ou associés) par la méthode U/Pb sur zircons, ont estimé la durée de la glaciation Sturtienne à ~ 60Ma (732.9 – 662.4 +/- 3.9Ma). Sur la base de ces résultats, il faut donc supposer que les événements glaciaires globaux sont extrêmement longs, leur durée pouvant atteindre la durée du Cénozoïque !

Cependant supposer de telles durées pour des événements glaciaires globaux a de nombreuses répercussions. En effet la pCO_2 associée à la fonte de la Terre boule de neige est directement dépendante de la durée de la glaciation. A terme, la lente accumulation du CO_2 volcanique génère un très puissant effet de serre qui conduit à une fonte brutale et irréversible des glaces de l'équateur aux pôles. En 2004, R. Pierrehumbert estima la valeur de CO_2 nécessaire pour enclencher la déglaciation à 290 mb (~ 1000 fois la pCO_2 pré-industrielle). Le dégazage volcanique aérien avoisinant ~5.4 10^{12} mol CO_2/an (Williams et al., 1992), 10Ma d'années seraient nécessaires pour atteindre le seuil de 290 mb si l'atmosphère était complètement isolée de l'océan. En 2008, Le Hir et al, ont démontré qu'en réalité une très faible surface (<3000km²) entre l'océan et l'atmosphère suffisait pour assurer une dissolution efficace des gaz atmosphériques dans l'océan. Dans ces conditions, plus de 30Ma seraient nécessaires pour atteindre les 290 mb de CO_2. Cette très bonne concordance entre la durée des glaciations estimée par les mesures radiochronologiques et le comportement du cycle du carbone est restée valable jusqu'en 2015.

L'incohérence entre ces deux conclusions émergea en 2015, lorsque Benn et co-auteurs précisèrent le mécanisme de la déglaciation. Ils montrèrent que la déglaciation débutait à des niveaux de CO_2 bien plus faibles (5-10 fois moindre, ~0,02-0,05bar). Plus surprenant encore, la déglaciation des continents débutait sans doute progressivement pour s'accélérer. Ce résultat pose un problème majeur car une pCO_2 de 50mbars comme seuil de déglaciation serait atteinte en 3Ma, 5 à 10 fois moins que la durée estimée par la géochronologie ! Pire la seconde glaciation globale, la glaciation Marinoenne semble bien plus courte (<10Ma).

Ces résultats soulèvent une question essentielle : (1) ***Est-il possible de maintenir la Terre dans un état glaciaire aussi longtemps (>60Ma) et si oui sous quelles conditions ?*** Résoudre cette question permettra également de déterminer ***comment se déroule la déglaciation*** et la vitesse de cet événement. (2) ***Comment ces deux événements*** *en apparence identique (glaciation Sturtienne et Marinoenne)* ***peuvent-ils avoir des durées si différentes ? (3)*** La réponse à ces points nous permettra également de déterminer ***quelles sont les contraintes environnementales*** induites par les glaciations prolongées et donc celles de la déglaciation (voir perspectives p54).

Stratégie

La première étape de ce projet consiste à simuler le cycle du carbone durant la phase glaciaire. Mais contrairement aux autres études qui supposait une altération à l'arrêt, le but de cette étape consiste à modéliser explicitement le cycle du carbone synglaciaire. Répondre à ce problème nécessite le développement de multiples couplages entre différents types de modèles : un modèle de climat couplé à une modèle de calotte de glace (à la manière de Benn et al. 2015) qui serait couplé à un modèle d'altération chimique des sols. La matrice de résultats du couplage de ces 3 modèles servirait à forcer un modèle de cycle du carbone dans lequel l'altération des silicates de la lithosphère océanique est explicitement implémentée. A l'heure actuelle, le modèle de glace (GRISLI, Riss et al, 2001), du cycle du carbone (COMBINE, Goddéris et Joachimski, 2004) et d'altération chimique des sols (WITCH, Goddéris et al, 2006) existent, et deux couplages sur les trois nécessaires ont été réalisés (Le Hir et al. 2009). Reste comme actuelle incertitude le modèle de climat 3D qui permettra de simuler, avec le plus de degré de liberté possible, le climat glaciaire. Le meilleur prétendant à cette fonction est le modèle LMDz (Hourdin et al, 2006), modèle ayant l'avantage d'avoir une physique et une dynamique de l'atmosphère d'une grande qualité, tout en offrant la possibilité de représenter l'océan par une couche de mélange océanique incluant le transport d'Ekman. Cette version développée par F. Codron (Pr. au LOCEAN) est actuellement en cours d'installation sur le calculateur national (IRENE, http://www.genci.fr/fr).

Une fois cette première étape franchie, il sera possible de calculer l'évolution de la pCO_2 atmosphérique durant la phase glaciaire ainsi que la chimie de l'océan. Si les sources ne varient pas, ce flux d'altération glaciaire peut être également contrait par le rapport $^{87}Sr/^{86}Sr$ publié par Jacobsen et Kaufman (1999). Il sera dés lors possible de proposer une relation durée de glaciation versus le seuil de déglaciation en CO_2.

En parallèle de ce volet purement modélisation, je souhaite également intégrer une application géochimique afin de rendre l'utilisation du signal de $\Delta^{17}O$ plus performant comme proxy de la paléopCO_2. A l'heure actuelle, la principale incertitude de ce proxy pour ces périodes réside dans les valeurs de $\Delta^{17}O$ et dans la difficulté de contraindre la droite de régression entre le $\delta^{18}O$ et le $\Delta^{17}O$. Actuellement le $\Delta^{17}O$ reste difficilement exploitable car l'utilisation du signal en $\delta^{18}O$ des calottes actuelles n'est pas transposable aux calottes équatoriales de la Terre boule de neige. Par exemple, le signal en $\Delta^{17}O$ mesuré dans les carbonates péri-glaciaires de la formation de Wilsonbreen (Svalbard) est compatible avec une paléo-pCO_2 allant de 35 et 350 fois la pCO_2 actuelle.

Ce problème est en passe d'être résolu en simulant les valeurs le rapport $^{18}O/^{16}O$ des inlandsis formés aux basses latitudes et dans des volumes d'une ampleur non connue sur le Phanérozoïque. Ces simulations seront réalisées avec une version de LMDz intégrant les isotopes de l'oxygène, simulations qui auront pour but de contraindre le $\delta^{18}O$ des calottes, et donc des eaux de fontes issues des glaciers, valeurs nécessaires pour contraindre le cycle isotopique de l'oxygène et donc la paléo-pCO_2.

EXPOSE SYNTHÉTIQUE DES RECHERCHES :

THÈME 3: De L'importance d'une régulation biologique

Le passage du 18ème au 19ème siècle marqua un tournant dans l'histoire des Sciences Naturelles. La naissance de la collecte scientifique minutieuse à l'échelle mondiale à travers des explorations devenues célèbres (Von Humbolt, D'Orbigny, Wallace, Darwin) permirent, en quelques décennies, l'élaboration de théories scientifiques majeures (la théorie de l'évolution notamment). Parmi ces grands scientifiques, nous devons à Alcide ***d'Orbigny*** *(1802-1857)*, élève de ***G. Cuvier*** *(1769-1832)*, d'étudier aujourd'hui encore l'histoire de la Terre à travers l'histoire du Vivant. Grand naturaliste, **D'Orbigny** ***signa l'acte de naissance de la biostratigraphie***. De part son exceptionnelle connaissance de l'anatomie comparée et influencé par la théorie du catastrophisme de son mentor G. Cuvier, d'Orbigny délimita chaque tranche de temps géologique (ou étage défini par un *stratotype*) comme la co-existence d'espèces (ou faune fossile), chaque période débutant par la disparition de la faune précédente lors d'une catastrophe.

Suivant cette approche, Sepkovski (1978) caractérisa à l'aide des fossiles d'invertébrés marins, les plus grandes ruptures de diversité, connues comme les *« Big Five »* : crise fini-Ordovicien (443Ma), Frasnien-Famennien (372Ma), Permo-Trias (252Ma), Trias-Jurassique (200Ma) et Crétacé-Paléogène (66Ma). Paradoxalement si nos connaissances des faunes passées (paléontologie ou paléobiologie) se sont considérablement accrues (Sepkovski 1978, 1979, 1984, Raup and Sepkovski 1982, http://paleodb.org), notre compréhension des interactions entre la biodiversité et l'environnement reste très rudimentaire. Aujourd'hui encore, lorsque nous étudions l'enregistrement paléontologique, bien souvent seul l'impact d'une perturbation environnementale est considéré et la plupart du temps via des corrélations directes.

L'objectif de cette partie est de montrer que la biosphère ne répond pas « passivement » aux perturbations. En effet, cette vision issue d'une approche focalisée sur la biodiversité oublie la composante biomasse de la biosphère. Ainsi une part importante de ce travail, débutée voilà 6 années, est d'introduire la totalité de la biosphère (biomasse + biodiversité) dans cette « équation ». Sans verser dans la théorie de Gaia (Lovelock et Margulis 1974), cette partie - encore très exploratoire - s'attachera à exprimer les relations complexes de la biosphère avec son environnement.

L'intégration de la biosphère dans les modèles n'a pas débuté nos travaux. En effet les organismes étant un stock transitoire de carbone organique, toute modulation rapide de ce stock modifie les équilibres inorganiques présentés dans les sections 1 et 2. De ce fait la biosphère a été très tôt intégrée dans les modèles biogéochimiques mais de manière rudimentaire. Afin de bien illustrer l'apport de ces travaux, voici une rapide présentation des simplifications utilisées jusqu'à présent.

BILAN : comment modéliser la dynamique du Vivant?

I. Comment les modèles intègrent-ils la biosphère ?

Le carbone actuel étant à plus de 98% contenu dans l'océan, les modèles qui calculent les cycles biogéochimiques à long-terme n'intègrent pas la biosphère continentale. Le déséquilibre du stock de carbone océanique face au contenu en carbone de l'atmosphère implique que la pCO_2 soit directement dépendante de l'équilibre chimique océan/atmosphère (fig. 17). Le temps de résidence du carbone dans l'atmosphère, via ses échanges avec l'océan, étant très bref (~8,5 ans), les teneurs en carbone atmosphérique et océanique sont nécessairement contrôlées par un mécanisme extrêmement efficace sans quoi l'habitabilité de la Terre ne pourrait être maintenue.

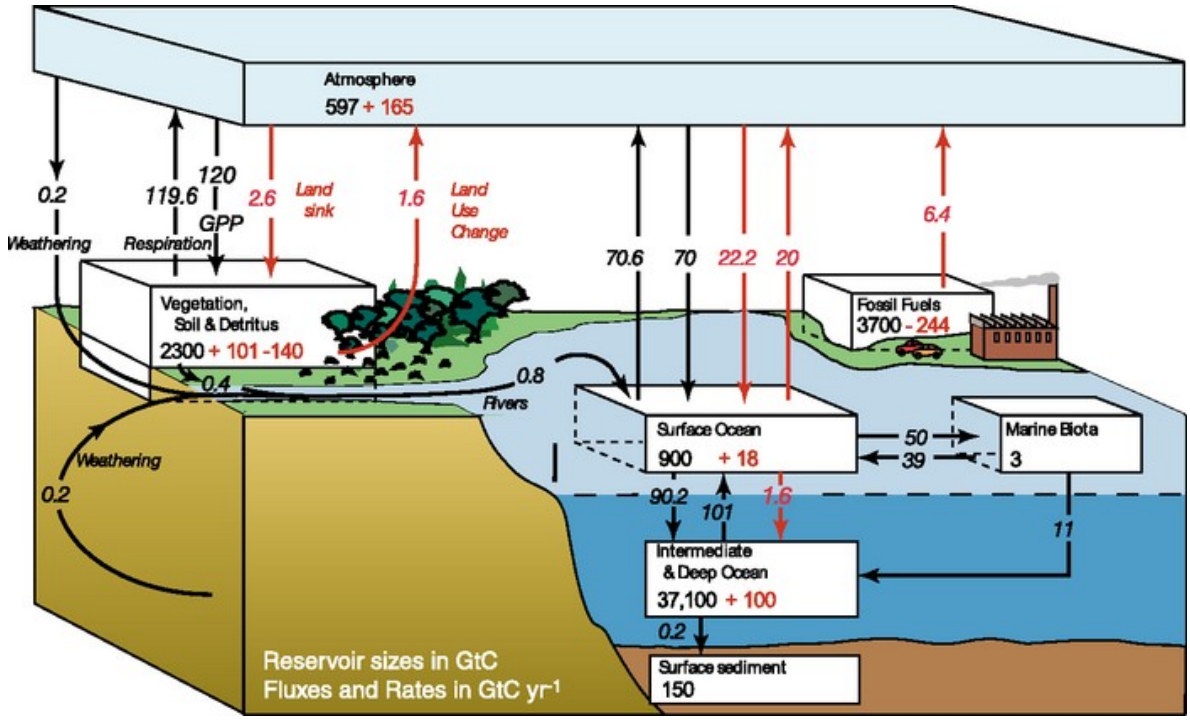

Figure **17**. En noir les flux et stocks naturels de carbone, en rouge ceux liés aux activités humaines. Temps caractéristique des échanges océan/atmosphère pour l'atmosphère (pré-anthropocène = 567/70 ~8.5ans) Source : rapport du GIEC (https://www.ipcc.ch/publications_and_data/ar4/wg1/en/ch7s7-3.html)

En 1981, Walker et collaborateurs (voir partie 1) ont démontré que l'altération chimique des silicates était le mécanisme de rétro-contrôle, processus inféodé au climat par sa dépendance à la température et au ruissellement, donc in fine à l'effet de serre et donc à la teneur de CO_2. Ce processus est lui-même modulé par la tectonique (Goddéris et al. 2014), la lithologie (Dessert et al. 2003) et le couvert végétal (Berner 2004). Mais ***cette régulation ne peut pas être exclusivement inorganique car 25 à 30 % du carbone émis par les volcans est substitué*** (fig.17) ***sous forme de carbone organique*** (Berner, 2004; Katz et al., 2005) ***par la biosphère.***

Le mécanisme qui « substitue » le carbone sous forme organique (cad un carbone réduit par l'action biologique ou C_{org}) est l'enfouissement de la matière organique sur les fonds océaniques (côtier comme profond). La quantité de C_{org} ainsi préservée dépend de la combinaison entre la productivité primaire (à 95 % issu de la photosynthèse oxygénique) et de l'efficacité de l'enfouissement du C_{org}. L'équation bilan résumant ces effets (fig. 18) montre que la préservation de la matière organique est à la fois une source de O_2 et un puits de CO_2.

$$C_{org} + O_2 \rightarrow CO_2 + H_2O + \text{énergie} \quad \text{(oxydation de la matière organique ou } C_{org})$$

Figure 18

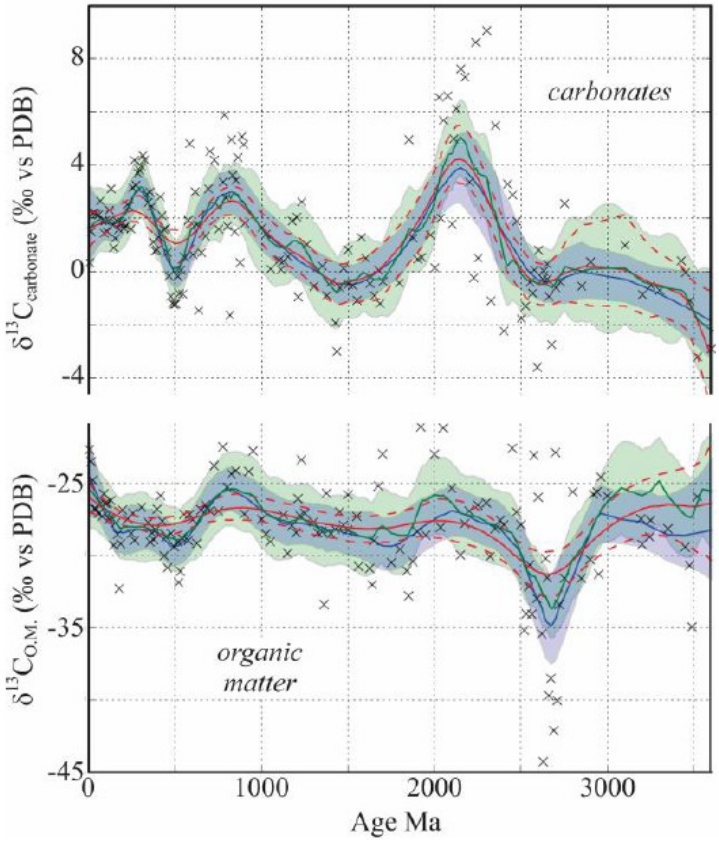

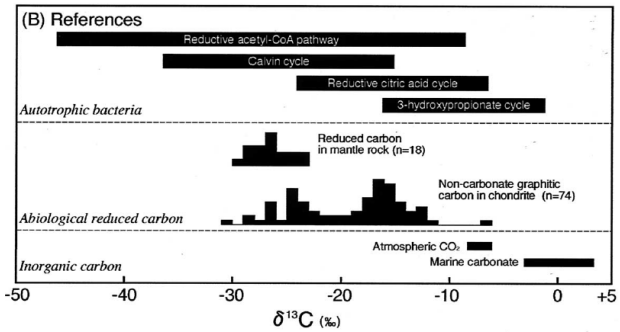

gauche : dispersion des valeurs du $\delta^{13}C_{carbonates}$ et $\delta^{13}C_{org}$ mesurés depuis 3.5Ga. (Krissansen-Totten et al., 2015), droite : dispersion du $\delta^{13}C_{org}$ des différents réservoirs (Ueno et al. 2004)

$$\delta^{13}C = \left(\frac{\left(\frac{^{13}C}{^{12}C}\right)_{sample} - \left(\frac{^{13}C}{^{12}C}\right)_{standard}}{\left(\frac{^{13}C}{^{12}C}\right)_{standard}} \right) * 1000$$

standard PDB : rostre béleminte (en $CaCO_3$) de la formation Pee Dee du Crétacé
Rapport ^{13}C /^{12}C du standard PDB = 0.011238
^{12}C = 98.885 %; ^{13}C = 1.1024 %; $^{14}C = 10^{-10}$ %

$$\delta^{13}C_{volc} = \delta^{13}C_{carbonates}(1-f) + \delta^{13}C_{org}(f) \quad \text{(équation du bilan de masse isotopique)}$$

En supposant que l'unique source de carbone est le volcanisme ($\delta^{13}C_{volc}$ = -5‰) et que le puits organique de carbone a un $\delta^{13}C_{org}$ = -25‰, alors l'inversion du signal du $\delta^{13}C_{carbonates}$ indique la valeur de f. Ainsi si $\delta^{13}C_{carbonates}$ = 0 ‰, alors f=0.2 (cad que 20 % du carbone émis par les volcans est substitué par l'enfouissement du C_{org})

Plus intéressant, en mesurant le $\delta^{13}C$ des carbonates océaniques il devient possible de connaître le ratio de carbone consommé par l'enfouissement du C_{org} / altération des silicates grâce au bilan de masse isotopique du carbone. En effet, en inversant le $\delta^{13}C_{carbonates}$, il est théoriquement possible d'estimer *f,* et donc le flux de CO_2 émis et d'O_2 consommé par le cycle organique du carbone.

Ce formalisme fut utilisé par Kump (1991) pour comprendre l'océan Strangelove de la limite K-Pg (66Ma). L'océan de cette période présente une absence de gradient du $\delta^{13}C_{carbonates}$ entre les zones pélagique et benthique, homogénéisation isotopique supposée due à une production primaire quasi-nulle. La très bonne corrélation entre le $\delta^{13}C_{carbonates}$ modélisé et celui mesuré (fig. 19) suggère que **du point de vue géochimique, réduire la biosphère à sa biomasse semble correcte**.

Cette approche est celle privilégiée dans le modèle GEOCARB développé par Berner (Berner, 2004; Bergman et al., 2004; Li and Eldefield, 2013).

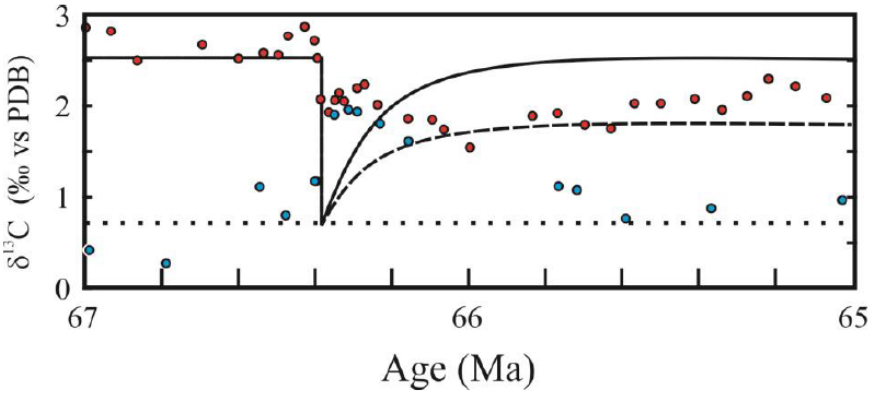

Figure 19 $\delta^{13}C_{carbonates}$ calculés versus $\delta^{13}C_{carbonates}$ mesurés (points, rouge pour les foraminifères pélagiques, et en bleu pour les benthiques) lors de la crise K-Pg (66Ma). (Zachos et al., 1999 Kump 2001).

Conceptuellement cette approche implique que le $\delta^{13}C_{carbonates}$ dépend d'un taux d'enfouissement de C_{org} qui varie (pour correspondre au $\delta^{13}C_{carbonates}$ mesuré) mais sans en connaître les processus responsables. Pour corriger cette limitation, les modèles biogéochimiques actuels calculent la composition isotopique des carbonates en fonction d'un $\delta^{13}C_{org}$ (qui reste fixé car issu de la photosynthèse prinicipalement) et d'une quantité de C_{org} enfouis explicitement dépendant de la productivité et de la teneur en O_2 dissout (GEOCLIM, Goddéris et al., 2014; GENIE, Ridgwell et al., 2007). Tout écart entre la modélisation et le $\delta^{13}C_{carbonates}$ mesuré est aujourd'hui attribué à la simplification des processus (exemple la mauvaise représentation de la limitation en phosphore de l'océan tant spatiale que temporelle, diagenèse simplifiée à l'extrême, altération des carbonates continentaux…).

Toutefois ce formalisme est lui aussi biaisé. En procédant ainsi le calcul du bilan de masse suppose que la biosphère ne dépend que des nutriments, et que donc les conditions environnementales ne l'influence qu'au mieux transitoirement en réduisant la quantité de nutriments disponibles. En d'autres termes la biosphère depuis 3.8Ga doit avoir les mêmes caractéristiques générales ; les grandes crises ne modifiant pas ces propriétés.

Cette hypothèse mérite d'être explorée compte tenu de ses implications tant biologiques, géochimiques que climatiques. En effet, le registre géologique nous montre une évolution irréversible des organismes et une réponse très variable bien que les perturbations soient en apparence assez semblables (événements volcaniques majeurs par exemple, Courtillot et Rennes, 2003). Ainsi, si nous souhaitons participer au débat débuté au 18ème siècle quant à l'origine des *« révolutions du Globe »* de Cuvier et plus globalement avancé dans la connaissance des liens entre le Vivant et de son Habitat, la dynamique du vivant doit être prise en compte dans l'équation.

Nos avancées sur cette question sont présentées ci-après à travers deux études fondatrices en terme de développement des outils.

II. ... et la Terre fût couverte de végétaux, la révolution du Dévonien

- article. 2011. Le Hir, G., Donnadieu, Y., Goddéris, Y., Meyer-Berthaud, B., Ramstein, G., Blakey, R., The climate change caused by the land plant invasion in the Devonian, Earth and Planetary Science Letters, vol. 310, p:203-212, doi:10.1016/j.epsl.2011.08.042

- projet ANR (blanc) ACCRO-Earth (Accidents in Climate Carbon cycle Regulation Of Earth, dirigé par G. Ramstein, 2008-2012)

Cent millions d'années après la glaciation fini-Ordovicienne, la Terre connaît un nouvel épisode froid, le second du Paléozoïque. Cette période glaciaire sera la plus longue et la plus intense du Phanérozoïque (fig.8) et durera tout au long du Carbonifère (360-300Ma). Si cet épisode glaciaire est étroitement lié à l'orogène Varisque (Goddéris et al. 2017), cette transition d'un monde chaud vers un monde froid a connu un prélude, celui de la mise en place des plantes terrestres.

Les premiers indices de la colonisation des continents par les plantes remontent à la période Ordovicienne (spores microscopique ~475 Ma), mais ce n'est que durant le Dévonien (416 à 359 Ma) que les plantes terrestres sont devenues suffisamment abondantes et diversifiées pour changer les déserts continentaux en paysages couverts de végétation, conditions propices à l'évolution d'une vie terrestre riche et complexe (Algeo and Scheckler, 1998). Cet événement de diversification a été comparé à l'« Explosion Cambrienne » en termes d'intensité et d'impact sur la biodiversité (fig. 20).

En parallèle de la colonisation des continents par les plantes, le passage du Dévonien moyen au supérieur montre une disparition des spores d'espèces inféodés aux régions subpolaires, un $\delta^{18}O$ des carbonates qui augmente, signe d'un réchauffement, et un gradient latitudinal de température « plat ». Paradoxalement, l'inversion du signal du $\delta^{13}C$ par GEOCARBIII ou GEOCARBSULF simulent une baisse du CO_2, prélude à l'ère glaciaire du Carbonifère (Van Geldern et al., 2006).

Le Dévonien supérieur est donc une période singulière où données et modélisation semblent contradictoire, les premières suggérant un réchauffement, là où les seconds indiquent une baisse de l'effet de serre.

On suspecte depuis une vingtaines d'années que la colonisation des continents par les végétaux puissent avoir des conséquences importantes sur le cycle global du carbone, et donc sur le climat (Berner, 1997). Les première études se sont focalisées sur l'impact du développement du système racinaire sur l'altération chimique dans les sols (Algeo and Scheckler, 1998; Beerling and Berner, 2005; Berner, 2004). Selon ces études la présence d'un couvert végétal augmenterait fortement l'altération des continents (jusqu'à un facteur 10)(Bormann et al., 1998; Moulton and Berner, 1998). C'est donc ce facteur d'altérabilité des surfaces continentales combiné au signal de $\delta^{13}C$ qui conduit le modèle GEOCARBIII a simulé une baisse de CO_2 à la fin du Dévonien (fig.14) (Berner, 2004). Cependant les plantes modifient également les propriétés de surface des continents : albédo, évapotranspiration, rugosité. Jusqu'en 2011, aucune étude n'avait été menée sur les effets liés à ces modifications, conséquence de la colonisation des continents par les plantes. Cette étude a été réalisée en collaboration avec B. Meyer-Berthaud, paléobotaniste à l'AMAP (botAnique et bioinforMatique de l'Architecture des Plantes) de Montpellier – notamment le travail de comparaison des flores fossiles et actuelles.

Afin d'explorer les interactions entre la végétation et le système climat-carbone, j'ai utilisé le modèle de climat-carbone GEOCLIM, auquel j'ai couplé un modèle de végétation développé pour l'occasion (SLAVE-Jr, un dérivé du modèle SLAVE, Friedlingstein et al., 1992). Ce couplage a permis de reconstruire l'évolution simultanée de la végétation, du cycle global du carbone et du climat durant le Dévonien. Pour tenir compte des données fossiles, trois types de végétation ont été pris en compte : i) des communautés de plantes primitives rasantes ou peu élevées, seules présentes au début du Dévonien, ii) des forêts de fougères arborescentes, apparues au Dévonien moyen et iii) des forêts d'arbres architecturalement proches des conifères modernes, apparus au Dévonien supérieur. Les caractéristiques biophysiques de ces plantes aujourd'hui éteintes ont été déduites d'analogues modernes présentant des caractéristiques biologiques les plus proches possibles et permises via une collaboration étroite avec les paléo-botanistes (B. Meyer-Berthaud)

Quatre intervalles de temps ont été explorés 1) la phase anté-colonisation (simulation No-Land-Plants, puis les 3 phases de cette colonisation depuis la base du Dévonien (LP1 puis LP2) jusqu'au Dévonien Supérieur (LP3). Les trois premières simulations correspondent à la reconstruction géographique à 400 Ma, la quatrième correspond à 370 Ma (fig.14). Les simulations No-LP et LP1 montrent l'évolution d'un monde sans plante vers un monde couvert sporadiquement par des plantes ne dépassante pas les 0.5-1 mètre (Prêles et associés). LP2 simule l'apparition des fougères arborescentes. Pour chaque simulation, la distribution spatiale des plantes est fonction de la température et de la quantité d'eau présente dans les sols. Les fougères ont par exemple des conditions de vie plus restrictives en terme de besoin en eau que les premières plantes (type Presles). LP3 simule l'apparition des *paléo-arbres* (Archeopteris) et utilise la reconstruction des continents à 370 Ma.

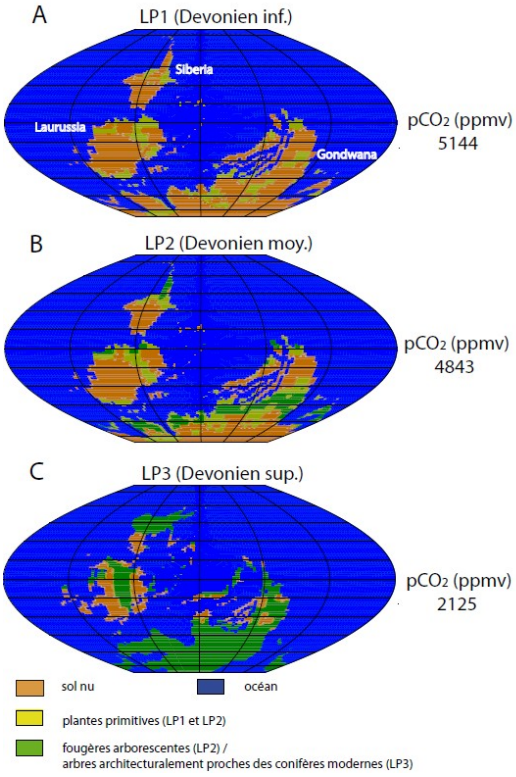

Figure 20 : répartition potentielle de la végétation au Dévonien. Les cartes montrent la répartition potentielle maximale de trois grandes périodes du Dévonien. La végétation, le climat et le cycle du carbone sont à l'équilibre.

Au cours du Dévonien, les sols désertiques laissent place à un couvert végétal de plus en plus dense et vert. Cette colonisation végétale est due à la plus faible dépendance des plantes vis-à-vis de l'eau, extension également favorisée par un climat globalement plus humide. Ainsi, en partant des données paléontologiques et d'analogues actuels, les premiers arbres (taxon des

Archeopteris) sont supposés accepter des milieux nettement plus secs que les fougères arborescentes (contenu en eau du sol supérieur à 30 % au lieu de 80 %). Cette évaluation du couvert végétal aurait diminué l'albédo de surface de plus de 10% à l'échelle globale.

D'un point de vue climatique la présence des *paléo-arbres* (Archeopteris) augmente les précipitations (et donc le ruissellement), et induit un réchauffement continental. Le réchauffement résulte de la baisse de l'albédo passant de 0,3 à des valeurs proches de 0,1. L'augmentation des précipitations et du ruissellement sont la conséquence des changements de la rugosité, de l'évapotranspiration mais également de l'albédo.

En réponse à cette baisse d'albédo, la température simulée tend dans un premier temps à augmenter, favorisant une accélération du cycle de l'eau sur le continent. Il en résulte un drainage plus important des sols et une augmentation de la consommation de CO_2 par l'altération continentale.

Après quelques milliers d'années, le modèle du cycle du carbone simule une baisse de 50 % du CO_2 atmosphérique alors que paradoxalement la température globale reste quasiment inchangée. En effet, malgré une chute de 4000 ppmv de la pCO_2 (fig. 21), le modèle simule une température des continents quasi-constante. Une analyse du bilan radiatif montre que la baisse de CO_2 est compensée par la baisse de l'albédo des continents. La rétroaction climat-carbone-végétation permet donc la mise en place d'un mécanisme assez unique dans l'histoire de la Terre où l'évolution de la température continentale est découplée de celle du CO_2.

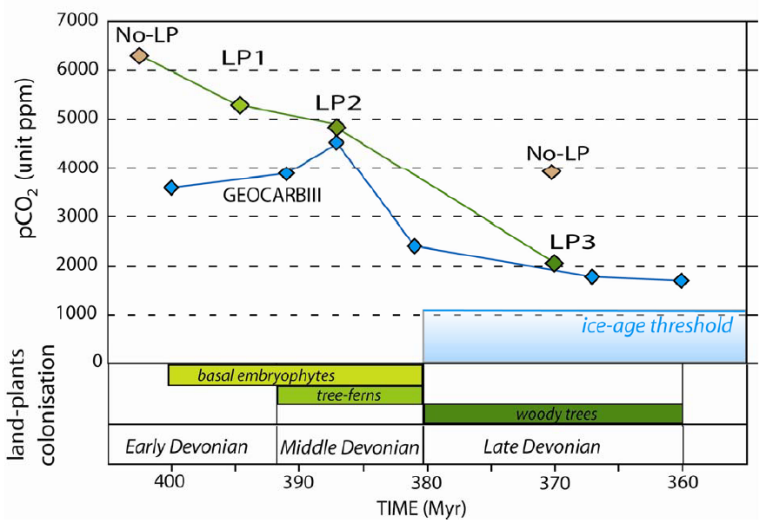

Figure 21 Evolution de la teneur en CO_2 simulée par GEOCLIM. L'effet de la géographie entre le début et la fin du Dévonien apparaît non négligeable avec une baisse du CO_2 de 6000 à 4000 ppm. Cette baisse s'explique par la migration du craton de la Laurussie (Laurentia + Baltica) à travers la zone de convergence intertropicale de 400 à 370 Ma qui va lors induire une augmentation de la consommation de CO_2. La sortie du craton sibérien des tropiques vers les moyennes latitudes induit également une hausse de consommation de CO_2. L'effet des plantes sur la teneur en CO_2 dans l'atmosphère est faible dans un premier temps (LP1 et LP2) mais prend beaucoup plus d'ampleur avec l'apparition des Archeopteris (2000 ppmv de différence entre No-LP pour 370 Ma et LP3).

Conclusion

Comme pour toutes études portant sur des périodes anciennes, de nombreuses incertitudes existent, les valeurs des paramètres bioclimatiques pour les premières plantes sont inconnues. Cependant mêmes des valeurs de premier ordre permettent de conclure que la rétroaction climat-carbone-végétation explique le découplage entre les estimations de température et de pression de CO_2, découplage jusque là resté inexpliqué.

III. Les révolutions du Globe aux extinctions de masse : la construction d'un modèle écosystémique simple couplé au modèle climat-carbone.

- article 2014 Mussard M, **Le Hir G**., Fluteau F., Lefebvre F., Goddéris Y. 2014. Modeling the carbon-sulfate interplays in climate changes related to the emplacement of Continental Flood Basalts., Geological Society of America vol; 505, p339-352, 2014. doi: 10.1130/2014.2505(17).

- projet SYSTER (2014) Modélisation des effets des grandes provinces basaltiques sur l'environnement et la productivité marine

- projet émergeance (2012-2015) (PI M. Bonifacie – IPGP) la reconstruction de la température des océans (le Crétacé)

- projet SYSTER (2016) la crise de la production carbonatée lors de l'extinction K-Pg (66Ma) (co-PI avec B ? Max_Sucheras CEREGE)

- projet SYSTER (2017) couplage des cycles biogéochimiques, du climat et de la biodiversité à l'échelle des temps géologiques (PI Y. Goddéris, GET-Toulouse)

- article 2019 (Le Hir et al.) Amplifying factors leading to the collapse of primary producers during the Chicxulub Impact and Deccan traps, GSA spécial issue

- article 2019 (E. Font et al.). Wildfire, environmental acidification and carbonate saturation overshoot linked to major Deccan eruptions - soumis

- Salomé Hennequin (travaux de thèse) – doctorante au GET, Toulouse (dir. Thèse Y. Goddéris)

Les cinq extinctions majeures du Phanérozoïque (Sepkoski, 1984) correspondent à des crises biologiques globales, courtes (parfois nettement inférieures au million d'années), affectant de nombreux groupes vivants. Chacune de ces extinctions de masse est marqué par une phase d'extinction suivie d'une phase de radiation. Ainsi la crise Permien-Trias (252 Ma) se distingue par une perte de biodiversité comprise entre 80 et 90 % des espèces d'invertébrés marins (Stanley 2016) en moins de 100 000 ans (Burgess et Bowling, 2015 ; Burgess et al. 2017).

Si plusieurs facteurs ont été évoqués comme causes de l'extinction Permien-Trias, la mise en place des trapps de Sibérie constitue aujourd'hui le facteur déclenchant le plus probable (Burgess et al. 2017). A l'opposé de la crise P-Tr, la crise de la limité Crétacé-Paléogène (66Ma) est la moins intense des cinq extinctions alors que la collision d'un astéroïde est survenu pendant la mise en place des traps du Deccan. Il apparaît ainsi que l'ampleur de la crise biologique n'est pas directement proportionnelle à l'intensité des facteurs l'ayant déclenchée. Si plusieurs causes peuvent expliquer cette décorrélation (Ganino et Arndt, 2009), les propriétés intrinsèques de la biosphère ont été jusqu'à aujourd'hui totalement occultées.

Pour explorer cette question, nous avons étudiés 2 crises: i) la crise P-Tr (252Ma) qui est la plus importante en intensité et 2) la crise K-Pg (66Ma), la plus récente et médiatisée mais également la mieux documentée.

3.1 Les effets climatiques – l'importance des pulses volcaniques

Les grandes provinces basaltiques sont connues pour être des événements volcaniques épisodiques, rares, de grande ampleur, sans équivalent récent[5]. L'analyse de la variation séculaire du champ magnétique enregistré par les coulées basaltiques indiquent que la mise en place de la phase paroxysmale est brève (< 1 Ma) et saccadée. Dans le cas des traps du Deccan, il a été estimé que la mise en place de plus de 80% du volume du traps s'est produite en environ 200 kans (Schoene et al. 2015, 2019), et que la moitié de ce volume résulte d'un faible nombre (~30) d'événements éruptifs d'ampleur exceptionnelle («mega-pulses») durant lesquels plusieurs milliers de km^3 (jusqu'à 10^4 km^3) de magma pourraient être émis en moins d'un siècle, voire quelques années (Chenet et al., 2008, 2009).

L'impact du volcanisme subaérien des traps sur l'environnement est classiquement attribué aux émissions massives de CO_2 et plus récemment de SO_2. Self et al (2008) et Chenet et al. (2008) ont estimé que la mise en place des traps du Deccan a injecté ~ 28000 Gt de CO_2 et de ~6800 Gt de SO_2 dans l'atmosphère. Si le gaz carbonique est bien connu comme gaz à effet de serre, les aérosols sulfatés, dérivés des émissions de SO_2, induisent au contraire une baisse des températures de surface. Cependant leur taille importante (~ µm) limite leur temps de résidence dans l'atmosphère. Comme les effets de ces deux composés agissent sur deux échelles de temps différentes (> siècle pour le CO_2, et <10ans pour les aérosols sulfatés), nous avons développé un modèle de dégazage rendant compte de l'aspect irrégulier du dégazage à travers des pulses intenses mais courts ainsi que de l'évolution chimique spécifique des espèces sulfatées.

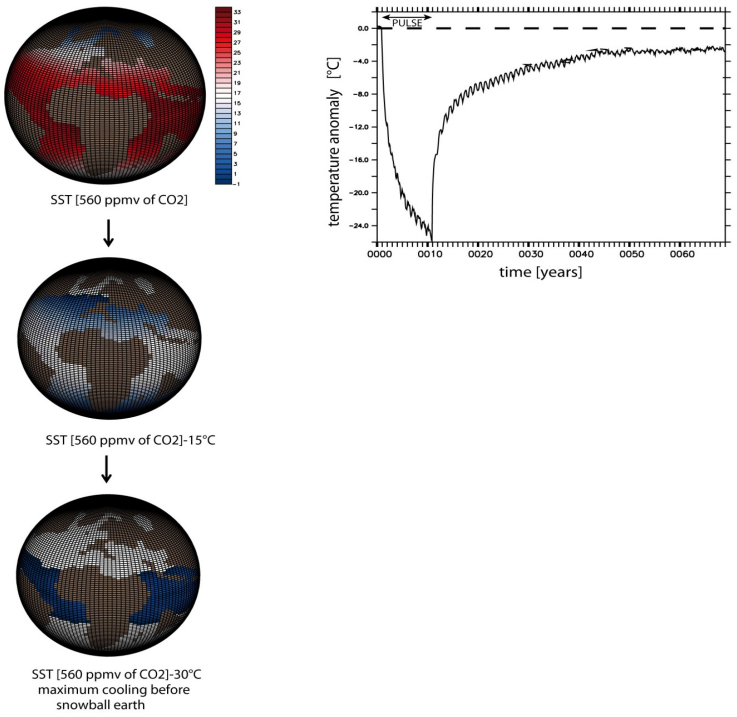

Figure 22 *modélisation d'un pulse froid en réponse à l'augmentation transitoire de dérivés soufrés (flux de 1Gt SO_2/an pendant 10ans) dans l'atmosphère. Ce refroidissement est estimé par des simulations climatiques intégrant la baisse d'ensoleillement en réponse à la présence d'aérosols sulfatés dans l'atmosphère. La température après 50 ans n'est pas revenue à son état initial du fait de la dissolution d'une part du CO_2 dans l'océan. On note ici le développement de la banquise jusqu'aux tropiques (30°). Ce scénario constitue donc le refroidissement maximal supposé, toute baisse de température additionnelle engendrerait un englacement total de la Terre (ce qui n'est pas produit selon les données dont nous disposons).*

En 2014, en considérant un dégazage par pulses (fig. 22), nous avons démontré qu'à long terme ces pics froids ont comme effet contre-intuitif d'accroître l'accumulation de CO_2. En effet comme chaque pulse la source de CO_2 est accrue, et le puits inorganique (altération) ralentie, ces effets combinés conduisent à terme (~ 200 kans) à augmenter la pCO_2 de 15-20 % (fig. 23) (Mussard et al. 2014).

5 même l'énorme taux de lave émis (~1 km^3/an) par le volcan sous marins au large de Mayotte est inférieur

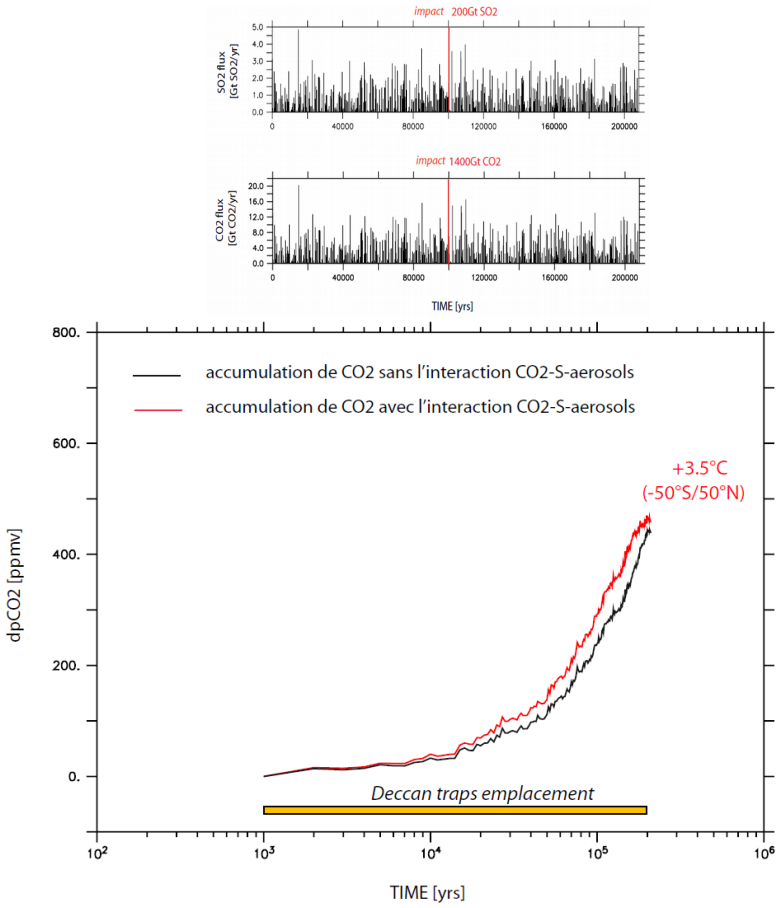

Figure 23. Séquence éruptive des traps du Deccan correspondant à la phase paroxysmale (~ 200 kans, Schoene et al. 2019). Cette séquence a été obtenue en utilisant la variation séculaire du champ magnétique (1an < durée d'un pulse < 100ans) et la quantité de gaz émis comme seuls facteurs forçants. L'impact de Chicxulub est indiqué en rouge
La pCO_2 n'augmente que lentement durant la mise en place du traps du Deccan (Mussard et al. 2014, Dessert et al. 2003, Caldeira and Rampino, 2000), son effet sur l'augmentation des températures est facilement masqué par les refroidissements abrupts causés par les fortes variations de dérivés soufrés. Après la mise en place des traps du Deccan, une fois l'atmosphère lessivée de ses composés soufrés, l'effet du CO_2 se manifeste (réchauffement).

3.2 l'importance des paramètres biologiques dans la compréhension d'une crise

Si le climat connaît des perturbations majeures, le cycle du carbone et plus globalement l'état géochimique de l'océan vont également changer. Ainsi Wignall et Bond (2015) ont proposé que les principales conséquences sur les écosystèmes marins étaient un changement de température ou de pH des eaux (Clarkson et al. 2015). Par conséquent, la biomasse immobilisée au sein de chaque espèce a vraisemblablement changé, modifiant les flux d'enfouissement du carbone dans les sédiments marins.

Pour représenter la distribution non homogène de la biomasse marine, nous avons discrétiser la biomasse en *n* « espèces ». Il est en réalité plus correct de parler de *groupe fonctionnel* car l'identité génétique des groupes n'est pas représentée, seules leurs caractéristiques fonctionnelles le sont. Chaque groupe fonctionnel (FT pour Functional Type) est représenté par un réservoir de carbone. A la différence des Plant Functional Type (PFT), les types fonctionnels ne sont pas exclusifs spatialement, de nombreux FT occupent le même espace (Le Quéré et al., 2005).

Ce réservoir y_i est alimenté par un taux de reproduction α_i et est vidé par un taux de mortalité ω_i (les deux grandeurs étant exprimées en mol C/an) :

$$\frac{dy_i}{dt} = \alpha_i - \omega_i$$

Le taux de reproduction va dépendre d'un nombre important de paramètres. Dans cette étude préparatoire, nous ne considérerons que le pH et la température. Par exemple, pour un producteur primaire et de manière simple, on peut représenter la dépendance à ces paramètres par une gaussienne centrée sur la valeur optimale de chaque paramètre b^i_1 et b^i_2, la tolérance à des changements de température ou de pH étant représentée par la largeur de la gaussienne c^i_1 et c^i_2:

$$\alpha_i = br_i \cdot a_1^i \cdot \exp\left[\frac{-\left(T - b_1^i\right)^2}{2\left(c_1^i\right)^2}\right] \cdot a_2^i \cdot \exp\left[\frac{-\left(pH - b_2^i\right)^2}{2\left(c_2^i\right)^2}\right] \cdot I_i \cdot F_{in}^P$$

Les facteurs a^i_1 et a^i_2 représentent l'efficacité de l'utilisation des nutriments. F^P_{in} est le flux de nutriment (ici le phosphore) disponible pour l'écosystème. Le facteur I_i représente la compétition avec les autres FT j pour l'accès aux ressources. L'originalité consistera à affecter aux paramètres a, b et c des valeurs aléatoires. De même pour le paramètre I : il sera aléatoirement fixé, simulant une compétition variable entre FT.

Cet aspect stochastique permet d'éviter un trop grand déterminisme lors de la définition des écosystèmes océaniques. Le taux de mortalité sera simplement exprimé comme un flux de carbone quittant le réservoir y_i et proportionnel au réservoir y_i lui-même, avec une constante de proportionnalité fixée aléatoirement (à l'intérieur d'une gamme définie pour chacun des paramètres). Cette approche peut sembler valable pour décrire le cycle du carbone car les producteurs primaires représentent la majeure partie du carbone organique de l'océan (biomasse). Ci-dessous une représentation du couplage utilisé pour intégrer l'écosystème *« rudimentaire »* au modèle climat-carbone (GEOCLIM) (fig. 24).

Le

de

la

les

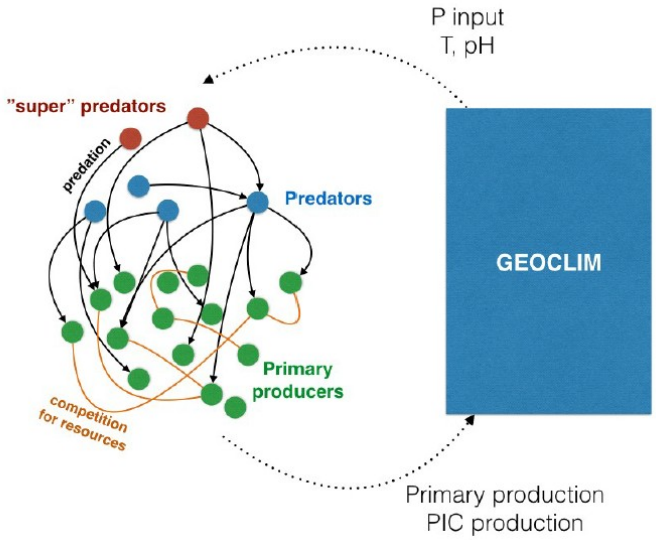

Figure 24
Le couplage avec le modèle GEOCLIM permet calculer l'état géochimique de l'océan via une description mathématique du cycle du carbone (élémentaire et isotopique), de l'alcalinité, du phosphore (seul nutriment modélisé), du strontium (élémentaire et isotopique), du lithium (élémentaire et isotopique), et de l'oxygène. GEOCLIM fournit à chaque bassin océanique de surface (4 bassins au total) le pH de l'eau de mer, la température et l'apport en phosphore soit par upwelling, soit par décharge continentale pour les mers épicontinentales. En retour, le modèle écosystémique fournira la productivité primaire globale que GEOCLIM utilisera pour calculer le flux de carbone exporté par l'activité biologique vers les réservoirs océaniques profonds et vers le sédiment.

3.2.1 l'amplification biologique de la perturbation inorganique

Pour illustrer les apports de cette approche, considérons la crise de la limite K-Pg (66 Ma). Cette crise connue pour être celle de la disparition des dinosaures est également marquée par une disparition très brutale et intense de producteurs primaires carbonatés. Parmi les 131 espèces de nannoplanctons calcaires connues, seule une dizaine a passé la crise (Bown et al. 2005). Cela correspond à une extinction de plus de 90 % de ce groupe alors que 50 % des producteurs primaires non-carbonatés s'éteignent (Mac Leod et al. 1997). De part la sensibilité des producteurs carbonatés au degré de saturation en calcite de l'océan, l'hypothèse d'une acidification brutale de l'océan fût très tôt envisagée (Prinn et Fegley, 1987 et D'Hondt et al. 1994).

En considérant la biomasse de l'océan comme la somme de 50 groupes fonctionnels – tous producteurs primaires – mais dont seuls 17 sont calcifiantes, nous avons pu mettre en évidence le rôle actif de la biosphère dans l'amplification des perturbations. En effet soumis à un stress environnemental majeur (pulse volcanique/impact de Chicxulub) combinant refroidissement intense et acidification des eaux de surface, les groupes fonctionnels réduisent la production primaire durablement. Ce stress environnemental décorrèle pendant un temps, l'abondance des nutriments (phosphore) et production primaire (fig. 25 a-b). Cette baisse de la production primaire intégrée sur la durée d'un pulse réduit sensiblement la part de C_{org} enfouit dans le sédiment.

Au final - ***sur la durée de mise en place d'un traps (ici 200 kans pour le Deccan) - cet effet cumulatif permet de constater une très forte différence dans l'augmentation de la pCO_2 ~ 40 %*** (fig. 25c).

Figure 25

a, b. interactions biosphère/climat-carbone lors d'un pulse (ou un impact) La capacité de la biosphère à transférer du carbone inorganique dissout (DIC) en carbone organique (Corg) particulaire (POC) - stocké durablement dans le sédiment - est fortement réduite. C'est donc au final une baisse d'efficacité du puits organique qui est ici modélisée, baisse liée à la décorrélation entre la quantité de nutriments disponible et la production primaire réalisée.

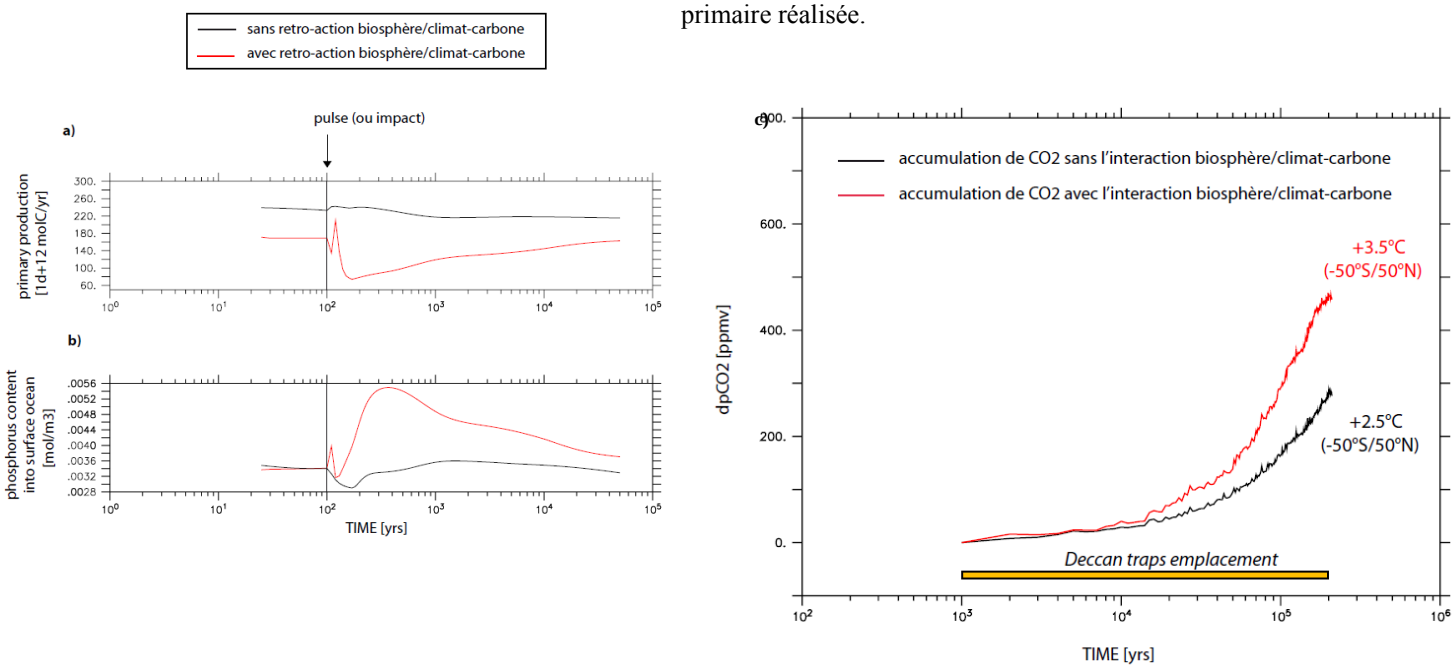

c) effets à long-terme (~ 200 kans soit la durée de mise en place de la phase paroxysmale du traps). La faiblesse du puits organique de carbone induit par le stress environnemental conduit à augmenter la pCO_2 de 40 % (courbe rouge) comparé à un cas où la biosphère dépend uniquement des nutriments disponibles (courbe noire) ;

Ce processus montre que la biosphère est un facteur qui amplifie la perturbation initiale, mais qu'elle ne peut en aucun cas l'enclencher. Tout débute ici avec une perturbation inorganique qui voit son intensité amplifiée sous l'action combinée de 2 mécanismes : i) un mécanisme lié au cycle organique du carbone – estimé dans le cas de cet assemblage de 50 groupes fonctionnels à plus de 40 %, ii) un second mécanisme inorganique moins intense qui résulte de l'interaction entre les composés atmosphériques CO_2-S-aerosols (+15-20 % environ).

3.2.2 la tolérance de la biosphère à l'origine de l'amplification

Une étude, menée par Salomé Hennequin (doctorante du GET, Toulouse), avec le même modèle mais appliquée à la crise P-Tr illustre que la tolérance des FT est à l'origine du mécanisme amplificateur. En testant divers assemblages de FT ayant une sensibilité à la température de plus en plus réduite, on observe une réponse croissante de la réponse à la perturbation initiale.

Comme pour la crise K-Pg, la perturbation initiale est inorganique et toujours supposée d'origine volcanique. En effet la mise en place des traps de Siberie constitue aujourd'hui le facteur déclenchant le plus probable (Burgess et al. 2017). La coïncidence de plusieurs perturbations majeures sont la base de cette hypothèse. La transition Permo-Trias (252Ma) se caractérise par une perte de biodiversité de plus de 90 % des espèces d'invertébrés marins en moins de 100 kans (Burgess et Bowling, 2015), dont les plus touchées furent ceux possédant des tests carbonatés développés et sensibles au phénomène d'hypercapnie (pression de CO_2 élevée au sein des organismes) (Knoll et al. 2007). En plus de cette perte de biodiversité, l'excursion négative du $\delta^{13}C$ (marqueur d'une injection massive de carbone léger (^{12}C)) suggère une baisse importante de la biomasse ; l'ensemble de ces perturbations s'opére dans un climat chaud, voire très chaud, les données géochimiques suggérant une augmentation des températures de surface océaniques de près de 10°C.

En testant un scénario de dégazage réaliste des traps de Sibérie (fig. 26) où la sensibilité à la température relativement forte (faible tolérance : variance -/+ 0.25°C), la réponse du cycle organique est très importante. Cet effet impacte le $\delta^{13}C_{carbonates}$, l'excursion en $\delta^{13}C_{carbonates}$ oscillant entre 1 et 2‰ (fig. 27 courbes vertes). A contrario, sans effet de tolérance (fig. 27 courbe noire), l'excursion du $\delta^{13}C_{carbonates}$ ne dépasse pas les 0.5 ‰.

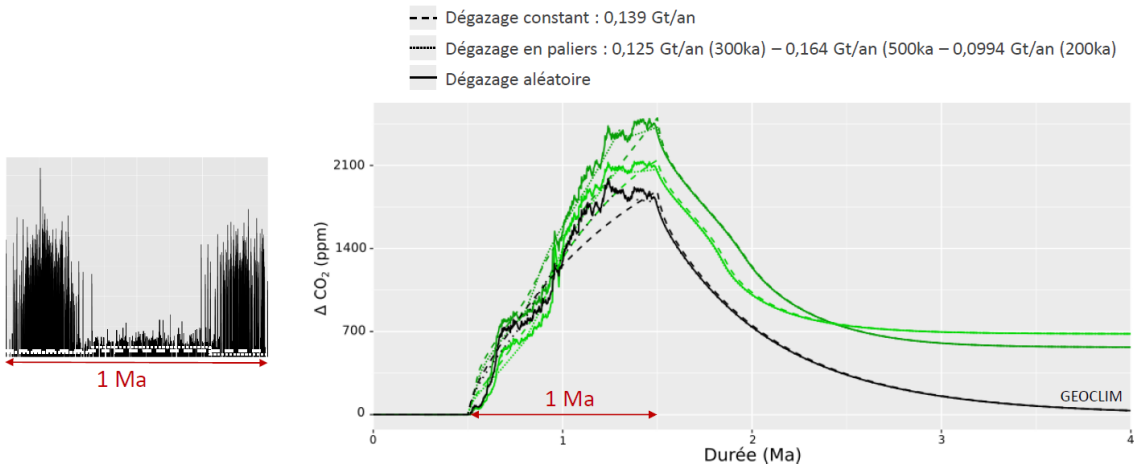

Figure 26 *A gauche,* série volcanique imposé représentant les émissions de CO_2 lors de la mise en place des traps de Siberie – les composés soufrés ne sont pas inclus ici. *A droite,* l'accumulation de CO_2 issue du dégazage selon 3 modes (courbes pleines, grasse ou standard). La courbe noir est le cas de référence où la biosphère n'évolue qu'en fonction des nutriments sans influence de la températures (ni du pH). Les courbes en couleur représentent les mêmes cas mais pour

une biosphère dépendante de la température et pour 2 températures d'optimum différentes (la tolérance à la température est volontairement faible (σ ± 0.25°C) pour amplifier la réponse).

Ces variations sont obtenues sans imposer un forçage autre que la perturbation géologique. A l'inverse de la simulation de Kump (1991) où l'homogénéisation du $\delta^{13}C_{carbonates}$ de l'océan est obtenue en imposant un flux nul de C_{org} enfouis. Dès lors, il devient possible d'expliquer les excursions de la limite P-Tr, sans invoquer de processus tiers (intrusion dans des niveaux de charbons, source mantellique anormalement négative, ou une biomasse entièrement anéantie C_{org} enfouis ~ 0.

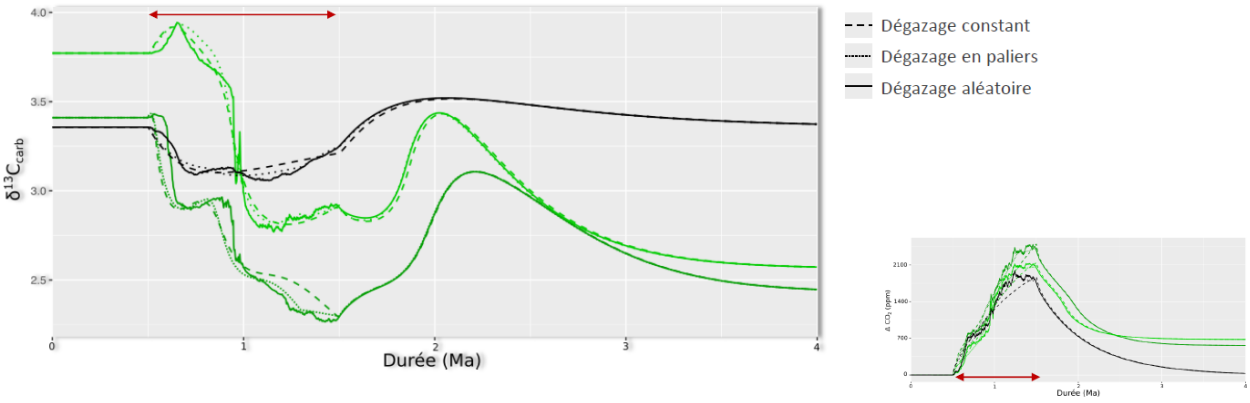

Figure 27 La réponse du $\delta^{13}C_{carbonates}$ à ces 9 cas. L'amplitude de l'excursion est bien plus prononcée si la biosphère est tolérante à la température (les deux couleurs vertes correspondent à une biosphère ayant la même tolérance à la température mais dont les optimums sont différents). On constate également que l'état post-crise est différent de l'état initial. Cette modification est liée à la réduction en biomasse de certains de groupes fonctionnels qui une fois devenu très minoritaire sont considérés comme éteints. Ainsi la structure de l'écosystème post-crise repose sur un panel de groupes fonctionnels réduit, à l'optimum climatique moyen différent du groupe initial au complet.

En réalisant une étude de sensibilité élargie, où les tolérances sont identiques (variance -/+ 0.25°C) mais où le panel de groupes fonctionnels testés est agrandie, on constate qu'à une même perturbation (ici le traps de Siberie, 252-251Ma) peut correspondre diverses tendances du $\delta^{13}C_{carbonates}$ (fig. 28). Comparé aux fluctuations mesurées dans les carbonates de la limite P-Tr, on observe que c'est en réalité le panel initial de groupe fonctionnel qui détermine la réponse et non la perturbation. La perturbation inorganique est l'élément déclenchant, mais son influence sur le résultat apparaît être de second ordre tant l'effet de la biosphère est important.

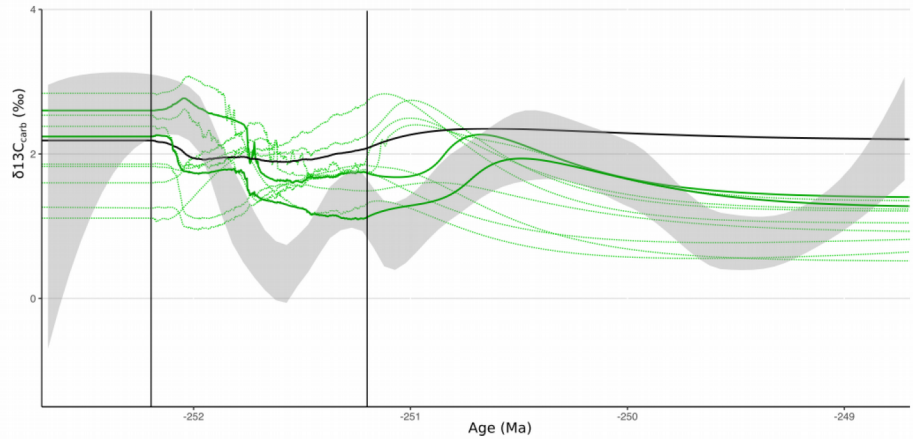

Figure 28 La zone grise représente l'intervalle de confiance (99%) du $\delta^{13}C_{carbonates}$ mesuré (Burgess et Bowring, 2015 et citations). Les courbes vertes les différentes solutions proposées pour divers « ecosystèmes » à la tolérance à la température importante (variance -/+ 0.25°C).

Conclusion

Bien que très exploratoire, ce travail sur le comportement de la biosphère peut nous suggérer quelques pistes pour comprendre les révolutions du Globe énoncées par Cuvier voilà plus de deux siècles.

- la biosphère réagit très vite à la perturbation. Ainsi sur les simulations de la crise K-Pg (66Ma) l'effet maximal de la perturbation est atteint après 100 kans, au-delà l'accumulation de nutriments commence à contre-balancer significativement le stress environnemental. Ce résultat correspond aux temps caractéristiques de la durée des crises observées dans l'enregistrement géologique.

- la perturbation initiale est toujours inorganique, la réponse étant amplifiée par la combinaison de deux rétro-actions i) inorganique (faible) et ii) organique (forte).

- l'amplification organique semble dépendante du degré de tolérance initiale des écosystèmes. La résilience des groupes fonctionnels n'est pas uniforme, il est donc fort probable que chaque assemblage de groupes fonctionnels réagissent différemment à une même perturbation. Si ce mécanisme se révèle valide, la résilience de la biosphère serait potentiellement la cause principale à la variabilité du taux d'extinction observé dans l'enregistrement géologique.

- la limitation de la productivité primaire lors de la perturbation permet l'accumulation de nutriments dans l'océan. Cette abondance de nutriments et les niches écologiques vacantes peuvent être considérées comme des facteurs favorisants la radiation post-crise.

Perspectives

IV. Vers une modélisation des extinctions de masse du Phanérozoïque et au-delà …

4.1 Des écosystèmes ou des types d'écosystèmes

Dans toutes les études menées jusqu'à présent, la biodiversité n'est considérée que par le prisme des producteurs primaires. Cette simplification trouve sa justification dans la part résiduelle de C_{org} qu'occupe les niveaux trophiques supérieurs. Cependant les crises ont été définies (cf les invertébrés marins de A. d'Orbigny et de Sepkovski (1978)) et sont étudiées, et concernent, l'ensemble des niveaux trophiques. Il apparaît donc essentiels d'inclure des niveaux trophiques supérieurs.

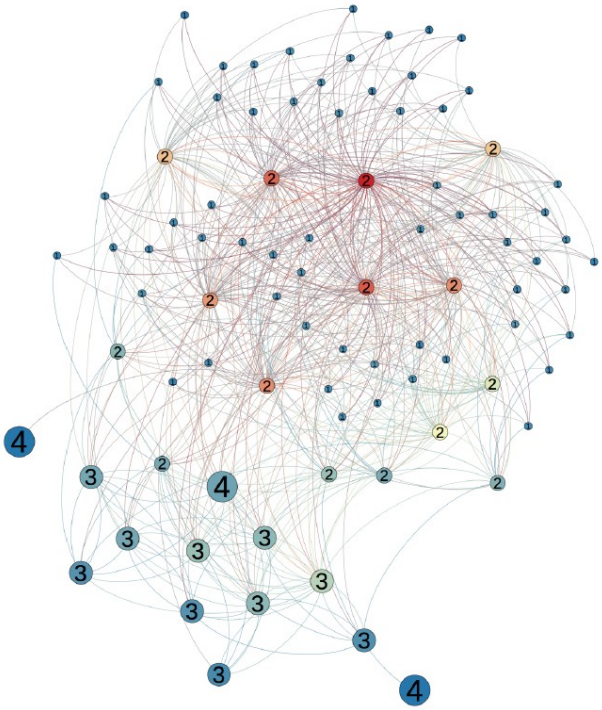

Figure 29 :
Exemple d'un réseau trophique du modèle d'écosystème incluant 4 niveaux trophiques. Les numéros indiquent le niveau trophique du groupe fonctionnel (1 : producteur primaire, …, 4 super-prédateur). Les flèches représentent les relations trophiques entre les divers groupes fonctionnels.

Inclure des niveaux trophiques supérieurs possède le double avantage : i) d'étudier le mécanisme d'extinction en cascade (c'est à dire l'impact de la disparition de la proie sur son prédateur et inversement) mais aussi ii) de voir si parmi les écosystèmes, certaines solutions sont plus résilientes que d'autres. Si les résultats précédents illustrent l'importance de la tolérance, plusieurs tests préliminaires révèlent l'existence de groupes fonctionnels hégémoniques et qui constituent la clé de voûte de la productivité marine. Dès lors l'ensemble du réseau trophique devient vulnérable si ces groupes fonctionnels sont tolérants ou pas aux variations des paramètres océaniques.

Stratégiquement, pour des raisons de croissance exponentielle des solutions, une approche à 4 niveaux a été choisie (producteurs, consommateurs, prédateurs et super-prédateurs (fig. 29) avec des relations trophiques entre chaque niveau. Ce développement a déjà abouti mais reste à être validé. Dans un futur proche, les relations de prédations seront inféodées à la taille respective des groupes fonctionnels.

4.2 Les tipping-points du système climat-carbone-biosphère

L'hypothèse de la causalité entre crise de biodiversité et traps a été proposée sur la base de l'enregistrement géologique (Rampino et Self, 1984 ; Courtillot et al., 1986). L'amélioration des techniques de datation et de corrélation radiométrique (p. ex. U/Pb sur zircon individuel) a permis de confirmer le synchronisme des grands épanchements basaltiques avec les extinctions de masse (Courtillot & Renne, 2003). Ces grandes provinces basaltiques sont connues pour être des événements volcaniques épisodiques, rares, de grande ampleur, sans équivalent récent.

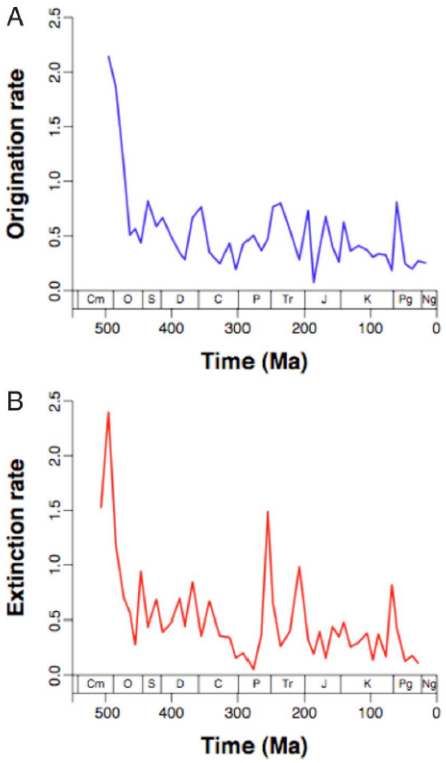

Figure 30 : Les courbes d'Alroy (2008) sont obtenus comme pour les courbes de Sepioski (1978 et ultérieurs) à partir des invertébrés marins. Cependant elles sont corrigées des artefacts de prélèvements.
Le taux d'origination représente la fréquence d'apparition de nouvelles espèces dans le registre fossile. A l'opposé, le taux d'extinction représente la fréquence de disparition d'une espèce du même registre fossile. Ces deux courbes sont des moyennes glissantes sur 10Ma.
Ci dessous la relation intensité de l'extinction / volume de basalte mis en place (Ganino et al. 2009)

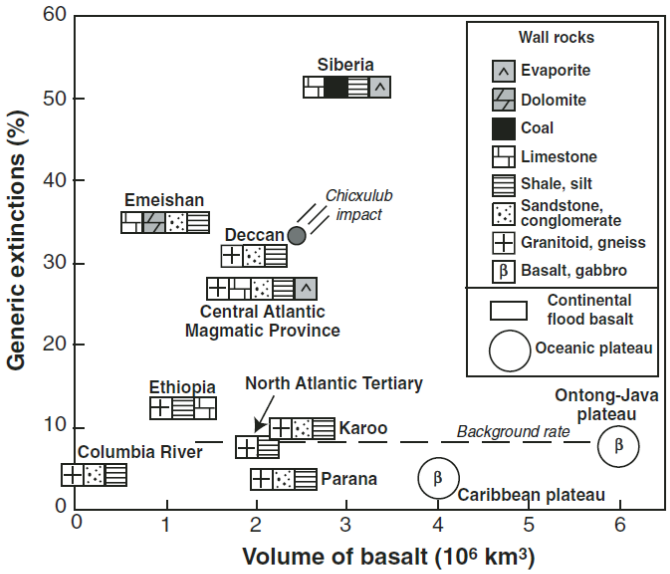

Figure 1. Percentage of generic extinctions (from Rhode and Muller, 2005) versus volume of erupted basalt from Courtillot and Renne (2003) for major LIPs. Two main populations of LIPs are evident, one for which the associated rate of extinction is close to the background rate (Columbia River to Ontong-Java plateau) and another for which the rate is far higher. Those in the latter group intrude sedimentary rocks that released abundant greenhouse or toxic gases.

La figure 30 nous montre l'absence de relation directe entre l'unicité de la cause (les traps) et le taux d'extinction déduit du registre fossile. Une solution fût proposée par Ganino et al. (2009) en considérant que la chimie des gaz émis fut altérée par les sédiments intrudés par des coulés basaltiques.

Dans la continuité des travaux proposés précédemment, nous souhaitons réaliser une approche sur l'ensemble du Phanérozoïque où plusieurs assemblages de groupes fonctionnels seront soumis à des dégazages d'intensités variables afin de contraindre la non-linéarité des réponses biologiques. Dans une approche analogue à celle menée voilà 40 ans sur les mécanismes de régulation du climat, ici ***nous souhaitons étudier les points d'équilibre du systèmes climat-carbone-biosphère et donc les points de bascule.*** Si ces points de bascules (tipping-points) sont

établis, alors un pas important sera franchi pour ***comprendre la singularité des 5 extinctions majeures du Phanérozoïque.*** Le pendant de cette question est de ***savoir si des extinctions de masses ont pu se produire dans un monde de micro-organismes – un monde Précambrien (<542Ma).***

4.3 Une extinction en masse de micro-organismes ? la Terre boule de neige...

En quoi est-ce important ? Comme la perturbation environnementale syn et post-glaciaire est dépendante de la durée et de la pCO_2, cette prospective a vocation à intégrer la biodiversité comme la dernière et ultime composante du système exosphérique. L'objectif final étant d'aider à la résolution d'un important mystère associé à la théorie de la Terre boule de neige à savoir la survie des organismes, question toujours non solutionnée à cette heure !

Cette intégration de la biodiversité dans des modèles jusqu'ici quantitatifs apparaît nécessaire à la vue des observations paléontologiques. En effet la présence de stromatolithes dans les carbonates post-glaciaires confirme la survivance d'organismes procaryotes aux glaciations extrêmes. De mêmes, des clades d'eucaryotes (algues) sont, semble t-il, déjà présents avant les glaciations globales, ainsi que des bilateria et des spongiaires comme le suggèrent les données moléculaires. La survivance de ces organismes, supposés moins résilients que les procaryotes, aux glaciations globales prolongées reste énigmatique. Ainsi, actuellement il semble qu'aucun lien direct et irréfutable ne puisse être avancé entre les glaciations globales et une extinction majeure similaire aux big-5 du Phanérozoïque. Cette singulière observation est à elle seule capable de remettre en cause l'existence des glaciations globales. Cette même constatation peut être faite concernant l'émergence des faunes de Doushanto en Chine (600-570 Ma) ou d'Ediacara en Australie (575-542 Ma) qui intervient plus de 30 Ma après la fin des glaciations globales.

Afin de quantifier les effets d'une glaciation globale et de sa déglaciation sur la biosphère marine, nous réaliserons un dernier (et ultime?) niveau de couplage entre le modèle - type Earth System - issu de l'assemblage LMDz-GRISLI-COMBINE-WITCH avec le modèle de biosphère.

En multipliant ainsi les couplages et en limitant autant que faire se peut les conditions limites, cette approche maximise le degré de liberté laissé au système, d'autant plus, qu'un panel important d'espèces types peut être testé (100 à 200). Ce modèle de biodiversité marine repose sur le caractère stochastique de la sensibilité des espèces aux variations environnementales. En testant un grand nombre de groupes fonctionnels, il devient dès lors possible d'évaluer le pourcentage potentiel de survie et d'extinction d'espèces pour divers scénarii.

A la différence des causes d'extinctions présentées précédemment (cad traps et météorite), ces scénarios seront issus de la prospective focalisée sur l'amplitude et la vitesse des perturbations environnementales entre la phase glaciaire et la phase post-glaciaire au Cryogenian (thème 2). Font et al (2006, 2019), sur la base des inversions du champ magnétique terrestre mesurées dans les carbonates post-glaciaires, estiment la déglaciation > 10^5 ans. A contrario les observations sédimentaires supposent une déglaciation plus rapide (~10^4ans)(Hoffman et al. 2007), soit une durée similaire à la dernière déglaciation intervenue à la transition Würm-Holocène.

Cette dernière prospective a été pensée pour s'intégrer à une thèse de doctorat intitulée *« quantifications des perturbations environnementales causées par une glaciation globale et leurs conséquences biologiques »*.

RÉFÉRENCES BIBLIOGRAPHIQUES

Alroy, J. « Dynamics of Origination and Extinction in the Marine Fossil Record ». *Proceedings of the National Academy of Sciences*, vol. 105, nº Supplement 1, août 2008, p. 11536-42. *DOI.org (Crossref)*, doi:10.1073/pnas.0802597105.

Beerling, D. J., et R. A. Berner. « Feedbacks and the Coevolution of Plants and Atmospheric CO2 ». *Proceedings of the National Academy of Sciences*, vol. 102, nº 5, février 2005, p. 1302-05. *DOI.org (Crossref)*, doi:10.1073/pnas.0408724102.

Beerling, David J., et Dana L. Royer. « Convergent Cenozoic CO2 History ». *Nature Geoscience*, vol. 4, nº 7, juillet 2011, p. 418-20. *DOI.org (Crossref)*, doi:10.1038/ngeo1186.

Bell, Elizabeth A., et al. « Potentially Biogenic Carbon Preserved in a 4.1 Billion-Year-Old Zircon ». *Proceedings of the National Academy of Sciences*, vol. 112, nº 47, novembre 2015, p. 14518-21. *DOI.org (Crossref)*, doi:10.1073/pnas.1517557112.

Benn, Douglas I., et al. « Orbitally Forced Ice Sheet Fluctuations during the Marinoan Snowball Earth Glaciation ». *Nature Geoscience*, vol. 8, nº 9, septembre 2015, p. 704-07. *DOI.org (Crossref)*, doi:10.1038/ngeo2502.

Bergman, N. M. « COPSE: A New Model of Biogeochemical Cycling over Phanerozoic Time ». *American Journal of Science*, vol. 304, nº 5, mai 2004, p. 397-437. *DOI.org (Crossref)*, doi:10.2475/ajs.304.5.397.

Berner, Robert A. « GEOCARBSULF: A Combined Model for Phanerozoic Atmospheric O2 and CO2 ». *Geochimica et Cosmochimica Acta*, vol. 70, nº 23, décembre 2006, p. 5653-64. *DOI.org (Crossref)*, doi:10.1016/j.gca.2005.11.032.

Blake, Ruth E., et al. « Phosphate Oxygen Isotopic Evidence for a Temperate and Biologically Active Archaean Ocean ». *Nature*, vol. 464, nº 7291, avril 2010, p. 1029-32. *DOI.org (Crossref)*, doi:10.1038/nature08952.

Bodiselitsch, B. « Estimating Duration and Intensity of Neoproterozoic Snowball Glaciations from Ir Anomalies ». *Science*, vol. 308, nº 5719, avril 2005, p. 239-42. *DOI.org (Crossref)*, doi:10.1126/science.1104657.

Bond, David P. G., et Paul B. Wignall. « Large Igneous Provinces and Mass Extinctions: An Update ». *Volcanism, Impacts, and Mass Extinctions: Causes and Effects*, Geological Society of America, 2014. *DOI.org (Crossref)*, doi:10.1130/2014.2505(02).

Bormann, Bernard T., et al. « [No title found] ». *Biogeochemistry*, vol. 43, nº 2, 1998, p. 129-55. *DOI.org (Crossref)*, doi:10.1023/A:1006065620344.

Bown, Paul. « Selective Calcareous Nannoplankton Survivorship at the Cretaceous-Tertiary Boundary ». *Geology*, vol. 33, nº 8, août 2005, p. 653-56. *DOI.org (Crossref)*, doi:10.1130/G21566AR.1.

Budyko, M. I. « The Effect of Solar Radiation Variations on the Climate of the Earth ». *Tellus*, vol. 21, nº 5, octobre 1969, p. 611-19. *DOI.org (Crossref)*, doi:10.1111/j.2153-3490.1969.tb00466.x.

Buick, Roger, et al. « Stromatolite Recognition in Ancient Rocks: An Appraisal of Irregularly Laminated Structures in an Early Archaean Chert-Barite Unit from North Pole, Western Australia ». *Alcheringa: An Australasian Journal of Palaeontology*, vol. 5, nº 3, janvier 1981, p. 161-81. *DOI.org (Crossref)*, doi:10.1080/03115518108566999.

Burgess, S. D., et al. « Initial Pulse of Siberian Traps Sills as the Trigger of the End-Permian Mass Extinction ». *Nature Communications*, vol. 8, nº 1, décembre 2017, p. 164. *DOI.org (Crossref)*, doi:10.1038/s41467-017-00083-9.

Burgess, Seth D., et Samuel A. Bowring. « High-Precision Geochronology Confirms Voluminous Magmatism before, during, and after Earth's Most Severe Extinction ». *Science Advances*, vol. 1, nº 7, août 2015, p. e1500470. *DOI.org (Crossref)*, doi:10.1126/sciadv.1500470.

Caldeira, Ken, et Michael R. Rampino. « Carbon Dioxide Emissions from Deccan Volcanism and a K/T Boundary Greenhouse Effect ». *Geophysical Research Letters*, vol. 17, nº 9, août 1990, p. 1299-302. *DOI.org (Crossref)*, doi:10.1029/GL017i009p01299.

Charlson, Robert J., et al. « Oceanic Phytoplankton, Atmospheric Sulphur, Cloud Albedo and Climate ». *Nature*, vol. 326, nº 6114, avril 1987, p. 655-61. *www.nature.com*, doi:10.1038/326655a0.

Charnay, B., et al. « Exploring the Faint Young Sun Problem and the Possible Climates of the Archean Earth with a 3-D GCM: A 3-D MODELING OF THE CLIMATES OF THE ARCHEAN EARTH ». *Journal of Geophysical Research: Atmospheres*, vol. 118, nº 18, septembre 2013, p. 10,414-10,431. *DOI.org (Crossref)*, doi:10.1002/jgrd.50808.

Chenet, A., et al. « 40K–40Ar Dating of the Main Deccan Large Igneous Province: Further Evidence of KTB Age and Short Duration ». *Earth and Planetary Science Letters*, vol. 263, nº 1-2, novembre 2007, p. 1-15. *DOI.org (Crossref)*, doi:10.1016/j.epsl.2007.07.011.

Chenet, Anne-Lise, et al. « Determination of Rapid Deccan Eruptions across the Cretaceous-Tertiary Boundary Using Paleomagnetic Secular Variation: Results from a 1200-m-Thick Section in the Mahabaleshwar Escarpment ». *Journal of Geophysical Research*, vol. 113, nº B4, avril 2008, p. B04101. *DOI.org (Crossref)*, doi:10.1029/2006JB004635.

Clarkson, M. O., et al. « Ocean Acidification and the Permo-Triassic Mass Extinction ». *Science*, vol. 348, nº 6231, avril 2015, p. 229-32. *DOI.org (Crossref)*, doi:10.1126/science.aaa0193.

Cohen, K. M., et al. « The ICS International Chronostratigraphic Chart ». *Episodes*, vol. 36, nº 3, septembre 2013, p. 199-204. *DOI.org (Crossref)*, doi:10.18814/epiiugs/2013/v36i3/002.

Condon, D. « U-Pb Ages from the Neoproterozoic Doushantuo Formation, China ». *Science*, vol. 308, nº 5718, avril 2005, p. 95-98. *DOI.org (Crossref)*, doi:10.1126/science.1107765.

Courtillot, Vincent, et al. « Deccan Flood Basalts at the Cretaceous/Tertiary Boundary? » *Earth and Planetary Science Letters*, vol. 80, nº 3-4, novembre 1986, p. 361-74. *DOI.org (Crossref)*, doi:10.1016/0012-821X(86)90118-4.

Courtillot, Vincent E., et Paul R. Renne. « On the Ages of Flood Basalt Events ». *Comptes Rendus Geoscience*, vol. 335, nº 1, janvier 2003, p. 113-40. *DOI.org (Crossref)*, doi:10.1016/S1631-0713(03)00006-3.

Dauphas, N., et J. F. Kasting. « Low in the Pore Water, Not in the Archean Air ». *Nature*, vol. 474, nº 7349, juin 2011, p. E1-E1. *DOI.org (Crossref)*, doi:10.1038/nature09960.

Denis, Michaël, et al. « Hirnantian Glacial and Deglacial Record in SW Djado Basin (NE Niger). » *Geodinamica Acta*, vol. 20, nº 3, juin 2007, p. 177-95. *DOI.org (Crossref)*, doi:10.3166/ga.20.177-195.

Dessert, Céline, et al. « Basalt Weathering Laws and the Impact of Basalt Weathering on the Global Carbon Cycle ». *Chemical Geology*, vol. 202, nº 3-4, décembre 2003, p. 257-73. *DOI.org (Crossref)*, doi:10.1016/j.chemgeo.2002.10.001.

Díaz-Martínez, Enrique, et Yngve Grahn. « Early Silurian Glaciation along the Western Margin of Gondwana (Peru, Bolivia and Northern Argentina): Palaeogeographic and Geodynamic Setting ». *Palaeogeography, Palaeoclimatology, Palaeoecology*, vol. 245, nº 1-2, mars 2007, p. 62-81. *DOI.org (Crossref)*, doi:10.1016/j.palaeo.2006.02.018.

Donnadieu, Y., et al. « A GEOCLIM Simulation of Climatic and Biogeochemical Consequences of Pangea Breakup: SIMULATION OF PANGEA BREAKUP ». *Geochemistry, Geophysics, Geosystems*, vol. 7, nº 11, novembre 2006, p. n/a-n/a. *DOI.org (Crossref)*, doi:10.1029/2006GC001278.

Donnadieu, Yannick, et al. « A 'Snowball Earth' Climate Triggered by Continental Break-up through Changes in Runoff ». *Nature*, vol. 428, nº 6980, mars 2004, p. 303-06. *DOI.org (Crossref)*, doi:10.1038/nature02408.

Finnegan, S., et al. « The Magnitude and Duration of Late Ordovician-Early Silurian Glaciation ». *Science*, vol. 331, nº 6019, février 2011, p. 903-06. *DOI.org (Crossref)*, doi:10.1126/science.1200803.

Font, E., et al. « Fast or Slow Melting of the Marinoan Snowball Earth? The Cap Dolostone Record ». *Palaeogeography, Palaeoclimatology, Palaeoecology*, vol. 295, nº 1-2, septembre 2010, p. 215-25. *DOI.org (Crossref)*, doi:10.1016/j.palaeo.2010.05.039.

Foriel, Julien, et al. « Biological Control of Cl/Br and Low Sulfate Concentration in a 3.5-Gyr-Old Seawater from North Pole, Western Australia ». *Earth and Planetary Science Letters*, vol. 228, nº 3-4, décembre 2004, p. 451-63. *DOI.org (Crossref)*, doi:10.1016/j.epsl.2004.09.034.

Friedlingstein, P., et al. « The Climate Induced Variation of the Continental Biosphere: A Model Simulation of the Last Glacial Maximum ». *Geophysical Research Letters*, vol. 19, nº 9, mai 1992, p. 897-900. *DOI.org (Crossref)*, doi:10.1029/92GL00546.

Ganino, Clément, et Nicholas T. Arndt. « Climate Changes Caused by Degassing of Sediments during the Emplacement of Large Igneous Provinces ». *Geology*, vol. 37, nº 4, avril 2009, p. 323-26. *DOI.org (Crossref)*, doi:10.1130/G25325A.1.

Gaucher, Eric A., et al. « Palaeotemperature Trend for Precambrian Life Inferred from Resurrected Proteins ». *Nature*, vol. 451, nº 7179, février 2008, p. 704-07. *DOI.org (Crossref)*, doi:10.1038/nature06510.

Ghienne, Jean-Francois, et al. « The Late Ordovician Glacial Sedimentary System of the North Gondwana Platform ». *Glacial Sedimentary Processes and Products*, édité par Michael J. Hambrey et al., Blackwell Publishing Ltd., 2009, p. 295-319. *DOI.org (Crossref)*, doi:10.1002/9781444304435.ch17.

Godderis, Y. « Tectonic Control of Chemical and Isotopic Composition of Ancient Oceans; the Impact of Continental Growth ». *American Journal of Science*, vol. 300, nº 5, mai 2000, p. 434-61. *DOI.org (Crossref)*, doi:10.2475/ajs.300.5.434.

Goddéris, Y., et al. « The Sturtian 'Snowball' Glaciation: Fire and Ice ». *Earth and Planetary Science Letters*, vol. 211, nº 1-2, juin 2003, p. 1-12. *DOI.org (Crossref)*, doi:10.1016/S0012-821X(03)00197-3.

Goddéris, Yves, Louis M. François, et al. « Modelling Weathering Processes at the Catchment Scale: The WITCH Numerical Model ». *Geochimica et Cosmochimica Acta*, vol. 70, nº 5, mars 2006, p. 1128-47. *DOI.org (Crossref)*, doi:10.1016/j.gca.2005.11.018.

Goddéris, Yves, Yannick Donnadieu, Sébastien Carretier, et al. « Onset and Ending of the Late Palaeozoic Ice Age Triggered by Tectonically Paced Rock Weathering ». *Nature Geoscience*, vol. 10, nº 5, mai 2017, p. 382-86. *DOI.org (Crossref)*, doi:10.1038/ngeo2931.

Goddéris, Yves, Yannick Donnadieu, Vincent Lefebvre, et al. « Tectonic Control of Continental Weathering, Atmospheric CO2, and Climate over Phanerozoic Times ». *Comptes Rendus Geoscience*, vol. 344, nº 11-12, novembre 2012, p. 652-62. *DOI.org (Crossref)*, doi:10.1016/j.crte.2012.08.009.

Goddéris, Yves, et Michael M. Joachimski. « Global Change in the Late Devonian: Modelling the Frasnian–Famennian Short-Term Carbon Isotope Excursions ». *Palaeogeography, Palaeoclimatology, Palaeoecology*, vol. 202, nº 3-4, janvier 2004, p. 309-29. *DOI.org (Crossref)*, doi:10.1016/S0031-0182(03)00641-2.

Gomes, R., et al. « Origin of the Cataclysmic Late Heavy Bombardment Period of the Terrestrial Planets ». *Nature*, vol. 435, nº 7041, mai 2005, p. 466-69. *DOI.org (Crossref)*, doi:10.1038/nature03676.

Gough, D. O. « Solar Interior Structure and Luminosity Variations ». *Solar Physics*, vol. 74, nº 1, novembre 1981, p. 21-34. *DOI.org (Crossref)*, doi:10.1007/BF00151270.

Grahn, Yngve, et Mário V. Caputo. « Early Silurian Glaciations in Brazil ». *Palaeogeography, Palaeoclimatology, Palaeoecology*, vol. 99, nº 1-2, novembre 1992, p. 9-15. *DOI.org (Crossref)*, doi:10.1016/0031-0182(92)90003-N.

Harland, W. B. « Critical Evidence for a Great Infra-Cambrian Glaciation ». *Geologische Rundschau*, vol. 54, nº 1, mai 1964, p. 45-61. *DOI.org (Crossref)*, doi:10.1007/BF01821169.

Herrmann, Achim D, et al. « Response of Late Ordovician Paleoceanography to Changes in Sea Level, Continental Drift, and Atmospheric PCO2: Potential Causes for Long-Term Cooling and Glaciation ». *Palaeogeography, Palaeoclimatology, Palaeoecology*, vol. 210, nº 2-4, août 2004, p. 385-401. *DOI.org (Crossref)*, doi:10.1016/j.palaeo.2004.02.034.

Herrmann, Achim D., et al. « The Impact of Paleogeography, PCO2, Poleward Ocean Heat Transport and Sea Level Change on Global Cooling during the Late Ordovician ». *Palaeogeography, Palaeoclimatology, Palaeoecology*, vol. 206, nº 1-2, avril 2004, p. 59-74. *DOI.org (Crossref)*, doi:10.1016/j.palaeo.2003.12.019.

Hoffman, P. F. « A Neoproterozoic Snowball Earth ». *Science*, vol. 281, nº 5381, août 1998, p. 1342-46. *DOI.org (Crossref)*, doi:10.1126/science.281.5381.1342.

Hoffman, Paul F., et Daniel P. Schrag. « The Snowball Earth Hypothesis: Testing the Limits of Global Change ». *Terra Nova*, vol. 14, nº 3, juin 2002, p. 129-55. *DOI.org (Crossref)*, doi:10.1046/j.1365-3121.2002.00408.x.

Hourdin, Frédéric, et al. « The LMDZ4 General Circulation Model: Climate Performance and Sensitivity to Parametrized Physics with Emphasis on Tropical Convection ». *Climate Dynamics*, vol. 27, nº 7-8, octobre 2006, p. 787-813. *DOI.org (Crossref)*, doi:10.1007/s00382-006-0158-0.

Hren, M. T., et al. « Oxygen and Hydrogen Isotope Evidence for a Temperate Climate 3.42 Billion Years Ago ». *Nature*, vol. 462, nº 7270, novembre 2009, p. 205-08. *DOI.org (Crossref)*, doi:10.1038/nature08518.

Jacobsen, Stein B., et Alan J. Kaufman. « The Sr, C and O Isotopic Evolution of Neoproterozoic Seawater ». *Chemical Geology*, vol. 161, nº 1-3, septembre 1999, p. 37-57. *DOI.org (Crossref)*, doi:10.1016/S0009-2541(99)00080-7.

Jouzel, J., et al. « Orbital and Millennial Antarctic Climate Variability over the Past 800,000 Years ». *Science*, vol. 317, nº 5839, août 2007, p. 793-96. *DOI.org (Crossref)*, doi:10.1126/science.1141038.

Kasting, James F. « Faint Young Sun Redux ». *Nature*, vol. 464, nº 7289, avril 2010, p. 687-89. *DOI.org (Crossref)*, doi:10.1038/464687a.

---. « The Evolution of the Prebiotic Atmosphere ». *Origins of Life*, vol. 14, nº 1-4, 1984, p. 75-82. *DOI.org (Crossref)*, doi:10.1007/BF00933642.

---. « Theoretical Constraints on Oxygen and Carbon Dioxide Concentrations in the Precambrian Atmosphere ». *Precambrian Research*, vol. 34, nº 3-4, janvier 1987, p. 205-29. *DOI.org (Crossref)*, doi:10.1016/0301-9268(87)90001-5.

Kasting, James F., et David Catling. « Evolution of a Habitable Planet ». *Annual Review of Astronomy and Astrophysics*, vol. 41, nº 1, septembre 2003, p. 429-63. *annualreviews.org (Atypon)*, doi:10.1146/annurev.astro.41.071601.170049.

Kasting, James F., et M. Tazewell Howard. « Atmospheric Composition and Climate on the Early Earth ». *Philosophical Transactions of the Royal Society B: Biological Sciences*, vol. 361, nº 1474, octobre 2006, p. 1733-42. *DOI.org (Crossref)*, doi:10.1098/rstb.2006.1902.

Katz, Miriam E., et al. « Biological Overprint of the Geological Carbon Cycle ». *Marine Geology*, vol. 217, nº 3-4, juin 2005, p. 323-38. *DOI.org (Crossref)*, doi:10.1016/j.margeo.2004.08.005.

Kiehl, J. T., et R. E. Dickinson. « A Study of the Radiative Effects of Enhanced Atmospheric CO_2 and CH_4 on Early Earth Surface Temperatures ». *Journal of Geophysical Research*, vol. 92, nº D3, 1987, p. 2991. *DOI.org (Crossref)*, doi:10.1029/JD092iD03p02991.

Kienert, Hendrik, et al. « Faint Young Sun Problem More Severe Due to Ice-Albedo Feedback and Higher Rotation Rate of the Early Earth: THE 3-D MODELLING OF FAINT YOUNG SUN PROBLEM ». *Geophysical Research Letters*, vol. 39, nº 23, décembre 2012, p. n/a-n/a. *DOI.org (Crossref)*, doi:10.1029/2012GL054381.

Knauth, L. Paul, et Samuel Epstein. « Hydrogen and Oxygen Isotope Ratios in Nodular and Bedded Cherts ». *Geochimica et Cosmochimica Acta*, vol. 40, nº 9, septembre 1976, p. 1095-108. *DOI.org (Crossref)*, doi:10.1016/0016-7037(76)90051-X.

Knauth, L. Paul, et Donald R. Lowe. « High Archean Climatic Temperature Inferred from Oxygen Isotope Geochemistry of Cherts in the 3.5 Ga Swaziland Supergroup, South Africa ». *GSA Bulletin*, vol. 115, nº 5, mai 2003, p. 566-80. *pubs.geoscienceworld.org*, doi:10.1130/0016-7606(2003)115<0566:HACTIF>2.0.CO;2.

Knoll, Andrew H., et al. « Paleophysiology and End-Permian Mass Extinction ». *Earth and Planetary Science Letters*, vol. 256, nº 3-4, avril 2007, p. 295-313. *DOI.org (Crossref)*, doi:10.1016/j.epsl.2007.02.018.

Krissansen-Totton, J., et al. « A Statistical Analysis of the Carbon Isotope Record from the Archean to Phanerozoic and Implications for the Rise of Oxygen ». *American Journal of Science*, vol. 315, nº 4, avril 2015, p. 275-316. *DOI.org (Crossref)*, doi:10.2475/04.2015.01.

Kump, Lee R. « Interpreting Carbon-Isotope Excursions: Strangelove Oceans ». *Geology*, vol. 19, nº 4, avril 1991, p. 299-302. *pubs.geoscienceworld.org*, doi:10.1130/0091-7613(1991)019<0299:ICIESO>2.3.CO;2.

Le Hir, Guillaume, et al. « Scenario for the Evolution of Atmospheric PCO2 during a Snowball Earth ». *Geology*, vol. 36, nº 1, 2008, p. 47. *DOI.org (Crossref)*, doi:10.1130/G24124A.1.

Lefebvre, Alice, et al. *Summary of Average Roughness Length Calculated from the Moored and Ship-Based ADCP Velocity Profiles on 17 Oct and 20 Oct around the Time of Maximum Velocity*. PANGAEA - Data Publisher for Earth & Environmental Science, 2013. *DOI.org (Datacite)*, doi:10.1594/pangaea.812063.

Lefebvre, Vincent, et al. « Was the Antarctic Glaciation Delayed by a High Degassing Rate during the Early Cenozoic? » *Earth and Planetary Science Letters*, vol. 371-372, juin 2013, p. 203-11. *DOI.org (Crossref)*, doi:10.1016/j.epsl.2013.03.049.

Li, Gaojun, et Henry Elderfield. « Evolution of Carbon Cycle over the Past 100 Million Years ». *Geochimica et Cosmochimica Acta*, vol. 103, février 2013, p. 11-25. *DOI.org (Crossref)*, doi:10.1016/j.gca.2012.10.014.

Lovelock, James E., et Lynn Margulis. « Atmospheric Homeostasis by and for the Biosphere: The Gaia Hypothesis ». *Tellus*, vol. 26, nº 1-2, février 1974, p. 2-10. *DOI.org (Crossref)*, doi:10.1111/j.2153-3490.1974.tb01946.x.

Lüthi, Dieter, et al. *CO2 Record from the EPICA Dome C 1999 (EDC99) Ice Core (Antarctica) Covering 650 to 800 Kyr BP Measured at the University of Bern, Switzerland*. PANGAEA - Data Publisher for Earth & Environmental Science, 2008. *DOI.org (Datacite)*, doi:10.1594/pangaea.710901.

Macleod, N., et al. « The Cretaceous-Tertiary Biotic Transition ». *Journal of the Geological Society*, vol. 154, nº 2, mars 1997, p. 265-92. *DOI.org (Crossref)*, doi:10.1144/gsjgs.154.2.0265.

Marin-Carbonne, J., et al. « The Silicon and Oxygen Isotope Compositions of Precambrian Cherts: A Record of Oceanic Paleo-Temperatures? » *Precambrian Research*, vol. 247, juillet 2014, p. 223-34. *DOI.org (Crossref)*, doi:10.1016/j.precamres.2014.03.016.

Millero, Frank J., et Alain Poisson. « International One-Atmosphere Equation of State of Seawater ». *Deep Sea Research Part A. Oceanographic Research Papers*, vol. 28, nº 6, juin 1981, p. 625-29. *DOI.org (Crossref)*, doi:10.1016/0198-0149(81)90122-9.

Moreau, Julien. « The Late Ordovician Deglaciation Sequence of the SW Murzuq Basin (Libya): Late Ordovician Deglaciation Sequence ». *Basin Research*, vol. 23, nº 4, août 2011, p. 449-77. *DOI.org (Crossref)*, doi:10.1111/j.1365-2117.2010.00499.x.

Mussard, Mickaël, et al. « Modeling the Carbon-Sulfate Interplays in Climate Changes Related to the Emplacement of Continental Flood Basalts ». *Volcanism, Impacts, and Mass Extinctions: Causes and Effects*, Geological Society of America, 2014. *DOI.org (Crossref)*, doi:10.1130/2014.2505(17).

Nardin, E., et al. « Modeling the Early Paleozoic Long-Term Climatic Trend ». *Geological Society of America Bulletin*, vol. 123, nº 5-6, mai 2011, p. 1181-92. *DOI.org (Crossref)*, doi:10.1130/B30364.1.

Nisbet, E. G., et N. H. Sleep. « The Habitat and Nature of Early Life ». *Nature*, vol. 409, nº 6823, février 2001, p. 1083-91. *DOI.org (Crossref)*, doi:10.1038/35059210.

Petoukhov, V., et al. « CLIMBER-2: A Climate System Model of Intermediate Complexity. Part I: Model Description and Performance for Present Climate ». *Climate Dynamics*, vol. 16, nº 1, janvier 2000, p. 1-17. *DOI.org (Crossref)*, doi:10.1007/PL00007919.

Pierrehumbert, R. T., et al. « Climate of the Neoproterozoic ». *Annual Review of Earth and Planetary Sciences*, vol. 39, nº 1, mai 2011, p. 417-60. *DOI.org (Crossref)*, doi:10.1146/annurev-earth-040809-152447.

Poussart, Pascale F., et al. « Late Ordovician Glaciation under High Atmospheric CO_2 : A Coupled Model Analysis ». *Paleoceanography*, vol. 14, nº 4, août 1999, p. 542-58. *DOI.org (Crossref)*, doi:10.1029/1999PA900021.

Prell, W. L., et al., éditeurs. *Proceedings of the Ocean Drilling Program, 117 Scientific Results*. Vol. 117, Ocean Drilling Program, 1991. *DOI.org (Crossref)*, doi:10.2973/odp.proc.sr.117.1991.

---, éditeurs. *Proceedings of the Ocean Drilling Program, 117 Scientific Results*. Vol. 117, Ocean Drilling Program, 1991. *DOI.org (Crossref)*, doi:10.2973/odp.proc.sr.117.1991.

Prinn, Ronald G., et Bruce Fegley. « Bolide Impacts, Acid Rain, and Biospheric Traumas at the Cretaceous-Tertiary Boundary ». *Earth and Planetary Science Letters*, vol. 83, nº 1-4, mai 1987, p. 1-15. *DOI.org (Crossref)*, doi:10.1016/0012-821X(87)90046-X.

Qiang, Xiaoke, et al. « New Eolian Red Clay Sequence on the Western Chinese Loess Plateau Linked to Onset of Asian Desertification about 25 Ma Ago ». *Science China Earth Sciences*, vol. 54, nº 1, janvier 2011, p. 136-44. *DOI.org (Crossref)*, doi:10.1007/s11430-010-4126-5.

Quere, Corinne Le, et al. « Ecosystem Dynamics Based on Plankton Functional Types for Global Ocean Biogeochemistry Models ». *Global Change Biology*, vol. 0, nº 0, octobre 2005, p. 051013014052005-??? *DOI.org (Crossref)*, doi:10.1111/j.1365-2486.2005.1004.x.

Raup, D. M., et J. J. Sepkoski. « Mass Extinctions in the Marine Fossil Record ». *Science*, vol. 215, nº 4539, mars 1982, p. 1501-03. *DOI.org (Crossref)*, doi:10.1126/science.215.4539.1501.

Reinhard, Christopher T., et Noah J. Planavsky. « Mineralogical Constraints on Precambrian ». *Nature*, vol. 474, nº 7349, juin 2011, p. E1-E1. *DOI.org (Crossref)*, doi:10.1038/nature09959.

Ridgwell, A., et al. « Marine Geochemical Data Assimilation in an Efficient Earth System Model of Global Biogeochemical Cycling ». *Biogeosciences*, vol. 4, nº 1, janvier 2007, p. 87-104. *DOI.org (Crossref)*, doi:10.5194/bg-4-87-2007.

Ritz, Catherine, et al. « Modeling the Evolution of Antarctic Ice Sheet over the Last 420,000 Years: Implications for Altitude Changes in the Vostok Region ». *Journal of Geophysical Research: Atmospheres*, vol. 106, nº D23, décembre 2001, p. 31943-64. *DOI.org (Crossref)*, doi:10.1029/2001JD900232.

Robert, François, et Marc Chaussidon. « A Palaeotemperature Curve for the Precambrian Oceans Based on Silicon Isotopes in Cherts ». *Nature*, vol. 443, nº 7114, octobre 2006, p. 969-72. *DOI.org (Crossref)*, doi:10.1038/nature05239.

Rooney, Alan D., et al. « A Cryogenian Chronology: Two Long-Lasting Synchronous Neoproterozoic Glaciations ». *Geology*, vol. 43, nº 5, mai 2015, p. 459-62. *DOI.org (Crossref)*, doi:10.1130/G36511.1.

Rosing, Minik T., et al. « No Climate Paradox under the Faint Early Sun ». *Nature*, vol. 464, nº 7289, avril 2010, p. 744-47. *DOI.org (Crossref)*, doi:10.1038/nature08955.

Rye, Rob, et al. « Atmospheric Carbon Dioxide Concentrations before 2.2 Billion Years Ago ». *Nature*, vol. 378, nº 6557, décembre 1995, p. 603-05. *DOI.org (Crossref)*, doi:10.1038/378603a0.

Sagan, C., et G. Mullen. « Earth and Mars: Evolution of Atmospheres and Surface Temperatures ». *Science*, vol. 177, nº 4043, juillet 1972, p. 52-56. *DOI.org (Crossref)*, doi:10.1126/science.177.4043.52.

Schoene, B., et al. « U-Pb Geochronology of the Deccan Traps and Relation to the End-Cretaceous Mass Extinction ». *Science*, vol. 347, nº 6218, janvier 2015, p. 182-84. *DOI.org (Crossref)*, doi:10.1126/science.aaa0118.

Seki, Osamu, et al. « Alkenone and Boron-Based Pliocene PCO2 Records ». *Earth and Planetary Science Letters*, vol. 292, nº 1-2, mars 2010, p. 201-11. *DOI.org (Crossref)*, doi:10.1016/j.epsl.2010.01.037.

Self, S., et al. « Sulfur and Chlorine in Late Cretaceous Deccan Magmas and Eruptive Gas Release ». *Science*, vol. 319, nº 5870, mars 2008, p. 1654-57. *DOI.org (Crossref)*, doi:10.1126/science.1152830.

Sepkoski, J. John. « A Kinetic Model of Phanerozoic Taxonomic Diversity I. Analysis of Marine Orders ». *Paleobiology*, vol. 4, nº 3, 1978, p. 223-51. *DOI.org (Crossref)*, doi:10.1017/S0094837300005972.

---. « A Kinetic Model of Phanerozoic Taxonomic Diversity II. Early Phanerozoic Families and Multiple Equilibria ». *Paleobiology*, vol. 5, nº 3, 1979, p. 222-51. *DOI.org (Crossref)*, doi:10.1017/S0094837300006539.

---. « A Kinetic Model of Phanerozoic Taxonomic Diversity. III. Post-Paleozoic Families and Mass Extinctions ». *Paleobiology*, vol. 10, nº 2, 1984, p. 246-67. *DOI.org (Crossref)*, doi:10.1017/S0094837300008186.

Sheldon, Nathan D. « Precambrian Paleosols and Atmospheric CO2 Levels ». *Precambrian Research*, vol. 147, nº 1-2, juin 2006, p. 148-55. *DOI.org (Crossref)*, doi:10.1016/j.precamres.2006.02.004.

Shields, Graham, et Ján Veizer. « Precambrian Marine Carbonate Isotope Database: Version 1.1: CARBONATE ISOTOPE DATABASE ». *Geochemistry, Geophysics, Geosystems*, vol. 3, nº 6, juin 2002, p. 1 of 12-12 12. *DOI.org (Crossref)*, doi:10.1029/2001GC000266.

Shukla, Sonali P., et al. « The Response of the South Asian Summer Monsoon Circulation to Intensified Irrigation in Global Climate Model Simulations ». *Climate Dynamics*, vol. 42, nº 1-2, janvier 2014, p. 21-36. *DOI.org (Crossref)*, doi:10.1007/s00382-013-1786-9.

Tang, M., et al. « Archean Upper Crust Transition from Mafic to Felsic Marks the Onset of Plate Tectonics ». *Science*, vol. 351, nº 6271, janvier 2016, p. 372-75. *DOI.org (Crossref)*, doi:10.1126/science.aad5513.

Tartèse, R., et al. « Warm Archaean oceans reconstructed from oxygen isotope composition of early-life remnants ». *Geochemical Perspectives Letters*, 2017, p. 55-65. *DOI.org (Crossref)*, doi:10.7185/geochemlet.1706.

Teitler, Yoram, et al. « Ubiquitous Occurrence of Basaltic-Derived Paleosols in the Late Archean Fortescue Group, Western Australia ». *Precambrian Research*, vol. 267, septembre 2015, p. 1-27. *DOI.org (Crossref)*, doi:10.1016/j.precamres.2015.05.014.

Trotter, J. A., et al. « Did Cooling Oceans Trigger Ordovician Biodiversification? Evidence from Conodont Thermometry ». *Science*, vol. 321, nº 5888, juillet 2008, p. 550-54. *DOI.org (Crossref)*, doi:10.1126/science.1155814.

Turner, Brian R., et al. « High Frequency Eustatic Sea-Level Changes during the Middle to Early Late Ordovician of Southern Jordan: Indirect Evidence for a Darriwilian Ice Age in Gondwana ». *Sedimentary Geology*, vol. 251-252, avril 2012, p. 34-48. *DOI.org (Crossref)*, doi:10.1016/j.sedgeo.2012.01.002.

Ueno, Yuichiro, et al. « Carbon Isotopes and Petrography of Kerogens in ~3.5-Ga Hydrothermal Silica Dikes in the North Pole Area, Western Australia ». *Geochimica et Cosmochimica Acta*, vol. 68, nº 3, février 2004, p. 573-89. *DOI.org (Crossref)*, doi:10.1016/S0016-7037(03)00462-9.

Valentine, James W., et Eldridge M. Moores. « Global Tectonics and the Fossil Record ». *The Journal of Geology*, vol. 80, nº 2, mars 1972, p. 167-84. *DOI.org (Crossref)*, doi:10.1086/627723.

van den Boorn, Sander H. J. M., et al. « Dual Role of Seawater and Hydrothermal Fluids in Early Archean Chert Formation: Evidence from Silicon Isotopes ». *Geology*, vol. 35, nº 10, 2007, p. 939. *DOI.org (Crossref)*, doi:10.1130/G24096A.1.

van Geldern, R., et al. « Carbon, Oxygen and Strontium Isotope Records of Devonian Brachiopod Shell Calcite ». *Palaeogeography, Palaeoclimatology, Palaeoecology*, vol. 240, nº 1-2, octobre 2006, p. 47-67. *DOI.org (Crossref)*, doi:10.1016/j.palaeo.2006.03.045.

Veizer, Ján, et al. « 87Sr/86Sr, Δ13C and Δ18O Evolution of Phanerozoic Seawater ». *Chemical Geology*, vol. 161, nº 1-3, septembre 1999, p. 59-88. *DOI.org (Crossref)*, doi:10.1016/S0009-2541(99)00081-9.

Walker, James C. G., et al. « A Negative Feedback Mechanism for the Long-Term Stabilization of Earth's Surface Temperature ». *Journal of Geophysical Research*, vol. 86, nº C10, 1981, p. 9776. *DOI.org (Crossref)*, doi:10.1029/JC086iC10p09776.

Williams, Stanley N., et al. « Global Carbon Dioxide Emission to the Atmosphere by Volcanoes ». *Geochimica et Cosmochimica Acta*, vol. 56, nº 4, avril 1992, p. 1765-70. *DOI.org (Crossref)*, doi:10.1016/0016-7037(92)90243-C.

Wolf, E. T., et O. B. Toon. « Hospitable Archean Climates Simulated by a General Circulation Model ». *Astrobiology*, vol. 13, nº 7, juillet 2013, p. 656-73. *DOI.org (Crossref)*, doi:10.1089/ast.2012.0936.

Yapp, Crayton J., et Harald Poths. « Ancient Atmospheric C02 Pressures Inferred from Natural Goethites ». *Nature*, vol. 355, nº 6358, janvier 1992, p. 342-44. *DOI.org (Crossref)*, doi:10.1038/355342a0.

Zachos, James C., et al. *(Table 1) Strontium Isotope Ratios of Planktonic Foraminifera and Ostracoda from ODP Hole 120-748B on the Kerguelen Plateau, Indian Ocean, Supplement to: Zachos, James C; Opdyke, Bradley N; Quinn, Terrence Michael; Jones, Charles E; Halliday, Alex N (1999): Early Cenozoic Glaciation, Antarctic Weathering, and Seawater 87Sr/86Sr: Is There a Link? Chemical Geology, 161(1-3), 165-180*. PANGAEA - Data Publisher for Earth & Environmental Science, 1999. *DOI.org (Datacite)*, doi:10.1594/pangaea.695370.

Zhisheng, An, et al. « Evolution of Asian Monsoons and Phased Uplift of the Himalaya–Tibetan Plateau since Late Miocene Times ». *Nature*, vol. 411, nº 6833, mai 2001, p. 62-66. *DOI.org (Crossref)*, doi:10.1038/35075035.

Zhou, Chuanming, et al. « New Constraints on the Ages of Neoproterozoic Glaciations in South China ». *Geology*, vol. 32, nº 5, 2004, p. 437. *DOI.org (Crossref)*, doi:10.1130/G20286.1.

CURRICULUM VITAE

Guillaume LE HIR

Maître de conférences de l'Université Paris Diderot — né le 27 Mars 1979
Institut de Physique du Globe de Paris (UMR CNRS 7154) — Pacsé, un enfant
Bureau 130; 1 rue Jussieu

tel : 33 (0)1 83 95 74 97
France mail : lehir@ipgp.fr

EXPERIENCE PROFESSIONNELLE

- Depuis 2009 - Maître de conférences à l'Université Paris Diderot
- 2008-2009 - ATER à l'Institut de physique du globe de Paris
- 2007-2008 - Post-doctorat de 8mois au LMTG (GET) - CIRAD (Montpellier)

  - CEA (Gif s/Yvette)
- 2003-2007 - nombreuses vacations d'enseignement (UVSQ, ENS-Paris, ...)
- 2002-2003 - enseignant de SVT dans le secondaire (lycée F. COUPRIN, Fontainebleau)

FORMATION

- Octobre 2004 – Novembre 2007 : Doctorat ED 143 Dynamique et Physico-chimie de la Terre et des Planètes (titre *comprendre et modéliser les glaciations du Néoprotérozoïque*, effectué au Laboratoire des Sciences du Climat et de l'Environnement (LSCE), UMR mixte CEA-CNRS-UVSQ.
- 2004 - DEA Géodynamique et Physique de la Terre, Filière "Sédimentologie et géochimie "
- 2002 Agrégation de Sciences de la Vie et de la Terre (spécialité Géologie) ENS Paris (rue d'Ulm) – Université Paris-Sud (Orsay)
- 1998- 2001 : 1er et 2ème cycles de biologie préparés à l'Université Paris-Sud (Orsay)

RECHERCHE

Mes activités de recherche concernent les changements climatiques pré-Quaternaires occasionnés par l'activité interne de la Terre (tectonique, volcanisme,...).

- *J'étudie* ***le couplage entre Terre interne et Terre externe afin de comprendre les mécanismes qui contrôlent l'évolution du climat*** *aux longues échelles de temps (>1Ma), comme ses perturbations plus brèves (<1Ma).*
- *Plus récemment, j'ai également étudié* ***les couplages du système climatique avec la biosphère*** *via l'intégration des propriétés fonctionnelles de la biosphère.*

- *Mes activités de recherche reposent sur l'utilisation des outils de la **modélisation numérique du climat mais aussi des cycles biogéochimiques (notamment celui du carbone) ainsi que de l'altération continentale.** L'intérêt de ces outils réside dans leur pouvoir de quantification des processus et rétroactions contrôlant le climat terrestre.*

ResearcherID: A-5676-2011

Thèses co-encadrées

- **Alexandre Pohl** (Soutenance effectuée le 16/11/2016) sujet : *Modélisation des changements climatiques et cryosphériques à l'Ordovicien.* Taux d'encadrement : 50%. Autre encadrant : Y. Donnadieu (DR CNRS).

- **Delphine Tardif** (thèse débutée le 01/10/2017) sujet : *Les moussons Asiatiques à la limité Eocène-Oligocène.* Taux d'encadrement : 33%. Autre encadrant : Y. Donnadieu (DR CNRS) et F. Fluteau (professeur IPGP).

- **Salomé Hennequin** (thèse débutée le 01/10/2017) sujet : *Etude des couplages entre l'évolution géologique des cycles biogéochimiques, du climat et de la biodiversité océanique,* Taux d'encadrement : 33%. Autre encadrant : G. Goddéris (DR CNRS) et F. Fluteau (professeur IPGP).

- **Mickael Mussard** (thèse abandonnée en Septembre 2014 suite à des soucis familiaux). sujet : *Quantification des perturbations environnementales liées aux traps du Deccan.* Début de thèse 01/10/2011 –Durée de la thèse 3ans. Taux d'encadrement : 50%. Autre encadrant : F. Fluteau (professeur IPGP).

- **Yoram Teitler** (Soutenance effectuée le 21/12/2012) sujet : *Climat et composition de l'atmosphère au Précambrien : des paléosols aux simulations numériques*. Durée de la thèse 4ans et 3mois. Taux d'encadrement : 33%. Autres encadrants : P. Philippot (Professeur -CNRS-IPGP), F. Fluteau (professeur IPGP).

Stages Masters

Clément Dufour (M1) sujet : *« évolution de l'albédo planétaire ».* 2011 (co-encadré avec Stéphane Jacquemoud, Université Dénis Diderot - Paris 7), **Nathan Jeiger** (M1) sujet : *« les perturbations climatiques liées aux changements de circulations océaniques au Cénozoïque »* (stages co-dirigé avec Y. Donnadieu, CNRS, LSCE centre de Saclay), **Pauline Galmiche** (M1) sujet : *« Analyse de la stabilité de la calotte Ouest Antarctique, quel rôle pour la surrection andine et le passage de Panama »* (stages co-dirigé avec Y. Donnadieu et P. Sepulchre, CNRS, LSCE centre de Saclay), **Alexandre Pohl** (M2) sujet : *Modélisation des changements climatiques et cryosphériques à l'Ordovicien.* 2nd semestre de l'année 2012-2013. Taux encadrement 33% (co-encadré par Yannick Donnadieu (CNRS), Christophe Dumas (CEA) du LSCE centre de Saclay)

Stages Licences

Léna Gurriaran (L2) sujet : *« le climat du Crétacé, l'importance de l'altération des silicates de la croûte océanique » Taux encadrement 100%* (stage non obligatoire)

RESPONSABILITES

- **Responsabilités au sein de l'université Paris 7 Denis Diderot – IPGP)**

  - Depuis 2016 : Directeur de la Licence Sciences de la Vie et de Terre (univ. Paris 7)
  - 2012 – 2017: Membre élu de la commission Recherche de l'Université Paris 7
  - 2012 – 2017: Membre élu de la commission des moyens de l'Université Paris 7
  - 2012 – 2017: Membre du conseil de l'UFR (université Paris 7-IPGP)
  - 2014- 2015: Directeur adjoint de l'UFR (université Paris 7-IPGP)

- **Responsabilités nationales**

  - depuis 2019: évaluateur HCERES pour les formations
  - 2014-2017: jury au concours de l'Agrégation externe de SVT
  - depuis 2014: membre du du GDR Climat Environnement Vie (CEV): les apports du pré-Quaternaire et co-responsable de la thématique – Volcanisme et Perturbations extrêmes du système Terre
  - depuis 2012: expert au CT1 (Comité thématique sur le climat) au comité GENCI (grand équipement national de calcul intensif)

- **Responsabilités Scientifiques**

  - 2018-2019 Responsable du projet INSU (comité SYSTER) « Paléomousson : de l'enregistrement continental au forçage orbital en Asie à l'Eocène »
  - 2017-2018 Participant au projet INSU (comité SYSTER) : *« Paléomousson » piloté par F. Fluteau (IPGP)*
  - 2017-2018 Participant au projet INSU (comité INTERVIE) : *« Couplages des cycles biogéochimiques, du climat et de la biodiversité à l'échelle des temps géologiques » piloté par Y. Goddéris (GET)*
  - 2016-2017 Participant au projet INSU (comité SYSTER) : *« Conséquences du grand bombardement tardif sur la Terre archéenne »* piloté par F. Fluteau (IPGP)
  - 2015-2016 Responsable (P.I.) du projet INSU (comité SYSTER) *: les glaciations du Néoprotérozoïque : un test pour comprendre la réponse du système Terre aux événements extrêmes à l'échelle de temps géologiques.*
  - 2015-2016 Participant au projet INSU (comité SYSTER) : *« Evolution de la production carbonatée pélagique à la limite K/Pg » piloté par B. Sucheras (CEREGE)*
  - 2013-2015 Participant au Svalbard project (PI. I Faichild et D. Benn) *« étude de la Terre boule de neige »* en tant que responsable du pôle modélisation

- 2013-2014 - Responsable (P.I.) du projet INSU (comité SYSTER) **:** *Modélisation des effets des grandes provinces basaltiques sur l'environement et la productivité marine* (2013-2014)
- 2009-2012 Participant au projet Emergeance *« quantifier et comprendre les variations des températures océaniques passées – projet modèle – données »,* responsable de la partie modélisation climat et cycles biogéochimiques (P.I. Bonifaci Magali, arrêt du projet : fin 2012
- 2009-2012 - Participation à l'ANR eLife en tant que responsable de la partie modélisation des climats anciens (P.I. de l'ANR eLife : Philippot Pascal, IPGP, arrêt de l'ANR : fin 2012)

ENSEIGNEMENT

J'enseigne essentiellement dans 3 grands domaines : **le climat, la biologie, et la géologie de terrain**.

i) les filières de formations aux futurs enseignants (40 %) - responsable d'une UE

ii) stage de terrain – modélisation 3D des structures géologiques (40%)

iii) en licence de géologie (20 %) - co-responsable de 2 UEs.

- **Présentation synthétique des enseignements**

	Heures Equivalents TD (CM=1,5TD-TP)							
UE	Filière	Niveau	Effectif	Formation	CM	TD	TP-Terrain	Heures Totales
Stage de terrain (Languedoc)	LVT	L2	40	initiale	0	0	30	30
Module de cartographie	LVT	L3	40 (2 groupes)	initiale	0	0	24	24
Préparation aux écrits	MEEF	M1	40	initiale	7	15	0	25,5
Préparation aux oraux	MEEF	M1	20 (2 groupes)	initiale	0	12	0	12
Exploitation géologique du sous-sol de Paris	MEEF	M1-M2	40 (2 groupes)	initiale	0	0	6	6
Stage de cartographie 3D (12 jours)	Masters géophysique	M1-M2	16	Initiale-continue	0	0	72	72
Biologie, Biochimie pour les géosciences	STEP	L1	72	Initiale	12	0	0	18
L'Homme et la Planète	STEP	L2	72	Initiale	10	0	0	15
** STEP Sciences de la Terre ,de l'Environnement et des Planètes Responsable de la Licence VT (décharge 32h)*								

Année	Heures équivalents TD
2015-2016	202
2016-2017	261,5
2017-2018	199,5
2018-2019	216.5

- **Pédagogie**

Ayant été moi-même enseignant dans le secondaire entre 2002-2003, je me suis impliqué, depuis mon recrutement à l'université Paris VII, dans les filières de formation aux futurs enseignants de SVT (ex prépa-CAPES, actuelles ESPE). J'ai eu l'opportunité d'être jury au concours de l'agrégation externe de SVT.
De ces expériences, j'ai décidé de m'investir en Licence (~ 60 % de mon temps – hors stage de terrain). Avec la réforme LMD, la licence est devenue le niveau crucial d'acquisition, à une période où les étudiants perçoivent encore mal l'intérêt des principes étudiés - spécialement si ces derniers sont présentés frontalement. Pour cette raison j'ai choisi de développer des approches pédagogiques :

- En supprimant les présentations type conférence et en réduisant les supports visuels à un nombre très réduit (3-4/2h de cours). En effet les cours magistraux sous forme de présentation type conférence (30-50 slides/heure) donnent un nombre d'informations visuelles bien trop grand pour un esprit qui n'est pas encore formé à sélectionner l'information. L'étudiant éprouve des difficultés à hiérarchiser l'importance des notions évoquées.

- Pour remplacer ce mode de présentation, j'ai choisi de repartir de la craie et du tableau noir (ou d'une mise en situation) afin de faire émerger une grande question, à partir de laquelle les notions d'importance sont construite. Cette approche, classique du secondaire, n'est possible que si le nombre d'étudiants reste modéré et devient délicate à appliquer dans un amphithéâtre.

- Lorsque cela est opportun, j'ai aussi opté pour l'insertion de l'étudiant dans la société. Cette approche repose sur la discussion du bien fondé scientifique de questions abordés dans l'actualité. La finalité de cette approche est de montrer comment est construit la savoir scientifique afin de permettre à l'étudiant de pouvoir discuter d'un point de vue scientifique l'actualité (ex : le réchauffement climatique et les derniers communiqués de presse du GIEC) et donc de s'affranchir des fakenews. Tous les cours ne sont pas propices à cette approche, cette approche est tout particulièrement développée dans l'UE « L'Homme et la Planète » où il est questions des problèmes environnementaux.

CONFERENCES (dernières années)

2017. Séminaire-invité à l'université de Lausanne (Suisse) en 2017 : « l'effondrement des producteurs primaires à la limite Crétacé-Paléogène »

2019. Séminaire-invité iSTEP (UMPC Paris) en 2019 « L'Apport de la modélisation biogéochimique à la compréhension de la crise K-Pg »

2019. Séminaire au GDR Climat Environnement Vie (CEV) – Lyon : « L'Apport de la modélisation biogéochimique à la compréhension de la crise K-Pg »

2019. Séminaire d'équipe au LSCE – Gif Sur Yvette - « L'Apport de la modélisation biogéochimique à la compréhension de la crise K-Pg »

Communications

2005- 2019: Nombreuses communications orales, posters en conférences internationales (Goldschmidt, EGU, GSA, AGU) et nationales (RST 2104, 2016)

PUBLICATIONS SCIENTIFIQUES

(* *étudiant encadré en thèse)*

Publications de rang A

1. 2007 Le Hir, G., Ramstein, G., Donnadieu, Y., Pierrehumbert, R.. Investigating plausible mechanisms to trigger a deglaciation from a hard snowball Earth. *Comptes Rendus de l'Académie des Sciences*, *snowball Earth special issue*, tome 339, n°3 et 4, p274-287,

2. 2008 Le Hir, G., Goddéris, Y., Ramstein, G., and Donnadieu, Y., Scenario for the evolution of atmospheric pCO2 during a snowball Earth. *Geology,* vol n36, n°1, p47-50,

3. 2008 Le Hir, G., Goddéris, Y., Donnadieu, Y., and Ramstein, G. A geochemical modeling study of the evolution of the chemical composition of seawater linked to a "snowball" glaciation. *Biogeosciences,* vol n°5, issue n°1, p253-267,

4. 2009 Le Hir, G., Goddéris, Y., Donnadieu, Y., Pierrehumbert, R, Halverson, G., Macouin M, Nedelec A., and Ramstein, G, The snowball Earth aftermath: exploring the limits of continental weathering processes, *Earth and Planetary Science Letter*, vol 277, issue 3-4, p453-463,

5. 2010 Le Hir, G., Donnadieu, Y., Krinner, G., and Ramstein, G. Toward Toward the snowball earth deglaciation… *Climate Dynamics*, vol 35, p285–297,

6. 2011 Le Hir, G., Donnadieu, Y., Goddéris, Y., Meyer-Berthaud, B., Ramstein, G., Blakey, R., The climate change caused by the land plant invasion in the Devonian, Earth and Planetary Science Letter, vol 310, p203-212

7. 2011 Nardin, E., Goddéris, Y., Donnadieu, Y., Le Hir, G., Blakey, R., Pucéat, E., Aretz, M., Modeling the early Paleozoic long-termed climatic trend, Geological Society of America Bulletin. Vol. 123, p: 1181-1192, doi: 10.1130/B30364.1

8. 2012 Abbot, D., Voigt, A., Branson, M; Pierrehumbert R., Pollard, D., Le Hir, G, Koll, D. Clouds and Snowball Earth deglaciation, Geophysical Research Letters. Vol. 39. DOI: 10.1029/2012GL052861

9. 2012 Goddéris, Y., Donnadieu, Y. Lefebvre, V., Le Hir, G ; Nardin, E 2012, Tectonic control of continental weathering, atmospheric CO2, and climate over Phanerozoic times Comptes rendus Geosciences. Vol: 344 Issue: 11-12 Pages: 52-662 DOI: 10.1016/j.crte.2012.08.009

10. 2013 Abbot, D., Voigt, A, Li, D. Le Hir, G ; Pierrehumbert, RT ; Branson, M ; Pollard, D ; Koll, D. Robust elements of Snowball Earth atmospheric circulation and oases for life. Journal of Geophysical Research-Atmospheres. Vol: 118 Issue: 12 Pages: 6017-6027 DOI: 10.1002/jgrd.50540

11. 2013 Goddéris Y.; Donnadieu Y.; Le Hir G.; Lefebvre V.; Nardin E. The role of paleogeography in the Phanerozoic history of atmospheric CO_2 and climate. Earth Science Reviews. 128,122-138, doi. 10.1016/j.earscirev.2013.11.004

12. 2014 *Mussard M, Le Hir G., Fluteau F., Lefebvre F., Goddéris Y. Modeling the carbon-sulfate interplays in climate changes related to the emplacement of Continental Flood

Basalts., Geological Society of America vol; 505, p339-352, 2014. doi: 10.1130/2014.2505(17).

13. 2014 *Teitler, Y; Le Hir, G; Fluteau, F; Philippot, P; Donnadieu, Y; Investigating the Paleoproterozoic glaciations with 3-D climate modeling, Earth and Planetary Science Letters, vol. 395, p:71-80, doi:10.1016/j.epsl.2014.03.044

14. 2014 Le Hir, G., *Teitler, Y., Fluteau, F., Donnadieu, Y., and Philippot, P. , The faint young Sun problem revisited with a 3-D climate–carbon model–Part 1,Climate of the Past,vol 10, p:697- 713, doi:10.5194/cp-10-697-2014

15. 2014 *Pohl, A; Donnadieu, Y; Le Hir, G; Buoncristiani, J-F; Vennin, E;, Effect of the Ordovician paleogeography on the (in) stability of the climate, Climate of the Past, 10, 2053-2066, doi:10.5194/cp-10-2053-2014

16. 2014 Godderis, Y.; Donnadieu, Y.; Le Hir, G. Lefebvre V., Nardin, E;, The role of palaeogeography in the Phanerozoic history of atmospheric CO2 and climate, Earth-Science Reviews, 128, 122- 138, DOI: 10.1016/j.earscirev.2013.11.004

17. 2015 *Teitler, Y., Philippot, P., Gérard, M., Le Hir G., Fluteau F., Ader M., Ubiquitous occurrence of basaltic-derived paleosols in the Late Archean Fortescue Group, Western Australia. PrecambrianResearch. doi:10.1016/j.precamres.2015.05.014

18. 2015 Benn D. Le Hir G., Bao H., Donnadieu Y, Dumas C., Fleming E.J., Hambrey M., McMillan E., Petronis M., Ramstein G., Stevenson C., Wynn P., Fairchild I. Orbitally forced ice sheet fluctuations during the Marinoan Snowball Earth glaciations. Nature Geoscience, vol.8, p704-707,, doi:10.1038/ngeo2502

19. 2015 Hoareau G., Bomou B., van Hinsbergen D., Carry N., Marquer D., Donnadieu Y., Le Hir G., Vrielynck G., Walter-Simonnet A.V. Did high Neo-Tethys subduction rates contribute to early Cenozoic warming? Climate of the Past, vol. 11, pp1751-1767, doi:10.5194/cp-11-1751

20. 2016 Pohl A., Donnadieu Y., Le Hir G.*, Ladant J.B., Dumas C., Alvarez-Solas J., Vandenbroucke T. Glacial onset predated Late Ordovician climate cooling. Paleoceanography, vol. 31, pp800-821. doi:10.1002/2016PA002928

21. 2016 Godderis, Y.; Le Hir, G.; Macouin, M.; Donnadieu Y., Hubert-Théou Lucie, Dera G. , Aretz M., Fluteau F., Lie Z.X., Halverson G. Paleogeographic forcing of the strontium isotopic cycle in the Neoproterozoic Gondwana Research Volume: 42 Pages: 151-162 DOI: 10.1016/j.gr.2016.09.013

22. 2017 Charnay B., Le Hir G., Fluteau F., Forget F., Catling D.C., A warm or a cold early Earth? New insights from a 3-D climate-carbon model, Volume 474, Pages 97-109. doi.org/10.1016/j.epsl.2017.06.029

23. 2017 Van der Meer, D. G.; van Saparoea, A; van Hinsbergen, D. J. J.; van de Wega R.M.B, Godderis Y., LeHir G., Donnadieu Y. Reconstructing first-order changes in sea level during the Phanerozoic and Neoproterozoic using strontium isotopes. Gondwana Research Volume: 44 Pages: 22-34. DOI: 10.1016/j.gr.2016.11.002

24. 2017 Pohl, A.*, Donnadieu, Y., Le Hir, G. and Ferreira, D.. The climatic significance of Late Ordovician-early Silurian black shales. Paleoceanography, 32(4): 397-423. DOI10.1002/2016PA003064

25. 2017 Hoffman P., Abbot D., Ashkenazy Y., Benn D., Brocks J.J., Cohen P., Cox G., Creveling J., Donnadieu Y., Erwin D., Fairchild I., Ferreira D., Goodman J., Halverson G., Jansen M., Le Hir G., Love G., Macdonald F., Maloof A., Partin C., Ramstein G., Rose B., Rose C., Sadler P., Tziperman E., Voigt A., Warren S. Snowball Earth climate dynamics and Cryogenian geology-geobiology, Science Advances, vol 3(11): DOI10.1126/sciadv.1600983

26. 2018 Pohl, A.*, Harper D., Donnadieu, Y., Le Hir G., Nardin E., Servais T. Possible patterns of marine primary productivity during the Great Ordovician Biodiversification Event, Lethaia, DOI 10.1111/let.12247

27. 2019 Michaud-Dubuy A., Carazzo G., Tait, S., Le Hir G, Fluteau F., Kaminiski E. Impact of wind direction variability on hazard assessment in Martinique (Lesser Antilles): the example of the 14 ka cal BP Bellefontaine Plinian eruption of Mount Pelée volcano Journal of Volcanology and Geothermal Research vol 381, Pages 193-208, doi.org/10.1013/j.volgeores.2019.06.004

28. Le Hir G., Fluteau, F., Sucheras, B., Goddéris, Y., Amplifying Factors Leading to the Collapse of Primary Producers during the Chicxulub Umpact and Deccan Traps, accepted Geological Society of America

Autres Publications

Chapitres de livres

Goddéris, Y., Le Hir, G., Donnadieu, Y.., 2011, Modelling the Snowball Earth,"Geological Society, London, Memoirs",36,1,151-161,,Geological Society of London, editor Armaud E, Shields G., Halverson G.

Le Hir, G., Paleomagnetism and climate, 2011, *CNFGG*

Donnadieu, Y Goddéris, Y., Le Hir, G., 2012, Neoproterozoic atmospheres and glaciation; *Treatise of Geochemistry vol. 13,* Editor Donald E. Canfield, James Farquhar, James F. Kasting

Le Hir, G. et Fluteau, F., 2012, la Climatologie, Encyclopedia Universalis

Goddéris, Y., Ramstein G., Le Hir, G., 2013, Le climat du Précambrien, in Paléoclimatologie, CNRS editions

Godderis, Y; Donnadieu, Y; Ramstein, G., Pucéat, E., Le Hir G., 2013, Le climat de la Terre à l'échelle destemps géologiques in Le Climat à découvert, CNRS éditions

Godderis, Y; Donnadieu, Y; Ramstein, G., Pucéat, E., Le Hir G., 2013, Le cycle du carbone à l'échelle des temps, CNRS éditions

Le Hir, G., La vie sur la Terre glacée, *La Recherche*, 2005

Le Hir, G., Goddéris, Y., Planète Blanche, *Sciences et Vie, Hors-série*, 2006

Le Hir, G. Goddéris, Y., La Terre boule de neige, *Les Dossiers de la Recherche*, 2007

Le Hir G. « la Terre boule de neige » bulletin de l'APBG (Association des professeurs de Biologie et Géologie) 2015

P. SanJoffre et G. Le Hir « La Terre boule de Neige, «Cataclysme climatique et tremplin biologique » Pour la Science, 2018

Pohl, A, Donnadieu, Y, Le Hir G., la modélisation peut elle aider à comprendre le climat d'il y a 450 Ma ? La Météorologie, n° 105, 2019 *(article invité suite à la remise du prix Prud'homme à A. Pohl pour sa thèse)*

RECUEIL DES TRAVAUX

Une sélection de 10 papiers est présentée dans la suite de ce manuscrit et classée par ordre chronologique de publication :

1. 2008 Le Hir, G., Goddéris, Y., Ramstein, G., and Donnadieu, Y., Scenario for the evolution of at mospheric pCO2 during a snowball Earth. *Geology,* vol n36, n°1, p47-50.

2. 2009 Le Hir, G., Goddéris, Y., Donnadieu, Y., Pierrehumbert, R, Halverson, G., Mac ouin M, Nedelec A., and Ramstein, G, The snowball Earth aftermath: explo ring the limits of continental weathering processes, *Earth and Planetary Science Letter*, vol 277, issue 3-4, p453-463,

3. 2011 Le Hir, G., Donnadieu, Y., Goddéris, Y., Meyer-Berthaud, B., Ramstein, G., Blakey, R., The climate change caused by the land plant invasion in the Devonian, Earth and Planetary Science Letter, vol 310, p203-212

4 2014 Le Hir, G., *Teitler, Y., Fluteau, F., Donnadieu, Y., and Philippot, P., The faint young Sun problem revisited with a 3-D climate–carbon model–Part 1,Climate of the Past,vol 10, p:697- 713, doi:10.5194/cp-10-697-2014

5. 2014 *Pohl, A; Donnadieu, Y; Le Hir, G; Buoncristiani, J-F; Vennin, E, Effect of the Ordovician paleogeography on the (in) stability of the climate, Climate of the Past, 10, 2053-2066, doi:10.5194/cp-10-2053-2014

6. 2014 Godderis, Y.; Donnadieu, Y.; Le Hir, G. Lefebvre V., Nardin, E, The role of palaeogeography in the Phanerozoic history of atmospheric CO2 and climate, Earth- Science Reviews, 128, 122- 138, DOI: 10.1016/j.earscirev.2013.11.004

7. 2015 Benn D. Le Hir G., Bao H., Donnadieu Y, Dumas C., Fleming E.J., Hambrey M., McMillan E., Petronis M., Ramstein G., Stevenson C., Wynn P., Fairchild I. Orbitally forced ice sheet fluctuations during the Marinoan Snowball Earth glaciations. Nature Geoscience, vol.8, p704- 707,, doi:10.1038/ngeo2502

8. 2016 Pohl A*., Donnadieu Y., Le Hir G. Ladant J.B., Dumas C., Alvarez-Solas J., Vandenbroucke T. Glacial onset predated Late Ordovician climate cooling. Paleoceanography, vol. 31, pp800-821,. doi:10.1002/2016PA002928

9. 2017 Charnay B., Le Hir G., Fluteau F., Forget F., Catling D.C., A warm or a cold early Earth? New insights from a 3-D climate-carbon model, Volume 474, Pages 97-109. doi.org/10.1016/j.epsl.2017.06.029

10 Le Hir G., Fluteau, F., Sucheras, B., Goddéris, Y., Amplifying Factors Leading to the Collapse of Primary Producers during the Chicxulub Impact and Deccan Traps,sous presse Geological Society of America

Scenario for the evolution of atmospheric pCO_2 during a snowball Earth

Guillaume Le Hir
Gilles Ramstein
Yannick Donnadieu
UMR CEA/CNRS/UVSQ, 1572 Laboratoire des Sciences du Climat et de l'Environnement, CE Saclay, Orme des Merisiers, Bât. 701, 91191 Gif sur Yvette Cedex, France
Yves Goddéris
UMR CNRS, 5563 Laboratoire des Mécanismes et Transferts en Géologie, Observatoire Midi-Pyrénées, 14, avenue Edouard Belin, 31400 Toulouse, France

ABSTRACT

The snowball Earth theory, initially proposed by J.L. Kirschvink to explain the Neoproterozoic glacial episodes, suggests that the Earth was globally ice covered at 720 Ma (Sturtian episode) and 640 Ma (Marinoan episode). The reduction of the water cycle and the growth of large ice sheets led to a collapse of CO_2 consumption through continental weathering and biological carbon pumping. As a consequence, atmospheric CO_2 built up linearly to levels allowing escape from a snowball Earth. In this contribution, we question this assumed linear accumulation of CO_2 into the atmosphere. Using a numerical model of the carbon-alkalinity cycles, we suggest that during global glaciations, even a limited area of open waters (10^3 km^2) allows an efficient atmospheric CO_2 diffusion into the ocean. This exchange implies that the CO_2 consumption through the low-temperature alteration of the oceanic crust persists throughout the glaciation. Furthermore, our model shows that rising CO_2 during the glaciation increases the efficiency of this sink through the seawater acidification. As a result, the atmospheric CO_2 evolution is asymptotic, limiting the growth rate of the atmospheric carbon reservoir. Even after the maximum estimated duration of the glaciation (30 m.y.), the atmospheric CO_2 is far from reaching the minimum deglaciation threshold (0.29 bar). Accounting for this previously neglected carbon sink, processes that decrease the CO_2 deglaciation threshold must be further explored.

Keywords: carbon cycle, seafloor weathering, snowball Earth, Neoproterozoic.

INTRODUCTION

Although processes and conditions required to trigger a snowball Earth (Kirschvink, 1992) have been intensively explored (Donnadieu et al., 2002, 2004a, 2004b; Schrag et al., 2002; Warren et al., 2002), studies related to the deglaciation of a snowball Earth remain scarce (Caldeira and Kasting, 1992; Higgins and Schrag, 2003; Pierrehumbert, 2005). The amount of atmospheric CO_2 needed to trigger the deglaciation from a globally ice-covered Earth was first evaluated at 0.12 bar (Caldeira and Kasting, 1992) and then modified at 0.29 bar by Pierrehumbert (2004) to account for the decreased solar luminosity in Neoproterozoic time. Using a more complex and comprehensive model (an atmospheric general circulation model, i.e., AGCM), Pierrehumbert (2005) demonstrated that the threshold value of 0.29 bar calculated with an energy balance model (EBM) was underestimated, and suggested that this value is at the lower end of the CO_2 levels required to deglaciate the snowball Earth.

In this contribution we focus on the various processes that may affect the way CO_2 would accumulate in a snowball atmosphere. It has been assumed that the drastic reduction of the continental weathering and the primary productivity occurring in a snowball Earth would have left the CO_2 outgassed by volcanoes free to accumulate in the atmosphere. Hoffman et al. (1998) calculated that atmospheric pCO_2 would reach 0.12 bar at the present outgassing rate after ~4 m.y. if no air-sea gas exchange took place, but that partial gas exchange through cracks in sea ice would increase this estimate. In contrast, Higgins and Schrag (2003) assumed that the ocean and atmosphere were in equilibrium with respect to CO_2 due to the air-sea gas exchange during the entire glacial event. However, in this later case an important additional factor able to modify the seawater chemistry, i.e., the low-temperature alteration of the oceanic crust, has to be considered if air-sea gas exchange took place. Because a large amount of the atmospheric CO_2 could be dissolved into the ocean, the ocean acidification promotes the removal of carbon through basaltic crust dissolution. This sink may have moved the simple linear atmospheric CO_2 accumulation toward an asymptotic evolution, raising the question of whether deglaciation melting can be reached.

CARBON CYCLE AND SEAFLOOR WEATHERING DURING SNOWBALL EVENTS

To investigate and quantify the carbon cycle evolution in a snowball environment, we designed a simple numerical model of the carbon-alkalinity cycles that includes the calculation of the seafloor weathering response to the acidification of the ocean (see Appendix). The model includes a box for the atmosphere, while the ocean is partitioned between a surface and a deep reservoir connected to a reservoir of water percolating through the oceanic crust, with a residence time of 2×10^4 yr (Elderfield and Schultz, 1996). The CO_2 exchange flux, F, at the ocean-atmosphere interface is calculated as a function of the gradient between the calculated atmospheric (pCO_2^{atm}) and dissolved oceanic pCO_2 (pCO_2^{ocean}):

$$F = \alpha\left(pCO_2^{atm} - pCO_2^{ocean}\right)\text{area}_{open}, \quad (1)$$

where α is the diffusion coefficient fixed at 16 mol/(yr m^2 PAL [Present Atmospheric Level]) (Etcheto et al., 1991), a value typical of high-latitude cold seawater, and area_{open} is the area of open water, a value considered as a model parameter that can be tested. pCO_2^{ocean} is estimated using Henry's law, fixing surface ocean temperature at 275 K during the snowball Earth. Carbonate speciation is calculated for each water reservoir at each time step. We assume an oceanic vertical mixing 100 times lower than the present-day thermohaline circulation (0.02 Sv) between the surface and deep ocean to account for the maximal expected overturning reduction due to the ice-covered ocean, because it seems physically improbable to completely shut down the general circulation (Zhang et al., 2001). Low-temperature seafloor alteration is calculated using laboratory kinetic laws (see Appendix). The dissolution of each mineral constitutive of the fresh basaltic crust (assumed to be a tholeiitic basalt) is modeled as a function of the temperature, T, of the water in contact with the basalt (fixed at 40 °C) (Brady and Gislason, 1997), and the pH of the percolating waters. The conclusions of this study partly depend on the model parameters, including the vertical mixing of the ocean, the present-day amplitude of the seafloor weathering, the water flux percolating the oceanic crust as well as its temperature, the seafloor spreading rate, the presence or absence of seafloor carbonates, and the area of open water. In the following we concentrate on the two last parameters, which are by far the most important. More details and

diagrams about sensitivity tests, regarding other important parameters such as the vertical mixing of the ocean and the efficiency of the seafloor weathering, can be found in GSA Data Repository Figures DR1 and DR2.[1]

Efficient Exchange Between the Ocean and Atmosphere

We first tested the minimal surface of open waters allowing an efficient diffusion of the atmospheric CO_2 into the ocean. Patches of open water were proposed in the original snowball Earth theory as refugia for living organisms (Kirschvink, 1992). Their existence has been confirmed by the study of Neoproterozoic formations (Hoffman and Maloof, 1999). To test the efficiency of the CO_2 diffusion from the atmosphere into the ocean, we define the diffusion efficiency E:

$$E = 1 - \frac{pCO_2\left(\text{area}_{\text{open}}\right)}{pCO_2\left(\text{hard snowball}\right)}, \qquad (2)$$

where $pCO_2(\text{area}_{\text{open}})$ is the CO_2 level reached after a simulation of 30 m.y., the maximum estimated duration of the snowball event (Hoffman et al., 1998), for a given free water area ($\text{area}_{\text{open}}$), and pCO_2 (hard snowball) is the same value assuming an ocean fully covered with ice. This E parameter is then normalized to its present-day value ($\text{area}_{\text{open}} = 363 \times 10^6$ km^2). In our set of model simulations, wherein the ice-free surface is varied from the present-day ocean surface (363×10^6 km^2) to 0 km^2, we calculate that above 3000 km^2, atmospheric CO_2 has enough time at the geologic time scale (here several millions of years) to dissolve within the ocean, and the area of open water is not a limiting factor for diffusion (Fig. 1). Below 3000 km^2, atmospheric CO_2 mixing into the ocean is limited. Today the surface of emerged active hydrothermal areas largely exceeds the 10^3 km^2 scale, being equal to 1.5×10^6 km^2 (Dessert et al., 2003). During global glaciations, emerged geothermal environments may be associated with small open water areas, maintained by heat production and lava flows. However, the existence of thick sea ice (Goodman, 2006) may reduce the contact between the patches of free waters and the whole ocean, limiting the CO_2 dissolution. For that reason, we cannot firmly state that the atmospheric CO_2 diffusion was fully efficient, but only 3000 km^2 of open waters in contact with the whole ocean are enough to achieve massive CO_2 dissolution.

[1]GSA Data Repository item 2008013, Figures DR1–DR3, supplementary information on the model and additional tests, is available online at www.geosociety.org/pubs/ft2008.htm, or on request from editing@geosociety.org or Documents Secretary, GSA, P.O. Box 9140, Boulder, CO 80301, USA.

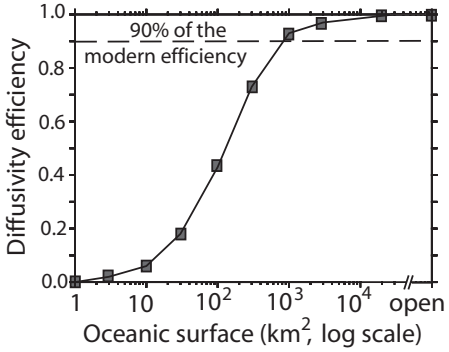

Figure 1. Normalized CO_2 diffusion efficiency as function of the ice-free oceanic surface.

Implications

If CO_2 is allowed to dissolve within the ocean during the building up of extremely high atmospheric carbon levels, seawater pH should drastically decrease and promote both deep-sea carbonates and oceanic basaltic crust dissolution.

Seafloor Weathering and Its Implication on the pCO_2

In the absence of deep seafloor sedimentary carbonates, the seawater acidification enhances the consumption of dissolved carbon through low-temperature alteration of the oceanic basaltic crust. Under the corrosive action of seawater percolating the crust at almost kilometric depth, basalts dissolve and release alkalinity, which is then removed through carbonate precipitation in veins from highly saturated pore waters (Alt and Teagle, 1999; Brady and Gislason, 1997; Spivack and Staudigel, 1994). The CO_2 consumption through seafloor basaltic weathering rises until the ocean is sufficiently acidified, so that consumption of carbon through seafloor weathering balances solid Earth outgassing.

The question is whether this theoretical steady-state CO_2 is higher than the required deglaciation threshold. In our scenario accounting for seafloor weathering, the atmospheric CO_2 build up does not rise linearly as in the classical snowball scenario (Fig. 2), but reaches an asymptotic value. Assuming a present-day total degassing rate of 7.15×10^{12} mol/yr (a value fixed to balance the present continental silicate and seafloor basalt CO_2 consumption rates) (Brady and Gislason, 1997; Gaillardet et al., 1999), we found that the atmospheric partial pressure does not exceed 0.17 bar within the estimated snowball duration of 12 m.y. (Bodiselitsch et al., 2005), because the seawater pH goes rapidly down to 6, increasing the seafloor weathering rate by a factor slightly above 4. Even after 30 m.y., the maximal duration for the snowball event (Hoffman et al., 1998), and with a volcanic outgassing rate enhanced by 20% (which is the maximum increase recorded over the past

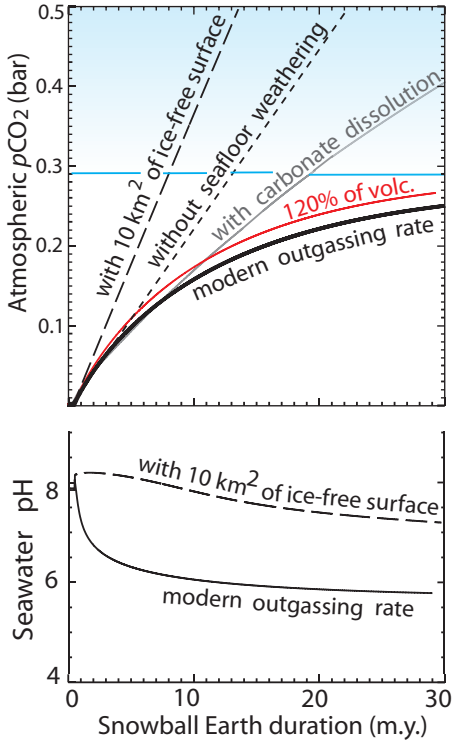

Figure 2. CO_2 evolution as function of the snowball Earth duration; 30 m.y. is maximum estimate. One run was performed with 10 km² of ice-free surface, all others with ice-free surface of 3000 km². Snowball earth deglaciation threshold (blue line) is 0.29 bar, estimated through an energy balance model simulation for a Neoproterozoic insolation. With a modern outgassing rate, the difference between the run with or without the seafloor weathering (black thick line and black dashed line, respectively) shows the impact of the CO_2 consumption by the low-temperature weathering of the basaltic seafloor. Higher volcanic degassing rate (red line) (1.2× present day; see text) would help at rising more rapidly the atmospheric CO_2 level but not sufficiently to overcome the deglaciation threshold. Because total degassing depends on the seafloor-spreading rate (Gaffin, 1987), the CO_2 consumption increases proportionally the surface of fresh seafloor basaltic rocks exposed to seawater. Below 10 km² of ice-free surface, the CO_2 diffusion becomes so weak that the atmosphere and ocean remain virtually isolated, the CO_2 accumulates in the atmosphere, and the seafloor weathering effect becomes negligible.

160 m.y.; Cogne and Humler, 2004), the CO_2 threshold of 0.29 bar required to escape the snowball glaciation cannot be reached (Fig. 2).

Buffering of Seawater pH through Carbonate Dissolution or Basaltic Weathering?

Seafloor sedimentary carbonate dissolution may have buffered seawater pH during the snowball glaciation, thus reducing the efficiency of seafloor weathering. However, maintain-

ing carbonate saturation (Higgins and Schrag, 2003) under 0.12 bar of CO_2 would require a calcium concentration in seawater twice its present-day level, corresponding to the dissolution of 2.5×10^{19} mol of carbonates if preglacial calcium concentration was close to its present-day value. If carbonate were of shelfal origin (pelagic carbonate producers being virtually absent), and considering the maximum past carbonate shelf extent of 15×10^6 km^2 (Walker et al., 2002), this would correspond to the dissolution of 66 m of carbonate sediments. This value would be even greater since the 0.12 bar threshold is largely underestimated (Pierrehumbert, 2004). Because sea level fell by more than 400 m during the glacial event (Hoffman et al., 2007), these shelf carbonates might not be available for dissolution.

However, carbonate slumps along continental slopes (Swart, 1992) or preglacial direct abiotic precipitation might have partly overlaid the deep seafloor with carbonates. We tested this hypothesis by running the model assuming that deep-sea carbonate dissolution occurs kinetically during the glacial event, forcing the seawater saturation index to 1. This corresponds to the maximum impact of carbonate dissolution on seawater chemistry, since dissolution stops when the saturation index reaches 1. We found that alkalinity rose to 18 equivalents/m^3 when CO_2 reached 0.29 bar, as a result of Ca^{2+} release by the carbonate dissolution and Ca^{2+}/Mg^{2+} exchange at mid oceanic ridges (Elderfield and Schultz, 1996). Seawater pH is calculated as 6.17, close to the 5.9 calculated in the absence of seafloor sedimentary carbonates. However, oceanic crust dissolution is sensitive to small pH changes. We calculate that, accounting for the maximum effect of carbonate buffering and because basaltic seafloor weathering is reduced, 0.29 bar of CO_2 can be reached in 19 m.y. This maximum effect corresponds to the dissolution of a 3-m-thick sedimentary carbonate layer spread over the global seafloor surface.

A possible anoxic state of the deep ocean may increase the pH of seawater during the snowball Earth. This would also result in decreased efficiency of the seafloor weathering. All along the glacial state, sulfate reduction may have produced alkalinity if the deep ocean was anoxic. The importance of this process depends upon the SO_4^{2-} level in seawater prior to the glacial event, and upon the availability of organic carbon in the water column and on the deep seafloor. A recent estimation shows that the SO_4^{2-} level might have been an order of magnitude below the present-day level (Hurtgen et al., 2002), thus largely below the dissolved inorganic carbon content of a snowball ocean, itself an order of magnitude above its present-day level in our calculations due to efficient atmospheric carbon dissolution. For that reason, we suggest that the ocean pH was still largely controlled by carbonate speciation, even during a snowball event.

CONCLUSION

If the snowball Earth occurred, it must have deglaciated. Our study shows that if the area of surface water in contact with the deep ocean is sufficient, the dissolution of the basaltic oceanic crust during the snowball glaciation may delay the atmospheric CO_2 rise required to reach the melting threshold, up to unacceptable time spans. The snowball theory thus requires either an extremely efficient dissolution of a large seafloor sedimentary carbonate reservoir whose existence remains hypothetical, or additional plausible processes able to decrease the CO_2 threshold through, for example, an albedo decrease, such as the deposition of dark fine volcanic ash on the ice and snow as suggested by Pierrehumbert (2004), or the existence of a thin equatorial ice (Goodman, 2006; Pollard and Kasting, 2005, 2006; Warren and Brandt, 2006).

APPENDIX: GEOCHEMICAL MODELING PROCEDURE

To simulate the evolution of the carbon content before the global glaciation, we first run the model according to Proterozoic preglacial conditions until a steady state is reached (Fig. DR3; see footnote 1). We use a standard silicate weathering law, where Ca^{2+} and Mg^{2+} weathering rates are proportional to global runoff and depend on mean global air temperature (Oliva et al., 2004). Continental carbonate weathering is proportional to global runoff times the concentration of Ca^{2+} in equilibrium with calcite at the calculated mean air temperature and atmospheric CO_2. Both air temperature and runoff are assumed to be a function of atmospheric CO_2. Biological productivity in the surface ocean is made dependent on the input flux of phosphorus from the deep ocean (to simulate upwelling consequences) and from the weathering of continental surfaces. These dependencies are used for the calibration procedure, because continental silicate, carbonate, and phosphorus weathering are shut down during the snowball glaciation.

To apply snowball conditions we instantaneously shut down all continental weathering fluxes to reproduce the consequences of the rapid growth of continental ice sheets and the strong weakening of the hydrological cycle. Surface water temperature is forced to drop from 20 °C to 2 °C, and the vertical mixing between the surface and deep ocean decreases from 21×10^6 m^3/s to 0.2×10^6 m^3/s. The model then evolves freely.

The α value used in equation 1 depends on wind speed (Wanninkhof, 1992). The wind action may be more efficient on one large surface than on several small. Since the total of ice-free surface is the sum of several small surfaces, K may be overestimated in our scenario. However in the extreme case wherein K is reduced by 10, the threshold surface required for an efficient exchange reaches 3×10^4 instead of 3×10^3 km^2, which remains very small. Note, however, that wind speed during the snowball event remains largely unknown, and the K we used is probably one of the best estimates that can be made.

Seafloor Weathering Parameterization

The deep ocean reservoir is in contact with a water reservoir incorporated into the oceanic crust. The temperature of the deep ocean is held constant at 275 K, and based on a present-day estimation (Elderfield and Schultz, 1996), the exchange water flux between the reservoir of percolating waters and the deep ocean is 0.2×10^6 m^3/s, given that 735×10^{13} kg/yr of water are involved in the water circulation off axis at low temperature.

The reservoir of percolating waters is depleted in carbon through low-temperature dissolution of the basaltic crust, under the corrosive action of seawater. The release of alkalinity through this process is assumed to finally lead to the precipitation of carbonate minerals from highly saturated waters in veins, thus removing carbon from the ocean-atmosphere system at the million year time scale. The global sink of carbon is estimated as ~$1.5–2.4 \times 10^{12}$ mol/yr (Alt and Teagle, 1999). Dissolution of seafloor basalts is calculated using laboratory kinetic laws to estimate the response of the H^+, OH^-, and H_2O promoted dissolution to change in seawater pH. The mineralogical composition of the crust is taken as the mineralogy of a tholeiitic basalt, containing 54% labradorite, 32% diopside, 9% basaltic glass, 4.3% apatite, and 1.3% forsterite. Kinetic constants are taken from the WITCH model database (Godderis et al., 2006; Drever, 1997). For each mineral, the overall dissolution rate R_{basalt} (in moles of Ca^{2+} released per m^2 of mineral per year) is estimated as following:

$$R_{basalt} = \sum_i d_i \exp\left(\frac{-E_i}{R \cdot T_p}\right) C_i^{n_i}, \qquad (A1)$$

where the sum extends up to all the dissolving species (H^+, OH^- and H_2O), while the index i stands for the dissolving species. E_i and d_i are, respectively, the activation energy and dissolution constant for each mineral depending on the species i promoted dissolution. T_p is the temperature of the percolating waters into the oceanic crust at which dissolution occurs, here fixed at 313 K. The value C_i stands for the concentration in the species i that promotes dissolution, while n_i is the order of the dissolution reaction. We assume that carbon consumption

through seafloor weathering (hereafter sfw) equals half of the alkalinity released through dissolution. The calculated overall CO_2 consumption flux F_{sfw} is multiplied by a constant area, representing the total mineral surface area exposed to dissolution:

$$F_{sfw} = SR \cdot area \cdot R_{basalt}. \quad (A2)$$

This constant is in fact a calibration constant that was fixed so that the total CO_2 consumption rate through seafloor weathering equals 1.6×10^{12} mol/yr under present-day conditions, within the lower range of recent estimations (Alt and Teagle, 1999; Spivack and Staudigel, 1994). SR is the seafloor spreading, normalized to its present-day value. It is kept constant at 1 in all simulations, except when assuming higher outgassing rate, itself corresponding to a higher seafloor-spreading rate. This overall kinetic formalism predicts a minimal basaltic dissolution rate at the present value of the ocean pH of 8.2.

ACKNOWLEDGMENTS

This work was supported by the ECLIPSE program (Environnement et Climat du Passé: Histoire et Evolution) of the Institut National des Sciences de l'Univers (INSU) of the French Centre National de la Recherche Scientifique (CNRS).We thank G. Halverson and P. Regnier for comments and corrections of this manuscript, and P. Sepulchre for his help and encouraging comments. Constructive comments by S. Warren, P. Hoffman, and anonymous reviewers helped to improve the manuscript.

REFERENCES CITED

Alt, J.C., and Teagle, D.A.H., 1999, The uptake of carbon during alteration of ocean crust: Geochimica et Cosmochimica Acta, v. 63, p. 1527–1535, doi: 10.1016/S0016–7037(99)00123–4.

Bodiselitsch, B., Koeberl, C., Master, S., and Reimold, W.U., 2005, Estimating duration and intensity of Neoproterozoic snowball glaciations from Ir anomalies: Science, v. 308, p. 239–242, doi: 10.1126/science.1104657.

Brady, P.V., and Gislason, S.R., 1997, Seafloor weathering controls on atmospheric CO2 and global climate: Geochimica et Cosmochimica Acta, v. 61, p. 965–973, doi: 10.1016/S0016–7037(96)00385–7.

Caldeira, K., and Kasting, J.F., 1992, Susceptibility of the early Earth to irreversible glaciation caused by carbon dioxide clouds: Nature, v. 359, p. 226–228, doi: 10.1038/359226a0.

Cogne, J.P., and Humler, E., 2004, Temporal variation of oceanic spreading and crustal production rates during the last 180 My: Earth and Planetary Science Letters, v. 227, p. 427–439, doi: 10.1016/j.epsl.2004.09.002.

Dessert, C., Dupre, B., Gaillardet, J., Francois, L.M., and Allegre, C.J., 2003, Basalt weathering laws and the impact of basalt weathering on the global carbon cycle: Chemical Geology, v. 202, p. 257–273, doi: 10.1016/j.chemgeo.2002.10.001.

Donnadieu, Y., Ramstein, G., Fluteau, F., Besse, J., and Meert, J., 2002, Is high obliquity a plausible cause for Neoproterozoic glaciations?: Geophysical Research Letters, v. 29, 23, doi: 10.1029/2002GL015902.

Donnadieu, Y., Godderis, Y., Ramstein, G., Nedelec, A., and Meert, J., 2004a, A 'snowball Earth' climate triggered by continental break-up through changes in runoff: Nature, v. 428, p. 303–306, doi: 10.1038/nature02408.

Donnadieu, Y., Ramstein, G., Fluteau, F., Roche, D., and Ganopolski, A., 2004b, The impact of atmospheric and oceanic heat transports on the sea-ice-albedo instability during the Neoproterozoic: Climate Dynamics, v. 22, p. 293–306, doi: 10.1007/s00382–003–0378–5.

Drever, J.I., 1997, The geochemistry of natural waters (third edition): Englewood Cliffs, New Jersey, Prentice-Hall, Inc., 436 p.

Elderfield, H., and Schultz, A., 1996, Mid-ocean ridge hydrothermal fluxes and the chemical composition of the ocean: Annual Review of Earth and Planetary Sciences, v. 24, p. 191–224, doi: 10.1146/annurev.earth.24.1.191.

Etcheto, J., Boutin, J., and Merlivat, L., 1991, Seasonal-variation of the CO2 exchange coefficient over the global ocean using satellite windspeed measurements: Tellus, ser. B, Chemical and Physical Meteorology, v. 43, p. 247–255, doi: 10.1034/j.1600–0889.1991.00017.x.

Gaffin, S., 1987, Ridge volume dependence on seafloor generation rate and inversion using long-term sealevel change: American Journal of Science, v. 287, p. 596–611.

Gaillardet, J., Dupre, B., Louvat, P., and Allegre, C.J., 1999, Global silicate weathering and CO2 consumption rates deduced from the chemistry of large rivers: Chemical Geology, v. 159, p. 3–30, doi: 10.1016/S0009–2541(99)00031–5.

Godderis, Y., Francois, L.M., Probst, A., Schott, J., Moncoulon, D., Labat, D., and Viville, D., 2006, Modelling weathering processes at the catchment scale: The WITCH numerical model: Geochimica et Cosmochimica Acta, v. 70, p. 1128–1147, doi: 10.1016/j.gca.2005.11.018.

Goodman, J.C., 2006, Through thick and thin: Marine and meteoric ice in a "Snowball Earth" climate: Geophysical Research Letters, v. 33, p. L16701, doi: 10.1029/2006GL026840.

Higgins, J.A., and Schrag, D.P., 2003, Aftermath of a snowball Earth: Geochemistry, Geophysics, Geosystems, v. 4, doi: 10.1029/2002GC000403.

Hoffman, P.F., and Maloof, A.C., 1999, Glaciation: The snowball theory still holds water: Nature, v. 397, p. 384, doi: 10.1038/17006.

Hoffman, P.F., Kaufman, A.J., Halverson, G.P., and Schrag, D.P., 1998, A Neoproterozoic snowball earth: Science, v. 281, p. 1342–1346, doi: 10.1126/science.281.5381.1342.

Hoffman, P.F., Halverson, G.P., Domack, E.W., Husson, M.H., Higgins, J.A., and Schrag, D.P., 2007, Are basal Ediacaran (635 Ma) postglacial "cap-dolostones" diachronous?: Earth and Planetary Science Letters, v. 258, p. 114–131.

Hurtgen, M.T., Arthur, M.A., Suits, N.S., and Kaufman, A.J., 2002, The sulfur isotopic composition of Neoproterozoic seawater sulfate: Implications for a snowball Earth?: Earth and Planetary Science Letters, v. 203, p. 413–429, doi: 10.1016/S0012–821X(02)00804-X.

Kirschvink, J.L., 1992, Late Proterozoic low-latitude glaciation: The snowball earth, *in* Schopf, J.W., and Klein, C., eds., The Proterozoic biosphere: Cambridge, Cambridge University Press, p. 51–52.

Oliva, P., Dupre, B., Martin, F., and Viers, J., 2004, The role of trace minerals in chemical weathering in a high-elevation granitic watershed (Estibere, France): Chemical and mineralogical evidence: Geochimica et Cosmochimica Acta, v. 68, p. 2223–2243, doi: 10.1016/j.gca.2003.10.043.

Pierrehumbert, R.T., 2004, High levels of atmospheric carbon dioxide necessary for the termination of global glaciation: Nature, v. 429, p. 646–649, doi: 10.1038/nature02640.

Pierrehumbert, R.T., 2005, Climate dynamics of a hard Snowball Earth: Journal of Geophysical Research, v. 110, D01111, doi: 10.1029/2004JD005162.

Pollard, D., and Kasting, J.F., 2005, Snowball Earth: A thin-ice solution with flowing sea glaciers: Journal of Geophysical Research-Oceans, v. 110, C07010, doi: 10.1029/2004JC002525.

Pollard, D., and Kasting, J.F., 2006, Snowball Earth: A thin-ice solution with flowing sea glaciers: Reply: Journal of Geophysical Research-Oceans, v. 111.

Schrag, D.P., Berner, R.A., Hoffman, P.F., and Halverson, G.P., 2002, On the initiation of a snowball Earth: Geochemistry, Geophysics, Geosystems, v. 3, doi: 10.1029/2001GC000219.

Spivack, A.J., and Staudigel, H., 1994, Low-temperature alteration of the upper oceanic-crust and the alkalinity budget of seawater: Chemical Geology, v. 115, p. 239–247, doi: 10.1016/0009–2541(94)90189–9.

Swart, R., 1992, Facies analysis of Late Proterozoic carbonate turbidites in the Zerrissene Basin, Damara-Orogen, Namibia: Journal of African Earth Sciences, v. 14, p. 283–294, doi: 10.1016/0899–5362(92)90105-L.

Walker, L., Wilkinson, B.H., and Ivany, L.C., 2002, Continental drift and Phanerozoic carbonate accumulation in shallow-shelf and deep-marine settings: Journal of Geology, v. 110, p. 75–87, doi: 10.1086/324318.

Wanninkhof, R., 1992, Relationship between windspeed and gas-exchange over the ocean: Journal of Geophysical Research-Oceans, v. 97, p. 7373–7382.

Warren, S.G., and Brandt, R.E., 2006, Snowball earth: A thin-ice solution with flowing sea glaciers: Comment: Journal of Geophysical Research-Oceans, v. 111, C09016, doi:10.1029/2005JC003411.

Warren, S.G., Brandt, R.E., Grenfell, T.C., and McKay, C.P., 2002, Snowball Earth: Ice thickness on the tropical ocean: Journal of Geophysical Research-Oceans, v. 107, no. C10, 3167, doi: 10.1029/2001JC001123.

Zhang, R., Follows, M.J., Grotzinger, J.P., and Marshall, J., 2001, Could the Late Permian deep ocean have been anoxic?: Paleoceanography, v. 16, p. 317–329, doi: 10.1029/2000PA000522.

Manuscript received 29 May 2007
Revised manuscript received 30 August 2007
Manuscript accepted 31 August 2007

Printed in USA

Earth and Planetary Science Letters xxx (2008) xxx–xxx

Contents lists available at ScienceDirect

Earth and Planetary Science Letters

journal homepage: www.elsevier.com/locate/epsl

The snowball Earth aftermath: Exploring the limits of continental weathering processes

Guillaume Le Hir [a], Yannick Donnadieu [a], Yves Goddéris [b,*], Raymond T. Pierrehumbert [c], Galen P. Halverson [d], Mélina Macouin [b], Anne Nédélec [b], Gilles Ramstein [a]

[a] LSCE, CNRS-CEA-UVSQ, Gif-sur-Yvette, France
[b] LMTG, CNRS-Université de Toulouse, Observatoire Midi-Pyrénées, Toulouse, France
[c] Dept of Geophysical Sciences, University of Chicago, Illinois, USA
[d] School of Earth and Environmental Sciences, University of Adelaide, North Terrace, Adelaide, SA 5005, Australia

ARTICLE INFO

Article history:
Received 22 May 2008
Received in revised form 10 October 2008
Accepted 10 November 2008
Available online xxxx

Editor: P. DeMenocal

Keywords:
snowball Earth
greenhouse
cap dolostones
weathering
modelling

ABSTRACT

Carbonates capping Neoproterozoic glacial deposits contain peculiar sedimentological features and geochemical anomalies ascribed to extraordinary environmental conditions in the snowball Earth aftermath. It is commonly assumed that post-snowball climate dominated by CO_2 partial pressures several hundred times greater than modern levels, would be characterized by extreme temperatures, a vigorous hydrological cycle, and associated high continental weathering rates. However, the climate in the aftermath of a global glaciation has never been rigorously modelled. Here, we use a hierarchy of numerical models, from an atmospheric general circulation model to a mechanistic model describing continental weathering processes, to explore characteristics of the Earth system during the supergreenhouse climate following a snowball glaciation. These models suggest that the hydrological cycle intensifies only moderately in response to the elevated greenhouse. Indeed, constraints imposed by the surface energy budget sharply limit global mean evaporation once the temperature has warmed sufficiently that the evaporation approaches the total absorbed solar radiation. Even at 400 times the present day pressure of atmospheric CO_2, continental runoff is only 1.2 times the modern runoff. Under these conditions and accounting for the grinding of the continental surface by the ice sheet during the snowball event, the simulated maximum discharge of dissolved elements from continental weathering into the ocean is approximately 10 times greater than the modern flux. Consequently, it takes millions of years for the silicate weathering cycle to reduce post-snowball CO_2 levels to background Neoproterozoic levels. Regarding the origin of the cap dolostones, we show that continental weathering alone does not supply enough cations during the snowball melting phase to account for their observed volume.

1. Introduction

Geological evidence suggests the occurrence of two global glaciations during the Neoproterozoic. The older glaciation, the Sturtian event, is commonly inferred to have occurred at ca. 700–680 Ma, while the latter, end-Cryogenian glaciation ended at 635 Ma (Hoffman et al., 2004; Condon et al., 2005). The melting of these snowball Earth events requires very high atmospheric pCO_2, so that the greenhouse warming overcomes the freezing feedback induced by a high sea-ice albedo. The amount of CO_2 required to initiate melting of a snowball was first calculated to be 0.12 bar (400 PAL) using a simple energy balance model (Caldeira and Kasting, 1992) but more recent modelling suggests it was above 0.2 bar (660 PAL) (Pierrehumbert, 2004). Geochemical evidence seems to confirm exceptionally high pCO_2 following at least the 635 Ma snowball event (Kaseman et al., 2005; Bao et al., 2008), but the behavior of this supergreenhouse climate under very high CO_2 levels is still poorly understood. Was it just a short pulse, lasting a few hundreds of kyrs, or was it longer-lived, with environmental consequences enduring for millions of years? According to the classic snowball Earth hypothesis the supergreenhouse drove a hyper-active hydrological cycle inducing intense continental weathering, such that CO_2 levels would have been drawn down from very high levels to preglacial levels in about 200 kyrs (Higgins and Schrag, 2003).

Up to now, this timespan subsequent to the snowball glacial event has never been investigated with a comprehensive climate model. In this contribution, four numerical models (Fig. 1) are used to investigate the evolution of the post glacial climate: (1) a 3D-climate model to characterize the super hothouse climate, (2) a continental weathering model to investigate the behaviour of the CO_2 weathering sink, (3) a simple carbon-alkalinity cycle model to simulate the evolution of the atmospheric CO_2 levels in the immediate aftermath of the snowball Earth, and (4) a simple eustatic model to investigate the

* Corresponding author.
E-mail address: godderis@lmtg.obs-mip.fr (Y. Goddéris).

0012-821X/$ – see front matter © 2008 Elsevier B.V. All rights reserved.
doi:10.1016/j.epsl.2008.11.010

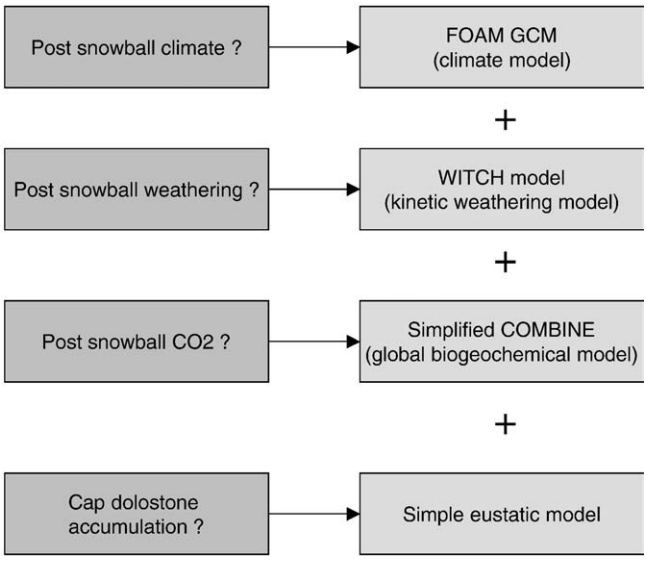

Fig. 1. General design of the simulations. At each level, a question is added and addressed using a specific model. When going down through the diagram, any new specific question requires the coupling of a hierarchy of models (specified by the sign '+').

consequences of post snowball continental weathering on cap dolostone accumulation. Our aim is to use numerical modelling to produce a first order reconstruction of the supergreenhouse climate and the timescale over which it is relaxed. Weathering processes are influenced by the air temperature controlling the dissolution rates of minerals, and by the continental runoff, which modulates dissolution through water-rock interactions and carries the weathering products to the oceans. We will first focus on climatic reconstructions of the supergreenhouse environment, after which the behaviour of the weathering sink under this climate will be discussed, and its consequences on the duration of the supergreenhouse will be investigated. Specifically, we will address the accumulation of cap dolostones which were deposited during the post glacial eustatic transgression and are a key element of the snowball hypothesis.

2. The climate of the snowball aftermath

2.1. Climate model description and simulation design

The climate of the post snowball is investigated with the general circulation climate model FOAM 1.5. The atmospheric component of FOAM is a parallelized version of NCAR's Community Climate Model 2 (CCM2) with the upgraded radiative and hydrologic physics incorporated in CCM3 v. 3.2 (Jacob, 1997). All simulations have been performed with an R15 spectral resolution (4.5°×7.5°) and 18 vertical levels. FOAM is used in mixed-layer mode, meaning the atmospheric model is linked to a 50-meter mixed-layer ocean with heat transport parameterized through diffusion. FOAM has been extensively applied to the study of ancient climate (Poulsen, 2003; Poulsen and Jacob, 2004; Donnadieu et al., 2006) and Pierrehumbert has demonstrated the validity of the FOAM radiative code in highly enriched CO_2 atmospheres such as the one hypothesized in the snowball Earth aftermath (Pierrehumbert, 2004). We have used a simplified paleogeographic model for the late Cryogenian (i.e. Marinoan) adapted from Macouin [pers.com] wherein the continental fragments of the former supercontinent Rodinia are clustered in low latitudes. An orography is assumed considering geological features (old orogenic belts and recent rifting) (Meert and Torsvik, 2003) [Macouin, pers. com.] (Fig. 2). We prescribe the presence of orogens and rifts (Meert and Torsvik, 2003) as elevated areas, between 500 and 1100 m (these relatively low altitudes are the consequence of the spectral smoothing implied by the model low surficial resolution), while the continental area outside uplifted surface has an elevation of 75 m. Solar luminosity is fixed at 94% of its present day value (1286 W/m^2) according to stellar evolution models (Gough, 1981). Orbital parameters are set at their present day values. Regarding continental runoff, a present day simulation of FOAM linked to the mixed-layer ocean predict a global value of 27 cm/yr, a value very close to the observed 25 cm/yr (Berner and Berner, 1987) or 22 cm/yr (Gaillardet et al., 1999).

The melting phase of the snowball Earth has never been investigated. Indeed, modelling the climate under several hundred times the present day CO_2 pressure and with the presence of melting icecaps but also of melting sea-ice glaciers remains an unsolved challenge in terms of numerical tools and of computational times. The aim of this paper is not to model in detail the deglaciation: rather the

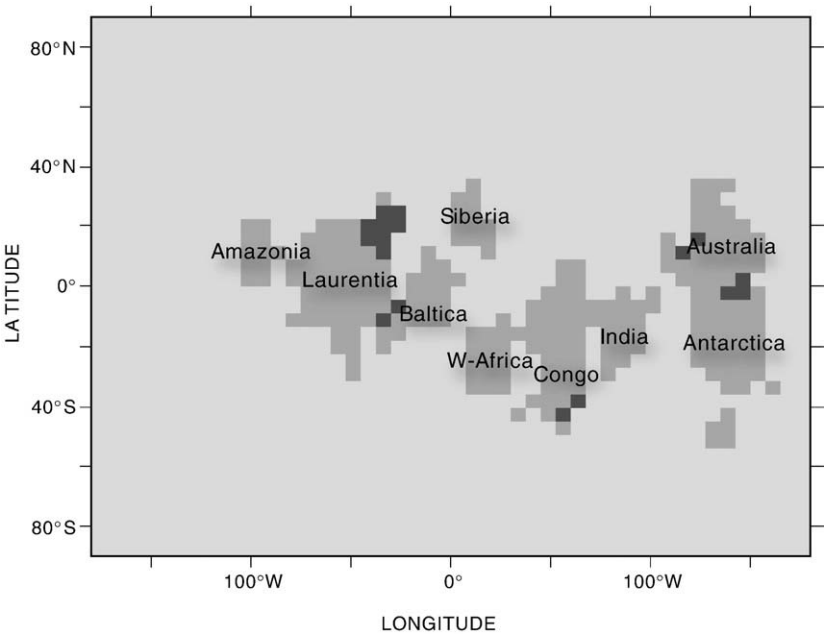

Fig. 2. End-Cryogenian (ca. 635 Ma) paleogeography used in the numerical modelling in this paper. Location of continental flood basalt provinces are shown in dark grey.

Please cite this article as: Le Hir, G., et al., The snowball Earth aftermath: Exploring the limits of continental weathering processes, Earth Planet. Sci. Lett. (2008), doi:10.1016/j.epsl.2008.11.010

focus here is on the supergreenhouse climate occurring just after the melting of the continental and sea ice. Considering the Neoproterozoic solar weakness and nonlinear relation between CO_2 concentration and the resultant greenhouse forcing, the following range of atmospheric CO_2 mixing ratios (400, 200, 100, 50, 25, 20, 15, and 10 PAL) has been used to model the influence of CO_2 concentrations on post-glacial temperature and runoff. The simulations reach equilibrium with the prescribed boundary conditions after 30 years. The analyses are done using the average of the next ten years. All the continents are assumed to be covered with a rocky regolith (visible albedo 0.24, infrared albedo 0.4, roughness 0.05 m, potential evaporation 0.1)

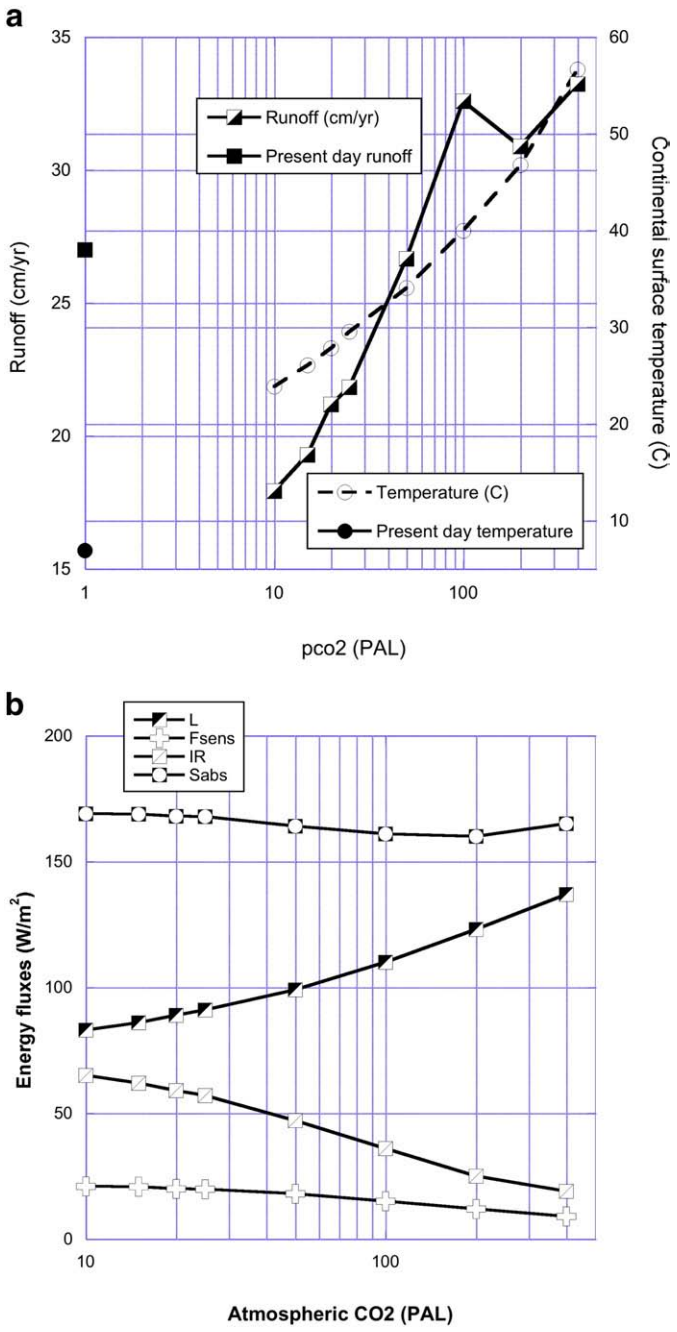

Fig. 3. a) Mean continental runoff and mean continental temperature calculated by the FOAM GCM under Neoproterozoic conditions and for various atmospheric CO_2 levels. The calculated present day values are also shown b) Energy fluxes calculated by the FOAM GCM under Neoproterozoic conditions and for various atmospheric CO_2 levels. *L* is the latent heat, F_{sens} the sensible heat, IR the surface infra-red cooling and S_{abs} the total incoming solar radiation adsorbed by the surface.

Table 1
Water vapor mixing ratio at 5 different CO_2 levels for Neoproterozoic conditions, 1 PAL equals 280 ppm

Atmospheric pCO_2 (PAL)	q_s	q	P (mm/mo)	Land ratio
400	0.064	0.052	141	0.88
200	0.042	0.035	127	0.96
100	0.029	0.024	113	0.94
50	0.022	0.018	102	0.88
10	0.014	0.011	85	0.825

q_s is the saturation water vapor mixing ratio at surface air temperature, in kg water per kg air. q is the actual water mixing ratio of the air, in kg water per kg air. P is the global mean precipitation in mm/month, and the "land ratio" is the ratio of the mean precipitation rate over land to the global mean precipitation rate.

2.2. Post snowball Earth climate: runoff and water cycle behaviour

Fig. 3a shows average terrestrial temperature and runoff evolution as a function of the atmospheric CO_2 mixing ratio. The mean continental temperature exhibits a roughly logarithmic response to CO_2 rise while runoff follows two pathways in our runs, a first one characterized by a logarithmic increase and a second one, above 100 PAL, characterized by a runoff saturating around 30–33 cm/yr which corresponds to a maximum increase of 22% when compared to the simulated runoff under present-day climate. This modest increase in runoff despite vastly higher pCO_2 sharply contrasts with the 7 fold increase in runoff assumed in the only other attempt to model silicate weathering rates under a post-snowball climate. In this previous study (Kump pers. com. in Higgins and Schrag, 2003), maximum runoff increase was estimated based on the inventory of the maximum amplitude of a variety of hydrological factors (Holland, 1978). As will be discussed further in Section 3, our result has important consequences for the rates of chemical weathering and geochemical evolution of the oceans following a snowball glaciation.

The weak increase in precipitation (and hence in runoff) with temperature in the post-Snowball world plays a key role in our results, and so merits some further discussion. In fact, a very similar phenomenon, although smaller, has attracted a lot of attention with regard to the effect of anthropogenic global warming on precipitation (notably Held and Soden, 2006). In particular, it has been found in virtually all climate simulations that increasing temperature by doubling or quadrupling CO_2 increases the precipitation much less than one would expect from the increase in saturation vapor pressure obtained from the Clausius-Clapeyron relation. Specifically, the Clausius-Clapeyron relation predicts that precipitation should increase by about 7% per degree of warming, whereas the actual figure for moderate warming is more like 2%. The presumed explanation for this disparity is that as the planet warms, atmospheric circulation becomes more sluggish, so that even though there is more water in the system, the rate at which it condenses into rain does not increase much (Vecchi et al., 2006). Atmospheric circulation weakens with the increase of atmospheric CO_2 levels in our simulations, in particular, the mean annual stream function zonally averaged is divided by 5 between the 20 PAL and the 400 PAL runs (figure not shown).

It has often been thought that infrared radiative cooling places an *a priori* constraint on precipitation, given that the dominant energy balance in the atmosphere is between latent heat release and radiative cooling (see Allen and Ingram, 2002 for a recent review of such arguments). However, Pierrehumbert (Pierrehumbert, 1999) showed that the argument is fallacious, or at least incomplete, since in principle the surface conditions can adjust to allow whatever column-integrated infrared cooling is necessary to accommodate the evaporation required to sustain a given precipitation level. In order to understand constraints on precipitation, a detailed consideration of the surface energy budget is unavoidable. In particular, it was argued

Please cite this article as: Le Hir, G., et al., The snowball Earth aftermath: Exploring the limits of continental weathering processes, Earth Planet. Sci. Lett. (2008), doi:10.1016/j.epsl.2008.11.010

that the evaporation from the surface is in effect limited by the supply of solar radiation absorbed at the surface, so that if one warms the climate by increasing CO_2 without changing the solar radiation, there comes a threshold above which all solar radiation is used to sustain evaporation, whereafter precipitation no longer increases with temperature. This argument was extended and made more quantitative in Pierrehumbert (2002), where it was pointed out that the evaporation can somewhat exceed the solar absorption, but that the excess tends to be limited by the properties of turbulent fluxes in a stable boundary layer. This limitation in the increase in precipitation rates with increased pCO_2 has important implications for silicate weathering, and it is these implications that we explore in the Snowball recovery simulations here.

Table 1 and Fig. 3b summarize key boundary layer and surface budget properties pertinent to the hydrological cycle. As CO_2 is increased from 10 PAL to 400 PAL, the low level saturation mixing ratio increases by a factor of 4.6, and the actual boundary layer mixing ratio increases by a similar factor. However, the global precipitation rate only increases by 60%, with a proportional increase over the continents. To understand this relationship, it is necessary to examine the components of the surface energy budget. The following equation describes the global energy budget of the Earth surface:

$$S_{abs} = L + F_{sens} + IR. \quad (1)$$

where S_{abs} is the global solar radiation absorbed by the surface, L is the latent heat flux (evaporation), F_{sens} is the sensible heat flux and IR the net infrared cooling of the surface. The mass flux of water due to evaporation is proportional to L, which hence determines the global precipitation rate. The net infrared cooling rate of the surface is the upward flux $\sigma T^4_{surface}$ minus the infrared back-radiation from the atmosphere. To the extent that F_{sens} and IR balance some of the incoming solar absorption, they capture energy that would otherwise be used to sustain evaporation. Both F_{sens} and IR increase as the surface is made increasingly warmer than the overlying atmosphere; they tend to be small when the air and surface temperatures are close, and moreover as the temperature increases and the boundary layer becomes more moist the net infrared cooling falls to zero because the atmosphere radiates to the ground at the same temperature as the ground radiates to the atmosphere. Looking at the calculated energy budget in the Fig. 3b, we see that the solar absorption remains nearly constant as CO_2 is increased, but that the sensible and infrared cooling falls precipitously as the climate is made warmer. The slack is taken up by evaporation, but the total "extra" energy in the 10 PAL case is only 86 W/m^2. Indeed, we see that by the time we reach the 400 PAL case, evaporation balances 82% of the surface absorbed solar radiation.

Thus, the limited increase in runoff in these simulations is seen as a robust consequence of the behavior of the surface energy budget. Nevertheless, it should be reminded that the runoff depends also on how available water vapor is redistributed between land and ocean. In our particular case where most of the continents are located in the tropical regions, deep atmospheric convection as well as sea surface temperature distribution should be two major factors controlling the water transport between the ocean and the continent. While we are confident in the way FOAM simulates the former one, the latter one may suffer from uncertainties owing to the use of the mixed-layer version of the FOAM model. Nevertheless, although we acknowledge that the mixed-layer model may bias our results, we suspect that the global energetic arguments developed in the paper remain the first order process controlling the absolute value of the global runoff. The use of a fully coupled climate model is warranted in order to provide a definitive answer. Potential shortcomings of our results may also come from the cloud parameterizations and its behaviour in a very different climate than the modern one. One of the primary determinants of cloud forcing is the cloud water content. The FOAM cloud water parameterization and its limitations were described in Pierrehumbert (2004). In particular, while the scale height of cloud water increases in a warming climate, allowing high clouds to become more optically thick in a warmer world, the base-level cloud water parameter is independent on temperature. Insofar as there is more supply of water vapor in a hotter world, it is not unreasonable to expect that clouds at all levels might have higher water vapor content. In that case, the present simulations may underestimate the cloud water content. To test the implications of this possibility, we performed another run with 400× present CO_2, but with the cloud water parameter increased by a factor of 2. As a test in this run, both the cloud albedo effect and the cloud greenhouse effect roughly doubled compared to the control case, but the net cloud forcing remained nearly the same, with a slight shift toward more net cooling in the subtropics and more warming at the poles. The higher albedo did, however, reduce the surface absorbed solar radiation from 167 W/m^2 in the 400 PAL control case to 150 W/m^2 in the thick-cloud case. In accordance, this also reduced the global mean precipitation rate from 141 mm/mo to 114 mm/mo. Thus, higher cloud water content further reduces the precipitation. Nevertheless, the factors governing cloud fraction are poorly understood. In particular, there is observational evidence that for warm rain processes, cloud fraction goes down with temperature, owing to increased precipitation efficiency (Rapp et al., 2005). This feedback is not present in the cloud fraction scheme we are using. This is a fruitful area for future inquiry.

3. Continental weathering during the supergreenhouse climate

We now consider the weathering pattern as a function of the simulated climate. As shown in Section 2, the simulated post-glacial period is warm and moderately humid, with maximum continental runoff limited at 33 cm/yr above 100 PAL CO_2. Depending on this climate regime, the silicate weathering acts as a restoring force of the carbon cycle that reduces atmospheric CO_2. Continental weathering is a function of climate, increasing with temperature and continental runoff as demonstrated by numerous field studies (Brady, 1991; White and Blum, 1995; Dessert et al., 2001; Oliva et al., 2003). Based on the compilation of the main cation fluxes exported by small basaltic and granitic catchments, Dessert et al. (2001) and Oliva et al. (2003) have proposed parametric relationships linking the climatic parameters (mean annual temperature and runoff) to CO_2 consumption by the dissolution of silicate minerals. These laws are strictly valid only for the present day environment and do not include a direct dependence of rock weathering on the acidity of rainwater (Oliva et al., 2003). Exporting these laws into the post-snowball environment is tricky for three reasons: (1) The climate is exotic and is beyond the validity field of the parametric laws. (2) The Earth surface might have been largely modified by the global glaciation. That is, dynamic glaciation persisting for several millions of years might have produced fine grained materials (i.e. rock flour) with very high reactive surface areas, promoting the dissolution of minerals and the atmospheric CO_2 consumption. (3) The very high levels of atmospheric CO_2 in the snowball Earth aftermath (100–400 PAL) would have acidified the rainfall. These CO_2 levels, which are potentially above the common soil CO_2 levels encountered today, have promoted the mineral dissolution rates. Because the use of parametric laws to describe continental weathering cannot account for these three major changes, it is necessary to investigate the runoff-temperature-weathering feedback with a mechanistic model of silicate rock weathering in natural environments.

3.1. Description of the continental weathering model

Here we utilize the WITCH weathering model (Goddéris et al., 2006), which was initially developed to simulate weathering processes in soil profiles and in river catchments above silicate bedrock and calibrated on a granitic watershed. It successfully

Please cite this article as: Le Hir, G., et al., The snowball Earth aftermath: Exploring the limits of continental weathering processes, Earth Planet. Sci. Lett. (2008), doi:10.1016/j.epsl.2008.11.010

describes the seasonal evolution of the chemical composition of soil solutions as a function of water-rock-biosphere interactions, as well as the mean annual chemical composition of the main stream. For present day studies, WITCH is coupled to a biospheric model that calculates the water circulation in the soil, the partial pressure of CO_2 below ground level as a result of root respiration and organic carbon decay, and the uptake and release of cations by the living and dead biomass. WITCH calculates the dissolution of minerals as a function of the soil solution composition at each time step through kinetic laws derived from transition state theory concept (Eyring, 1935). The kinetic and thermodynamic parameters have been experimentally determined. Four dissolving species are accounted for (H^+, OH^-, H_2O and organic ligands, but hereafter the organic ligands dissolution will be neglected due to absence of terrestrial vegetation). The dissolution rate of a given mineral R_s is thus equals to:

$$R_s = A \cdot S_w \cdot \left[\sum_i k_i \exp\left(\frac{-E_a^i}{RT}\right) \cdot a_i^{n_i} \cdot f_{inh}\right](1-\Omega^s) \quad (2)$$

where A stands for the mineral reactive surface (m^2/m^3 of soil), S_w is the soil moisture saturation (function of the water volumetric content, Sverdrup and Warfinge, 1995), k_i and E_a^i are the dissolution rate constant and the activation energy for the i species-promoted dissolution, a_i and n_i stand for the activity of species i and the order of reaction with respect to the dissolving species i, respectively. f_{inh} describes the inhibiting effect of aqueous species on mineral dissolution (Oelkers et al., 1994; Schott and Oelkers, 1995; Devidal et al., 1997). Finally, the effect of departure from equilibrium on mineral dissolution/precipitation rates is accounted for by the factor $(1-\Omega^s)$, where Ω stands for the solution saturation index with respect to the particular solid and s is a stoichiometric number.

The WITCH model includes 32 silicate minerals. The number of soil layers that are modelled can be adapted to any specific problem. The mineral reactive surface is calculated according to a simple parametric law assumed to be an approximation of the solid BET surface (Brunauer et al., 1938; Sverdrup and Warfinge, 1995):

$$A = \left(8.0x_{clay} + 2.2x_{silt} + 0.3x_{sand} + 0x_{coarse}\right) \cdot \rho \quad (3)$$

where x_{clay}, x_{silt}, x_{sand} and x_{coarse} represent the textural fractions of the clay, silt, sand and coarse materials in the soil, such that $x_{clay}+x_{silt}+x_{sand}+x_{coarse}=1$. ρ is the soil density in g/m^3. We also include continental calcite and dolomite dissolution in the WITCH model. Because carbonate dissolution is several orders of magnitude faster than silicate dissolution, we assume that continental waters are at equilibrium respectively with the carbonate phases when their abundance exceeds 2% by volume of the bedrock (thus when carbonate rock is the dominant phase, geochemically speaking), and with the CO_2 partial pressure below ground level. The solubility product of dolomite is calculated as a function of the air temperature T (Drever, 1997):

$$K_{dol} = 10^{-17.09} \exp\left[-\frac{39480}{R} \cdot \left(\frac{1}{298.15} - \frac{1}{T}\right)\right] \quad (4)$$

where the standard enthalpy of reaction is in J/mol and R is the perfect gas constant.

For calcite, the solubility product is given by Drever (1997):

$$K_{cal} = 10^{-8.48} \exp\left[-\frac{9610}{R} \cdot \left(\frac{1}{298.15} - \frac{1}{T}\right)\right] \quad (5)$$

3.2. Design of the WITCH simulations

A number of parameters have to be fixed for using the WITCH model in the Neoproterozoic context. (1) The dissolution of minerals by organic ligands, and exchanges of elements with the living and dead biomass are set to zero because of the absence of continental vegetation at this time. (2) Since we aim at constraining the maximum CO_2 consumption in the post snowball environment, we assume granitic lithology covering all continental surface except where the occurrence of basaltic outcrops can be reasonably inferred from geological data (see compilation by Goddéris et al., 2003 and Fig. 2). Mineralogy of the granite and basalt used in WITCH are shown on Table 2. Carbonate weathering does not consume CO_2 on a 10^5 to 10^6 year timescale. Its role during the melting phase will be discussed in Section 5 (3) The volumetric content of water in the weathering profile has to be fixed. This parameter is important as it defines the fraction of the total reactive mineral surface that is wet and weatherable. In a first step, we fix it to a standard value of 0.2 m^3 water/m^3 soil. In a second step, we use the soil water content simulated by FOAM. (4) Given the assumed absence of soil biomass, CO_2 level is fixed in pore spaces to the atmospheric concentration. The WITCH model does not include a carbon budget of the below ground solutions so far. This means that the model is providing unlimited CO_2 to the water solutions, resulting in a possible slight overestimation of the weathering rates. (5) Assumptions about the thickness of the weathering profile and its texture are required in the model. We have chosen a shallow two layer structure with a thickness of 25 cm for the surface layer and of 100 cm for the deepest one. These relatively shallow thicknesses have been chosen based on the influence of persistent mechanical weathering during glaciation (Donnadieu et al., 2003), which would not allow the survival of any pre-glacial thick soil profiles. The soil system is assumed to have been largely reset by the glacial event. A sensitivity test to soil thickness is performed below. (6) With regards to the grain size, three tests have been run in which the reactive surface is changed according to Eq. (3) and intended to span the range of materials observed on the present earth surface. (7) temperature of the weathering profiles is taken from the GCM output field for the various atmospheric CO_2, and the GCM runoff is assumed to be equal to the vertical drainage of the weathering profile for each continental grid element. This assumption is valid because of the large size of the continental pixels in this study: all the water flowing through the weathering profiles can be assume to end up in a river draining the pixel.

3.3. Weathering rates in a supergreenhouse environment

Under 400 PAL, calculated CO_2 consumption by silicate weathering (Fig. 4a and b) ranges from 2.4 to 28 times the present-day flux, as estimated by Gaillardet et al. (1999), with the lowest value calculated assuming a coarse grain size (sand) material with reactive surface of 0.5×10^6 m^2/m^3 (LR run, Table 3). While such a coarse-grained surface layer on the continents is unlikely due to grinding by glaciers, this test provides a useful absolutely minimum level of silicate weathering to be expected. To test the sensitivity of weathering rates as a function of the mineral reactive surface, a finer grain size is used (MR run, Table 3), which yields a 6-fold increase over present day CO_2 consumption (Fig. 5a), showing that the mineral reactive surface is a crucial factor governing the post glacial weathering. In order to represent the Earth surface resulting from a global ice cover more precisely, we apply the reactive surface value measured on loesses derived from glacial erosion during the Last Glacial Maximum (Kahle et al., 2002) (13×10^6 m^2/m^3, HR run, Table 3) to the full 1.25 m-thick soil profile. In this run, which yields what we regard as a maximum value for weathering rates, the CO_2 consumption rate is 10 times

Table 2
Standard mineralogy for the silicated lithologies (in percent)

Granite	Quartz 31%	Orthose 26.5%	Andesine 42%	Apatite 0.3%
Basalt	Labradorite 45%	Basaltic glass 17.7%	Diopside 34%	Forsterite 2% Apatite 1.3%

Please cite this article as: Le Hir, G., et al., The snowball Earth aftermath: Exploring the limits of continental weathering processes, Earth Planet. Sci. Lett. (2008), doi:10.1016/j.epsl.2008.11.010

greater than the present-day value (Fig. 4a). A second run on a 6 m thick loess layer over the whole continental surface (Fig. 4a, run HR/thick) results in an increase in the calculated CO_2 consumption by a factor of only 2 to 3, which shows that predicted weathering rates are a non-linear function of loess thickness. This relationship is due to the limitation in weathering rates by the increase in the saturation state of pore water with respect to the primary silicate minerals as it percolates through the soil horizon. The result is significant because continental runoff is not commensurate with increased CO_2 levels, meaning soil waters rapidly reach oversaturation with respect to primary minerals.

Predicted CO_2 consumption by silicate weathering at low CO_2 levels (10 PAL) are all at least an order of magnitude below the present value of 11.7×10^{12} mol CO_2/yr (Gaillardet et al., 1999). These low predicted values are mainly driven by (1) the low below ground CO_2 levels (fixed at 10 PAL, which can be regarded as a lower hand value for

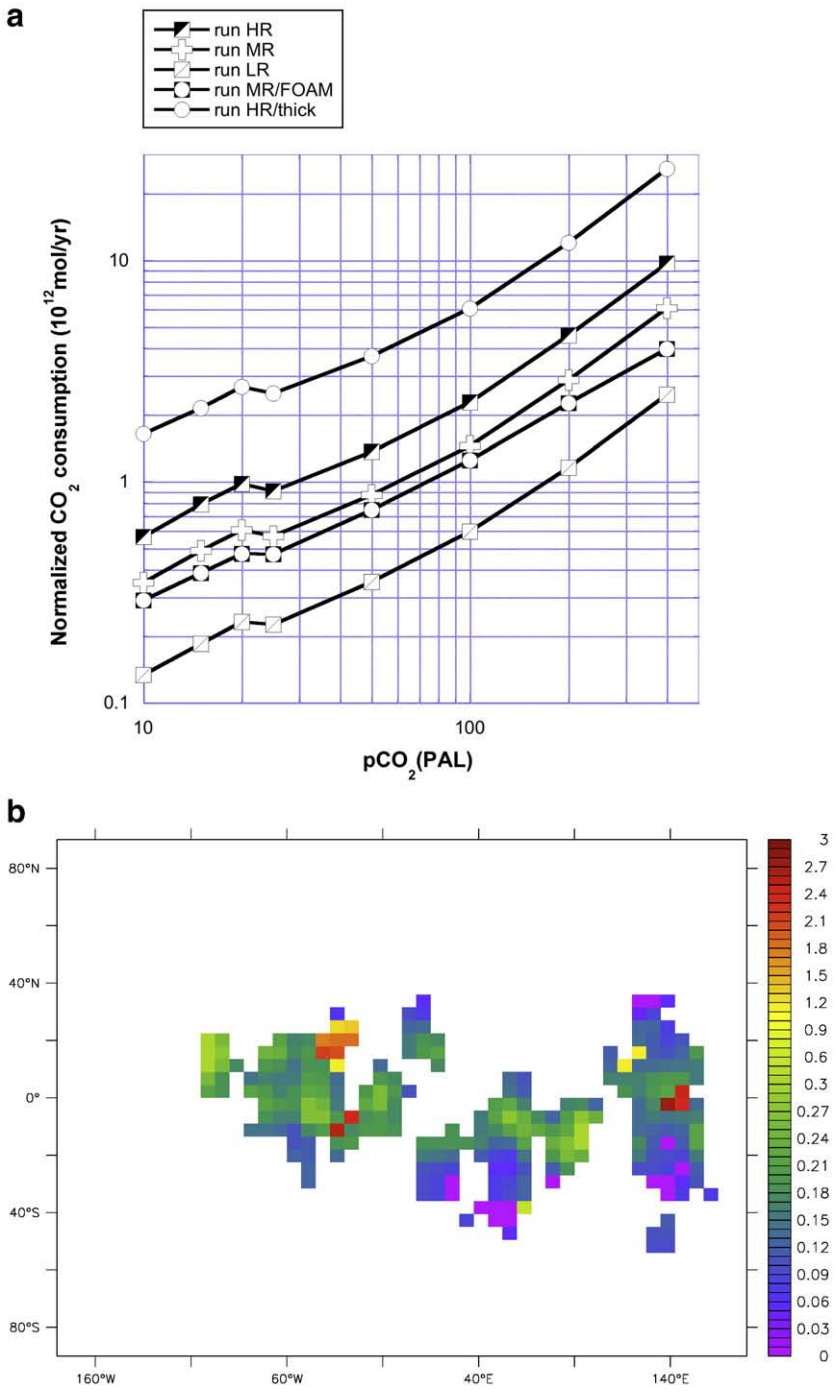

Fig. 4. a) Total CO_2 consumption by continental silicate weathering at various pCO_2 levels normalized to the present day value, as calculated by the WITCH model forced with the climatic output of the FOAM GCM. HR: high reactivity experiment, MR: middle reactivity experiment, LR: low reactivity experiment, HR/thick: high reactivity experiment with a 6 m-thick loess, and MR/FOAM: middle reactivity experiment with the water volumetric content of the loess calculated by FOAM. b) Calculated pattern of the CO_2 consumption by continental silicate weathering. at 400 PAL by the WITCH model(MR simulation, in 10^{12} mol/yr). Basaltic outcrop are identified by a higher flux.

Please cite this article as: Le Hir, G., et al., The snowball Earth aftermath: Exploring the limits of continental weathering processes, Earth Planet. Sci. Lett. (2008), doi:10.1016/j.epsl.2008.11.010

Table 3
WITCH simulations

WITCH simulation set	Temperature and runoff	Loess reactive surface (upper layer)	Water volumetric content of the loess
HR	FOAM	13×10^6 m^2/m^3	20%
MR	FOAM	6.2×10^6 m^2/m^3	20%
LR	FOAM	0.51×10^6 m^2/m^3	20%
MR/FOAM	FOAM	6.2×10^6 m^2/m^3	FOAM

All sets of run are using the FOAM climatology. Reactive surface of the upper layer (0.25 m thick) for the MR run (LR run) is calculated according to Eq. (3), assuming a grain size distribution with 25% clay and 75% silt materials (50% sandy and 50% coarse materials). Reactive surface of the upper layer for the HR run is prescribed at 13×10^6 m^2/m^3 based on Ref. The lower layer (1 m thick) contains sandy (50%) and coarse (50%) materials in all runs (yielding a reactive surface of 0.51×10^6 m^2/m^3), except for the HR run where we assumed a mineral reactive surface of the lower layer of 1×10^6 m^2/m^3.

present day soils), (2) the absence of organic acid produced by the biotic activity, (3) the relative aridity of the continental surfaces, (4) the smaller total continental surfaces (100×10^6 km^2 in the Neoproterozoic, compared to the 150×10^6 km^2 today).

4. Duration of the post-snowball supergreenhouse climate

Because the increase in CO_2 consumption by silicate weathering does not scale linearly with higher CO_2 levels, the post-snowball supergreenhouse climate should last much longer than the few hundred thousands years envisaged in the original snowball Earth model (Higgins and Schrag, 2003; Hoffman et al., 1998). Indeed, long term atmospheric CO_2 evolution is controlled by the balance between the solid Earth degassing and the total silicate weathering (Walker et al., 1981; Berner, 2004). No clear consensus exists concerning changes in the CO_2 outgassing flux in the geological past (Gaffin, 1987; Rowley, 2002; Cogné and Humler, 2004); thus we conservatively assume that the total solid earth degassing rate during the late Neoproterozoic was close to its present day value. Modelling the evolution of atmospheric CO_2 through geological times during a timespan where silicate weathering largely exceeds solid Earth degassing requires at least the calculation of the alkalinity and carbon budget of the surficial reservoirs (ocean+atmosphere), as well as the carbonate speciation in seawater. To perform these calculations, we use a simplified version of the COMBINE model (Goddéris and Joachimski, 2004), a box model with two oceanic reservoirs (surface and deep) and one for the atmosphere that has previously been applied to simulating the geochemical evolution of the snowball ocean (Le Hir et al., 2008a,b). CO_2 consumption by silicate weathering is taken from the FOAM/WITCH simulations, as a function of atmospheric CO_2. Since the WITCH model only gives cation and CO_2 consumption fluxes for the 8 solved climate scenarios (at 400, 200, 100, 50, 25, 20, 15 and 10 PAL CO_2), a linear interpolation for each continental grid cell (Fig. 2) is performed to define a continuous trend for cation fluxes as a function of atmospheric CO_2 between 400 and 10 PAL. Through this interpolation, we start from the CO_2 consumption fluxes calculated for each continental grid cell by the WITCH model, depending on the FOAM temperature and runoff, and end up with a simple trend describing the global CO_2 consumption through silicate rock weathering as a function of atmospheric CO_2. This interpolated flux is then incorporated at each timestep into the simplified COMBINE numerical model (Le Hir et al., 2008a,b). Since no GCM simulation was performed above 400 PAL our CO_2 history begins at 0.12 bar.

Fig. 5 shows the atmospheric CO_2 evolution in the aftermath of snowball Earth. Four shapes of global CO_2 consumption have been used to decipher the role of weathering parameters in controlling how atmospheric CO_2 would have decreased in the snowball aftermath. Using the FOAM water volumetric content (MR/FOAM run), the continental weathering becomes less efficient due to enhanced dryness of the weathering profiles. Indeed, the hothouse climate plays an inhibiting role on weathering by dropping the soil water volumetric content below 20% which was the fixed value of the other experiments. Nevertheless, changes linked to the use of the FOAM water volumetric content remain minor. This is the result of the first order control played by the runoff on the weathering, bringing waters in contact with the minerals and transporting the weathering products. The soil water content only plays a secondary role on how long the runoff interacts with the minerals (i.e. residence time). Hence, the simulated CO_2 reductions are of the same order for the MR/FOAM run and the MR run. Larger effects are visible when changing the reactive surface (HR run) and even more when also changing the soil thickness (HR/thick run). After 1 million years, atmospheric CO_2 decreases to 100 PAL, 70 PAL and 20 PAL for MR, HR and HR/thick runs, respectively. Recovery timescales are thus dependent on the weathering profile parameters, though the HR run is probably the one better representing soil conditions that may have occurred after several million years of global glaciation. Hence, we can conclude that the recovery timescale from a snowball Earth is 1) on the order of a few million years in any case and 2) mostly dependent on the soil thickness, the reactive surface, and the runoff pattern.

5. The deglaciation and the cap dolostone deposition, a model-data discussion

Is it possible to explore the weathering rates during the melting phase itself? As discussed above, modelling the melting of a snowball Earth at very high CO_2 levels using a coupled ice-sheet — climate model remains a technical challenge for a while because of computational limitations. Our GCM cannot at present handle rapidly melting ice sheets and sea glaciers in the initial stages of the high CO_2 world. Nevertheless, guesses can be assumed regarding the continental runoff and temperature resulting from the melting phase. A

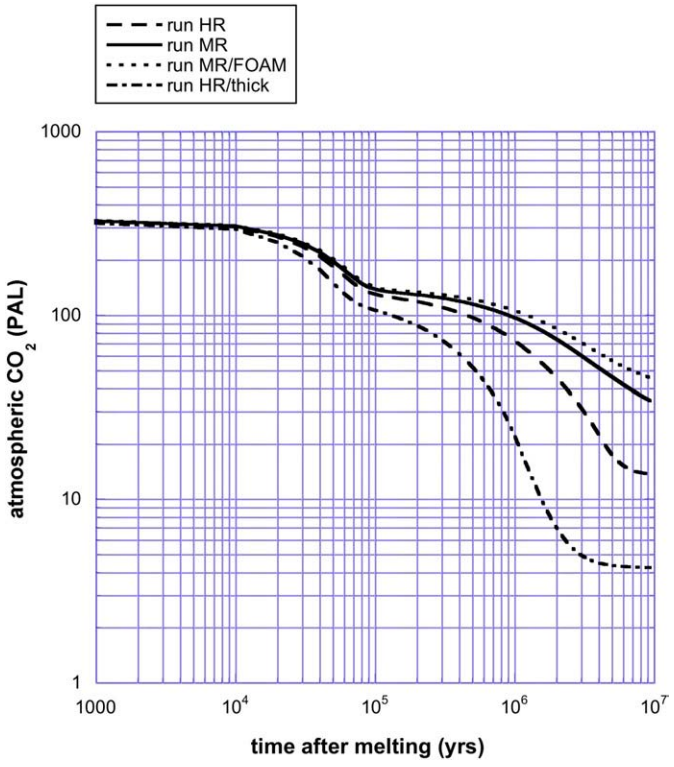

Fig. 5. Post-snowball atmospheric CO_2 evolution calculated by the simplified COMBINE geochemical module, using the weathering rates calculated by the WITCH mechanistic weathering model in the four cases described above.

Please cite this article as: Le Hir, G., et al., The snowball Earth aftermath: Exploring the limits of continental weathering processes, Earth Planet. Sci. Lett. (2008), doi:10.1016/j.epsl.2008.11.010

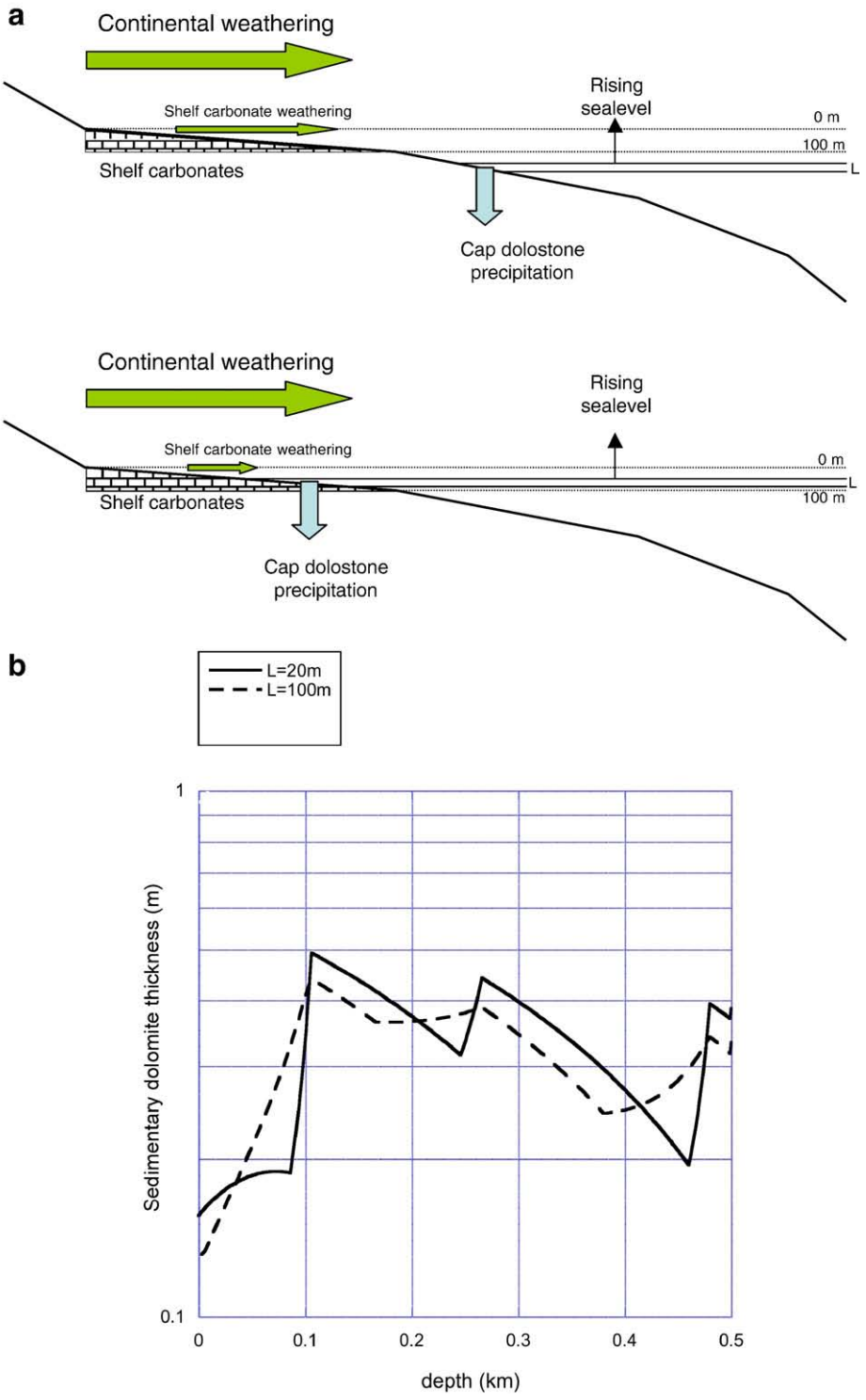

Fig. 6. a) Numerical model used to calculate the deposition rate of the cap dolostones. b) Cap dolostones thickness accumulated during the deglaciation phase (lasting 10 kyr), as a function of the level below the pre-glacial sealevel (assumed to be located at 0 m). 0.5 km represents the sea-level drop linked to Neoproterozic global glaciations. *L* denotes the thickness of the water layer intercepting the seafloor and from which cap dolostone are precipitated.

previous modelling study coupling a climate and an ice-sheet models calculates a land-ice volume reaching ~200×10^6 km^3 for a global glaciation (Donnadieu et al., 2003), a value in close agreement with a glacio-eustatic sea level fall of 500 m or more deduced from the stratigraphic record of end-Cryogenian glaciation in Namibia (Hoffman et al., 2007). If the melting spans 10 kyrs (Hoffman et al., 2007) and if the icecap melts linearly with time, this would correspond to a runoff flux of 20 cm/yr during 10 kyr. The contribution of rainfall to this runoff cannot be estimated accurately without a coupled GCM-ice sheet simulation of the melting of the snowball. This is a fruitful area for future inquiry. Indeed, during deglaciation, it is possible that precipitation was focused on low latitude continents owing to newly formed ice-free oceanic areas and to resulting steep meridional temperature gradient (Peyser and Poulsen, 2008), but this process cannot be explored here. Regarding temperature, we assume that the melt waters responsible for the dissolution of the minerals are around

Please cite this article as: Le Hir, G., et al., The snowball Earth aftermath: Exploring the limits of continental weathering processes, Earth Planet. Sci. Lett. (2008), doi:10.1016/j.epsl.2008.11.010

1 °C. At such a low temperature, the solubility of carbonate minerals increases, but silicate weathering is strongly inhibited. Atmospheric CO_2 is fixed at 400 PAL. Under such conditions (*Deglac* run), the predicted silicate weathering flux obtained by WITCH only consumes 15.11×10^{12} mol CO_2/yr despite very high CO_2 pressure acidifying the percolating solutions. This value is only slightly above the present day estimate (Gaillardet et al., 1999). The net atmospheric pCO_2 drawdown linked to silicate weathering itself is insignificant owing to the melting phase duration (10 kyr) and the high atmospheric CO_2 content. This result is in agreement with the observation that the maximum silicate weathering is reached after cap dolostone deposition, i.e. after the melting and transgressive phase, as shown by Sr and Ca isotope data (Kaseman et al., 2005; Nédélec et al., 2007; Nogueira et al., 2007).

While silicate weathering rates during the deglaciation would have been relatively low, carbonate weathering should have been much higher because the dissolution of carbonate minerals is enhanced by the low temperature. Higgins and Schrag (2003) argued that the carbonate weathering flux might be responsible for the accumulation of the 18 m-thick (on average) post-glacial cap dolostones (Hoffman et al., 2007) during the melting phase, mainly resulting from the weathering of emerged carbonate platforms and intra-cratonic carbonate outcrops. To test this hypothesis, an additional carbonate lithology is added to the model, randomly along the coast line so that the carbonate weathering can be investigated with WITCH. Indeed, given the low sea-level prior to deglaciation, large carbonate (calcite and dolomite) platforms would have been exposed to subaerial weathering. The exact location of the carbonate outcrops is not important in this numerical experiment, since global climate is assigned at a fixed value for each continental grid element (runoff = 20 cm/yr, temperature = 1 °C), whatever its location. Assuming that these carbonate platforms accumulate prior to the snowball Earth beneath a 100 m-thick epicontinental oceanic layer, their maximum areal extent cannot exceed 20×10^6 km^2, assuming a present day oceanic hypsometry. In addition to these emerged carbonate shelves, ancient carbonates in the continental interior would also have been subjected to weathering. Today, intra-continental carbonate outcrops cover about 20×10^6 km^2 of the land surface (Amiotte-Suchet et al., 2003). We use the same value for the Neoproterozoic continental surface. Thus, the assumed maximum carbonate surface area in the direct aftermath of the snowball (as long as sealevel is below the 100 m depth level) was 40×10^6 km^2. In our model, 50% of these outcrops are assumed to be calcite and 50% dolomite and the water draining these areas are assumed to be saturated with respect to the relevant carbonate mineral. The WITCH simulation can be performed at very high CO_2 levels. Indeed we prescribe the climate for each continental grid element (constant runoff and temperature). The FOAM GCM output are not used here and the 400 PAL threshold is not a limitation for the WITCH model. Because it has been suggested that 400 PAL might be too low (Pierrehumbert, 2004) to melt the snowball Earth, we perform our simulations assuming that the CO_2 level was around 1000 PAL, thus further maximizing the continental weathering rates and consequently the cap-carbonates deposition rate.

Since the WITCH model calculates the Mg^{2+} and Ca^{2+} flux to the ocean, we can convert these fluxes in thickness of cap dolostones being deposited, assuming that chemical conditions for cap dolostones to precipitate are satisfied (Font et al., 2006), a deposition surface and a mean density of 2600 kg/m^3 for the sedimentary carbonates. We deliberately choose this mass balance method since the kinetics of cap dolostone precipitation is not known. To be as realistic as possible, we build up a numerical model calculating the deposition surface as a function of the sealevel during the melting phase (the so-called "hypsometric model", Fig. 1). The depositional surface is estimated assuming the present day oceanic hypsometry, and that cap dolostones where deposited within a water layer of thickness L (Fig. 6a). This water layer rises from the slope along the shelf, as the oceanic volume rises linearly in response to the icecap melting, forcing sealevel to rise. The interception between the seafloor surface and this water layer defines the area of cap dolostones accumulation. All Mg^{2+} originating from continental weathering is assumed to precipitate instantaneously on this area, assuming consequently that the chemical conditions required to precipitate dolostones are satisfied within the considered water layer. We also account for the decrease in the surface of emerged carbonate platforms once the sealevel reaches 100 m below its pre-perturbation value (see Fig. 6a).

With $L = 20$ m, we found that, if the melting phase lasts 10 kyr, a maximum of 50 cm of cap dolostones could be accumulated by using all the Mg^{2+} from coeval continental weathering (Fig. 6b). The calculated thickness of cap-carbonates is not heavily dependent on the assumed thickness L of the water layer in which cap dolostones are deposited (Fig. 7), nor on the duration of the melting phase (since a longer duration implies a lower runoff, and hence a lower weathering). The calculated thickness of the cap dolostones is about 40 times lower than the mean compiled value of 18.5 m (Hoffman et al., 2007), although this is the mean arithmetic thickness, without weighting by the original depositional area. To reconcile the model output with the data would require that the surface of dolomitic outcrop being weathered was 40 times greater than the assumed 20×10^6 km^2, which is clearly unrealistic. Conversely, if we allow that the area over which cap dolostones were precipitated was lower by a factor of 10, then cap dolostones on average 5 meters thick would have been deposited. While the base-Ediacarian cap dolostones in Namibia and Death Valley, for example, are very thick, the equivalent cap dolostones in Svalbard, East Greenland, northern Norway, Australia, and elsewhere are on average much thinner. If these thinner cap dolostones are in fact more typical and their areal extent restricted, then the carbonate weathering model for cap dolostone precipitation may in fact be valid. This also suggests that the thickness of cap dolostones was heterogeneous over continental shelves and that high average thicknesses of preserved cap dolostones are a preservational bias. In addition, as noted above, we do not take into account the runoff component resulting from the precipitation occurring during the deglaciation itself but the one resulting from the continental ice cover melting. Although an accurate estimate of the former one depends on coupled GCM ice-sheet simulations in this peculiar context, we can note that the runoff calculated by FOAM at 400 PAL saturates around 30–33 cm/yr. By adding both components (the one from the ice-sheet melting and the one from the ocean-atmosphere system), we obtain a mean thickness of 82 cm, a value which remains far for the one suggested by Hoffman et al. (Hoffman et al., 2007). Hence, even with the shortcomings of our model, our results still support the possibility that thinner cap dolostones are in fact more typical during the aftermath of the snowball Earth. This conclusion remains to be confirmed in the future.

Alternatively, the timescale for cap dolostone precipitation may be grossly underestimated. In fact, the timescale of cap dolostone precipitation is a subject of significant debate (Hoffman et al., 2007). Importantly, the stratigraphic context of the cap dolostone unambiguously constrains its timing of deposition to the period spanning the post-glacial eustatic rise in sea level. Rapid deposition of the cap dolostone (2000–10000 years; Hoffman et al., 2007) has thus been inferred based on modelled high rates of ice sheet decay at the end of the snowball (Hyde et al., 2000) and by analogy with Quaternary deglaciation (Bard et al., 1990). However, magnetostratigraphic data from multiple successions imply that cap dolostones span multiple magnetic reversal events (Trindade et al., 2003; Kilner et al., 2005), suggesting that the cap dolostones accumulated over several hundreds of thousands of years. Whether this timescale may be reconciled with the climate models is still an open question, pending on a careful modeling of the melting phase.

6. Conclusion

In this study, we force a numerical model predicting continental weathering with 3D-climate model output to investigate the climate

Please cite this article as: Le Hir, G., et al., The snowball Earth aftermath: Exploring the limits of continental weathering processes, Earth Planet. Sci. Lett. (2008), doi:10.1016/j.epsl.2008.11.010

and weathering response during the supergreenhouse climate following the snowball Earth event. The main conclusion of this study is that post-glacial silicate weathering was likely not as vigorous as commonly assumed (Higgins and Schrag, 2003; Hoffman et al., 2007). This result is largely due to the non-linear relationship between average continental temperatures and runoff rates under very high CO_2 levels. This relative dryness of the supergreenhouse climate is linked to physical constraints governing the surface energy budget. Indeed the energy released by the evaporation cannot overcome the net solar energy absorbed in surface. Since the incoming solar energy is not enhanced by increasing CO_2, the evaporation rates, and thus the intensity of the hydrological cycle, level off at high CO_2 levels. For example, even at 400 times the present CO_2 pressure, continental runoff is only 22% higher than the calculated present day values. As a consequence, under a 400 PAL CO_2 climate, our simulated discharge of dissolved elements from continental weathering into the ocean shows at best a 10-fold increase compared to the present-day estimate. As a consequence, the time required to restore CO_2 concentrations to roughly pre-glacial levels is on the order of a few million years, rather than a few thousand years, as has been previously assumed (Higgins and Schrag, 2003). Hence, an unusually warm climate may have persisted for many million years, thus extending the duration of the environmental filter on the biospheric evolution. A more protracted timescale for the recovery from the post-snowball super-greenhouse should be testable using isotopic proxies (e.g. $^{87}Sr/^{86}Sr$, $\delta^{26}Mg$) of the continental weathering.

A final important result of our linked numerical models is that, assuming a timescale of deglaciation of 10 kyr, total continental weathering (carbonate+silicate) supplies only enough Mg^{2+} to accumulate a maximum of 50 cm of cap dolostone over the continental shelves, which is over an order of magnitude lower than the calculate average global thickness of base-Ediacaran cap dolostones (Hoffman et al., 2007). Our history of continental rock dissolution in the aftermath of the snowball glaciation is also in agreement with the isotopic proxies for continental weathering that suggest that the major increase in silicate weathering occurred directly after cap dolostone deposition (Kaseman et al., 2005).

Acknowledgments

This study was funded by the French National Agency for Research program ANR-06-BLAN-0347 and by the CNRS/INSU through the ECLIPSE program. We thank Praksys for the maintenance of the cluster of PC at the LMTG (www.praksys.org). We thank Lee Kump and an anonymous referee for their insightful reviews, and Peter deMenocal for the quality of the editorial procedure.

References

Allen, M.R., Ingram, J., 2002. Constraints on future changes in climate and the hydrologic cycle. Nature 419, 224–232.
Amiotte-Suchet, P., Probst, J.L., Ludwig, W., 2003. World wide distribution of continental rock lithology: implications for atmospheric/soil CO_2 uptake by continental weathering and alkalinity river transport to the oceans. Glob. Biogeochem. Cycles 17, doi:10.1029/2002GB001891.
Bao, H.M., Lyons, J.R., Zhou, C., 2008. Triple oxygen isotope evidence for elevated CO_2 levels after a Neoproterozoic glaciation. Nature 453, 504–506.
Bard, E., Hamelin, B., Fairbanks, R.G., Zindler, A., 1990. Calibration of the ^{14}C timescale over the past 30.000 years using mass spectrometric U–Th ages from Barbados corals. Nature 345, 405–410.
Berner, R.A., 2004. The Phanerozoic Carbon Cycle. Oxford University Press, New York. 150 pp.
Berner, E.K., Berner, R.A., 1987. The global water cycle: geochemistry and environment. Prentice Hall. 397 pp.
Brady, P.V., 1991. The effect of silicate weathering on global temperature and atmospheric CO_2. J. Geophys. Res. 96, 18101–18106.
Brunauer, S., Emmett, P.H., Teller, E., 1938. Adsorption of gases in multimolecular layers. J. Am. Chem. Soc. 60, 309–319.
Caldeira, K., Kasting, J.F., 1992. Susceptibility of the early Earth to irreversible glaciation caused by carbon dioxide clouds. Nature 359, 226–228.
Cogné, J.P., Humler, E., 2004. Temporal variation of oceanic spreading and crustal production rates during the last 180 My. Earth Planet. Sci. Lett. 227, 427–439.
Condon, D., Zhu, M.Y., Bowring, S., Wang, W., Yang, A.H., Jin, Y.G., 2005. U–Pb ages from the Neoproterozoic Doushantuo Formation, China. Science 308, 95–98.
Dessert, C., Dupré, B., François, L.M., Schott, J., Gaillardet, J., Chakrapani, G.J., Bajpai, S., 2001. Erosion of Deccan Traps determined by river geochemistry: impact on the global climate and the $^{87}Sr/^{86}Sr$ ratio o.f seawater. Earth Planet. Sci. Lett. 188, 459–474.
Devidal, J.L., Schott, J., Dandurand, J.L., 1997. An experimental study of kaolinite dissolution and precipitation kinetics as a function of chemical affinity and solution composition at 150 °C, 40 bars, and pH 2, 6.8, and 7.8. Geochim. Cosmochim. Acta 61, 5165–5186.
Donnadieu, Y., Fluteau, F., Ramstein, G., Ritz, C., Besse, J., 2003. Is there a conflict between the Neoproterozoic glacial deposits and the snowball Earth interpretation: an improved understanding with numerical modeling. Earth Planet. Sci. Lett. 208, 101–112.
Donnadieu, Y., Pierrehumbert, R.T., Fluteau, F., Jacob, R., 2006. Modelling the primary control of paleogeography on Cretaceous climate. Earth Planet. Sci. Lett. 248, 426–437.
Drever, J.I., 1997. The geochemistry of natural waters. Prentice Hall, Upper Saddle River, New Jersey 07458. 436 pp.
Eyring, H., 1935. The activated complex in chemical reactions. J. Chem. Phys. 3, 107–115.
Font, E., Nédélec, A., Trindade, R., Macouin, M., Charrière, A., 2006. Chemostratigraphy of the Neoproterozoic Mirassol d'Oeste cap dolostones (Mato Grosso, Brazil): a model for Marinoan cap dolostone formation. Earth Planet. Sci. Lett. 250, 89–103.
Gaffin, S., 1987. Ridge volume dependence on seafloor generation rate and inversion using long term sealevel change. Am. J. Sci. 287, 596–611.
Gaillardet, J., Dupré, B., Louvat, P., Allègre, C.J., 1999. Global silicate weathering and CO_2 consumption rates deduced from the chemistry of the large rivers. Chem. Geol. 159, 3–30.
Goddéris, Y., Joachimski, M.M., 2004. Global change in the late Devonian: modelling the Frasnian–Famennian short-term carbon isotope excursions. Palaeogeogr. Palaeoclimatol. Palaeoecol. 202, 309–329.
Goddéris, Y., Nédelec, A., Donnadieu, Y., Dupré, B., Dessert, C., François, L.M., Grard, A., Ramstein, G., 2003. The Sturtian glaciation: Fire and ice. Earth Planet. Sci. Lett. 211, 1–12.
Goddéris, Y., François, L.M., Probst, A., Schott, J., Moncoulon, D., Labat, D., Viville, D., 2006. Modelling weathering processes at the catchment scale with the WITCH numerical model. Geochim. Cosmochim. Acta 70, 1128–1147.
Gough, D.O., 1981. Solar interior structure and luminosity variations. Sol. Phys. 74, 21–34.
Held, I.M., Soden, B.J., 2006. Robust responses of the hydrological cycle to global warming. J. Clim. 19, 5686–5699.
Higgins, J.A., Schrag, D.P., 2003. Aftermath of a snowball Earth. Geochem. Geophys. Geosyst. 4, doi:10.1029/2002GC000403.
Hoffman, P.F., Kaufman, A.J., Halverson, G.P., Schrag, D.P., 1998. A Neoproterozoic Snowball Earth. Science 281, 1342–1346.
Hoffman, P.F., Halverson, G.P., Schrag, D.P., 2004. On the consistent sequence of mineralogy and bedforms in post-glacial cap carbonates of Marinoan (ca 635 Ma) age on different paleomargins: steady-state ocean stratification during a post-snowball Earth marine transgression ? Annual Geological Society of America Annual meeting, Denver.
Hoffman, P.F., Halverson, G.P., Domack, E.W., Husson, J.M., Higgins, J.A., Schrag, D.P., 2007. Are basal Ediacaran (635 Ma) post-glacial "cap-dolostones" diachronous ? Earth Planet. Sci. Lett. 258, 114–131.
Holland, H.D., 1978. The chemistry of Oceans and Atmosphere. Wiley, New York. 351 pp.
Hyde, W.T., Crowley, T.J., Baum, S.K., Peltier, W.R., 2000. Neoproterozoic "snowball Earth" simulations with a coupled climate/ice sheet model. Nature 405, 425–429.
Jacob, R., 1997. Low frequency variability in a simulated atmosphere ocean system. Univ. Wisconsin-Madison.
Kahle, M., Kieber, M., Reinhold, J., 2002. Carbon storage in loess derived surface soils from Central Germany: influence of mineral phase variables. J. Plant. Nutr. Soil Sci. 165, 141–149.
Kaseman, S.A., Hawkesworth, C.J., Prave, A.R., Fallick, A.E., Pearson, P.N., 2005. Boron and calcium isotope composition in Neoproterozoic carbonate rocks from Namibia: evidence for extreme environmental change. Earth Planet. Sci. Lett. 231, 73–86.
Kilner, B., MacNiocaill, C., Brasier, M., 2005. Low-latitude glaciation in the Neoproterozoic of Oman. Geology 33, 413–416.
Le Hir, G., Goddéris, Y., Donnadieu, Y., Ramstein, G., 2008a. A geochemical modelling study of the evolution of the chemical composition of seawater linked to a snowball glaciation. Biogeosciences 5, 253–267.
Le Hir, G., Goddéris, Y., Ramstein, G., Donnadieu, Y., 2008b. A scenario for the evolution of the atmospheric pCO_2 during a snowball Earth. Geology 36, 47–50.
Meert, J.G., Torsvik, T.H., 2003. The making and unmaking of a supercontinent: Rodinia revisited. Tectonophysics 375, 261–288.
Nédélec, A., Affaton, P., France-Lanord, C., Charrière, A., Alvaro, J.J., 2007. Sedimentology and chemostratigraphy of the Bwipe Neoproterozoic cap carbonates (Ghana, Volta Basin): a record of microbial activity in a peritidal environment. C. R. Geosci. 339, 516–518.
Nogueira, A.C.R., Riccomini, C., Sial, A.N., Moura, C.A.V., Trindade, R., Fairchild, T.R., 2007. Carbon and strontium isotope fluctuations and paleoceanographic changes in the late Neoproterozoic Araras carbonate platform, southern Amazon craton, Brazil. Chem. Geol. 237, 168–190.
Oelkers, E.H., Schott, J., Devidal, J.L., 1994. The effect of aluminum, pH and chemical affinity on the rates of aluminosilicate dissolution reactions. Geochim. Cosmochim. Acta 58, 2011–2024.
Oliva, P., Viers, J., Dupré, B., 2003. Chemical weathering in granitic crystalline environments. Chem. Geol. 202, 225–256.

Please cite this article as: Le Hir, G., et al., The snowball Earth aftermath: Exploring the limits of continental weathering processes, Earth Planet. Sci. Lett. (2008), doi:10.1016/j.epsl.2008.11.010

Peyser, C.E., Poulsen, C.J., 2008. Controls on Permo-Carboniferous precipitation over tropical Pangaea: a GCM sensitivity study. Palaeogeogr. Palaeoclimatol. Palaeoecol. 268, 181–192.
Pierrehumbert, R.T., 1999. Subtropical water vapor as a mediator of rapid global climate change. In: Clarks, P.U., Webb, R.S., Keigwin, L.D. (Eds.), Mechanisms of global change at the Millenial time scales. Geophys. Monogr. Ser., vol. 112. American Geophysical Union, Washington D.C., p. 394.
Pierrehumbert, R.T., 2002. The hydrologic cycle in deep-time climate problems. Nature 419, 191–198.
Pierrehumbert, R.T., 2004. High levels of atmospheric carbon dioxyde necessary for the termination of global glaciation. Nature 429, 646–649.
Poulsen, C.J., 2003. Absence of a runaway ice-albedo feedback in the Neoproterozoic. Geology 31, 115–118.
Poulsen, C.J., Jacob, R.L., 2004. Factors that inhibit snowball Earth simulation. Paleoceanography 19, doi:10.1029/2004PA001056.
Rapp, A.D., Kummerow, C., Berg, W., Griffith, B., 2005. An evaluation of the proposed mechanism of the adaptative infrared iris hypothesis using TRMM VIRS and PR measurements. J. Clim. 18, 4185–4194.
Rowley, D.B., 2002. Rate of plate creation and destruction: 180 Ma to present. Geol. Soc. Am. Bull. 114, 927–933.
Schott, J., Oelkers, E.H., 1995. Dissolution and crystallization rates of silicate minerals as a function of chemical affinity. Appl. Chem. 67, 903–910.
Sverdrup, H., Warfinge, P., 1995. Estimating field weathering rates using laboratory kinetics. Rev. Mineral. 31, 485–541.
Trindade, R.I.F., Font, E., D'Agrella-Filho, M.S., Nogueira, A.C.R., Riccomini, C., 2003. Low-latitude and multiple geomagnetic reversals in the Neoproterozoic Puga cap carbonate, Amazon craton. Terra Nova 15, 441–446.
Vecchi, G.A., Soden, B.J., Wittenberg, A.T., Held, I.M., Leetma, A., Harrison, M.J., 2006. Weakening of tropical Pacific atmospheric circulation due to anthropogenic forcing. Nature 441, 73–76.
Walker, J.C.G., Hays, P.B., Kasting, J.F., 1981. A negative feedback mechanism for the long-term stabilization of Earth's surface temperature. J. Geophys. Res. 86, 9776–9782.
White, A.F., Blum, A.E., 1995. Effects of climate on chemical weathering in watersheds. Geochim. Cosmochim. Acta 59, 1729–1747.

Please cite this article as: Le Hir, G., et al., The snowball Earth aftermath: Exploring the limits of continental weathering processes, Earth Planet. Sci. Lett. (2008), doi:10.1016/j.epsl.2008.11.010

Earth and Planetary Science Letters 310 (2011) 203–212

Contents lists available at SciVerse ScienceDirect

Earth and Planetary Science Letters

journal homepage: www.elsevier.com/locate/epsl

The climate change caused by the land plant invasion in the Devonian

Guillaume Le Hir [a,*], Yannick Donnadieu [b], Yves Goddéris [c], Brigitte Meyer-Berthaud [d,e], Gilles Ramstein [b], Ronald C. Blakey [f]

[a] Institut de Physique du Globe de Paris, Université Paris7-Denis Diderot, 1 rue Jussieu, 75005 Paris, France
[b] LSCE, CNRS-CEA-UVSQ, Gif-sur-Yvette, France
[c] Geosciences-Environnement-Toulouse, CNRS-Université de Toulouse, Observatoire Midi-Pyrénées, Toulouse, France
[d] Université Montpellier 2, UMR AMAP, Montpellier, F-34000, France
[e] CNRS, UMR AMAP, Montpellier, F-34000, France
[f] Northern Arizona University, Flagstaff, USA

ARTICLE INFO

Article history:
Received 2 March 2011
Received in revised form 15 July 2011
Accepted 30 August 2011
Available online 29 September 2011

Editor: P. DeMenocal

Keywords:
Devonian
land plants
trees
climate modeling
Palaeozoic
carbon cycle

ABSTRACT

Land plants invaded continents during the Mid-Paleozoic. Their spreading and diversification have been compared to the Cambrian explosion in terms of intensity and impact on the diversification of life on Earth. Whereas prior studies were focused on the evolution of the root system and its weathering contribution, here we used a coupled climate/carbon/vegetation model to investigate the biophysical impacts of plant colonization on the surface climate through changes in continental albedo, roughness, thermal properties, and potential evaporation. From the Early to the Late Devonian, our model simulates a significant atmospheric CO_2 drop from 6300 to 2100 ppmv that is due to an increase in the consumption of CO_2 though continental silicate weathering. The continental drift and the climatic changes promoted by land plants explain this trend. The simulated CO_2 drawdown is paradoxically associated with unchanged temperatures. We show here that the CO_2 drop is counteracted by a large warming resulting from the surface albedo reduction caused by the appearance of an extended plant-cover. If CO_2 is consensually assumed as the main driver of the Phanerozoic climate, this paper demonstrates that, during land-plant invasion, the modifications of soil properties could have played in the opposite direction of the carbon dioxide fall, hence maintaining warm temperatures during part of the Devonian.

1. Introduction

Earliest bryophyte-like plants evolved in the mid-Ordovician (~470 Ma). Land plants diversified but remained reduced in size following the origin of the first vascular organisms approximately 450 million years ago, then gradually increased in height and complexity during the Early Devonian (~415 Ma), achieved the tree habit in the Middle Devonian (~390 Ma), and evolved large leaves and subsequently seeds, in the Late Devonian (~365 Ma) (Algeo and Scheckler, 1998; Beerling et al., 2001; Kenrick and Crane, 1997; Stein et al., 2007). The first stages of plant colonization were confined to wetlands (Greb et al., 2006). Prior to the Early Devonian, the interplay between plants and their immediate abiotic environment is considered as insignificant due to their small size, shallow root system, and lack of leaves (Driese and Mora, 2001). Land plants then progressively colonized all habitats in lowlands. Seed plants ultimately inhabited drier habitats, possibly uplands, in the late Late Devonian (Algeo and Scheckler, 1998; Fairon-Demaret and Hartkopf-Fröder, 2004). The rise of large vascular plants with an extended leaf-cover and their expansion into extrabasinal settings led to substantial changes in the terrestrial landscapes, and therefore in the global environment.

It is frequently assumed that the increase in plant size and a wider geographic distribution promoted chemical weathering processes (Algeo and Scheckler, 1998; Beerling and Berner, 2005; Berner, 2004). Studies on the fluxes of dissolved cations for water draining forested and bare surfaces have suggested an enhancement of the weathering by factors ranging from 3 to 10 (Berner, 2004; Bormann et al., 1998; Moulton and Berner, 1998). Based on these field results, carbon cycle models estimate that the paleo-pCO_2 should probably be 2 to 5 times higher if vascular plants had never evolved (Berner, 1987, 1991, 2001, 2006). These studies were focused on the acceleration of the continental weathering rate owing to deeply rooted soils. Conversely and to our knowledge, none modeling studies have investigated how changes in the surface properties may have affected the water cycle, the continental weathering rate and hence the climate in response to the land plant invasion during the Paleozoic. Indeed, apart from directly impacting the weathering rates as described above, vascular plants also promote transpiration, reduce the surface

* Corresponding author at: Institut de Physique du Globe de Paris, 1, rue Jussieu, 75238 Paris cedex 05, France. Tel.: +33 1 83 95 74 97.
E-mail address: lehir@ipgp.fr (G. Le Hir).

0012-821X/$ – see front matter © 2011 Elsevier B.V. All rights reserved.
doi:10.1016/j.epsl.2011.08.042

albedo, and increase the soil roughness (Algeo et al., 2001; Berner, 2001; Donnadieu et al., 2009). Because continental temperature and runoff directly influence the chemical weathering, quantifying such changes appears essential to better constrain the climatic evolution in relation with the plant continental invasion and the carbon cycle perturbation. To explore the climate–vegetation interplay, we have used a fully coupled 3D carbon–climate–vegetation model (Fig. 1) to simulate the long-term climate evolution during the advent of the land plants. Finally, by using a set of sensitivity experiments, we have determined how each characteristic of the Devonian vegetation has influenced the climate.

2. Methods and tools

2.1. Climate–carbon model (GEOCLIM)

All experiments conducted in this study are performed with the GEOCLIM model (Donnadieu et al., 2004, 2006; Le Hir et al., 2009). This model includes a General Circulation Model (GCM), here FOAM (for Fast Ocean Atmosphere Model) (Jacob, 1997) where the ocean is represented by a 50 m depth mixed-layer (slab ocean), coupled to a box model of the geological carbon–alkalinity cycles (COMBINE (Godderis and Joachimski, 2004)) (Fig. 1). The spatial resolution of GEOCLIM (7.5° long × 4.5° lat) allows us to capture the evolution of the main features of Devonian geographies and their impacts on the carbon cycle. According to a given set of boundary conditions (paleogeographic configuration, solar constant, and solid Earth degassing), GEOCLIM calculates the corresponding steady-state atmospheric CO_2 and climate pattern. The pCO_2 calculation relies on interactive processes loop between the FOAM and COMBINE models. Fixing the solid Earth CO_2 degassing to a constant value, the GEOCLIM model estimates the pCO_2 required to balance the degassed carbon flux by the flux of carbon consumed through continental silicate weathering (Walker et al., 1981). The outgassed rate of carbon is kept constant at its supposed present day value: 6.8×10^{12} mol CO_2 yr^{-1} required to balance the present day CO_2 consumption by silicate weathering, (Gaillardet et al., 1999), which appears to be a conservative assumption, due to the lack of consensus about the Earth degassing rate for the last 200 million years (see discussion in Donnadieu et al. (2006)). The carbon consumption flux through silicate weathering is calculated by COMBINE using phenomenological laws (Dessert et al., 2003; Oliva et al., 2004). The model accounts for the weathering of basaltic and granitic outcrops (all grid cells have rock types in modern proportions: 4% of basalt/96% of granite).

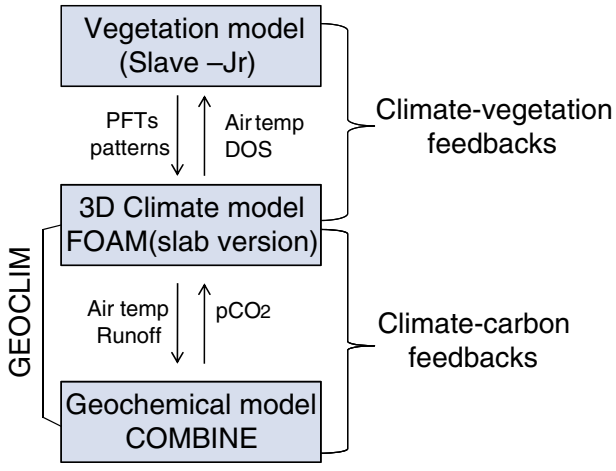

Fig. 1. Models architecture. The GEOCLIM model comes from the coupling of the FOAM model and of the COMBINE model. DOS is degree of saturation of soils, Air temp is the annual mean continental air temperature at the surface level, Plant Functional Types (PFT) are fully described in Section 2.3 and Table 1.

$$F_{sw} = k \sum_j A_j \; Run_j \;\; \exp\left[-\frac{E_a}{R}\left(\frac{1}{T_j}-\frac{1}{T_0}\right)\right] \quad (1)$$

where T_j is the mean annual temperature and Run_j the mean annual runoff of the continental grid box j. A_j is the area of the grid box. E_a is an apparent activation energy set at 48,200 J/mol for granites (Oliva et al., 2004) and 42,300 J/mol for basalts (Dessert et al., 2001). k is a constant calibrated for each lithology, so that total continental silicate weathering consumes a total amount of $6.8 \cdot 10^{12}$ mol/yr of CO_2, 30% being consumed by basalt weathering (Dessert et al., 2003).

The climatic variables T_j and Run_j are computed by FOAM forced by a large range of pCO_2 (30, 25, 20, 15, 10, 8, 6 and 4PAL, one PAL (Preindustrial Atmospheric Level) being equal to 280 ppmv). Climate reaches equilibrium with the prescribed boundary conditions after 30 simulated years; the analyses are performed on the average of the next ten simulated years. Starting from an arbitrary atmospheric CO_2 value, the GEOCLIM model calculates the temperature and runoff of each grid cell through a linear interpolation of the temperature and runoff predicted by each climatic simulation and for each continental grid cell. A new CO_2 consumption through silicate weathering is then estimated for each grid box with Eq. (1). This flux is summed up over the whole continental surface and total silicate weathering is estimated, and consequently a new atmospheric CO_2. This procedure is repeated until a steady-state is reached that corresponds to a stable CO_2 and climate. For more details, an exhaustive GEOCLIM description can be found in Donnadieu et al. (2006).

2.2. Vegetation model description (SLAVE-Jr) and coupling procedure

Similar to Donnadieu et al. (2009), we improve the GEOCLIM model by incorporating a dynamic model for the vegetation to account for the vegetation impact on the climate. Indeed, the influence of vegetation on climate occurs through the fluxes of energy, water vapor and momentum between land and atmosphere. Vegetation modifies the albedo of the continental surfaces and absorbs part of the heat which modifies the sensible heat flux. Plants also transpire and change the latent heat flux. Furthermore, they hinder air movements which transfer momentum to the atmosphere. The calculated vegetation distribution directly impacts on the following physical parameters in FOAM: (1) the albedo of each continental grid element, (2) its thermal properties, (3) its roughness (height of plants governing the aerodynamic resistance of wind speed), (4) and its potential evaporation (incorporating stomata effect).

Consequently, to explore vegetation/climate interplays, the main improvement of GEOCLIM is the coupling with the vegetation model SLAVE-Junior (hereafter SLAVE-Jr) so that vegetation distribution can be coevally calculated with the climatic reconstruction. SLAVE-Jr is a slightly modified version of SLAVE (Freidlingstein, 1995; Friedlingstein et al., 1992) adapted for deep-time purpose. It originally represented 9 vegetation types, but for the Devonian, only three vegetation types (basal embryophyte communities, cladoxylopsid forests comprising tree fern-like trees, and *Archeopteris* forests consisting of woody trees) are considered as appropriate representation of main steps in the land-plant evolution and given our limited knowledge of the biosphere characteristics in the Devonian.

The spatial distribution of each vegetation type is based on two climatic variables: (1) the annual mean continental temperature, and (2) water availability for plants (or degree of saturation of the soil) for each grid point. The degree of saturation (hereafter DOS) is defined as the water volume (soil moisture variable) divided by the maximum water content in the soil (15 cm, bucket model

assumption). This water content is directly governed by the water availability to the pore space and ranges from 0 (dry) to 1 (saturated). In contrast with modern plants, the shallow root systems of the first land plants were probably limited by the available soil water. This parameterization tends to better account for this effect. Concerning the temperature sensitivity, we consider that a grid box with an annual continental temperature below 0 °C is a factor prohibiting the growth of the tree ferns that are not adapted to cold seasons. Explicit conditions to install vegetation types for Plant Functional Types (hereafter PFT1, PFT2 and PFT3) are given in Table 1b.

To couple FOAM with SLAVE-Jr, we have written a *python* program (*python* is a dynamic object-oriented programming language) that changes the climatic parameters in the FOAM boundary files according to the vegetation distribution given by SLAVE-Jr. Starting from the climate and atmospheric information as inputs, SLAVE-Jr dynamically computes spatially explicit transient vegetation composition in terms of plant functional groups, and their associated water budgets. In the coupling procedure, FOAM is run for five years, the annual terrestrial temperature and precipitations of the last year are saved to force SLAVE-Jr which calculates the PFT pattern. This process is repeated throughout the first 20 model years to take into account the vegetation–climate feedbacks, a time to ensure that the vegetation reaches the equilibrium coevally with the climatic conditions. The climates calculated by the coupled FOAM–SLAVE-Jr model are then used in COMBINE to estimate past atmospheric CO_2 and steady state climate following the procedure described above. We eventually reach a climate at steady-state associated with a biome distribution for each simulated geological period in equilibrium with the calculated pCO_2.

2.3. Devonian land plants

Previous conclusions on early land plant evolution distinguished three successive phases in the terrestrialization of plants (Kenrick and Crane, 1997). (1) The "Eoembryophytic phase" when most land plants are at a bryophytic grade of organization is followed by (2) an "Eotracheophytic phase" corresponding to the rise of the earliest vascular plants in the Silurian and Early Devonian. (3) The "Eutracheophytic phase", which is the main focus of this paper, initiates in the Early Devonian and corresponds to an extensive diversification of the morphologies and reproductive strategies of land plants. During this phase, the evolution of trees that occurred separately in different clades represents a major breakthrough with a putative impact on climate changes (Algeo et al., 2001; Beerling and Berner, 2005). Interestingly, subdividing the "Eutracheophytic phase" based on the presence versus the absence of trees and on the successive dominant types of trees of the Devonian results in recognizing the Early, Middle and Late Devonian respectively as three significant phases in the evolution of land plants (see below).

An accurate appraisal of the composition, structure, ecological requirements and geographical distribution of the palaeovegetations for each phase is currently difficult. Our assessments are based on extrapolations from the limited number of palaeoecological studies that have been realized so far, most from Euramerican localities (Cressler et al., 2010; Driese et al., 1997; Hotton et al., 2001; Mintz et al., 2010; Scheckler, 1986; Steemans et al., 2010).

Finally, assessing the most appropriate extant analogs for the Devonian vegetations in order to parameterize the land surface features of past landscapes is also a challenge. Our approach consists of adopting the same criteria to define the main vegetation types of the Devonian as those used by Matthews (1984) to classify the extant types of vegetation. These criteria include the height, presumed density and main physiological traits of the dominant lifeforms. Because we use ecological rather than systematic criteria, and despite the fact that they comprise no closely related plants, we assume that the extant types of vegetation we have selected are the closest available analogs for the Devonian forms (hereafter called PFTs for Plant Functional Types). We then derive the land-surface properties for the Devonian PFTs from the values of the corresponding extant vegetation types provided by Matthews (1984) and Hack et al. (1993). Considering these assumptions, the proposed vegetation types and extant analogs used to parameterize land-surface boundary conditions for the Devonian (up to the mid-Famennian) are the following. They are summarized in Table 1.

(1) Vegetated Early and Middle Devonian landscapes were dominated by PFT1 which comprises basal land plants. These include the eotracheophytic rhyniophytes and rhyniophytoids, and the eutracheophytic zosterophylls, early lycopsids and basal euphyllophytes of low to moderate stature. These plants are shallowly rooted and characterized by a homosporous reproduction necessitating free water for fertilization. Interpreted as obligate dwellers of wet substrates (Greb et al., 2006), some may have withstood seasonal freezing or aridity (Wellman and Gray, 2000; Wellman et al., 2000). Many formed

Table 1
Devonian vegetation (upper part) and boundary conditions (lower part).

Simulations	Periods	Main plant type	Height	Density	Phenology	Morphology of photosynthetic structures	Closest extant vegetation analog (Matthews, 1984)
LP1	Early Devonian	PFT1, basal embryophytes	0.5–1 m up to 2 m	–	–	Narrow, dissected	Grassland/forb formation
LP2	Mid-Devonian (or Late Early Devonian)	PFT1, basal embryophytes	0.5–1 m up to 2 m potentially >5 m	–	–	Narrow, dissected	Grassland/forb formation
		PFT2, Tree-ferns (Cladoxylopsid)	Potentially >5 m	Open stands	Evergreen	Narrow, dissected	Evergreen needleaved
LP3	Late Devonian (mid Frasnian to mid-Famennian)	PFT3, Woody trees (*Archeopteris*)	Potentially >5 m	Closed forest	Evergreen	Broad-leaved	Rainforest

Surface properties (PFT)	Albedo (%) (total/vis/near IR)	Roughness (m)	Evapotranspiration coefficient	Thermal property	Climate conditions required to install land plants
Rocky desert	32/24/40	0.05	0.1	7	
Basal embryophytes (PFT1)	20.5/9/32	0.1	0.1	6	0.5<DOS<0.8
Tree-ferns (PFT2)	19.5/14/25	1	0.25	5	0.8<DOS and annual temp>0 °C
Woody trees (PFT3)	12/6/18	2	0.25	4	0.3<DOS

To define Devonian plant properties, we used values of their respective analog extracted from the Matthews classification (1984) (see Section 2.3 for an exhaustive discussion concerning the choice of modern analogs). Then, land surface boundary conditions are specified in FOAM using vegetation-related surface features. The data base used to prescribe the plant albedo is the NASA Tech. Memo (Matthews, 1984). For the roughness, evapo-transpiration coefficient, and thermal property, values come from the NCAR Tech. Note (Hack et al., 1993). The surface extension conditions are determined as a function of assumptions based on paleo-botanical features (see Section 2.3).

monotaxic patches of clonal plants forming dense stands that excluded other species (Hotton et al., 2001). The closest analogs found in Matthews (1984) are "tundra formations" (referred to as # 16 in Matthews' Table 1) and "grasslands" (referred to as # 19 in Matthews' Table 1). The former consists of dwarf-scrub communities, the latter to either actual grasslands or to forb formations, i.e. formations of non graminoid herbaceous plants such as ferns that include plants exceeding 50 cm in height. "Tundra formations" are more appropriate analogs for the eotracheophytic vegetations of late Silurian and earliest Devonian age. However, in order to take into account the increase in size of the plants accompanying the diversification of the early eutracheophytes prior to the advent of the tree habit, we have selected the "grasslands/forb formations" as the closest analogs for the Early and Middle Devonian vegetation types devoid of trees. This vegetation type better corresponds to the communities reported from the Emsian Battery Point Formation from Gaspé (Québec) for example (Hotton et al., 2001). Selecting "tundra formations" as the closest analog for PFT1 would have probably underestimated the impact of this PFT for both the late Early Devonian and the Middle Devonian. Our choice of "grasslands/forb formations" probably overestimates the impact of this PFT for the Lochkovian and Pragian stages of the Devonian. The ecological requirements mentioned above for PFT1 supposes a small range of acceptance concerning the DOS (from 0.5 to 0.8) and absence of limitation for the temperature.

(2) The Middle Devonian saw the rise of PFT2 which corresponds to the earliest tree communities. It comprised tree fern-like cladoxylopsids that could exceed 5 m in height (Stein et al., 2007). By analogy with extant trees, the limited extent of their root system and narrowness of their crown lacking large laminate leaves suggest that these cladoxylopsids may have lived in open stands. Photosynthesis was performed by distal branches that were green and may have superficially resembled those of extant Cupressaceae. Stumps rooted in paleosols indicate that they occupied wetlands (Driese et al., 1997; Mintz et al., 2010). For these reasons, we choose Matthews (1984) "evergreen needle-leaved woodlands" (referred to as # 10 in Matthews' Table 1), a composite vegetation type comprised of 50% of evergreen woodlands, 25% of "grasslands" and 25% of barren surface, as the closest analog for the cladoxylopsid forests with the requirements for an elevated DOS (here fixed over 0.8) of their habitat. Because of the large amount of living cells characterizing their trunk, cladoxylopsid trees probably avoided freezing climates (Meyer-Berthaud et al., 2010) which exclude lands experiencing temperatures below zero and long cold seasons. Indeed, no indication of seasonality such as growth rings or differences in the size of the branch scars along the trunk has been reported for these trees, which suggests their preference for equable environmental conditions.

(3) In the Late Devonian spread a second type of forests, PFT3, comprised of the progymnosperm genus *Archeopteris*. *Archeopteris* had a worldwide distribution that ranged from low to high paleolatitudes (Anderson et al., 1995; Cressler et al., 2010; Retallack, 1997). These trees, which may have reached 40 m in height, possessed large leaves and an extended root system. Their trunks, branches, and roots were essentially made of wood. They formed dense shady forests, a strategy that overcame the necessity of moisture linked to their heterosporous reproduction (Beck, 1964; Driese et al., 1997). Because of these traits — depth of the root system, wood instead of living cells as the essential component of the biomass, optimal environment for reproduction independent from external conditions and provided by the forest itself — we assume that the Late Devonian PFT3, could survive with a DOS below 30%. In addition, the structural resemblance of *Archeopteris* with that of extant conifers suggests that these trees may have supported freezing conditions and suppose an absence of thermal restriction for their colonization. They inhabited diverse types of habitats from poorly to well-drained lowlands (Driese et al., 1997; Scheckler, 2001), and showed a wide range of ecological strategies including opportunistic growth (Mintz et al., 2010). They had the ability to stop their growth, produce growth rings (Arnold, 1930; Lemoigne et al., 1983), and generate epicormic shoots (Meyer-Berthaud et al., 2000), a set of traits that may have favored their settlements in habitats subjected to environmental stresses or even disturbances, and under a wider range of climatic conditions than any of the other trees of the Late Devonian (Cressler, 2006; Cressler et al., 2010; Fairon-Demaret et al., 2001). *Archeopteris* shed leafy branches instead of leaves. But the deciduous/persistent character of the leafy branches is equivocal (Beck, 1971). Many woody remains of *Archaeopteris* from equatorial and paleotropical deposits show either subtle (Lemoigne et al., 1983; Meyer-Berthaud et al., 1997; Snigirevskaya and Snigirevsky, 2001) or no growth rings (Arnold, 1930; Galtier et al., 1996; Meyer-Berthaud et al., 2004), suggesting that leafy branches remained attached to the trees for several years (Falcon-Lang, 2000). Added to the height and density of the stands, the persistency of the leafy units resulted in forests that were presumably closed and evergreen which legitimizes our choice for "rainforests" as the closest extant analogs for most of the PFT3 represented in the fossil record. Dense broad-leaved forests thrived at high paleolatitudes (85°S) during the Permian (Taylor et al., 1992) and shed their leaves during winter, a strategy possibly adopted by their Late Devonian counterparts. However, although archaeopterid spores have been recorded in the Givetian (385–392 Ma) of Antarctica, and compressions of leafy branches in the Famennian (374–359 Ma) of South Africa, no woody remains were yielded from high paleolatitude outcrops of Devonian age, and the phenology of archaeopterid forests in these zones is unknown. Treating all Late Devonian forests as a single PFT analogous to extant rainforests is another limitation of this study which may overestimate the impact of the actual vegetation at this time.

Evidence for the occurrence of early seed plants before the late Famennian is poor. Published analyses of the distribution of plants in the late Famennian localities of the Catskill Delta show that early seed plants were ruderal in disturbed habitats within lowlands (Cressler et al., 2010; Scheckler, 1986). This indicates the pivotal role of such plants in ecological successions but does not infer that these plants covered large surfaces in the Devonian landscapes even if it is suspected that they have been more significant than suggested by their record at this time (Fairon-Demaret and Hartkopf-Fröder, 2004). Because of these uncertainties about the actual distribution of this plant group in Late Devonian landscapes, especially in uplands, and the spatial resolution of the model, we choose to follow a conservative approach and did not take into account the seed plants in this work.

2.4. Boundary conditions and simulation design

The only three forcing functions are the solid Earth degassing rate (here fixed at its present-day value due to the lack of constraints), the continental configuration, and the slowly increasing solar constant. In the present study, we use the palaeogeographies from Ron Blakey (2003), where the Devonian is mainly characterized by a southward migration of Gondwanaland while Laurentia, Baltica and Siberia cratons remained located at low latitudes. To represent this continental drift, two maps have been used for the Devonian. The first one is

assumed to be representative of the 400–370 Ma interval (Early and Middle Devonian), and the second one stands for the 370–360 Ma interval (Late Devonian). Concerning the solar constant, we have supposed that the solar luminosity increases from 1323 W/m^2 (3.3% reduction relative to present day value) in the Early Devonian to 1326 W/m^2 in the Late Devonian, according to stellar evolution models (Gough, 1981).

To model the land plant invasion and investigate climate–carbon–vegetation interplays, five GEOCLIM runs are presented in this contribution. We first quantify the effect of the continental drifting between the Early and the Late Devonian without plants (no land-plant simulations, Table 2). For these runs, we prescribe a continental surface covered by a rocky regolith (Tables 1 and 2). Then, the land-plant invasion is modeled by three sets of simulations (land-plant runs or LP, see Tables 1–2). LP1 simulations represent the Earliest Devonian case characterized by the existence of primitive plants (PFT1). LP2 runs simulate the Middle Devonian (or Late Early Devonian) where PFT1 and PFT2 coexist. Both LP1 and LP2 are performed assuming an Early Devonian continental configuration. Finally LP3 simulation describes the Late Devonian vegetation dominated by woody trees (PFT3). The Late Devonian continental configuration is used for LP3. For all the LP (for land plant) simulations, GEOCLIM is coupled to the terrestrial biosphere model SLAVE-Jr. In addition, sensitivity runs have been performed to test the robustness of our results according to the boundary conditions that we have initially fixed (see Sections 3.4 and 3.5).

3. Surface climate and vegetation interplays during the land-plant invasion

The impact of plant colonization on the surface climate is investigated using a series of general circulation model simulations, coupled to a carbon and vegetation models. Since the modeling outputs are vegetation maps, CO_2 and climate, those three aspects will be successively described.

3.1. Calculated vegetation maps during Devonian

In vegetation maps calculated by the LP1 run, basal embryophytes (Fig. 2A) are mainly restricted to the coastal environments of north Gondwana, Laurussia and north Siberia. This limited expansion is the result of (1) an arid climate persisting during the Early Devonian due to the continental configuration, and (2) the water requirement of basal embryophytes (Table 1b). Looking at LP2 simulations, the distribution of basal embryophytes remains quasi-unchanged, but the new PFT2, consisting of "tree ferns", spreads into low latitudes (<15°latitudes) settling in the wet environments (P-E$_{low\ latitudes}$>100 cm/yr) (Fig. 2B). Mid-latitudes (40 to 50°) also take advantage of soil remaining humid throughout the year due to the sea-side proximity (P-E$_{mid\ latitudes}$>40 cm/yr). Between 15° and 30° of latitudes, the subsiding branch of the Hadley cell promotes the development of subtropical arid deserts and explains why these regions remain free of vegetation (P-E<20 cm/yr). Regarding LP3 simulations, 75% of continents are potentially colonized by land plants (PFT3), the remaining 25% being too dry (deserts) to be invaded (but this ratio is slightly depending on topography assumptions). This expansion is the result of less restrictive living conditions (Table 1b). A second cause is related to the tectonic setting. The land distribution, coupled to the sea-level rise, reduces the continental aridity. These two features facilitate the spreading of plants during the Late Devonian, even at high latitudes (Fig. 2C). It should be noted that Fig. 2 displays

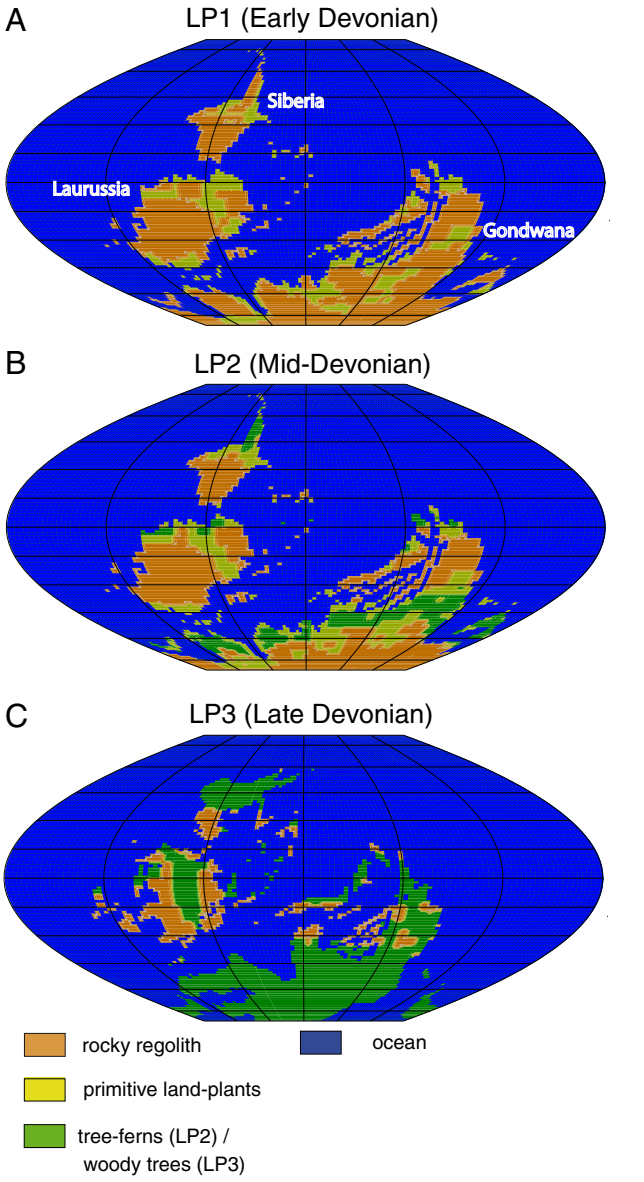

Fig. 2. Devonian potential vegetation distribution. Maps show the maximal potential distribution pattern for three timeslices, in equilibrium with the calculated pCO_2 (respectively 5144, 4843 and 2125 ppmv for LP1, LP2 and LP3 runs).

Table 2
Main modeling results.

Simulations	Early Devonian			Late Devonian	
	No land plants	LP1	LP2	No land plants	LP3
Surface (10^6 km²)					
Rocky regolith	122	95	72	104	27
Primitive plants	–	27	30	–	–
Giant ferns	–	–	20	–	–
Tree-like	–	–	–	–	77
Cont albedo (%)	32.0	29.9	27.0	32.0	17.2
Planetary albedo (%)	17.8	17.5	17.2	17.4	15.8
pCO_2 (ppmv)	6296	5144	4843	3954	2125
Tcont (°C)	16.2	15.5	15.5	16.9	16.5
SST (°C)	26.5	25.9	26.0	24.6	23.7
T_{global} (°C)	24.1	23.4	23.5	23.1	22.2
Runoff (cm/yr)	36.6	36.4	36.3	41.3	40.0
Cont. precip (cm/yr)	103.1	103.8	107.6	112.3	129.5
Cont. evap (cm/yr)	66.4	67.3	71.3	70.9	89.4
Cont. latent heat flux (W/m²)	53.8	54.6	57.8	57.5	72.6

The continental albedo does not include the snow-cover. Planetary albedo computed in clear sky.

maps of potential vegetation, without representing the plant abundance, or the associated productivity.

3.2. Devonian simulations predict an important pCO_2 reduction

Regarding runs performed without vegetation (No-LP runs), the pCO_2 drops from 6300 to 3950 ppmv throughout the Devonian (Table 2). This long-term reduction is mainly due to modifications of the global runoff simulated between the Upper and Lower Devonian, respectively 36.6 and 41.3 cm/yr (Table 2). In the Lower Devonian case, in order to consume the $6.8 \cdot 10^{12}$ mol of carbon released by volcanoes, the CO_2 has to rise (6296 ppmv) until the Earth surface is warm enough ($T_{global} = 24.1$ °C) to counteract the inhibition of weathering by low runoff and balance the solid Earth prescribed degassing. Conversely, the Upper Devonian configuration predicts a wetter climate (+11.4% of runoff, and +8.2% for precipitations, in annual mean), and thus requires a lower pCO_2 (3954 ppmv) to reach the same continental silicate weathering rate.

Fig. 3a shows the silicate weathering fluxes for both continental configurations at the same atmospheric CO_2 concentration (4200 ppmv). Two main differences arise, the first one over the tropical latitudes and the second one over the northern mid-latitudes. They are due to the general northward drift of continents from the Lower Devonian to the Upper Devonian that brings the Laurussia plate into the intertropical convergence zone and the Siberia plate from the tropical divergence zone to the wetter middle latitudes of the Northern hemisphere. These patterns of the plates drifting result in an increase of the silicate weathering through an increase of the continental runoff and promote a more efficient CO_2 consumption.

Fig. 4 shows the simulated atmospheric CO_2 concentrations during the land-plant colonization. The first step of land-plant appearance (i.e. the basal embryophytes, PFT 1) induces a decrease of pCO_2 of 1100 ppmv (from 6296 to 5144 ppmv) compared to the run performed without land plants. An additional 300 ppmv CO_2 decrease is simulated when including the arborescent cladoxylopsids vegetation (PFT 2). Finally, during the Late Devonian, the emergence of the PFT3 associated to the continental drift causes the largest effect on atmospheric CO_2 level with a decrease of more than 2500 ppmv (from 4843 to 2125 ppmv, where 1800 ppmv of reduction is the contribution accountable to land plants, see Fig. 4 and Table 2). These successive steps, in atmospheric CO_2 levels, are the results of an increase in the CO_2 consumption over low latitudes for all simulations and over the southern mid-latitudes for the LP3 runs. Regarding zonal weathering, runoff and temperature profiles at a fixed pCO_2 (Fig. 3b–d), we show that the three steps of the colonization of the land plants have induced a general increase of the continental temperature at all latitudes and a more complex modification of the runoff pattern with positive and negative anomalies. Nevertheless, when comparing runoff modifications and the changes in the weathering fluxes, one can easily attribute most of the increase in the CO_2 consumption to the runoff modifications promoted by the rise of land plants (Fig. 3d) and by the continental drift.

3.3. Climate evolution: a temperature decoupled from the pCO_2

While our model simulates a huge CO_2 decrease, the world-wide surface temperature remains rather stable during the Devonian, respectively 23.4, 23.5 and 22.2 °C for LP1, LP2 and LP3 simulations (Table 2). For instance, despite a significant drop in CO_2 (4843 to 2125 ppmv) from LP2 (Middle Devonian) to LP3 (Late Devonian), the temperature remains paradoxically quasi-unchanged (from 23.5 to 22.2 °C), whereas runoff is significantly boosted (36.3 to 40 cm/yr).

To explain this unusual behavior linked to the land-plant expansion, we compare the Earth energy budget evolution from 400 Ma (No-LP runs) to 370 Ma (LP3) to estimate the impact of the vegetated surface rise. At the global scale and in clear sky diagnostic, the net solar flux absorbed at the TOA (Top of Atmosphere) increases by 6.4 W/m² over the course of the Devonian. This result is explained by the significant reduction of the planetary Earth albedo (from 17.8 to 15.8%) caused by the continental albedo decrease (32.0 to 17.2%, see Table 2). However this albedo reduction does not provide a net warming. Indeed, as our model includes carbon–climate feedbacks, the transient warming caused by the albedo reduction is counteracted by the increase of the weathering rate which drives a pCO_2 drawdown. In consequence, the continental heating provided by the land-plant spreading is balanced by the cooling caused by the CO_2 drawdown. According to the relationship linking the pCO_2 and its radiative forcing, the CO_2 dropping from 6296 to 2125 ppmv creates a negative forcing estimated to −8.9 W/m² (computation based on the standard radiative model of Kiehl and Dickinson (1987)). Hence our model predicts a pCO_2 decrease over the course of the Devonian paradoxically associated to a mean global temperature remaining constant.

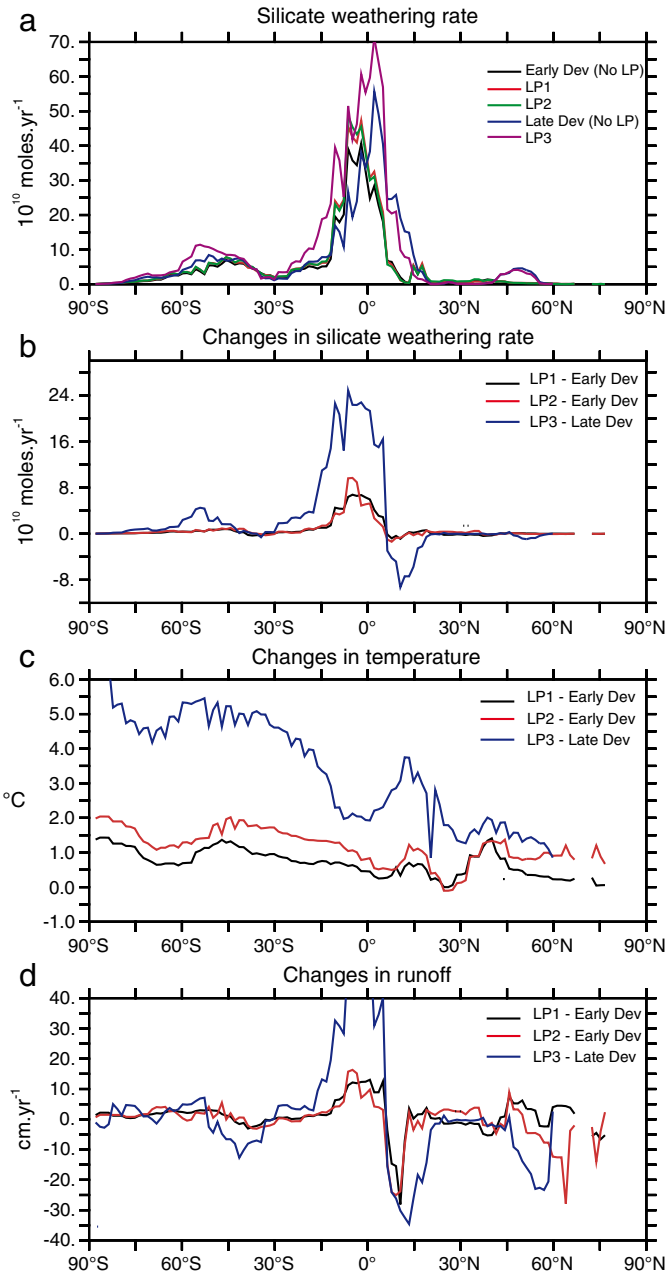

Fig. 3. Simulated silicate weathering rates, runoff and surface temperatures anomalies at a prescribed pCO_2 (15PAL or 4200 ppmv) for various timeslices and run conditions.

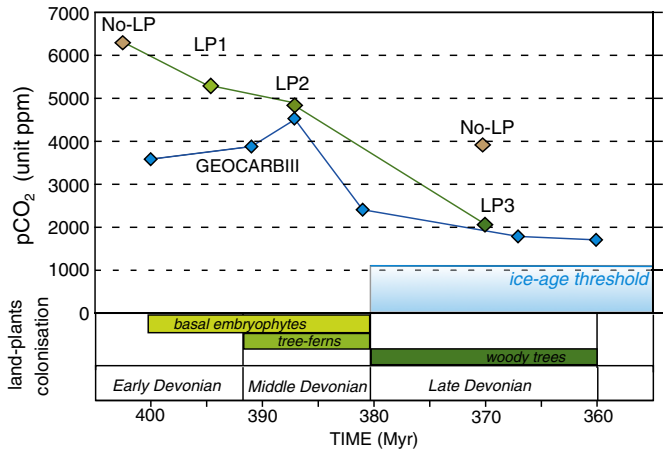

Fig. 4. Simulated pCO_2 obtained with GEOCLIM/SLAVE-JR (green curve) through the Devonian. The blue curve represents pCO_2 estimations based on GEOCARBIII (modified from Van Geldern et al., 2006). Light brown diamonds represent pCO_2 obtained with GEOCLIM without land plants (no-LP runs). The ice-age threshold has been estimated close to 4PAL (1120 ppmv) using the Late Devonian conditions.

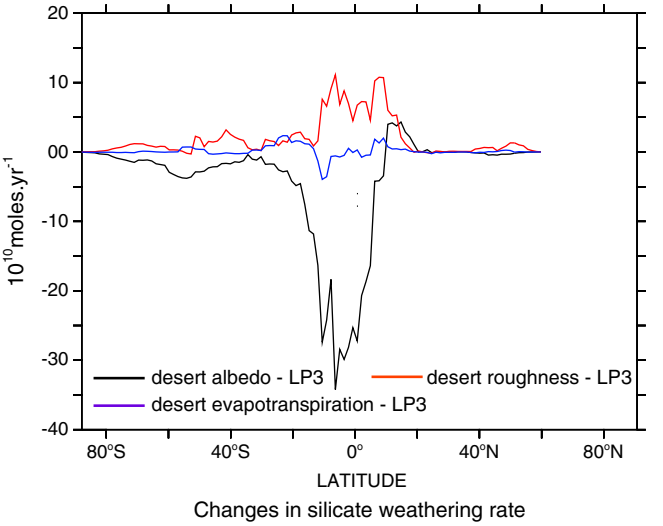

Fig. 5. Sensitivity test to plants surface properties. In each simulation one element of the reference run is replaced by the corresponding desert value (albedo, roughness and evapotranspiration coefficient). To avoid climate–carbon feedbacks and isolate the climate–vegetation interplays, the pCO_2 is fixed at 15PAL.

3.4. Impact of the land plants on the water cycle and weathering rates

In Section 3.2, we have demonstrated that the increase of the silicate weathering was due to an increase in the runoff. Coevally with the colonization of the continental surfaces by land plants, three physical parameters of the climatic model are impacted: the potential evaporation, the roughness and the albedo of the surface. Each of these parameters may modify the continental runoff and hence weathering rates. Regarding Early and Mid-Devonian simulations (LP1, LP2), the enhancement of the runoff (Fig. 3d) and associated weathering rates remain moderate (Fig. 3c). Indeed, (1) basal embryophytes have surface characteristics similar to the rocky regolith, and (2) the arborescent cladoxylopsids vegetation remains too confined ($20 \cdot 10^6$ km²) to significantly affect the global climate via an albedo reduction or via the evapotranspiration process (Table 2). The largest effect occurs during the Late Devonian where runoff and temperature patterns show large positive anomalies (Fig. 3c and d). Another diagnostic obtained with a roughly constant continental temperature but a changing pCO_2 (Table 2) shows that the runoff reaches 40 cm/yr in LP3, compared to 36 cm/yr in LP1 and LP2 runs.

To identify the mechanisms that modify the runoff and consequently the weathering, a supplementary set of sensitivity simulations have been performed, wherein one element of the reference run (albedo, roughness or potential evaporation coefficient) is replaced by the corresponding value typical of a rocky regolith. To inhibit the carbon–climate feedback, the pCO_2 is fixed at 4200 ppmv (15PAL). Regarding the anomalies obtained for weathering rates (Fig. 5), a large difference occurs when the vegetation albedo (0.12) is replaced by its desert value (0.32) (Fig. 5, black curve). This result suggests that a higher continental albedo decreases the runoff, and hence the weathering efficiency. A second order factor is the roughness affecting the latent and sensible heat fluxes. A surprising result is the unchanged pattern when the potential evaporation factor is set to its desert value, which supposes a minor effect caused by the evapo-transpiration process. Consequently the runoff, which drives weathering changes, is mainly controlled by the decrease in surface albedo promoted by the spreading of dense forests.

3.5. Importance of the plant albedo

The results of this study suggest that the land plant albedo largely drives an enhancement of the silicate weathering and a decrease in CO_2. As the plant albedo also governs the global hydrological cycle at the first order, it must be considered with care in order to account for the long term response of land plants. To investigate the impact of our parameterization concerning the plant albedo, two alternative albedo scenarios have been tested. In the first one, Late Devonian plants have the tree-fern albedo (19.5%) instead of the woody trees forests (12%). In the second case, we have replaced the initial PFT3 albedo by the basal embryophytes value (20.5%). In all cases the plant pattern distribution and other surface properties are kept constant, and correspond to LP3 run values.

As expected, our results indicate that tree-fern and basal embryophyte albedo lead to the calculation of higher pCO_2, respectively 3161 and 2979 ppmv, in the Late Devonian (compared to 2125 ppmv in the original LP3 run). We have calculated the climate sensitivity to Land Cover Change (LCC, see method in Appendix A), which corresponds to the warming caused by the land albedo radiative forcing. According to our model, when the LCC produces a forcing of 1 W/m² on the continent, the continental temperature increases by ~0.2 °C. The same calculation as a function of the continental albedo suggests a ratio of 1 °C for each 0.036 albedo variation. Hence, assuming that the pre-land plants' surface is correctly represented by a rocky desert, the progressive change of the continental albedo to the Late Devonian, from 32.0 to 17.2% (Table 2) indicates that land plants have induced a global warming of at least 4 °C. It should be noted that this warming is not observed in simulations due to the parallel reduction of the pCO_2 (see Section 3.2).

4. Discussion

In such deep time periods, it remains difficult to compare our predicted plant distributions with a coarse resolution to the fossil record (frequently punctual in time and space and allochthonous). However several similarities could be distinguished. For Mid-Devonian (LP2), the modeled phytogeography matches reasonably the fossils outcrops based on spore and megafossil assemblages (Edwards and Wellman, 2001; Scotese et al., 1999), except for South Laurussia. Indeed, according to our model, this region located between 15 and 30°S latitude, is too arid to bear any primitive land-plant implantation. This pattern makes sense because, beyond 20° of latitude, the subsiding branch of the Hadley cell leads to the development of subtropical arid zones. Nevertheless, we also emphasize that the use of the ocean slab model commonly induces slightly extended subsiding regions. Hence, the equator belt, with a very humid and warm climate, tends to be too narrow.

The Middle and Upper Devonian are considered as periods characterized by a weak latitudinal temperature gradient due to generally warm climatic conditions (Joachimski et al., 2009; Van Geldern et al., 2006; Veizer et al., 1999). Indeed miospores typical of mid-to-high latitude environment disappeared in the Mid-Devonian and tropical forms spread into subpolar regions during the Late Devonian. Similarly the $^{87}Sr/^{86}Sr$ records in carbonates tend to show an intensified weathering during the Late Devonian (Van Geldern et al., 2006), although the interpretation of the $^{87}Sr/^{86}Sr$ as indicative of weathering intensity is highly disputable (Godderis and Francois, 1995; Godderis et al., 2008; Nardin et al., 2010). Finally the oxygen isotopic composition of the surface seawater recorded in sedimentary calcite suggests a global warming during the Late Devonian. However, a global warming episode in the Middle–Late Devonian would be anti-correlated with the CO_2 evolution simulated by numerical models such as GEOCARBIII or GEOCARBSULF which predicts a drastic decrease from approximately 3400 to 1100 ppmv (Van Geldern et al., 2006). To reconcile proxies recording a global warming and the modeled evolution of the global carbon cycle during the Devonian, a likely solution would be that the negative climatic forcing driven by the pCO_2 reduction would be transiently overcome by a positive forcing linked to decrease continental albedo associated with a rapid land-plant expansion during the Middle to Late Devonian (Joachimski et al., 2009; Van Geldern et al., 2006). The present study yields tropical sea surface temperatures of 28 °C, 24.7 °C and 26.5 °C for the No-LP, LP2 and LP3 simulations, respectively. Using the Joachimski et al. temperature trend, we get tropical SSTs estimates of 28–32 °C at the Silurian–Devonian boundary (=No-LP), 21–25 °C in the Middle Devonian (=LP2), and 28–32 °C in the Late Devonian (=LP3). Trend in temperature from the Early to the Middle Devonian is in fairly good agreement between our study and the one of Joachimski et al. (2009), although our cooling trend is a bit weaker than the one estimated with data. However, the Late Devonian estimates from data are clearly warmer than our estimates. The model-data disagreement suggests either that (1) pCO_2 did not decline as much during this interval, or (2) the positive radiative forcing associated with Earth-surface albedo changes was larger than that calculated in the present-study. For example, we estimate that the land plant albedo changes associated to their massive extension could provide an important warming (+4.6 °C) if the pCO_2 is not influenced by the inorganic carbon feedback. In addition, moderate differences in term of CO_2 may come from other processes not included in our carbon cycle model (roots, organic burial).

In addition, our results have to be interpreted with caution. During the Latest Devonian, it seems that other factors may have supplanted the effect of the tectonic and of the land plant invasion. Indeed, a cold event recorded by the $\delta^{18}O$ in brachiopod and conodont tests is found at the Famennian (365 Ma) (Algeo and Scheckler, 1998; Algeo et al., 2001). Regarding the timing of major changes occurring during the latest Devonian and in agreement with the "Devonian Plant Hypothesis" (Algeo et al., 2001), it could be suggested that the spread of seed plants into upland areas may have been the factor that reduced pCO_2 to levels triggering a continental glaciation event (Fig. 4).[1]

Previous modeling studies suggest that during the Devonian, atmospheric CO_2 was reduced by a factor of 2 (Berner, 2004; Berner and Kothavala, 2001) due to vast quantities of carbon previously located in the atmosphere and now stored in the sedimentary layer. The most accepted mechanism to explain this downward trend was the enhancement of chemical weathering during land plant colonization, through root respiration, mechanical effect of roots and organic acid release (Berner, 1994; Berner and Kothavala, 2001; Ekart et al., 1999; Mora et al., 1996; Yapp and Poths, 1992). This study shed light on other processes, notably the changes in surface properties, which may increase the silicate weathering enough to decrease atmospheric CO_2 by a factor of 1.55 ± 0.3 (see footnote) according to the vegetation albedo value assumed (from 0.12 to 0.2). Therefore this decrease in CO_2 is of the same order of magnitude as prior estimations which are based on other processes. Hence surface property changes are one of the major actors involved in the CO_2 reduction during Mid-Paleozoic.

The processes we pointed out in this paper are robust, nevertheless their impact on precipitation, silicate weathering and finally, atmospheric CO_2 is certainly model dependent essentially because of our limited knowledge of Devonian vegetation. For example, in an atmospheric general circulation model (here FOAM), the runoff pattern is significantly affected by topography, a factor very difficult to constrain in deep times notably due to the absence of proxies. For example the Eastern/Western Laurussia remains not vegetated in the Late Devonian (LP3) because humid air masses tend to be locked on the central orogenic belt of the Laurussia. A second limitation of our study concerns obviously the physical properties used in SLAVE-Jr to mimic the Devonian vegetation. We are aware that representing the complexity of the vegetation by one or two PFT, for a flora which was already much diversified during the Devonian, is a crude simplification. However we motivate this choice by the necessity to distinguish fundamental steps in the land-plant invasion, with a time resolution coherent with the other boundary conditions we used, notably the geography.

5. Conclusion

In the present contribution, we explore the impact of the land plant evolution during the Devonian on the evolution of the global carbon cycle and climate. The numerical model used (GEOCLIM) couples a 3D-climate model to a model of the global biogeochemical cycles and to a simple model for vegetation dynamics adapted to Devonian conditions. More specifically, we quantify the impact of the changing continental conditions during terrestrialization (albedo, roughness, thermal properties and potential evaporation) on the climate and hence on the CO_2 consumption through continental silicate weathering; we also account for the continental drift.

We found that, in response to the continental drift, the atmospheric CO_2 decreases from 6300 ppmv to 3950 ppmv from the Early to the Middle Devonian. This decrease is triggered by the drifting of Laurussia and Siberia into more humid latitudinal belts over the course of the Devonian. The Late Devonian pCO_2 is further reduced to 1800 ppmv by the spreading of the land plants on continental surfaces. This further decrease is mainly triggered by decreasing continental albedo, which warms the continental surfaces and hence promotes CO_2 consumption by silicate rock weathering.

A salient result of our simulations is that the evolutionary development and the spread of land plants during the Devonian have been an important controlling factor of the Paleozoic climatic evolution. We show that continental surface changes induced by land plants and tectonic drift have produced a large CO_2 drawdown without being associated to a global cooling, because the cooling trend is counteracted by a warming trend resulting from the surface albedo reduction. Future works should now integrate our results to the previously modeled effects of the land plant expansion during the Devonian, as the impact of plant rooting on the weathering rates, and the burial of terrestrial organic carbon.

Acknowledgements

This work has been funded by the French National Agency for Research, project ANR-06-BLAN-0347-01. Y.D. thanks the ANR project

[1] 1.85 is reached for a pCO_2 decrease from 3954 to 2125 ppm (Table 2), and only 1.25 for a drop from 3954 to 3161 ppmv of CO_2. These two end-members represent the CO_2 reduction predicted for an albedo reduction from 0.32 to respectively 0.12 and 0.20.

COLORS (no. ANR-09-JCJC-0105). We thank Pierre Friedlingstein for providing the original SLAVE model. AMAP (Botany and Computational Plant Architecture) is a joint research unit which associates CIRAD (UMR51), CNRS (UMR5120), INRA (UMR931), IRD (R123), and Montpellier 2 University (UM27); http://amap.cirad.fr/.

We gratefully acknowledge Thomas Algeo and an anonymous reviewer for providing constructive comments on this manuscript, and Peter DeMenocal for the quality of the editorial procedure. This is IPGP contribution no. 3218.

Appendix A

The Land Cover Change (LCC) is determined as the ΔTemp/ΔSNFSC where LP3 is the simulation of reference. The LCC being computed with an unchanged pCO_2, all results are obtained with a pCO_2 fixed at 10PAL (2800 ppmv). All simulations are done with LP3 boundary conditions, except the vegetation albedo. SNFSC represents the solar net flux absorbed at the surface in clear sky diagnostic.

Simulations	LP3	LP3 — scenario 1	LP3 — scenario 2
Vegetal albedo (vis/IR)	0.06/0.18	0.14/0.25	0.09/0.32
Continental albedo (%)	17.2	22.7	23.5
SNFSC (W/m^2)	199.5	190.4	190.0
Continentale temp (°C)	18.3	16.8	16.6
LCC ($°C/Wm^{-2}$)	–	0.17	0.18

References

Algeo, T.J., Scheckler, S.E., 1998. Terrestrial-marine teleconnections in the Devonian: links between the evolution of land plants, weathering processes, and marine anoxic events. Philos. Trans. R. Soc. B-Biol. Sci. 353 (1365), 113–128.

Algeo, T.J., Scheckler, S.E., Maynard, B., 2001. Effects of the Middle to Late Devonian spread of vascular land plants on weathering regimes, marine biotas, and global climate. In: Gensel, P.G., Edwards, D. (Eds.), Plants Invade the Land: Evolutionary and Environmental Perspectives, 213–236. Columbia University Press, New York.

Anderson, H.M., Hiller, N., Gess, R.W., 1995. Archeopteris (progymnospermopsida) from the Devonian of Southern Africa. Bot. J. Linn. Soc. 117 (4), 305–320.

Arnold, C.A., 1930. The genus *Callixylon* from the Upper Devonian of central and western New York. T. Pap. Mic. Acad. Sci. 11, 1–50.

Beck, C.B., 1964. Predominance of *Archaeopteris* in Upper Devonian flora of western Catskills and adjacent Pennsylvania. Bot. Gaz. 125 (2), 126–128.

Beck, C.B., 1971. On the anatomy and morphology of lateral branch systems of *Archaeopteris*. Am. J. Bot. 58 (8), 758–784.

Beerling, D.J., Berner, R.A., 2005. Feedbacks and the coevolution of plants and atmospheric CO_2. Proc. Natl. Acad. Sci. U. S. A. 102 (5), 1302–1305.

Beerling, D.J., Osborne, C.P., Chaloner, W.G., 2001. Evolution of leaf-form in land plants linked to atmospheric CO_2 decline in the Late Palaeozoic era. Nature 410 (6826), 352–354.

Berner, R.A., 1987. Models for carbon and sulfur cycles and atmospheric oxygen — application to Paleozoic geologic history. Am. J. Sci. 287 (3), 177–196.

Berner, R.A., 1991. A model for atmospheric CO_2 over Phanerozoic time. Am. J. Sci. 291 (4), 339–376.

Berner, R.A., 1994. GEOCARBII — a revised model of atmospheric CO_2 over Phanerozoic time. Am. J. Sci. 294 (1), 56–91.

Berner, R.A., 2001. The effect of the rise of land plants on atmospheric CO_2 during the Paleozoic. In: Gensel, P.G., Edwards, D. (Eds.), Plants Invade the Land: Evolutionary and Environmental Perspectives, 173–178. Columbia University Press, New York.

Berner, R.A., 2004. The Phanerozoic Carbon Cycle: CO_2 and O_2. Oxford University Press, p. 158.

Berner, R.A., 2006. GEOCARBSURF: a combined model for Phanerozoic atmospheric O_2 and CO_2. Geochim. Cosmochim. Acta 70, 5653–5664.

Berner, R.A., Kothavala, Z., 2001. GEOCARB III: a revised model of atmospheric CO_2 over Phanerozoic time. Am. J. Sci. 301 (2), 182–204.

Blakey, R.C., 2003. Carboniferous–Permian paleogeography of the assembly of Pangea. In: Wong, T.E. (Ed.), XVth International Congress on Carboniferous and Permian Stratigraphy. Royal Netherlands Academy of Arts and Sciences, Utrecht, the Netherlands, pp. 443–465.

Bormann, B.T., Wang, D., Bormann, F.H., Benoit, G., April, R., Snyder, M.C., 1998. Rapid, plant-induced weathering in an aggrading experimental ecosystem. Biogeochemistry 43 (2), 129–155.

Cressler III, W.L., 2006. Plant paleoecology of the Late Devonian Red Hill locality, north-central Pennsylvania, an *Archaeopteris*-dominated wetland plant community and early tetratop site. In: Greb, S.F., DiMichele, W.A. (Eds.), Geological Society of America, Boulder, CO, Special Paper, Wetlands through Time (399), pp. 79–102.

Cressler III, W.L., Daeschler, E.B., Slingerland, R., Peterson, D.A., 2010. Terrestrialization in the Late Devonian: a palaeoecological overview of the Red Hill site, Pennsylvanian, USA. In: Vecoli, M., Clément, G., Meyer-Berthaud, B. (Eds.), Geological Society, London, Special Publications, The Terrestrialization Process: Modelling Complex Interactions at the Biosphere–Geosphere Interface (339), pp. 111–128.

Dessert, C., Dupre, B., Francois, L.M., Schott, J., Gaillardet, J., Chakrapani, G., Bajpai, S., 2001. Erosion of Deccan Traps determined by river geochemistry: impact on the global climate and the Sr-87/Sr-86 ratio of seawater. Earth Planet. Sci. Lett. 188 (3–4), 459–474.

Dessert, C., Dupre, B., Gaillardet, J., Francois, L.M., Allegre, C.J., 2003. Basalt weathering laws and the impact of basalt weathering on the global carbon cycle. Chem. Geol. 202 (3–4), 257–273.

Donnadieu, Y., Godderis, Y., Ramstein, G., Nedelec, A., Meert, J., 2004. A 'snowball Earth' climate triggered by continental break-up through changes in runoff. Nature 428 (6980), 303–306.

Donnadieu, Y., Godderis, Y., Pierrehumbert, R., Dromart, G., Fluteau, F., Jacob, R., 2006. A GEOCLIM simulation of climatic and biogeochemical consequences of Pangea breakup. Geochem. Geophys. Geosyst. 7, Q11019.

Donnadieu, Y., Godderis, Y., Bouttes, N., 2009. Exploring the climatic impact of the continental vegetation on the Mezosoic atmospheric CO_2 and climate history. Clim. Past 5 (1), 85–96.

Driese, S.G., Mora, C.I., 2001. Diversification of Siluro-Devonian plant traces in paleosols and influence on estimates of paleoatmospheric CO_2 levels. In: Gensel, P.G., Edwards, D. (Eds.), Plants Invade the Land: Evolutionary and Environmental Perspectives. Columbia University Press, New York, pp. 237–253.

Driese, S.G., Mora, C.I., Elick, J.M., 1997. Morphology and taphonomy of root and stump casts of the earliest trees (Middle to Late Devonian), Pennsylvania and New York, USA. Palaios 12 (6), 524–537.

Edwards, D., Wellman, C.H., 2001. Embryophytes on land: the Ordocvician to Lochkovian (Lower Devonian) record. In: Gensel, P.G., Edwards, D. (Eds.), Plants Invade the Land: Evolutionary and Environmental Perspectives, Columbia, pp. 3–28.

Ekart, D.D., Cerling, T.E., Montanez, I.P., Tabor, N.J., 1999. A 400 million year carbon isotope record of pedogenic carbonate: implications for paleoatmospheric carbon dioxide. Am. J. Sci. 299 (10), 805–827.

Fairon-Demaret, M., Hartkopf-Fröder, C., 2004. Late Famennian plant mesofossils from the Refrath 1 Borehole (Bergisch Gladbach-Paffrath Syncline; Ardennes-Rhenish Massif, Germany). Cour. Forsch.-Inst. Senckenberg 251, 89–121.

Fairon-Demaret, M., Leponce, I., Streel, M., 2001. *Archaeopteris* from the Upper Famennian of Belgium: heterospory, nomenclature, and palaeobiogeography. Rev. Palaeobot. Palynol. 115 (1–2), 79–97.

Falcon-Lang, H.J., 2000. The relationship between leaf longevity and growth ring markedness in modern conifer woods and its implications for palaeoclimatic studies. Palaeogeogr. Palaeoclimatol. Palaeoecol. 160 (3–4), 317–328.

Freidlingstein, P., 1995. Modélisation du cycle du carbone biosphérique et étude du couplage biosphère–atmosphère, of Brussel Brussel.

Friedlingstein, P., Delire, C., Muller, J.F., Gerard, J.C., 1992. The climate induced variation of the continental biosphere — a model simulation of the last glacial maximum. Geophys. Res. Lett. 19 (9), 897–900.

Gaillardet, J., Dupre, B., Louvat, P., Allegre, C.J., 1999. Global silicate weathering and CO_2 consumption rates deduced from the chemistry of large rivers. Chem. Geol. 159 (1–4), 3–30.

Galtier, J., Paris, F., ElAouadDebbaj, Z., 1996. The occurrence of Callixylon in the upper Devonian of Morocco and its palaeogeographical significance. C. R. Acad. Sci. Ser. IIa: Fascicule Sci. Terre Planets 322 (10), 893–900.

Godderis, Y., Francois, L.M., 1995. The Cenozoic evolution of the strontium and carbon cycles: relative importance of continental erosion and mantle exchanges. Chem. Geol. 126 (2), 169–190.

Godderis, Y., Joachimski, M.M., 2004. Global change in the Late Devonian: modelling the Frasnian–Famennian short-term carbon isotope excursions. Palaeogeogr. Palaeoclimatol. Palaeoecol. 202 (3–4), 309–329.

Godderis, Y., Donnadieu, Y., Tombozafy, M., Dessert, C., 2008. Shield effect on continental weathering: implication for climatic evolution of the Earth at the geological timescale. Geoderma 145 (3–4), 439–448.

Gough, D.O., 1981. Solar interior structure and luminosity variations. Sol. Phys. 74 (1), 21–34.

Greb, S.F., Dimichele, W.A., Gastaldo, R.A., 2006. Evolution and importance of wetlands in earth history. Geol. Soc. Am. 399, 1–40 (special paper).

Hack, J.J., Boville, B.A., Briegleb, B.P., Kiehl, J.T., Rasch, P.J., Williamson, D.L., 1993. Description of the NCAR Community Climate Model (CCM2). NCAR Technical Note NCAR/TN-382+STR: 108.

Hotton, C., Hueber, F., Griffing, D., Bridge, J., 2001. Early terrestrial plant environments: an example from the Emsian of Gaspé, Canada. In: Gensel, P.G., Edwards, D. (Eds.), Plants Invade the Land: Evolutionary and Environmental Perspectives, 179–212. Columbia University Press, New York, pp. 179–212.

Jacob, R., 1997. Low frequency variability in a simulated atmosphere ocean system.

Joachimski, M.M., Breisig, S., Buggisch, W., Talent, J.A., Mawson, R., Gereke, M., Morrow, J.R., Day, J., Weddige, K., 2009. Devonian climate and reef evolution: insights from oxygen isotopes in apatites. Earth Planet. Sci. Lett. 284 (3–4), 599–609.

Kenrick, P., Crane, P.R., 1997. The origin and early evolution of plants on land. Nature 389 (6646), 33–39.

Kiehl, J.T., Dickinson, R.E., 1987. A study of the radiative effects of enhanced atmospheric CO_2 and CH_4 on early Earth surface temperatures. J. Geophys. Res. Atmos. 92 (D3), 2991–2998.

Le Hir, G., Donnadieu, Y., Godderis, Y., Pierrehumbert, R.T., Halverson, G.R., Macouin, M., Nedelec, A., Ramstein, G., 2009. The snowball Earth aftermath: exploring the limits of continental weathering processes. Earth Planet. Sci. Lett. 277 (3–4), 453–463.

Lemoigne, Y., Iurina, A., Snigirevskaya, N., 1983. Révision du genre *Callixylon* Zalessky 1911 (*Archaeopteris*) du Dévonien. Palaeontographica 186B, 81–120.

Matthews, E., 1984. Prescription of land-surface boundary-conditions in GISS GCM II: a simple method based on fine-resolution data bases. NASA Tech. Memo. 86096, 1–21 June.

Meyer-Berthaud, B., Wendt, J., Galtier, J., 1997. First record of a large Callixylon trunk from the late Devonian of Gondwana. Geol. Mag. 134 (6), 847–853.

Meyer-Berthaud, B., Scheckler, S.E., Bousquet, J.L., 2000. The development of *Archaeopteris*: new evolutionary characters from the structural analysis of an early Famennian trunk from southeast Morocco. Am. J. Bot. 87 (4), 456–468.

Meyer-Berthaud, B., Rücklin, M., Soria, A., Belka, Z., Lardeux, H., 2004. Frasnian plants from the Dra Valley, southern Anti-Atlas, Morocco. Geol. Mag. 141 (6), 675–686.

Meyer-Berthaud, B., Soria, A., Decombeix, A.-L., 2010. The land plant cover in the Devonian: a reassessment of the evolution of the tree habit. In: Vecoli, M., Clément, G., Meyer-Berthaud, B. (Eds.), The Terrestrialization Process: Modelling Complex Interactions at the Biosphere–geosphere Interface. : Special Publications, 339. Geological Society, London, pp. 59–70.

Mintz, J.S., Driese, S.G., White, J.D., 2010. Environmental and ecological variability of middle Devonian (Givetian) forests in Appalachian basin paleosols, New York, United States. Palaios 25 (1–2), 85–96.

Mora, C.I., Driese, S.G., Colarusso, L.A., 1996. Middle to late Paleozoic atmospheric CO_2 levels from soil carbonate and organic matter. Science 271 (5252), 1105–1107.

Moulton, K.L., Berner, R.A., 1998. Quantification of the effect of plants on weathering: studies in Iceland. Geology 26 (10), 895–898.

Nardin, E., Goddéris, Y., Donnadieu, Y., Le Hir, G., Blakey, R.C., Pucéat, E., Aretz, M., 2010. Modeling the early Paleozoic long-term climatic trend. Geol. Soc. Am. Bull. 123 (5–6), 1181–1192.

Oliva, P., Dupre, B., Martin, F., Viers, J., 2004. The role of trace minerals in chemical weathering in a high-elevation granitic watershed (Estibere, France): chemical and mineralogical evidence. Geochim. Cosmochim. Acta 68 (10), 2223–2243.

Retallack, G.J., 1997. Early forest soils and their role in Devonian global change. Science 276 (5312), 583–585.

Scheckler, S.E., 1986. Ancestral character states of Archeopteridales (progymnospermopsida). Am. J. Bot. 73 (5), 704–705.

Scheckler, S.E., 2001. Afforestation — the first forests. In: Briggs, D.E.G., Crowther, P. (Eds.), Palaeobiology, II. Blackwell Science Ltd, Oxford, pp. 67–71.

Scotese, C.R., Boucot, A.J., McKerrow, W.S., 1999. Gondwanan palaeogeography and palaeoclimatology. J. Afr. Earth Sci. 28 (1), 99–114.

Snigirevskaya, N.S., Snigirevsky, S.M., 2001. New locality of *Callixylon* (Archaeopteridaceae) in the Late Devonian of Andoma Mountain (Vologda Region, north-west Russia) and its importance for the reconstruction of archaeopterid distribution. Acta Palaeobotanica 41, 97–105.

Steemans, P., Wellman, C.H., Gerrienne, P., 2010. Palaeogeographic and palaeoclimatic considerations based on Ordovician to Lochkovian vegetation. In: Vecoli, M., Clément, G., Meyer-Berthaud, B. (Eds.), The Terrestrialization Process: Modelling Complex Interactions at the Biosphere–geosphere Interface. : Geological Society, London, Special Publications. The Geological Society of London, pp. 47–56.

Stein, W.E., Mannolini, F., Hernick, L.V., Landing, E., Berry, C.M., 2007. Giant cladoxylopsid trees resolve the enigma of the Earth's earliest forest stumps at Gilboa. Nature 446 (7138), 904–907.

Taylor, E.L., Taylor, T.N., Cuneo, N.R., 1992. The present is not the key to the past — a polar forest from the Permian of Antarctica. Science 257 (5077), 1675–1677.

Van Geldern, R., Joachimski, M.M., Day, J., Jansen, U., Alvarez, F., Yolkin, E.A., Ma, X.P., 2006. Carbon, oxygen and strontium isotope records of Devonian brachiopod shell calcite. Palaeogeogr. Palaeoclimatol. Palaeoecol. 240 (1–2), 47–67.

Veizer, J., Ala, D., Azmy, K., Bruckschen, P., Buhl, D., Bruhn, F., Carden, G.A.F., Diener, A., Ebneth, S., Godderis, Y., Jasper, T., Korte, C., Pawellek, F., Podlaha, O.G., Strauss, H., 1999. Sr $^{87}/^{86}$, $\delta^{13}C$ and $\delta^{18}O$ evolution of Phanerozoic seawater. Chem. Geol. 161, 59–88.

Walker, J.C.G., Hays, P.B., Kasting, J.F., 1981. A negative feedback mechanism for the long-term stabilization of Earth's surface-temperature. J. Geophys. Res.-Oceans Atmos. 86 (NC10), 9776–9782.

Wellman, C.H., Gray, J., 2000. The microfossil record of early land plants. Philos. Trans. R. Soc. London, Ser. B-Biol. Sci. 355 (1398), 717–731.

Wellman, C.H., Habgood, K., Jenkins, G., Richardson, J.B., 2000. A new plant assemblage (microfossil and megafossil) from the Lower Old Red Sandstone of the Anglo-Welsh Basin: its implications for the palaeoecology of early terrestrial ecosystems. Rev. Palaeobot. Palynol. 109 (3–4), 161–196.

Yapp, C.J., Poths, H., 1992. Ancient atmospheric CO_2 pressures inferred from natural goethites. Nature 355 (6358), 342–344.

Clim. Past, 10, 697–713, 2014
www.clim-past.net/10/697/2014/
doi:10.5194/cp-10-697-2014

Climate of the Past
Open Access

The faint young Sun problem revisited with a 3-D climate–carbon model – Part 1

G. Le Hir[1], Y. Teitler[1,*], F. Fluteau[1], Y. Donnadieu[2], and P. Philippot[1]

[1]IPGP, Institut de Physique du Globe de Paris, Sorbonne Paris cité, Université Paris Diderot, UMR7154, 75005, France
[2]LSCE, CNRS-CEA-UVSQ, 91191 Gif-sur-Yvette, France
[*]now at: Centre for Exploration Targeting, University of Western Australia, Crawley, Australia

Correspondence to: G. Le Hir (lehir@ipgp.fr)

Received: 6 February 2013 – Published in Clim. Past Discuss.: 22 March 2013
Revised: 17 February 2014 – Accepted: 18 February 2014 – Published: 3 April 2014

Abstract. During the Archaean, the Sun's luminosity was 18 to 25 % lower than the present day. One-dimensional radiative convective models (RCM) generally infer that high concentrations of greenhouse gases (CO_2, CH_4) are required to prevent the early Earth's surface temperature from dropping below the freezing point of liquid water and satisfying the faint young Sun paradox (FYSP, an Earth temperature at least as warm as today). Using a one-dimensional (1-D) model, it was proposed in 2010 that the association of a reduced albedo and less reflective clouds may have been responsible for the maintenance of a warm climate during the Archaean without requiring high concentrations of atmospheric CO_2 (pCO_2). More recently, 3-D climate simulations have been performed using atmospheric general circulation models (AGCM) and Earth system models of intermediate complexity (EMIC). These studies were able to solve the FYSP through a large range of carbon dioxide concentrations, from 0.6 bar with an EMIC to several millibars with AGCMs. To better understand this wide range in pCO_2, we investigated the early Earth climate using an atmospheric GCM coupled to a slab ocean. Our simulations include the ice-albedo feedback and specific Archaean climatic factors such as a faster Earth rotation rate, high atmospheric concentrations of CO_2 and/or CH_4, a reduced continental surface, a saltier ocean, and different cloudiness. We estimated full glaciation thresholds for the early Archaean and quantified positive radiative forcing required to solve the FYSP. We also demonstrated why RCM and EMIC tend to overestimate greenhouse gas concentrations required to avoid full glaciations or solve the FYSP. Carbon cycle–climate interplays and conditions for sustaining pCO_2 will be discussed in a companion paper.

1 Introduction

Sagan and Mullen (1972) argued from solar models that, in the early Archaean, the young Sun's luminosity was 25 % lower compared to now. According to climate models, the weakness of the young Sun's brightness would have implied that Earth's surface temperature was well below the freezing point of water during the first two billion years of its history. A completely frozen Earth, however, conflicts with evidence of the presence of liquid water at the surface and life development during the Archaean. More intriguingly, geological evidence suggests that the Archaean climate was similar or even warmer than the present-day climate. Greenhouse gases, and more specifically carbon dioxide, were soon put forward as good candidates for solving this issue known as the "faint young Sun paradox" (FYSP; see Feulner, 2012 for a detailed review). Using a vertical one-dimensional radiative convective climate model (RCM), Kasting (1984, 2010) calculated that an atmospheric carbon dioxide partial pressure (pCO_2) of 0.3 bar or $\sim$ 1000 times the preindustrial atmospheric level (PAL) (i.e. 0.28 mbar or 280 ppm) was needed to maintain a mean global surface temperature of 15 °C for a Sun 75 % dimmer than today.

In parallel with the modelling approach, atmospheric carbon dioxide concentration was semi-quantitatively estimated from Archaean palaeosols. Considering the absence of siderite in 2.8 Ga-old palaeosols, Rye et al. (1995) suggested from thermodynamical modelling that the pCO_2 had not exceeded $\sim$ 0.04 bar (or $\sim$ 130 PAL) during the Late Archaean. Questioning the relevance of the Rye et al. (1995) approach, Sheldon (2006) conducted mass-balance calculations of weathering in several Archaean to Palaeoproterozoic

palaeosols and proposed that the pCO_2 fluctuated from 3 mbar to 26 mbar (i.e. 11 to 93 PAL) from 2.2 to 1.0 Ga. More recently, Driese et al. (2011), using palaeoweathering indicators, suggested moderate CO_2 partial pressures of about 10 mbar at 2.7 Ga ago. Given the composition of iron-rich minerals found in Archaean banded iron formations (BIFs), Rosing et al. (2010) argued that the coexistence of magnetite (i.e. Fe_3O_4, a moderately oxidised mineral) and siderite (i.e. $FeCO_3$, a reduced mineral) in BIF was dependent on the atmospheric level in di-hydrogen (pH_2). Di-hydrogen (H_2) is a nutrient for methanogenic bacteria, and biological constraints impose a minimum pH_2. Using this constraint, Rosing et al. (2010) defined an upper limit for pCO_2 of about 0.9 mbar (900 ppmv or 3.2 PAL). Such a low pCO_2 has been the core of vivid debate among specialists, notably because BIFs are formed in marine environments far from thermodynamic equilibrium with the atmosphere and therefore are poor proxies of the early Earth atmosphere composition (Dauphas and Kasting, 2011; Reinhard and Planavsky, 2011).

Given the difficulties in estimating the partial pressure of atmospheric greenhouse gases on the primitive Earth, other mechanisms influencing climate such as changes in cloud properties have been explored. The mean forcing of clouds results from two opposite effects (Pierrehumbert, 2010). Clouds are highly reflective in the spectrum of visible solar radiation (shortwave radiation) and highly absorbent in the spectrum of thermal terrestrial radiation (longwave radiation). This leads to two well-known opposite effects; the shortwave reflection effect contributing to the planetary albedo and the longwave absorption effect contributing to the greenhouse. These mechanisms are related to the cloud type, the greenhouse effect being stronger than the albedo effect in the case of cirrus clouds, which are quite transparent at visible wavelengths but good absorbers of thermal terrestrial radiation. Using a one-dimensional radiative model, Goldblatt and Zahnle (2011b) estimated that in order to compensate for a weak Sun, Earth must have been entirely cloud-covered with poorly reflective (i.e. absence of stratus) but 3.5 times thicker clouds than today. In the absence of a mechanism able to change cloud properties in such proportions, the authors concluded that this scenario was highly unlikely. Goldblatt and Zahnle (2011b) also challenged Rosing et al.'s (2010) hypothesis that thinner clouds, caused by sparse cloud condensation nuclei (CCN), could have acted as an alternative to atmospheric greenhouse gases to warm up the early Earth's surface. In the present-day atmosphere, abundant CCN permit the formation of small liquid water droplets, leading to optically dense and highly reflective clouds because of their direct scattering effect (Charlson et al., 1987). During the Archaean, the concentration of CCN would have been about 10 to 20 % of its natural present-day level due to lower organic and inorganic sources. As a consequence, fewer droplets, but of larger size, would have formed optically thin clouds characterised by a low scattering of shortwave radiations and shorter lifetime. This hypothesis had been quantified with RCM simulations (Rosing et al., 2010). However, using a more realistic treatment of clouds, Goldblatt and Zahnle (2011b) demonstrated that the radiative forcing due to such changes in cloud properties has been overestimated.

To go one step further in the understanding of the FYSP, Kienert et al. (2012) conducted the first 3-D climate modelling of the Archaean climate using the EMIC (Earth system models of intermediate complexity) CLIMBER, which consists in an ocean general circulation model coupled with a simplified, low-resolution atmosphere. Using Archaean boundary conditions including a reduced incoming solar radiation, a faster Earth rotation and a reduced continental surface, CLIMBER simulates a present-day climate for a carbon dioxide partial pressure fixed at 0.6 bar. The authors explained their results by the ice-albedo feedback, which is enhanced during the Archaean due to a faster Earth rotation rate. This result contrasts with conclusions obtained by Jenkins (1993b) and Jenkins et al. (1993) with CCMAO (CCMAO was the version of the NCAR model at the beginning of the 90s, an atmospheric GCM coupled to a swamp ocean without heat capacity), where a faster rotation rate would have induced a warmer climate. The recent modelling of Archaean climate by Charney et al. (2013) using LMDz (an atmospheric GCM coupled to a slab ocean developed by Laboratoire de Météorologie Dynamique) challenged the CLIMBER results (Kienert et al., 2012, 2013) and revealed a very limited impact of the faster Earth rotation. However, LMDz results suggest that, for 3.8 Ga-old conditions, 100 mbar of carbon dioxide and 2 mbar of CH_4 are required to maintain an Earth climate as warm as today. Similar results are predicted for the Late Archaean (2.7 Ga), with the atmospheric GCM coupled to a slab ocean CAM3 (Wolf and Toon, 2013), where a combination of 20 mbar of CO_2 and 1 mbar of CH_4 is required to yield a global mean surface temperature near that of the present day.

To understand why AGCMs (Charney et al., 2013; Wolf and Toon, 2013; Kunze et al., 2014), EMIC (Kienert et al., 2012, 2013) and RCMs (Rosing et al., 2010; Kasting, 1984) differ in simulating the early Earth climate, we investigated the Precambrian climate using an atmospheric general circulation model coupled to a slab ocean FOAM. The paper is organised as follows. First, we estimate the radiative deficit required for the onset of a pan-glaciation. We run experiments ranging from 3.5 to 1 Ga to explore the impacts of Archaean boundary conditions (solar constant, palaeogeography, amount of emerged continental surface, and cloud properties). Second, we investigate the faint young Sun problem by performing additional sets of simulations where the effects of greenhouse gases (CO_2 and CH_4), saltier oceans, faster Earth rotation or sea ice albedo are tested. Finally, we compare our results with the above-mentioned studies to explore the causes of observed differences among RCMs,

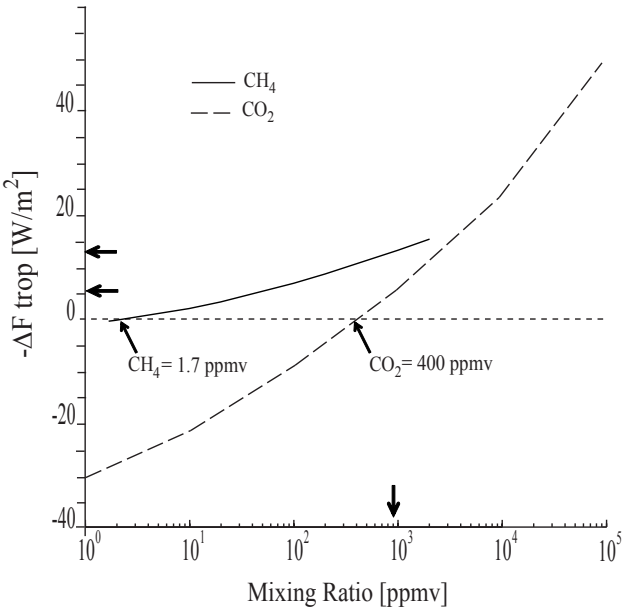

Fig. 1. Net long-wave fluxes computed for CO_2 and CH_4 with the FOAM radiative code (NCAR ccm3) (the total atmospheric is held constant, 1 bar). Thick arrows indicate the radiative forcing corresponding to 0.9 mbar of CO_2 and CH_4. Using the present-day atmosphere as a reference, the change in net flux at the tropopause (ΔF_{trop}) is 19 W m^{-2}, which reduces to 6 and 13 W m^{-2} for 0.9 mbar of CO_2 and CH_4, respectively.

EMIC and AGCMs, and discuss how these models differ in representing the ice-albedo feedback mechanism.

2 Model description and simulation specifications

2.1 Model description

Climate simulations were run with the atmospheric general circulation climate model (AGCM) FOAM 1.5. The atmospheric component of FOAM is a parallelised version of NCAR's Community Climate Model 2 (CCM2) with the upgraded radiative and hydrologic physics incorporated in CCM3 v. 3.2 (Jacob, 1997). All simulations were performed with an R15 spectral resolution ($4.5° \times 7.5°$) and 18 vertical levels. The radiative code (extracted from NCAR CCM3) has already shown its validity in atmospheres highly enriched in CO_2 (Pierrehumbert, 2004; Le Hir et al., 2010). The infrared absorption has been computed (Fig. 1) to replace CO_2-CH_4 conversion proposed by Rosing et al. (2010). Under an enriched CH_4 atmosphere, no significant differences are observed compared to prior estimates (Kiehl and Dickinson, 1987; Halevy et al., 2009). FOAM integrates the CCM3 version of cloud water parameterisation. As in the CCM3, cloud optical properties and liquid water droplet clouds used the Slingo (1989) parameterisation, where the liquid water droplet clouds (Cloud Water Path or CWP) is determined by integrating the liquid water concentration (q_{clw}):

$$\text{CWP} = \int q_{\text{clw}}.\text{d}z \text{ where } q_{\text{clw}} = q_{\text{clw0}} e^{(-z/H_{\text{clw}})} \quad (1)$$

z being the altitude, q_{clw0} an empirical constant equals to 0.21 g m^{-3} and H_{clw} the scale height representing the total precipitable water column, which is dependent of the precipitable water (q_{tot}). This last equation implies an exponential decay for in-cloud water concentration,

$$H_{\text{clw}} = 700 \ln(1 + q_{\text{tot}}) \quad (2)$$

with q_{tot} being computed by integrating the specific humidity Q (in kg kg^{-1}) over dp, p being the pressure and g the gravitational acceleration (9.8 m s^{-2}):

$$q\_\text{tot} = 1/g * \int Q \, \text{d}p. \quad (3)$$

FOAM is used in mixed-layer mode, meaning the atmospheric model is linked to a 50 m mixed-layer ocean with heat transport parameterised through diffusion. The diffusive rate of the slab ocean (Q_{flux}) is derived from the net surface fluxes and fixed to represent sea ice-covered seas based on estimates of the present-day sea ice mass budget. The sea ice module uses the thermodynamics of NCARs to compute ice fraction (growth and melting), snow cover, and penetrating radiation, and includes a Semtner model to calculate the sea ice temperature. The sea ice module does not treat sea ice dynamics, a lack which may slow the sea ice flow and underestimate the sea ice cover (Voigt and Abbot, 2012). Sea ice albedo is fixed at 0.7 (visible spectrum) and 0.5 (near-infrared spectrum).

2.2 Boundary conditions and experimental design

In this section, we describe boundary conditions used to explore the effects of solar constants, palaeogeography (amount of continental surface), and cloud properties from 3.5 to 1 Ga ago. Sets of simulations are summarised in Table 1.

2.2.1 Solar irradiance and palaeogeographies

Following Gough's formula (1981), the solar constant has been increased by 19 %, from 3.5 Ga (1053 W m^{-2}) to 1 Ga (1258 W m^{-2}) (Fig. 2a). Orbital parameters were set at their present-day values (orbital eccentricity: 0.016724, obliquity: 23.4463, vernal equinox latitude of perihelion: 77.9610) in all experiments. We varied the continental surface in response to the crustal growth and emergence, a process which affected the mean surface albedo ($\alpha_{\text{ocean}} = 0.06$, $\alpha_{\text{bare soil}} = 0.32$). Different scenarios ranging from a progressive formation to a quasi-instantaneous formation of all continental crust have been proposed (see Lowe and Tice, 2007 for a detailed review). Here we considered a gradual continental growth (Fig. 2b), consistent with the changes of $^{87}Sr/^{86}Sr$

Table 1. Simulations performed in the Sect. 3 (ΔF_{trop} is held constant and equals to $+19\,\text{W m}^{-2}$).

set of simulations	Boundary conditions *Paleogeography*	*Solar constant*	LOD (hours)	Droplet size(µm)	seawater freezing point
modern clouds	3.5-1Ga (Fig. 2b)	3.5-1Ga (Fig. 2a)	24	5–10	−1.8 °C
no clouds	"	"	24	/	"
Large droplet clouds	"	"	24	20	"

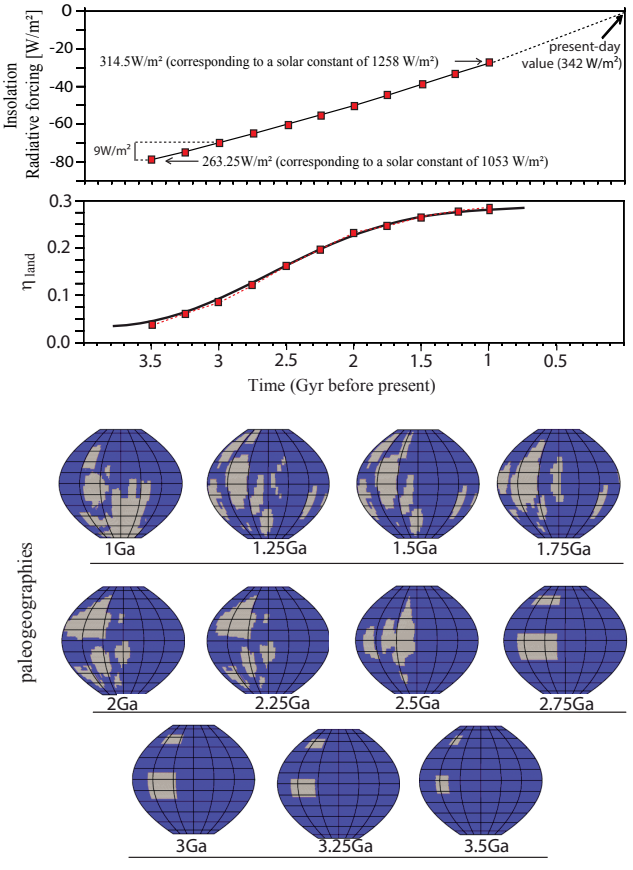

Fig. 2. Boundary conditions for solar constant (upper part) and continental growth (lower part). η_{land} is the emerged surface/Earth surface ratio (the present-day surface is $146 \times 10^6\,\text{km}^2$ or 29 % of the Earth's surface). Each red square represents the boundary conditions used in our sets of simulations.

(Godderis and Veizer, 2000) and δ^{34}S throughout the Archaean and early Proterozoic. Accordingly, the surface of the emerged continents increased from 4 % at 3.5 Ga to 27.5 % at 1 Ga. Palaeogeographies were reconstructed based on paleomagnetic data from 1 to 2.5 Ga (Pesonen et al., 2003). 3.5 to 2.75 Ga plate reconstructions being poorly constrained, continents were assumed to be located at low and mid latitudes. The elevation of land points was fixed at 200 m in all experiments.

2.2.2 Radiative forcing by greenhouse gases and ozone amounts

To set up boundary conditions correctly, we estimated the greenhouse radiative forcing provided by the combination of 0.9 mbar of CO_2 and CH_4 (i.e. CO_2 and CH_4 concentrations used by Rosing et al. (2010) and also tested by Charney et al. (2013)), rather than directly use pCO_2 and pCH_4 as boundary conditions. This was motivated because the assumption of such a low CO_2/high CH_4 is likely incorrect (Dauphas and Kasting, 2011; Reinhard and Planavsky, 2011). Moreover, Rosing et al. (2010) ignored the organic haze formation ($[CH_4]/[CO_2] > 0.2$ (Haqq-Misra et al., 2008)). Since it makes little difference whether radiative forcing is controlled by CO_2 or CH_4 (Hansen et al., 1997), this approach avoids doubtful assumptions about the Archaean/Proterozoic atmosphere composition. Hence, using the present-day atmosphere as a reference, the change in net radiative flux at the tropopause (ΔF_{trop}, Fig. 1) equals $19\,\text{W m}^{-2}$ ($\Delta F_{\text{trop}} = 6$ and $13\,\text{W m}^{-2}$ for 0.9 mbar of CO_2 and CH_4, respectively).

In addition, due to the low oxygen content of the Archean atmosphere imposed by sulfur mass independent fractionation (S-MIF) of sedimentary sulfides and sulfates (10^{-5} Present Atmospheric Level, PAL, Farquhar et al., 2001; Pavlov et al., 2000), the stratospheric ozone layer was removed in all experiments prior to 2.25 Ga and constrained to the present-day value in other experiments. The absence of an ozone layer precluded the formation of a stratospheric temperature inversion and resulted in a 40 km-thick atmosphere without temperature stratification (corresponding to the topmost atmospheric grid points in the AGCM). The global mean lapse rate from the surface to the 200 hPa level was not significantly affected by the absence of the ozone layer, and only a slight mean global cooling (0.7 °C) was simulated at the Earth's surface (Appendix Fig. A1). Induced cooling of surface temperature (1 to 2 °C) associated with the removal of the ozone layer is in good agreement with previous studies (Kasting, 1984; Kiehl and Dickinson, 1987; Wolf and Toon, 2013; Kunze et al., 2014).

2.2.3 Experimental design and assumptions for clouds

We performed sets of numerical experiments ranging from 3.5 to 1 Ga ago with a 0.25 Ga time increment. To avoid any effect of initial boundaries, simulations were initiated with warm conditions (present-day as starting point) and driven toward colder conditions (step-like decrease in the Sun's brightness). Each run lasted several tens of years until a steady state was reached for a decade or more. Climatic variables are averaged over the last decade.

To test the radiative impact of clouds, we considered three scenarios involving modern clouds, no cloud at all (cloud fraction fixed to 0), and clouds with large droplets (Table 1). A change in cloud droplet size affects scattering and therefore the cloud albedo (Pierrehumbert, 2010). For the parameterisation of Slingo (1989) implemented in FOAM, the cloud optical properties (OP_{clds}) for short-wave radiations were defined as

$$OP_{clds} = CWP[a + b/r_e], \quad (4)$$

where a and b are the cloud radiative coefficients (different for ice or liquid water clouds), CWP the cloud water path ($g\,kg^{-1}$) and r_e the effective droplet radius (droplet radius affected by its distribution).

In FOAM, liquid cloud droplet radii of modern clouds vary from 5 to 10 µm over landmasses and are fixed at 10 µm over oceans. This distinction is made to account for enhanced cloud drop nucleation that can occur over CCN-rich land areas. On the modern Earth, non-anthropogenic production of CCN is essentially related to soil dust formation, volcanic sulfate aerosols and dimethylsulfide (DMS) produced by planktonic eukaryotic algae (Charlson et al., 1987; Andreae and Rosenfield, 2008). In the absence of planktonic algae during the Archaean, the scarcity of emerged terrestrial surfaces and subaerial volcanism were considered as the possible, yet speculative, causes for the low CCN availability in the early Earth atmosphere (Rosing et al., 2010). To quantify the influence of large liquid droplets on climate, we ran a set of experiments in which we used the mean radius of liquid droplets of 20 µm[1] used by Rosing et al. (2010) over both the oceans and continents. Cloud droplets exceeding 15 µm being rarely observed (Bréon et al., 2002), this set of simulations should be regarded as an end member. Although large liquid water droplets of 20 µm diameter are expected to reduce cloud albedo (scattering effect), they also tend to rain out more rapidly (Boucher et al., 1995). According to the relationship established by Kump and Pollard (2008), the enhancement of cloud-to-precipitation rate varies as

$$\text{cloud-to-precipitation rate} = (r_e/r_{eo})^n, \quad (5)$$

where r_e represents the new effective radius (20 µm), r_{eo} the modern effective radius (assumed to be 10 µm, as oceans cover a large fraction of the Earth's surface), and n the parameter of enhanced rain-out (here $n = 3$). The literature features a wide range of values for the enhanced rain-out parameter; here we used an intermediate value suggesting a mid-strength feedback between 1 and 5.37 (Goldblatt and Zahnle, 2011b; Penner et al., 2006; Charney et al., 2013). As the cloud lifetime cannot be changed in the absence of a cloud microphysics module, we increased the precipitable water by 8 to represent the enhanced rain-out. Albeit speculative (see Sect. 2.1), we showed that CWP fluctuations are only governed by the air moisture (Appendix Fig. A2).

[1] The effective radius of 20 µm used by Rosing et al. (2010) was finally revised to 17 µm (Goldblatt and Zahnle, 2011a).

3 Results: estimating pan-glaciation thresholds

Figure 3 shows the radiative deficit required to induce a pan-glaciation, the global mean surface temperature and the mean planetary albedo. It is worth emphasising that the results presented here are not representative of climate evolution over the Precambrian era because only part of the boundary conditions used are realistic (solar luminosity, palaeogeography, fraction of emerged land). Other boundary conditions including the greenhouse gas radiative forcing ($\Delta F_{trop} = +19\,W\,m^{-2}$) are unrealistic. However, these were implemented in our model to allow comparison with previous simulations (Charney et al., 2013; Rosing et al., 2010) and to determine the radiative forcing threshold values required for the onset of pan-glaciations. The experiments (Exp) are labelled from 3.5 to 1 Ga according to the boundary conditions used.

3.1 Influence of the solar constant

Figure 3b (blue curve) represents the global mean surface temperature (Ts) simulated using the present-day cloud parameterisation. Ts is as low as −75 °C in Exp(3.5 Ga) and increases linearly up to −65 °C in Exp(2.5 Ga). The planetary albedo always exceeds 0.65 (Fig. 3c, blue curve) when the Earth is ice covered. An abrupt change, expressed by a shift of both temperature and albedo, is observed between Exp(2.5 Ga) and Exp(2.25 Ga). In Exp(2.25 Ga), Ts reaches −20 °C and the albedo drops to 0.45. This corresponds to a partially frozen Earth where sea ice spreads up to 30° latitude in both hemispheres. Between Exp(2.25 Ga) and Exp(1.75 Ga), a slight global warming of about 5 °C is observed, followed by a marked change of some 24 °C between Exp(1.75 Ga) and Exp(1.25 Ga), and a final slight warming of 4 °C between Exp(1.25 Ga) and Exp(1 Ga).

From these experiments, three climate states can be defined; a snowball Earth between Exp(3.5 Ga) and Exp(2.5 Ga), a partially frozen Earth between Exp(1.75 Ga) and Exp(2.25 Ga), and a weakly frozen Earth between Exp(1 Ga) and Exp(1.25 Ga). Although the solar brightness increased sub-linearly between 3.5 and 1 Ga, the global mean surface temperature changed dramatically during this time

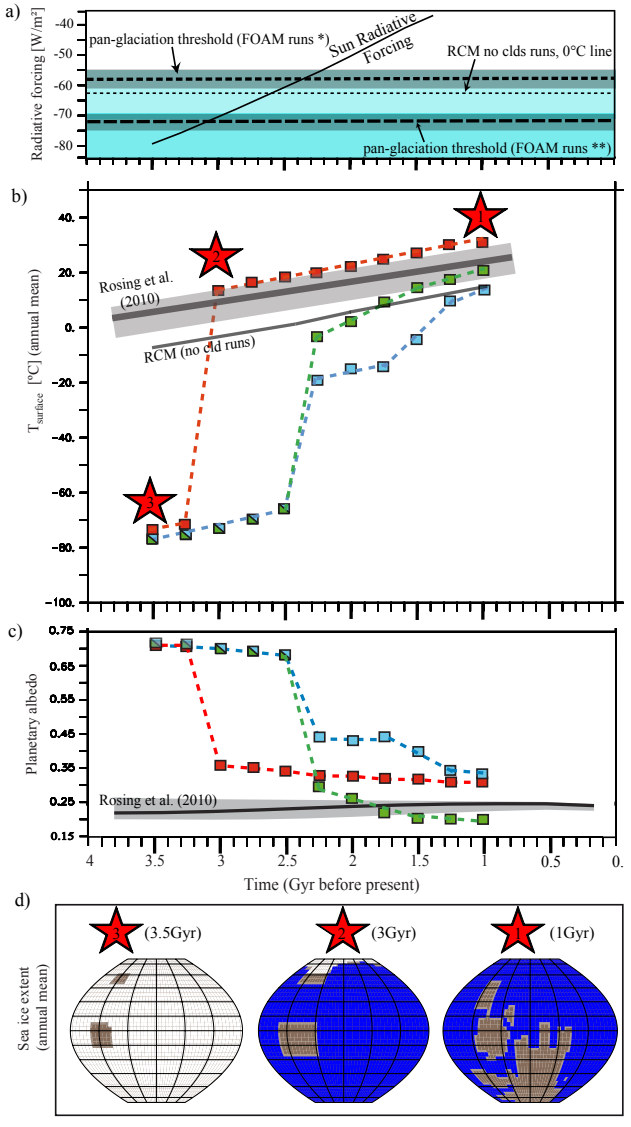

Fig. 3. 3-D climate simulations from 3.5 to 1 Ga with a greenhouse radiative forcing by CO_2 and CH_4 fixed to 19 W m^{-2} (ΔF_{trop}; see Fig. 1). **(a)** Radiative deficit required for the onset of a pan-glaciation with RCM (no cloud runs, surface albedo fixed to 0.264), FOAM runs (* modern clouds and cloud-free runs and ** large-droplet clouds (20 µm)). Grey lines represent uncertainties related to temporal resolution (0.25 Ga). **(b)** Evolution of surface temperature versus time assuming increasing irradiance and linear continental growth (see Fig. 2). Grey line is from Rosing et al. (2010). Blue and red curves were obtained using liquid droplet sizes of 5 to 10 µm (modern clouds) and 20 µm (clouds with large droplets), respectively. Green squares represent the cloud-free scenario. **(c)** Evolution of planetary albedo versus time (α_{ocean} 0.06, $\alpha_{\text{rocky desert continents}}$ 0.32, α_{seaice} 0.5, α_{snow} 0.8). **(d)** Red stars represent sea ice extent (white) predicted with runs performed with large (20 µm) droplets (Fig. 3b, c shows the corresponding temperature/albedo).

period (Fig. 3b). Between 1 and 1.25 Ga, the solar brightness is high enough to restrict the sea ice capping to the high latitudes ($\sim 60°$) and to bring the equator-pole surface temperature gradient to the present-day level. Between Exp(1.25 Ga) and Exp(1.75 Ga), sea ice spreads towards the equator up to 30° of latitude due to the reduced incoming solar radiation. Between Exp(1.75 Ga) and Exp(2.25 Ga), the sea ice maximum extent remains located in the vicinity of the tropics. This is due to a latitudinal gradient of temperature two times higher than in the Exp(1 Ga), which arises from a strong meridional energy transport by the atmosphere and oceans. For a solar constant lower than 1148 W m^{-2} (2.25 Ga), the solar brightness is low enough to drive climate towards snowball Earth conditions. Hence, for a fixed greenhouse-gas concentration of $\Delta F_{\text{trop}} = +19$ W m^{-2}, the solar constant evolution and its interplay with the ice-albedo feedback appear as the predominant factor governing the Earth's climate. This contrast with the RCM results (Fig. 3a) where the albedo is held constant at 0.264 (Goldblatt and Zahnle, 2011b) due to the absence of the ice-albedo feedback.

3.2 Influence of continental surfaces

A lower surface albedo due to a reduced continental area ($\alpha_{\text{bare soil}} = 0.32$, $\alpha_{\text{ocean}} = 0.06$) has been suggested as a solution to the FYSP (Schatten and Endel, 1982; Rosing et al., 2010; but see Walker et al., 1982 and Golbatt and Zanhle, 2011, for a controversy). No-cloud experiments show that the planetary albedo, which corresponds to the surface albedo, fluctuates with the growth of sea ice (Fig. 3b, green curve). Using the amount of energy reaching the Earth (expressed by $F = S/4(1\text{-}\alpha)$, with $\Delta\alpha = 0.10$ and $S = 1148$ W m^{-2}), we estimated the radiative forcing induced by the ice-albedo feedback to -29 W m^{-2} (cooling effect) between 1 and 2.25 Ga. This calculation shows that a slight change in the sea ice surface ($\alpha_{\text{sea-ice}} = 0.6$) can easily overcome the influence of a smaller continental area on the surface albedo ($\alpha_{\text{bare soil}} = 0.32$, $\alpha_{\text{ocean}} = 0.06$). These results demonstrate that the surface albedo is mainly governed by the sea ice extension, the growth of continental surfaces being a second-order factor. This conclusion is to challenged when the climate–carbon cycle feedbacks will be considered (Walker et al., 1981; Godderis and Veizer, 2000) (see companion paper).

3.3 Influence of clouds

Cloud experiments performed at 1 Ga show that the cloud radiative forcing is equal to -10 and -20 W m^{-2} at high and mid-latitudes, respectively (Fig. 4b). Accordingly, the absence of clouds seems to limit the sea ice spreading at high latitudes and to prevent the increase in the planetary albedo (Fig. 3c). This mechanism can explain why cloud-free experiments result in a warmer climate than those using modern clouds (Fig. 3b, green curve). Surprisingly, the shift

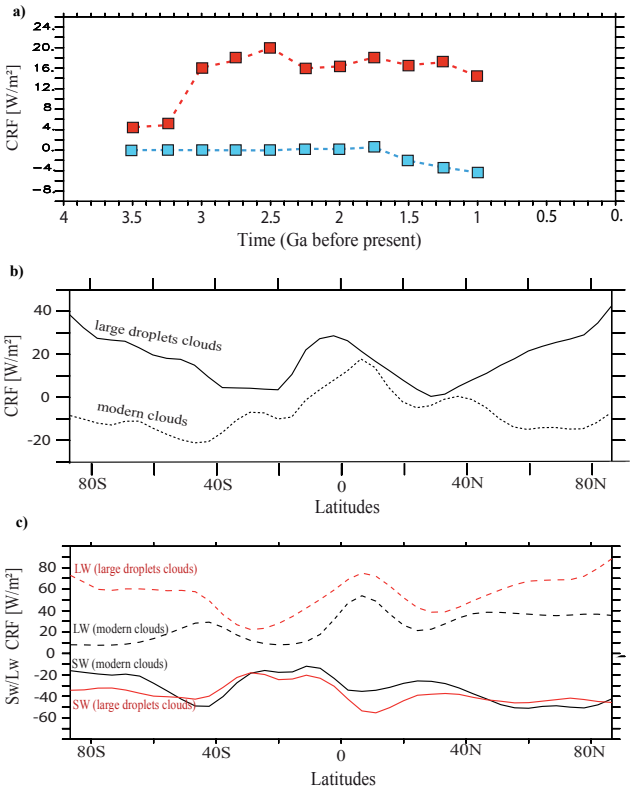

Fig. 4. (a) Net cloud radiative forcing (CRF, unit $\mathrm{W\,m^{-2}}$) versus time. Blue squares represent runs with modern clouds. Large-droplet clouds (red squares) result in a positive forcing because the effect of infrared trapping overcomes that of scattering. **(b)** CRF as a function of latitude for simulations performed at 1 Ga. The black line represents large-droplet clouds and the dashed line the modern cloud parameterisation. **(c)** Simulations performed using 1 Ga boundary conditions. Dashed lines represent long-wave (LW) budget of clouds (greenhouse effect), continuous lines their short-wave budget (albedo effect).

from a snowball state toward a partially ice-free Earth occurs between 2.5 and 2.25 Ga in both types of experiments. However, this apparent synchronicity is due to the relatively long duration increment of 250 Ma used between experiments. Since the incoming solar energy varies by as much as $5\,\mathrm{W\,m^{-2}}$ between 2.5 and 2.25 Ga (Fig. 2), it is not possible to evaluate with precision when the pan-glaciation occurs. In addition, it cannot be excluded that in a cold climate environment, the cloud scheme of FOAM underestimates the cloud radiative forcing (Abbot et al., 2012).

3.4 Effects of the cloud droplet size

The use of large liquid droplets (20 µm) increases the global mean surface temperature by about 20 to 35 °C compared to present-day droplet sizes (Fig. 3, red curves). In the large-droplet experiments, the shift towards snowball state occurs between 3 and 3.25 Ga with a mean global surface temperature of 13 °C. In contrast, modern clouds experiments result in a non-snowball state at 2.25 Ga with a mean global surface temperature of −19 °C. To explain why large-droplet experiments are in contrast to modern cloud simulations, we examined how clouds affect the Earth's budget. The cloud radiative forcing (CRF) obtained with large droplets was positive in all experiments (Fig. 4a). As an example, in the 1 Ga run, a net CRF of $14\,\mathrm{W\,m^{-2}}$ was obtained using large droplets instead of $-4\,\mathrm{W\,m^{-2}}$ for modern cloud simulation, a result in agreement with Goldblatt and Zahnle (2011b). In detail, clouds with large droplets generate a positive CRF at high latitudes ($+40\,\mathrm{W\,m^{-2}}$), preventing sea ice formation (Fig. 4b). Inhibiting sea ice formation limits the ice-albedo feedback efficiency and maintains the planetary albedo at low values (Fig. 3c, red curve). This change in CRF results from the combination of a slightly lower negative CRF at short wavelength (scattering effect) and a much higher positive CRF at large wavelength (IR trapping; Fig. 4c). As a consequence, even low-elevation clouds (the most reflective clouds) yield a positive CRF, as already shown by Goldblatt and Zahnle (2011b). The increase in evaporation due to warmer oceans enhances the cloud water content. This mechanism increases in turn the greenhouse effect because it amplifies the cloud emissivity ($\varepsilon_{\mathrm{cld}}$) expressed as

$$\varepsilon_{\mathrm{cld}} = 1 - e^{(-D * \mathrm{Kabs} * \mathrm{CWP})}, \quad (6)$$

where D is a diffusivity factor (1.66), Kabs is the longwave absorption coefficient ($\mathrm{m^2\,g^{-1}}$) and CWP is the cloud liquid water path.

4 Resolution of the faint young Sun problem: sensitivity tests

Fixing the change in the net radiative flux at the tropopause to $19\,\mathrm{W\,m^{-2}}$ (Fig. 1), none of the experiments can prevent the onset of pan-glaciation. The Earth's surface temperature threshold before shifting into a snowball Earth varies from −19 °C, using modern clouds, to +13 °C, using large-droplet clouds. The estimated radiative deficit required for the onset of a pan-glaciation between -57.5 ± 2.5 and $-72 \pm 2.5\,\mathrm{W\,m^{-2}}$ results in a threshold value between 21.5 ± 2.5 and $6.5 \pm 2.5\,\mathrm{W\,m^{-2}}$, respectively, to solve the FYSP (Fig. 3a). In the following, several warming parameters (greenhouse gas concentrations, ice albedo, a faster rotation rate and/or saltier oceans) able to generate an early Archaean climate at least as warm as today are tested at about 3.5 Ga.

4.1 Effects of greenhouse gases and ice albedo

Assuming a solar constant of $1053\,\mathrm{W\,m^{-2}}$ (77 % of the present-day value), an idealised geography, no ozone layer and two different cloud parameterisations (modern clouds and clouds with large droplets), the radiative forcing was enhanced either by increasing the concentrations of greenhouse

Table 2. Resolutions of the Faint Young Sun Problem: sensitivity tests (Sect. 4.1).

set of simulations	Boundary conditions	pCO_2 (10^{-3}bar)	pCH_4 (10^{-6}bar)	Ice albedo Vis/nIR	ΔF_{trop} (W m^{-2})	Droplet size (μm)	Global Ts (°C)
Run1	3.5 Ga	2.4	300	0.7/0.5	+24	20	14.2
Run2	"	25.2	1.7	"	+34	"	18.5
Run3	"	16.8	"	"	+30	"	15.7
Run4	"	25.2	"	"	+34	5–10	−73
Run5	"	56.0	"	"	+41	"	15.5
Run6	"	112.0	"	"	+49	"	21.1
Run7	"	25.2	"	0.5/0.5*	+34	"	−10.5

* Visible snow albedo fixed to 0.7 (instead of 0.9).

gases (pCO_2 and/or pCH_4) or by reducing the ice albedo from 0.6 to 0.5 (e.g. Warren et al., 2002). A summary of the simulations and global mean surface temperatures is given in Table 2.

When clouds with large droplets are considered, a radiative forcing at the tropopause (ΔF_{trop}) of +24 W m^{-2} yields an Earth surface temperature not significantly different from its present-day value (14.2 °C). Such a radiative forcing, which corresponds to 2.4 mbar of CO_2 and 0.3 mbar of CH_4, is able to solve the FYSP (Fig. 1). These results, which are in agreement with Charney al. (2013), and support the hypothesis defended by Rosing et al. (2010), are strongly dependent on the boundary conditions used. As an example, considering a modern pCH_4, the pCO_2 required to maintain a warm climate is about 16.8 mbar (run3, Table 2). When both pCH_4 and droplet sizes are fixed to their modern values, a pCO_2 of 56 mbar is required to simulate a mean temperature of 15 °C (run5, Table 2). In addition, ice albedo represents another factor that can affect the FYSP. When reducing the ice albedo by 0.1, the model simulates a colder climate, although the equator region remains ice free (run 7, Table 2). Climate response to varying ice albedo suggests the need for a good treatment of sea ice (notably for the sea ice dynamics), and also explains why the calculated greenhouse gas concentrations required for solving the FYSP are model dependent, most of them using different values for ice albedo (0.65 for LMDz; Charney et al., 2013, 0.68 (visible) to 0.3 (nearIR) for CAM3; Wolf and Toon, 2013, and 0.5–0.75 for EMAC, Kunze et al., 2014).

4.2 Effects of faster Earth rotation rate and saltier oceans

Palaeozoic rhythmites, mollusc shells and coral fossil records indicate that the Earth rotated faster in the deep past leading to a shorter Length Of the Day (LOD) (Walker and Zahnle, 1986). Between 3.8 and 2.5 Ga, the LOD increased from 14 to 18 h. Jenkins (1993a) and Jenkins et al. (1993) tested the effects of a shorter LOD on the early Earth climate using an atmospheric GCM coupled to a swamp ocean. He demonstrated that a faster rotation (corresponding to a LOD of ∼ 14 h) reduces the mean global cloudiness by 20 % and increases the mean global surface temperature by 2 °C. In fact this global warming hides local temperature changes, namely a cooling at the poles and a warming at the tropics due to the weakening of transient eddies carrying the heat from low to high latitudes. Hence, faster Earth rotation may have caused the climate to be more sensitive to the ice-albedo feedback (Kienert et al., 2012). To check this assumption, we ran a set of experiments assuming a LOD of 16 h (∼ 3.5 Ga). Another peculiar feature of the Archaean Earth is the occurrence of saltier oceans. Knauth (2005) suggested a long-term decline in ocean salinity throughout the Precambrian in parallel with the development of sedimentary basins and climatic conditions able to form and preserve halite (NaCl) deposits. As a consequence, the salinity of Archaean oceans may have been close to 60 ‰ (in comparison with 35 ‰ at the present-day) (Knauth, 2005; Foriel et al., 2004). Because a higher salinity lowers the seawater freezing temperature (Millero and Poisson, 1981), sea ice formation could have been delayed, potentially reducing the influence of the ice-albedo feedback. Since the atmospheric GCM FOAM is coupled with a slab ocean, a higher salinity cannot be taken into account. To mimic saltier oceans, we fixed the seawater freezing point at −3.3 °C following the equation of state of seawater proposed by Millero and Poisson (1981). Note that heat diffusion in our mixed-layer ocean was not adjusted in the Earth's rotation rate and salinity experiments (Table 3).

Accounting for saltier oceans, FOAM simulates a warming at high latitudes (Fig. 5), restricting sea ice formation and reducing the Earth's sensitivity to the ice-albedo feedback. More intriguing is the response induced by a faster Earth rotation. In present-day conditions, a change in day length from 24 to 16 h causes a global mean surface warming of about 2 °C (from 14.5 to 16.3 °C, Appendix Fig. A1), in agreement with previous results (Jenkins, 1993b). However, the warming is not homogeneous. Due to the reduced latitudinal heat transport and change in the cloud pattern, a faster Earth rotation warms up low latitudes but cools down high latitudes (Appendix Fig. A1), the warming of low latitudes overcoming the cooling of high latitudes. However,

Table 3. Simulations carried out with a $\Delta F_{\text{trop}} = +24\,\text{W m}^{-2}$ (Sect. 4.2). Note that heat diffusion in our mixed-layer ocean was not adjusted in the rotation rate and salinity experiments.

set of simulations	Boundary conditions *Paleogeography Solar*	*constant*	LOD (hours)	Droplet size(µm)	Seawater freezing	Mean surface temperature
Standard conditions	3.5 Ga	$1053\,\text{W m}^{-2}$	24	20	−1.8 °C	14.2 °C
Saltier ocean	"	"	24	"	−3.3 °C	15.0 °C
Faster Rotation	"	"	16	"	−1.8 °C	14.2 °C
Early Earth	"	"	16	"	−3.3 °C	14.4 °C

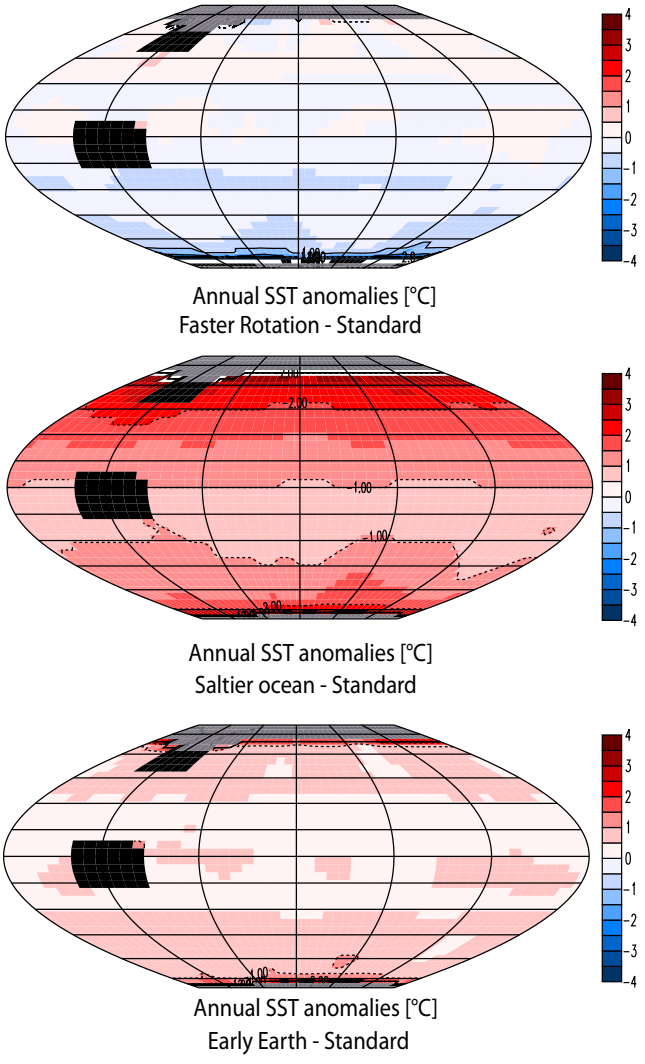

Fig. 5. Sea surface temperature anomalies (ΔSST) as a result of a faster Earth rotation rate (LOD = 16 h) and/or saltier ocean. Simulations performed with 3.5 Ga boundary conditions with large-droplet clouds and a $\Delta F_{\text{trop}} = +24\,\text{W m}^{-2}$ (standard conditions). The saltier ocean experiment uses standard conditions associated with an ocean two times saltier; the faster rotation experiment has a length of day of 16 h; the early Earth experiment combines both.

in colder conditions, a shorter LOD leads to the opposite trend: the sea ice formation at high and mid latitudes is facilitated, increasing the albedo and amplifying the cooling (Fig. 5). Consequently, when both a shorter LOD and saltier oceans are considered, their effects are balanced (a shorter LOD increases the Earth's sensitivity to the ice-albedo feedback while saltier oceans reduce it). This explains why these processes do not affect the solution of the FYSP (Fig. 5). It is noteworthy that our faster rotation simulation agrees with LMDz, but not CLIMBER (Kienert et al., 2012). One of the main reasons for such a difference is discussed below.

5 Discussion

FOAM, like other atmospheric GCMs, relies on a physical basis, which means that mechanisms and feedbacks are explicitly accounted for. Goldblatt and Zahnle (2011b) challenged the use of GCMs given that sub-grid scale parameterisation of clouds in these models precludes their use in palaeoclimate modelling. Here, we discuss differences between AGCMs and other categories of climate models (RCMs and EMIC) and argue that AGCMs are relevant and accurate tools for investigating deep-time climates.

5.1 FYSP resolutions: FOAM versus CLIMBER (EMIC)

FOAM results largely disagree with CLIMBER (Kienert et al., 2012, 2013). For instance, using CLIMBER, Kienert et al. (2012, 2013) suggested that a pCO_2 of 0.6 bar is required to generate a mean global temperature of 15 °C (for a 3.8 Ga solar constant of $1023\,\text{W m}^{-2}$) and that a faster rotation rate strongly impacts the ice-albedo feedback. This is at odd with the results obtained with FOAM in the present study. One of the reasons why CLIMBER yields opposite results to atmospheric GCMs essentially because of the different lapse rate parameterisation. Kienert et al. (2013) used Outgoing Longwave Radiation in clear-sky diagnostic (OLR) to check the validity of longwave radiative transfer, fixing the thermal structure of the atmosphere according to the lapse rate given in Halevy et al. (2009). However, they omitted to quantify OLR fluctuations caused by CLIMBER lapse rate parameterisation. As shown by Pierrehumbert (2004), the lapse rate

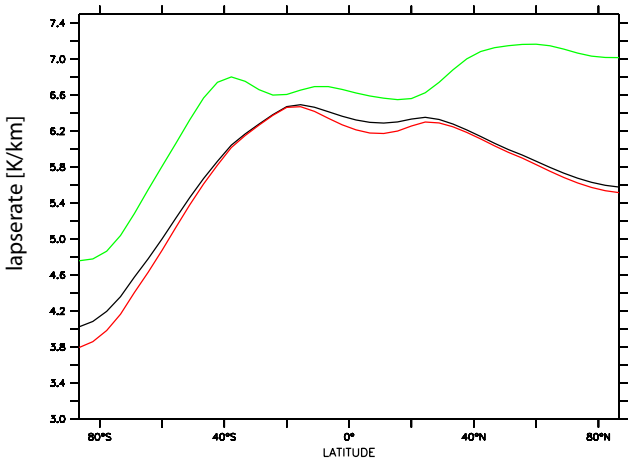

Fig. 6. Lapse rates (annual mean) calculated by CLIMBER lapse rate formula and FOAM using 1 Ga conditions (no clouds). Black curve represents the standard formulation in CLIMBER (Petoukhov et al., 2000), the red line is the calculation adapted for a faster rotation in CLIMBER (Kienert et al., 2012, 2013). The green line represents the FOAM lapse rate.

governs the sensitivity of climate to CO_2 so that the greenhouse effect (G) is expressed as

$$G(\mathrm{W\,m^{-2}}) = \sigma \mathrm{Ts}^4 - \mathrm{OLR}, \quad (7)$$

where Ts is the surface temperature (K), σ the Stefan–Boltzmann constant. OLR corresponds to the energy lost by the Earth as infrared radiation at the top of the atmosphere.

The CLIMBER lapse rate is based on a theoretical approach (Petoukhov et al., 2000) and was developed to fit empirical data such as

$$\text{lapse rate} = \Gamma_0 + \Gamma_1(\mathrm{Ts} - 273.16\,\mathrm{K}) * (1 - a_\mathrm{q} * Q^2) - \Gamma_2 * n_\mathrm{cld}, \quad (8)$$

where Γ_0, Γ_1 and Γ_2 are lapse rate parameters ($\Gamma_0 = 5.2 \times 10^{-3}$ K m^{-1}, $\Gamma_1 = 5.5 \times 10^{-5}$ K m^{-1}, $\Gamma_2 = 10^{-3}$ K m^{-1}), Q is the surface-specific humidity (kg kg^{-1}), n_cld the cumulus cloud amount and $a_\mathrm{q} = 10^3$ (kg kg)$^{-2}$. Kienert et al. (2012, 2013) updated this formula to account explicitly for a faster Earth rotation rate such as $\Gamma_0 = 5.1 \times 10^{-3}$ K m^{-1}, $\Gamma_1 = 6.1 \times 10^{-5}$ K m^{-1}, $\Gamma_2 = 0.9^{-3}$ K m^{-1} and $a_\mathrm{q} = 1.171 \times 10^3$ (kg kg)$^{-2}$. To illustrate CLIMBER lapse rate parameterisation better, we used FOAM outputs (i.e. Ts and Q). To suppress the cloud effects, we extracted outputs from a run performed at 1 Ga with no clouds; therefore n_cld is fixed to 0 (lapse rates computed with clouds are available in Appendix Fig. A3). In CLIMBER the radiative transfer depends on Ht (troposphere height), so we calculated lapse rates for the entire troposphere (from the Earth's surface to an atmospheric pressure level of 254 mbar).

Figure 6 shows lapse rates for different case scenarios: (1) with the standard formula implemented in CLIMBER (Petoukhov et al., 2000), (2) using the adapted formula in case of a faster rotation (Kienert et al., 2012, 2013) and (3) using FOAM. For the same values of Ts and Q, we show that the lapse rate is systematically underestimated with CLIMBER, hence inducing warmer temperature and a higher thermal radiation flux loss at the tropopause (the unusual shape of the lapse rate is explained by the northern hemisphere which is almost entirely oceanic, see Fig. 2b). Therefore, for the same $p\mathrm{CO_2}$, CLIMBER results in a less efficient greenhouse effect. This artefact in the CLIMBER lapse rate explains why this EMIC needs such a large $p\mathrm{CO_2}$ when a present-day Earth rotation is considered (Kienert at al., 2012). The required $p\mathrm{CO_2}$ is even higher when a faster Earth rotation is imposed. Although the authors discussed the uncertainties linked to CLIMBER radiative module (Kienert et al., 2013), they omitted lapse rate/OLR interplays. In addition to possible effects of ocean and sea ice dynamics and an ice albedo above classical values, this omission could explain why Kienert et al. (2012, 2013) proposed such a high $p\mathrm{CO_2}$ to solve the FYSP.

5.2 Pan-glaciation thresholds and ice-albedo feedback: AGCMs versus RCMs

It is noteworthy that atmospheric GCMs are able to maintain a large fraction of open oceans (i.e. above the seawater freezing point) with very moderate amounts of greenhouse gases, 0.9 mbar of CO_2 and CH_4 for LMDz (3.8 Ga), 3.7 mbar of CO_2 for EMAC (3.5 Ga) and 5 mbar of CO_2 for CAM3 (2.7 Ga), a result that contrasts with RCM estimates (0.04 bar of CO_2 at 3.5 Ga, Kasting, 1987). RCMs assume that a drop of the mean temperature below 0 °C leads to a runaway glaciation, and therefore induces high $p\mathrm{CO_2}$ in order to maintain ice-free oceans during the Archaean. However, stable climates have been simulated using AGCMs while the global mean surface temperature falls well below 0 °C (Charney et al., 2013; Wolf and Toon, 2013; Kunze et al., 2014, this study). Wolf and Toon (2013) suggested that the difference in the temperature leading to a runaway glaciation was the reason for the high estimates of $p\mathrm{CO_2}$ by RCMs.

To better understand why RCMs are not able to calculate the threshold temperature allowing the onset of runaway glaciations, we implemented an albedo dependency on temperature in the RCM developed by MacKay and Khalil (1991). It should be noted that Wang and Stone (1980) incorporated this process, but for unknown reasons, all RCM experiments kept a surface albedo held constant. This lack had biased the climate response and the Earth was maintained unfrozen for unrealistic reasons. To represent the ice-albedo feedback, we used the formula given by Pierrehumbert et al. (2011) where the Earth albedo is assumed to be

- Ice-free for $T > T_0 = 20$ °C, with an albedo (α_o) = 0.2
- Totally ice covered for $T < T_\mathrm{freeze}$, with an albedo (α_freeze) = 0.6

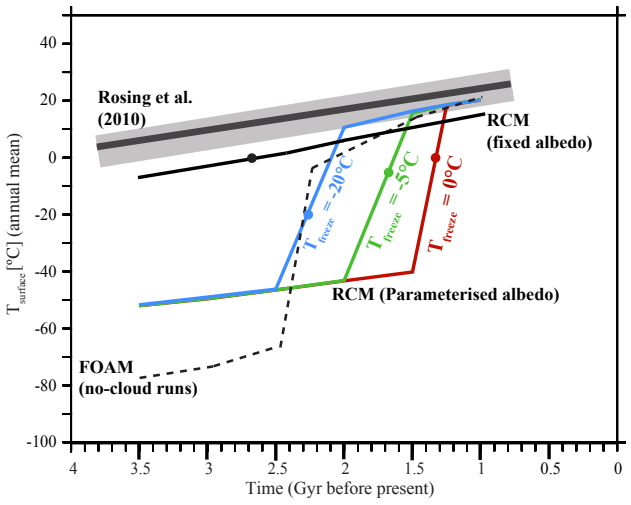

Fig. 7. RCM simulations showing the evolution of the surface temperature versus time between 3.5 and 1 Ga, with and without the ice-albedo feedback, and assuming increasing irradiance in the absence of clouds and a greenhouse radiative forcing of 19 W m^{-2}. Blue, green and red curves were obtained using the ice-albedo feedback formula from Pierrehumbert et al. (2011) where T_{freeze} values (−20 °C, −5 °C, 0 °C) represent the freezing temperature for the Earth (snowball Earth threshold). The black curve is obtained using a surface albedo fixed at 0.264 (absence of ice-albedo feedback). Rosing et al. (2010) and FOAM runs are described in Fig. 3.

– Partially ice covered for $T_{\text{freeze}} < T < T_0$, the albedo is interpolated according to the formula:

$$\alpha(T) = \alpha_{\text{o}} + (\alpha_{\text{freeze}} - \alpha_{\text{o}})[(T - T_0)^2/(T_{\text{freeze}} - T_0)^2] \quad (9)$$

where T is the Earth's temperature and T_{freeze} is the threshold temperature for the onset on global glaciations. The difference between T_{freeze} and T_0 is a measure of the meridional temperature gradient and therefore represents the efficiency of latitudinal heat transport. Because Wolf and Toon (2013) proposed that the freezing temperature is the main factor explaining differences between RCMs and AGCMs, we tested several T_{freeze} values (−20 °C, −5 °C, 0 °C). To avoid the difficulty of figuring out how to represent cloud changes between FOAM and RCM we removed clouds, so that the albedo corresponds to the planetary albedo incorporating the effects of Rayleigh scattering, atmospheric solar absorption and the reflective properties of the surface.

The RCM and FOAM are forced with the same boundary conditions, that is a net radiative forcing of +19 W m^{-2} and no clouds. In the absence of the ice-albedo feedback ($\alpha = 0.264$), the RCM simulates a linear increase in the mean temperature through time, the threshold value of 0 °C (supposed to represent the threshold temperature for runaway glaciations) being reached at about 2.6 Ga (Fig. 7). In contrast, RCM experiments that include the ice-albedo feedback show a drastic shift in the evolution of the mean temperature through time, similar to the one observed in FOAM experiments. More interestingly, when the ice-albedo feedback is parameterised such as the threshold temperature for the onset of snowball Earth (T_{freeze}) equals −20 °C, the timing of the shift from snowball Earth to ice-free conditions is similar in RCM and FOAM experiments. This similarity occurs because RCM mimics the latitudinal air surface temperature gradient of FOAM ($\Delta T = 40$ °C from equator to 45° of latitudes – sea ice latitudes). This calculation illustrates an essential weakness of RCM: their inability to calculate T_{freeze} in the absence of latitudinal heat transport. In AGCMs, T_{freeze} varies with the prescribed boundary conditions (for example in FOAM, the maximum latitudinal extent of the ice cap before the shift to runaway glaciation varies from 30° to 45° and 70° for experiments using modern clouds, cloud-free, and large-droplet clouds, respectively). This extent is controlled by the change in ocean heat flux, a process which cannot be captured by RCMs. Faster rotation and saltier oceans also slightly affect T_{freeze}. Consequently, AGCMs, in contrast to RCMs, more faithfully represent the ice-albedo feedback and hence the climatic transition towards snowball Earth.

5.3 Pan-glaciation thresholds and ice-albedo feedback: FOAM versus other AGCMs

The recent use of atmospheric GCMs for investigating the FYSP offered a great opportunity to compare FOAM with CAM3 (Wolf and Toon, 2013) LMDz (Charney et al., 2013) and EMAC (Kunze et al., 2014). All these studies suggested that Earth is less prone to full glaciations. Using a 2.7 Ga-old solar constant of 1093 W m^{-2} and 1 mbar of CO_2 and CH_4 (other parameters being held at present-day values), CAM3 simulates a mean surface temperature close to 2 °C (Wolf and Toon, 2013). For the same conditions, FOAM yields a full glaciation. A small difference in ice albedo of 0.68(vis)/0.3 (nearIR) with CAM3 and 0.7(vis)/0.5(nearIR) with FOAM seems to explain the different behaviour. Although minor, this difference has important consequences on the impact of the ice-albedo feedback when Earth becomes ice-covered (ice line spreads down to 30–40°; run 7 of Table 2). Using a 3 Ga-old solar constant (1082 W m^{-2}) and 0.9 mbar of CO_2, LMDz does not simulate a full glaciation (Charney et al., 2013). This behaviour arises from both the prescribed boundary conditions and heat transport. Charney et al. (2013) made the hypothesis that Earth was an aquaplanet at 3 Ga. In such conditions, LMDz simulates larger amount of water vapour, which enhances heat transport to high latitudes and decreases the equator-pole temperature gradient, so that the ice-albedo feedback becomes less efficient and the runaway glaciation is delayed. This result is in good agreement with the result of Kunze et al. (2014) who also assumed a water-covered world for the early Archaean (3.5 Ga, solar constant 1046 W m^{-2}). Using EMAC, they showed that it was possible to get a stable ice-free ocean at low latitudes (surface temperature equals to −9 °C) with moderate CO_2 concentrations (3670 ppmv).

For comparison, LMDz prevents the early Earth (3.8 Ga, 1025 $W m^{-2}$) from completely freezing with a greenhouse forcing corresponding to 0.9 mbar of a CO_2 combined to 0.9 mbar of CH_4 (Charney et al., 2013).

LMDz simulations also investigated the effect of CCN. Performing simulations with larger droplets (droplet radius set to 17 instead of 20 µm in our study), Charney et al. (2013) suggested a strong impact on the terrestrial radiative budget, in agreement with this study. More interestingly, both AGCMs simulate an increase in the cloud water path in low-altitude clouds located at high latitudes. Since the use of these two different cloud schemes shows similar behaviour, we suspect that the warming driven by high-latitude clouds inhibiting sea ice formation is not model dependent (see Sect. 3.4).

Other processes such as pressure broadening of CO_2 and H_2O by high atmospheric pressure (Goldblatt et al., 2009) or high concentrations of H_2 (Wordsworth and Pierrehumbert, 2013), which are not treated here, could also warm up the early Earth and affect the FYSP solutions. In addition, several processes are missing in this study, which are potential sources of uncertainties. The use of a slab ocean, with heat transport parameterised through diffusion, precludes the faithful representation of the meridional ocean heat transport. Indeed, during the Archaean the oceanic heat transport should supposedly be enhanced due to the smaller land fraction (Endal and Schatten, 1982). We also acknowledge that saltier oceans possibly lead to a weaker overturning (Williams et al., 2010). These conflicting assessments concerning ocean circulation, and their respective influence on the FYSP, could be explored using a fully coupled dynamic ocean model, an investigation which has not been conducted here. The last limitation relative to the use of a slab ocean is the absence of sea ice dynamics, which tends to slow the sea ice flow (Voigt and Abbot, 2012). This lack may change the radiative deficit triggering the onset of pan-glaciation and underestimate the greenhouse gas concentrations required to keep the early Earth unfrozen.

Obviously atmospheric GCMs still have limitations (Hack, 1998; Abbot et al., 2012; Stevens and Bony, 2013) and results can slightly differ according to their respective parameterisations or boundary conditions. However, as fully dynamic models, AGCMs represent a powerful tool for improving our understanding of deep past Earth climates, capturing cloud mechanisms involved in global warming, as well as time-dependent factors (e.g. palaeogeography, rotation rate). However, constraints on paleo-pCO_2 gained from climate modelling studies cannot be directly compared to geological data because all these studies omit to consider the carbon cycle-climate equilibrium. To estimate more accurately pCO_2 and the Earth's surface temperature evolution, we associated the atmospheric GCM simulations discussed in this paper with a geochemical model to investigate the carbon cycle climate during the Archaean (see companion paper).

6 Conclusions

FOAM, like other AGCMs, suggests a faint young Sun problem less problematic than initially assumed and solves the FYSP with a composition of greenhouse gases one order a magnitude lower than RCM or EMIC. Accounting for a 23 % weaker Sun at 3.5 Ga, we show that a moderate radiative forcing of 41 $W m^{-2}$ is sufficient to maintain the mean global surface temperature close to its present-day value. Assuming a high pCH_4 in the Archaean atmosphere (Pavlov et al., 2000; Catling et al., 2007), we show that such a moderate radiative forcing can be provided by the combination of 1 (0.3) mbar of methane and 11.5 (16) mbar of carbon dioxide. The presence of large-droplet clouds can theoretically provide significant warming so that lower CO_2 and CH_4 partial pressures are required for the maintenance of an ice-free surface. We demonstrated, however, that such changes in cloud properties cannot alone provide sufficient warming to solve the FYSP with low (0.9 mbar) pCO_2 as defended by Rosing et al. (2010).

This study highlights the central role of AGCMs over RCMs in investigating glacial thresholds. RCMs overestimate the early Archaean pCO_2 (i.e. 0.2–0.3 bar) required to keep equatorial waterbelts ice free due to their inability to calculate the correct threshold mean temperature for the onset of full glaciation (i.e. T_{freeze}). Applying Archaean boundary conditions, our AGCM simulations show a wide range of possible values for T_{freeze}, from −20 to 13 °C, according to the latitudinal temperature gradient. In contrast, RCMs use a fixed T_{freeze} value (0 °C, the freezing point of seawater) and therefore inaccurately estimate the poleward heat transport. The weak sensitivity of CLIMBER to CO_2 could be explained by its lapse rate calculation, which overestimates the energy leaving the Earth as infrared radiation. Our AGCM supports the main conclusions arising from previous AGCMs, but predicts an early Earth more inclined to full glaciation. Higher ice albedo is a likely cause for the stronger ice-albedo feedback in FOAM compared to CAM3. LMDz and EMAC simulate warmer climate due to a weaker ice-albedo feedback inherited from the absence of continents, a boundary condition that enhances poleward moist heat fluxes. However, all these studies cannot simulate ocean and sea ice dynamics, a limitation which may underestimate the greenhouse gas concentrations required to keep the early Earth unfrozen. Following this step forward in the understanding of physical processes able to solve the FYSP, we now consider carbon cycle–climate interplays to provide a complete picture of the faint young Sun problem (companion paper).

Acknowledgements. We thank the two anonymous referees for their very insightful reviews which considerably improved the quality of the manuscript, and the editorial board for the quality of the review procedure. This work was granted access to the HPC resources of CCRT under allocation 2014-017013 made

by GENCI (Grand Equipement National de Calcul Intensif). This work was supported by ANR eLIFE2 and LabexUnivEarth (ANR-10-LABX-0023 and ANR-11-IDEX-0005-02). This is IPGP contribution 3494.

Edited by: M. Claussen

The publication of this article is financed by CNRS-INSU.

References

Abbot, D. S., Voigt, A., Branson, M., Pierrehumbert, R. T., Pollard, D., Le Hir, G., and Koll, D. D. B.: Clouds and snowball Earth deglaciation, Geophys. Res. Lett., 39, L20711, doi:10.1029/2012GL052861, 2012.

Andreae, M. O. and Rosenfeld, D.: Aerosol–cloud–precipitation interactions. Part 1. The nature and sources of cloud-active aerosols, Earth-Sci. Rev., 89, 13–41, doi:10.1016/j.earscirev.2008.03.001, 2008.

Boucher, O., Le Treut, H., and Baker, M. B.: Precipitation and radiation modeling in a general circulation model: Introduction of cloud microphysical processes, J. Geophys. Res., 100, 16395–16414, doi:10.1029/95JD01382, 1995.

Bréon, F. M., Tanré, D., and Generoso, S.: Aerosol Effect on Cloud Droplet Size Monitored from Satellite, Science, 295, 834–838, doi:10.1126/science.1066434, 2002.

Catling, D. C., Claire, M. W., and Zahnle, K. J.: Anaerobic methanotrophy and the rise of atmospheric oxygen, Phil. Trans. R. Soc., 365, 1867–1888, doi:10.1098/rsta.2007.2047, 2007.

Charlson, R. J., Lovelock, J. E., Andreae, M. O., and Warren, S. G.: Oceanic Phytoplankton, atmospheric sulfur, cloud albedo and climate, Nature, 326, 655–661, 1987.

Charney, B., Forget, F., Wordworth, R., Leconte, J., Millour, E., Codron, F., and Spiga, A.: Exploring the faint young Sun problem and the possible climates of the Archean Earth with a 3-D GCM, J. Geophys. Res., 118, 10414–10431, doi:10.1002/jgrd.50808, 2013.

Dauphas, N. and Kasting, J. F.: Low pCO_2 in the pore water, not in the Archean air, Nature, 474, E2–E3, doi:10.1038/nature09960, 2011.

Driese, S. G., Jirsa, M. A., Ren, M., Brantley, S. L., Sheldon, N. D., Parker, D., and Schmitz, M.: Neoarchean paleoweathering of tonalite and metabasalt: implicationsq for reconstructions of 2.69 Ga early terrestrial ecosystems and paleoatmospheric chemistry, Precambrian Res., 187, 1–17, doi:10.1016/j.precamres.2011.04.003, 2011.

Farquhar, J., Airieau, S., and Thiemens, M. H.: Observation of wavelength-sensitive mass-independent sulfur isotope effects during SO_2 photolysis: Implications for the early atmosphere, J. Geophy. Res.-Planets, 106, 32829–32839, 2001.

Feulner, G.: The faint young sun problem, Rev. Geophys., 50, RG2006, doi:10.1029/2011RG000375, 2012.

Foriel, J., Philippot, P., Rey, P., Somogyi, A., Banks, D., and Menez, B.: Biological control of Cl/Br and low sulfate concentration in a 3.5-Gyr-old seawater from North Pole, Western Australia, Earth Planet. Sci. Lett., 228, 451–463, 2004.

Godderis, Y. and Veizer, J.: Tectonic control of chemical and isotopic composition of ancient oceans: the impact of continental growth, Am. J. Sci., 300, 434–461, 2000.

Goldblatt, C. and Zahnle, K. J.: Faint Young Sun Paradox remains, Nature, 474, E1, doi:10.1038/nature09961, 2011a.

Goldblatt, C. and Zahnle, K. J.: Clouds and the Faint Young Sun Paradox, Clim. Past, 7, 203–220, doi:10.5194/cp-7-203-2011, 2011b.

Goldblatt, C., Claire, M. W., Lenton, T. M., Matthews, A. J., Watson. A. J., and Zahnle, K. J.: Nitrogen-enhanced greenhouse warming on early Earth, Nat. Geosci., 2, 891–896, doi:10.1038/NGEO692, 2009.

Gough, D. O.: Solar interior structure and luminosity variations, Sol. Phys., 74, 21–34, 1981.

Hack, J. J.: Sensitivity of the simulated climate to a diagnostic formulation for cloud liquid water, J. Climate, 11, 1497–1515, 1998.

Halevy, I., Pierrehumbert, R. T., and Schrag, D. P.: Radiative transfer in CO_2-rich paleoatmospheres, J. Geophys. Res., 114, D18112, doi:10.1029/2009JD011915, 2009.

Hansen, J., Sato, M., and Ruedy, R.: Radiative Forcing and climate response, J. Geophys. Res., 102, 6831–6864, 1997.

Haqq-Misra, J. D., Domagal-Goldman, S. D., Kasting, P. J., and Kasting, J. F.: A revised, hazy methane greenhouse for the archean Earth, Astrobiology, 8, 1127–1137, 2008.

Jacob, R.: Low frequency variability in a simulated atmosphere ocean system, PhD Thesis, University of Wisconsin-Madison, 1997–310, 1997.

Jenkins, G. S.: The effects of reduced land fraction and solar forcing on the general circulation results from the NCAR CCM, Glob. Planet. Change, 7, 321–333, 1993a.

Jenkins, G. S.: A General Circulation Model Study of the Effects of Faster Rotation Rate, Enhanced CO_2 Concentration, and Reduced Solar Forcing' Implications for the Faint Young Sun Paradox, J. Geophys. Res., 98, 20803–20811, 1993b.

Jenkins, G. S., Marshall, H. G., and Kuhn, W. R.: Precambrian climate – the effects of land area and Earth's rotation rate, J. Geophys. Res.-Atmos., 98, 8785–8791, doi:10.1029/93JD00033, 1993.

Kasting, J. F.: The evolution of the prebiotic atmosphere, Origins Life Evol. B., 14, 75–82, 1984.

Kasting, J. F.: Theoretical constraints on oxygen and carbon-dioxide concentrations in the Pre-cambrian atmosphere, Precambrian Res., 34, 205–229, 1987.

Kasting, J. F.: Early Earth faint young sun redux, Nature, 464, 687–689, 2010.

Kiehl, J. T. and Dickinson, R. E.: A study of the radiative effects of enhanced atmospheric CO_2 and CH_4 on early Earth surface temperatures, J. Geophys. Res.-Atmos., 92, 2991–2998, 1987.

Kienert, H., Feulner, G., and Petoukhov, V.: Faint young sun problem more severe due to ice-albedo feedback and higher rotation rate of the early Earth, Geophys. Res. Lett., 39, L23710, doi:10.1029/2012GL054381, 2012.

Kienert, H., Feulner, G., and Petoukhov, V.: Albedo and heat transport in 3-D model simulations of the early Archean climate, Clim. Past, 9, 1841–1862, doi:10.5194/cp-9-1841-2013, 2013.

Knauth, L. P.: Temperature and salinity history of the Precambrian ocean: implications for the course of microbial evolution, Palaeogeogr. Palaeocl., 219, 53–69, 2005.

Kump, L. R. and Pollard, D.: Amplification of cretaceous warmth by biological cloud feedbacks, Science, 320, 195–195, 2008.

Kunze, M., Godolt, M., Langematz, U., Grenfell, J. L., Hamann-Reinus, A., and Rauer, H.: Investigating the early Earth faint young Sun problem with a general circulation model, Planet. Space Sci., doi:10.1016/j.pss.2013.09.011, in press, 2014.

Le Hir, G., Donnadieu, Y., Krinner, G., and Ramstein, G.: Toward the snowball earth deglaciation, Clim. Dynam., 35, 285–297, 2010.

Lowe, D. R. and Tice, M. M.: Tectonic controls on atmospheric, climatic, and biological evolution 3.5–2.5 Ga, Precambrian Res., 158, 177–197, 2007.

MacKay, R. M. and Khalil, M. A. K.: Theory and Development of a One Dimensional Time Dependant Radiative Convective Climate Model, Chemosphere, 22, 383–417, 1991.

Millero, F. J. and Poisson, A.: International one-atmosphere equation of state of seawater, Deep-Sea Res. Pt. I, 28, 625–629, 1981.

Pavlov, A. A., Kasting, J. F., Brown, L. L., Rages, K. A., and Freedman, R.: Greenhouse warming by CH_4 in the atmosphere of early Earth, J. Geophys. Res.-Planets, 105, 11981–11990, 2000.

Penner, J. E., Quaas, J., Storelvmo, T., Takemura, T., Boucher, O., Guo, H., Kirkevåg, A., Kristjánsson, J. E., and Seland, Ø.: Model intercomparison of indirect aerosol effects, Atmos. Chem. Phys., 6, 3391–3405, doi:10.5194/acp-6-3391-2006, 2006.

Petoukhov, V., Ganopolski, A., Brovkin, V., Claussen, M., Eliseev, A., Kubatzki, C., and Rahmstorf, S.: CLIMBER-2: a climate system model of intermediate complexity. Part I: model description and performance for present climate, Clim. Dynam. 16, 1–17, doi:10.1007/PL00007919, 2000.

Pesonen, L. J., Elming, S. A, Mertanen, S., Pisarevsky, S., D'Agrella-Filho, M. S., Meert, J. G., Schmidt, P. W., Abrahamsen, N., and Bylund, G.: Palaeomagnetic configuration of continents during the Proterozoic, Tectonophysics, 375, 289–324, 2003.

Pierrehumbert, R. T.: High levels of atmospheric carbon dioxide necessary for the termination of global glaciation, Nature, 429, 646–649, 2004.

Pierrehumbert, R. T.: Principles of Planetary Climate, Cambridge University Press, 652 pp., 2010.

Pierrehumbert, R. T., Abbot, D. S., Voigt., A., and Koll, D.: Climate of the Neoproterozoic Annual, Rev. Earth Planet. Sci., 39, 417–460, doi:10.1146/annurev-earth-040809-152447, 2011.

Reinhard, C. T. and Planavsky, N. J.: Mineralogical constraints on Precambrian pCO_2, Nature, 474, E1–E2, doi:10.1038/nature09959, 2011.

Rosing, M. T., Bird, D. K., Sleep, N. H., and Bjerrum, C. J.: No climate paradox under the faint early Sun, Nature, 464, 744–747, doi:10.1038/nature08955, 2010.

Rye, R., Kuo, P. H., and Holland, H. D.: Atmospheric carbon-dioxide concentrations before 2.2-billion years ago, Nature, 378, 603–605, 1995.

Sagan, C. and Mullen, G.: Earth and Mars – evolution of atmospheres and surface tempera-tures, Science, 177, 52–56, doi:10.1126/science.177.4043.52, 1972.

Schatten, K. H. and Endal, A. S.: The faint young Sun climate paradox – volcanic influence, Geophys. Res. Lett., 9, 1309–1311, doi:10.1029/GL009i012p01309, 1982.

Sheldon, N. D.: Precambrian paleosols and atmospheric CO_2 levels, Precambrian Res., 147, 148–155, 2006.

Slingo, A.: A GCM parameterization for the shortwave radiative properties of water clouds, J. Atmos. Sci., 46, 1419–1427, 1989.

Stevens, B. and Bony, S.: What Are Climate Models Missing?, Science, 340, 1053–1054, doi:10.1126/science.1237554, 2013.

Voigt, A. and Abbot, D. S.: Sea-ice dynamics strongly promote Snowball Earth initiation and destabilize tropical sea-ice margins, Clim. Past, 8, 2079–2092, doi:10.5194/cp-8-2079-2012, 2012.

von Paris, P., Rauer, H., Grenfell, J. L., Patzer, B., Hedelt, P., Stracke, B., Trautmann, T., and Schreier, F.: Warming the early earth-CO_2 reconsidered, Planet. Space Sci., 56, 1244–1259 doi:10.1016/j.pss.2008.04.008, 2008.

Walker, J. C. G.: Climatic factors on the Archean Earth, Palaeogr. Palaeocl., 40, 1–11, doi:10.1016/0031-0182(82)90082-7, 1982.

Walker, J. C. G. and Zahnle, K. J. Lunar nodal tide and distance to the Moon during the Pre-cambrian, Nature, 320, 600–602, 1986.

Walker, J. C. G., Hays, P. B., and Kasting, J. F.: A Negative Feedback Mechanism For The Long-Term Stabilization of Earth's Surface-Temperature, J. Geophys. Res.-Ocean. Atmos., 86, 9776–9782, 1981.

Wang, W. and Stone, P. H.: Effect of Ice-Albedo Feedback on Global Sensitivity in a One-Dimensional Radiative-Convective Climate Model, J. Atmophs. Sci., 37, 545–552, 1980.

Warren, S. G., Brandt, R. E., Grenfell, T. C., and McKay, C. P.: Snowball Earth: Ice thickness on the tropical ocean, J. Geophys. Res.-Ocean., 107, 31-1–31-18, doi:10.1029/2001JC001123, 2002.

Williams, P. D., Guilyardi, E., Madec, G., Gualdi, S., and Scoccimarro, E.: The role of mean ocean salinity in climate, Dynam. Atmos. Oceans, 49, 108–123, doi:10.1016/j.dynatmoce.2009.02.001, 2010.

Wolf, E. T. and Toon, O. B.: Hospitable Archean Climates Simulated by a General Circulation Model, Astrobiology, 13, 656–673, doi:10.1089/ast.2012.0936, 2013.

Wordsworth, R. and Pierrehumbert, R.: Hydrogen-nitrogen greenhouse warming in Earth's early atmosphere, Science, 339, 64–67, doi:10.1126/science.1225759, 2013.

Appendix A

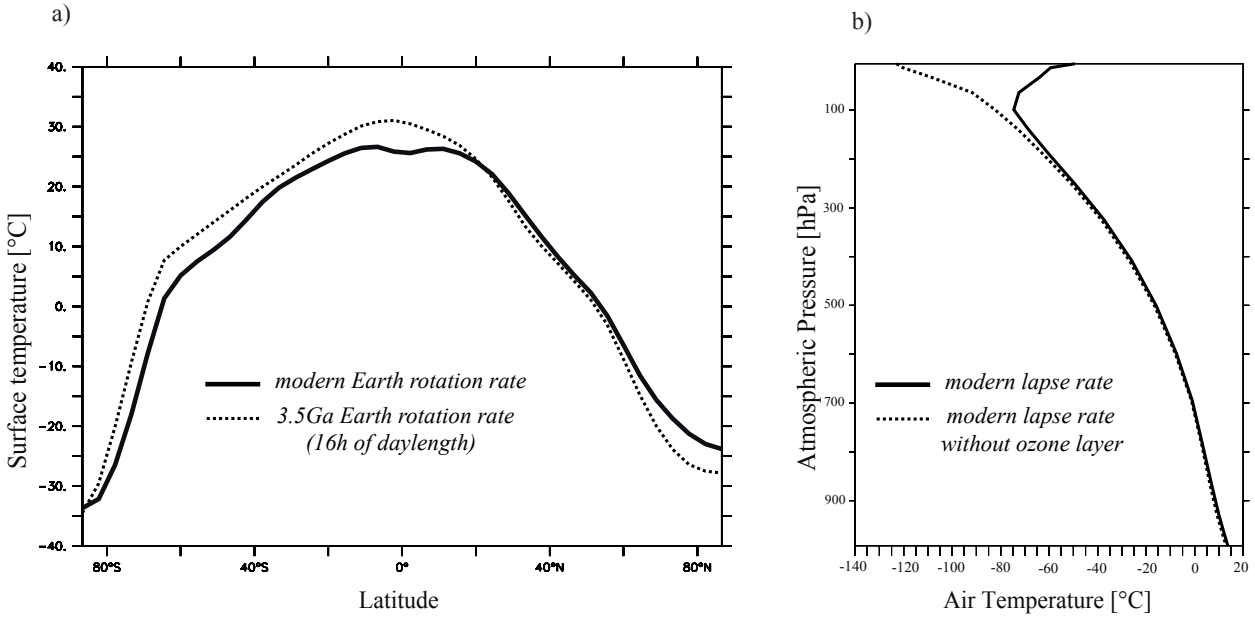

Fig. A1. (a) Temperature gradient as a function of Earth rotation rates. **(b)** Atmospheric lapse rate as a function of ozone layer presence/removal. Simulations performed under present-day boundary conditions.

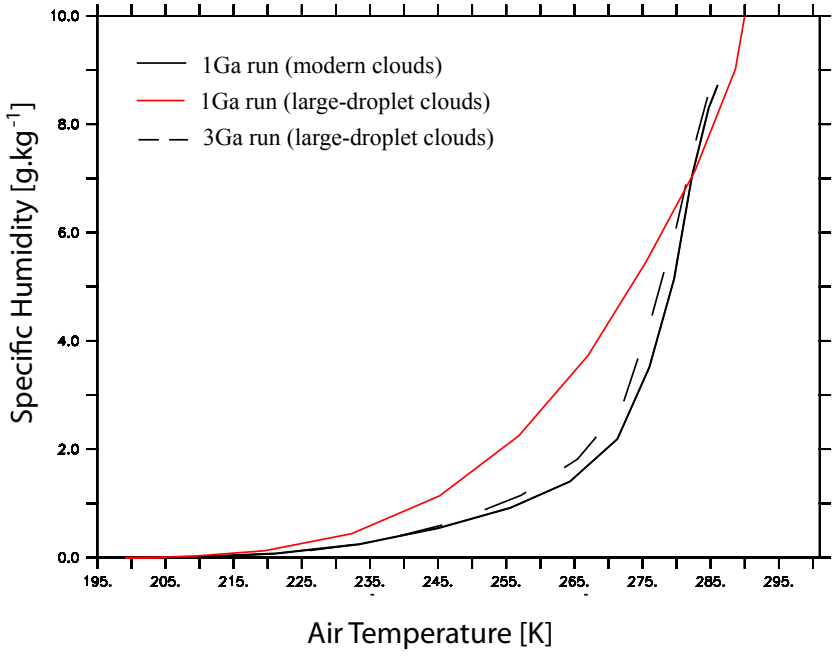

Fig. A2. Specific humidity response to varying air temperature. The Earth's global temperature equals 12.9 °C (1 Ga, modern clouds), 30.4 °C (1 Ga, large-droplet clouds) and 12.3 °C (1 Ga, large-droplet clouds).

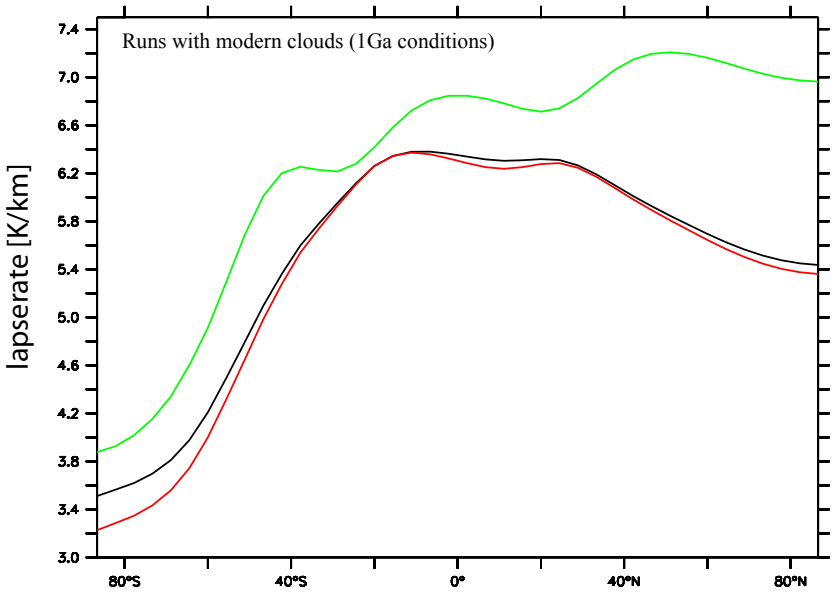

Fig. A3. Lapse rates (annual mean) using 1 Ga boundary conditions (modern clouds parameterization), calculated by the CLIMBER lapse rate formula and FOAM using the same conditions. Black curve represents the standard formulation in CLIMBER (Petoukhov et al., 2000), the red line is the calculation adapted for a faster rotation in CLIMBER (Kienert et al., 2012, 2013). The green line represents the FOAM lapse rate.

Clim. Past, 10, 2053–2066, 2014
www.clim-past.net/10/2053/2014/
doi:10.5194/cp-10-2053-2014

Climate of the Past
Open Access

Effect of the Ordovician paleogeography on the (in)stability of the climate

A. Pohl[1], Y. Donnadieu[1], G. Le Hir[2], J.-F. Buoncristiani[3], and E. Vennin[3]

[1]LSCE – Laboratoire des Sciences du Climat et de l'Environnement, UMR8212 – CNRS-CEA-UVSQ, CEA Saclay, Orme des Merisiers, 91191 Gif-sur-Yvette Cedex, France
[2]IPGP – Institut de Physique du Globe de Paris, Université Paris7-Denis Diderot, 1 rue Jussieu, 75005 Paris, France
[3]Laboratoire Biogéosciences, UMR/CNRS 6282, Université de Bourgogne, 6 Bd Gabriel, 21000 Dijon, France

Correspondence to: A. Pohl (alexandre.pohl@lsce.ipsl.fr)

Received: 23 May 2014 – Published in Clim. Past Discuss.: 2 July 2014
Revised: 8 October 2014 – Accepted: 14 October 2014 – Published: 26 November 2014

Abstract. The Ordovician Period (485–443 Ma) is characterized by abundant evidence for continental-sized ice sheets. Modeling studies published so far require a sharp CO_2 drawdown to initiate this glaciation. They mostly used non-dynamic slab mixed-layer ocean models. Here, we use a general circulation model with coupled components for ocean, atmosphere, and sea ice to examine the response of Ordovician climate to changes in CO_2 and paleogeography. We conduct experiments for a wide range of CO_2 (from 16 to 2 times the preindustrial atmospheric CO_2 level (PAL)) and for two continental configurations (at 470 and at 450 Ma) mimicking the Middle and the Late Ordovician conditions. We find that the temperature-CO_2 relationship is highly non-linear when ocean dynamics are taken into account. Two climatic modes are simulated as radiative forcing decreases. For high CO_2 concentrations ($\geq$ 12 PAL at 470 Ma and $\geq$ 8 PAL at 450 Ma), a relative hot climate with no sea ice characterizes the warm mode. When CO_2 is decreased to 8 PAL and 6 PAL at 470 and 450 Ma, a tipping point is crossed and climate abruptly enters a runaway icehouse leading to a cold mode marked by the extension of the sea ice cover down to the mid-latitudes. At 450 Ma, the transition from the warm to the cold mode is reached for a decrease in atmospheric CO_2 from 8 to 6 PAL and induces a $\sim 9\,^{\circ}C$ global cooling. We show that the tipping point is due to the existence of a 95 % oceanic Northern Hemisphere, which in turn induces a minimum in oceanic heat transport located around 40° N. The latter allows sea ice to stabilize at these latitudes, explaining the potential existence of the warm and of the cold climatic modes. This major climatic instability potentially brings a new explanation to the sudden Late Ordovician Hirnantian glacial pulse that does not require any large CO_2 drawdown.

1 Introduction

The Ordovician Period (485–443 Ma) is characterized by fundamental changes in the living organisms of our planet. Following the Cambrian explosion, the Early Ordovician is characterized by a major radiation in marine life and critical changes in paleoecology during the Great Ordovician Biodiversification Event (GOBE) through the rise of the Paleozoic evolutionary fauna (Servais et al., 2010). This time of marine diversification is yet interrupted by the second of the five biggest extinctions of the Phanerozoic Eon in terms of the percentage of genera and families lost (Sheehan, 2001). Trotter et al. (2008) proposed a critical role of the oceanic thermal state during the GOBE, showing that the long-term cooling from a very warm ocean to present-day-like temperatures during the Early to Middle Ordovician may have led to optimal conditions for widespread taxonomic radiations and the appearance of complex communities. Cooler conditions in the Late Ordovician are generally associated with the onset of large ice sheets over the southern Gondwana (e.g., Ghienne et al., 2007). The growth and the reduction of these ice sheets are concomitant with the two pulses of the global extinction (Sheehan, 2001). Thus, a very close binding relationship may have existed between global climate and organismal evolution during the Ordovician.

Atmospheric CO_2 concentration largely constrained climate evolution over the history of the Earth (Berner, 2006). The Ordovician glaciation stands out from the crowd since it occurred under high CO_2 values. Climate proxies (Yapp and Poths, 1992) and continental weathering models (Berner, 2006; Nardin et al., 2011) indicate that the Ordovician CO_2 atmospheric partial pressure (pCO_2) was equal to some 8–20 times its preindustrial atmospheric level (1 PAL = 280 ppm). Fainter Sun (Gough, 1981) somewhat reduces this apparent discrepancy between high CO_2 levels and glacial inception by suggesting that the solar constant was lower in the past. Nevertheless, it seems insufficient; the best hypotheses today consider a Late Ordovician drop in CO_2 to be the trigger of glaciation (Brenchley et al., 1994; Kump et al., 1999; Villas et al., 2002; Lenton et al., 2012). A glacial threshold of 14 to 8 PAL has been found with various models, from a conceptual energy balance model (EBM) (Crowley and Baum, 1991) to a more complex general circulation model (GCM) coupled to an ice-sheet model (Herrmann et al., 2003). Various data suggest that the lower CO_2 levels are probably the best estimates (Vandenbroucke et al., 2010; Pancost et al., 2013).

While the role of the pCO_2 has been fully investigated to explain the Ordovician glacial onset, much less has been done about the effect of ocean dynamics. Most of the modeling studies used atmospheric GCMs with slab mixed-layer oceans (Crowley et al., 1993; Crowley and Baum, 1995; Gibbs et al., 1997; Herrmann et al., 2003, 2004b). In these models, there are no currents and the poleward oceanic heat transport (OHT) is prescribed through a diffusion coefficient. Ocean dynamics are thus totally absent. Herrmann et al. (2004b) gave a precursory approach of this question by varying the diffusion coefficient in the slab model GENESIS. They found that the paleogeographical evolution and a drop in CO_2 were only preconditioning factors that were not sufficient to trigger continental glaciation during the Hirnantian. Additional changes, such as a sea level drop or a lowered OHT, were necessary to cause glaciation within a reasonable CO_2 interval (8–18 PAL). These results suggest that the ocean played a fundamental role in the Late Ordovician. But, as Herrmann et al. (2004a) noticed later, the non-dynamical ocean precluded any further investigation. Only two studies have so far investigated the role of ocean dynamics in the Late Ordovician climate changes. Poussart et al. (1999) coupled an energy/moisture balance model to an oceanic GCM and to a sea ice model. They demonstrated that the Ordovician geographical configuration may have led to critical changes in the OHT with an up to 42 % increase in the southern OHT compared to present-day and a highly asymmetric OHT relative to the equator. These results point out a major limitation inherent to the slab models that are unable to explicitly resolve the OHT, which value and pattern are often prescribed based on present-day estimates. Poussart et al. (1999) also demonstrated an important sensitivity of the oceanic overturning circulation to changes in the ice–snow albedo parameters, highlighting a strong coupling between atmospheric and oceanic components in the Ordovician climate. Herrmann et al. (2004a) forced an oceanic GCM with the GENESIS outputs from Herrmann et al. (2004b). They compared the results obtained for two Late Ordovician paleogeographical configurations. They noticed a significant impact of paleogeography on the oceanic overturning circulation and thus on the OHT. They moreover demonstrated a non-linear response of the OHT to the atmospheric forcing. Their uncoupled modeling procedure however did not allow for any feedback of ocean on global climate.

Here, we propose to extend previous studies by exploring the effects of changed radiative forcing due to CO_2 decrease on the Ordovician climate with the fully coupled ocean–atmosphere–sea ice GCM FOAM (Jacob, 1997) for two time intervals within the Middle and Late Ordovician. The climate model and the experimental setup are briefly described in Sect. 2. The modeling results are presented in Sect. 3. The main results are discussed in Sect. 4 and a conclusion is given in Sect. 5.

2 Model description and experimental setup

2.1 The coupled climate model FOAM

We used the Fast Ocean Atmosphere Model (FOAM) version 1.5, a 3-D GCM with coupled components for ocean, atmosphere, and sea ice (Jacob, 1997). The atmospheric module is a parallelized version of the National Center for Atmospheric Research's (NCAR) Community Climate Model 2 (CCM2) with the upgraded radiative and hydrologic physics from CCM3 version 3.2 (Kiehl et al., 1998). It was run at a R15 spectral resolution ($4.5° \times 7.5°$) with 18 vertical levels. The ocean module, the Ocean Model version 3 (OM3), is a 24-level z coordinate ocean GCM providing a $1.4° \times 2.8°$ resolution. The sea ice module uses the thermodynamic component of the CSM1.4 sea ice model, which is based on the Semtner 3-layer thermodynamic snow/ice model (Semtner, 1976). The coupled model, FOAM, is well designed for paleoclimate studies. It has no flux correction and its quick turnaround time allows for long millennium-scale integrations. FOAM has been widely used in paleoclimate studies (Poulsen and Jacob, 2004; Donnadieu et al., 2009; Zhang et al., 2010; Dera and Donnadieu, 2012; Lefebvre et al., 2012) including for the Ordovician (Nardin et al., 2011).

It is noteworthy that no land ice component was included. Correctly simulating deep-time ice sheets constitutes a whole study as such (see for example the review from Pollard, 2010) and it was therefore left for future work. Preliminary simulations conducted for the Late Ordovician (not shown here) however confirm that the climatic behavior demonstrated in this study persists in the presence of continental-sized ice sheets.

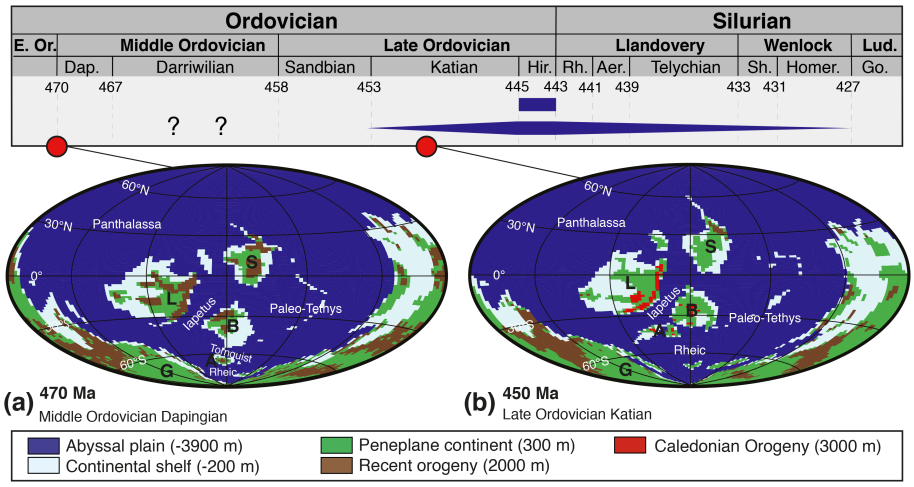

Figure 1. Continental configurations with the FOAM ocean grid based on the paleogeographical reconstructions from Blakey (2007), with the color code for the bathymetric and topographic categories used in this study. G: Gondwana, A: Avalonia, B: Baltica, L: Laurentia, S: Siberia. Ocean names are shown. Each time slice is replaced on the synthetic Ordovician glaciation chronology (inspired from Finnegan et al., 2011). Age limits are taken from the geological time scale v2014/02 (International Commission on Stratigraphy, 2014). Question marks are time intervals when hypothetical first ice sheets may have appeared according to Turner et al. (2012). Blue bars represent the two scenarios considered today for the duration of the Ordovician glaciation (see Sect. 2.2. for a full description).

2.2 Experimental setup

Spjeldnaes (1962), working on floro–faunal data, was the first to postulate a glaciation during the Ordovician. Since then, numerous studies widely documented the Ordovician glacial sedimentary record in North Africa (e.g., Beuf et al., 1971; Denis et al., 2007; Ghienne et al., 2007), South Africa (e.g., Young et al., 2004) and South America (e.g., Díaz-Martínez and Grahn, 2007). Dating these deposits remains highly difficult (e.g., Díaz-Martínez and Grahn, 2007) and geochemical methods bring conflicting results (see for example Trotter et al., 2008 and Finnegan et al., 2011). As a consequence, the duration of the glaciation is still not well constrained. Two models are still debated: a short-lived (< 2 Myr) glaciation limited to the Late Ordovician Hirnantian (445–443 Ma) (Brenchley et al., 1994, 2003; Sutcliffe et al., 2000), or a long-lived glaciation (> 20 Myr) that extended from the Late Ordovician Katian to the Silurian Wenlock, with the Hirnantian only representing the glacial maximum (Saltzman and Young, 2005; Loi et al., 2010; Finnegan et al., 2011) (Fig. 1). Some authors even propose a Darriwilian ice age based on eustatic cyclicities (Turner et al., 2012).

In this study, simulations were carried out for two paleogeographical configurations reconstructed by Blakey (2007), one for 470 Ma (Middle Ordovician Dapingian) and one for 450 Ma (Late Ordovician Katian) (Fig. 1). These two reconstructions have been chosen to be respectively representative of the following: (i) the pre-glacial interval; (ii) the undisputable Late Ordovician glacial interval. The 450 Ma reconstruction is considered here as a good estimate for the Late Ordovician Hirnantian (445 Ma). The paleogeographical changes are limited at that timescale and they are assumed to not critically impact global climate. Since previous studies have revealed the major role played by the topography to initiate glacial conditions during the Ordovician (Crowley and Baum, 1995), we defined five realistic topographic classes (Fig. 1). The ocean model bathymetry is a flat-bottom case. As Ordovician vegetation was limited to non-vascular plants (Steemans et al., 2009; Rubinstein et al., 2010) – the coverage of these can hardly be estimated – we imposed a bare soil (rocky desert) at every land grid point. No ice sheet was prescribed on the land. The solar luminosity was set 3.5 % below present according to the model of solar physics provided by Gough (1981), and we used the "cold summer orbital configuration" (CSO). The CSO is defined with an obliquity of 22.5°, an eccentricity of 0.05 and a longitude of perihelion of 270°. Because most explanatory hypotheses require a major pCO_2 fall to initiate glacial conditions in the Middle–Late Ordovician (Brenchley et al., 1994; Kump et al., 1999; Villas et al., 2002; Lenton et al., 2012), we finally used five pCO_2 values representative for presumed Ordovician conditions: 4, 6, 8, 12 and 16 PAL. A lower value, 2 PAL, was also tested in order to better understand the climatic behavior although this pCO_2 clearly stands beyond the lower bound of the pCO_2 range defined for the Ordovician Period. For each simulation, the model was run until deep ocean equilibrium was reached, which means 2000 years of integration except for the 450 Ma experiment with the pCO_2 set to 6 PAL that required 1000 years more.

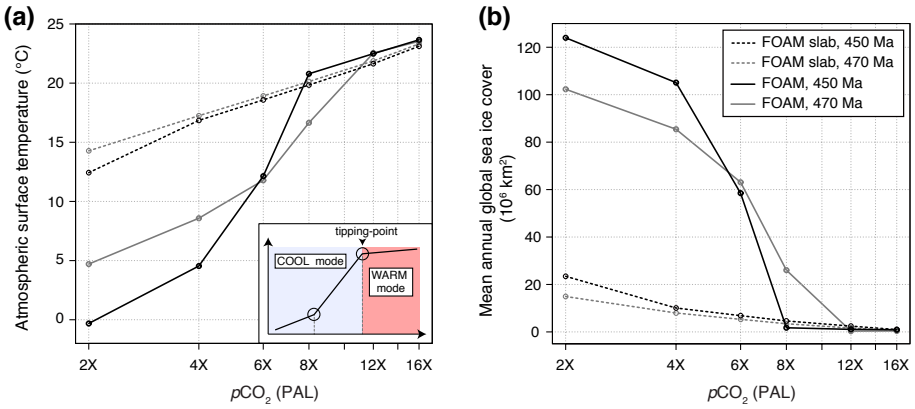

Figure 2. (a) Mean annual, globally averaged surface air temperature for various pCO_2 values from 2 to 16 PAL, with the slab-version of FOAM and with the fully coupled ocean–atmosphere–sea ice version of FOAM at 470 and at 450 Ma. The sketch illustrates the explanations provided in the main text. Note the logarithmic scale on the x axis. **(b)** Same plot as **(a)**, for the mean annual global sea ice cover expressed in M km^{-2}.

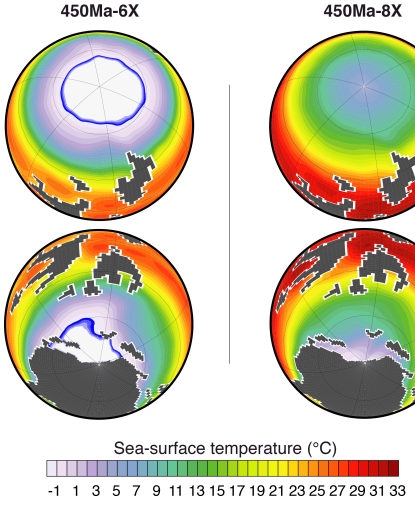

Figure 3. SST (color shading) and permanent sea ice cover (blue-white shading) simulated at 450 Ma with the fully coupled version of FOAM within the cold climatic mode (at 6 PAL) and within the warm climatic mode (at 8 PAL). The permanent sea ice cover is defined as the sum of all grid points whose at least 80 % of the surface is covered by sea ice during a year, allowing to discard temporary sea ice cover by icebergs or rapidly advancing and retreating ice fronts. The gray mask stands for continental masses.

3 Climate simulation results

3.1 Sensitivity to an atmospheric CO_2 decrease

Figure 2 presents the relationship between the global mean surface air temperature (SAT) and the pCO_2 for all the simulations discussed in this paper. For comparison with the previous studies undertaken with slab oceans (Crowley et al., 1993; Crowley and Baum, 1995; Gibbs et al., 1997; Herrmann et al., 2003, 2004b), we first ran FOAM with a 50 m deep mixed-layer slab ocean (black dashed lines in Fig. 2). All boundary conditions were kept the same as for the runs with the ocean–atmosphere GCM (see Sect. 2.2) and we followed the usual conventions by setting the diffusion coefficient so that total OHT reaches its present value. As expected from previous studies, the Late Ordovician (450 Ma) climate system is sensitive to a pCO_2 decrease and the temperature–CO_2 relationship is linear in a log-axis graph (Fig. 2a). The model sensitivity, 3 °C per halving of CO_2, lies very close to the value 2.5 °C obtained by Herrmann et al. (2003). It is however noteworthy that, for an identical atmospheric forcing value, climate is systematically warmer compared to GENESIS (Gibbs et al., 1997; Herrmann et al., 2004b). An immediate explanation lies in the prescribed solar constant. We chose a solar constant 3.5 % weaker than today following the parametric law from Gough (1981). Previous studies mostly used a 4.5 % depressed insolation compared to present-day (Crowley and Baum, 1995; Gibbs et al., 1997; Herrmann et al., 2003, 2004b), following the constant rate of decrease of 1 % every hundred million years proposed by Crowley and Baum (1992). Both values are within the range −3.5 to −5 % defined by Endal and Sofia (1981), but our weaker decrease of the solar constant logically results in higher temperatures. We must note that modeled absolute temperatures are also sensitive to ice albedo and cloud parameterizations and are thus highly model-dependent (see for example Braconnot et al., 2012). Proposing absolute climate estimates for the Ordovician remains highly challenging and lies far beyond the main purpose of our study. Aside that absolute temperature offset, FOAM produces a trend similar to results previously published when it is used as a slab.

Using the same (450 Ma) paleogeographical configuration, FOAM experiments with ocean dynamics lead to a much different climatic response to the CO_2 forcing. The temperature-CO_2 relationship is non-linear (Fig. 2a). Two

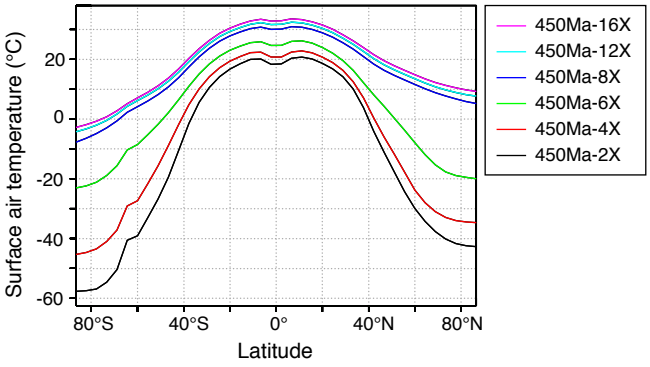

Figure 4. Mean annual, zonally averaged SAT simulated for each pCO_2 at 450 Ma with the fully coupled version of FOAM.

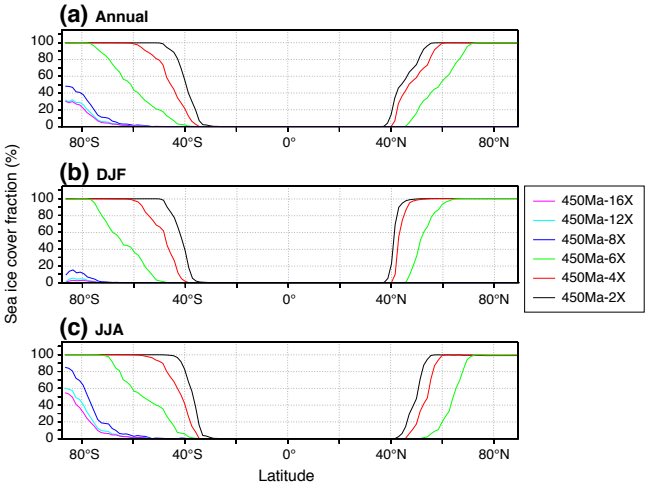

Figure 5. Zonally averaged sea ice cover fraction (expressed in percents) simulated for each pCO_2 at 450 Ma with the fully coupled version of FOAM. DJF: December, January and February. JJA: June, July and August.

climatic modes are simulated as forcing parameters slowly change.

– For high CO_2 concentrations (≥ 8 PAL), the warm mode is marked by a hot climate (Figs. 2a and 3) and no sea ice in the Northern Hemisphere (NH) (Figs. 2b and 3). The model sensitivity is similar to the one obtained with the slab (3 °C per halving of CO_2) and lies within the range 2.1–4.7 °C defined with various up-to-date GCMs for present-day simulations (IPCC, 2013). The temperature decrease associated to a CO_2 drop is almost evenly distributed at all latitudes (Fig. 4).

– When atmospheric forcing is decreased from 8 to 4 PAL, the annual global mean SAT falls by 8.65 °C from 8 to 6 PAL, and by 7.6 °C from 6 to 4 PAL. The Ordovician climate abruptly enters a cool climatic mode characterized by a fast extension of the sea ice cover (Figs. 2, 3 and 5). A tipping point is reached, a slight pCO_2 drop leading to a sharp cooling. The temperature decrease associated to a halving of CO_2 (from 8 to 4 PAL), −16 °C, lies far beyond the IPCC (2013) upper bound. The SAT drop is unevenly distributed against the latitudes. The minimum mean annual cooling is observed in the tropics (up to −5 °C from 8 to 6 PAL) whereas the maximum cooling (up to −27 °C from 8 to 6 PAL) occurs in both hemispheres at polar latitudes (Fig. 4). The amplification of the thermal response at high latitudes is due to the sea ice albedo positive feedback. The hemispheric sea ice cover (Table 1, Fig. 5b and c) suggests in particular a strong relationship between the NH sea ice extension and the global climate state. No ice is present in the NH within the warm mode (Fig. 3), and it is the expansion of the sea ice from the North Pole that marks the shift to the cold climatic mode. It is noteworthy here that the simulation of the sea ice in the model FOAM has been proven correct enough in the modern climate to be reasonably extended to paleoclimate studies. The reader is invited to refer to the study from Lefebvre et al. (2012, paragraph 14) for the whole analysis.

– From 4 to 2 PAL, the Earth's climate is still in cold mode but the SAT drop tends to slow down. Another threshold is crossed and the model sensitivity decreases back to a level characteristic of glacial climate (∼ 5 °C per CO_2 halving, see Berner and Kothavala, 2001). The climate change does not differ so much from the cooling occurring within the warm climatic mode between 16 and 8 PAL for a corresponding halving of CO_2, though glacial conditions still provide a higher global sensitivity (Kothavala et al., 1999) and an enhanced polar cooling. Sea ice continues to grow almost with the same intensity in the Southern Hemisphere (SH) but its spread is very limited in the NH (Table 1), where the sea ice edge stabilizes near 40° N (Fig. 5a).

The simulations were replicated for the 470 Ma continental configuration. A similar evolution is observed. With the slab model (Fig. 2), the temperature-CO_2 relationship is still linear in the log-axis graph. For the coupled runs (Fig. 2 and Table 1), two phases of stable climate are separated by a major climatic instability within the interval 12–6 PAL. The tipping point showing the shift from the warm to the cold climatic mode is reached this time between 12 and 8 PAL and is still associated to a sudden extension of the sea ice in the NH. Three main conclusions follow from theses results: (i) the climatic instability originates in ocean dynamics, as it is not observed with the slab, (ii) NH sea ice cover plays a critical role in the shift to the cold climatic mode, (iii) reaching the cold climatic mode requires a lower CO_2 level at 450 Ma than at 470 Ma.

Table 1. Overview of the coupled simulations. The name of each experiment includes the age of the paleogeography used in input followed by the pCO_2 expressed in PAL. These abbreviations are used throughout the manuscript. Slab runs are not shown.

Simulations	pCO_2 (ppm)	Surface air temperature (°C)	Global temperature of the Ocean (°C)	Mean annual global sea ice cover (10^6 km^2)	Mean annual Southern Hemisphere sea ice cover (10^6 km^2)	Mean annual Northern Hemisphere sea ice cover (10^6 km^2)
450 Ma-2X	560	−0.3	1.8	123.9	49.3	74.6
450 Ma-4X	1120	4.5	2.5	105.1	35.2	69.9
450 Ma-6X	1680	12.1	4.1	58.5	15.5	43.0
450 Ma-8X	2240	20.8	9.0	1.8	1.8	0.0
450 Ma-12X	3360	22.5	11.4	1.1	1.1	0.0
450 Ma-16X	4480	23.7	12.7	0.9	0.9	0.0
470 Ma-2X	560	4.7	2.3	102.3	28.3	74.0
470 Ma-4X	1120	8.6	3.1	85.4	19.2	66.2
470 Ma-6X	1680	11.8	3.9	63.1	10.9	52.2
470 Ma-8X	2240	16.7	6.7	26.0	3,2	22.8
470 Ma-12X	3360	22.5	11.1	0.3	0.3	0.0
470 Ma-16X	4480	23.5	12.0	0.4	0.4	0.0

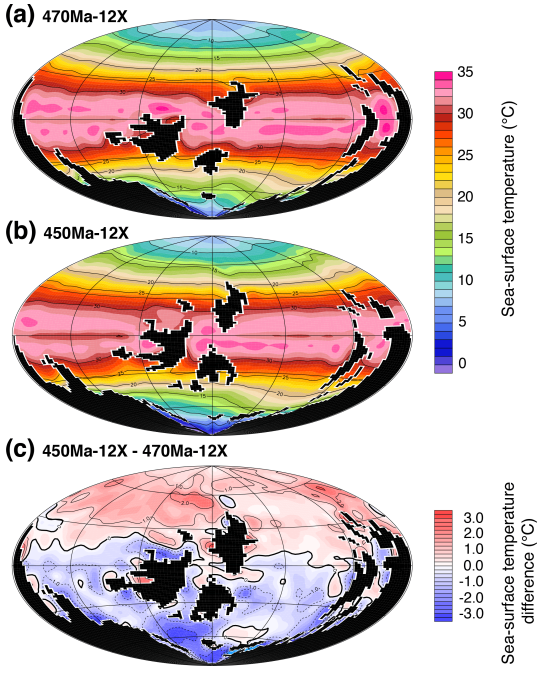

Figure 6. Comparison of the SST simulated at 12 PAL with the fully coupled version of FOAM for the two continental configurations used in this study. The black mask stands for continental masses. Note that, for the plot presented in **(c)**, the mask actually represents all the grid points where the SST difference could not be calculated, cumulating each point that is a continent either in the 450 or in the 470 Ma configuration.

This type of non-linearity within the Earth climate system has been extensively studied in the past few years. We will in particular discuss our results in the light of the major studies from Rose and Marshall (2009) and Ferreira et al. (2011) in Sect. 4, but we propose for now to continue our analysis by focusing on the response of ocean dynamics to the paleogeographical changes occurring between 470 and 450 Ma.

3.2 Sensitivity of ocean dynamics to the paleogeography

The shift from the warm to the cold climatic mode occurs between 12 and 8 PAL at 470 Ma, and between 8 and 6 PAL at 450 Ma. In order to constrain why the 450 Ma climatic system has a lower CO_2 threshold, we compare the climatic features at both time slices for the same pCO_2. We use the simulations preceding the tipping points (12 PAL) to identify the preconditioning factors for the climatic instability. These two simulations have a same global SAT (22.5 °C, Table 1) and a close global ocean temperature (11.1 °C at 470 Ma and 11.4 °C at 450 Ma, Table 1) that make the comparison reasonable.

Figure 6 displays the sea-surface temperatures (SST) for the 470 Ma-12X and the 450 Ma-12X experiments together with the SST difference between these two simulations. From 470 to 450 Ma, the SH cools and the NH warms (Fig. 6c). The temperature changes are on the order of a few degrees, locally up to 3 °C in both hemispheres. Assuming that the NH sea ice extension plays a major role in the abrupt transition from one climatic state to another through the sea ice albedo positive feedback (see Sect. 3.1), the NH warming observed in Fig. 6c appears as the key point accounting for the increasing stability from 470 to 450 Ma. It becomes more difficult to form sea ice and thus to trigger the albedo feedback in the NH through time, and a lower CO_2 concentration is required to enter the cool climatic mode at 450 Ma.

The origin of the temperature pattern observed in Fig. 6c is investigated through the study of the oceanic heat transport (Fig. 7). From 470 to 450 Ma, the NH is marked by

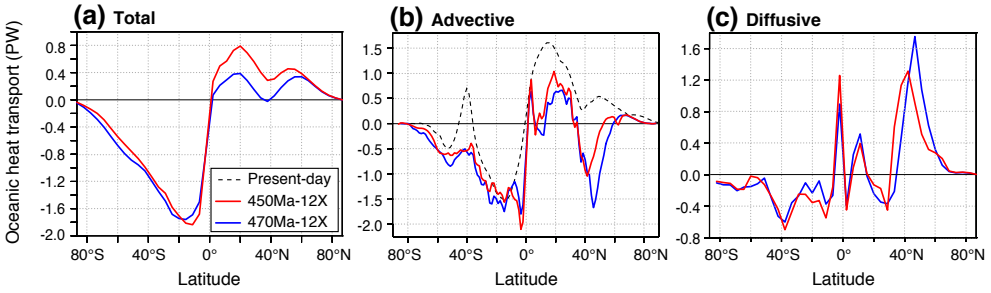

Figure 7. Comparison of the total, advective and diffusive OHT simulated with the fully coupled version of FOAM at 12 PAL for the two continental configurations used in this study. The OHT is given in petawatts (1 PW = 10^{15} W). The present-day curve is the control experiment conducted at present-day conditions with the up-to-date IPSL (Institut Pierre Simon Laplace) CM4 GCM (see the main text for explanations).

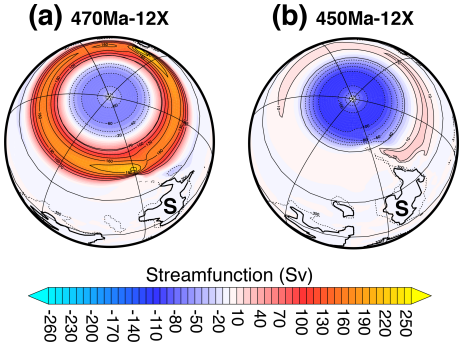

Figure 8. Siberia's northward drift and the consequences on the longitudinal stream function. Eastward stream is positive (red), westward stream is negative (blue). The stream function is integrated over the whole water column. S: Siberia. Simulations were conducted with the fully coupled version of FOAM. It is noteworthy that the northward drift of Siberia from the Middle to the Late Ordovician is a robust feature of all available Ordovician paleogeographical reconstructions published so far, including the maps from Torsvik and Cocks (Cocks and Torsvik, 2007, Fig. 6a; Torsvik and Cocks, 2013: Fig. 2.12, 2.14 and 2.15), Golonka and Gaweda (2012, Figs. 6 and 7) and Scotese and McKerrow (1991, Figs. 4 and 5).

a significant increase in the northward OHT exceeding 100 % at 20° N (from 0.4 to 0.8 PW respectively, Fig. 7a). In the SH, a slight decrease in the southward OHT is observed at all latitudes except for a narrow latitudinal band between 6 and 18° S (Fig. 7a). This new energy redistribution brings more heat to the NH and less to the SH. As a direct consequence, the NH warms from 470 to 450 Ma, and the SH cools.

Dividing the total OHT into its advective and diffusive components (Fig. 7b and c) reveals a striking feature within the NH advective heat transport between ∼ 35 and ∼ 65° N (Fig. 7b). The transport is negative, meaning a southward heat transport, which is a priori unexpected in the NH. The advective heat transport scales as $\sim \Psi \times \Delta T \times \rho \times C_p$ where Ψ is the strength of the overturning circulation, ΔT the temperature difference between the northward and the southward limbs of the overturning circulation, ρ the water density and C_p the water specific heat. A negative heat transport implies a southward transport of surface warm waters. The southward water flow results from an intense wind-driven eastward circumpolar current that develops at these latitudes in the absence of landmasses (Fig. 8). As a consequence of the Ekman deflection, the water masses are deviated to the right of the main eastward stream and thus constitute a southward mass transport. From 470 to 450 Ma, the northward drift of Siberia (Fig. 8) inhibits the zonal current and the associated Ekman cell, explaining why the reverse OHT weakens through time (Fig. 7b). A similar reverse advective OHT is observed in present-day experiments in the SH due to the Antarctica Circumpolar Current. Figure 7b shows the results obtained for a present-day experiment conducted with a state-of-the-art ocean–atmosphere–vegetation coupled model: the IPSL CM4 GCM (Marti et al., 2010). A reverse heat transport is obtained near 40° S. From this point of view, the Ordovician quasi-oceanic NH keeps some common features with our present-day ∼ 80 % oceanic SH.

The global Northern Hemisphere OHT strengthening, from 470 to 450 Ma (Fig. 7a), is due to an increase of the transport in three main areas (Fig. 9), the location of which turns out to be constrained by changes in the overturning circulation (Fig. 10).

- Between 5 and 30° N, the advective OHT increases (Fig. 7b) in response to the intensifying surface subtropical cell that directly brings heat from the equator.

- Between 30 and ∼ 42° N, the diffusive OHT increases (Fig. 7c) as a consequence of the strengthening of the subtropical cell. Much more heat is "deposited" at 30° N, which imposes a strong temperature gradient. Heat diffuses from the warm tropical latitudes where the heat is "deposited" to the cold waters at higher latitudes.

- Between ∼ 42 and 60° N, the southward advective OHT weakens through time (Fig. 7b). The northward drift of Siberia inhibits the 40° N zonal current (Fig. 8): the

counter-clockwise cell associated to the zonal current acts over the entire water column at 470 Ma and not beyond 2500 m at 450 Ma. Hence less cold waters are brought from the high latitudes to the mid-latitudes resulting in an increased net northward heat transport. An additional process is the northward deflection of surface warm currents by Siberia at 450 Ma. This can be seen by comparing the isotherms 20 and 15 °C in Fig. 6a and b. Although it is restricted to upper levels oceanic waters, this second mechanism is significant because the first tens of meters represent an important heat reservoir of the ocean.

The most significant outstanding issue is to determine why the temperature drawdown occurring through the tipping point is sharper at 450 than at 470 Ma. Although the tipping point occurs at lower CO_2 at 450 Ma, the two paleogeographical configurations present almost the same global SAT and an equivalent sea ice cover at 6 PAL (Fig. 2 and Table 1). Paradoxically, this sharper response through the 450 Ma tipping point is due to the paleogeographically induced increase in the Northern Hemisphere OHT that previously inhibited the cooling. While the NH warms from 470 to 450 Ma (Fig. 6c), the NH equator-to-pole temperature profile flattens (not shown here). These changes are observed within the warm mode at 12 PAL, but they are critical since they constitute the preconditioning factors for the differential climatic sensitivity as climate shifts to the cold climatic mode. The flattened 450 Ma SST gradient delays the tipping point to a certain extent by inhibiting sea ice growth at polar latitudes, but it increases the global climate sensitivity to the radiative forcing as soon as NH sea ice begins to expand.

4 Discussion

The potential existence of multiple equilibria in the climate system has a long story in the literature. Lorenz (1968) discussed whether the physical laws governing climate are "transitive", supporting a unique climate state, or "intransitive" leading to several sets of long-term statistics. Two main mechanisms supporting climate intransitivity have so far emerged. The first mechanism originates in the study of Stommel (1961) who showed that the thermohaline circulation may sustain two stable regimes depending on whether the driver of the circulation, the density difference, is dominated by the temperature or the haline gradient, leading respectively to an intense or a weak circulation. This concept motivated later a wealth of studies linking the last glacial abrupt events to these multiple thermohaline states, studies that are today well known as "fresh water hosing" experiments (see for example Kageyama et al., 2013). The second mechanism is the ice albedo positive feedback. It was independently introduced by Budyko (1969) and Sellers (1969). The authors developed simple one-dimension climate models in which surface temperature is computed by taking into

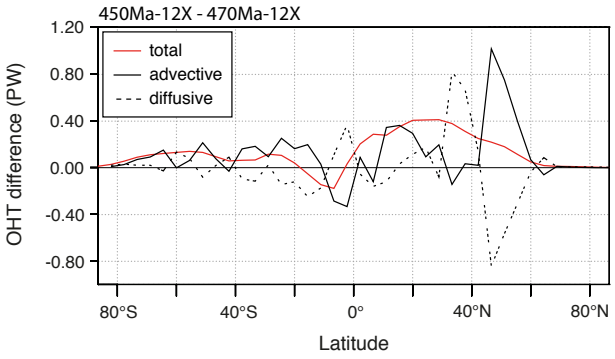

Figure 9. Difference in total, advective and diffusive OHT between the 450 Ma-12X and the 470 Ma-12X simulations.

account the local radiative budget and the meridional heat transport. Two stable climate states are obtained for a same solar forcing depending on the initial conditions, describing a classical hysteresis loop: a warm state with a small sea ice cap or no sea ice at all (Eq3, Fig. 11a), and a cold completely ice-covered state (Eq1, Fig. 11a). A large sea ice cap of finite size extending to the mid-latitudes constitutes another analytical solution, but this third equilibrium turns out to be very unstable and thus not realizable (Eq2 in Fig. 11a; Rose and Marshall, 2009). Critical non-linearities are observed at both latitudinal extremes (Rose and Marshall, 2009 and references therein). At low latitudes, near the equator, the "large ice cap instability" rules. An sea ice margin reaching these latitudes expands up to the equator ("snowball" state Eq1, Fig. 11a). At very high latitudes, this is the "small ice cap instability" (SICI): a reduced sea ice cover will either completely disappear or spread until it forms a small ice cap restricted to the high latitudes (warm state, Eq3 in Fig. 11a). In the absence of the equilibrium Eq2, a unique sea ice cap of large (beyond the SICI domain) but finite (no snowball state) size is obtained for a given climatic forcing (Fig. 11b). A comprehensive review of the successive improvements associated to the energy balance models (EBMs) is provided by North et al. (1981).

Recently, Rose and Marshall (2009) managed to stabilize the equilibrium Eq2 by extending the previous EBMs through two key processes: (i) the effect by which sea ice insulates the ocean surface from the atmosphere, (ii) the wind-driven structure of the OHT. A primary maximum at low-latitudes accounts for the heat transport by the subtropical gyre and a secondary maximum at high latitudes for the OHT generated by the subpolar gyre, with a local minimum in between (Fig. 11c). Contrary to classical EBMs in which the OHT describes a large parabolic curve from the equator to the pole (Fig. 11b), the OHT pattern from Rose and Marshall (2009) shows a local minimum at mid-latitudes where the sea ice edge can stably rest. This OHT structure is closer to the observations (see for example Garnier et al., 2000). Within the improved EBM of Rose and Marshall (2009), the small ice cap instability does not exist anymore: sea ice

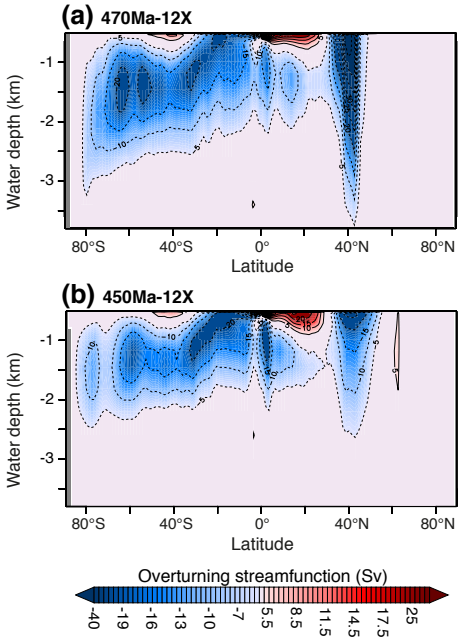

Figure 10. Comparison of the global meridional overturning circulation simulated at 12 PAL with the fully coupled version of FOAM for the two continental configurations used in this study. Red shading and solid contours indicate a clockwise circulation, blue shading and dashed contours indicate a counter-clockwise circulation.

caps of various size can persist at polar latitudes. Because the equilibrium Eq2 is now stable, two sea ice caps of large but finite size can be sustained for the same climatic forcing (e.g., for F5 in Fig. 11c). The position of the sea ice edge in the equilibrium Eq2 is captured within the position of the mid-latitude OHT minimum and thus very stable when external forcing is varied.

The question however still remained if the mid-latitude equilibrium Eq2 would hold in a more complex climate model with many degrees of freedom and a strong internal variability. Ferreira et al. (2011) demonstrated multiple equilibria using an up-to-date ocean GCM (the MITgcm) on two idealized configurations: a purely aqua planet, and an ocean planet with a strip of land extending from one pole to the other. The three states from Rose and Marshall (2009) are obtained: (i) a warm, ice-free state, (ii) a cold state with sea ice extending down to mid-latitudes, (iii) and the completely ice-covered "snowball" state. The authors highlight the consistency of their results with the study of Rose and Marshall (2009). In their complex GCM, the multiple equilibria owe their existence to the latitudinal structure of the OHT. The authors moreover extend the previous results from Rose and Marshall (2009) by demonstrating that no OHT minimum is required. A weak high-latitude OHT within the subpolar gyre is sufficient to stabilize a finite sea ice cap at mid-latitudes, in that critical weak-OHT zone situated between the subtropical and the subpolar gyres that they widely refer to as the "OHT convergence".

Here, we have investigated the Ordovician climate sensitivity to a varying radiative forcing. The hallmark of our results is the existence of a global climatic instability in the NH. A tipping point separates two climatic modes: a warm mode with no sea ice in the NH, and a cold mode with sea ice extending down to the mid-latitudes (Fig. 5a). In the light of the results from Rose and Marshall (2009) and Ferreira et al. (2011), these climatic modes respectively correspond to the classical warm mode obtained with an EBM and to the third equilibrium previously described, respectively Eq3 and Eq2 in Fig. 11. The simulations marked by a weak pCO_2 stabilize in Eq2, whereas the experiments conducted with high CO_2 levels lead to the warm state of Eq3.

It is noteworthy that the latitudinal position at which the sea ice edge stabilizes within the cold climatic mode effectively lies immediately poleward of the Northern Hemisphere OHT convergence (Fig. 12, $\sim 40°$ N), which is a key prediction from Rose and Marshall (2009) and Ferreira et al. (2011). According to these authors, the strong low-latitude OHT encounters here a weaker transport and heat is "deposited", thus preventing the sea ice edge from moving further equatorward.

The fact that the ice edge is strongly enslaved to the OHT convergence (Fig. 12; Rose and Marshall, 2009) explains why the model returns to its initial sensitivity below 4 PAL (see Sect. 3.1). Ice cannot spread further and stabilizes. The sea ice albedo feedback is geometrically stopped by the subtropical high-OHT barrier and cooling is consequently slowed-down.

The comparison of Fig. 11b and c permits to explain why tipping points were not previously observed for the Ordovician. Similarly to the classical EBMs, the slab models use a purely diffusive transport. The resulting OHT describes the same large parabolic curve from the equator to the pole (Fig. 12). There is no OHT minimum or more largely no OHT convergence where the sea ice edge could rest to make the mid-latitude equilibrium stable. Climate cannot switch between stable states which inhibits the climatic instability.

In addition, the similarity between EBMs and slab models explains the results from Gibbs et al. (1997) who observed with the slab model GENESIS a runaway icehouse that they interpreted as resulting from the small ice cap instability. As it was previously explained, this mechanism is not observed anymore when the OHT structure is taken into account, but it is a classical feature of the EBMs and by extension of all models that use a diffusive OHT. We emphasize that the runaway icehouse proposed by Gibbs et al. (1997) and the climatic instability suggested in this study rely on much different mechanisms.

The absence of ocean dynamics in the slab models makes their response to an atmospheric forcing much different from the ocean–atmosphere GCM when simulating time periods of particular land-sea configuration as it is the case for the

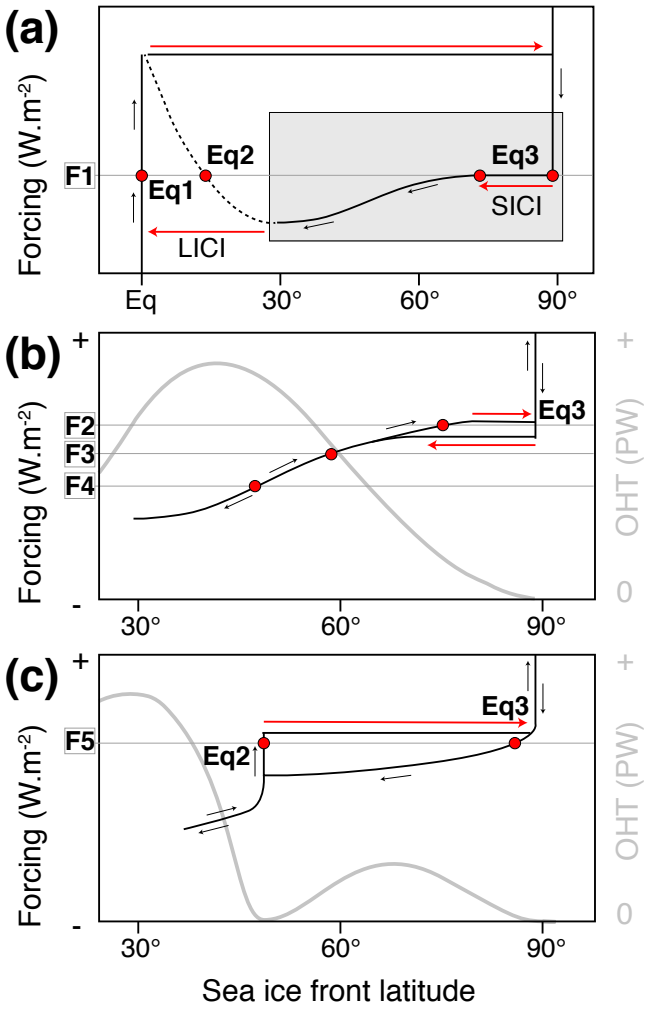

Figure 11. **(a)** Graph showing the latitude of the sea ice front (x axis) vs. the climatic forcing (y axis) for a classical Budyko–Sellers type EBM. Dark arrows indicate the pathway described by the model through a whole cycle of forcing decrease and increase. Red arrows account for major climatic instabilities. Red circles represent the sea ice edge latitudes corresponding to each analytical solution for a given climatic forcing F1. Dashed lines represent regions that are correct analytical solutions, but are unable to be realized within the model due to instability. SICI: small ice cap instability; LICI: large ice cap instability. **(b)** represents the same plot as **(a)**, while focusing on the domain shaded in grey in **(a)**. The forcing is decreased and then increased without reaching the snowball equilibrium Eq1. Several forcing values (F2, F3 and F4) are represented, each one leading to a single sea ice cap of finite size (red circles). The OHT pattern corresponding to the purely diffusive transport characteristic of classical EBMs is overlayed in grey (right y axis). **(c)** Same plot as **(b)** for the extended EBM from Rose and Marshall (2009) (see the main text for explanations) in which the OHT pattern is modified (grey curve). Note the two sea ice caps of finite size corresponding to the forcing level F5. **(a)** is adapted from North et al. (1981), **(b)** and **(c)** are modified after Rose and Marshall (2009).

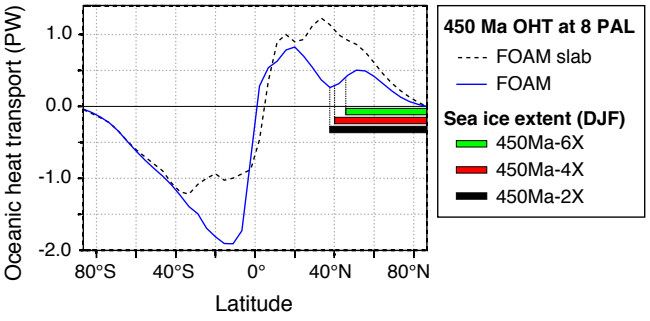

Figure 12. Comparison of the total OHT at 450 Ma and at 8 PAL for the slab version of FOAM and for the fully coupled version of FOAM. The OHT pattern is relatively stable when CO_2 is varied. Color bars represent the maximum (boreal winter) Northern Hemisphere sea ice extent simulated within the cold climatic mode at 450 Ma with the fully coupled model.

Ordovician. An efficient way to overcome that apparent deficiency would be to impose the structure of the latitudinal OHT, as Rose and Marshall (2009) did in their extended EBM. The decisive answer is brought by Ferreira et al. (2011), who tested this hypothesis within the MIT-gcm used as a slab. With the simple diffusive coefficient, the mid-latitude equilibrium is not stable, as for classical EBMs. However, by imposing the OHT deduced from their coupled runs to the slab, they managed to reproduce exactly the same climatic response as with their complex GCM. These results confirm that the differential behavior of ocean–atmosphere and slab–atmosphere GCMs lies within ocean dynamics through the OHT.

The Ordovician Period turned out to bring a favorable paleogeographical context to propose the sudden shift between different climate states on a realistic configuration. The stabilization of a sea ice edge at mid-latitudes requires a wind-driven latitudinal OHT structure, a condition that can be reached only in an oceanic context. It is notably the case of the Ordovician 95 % oceanic NH which ocean zonal circulation is not hampered by continental masses. If continents were largely distributed at all latitudes, then continental edges would strongly alter the pattern originally imposed by the winds and by the Ekman pumping mechanism. The OHT may thus be more even at all latitudes, as it is the case in our study in the SH due to the supercontinent Gondwana (Figs. 1 and 12). No OHT convergence would be obtained and the OHT pattern would become very similar to the one imposed by a simple diffusion coefficient. From this point of view, it is logical that the global instability lies in our study in the oceanic NH, and it would anyway be inconceivable to obtain a similar behavior in the SH.

5 Conclusions

We have examined the response of the Ordovician climate to a decreasing pCO_2 for two continental configurations at 470 and at 450 Ma with the coupled ocean, atmosphere and sea ice GCM FOAM. We have found the existence of tipping points in the Ordovician climate owing to the particular paleogeography with a quasi-oceanic Northern Hemisphere. As a result, the climate may have abruptly shifted from a warm climatic mode to a cold climatic mode. Warm SST and no sea ice in the NH characterize the warm mode, whereas much colder SST and a large sea ice extension to the mid-latitudes mark the cool mode. We also note that subtle changes occurring in the continental configuration between 470 and 450 Ma make the latter less sensitive to the radiative forcing. Indeed, the shift from the warm to the cold climatic mode takes place between 12 and 8 PAL at 470 Ma, and between 8 and 6 PAL at 450 Ma. One potential mechanism relies on the changes occurring in the oceanic heat transport between the two simulated time periods. The paleogeographical evolution promotes a larger northward oceanic heat transport at 450 Ma which in turn induces warmer Northern Hemisphere SST. Spread of sea ice becomes more difficult and a lower CO_2 level is required to enter the cold climatic mode. The fact that the tipping point is reached for a higher CO_2 level at 470 Ma whereas climate was warm at that time (e.g., Trotter et al., 2008), implies that the pCO_2 must have been high during the Middle Ordovician, thus precluding climate to reach the climatic instability.

The tipping point is due to a climatic instability occurring in the quasi-oceanic Northern Hemisphere. The instability relies on the sudden shift from a warm climate to a climatic equilibrium characterized by a sea ice front resting at mid-latitudes. This particular climate state has been widely discussed in the literature and proven to require a wind-driven latitudinal structure of the OHT (Rose and Marshall, 2009; Ferreira et al., 2011). The classical EBMs and slab models use a purely diffusive OHT and are by construction unable to stabilize an ice edge at the mid-latitudes (Rose and Marshall, 2009; Ferreira et al., 2011), explaining why that behavior was never noticed in previous studies about the Ordovician climate (e.g., Gibbs et al., 1997; Herrmann et al., 2004b). Published studies performed with idealized land–sea configurations however demonstrate that this limitation may be overcome by imposing a latitudinally varied diffusion coefficient reproducing the OHT structure. Such extended EBMs and slab models successfully reproduce the behavior of the more complex ocean–atmosphere GCMs (Rose and Marshall, 2009; Ferreira et al., 2011).

The Late Ordovician Hirnantian is characterized by the rapid growth of large ice sheets (e.g., Ghienne et al., 2007; Loi et al., 2010; Finnegan et al., 2011). Recent geochemical data suggest an abrupt tropical SST cooling at that time (Trotter et al., 2008; Finnegan et al., 2011). Several CO_2 sinks have been proposed to explain cooling but no consensus has been found so far (Brenchley et al., 1994; Kump et al., 1999; Villas et al., 2002; Lenton et al., 2012). In this context, the tipping point becomes a very interesting working hypothesis. It requires only a slight CO_2 decrease and at the same time induces a sharp global temperature drawdown, in the same order of magnitude as the Hirnantian cooling observed by Trotter et al. (2008) and Finnegan et al. (2011). The climatic instability demonstrated in this study therefore represents a step forward in understanding the Ordovician glacial events and provides in particular a minimal hypothesis for the Hirnantian abrupt cooling and associated glacial pulse. Our results also shed a new light on the CO_2 sinks envisaged to reduce the pCO_2 at that time. We now suggest that a moderate sink (e.g., Young et al., 2009; Nardin et al., 2011) may have been sufficient, thus making relevant some mechanisms that have been neglected so far because of their moderate impact on the pCO_2.

Acknowledgements. We thank Mark Williams and one anonymous referee for their constructive remarks that have greatly improved this paper. We thank Pierre Sepulchre for providing the IPSL CM4 GCM run. We are also grateful to David G. Ferreira for his constructive and helpful comments. This work was granted access to the HPC resources of TGCC under the allocation 2014-012212 made by GENCI.

Edited by: A. Haywood

References

Berner, R. A.: GEOCARBSULF: a combined model for Phanerozoic atmospheric O_2 and CO_2, Geochim. Cosmochim. Ac., 70, 5653–5664, doi:10.1016/j.gca.2005.11.032, 2006.

Berner, R. A. and Kothavala, Z.: GEOCARB III: a revised model of atmospheric CO_2 over Phanerozoic time, Am. J. Sci., 301, 182–204, doi:10.2475/ajs.301.2.182, 2001.

Beuf, S., Biju-Duval, B., De Charpal, O., Rognon, P., Gariel, O., and Bennacef, A.: Les grès du Paléozoïque Inférieur au Sahara, Technip, Paris, 464 pp., 1971.

Blakey, R. C.: Carboniferous-Permian paleogeography of the assembly of Pangea, in: Fifteenth International Congress on Carboniferous and Permian Stratigraphy, edited by: Wong, T. E., Utrecht, the Netherlands, pages 443–465, Royal Netherlands Academy of Arts and Sciences, Amsterdam, 2007.

Braconnot, P., Harrison, S. P., Kageyama, M., Bartlein, P. J., Masson-Delmotte, V., Abe-Ouchi, A., Otto-Bliesner, B., and Zhao, Y.: Evaluation of climate models using palaeoclimatic data, Nat. Clim. Change, 2, 417–424, doi:10.1038/NCLIMATE1456, 2012.

Brenchley, P. J., Marshall, J. D., Carden, G., Robertson, D., Long, D., Meidla, T., Hints, L., and Anderson, T. F.: Bathymetric and isotopic evidence for a short-lived Late Ordovician glaciation in a greenhouse period, Geology, 22, 295–298, doi:10.1130/0091-7613(1994)022<0295:BAIEFA>2.3.CO;2, 1994.

Brenchley, P. J., Carden, G. A., Hints, L., Kaljo, D., Marshall, J. D., Martma, T., Meidla, T., and Nõlvak, J.: High-

resolution stable isotope stratigraphy of Upper Ordovician sequences: constraints on the timing of bioevents and environmental changes associated with mass extinction and glaciation, Geol. Soc. Am. Bull., 115, 89–104, doi:10.1130/0016-7606(2003)115<0089:HRSISO>2.0.CO;2, 2003.

Budyko, M. I.: The effect of solar radiation variations on the climate of the Earth, Tellus, 21, 611–619, doi:10.1111/j.2153-3490.1969.tb00466.x, 1969.

Cocks, L. R. M. and Torsvik, T. H.: Siberia, the wandering northern terrane, and its changing geography through the Palaeozoic, Earth-Sci. Rev., 82, 29–74, doi:10.1016/j.earscirev.2007.02.001, 2007.

Crowley, T. J. and Baum, S. K.: Toward reconciliation of Late Ordovician (~ 440 Ma) glaciation with very high CO_2 levels, J. Geophys. Res.-Atmos., 96, 22597–22610, doi:10.1029/91JD02449, 1991.

Crowley, T. J. and Baum, S. K.: Modeling late Paleozoic glaciation, Geology, 2, 507–510, doi:10.1130/0091-7613(1992)020<0507:MLPG>2.3.CO;2, 1992.

Crowley, T. J. and Baum, S. K.: Reconciling Late Ordovician (440 Ma) glaciation with very high (14X) CO_2 levels, J. Geophys. Res.-Atmos., 100, 1093–1101, doi:10.1029/94JD02521, 1995.

Crowley, T. J., Baum, S. K., and Kim, K. Y.: General circulation model sensitivity experiments with pole-centered supercontinents, J. Geophys. Res.-Atmos., 98, 8793–8800, doi:10.1029/93JD00122, 1993.

Denis, M., Buoncristiani, J.-F., Konate, M., Ghienne, J.-F., and Guiraud, M.: Hirnantian glacial and deglacial record in SW Djado Basin (NE Niger), Geodin. Acta, 20, 177–195, doi:10.3166/ga.20.177-195, 2007.

Dera, G. and Donnadieu, Y.: Modeling evidences for global warming, Arctic seawater freshening, and sluggish oceanic circulation during the Early Toarcian anoxic event, Paleoceanography, 27, PA2211, doi:10.1029/2012PA002283, 2012.

Díaz-Martínez, E. and Grahn, Y.: Early Silurian glaciation along the western margin of Gondwana (Peru, Bolivia and northern Argentina): Palaeogeographic and geodynamic setting, Palaeogeogr. Palaeocl., 245, 62–81, doi:10.1016/j.palaeo.2006.02.018, 2007.

Donnadieu, Y., Goddéris, Y., and Bouttes, N.: Exploring the climatic impact of the continental vegetation on the Mezosoic atmospheric CO_2 and climate history, Clim. Past, 5, 85–96, doi:10.5194/cp-5-85-2009, 2009.

Endal, A. S. and Sofia, S.: Rotation in solar-type stars, I – Evolutionary models for the spin-down of the sun, Astrophys. J., 243, 625–640, doi:10.1086/158628, 1981.

Ferreira, D., Marshall, J., and Rose, B.: Climate determinism revisited: multiple equilibria in a complex climate model, J. Climate, 24, 992–1012, doi:10.1175/2010JCLI3580.1, 2011.

Finnegan, S., Bergmann, K., Eiler, J. M., Jones, D. S., Fike, D. A., Eisenman, I., Hughes, N. C., Tripati, A. K., and Fischer, W. W.: The magnitude and duration of Late Ordovician-Early Silurian glaciation, Science, 331, 903–906, doi:10.1126/science.1200803, 2011.

Garnier, E., Barnier, B., Siefridt, L., and Béranger, K.: Investigating the 15 years air-sea flux climatology from the ECMWF re-analysis project as a surface boundary condition for ocean models, Int. J. Climatol., 20, 1653–1673, doi:10.1002/1097-0088(20001130)20:14<1653::AID-JOC575>3.0.CO;2-G, 2000.

Ghienne, J.-F., Le Heron, D., Moreau, J., Denis, M., and Deynoux, M.: The Late Ordovician glacial sedimentary system of the North Gondwana platform, in: Glacial sedimentary processes and products, Special Publication, edited by: Hambrey, M., Christoffersen, P., Glasser, N., Janssen, P., Hubbard, B., and Siegert, M., 39, 295–319, International Association of Sedimentologists, Blackwells, Oxford, 2007.

Gibbs, M. T., Barron, E. J., and Kump, L. R.: An atmospheric pCO_2 threshold for glaciation in the Late Ordovician, Geology, 25, 447–450, doi:10.1130/0091-7613(1997)025<0447:AAPCTF>2.3.CO;2, 1997.

Golonka, J. and Gaweda, A.: Plate tectonic evolution of the southern margin of Laurussia in the Paleozoic, in: Tectonics – Recent advances, edited by: Sharkov, E., 261–282, InTech, 2012.

Gough, D. O.: Solar interior structure and luminosity variations, Sol. Phys., 74, 21–34, doi:10.1007/BF00151270, 1981.

Herrmann, A. D., Patzkowsky, M. E., and Pollard, D.: Obliquity forcing with 8–12 times preindustrial levels of atmospheric pCO_2 during the Late Ordovician glaciation, Geology, 31, 485–488, doi:10.1130/0091-7613(2003)031<0485:OFWTPL>2.0.CO;2, 2003.

Herrmann, A. D., Haupt, B. J., Patzkowsky, M. E., Seidov, D., and Slingerland, R. L.: Response of Late Ordovician paleoceanography to changes in sea level, continental drift, and atmospheric pCO_2: potential causes for long-term cooling and glaciation, Palaeogeogr. Palaeocl., 210, 385–401, doi:10.1016/j.palaeo.2004.02.034, 2004a.

Herrmann, A. D., Patzkowsky, M. E., and Pollard, D.: The impact of paleogeography, pCO_2, poleward ocean heat transport and sea level change on global cooling during the Late Ordovician, Palaeogeogr. Palaeocl., 206, 59–74, doi:10.1016/j.palaeo.2003.12.019, 2004b.

International Commission on Stratigraphy: International Chronostratigraphic Chart v2014/02, available at: www.stratigraphy.org, 2014.

IPCC: Climate Change 2013: The physical science basis, in: Contribution of Working Group I to the Fifth Assessment Report of the Intergovernmental Panel on Climate Change, edited by: Stocker, T. F., Qin, D., Plattner, G.-K., Tignor, M., Allen, S. K., Boschung, J., Nauels, A., Xia, Y., Bex, V., and Midgley, P. M., Cambridge University Press, Cambridge, UK and New York, NY, USA, 1535 pp., 2013.

Jacob, R. L.: Low frequency variability in a simulated atmosphere ocean system, Ph.D. thesis, University of Wisconsin-Madison, 1997.

Kageyama, M., Merkel, U., Otto-Bliesner, B., Prange, M., Abe-Ouchi, A., Lohmann, G., Ohgaito, R., Roche, D. M., Singarayer, J., Swingedouw, D., and Zhang, X.: Climatic impacts of fresh water hosing under Last Glacial Maximum conditions: a multi-model study, Clim. Past, 9, 935–953, doi:10.5194/cp-9-935-2013, 2013.

Kiehl, J. T., Hack, J. J., Bonan, G. B., Boville, B. A., Williamson, D. L., and Rasch, P. J.: The national center for Atmospheric Research community climate model: CCM3, J. Climate, 11, 1131–1149, doi:10.1175/1520-0442(1998)011<1131:TNCFAR>2.0.CO;2, 1998.

Kothavala, Z., Oglesby, R. J., and Saltzman, B.: Sensitivity of equilibrium surface temperature of CCM3 to systematic changes in atmospheric CO_2, Geophys. Res. Lett., 26, 209–212, doi:10.1029/1998GL900275, 1999.

Kump, L. R., Arthur, M. A., Patzkowsky, M. E., Gibbs, M. T., Pinkus, D. S., and Sheehan, P. M.: A weathering hypothesis for glaciation at high atmospheric pCO_2 during the Late Ordovician, Palaeogeogr. Palaeocl., 152, 173–187, doi:10.1016/S0031-0182(99)00046-2, 1999.

Lefebvre, V., Donnadieu, Y., Sepulchre, P., Swingedouw, D., and Zhang, Z.-S.: Deciphering the role of southern gateways and carbon dioxide on the onset of the Antarctic Circumpolar Current, Paleoceanography, 27, PA4201, doi:10.1029/2012PA002345, 2012.

Lenton, T. M., Crouch, M., Johnson, M., Pires, N., and Dolan, L.: First plants cooled the Ordovician, Nat. Geosci., 5, 86–89, doi:10.1038/ngeo1390, 2012.

Loi, A., Ghienne, J.-F., Dabard, M. P., Paris, F., Botquelen, A., Christ, N., Elaouad-Debbaj, Z., Gorini, A., Vidal, M., Videt, B., and Destombes, J.: The Late Ordovician glacio-eustatic record from a high-latitude storm-dominated shelf succession: the Bou Ingarf section (Anti-Atlas, Southern Morocco), Palaeogeogr. Palaeocl., 296, 332–358, doi:10.1016/j.palaeo.2010.01.018, 2010.

Lorenz, E. N.: Climatic determinism, Meteor. Mon., 8, 1–3, 1968.

Marti, O., Braconnot, P., Dufresne, J. L., Bellier, J., Benshila, R., Bony, S., Brockmann, P., Cadule, P., Caubel, A., Codron, F., Noblet, N., Denvil, S., Fairhead, L., Fichefet, T., Foujols, M. A., Friedlingstein, P., Goosse, H., Grandpeix, J. Y., Guilyardi, E., Hourdin, F., Idelkadi, A., Kageyama, M., Krinner, G., Lévy, C., Madec, G., Mignot, J., Musat, I., Swingedouw, D., and Talandier, C.: Key features of the IPSL ocean atmosphere model and its sensitivity to atmospheric resolution, Clim. Dynam., 34, 1–26, doi:10.1007/s00382-009-0640-6, 2010.

Nardin, E., Goddéris, Y., Donnadieu, Y., Le Hir, G., Blakey, R. C., Pucéat, E., and Aretz, M.: Modeling the early Paleozoic long-term climatic trend, Geol. Soc. Am. Bull., 123, 1181–1192, doi:10.1130/B30364.1, 2011.

North, G. R., Cahalan, R. F., and Coakley, J. A.: Energy balance climate models, Rev. Geophys., 19, 91–121, 80R1502, doi:10.1029/RG019i001p00091, 1981.

Pancost, R. D., Freeman, K. H., Herrmann, A. D., Patzkowsky, M. E., Ainsaar, L., and Martma, T.: Reconstructing Late Ordovician carbon cycle variations, Geochim. Cosmochim. Ac., 105, 433–454, doi:10.1016/j.gca.2012.11.033, 2013.

Pollard, D.: A retrospective look at coupled ice sheet – climate modeling, Climate Change, 100, 173–194, doi:10.1007/s10584-010-9830-9, 2010.

Poulsen, C. J. and Jacob, R. L.: Factors that inhibit snowball Earth simulation, Paleoceanography, 19, PA4021, doi:10.1029/2004PA001056, 2004.

Poussart, P. F., Weaver, A. J., and Barnes, C. R.: Late Ordovician glaciation under high atmospheric CO_2: a coupled model analysis, Paleoceanography, 14, 542–558, doi:10.1029/1999PA900021, 1999.

Rose, B. E. J. and Marshall, J.: Ocean heat transport, sea ice, and multiple climate states: insights from energy balance models, J. Atmos. Sci., 66, 2828–2843, doi:10.1175/2009JAS3039.1, 2009.

Rubinstein, C. V., Gerrienne, P., de la Puente, G. S., Astini, R. A., and Steemans, P.: Early Middle Ordovician evidence for land plants in Argentina (eastern Gondwana), New Phytol., 188, 365–369, doi:10.1111/j.1469-8137.2010.03433.x, 2010.

Saltzman, M. R. and Young, S. A.: Long-lived glaciation in the Late Ordovician? Isotopic and sequence-stratigraphic evidence from western Laurentia, Geology, 33, 109–112, doi:10.1130/G21219.1, 2005.

Scotese, C. R. and McKerrow, W. S.: Ordovician plate tectonic reconstructions, in: Advances in Ordovician geology, edited by: Barnes, C. R. and Williams, S. H., 90–9, 271–282, Geological Survey of Canada, 1991.

Sellers, W. D.: A global climatic model based on the energy balance of the earth-atmosphere system, J. Appl. Meteorol., 8, 392–400, doi:10.1175/1520-0450(1969)008<0392:AGCMBO>2.0.CO;2, 1969.

Semtner Jr, A. J.: A model for the thermodynamic growth of sea ice in numerical investigations of climate, J. Phys. Oceanogr., 6, 379–389, doi:10.1175/1520-0485(1976)006<0379:AMFTTG>2.0.CO;2, 1976.

Servais, T., Owen, A. W., Harper, D. A., Kröger, B., and Munnecke, A.: The Great Ordovician Biodiversification Event (GOBE): the palaeoecological dimension, Palaeogeogr. Palaeocl., 294, 99–119, doi:10.1016/j.palaeo.2010.05.031, 2010.

Sheehan, P. M.: The late Ordovician mass extinction, Annu. Rev. Earth Pl. Sc., 29, 331–364, doi:10.1146/annurev.earth.29.1.331, 2001.

Spjeldnaes, N.: Ordovician climatic zones, Norsk Geol. Tidsskr., 41, 45–77, 1962.

Steemans, P., Le Herissé, A., Melvin, J., Miller, M. A., Paris, F., Verniers, J., and Wellman, C. H.: Origin and radiation of the earliest vascular land plants, Science, 324, 353–353, doi:10.1126/science.1169659, 2009.

Stommel, H.: Thermohaline convection with two stable regimes of flow, Tellus, 13, 224–230, doi:10.1111/j.2153-3490.1961.tb00079.x, 1961.

Sutcliffe, O. E., Dowdeswell, J. A., Whittington, R. J., Theron, J. N., and Craig, J.: Calibrating the Late Ordovician glaciation and mass extinction by the eccentricity cycles of Earth's orbit, Geology, 28, 967–970, doi:10.1130/0091-7613(2000)28<967:CTLOGA>2.0.CO;2, 2000.

Torsvik, T. H. and Cocks, L. R. M.: New global palaeogeographical reconstructions for the Early Palaeozoic and their generation, in: Early Palaeozoic biogeography and palaeogeography, edited by: Harper, D. A. T. and Servais, T., 38, 5–24, Geological Society of London, Memoirs, 2013.

Trotter, J. A., Williams, I. S., Barnes, C. R., Lécuyer, C., and Nicoll, R. S.: Did cooling oceans trigger Ordovician biodiversification? Evidence from conodont thermometry, Science, 321, 550–554, doi:10.1126/science.1155814, 2008.

Turner, B. R., Armstrong, H. A., Wilson, C. R., and Makhlouf, I. M.: High frequency eustatic sea-level changes during the Middle to early Late Ordovician of southern Jordan: Indirect evidence for a Darriwilian Ice Age in Gondwana, Sediment. Geol., 251, 34–48, doi:10.1016/j.sedgeo.2012.01.002, 2012.

Vandenbroucke, T. R., Armstrong, H. A., Williams, M., Paris, F., Zalasiewicz, J. A., Sabbe, K., Nõlvak, J., Challands, T. J., Verniers, J., and Servais, T.: Polar front shift and atmospheric CO_2 during the glacial maximum of the Early Pa-

leozoic Icehouse. P. Natl. Acad. Sci., 107, 14983–14986, doi:10.1073/pnas.1003220107, 2010.

Villas, E., Vennin, E., Álvaro, J. J., Hammann, W., Herrera, Z. A., and Piovano, E. L.: The late Ordovician carbonate sedimentation as a major triggering factor of the Hirnantian glaciation, B. Soc. Geol. Fr., 173, 569–578, doi:10.2113/173.6.569, 2002.

Yapp, C. J. and Poths, H.: Ancient atmospheric CO_2 pressures inferred from natural goethites, Nature, 355, 342–344, doi:10.1038/355342a0, 1992.

Young, G. M., Minter, W., and Theron, J. N.: Geochemistry and palaeogeography of upper Ordovician glaciogenic sedimentary rocks in the Table Mountain Group, South Africa, Palaeogeogr. Palaeocl., 214, 323–345, doi:10.1016/j.palaeo.2004.07.029, 2004.

Young, S. A., Saltzman, M. R., Foland, K. A., Linder, J. S., and Kump, L. R.: A major drop in seawater $^{87}Sr/^{86}Sr$ during the Middle Ordovician (Darriwilian): Links to volcanism and climate?, Geol., 37, 951–954, doi:10.1130/G30152A.1, 2009.

Zhang, Z.-S., Yan, Q., and Wang, H.-J.: Has the Drake passage played an essential role in the Cenozoic cooling?, Atmos. Ocean. Sci. Lett., 3, 288–292, 2010.

Earth-Science Reviews 128 (2014) 122–138

Contents lists available at ScienceDirect

Earth-Science Reviews

journal homepage: www.elsevier.com/locate/earscirev

The role of palaeogeography in the Phanerozoic history of atmospheric CO_2 and climate

Yves Goddéris [a,*], Yannick Donnadieu [b], Guillaume Le Hir [c], Vincent Lefebvre [a], Elise Nardin [a]

[a] Géosciences-Environnement Toulouse, CNRS-Observatoire Midi-Pyrénées, Toulouse, France
[b] Laboratoire des Sciences du Climat et de l'Environnement, CNRS-CEA, Gif-sur-Yvette, France
[c] Institut de Physique du Globe de Paris, Paris, France

ARTICLE INFO

Article history:
Received 27 June 2013
Accepted 9 November 2013
Available online 16 November 2013

Keywords:
Carbon cycle
Climate
Palaeogeography
Phanerozoic
Weathering
Modelling

ABSTRACT

The role of the palaeogeography on the geological evolution of the global carbon cycle has been suspected since the development of the first global geochemical models in the early 80s. The palaeogeography has been rapidly recognized as a key factor controlling the long-term evolution of the atmospheric CO_2 through its capability of modulating the efficiency of the silicate weathering. First the role of the latitudinal position of the continents has been emphasized: an averaged low latitudinal position promotes the CO_2 consumption by silicate weathering, and is theoretically associated to low CO_2 periods. With the increase of model complexity and the explicit consideration of the hydrological cycle, the importance of the continentality factor has been recognized: periods of supercontinent assembly coincide with high pCO_2 values due to the development of arid conditions which weaken the silicate weathering efficiency. These fundamental feedbacks between climate, carbon cycle and tectonic have been discovered by pioneer modelling studies and opened new views in the understanding of the history of Earth's climate. Today, some of the key features of the Phanerozoic climate can be explained by: (1) continental drift; (2) small continental blocks moving to tropical belts; and (3) modulation of the climate sensitivity to CO_2 by palaeogeography changes. Those results emphasize the need for a careful process-based modelling of the water cycle and climate response to the continental drift.

Contents

1. Introduction

Palaeogeography and Earth climate are tightly linked. As noticed by Hay et al. (1990), the existence of a link between the latitudinal

* Corresponding author. Tel.: +33 5 61 33 26 15; fax: +33 5 61 33 25 60.
E-mail address: yves.godderis@get.obs-mip.fr (Y. Goddéris).

0012-8252/$ – see front matter © 2013 Published by Elsevier B.V.
http://dx.doi.org/10.1016/j.earscirev.2013.11.004

distribution of land mass and the continental climate has been first postulated by Lyell (1830), almost a century before the publication of the continental drift theory (Wegener, 1912). Assuming a constant land surface, Lyell (1830) proposes that filling the Arctic region with emerged continents at the expense of equatorial territories would result in a severe polar glaciation and in a drop of the global temperature. Then comes the continental drift theory (Wegener, 1912) and the prediction of Köppen and Wegener (1924) that if all continents are located in the equatorial area for a given past period, continental and shelfal markers of climate will all indicate warm conditions, making a strong case for a link between palaeogeography and climate.

Since the end of the seventies, an abundant literature deals with the link between continental configuration and climate. Land mass distribution modifies the regional and global climate (Gyllenhaal et al., 1991), through changes in the oceanic circulation (Kennett, 1977; von der Heydt and Dijkstra, 2006; Lagabrielle et al., 2009 and reference therein; Lefebvre et al., 2012; Zhang et al., 2012), albedo feedbacks (Hay et al., 1990; Horton et al., 2010), and direct impact on the precipitation/evaporation balance (Barron et al., 1989; Otto-Bliesner, 1995). In addition to geological features, climate modelling studies explore the role of the continental configuration on pCO_2 thresholds needed to explain ice/green-house successions (Barron and Washington, 1982; Crowley and Baum, 1991, 1995; Barron et al., 1993; Gibbs et al., 1997; Hyde et al., 1999; Herrmann et al., 2004; Donnadieu et al., 2006; Craggs et al., 2012; Horton et al., 2012; Spicer et al., 2008). However all these studies share a common characteristic: they prescribe atmospheric greenhouse gas levels. Specifically, CO_2 level is a boundary condition and is thus assumed to be an external forcing of the climate system, whatever the continental configuration.

But things are more complex. Since weathering of Ca–Mg silicates of crustal rocks consumes atmospheric CO_2 at a rate depending on the Earth's climate, CO_2 levels are necessarily depending on the palaeogeography at long-term scale. Basically, the rock mineral dissolution directly depends: (1) on the availability of water, thus on the continental area located within humid climatic belts; and (2) on the temperature, thus on the latitudinal distribution of the continents. Surprisingly, the interplay between palaeogeography and global carbon cycle has not been often studied in the recent years, despite the fact that it may be potentially a first order forcing of climate at the geological timescale. Instead of working on the geography effect, most of the efforts have been concentrated on the role of land plants (Berner, 2004), and of mountain building and physical erosion (Raymo et al., 1988; Raymo, 1991).

In this contribution, we propose an overview of the studies devoted to the impact of palaeogeography on the long-term carbon cycle ($>10^5$ yrs). We show that continental precipitations and runoff are highly sensitive to the palaeogeography. We demonstrate that the continental configuration is a first order factor controlling the atmospheric CO_2 level and the Earth's climate evolution.

2. Pioneer modelling studies of the impact of palaeogeography on the global carbon cycle

According to the Earth thermostat theory (Walker et al., 1981), for a given solid Earth CO_2 degassing, the total CO_2 consumption by continental weathering should be the same, whatever the location of continents. This is a direct consequence of the short response time of carbon and alkalinity in the ocean–atmosphere system, respectively 200 and 3 kyr (François and Goddéris, 1998) and of the negative feedback exerted by climate on weathering (Walker et al., 1981). The CO_2 consumption by silicate weathering is always tracking the CO_2 supply by solid Earth degassing, to avoid too large CO_2 fluctuations and repeated climatic catastrophe (Berner and Caldeira, 1997).

Marshall et al. (1988) first proposed that the palaeogeography might be a key parameter of the evolution of the geological carbon cycle (Table 1). They found that atmospheric CO_2 must be at high levels when most of the continents are located around the poles. Conversely, CO_2 must be low and global climate cold when continents are located around the equator. They argue that this is a direct consequence of a promoted CO_2 consumption by continental silicate rock dissolution when continents are located in the warm equatorial belt. Because temperatures are higher at the equator than at the pole, Marshall et al. (1988) note that the weatherability (i.e., the susceptibility to weathering) is higher when continents are close to the equator. As a consequence, the same total weathering flux will be reached at a much lower CO_2 level compared to a world where continents are located at the pole. Although their study was conceptual with generic continental configurations, Marshall et al. (1988) had already proposed that the late Precambrian glaciations might have been promoted by an equatorial location of the continents.

Worsley and Kidder (1991) further explore the Marshall et al. (1988) hypothesis through additional qualitative considerations. Similarly to Marshall et al., they suggest that a ring world (all continents located along the equator) should be characterized by lower atmospheric CO_2 (and hence colder global conditions) than a cap world (all continents around the poles). Provocatively, Worsley and Kidder (1991) even propose that the averaged latitude of the continents alone specify CO_2 levels.

Marshall and collaborators were the first to couple a process-based climate model with a mathematical description of the continental weathering. The climate model used was quite simple: an energy-balanced model (EBM). This model calculates the Earth surface temperature as a function of latitude accounting for the vertical budget of energy and for the meridional heat transport. Similar models, coupling a description of the carbon cycle with a zonal energy-balanced model, have been used to explore the Phanerozoic CO_2 history (François and Walker, 1992; Goddéris and François, 1995; Goddéris and Joachimski, 2004; Tajika, 2007). However, it is important to note that if EBM models are reliable in terms of temperature predictions, they lack a physical description of the water cycle and, as such, are not able to calculate accurately the runoff, a key parameter of continental weathering (Dessert et al., 2003; Oliva et al., 2003). To overcome this limitation, a new generation of models has been developed.

3. Exploring the role of palaeogeography on the water and carbon cycle

Continental silicate weathering and associated CO_2 sink are heavily dependent on continental runoff, which is the difference between rainfall and evapotranspiration. As such, the relationship between palaeogeographical setting and hydrological cycle must be understood, and this was beyond the abilities of the energy-balanced models previously used. The first study exploring the role of the continent distribution on the hydrologic cycle with an appropriate model was performed in 1989 by Barron and co-authors. They note that the water cycle is an essential part of the geochemical cycles (weathering, erosion, sedimentation), and that too much attention has been paid to temperature reconstructions at the expense of water cycle reconstructions. They explore the role of palaeogeography on the water cycle with the NCAR Community Climate Model (spatial resolution of 7.5° long × 4.5° lat). Contrary to energy-balanced models, the CCM includes a calculation of evaporation and condensation, and cloud cover. Such 3D climate models (also called General Circulation Models or GCM) explicitly simulate the water cycle, calculating the evaporation and rainfall on a 2-D map of the world, and the three-dimensional transport of water vapour in the atmosphere. Their main finding is that continental positions can strongly alter the hydrologic cycle (rainfall and runoff) if their positions affect the supply of moisture to the atmosphere. This is particularly the case in a simulation assuming a continuous belt of continents between 15°S and 15°N. Compared to the present day, this ring world is 8 °C globally warmer, but global rainfall is maintained at its present day rate because the area of intense evaporation along the equator is lacking oceanic surfaces. Because of this intense continental evaporation, continental runoff

Table 1
A synthesis of numerical models exploring the role of palaeogeography on the geological carbon cycle.

Model	Palaeogeography	Mechanistic calculation of the air temperature	Mechanistic calculation of the water cycle component	Spatial resolution	Parametric calculation of the air temperature	Parametric calculation of the continental runoff
Marshall et al. (1988)	Conceptual	X	X	Zonal		
Barron et al. (1989)	Conceptual and realistic	X	X	7.5°long × 4.5° lat (atmosphere) slab ocean		
Worsley and Kidder (1991)	Conceptual					
Otto-Bliesner (1995)	Realistic	X	X	11.6°lat × 11.25°long (atmosphere) slab ocean		
Gibbs et al. (1997)	Realistic	X	X	4.5°lat × 7.5°long (atmosphere) slab ocean		
Berner (2004) and all GEOCARB versions				Global, no spatial resolution	X	X
Donnadieu et al. (2004)	Realistic	X	X	10°lat × 50° long (atmosphere) zonal dynamic ocean		
Donnadieu et al. (2006, 2009), Goddéris et al. (2008a, 2008b), Nardin et al. (2011) GEOCLIM model	Realistic	X	X	4.5°lat × 7.5°long (atmosphere) slab ocean		

decreases by a factor of 2 in this extreme ring configuration, with respect to present day runoff. Despite lower continental rainfall, a world with all the continents located beyond 50° latitude (polar location, cap world) displays a much higher runoff rate. These results contradict the finding of Worsley and Kidder (1991). If weathering is firstly dependent on runoff, then a cap world would be more weatherable than a ring world, thus characterized by a lower CO_2 level.

Otto-Bliesner (1995) further investigates the palaeogeographical forcing of runoff by running the NCAR 3D atmospheric general circulation model (i.e., AGCM) of the climate for 14 time slices spanning the Phanerozoic. The palaeogeographical reconstructions are taken from Scotese (www.scotese.com). Aiming at isolating the palaeogeographical effect on the global climate with a focus on the water cycle, Otto-Bliesner (1995) has fixed the CO_2 level at 280 ppmv, the solar constant at its present day value, and has assumed flat continents (no mountains) covered by rocky deserts. She finds that the relationship between runoff and palaeogeography is critical but more complex than the Marshall et al. (1988) and Worsley and Kidder (1991) simple scheme. The size, and not only the location of continents, must be considered. As long as continents are small and widely dispersed, precipitations can reach easily the inland areas. As a consequence, rainfall is not a limiting factor for runoff. Rather evaporation becomes the limiting factor, especially if the continents are located in the tropics, as already noticed by Barron et al. (1989). In this specific configuration (small continents and low latitude averaged location), runoff stays low, being constrained by the intense evaporation and responds weakly to global warming induced by a given CO_2 rise. Conversely, if small continents are moving poleward, the associated decreasing temperature induces a decrease in evaporation, possibly promoting runoff, and hence CO_2 consumption by weathering. Once cratons are aggregated into large continents (such as the Pangea), inland rainfall is strongly reduced and becomes limiting for runoff, instead of evaporation. Runoff is kept at low levels but its response to global warming events becomes stronger, forced by the rise in rainfall. Otto-Bliesner (1995) evidences the complex interplay between latitudinal location of the continents and their size. She emphasizes that the sensitivity of runoff to global warming might be very small for particular continental configuration, namely for small continents located at low latitudes.

In 1991, Bluth and Kump paved the way to a spatially-resolved calculation of the past weathering rates by defining lithological maps for the geological past, with a resolution of 2°long × 2°lat. Using their Quaternary map, they first calculated the weathering rates and fluxes during the last glacial maximum (Gibbs and Kump, 1994). In this study, the authors emphasize the importance of accounting for the spatial distribution in runoff when reconstructing past weathering rates. Going then into the distant past, Gibbs et al. (1999) explicitly calculate the spatial distribution of the weathering rates of the continents over the last 250 Myr, using a 3D general circulation model for the atmosphere (GENESIS v1.02). The solar constant is kept at present day value and two sets of simulation are performed: one assuming a constant CO_2 level of 340 ppmv, and one at high CO_2 taken from simulations of the GEOCARB geochemical model (Berner, 1991). The continental runoff and temperature maps generated by the climate model for each time slice are used to calculate weathering rate for each of the 5 main lithological types (granite, basalt, carbonate, shale and sandstone). The fundamental conclusion of their work is that the overarching effect of continental collision and accretion is increased continentality (first identified by Kutzbach and Gallimore in 1989 for Pangean climates), which inhibits runoff and hence CO_2 consumption by silicate weathering. Times of super continent assembly should correspond to periods of high pCO_2, keeping all other parameters constant, such as the solid Earth degassing rate. Overall, chemical erosion is limited by the supply of water, which depends heavily on the palaeogeographical setting (super continent versus dispersed continents).

4. Coupling climate and carbon cycle

4.1. GEOCARB and similar models

All the above models (Marshall et al., 1988; Worsley and Kidder, 1991; Otto-Bliesner, 1995; Gibbs et al., 1999) give insights into the role of palaeogeography on silicate weathering without computing the CO_2 levels. This has been achieved by another type of model, the most cited being the GEOCARB model (versions I, II, III, and GEOCARBSULF; Berner, 2004, 2006). The models of the GEOCARB family compute the Phanerozoic atmospheric CO_2 through the solving of a set of equations, the most important being the carbon and alkalinity balance at the million year timescale, the carbon isotopic balance, the expression of silicate weathering as a function of environmental parameters such as the vegetation cover, physical erosion, and climate. The GEOCARB models being zero-dimensional, they only calculate a mean global temperature and runoff, without resolving the spatial distribution of the continental climate. In details, mean global runoff and temperature are calculated through the solving of two equations.

$$T_{glob} = T_0 + \Gamma \log(pCO_2) - W_s \frac{t}{570} + geog \quad (1)$$

$$R_{glob} = R_0 \left[1 + Y\left(T_{glob} - T_0\right)\right] f_D \quad (2)$$

In Eq. (1), T_0 is the present day global air temperature, Γ is a parameter fixing the sensitivity of temperature to CO_2 variations, pCO_2 is the atmospheric CO_2 partial pressure in PAL (Pre-industrial Atmospheric Level), W_s is the rate of temperature rise with time related to the increase in the solar constant. In this equation, two parameters are functions of the continental configuration. Firstly the factor *geog* is the correction applied to the calculation of T_{glob} in response to continental drift. This factor is taken from Otto-Bliesner (1995) and is equal to the mean air continental temperature anomaly (relative to the present day control run) for each geological time slice from the simulations described above ($pCO_2 = 1$ PAL, no mountains, present day solar constant). Second, Γ is the sensitivity of the air temperature to a CO_2 change for a given palaeogeography. Two values are adopted for the Phanerozoic: 3.3 for a priori warm climate modes (before 340 Ma, and between 260 and 40 Ma, corresponding to a global warming of 2.3 °C for a CO_2 doubling), and 4 for other periods assumed to be cold (2.8 °C warming for a CO_2 doubling). Those values come from GCM simulation at various CO_2 levels for the present day (assumed to be representative of the Phanerozoic cold modes) and the mid-Cretaceous (a model for warm modes) configurations (Hay et al., 1999; Kothavala et al., 1999). Recently, Park and Royer (2011) have revisited the value of the Γ parameter, increasing it strongly during the cold phase of the Phanerozoic (Γ=8.7 to 11.5, corresponding to a 6 to 8 °C warming for a CO_2 doubling). Whatever the absolute values, it is important to note that the values of *geog* and Γ are fixed prior to the GEOCARB simulations, and do not evolve as a function of the calculated atmospheric CO_2. They are thus forcing functions and may introduce some inconsistency in the model: for instance low calculated CO_2 may be coeval with low climate sensitivity Γ.

In Eq. (2), R_0 is the present day runoff, Y is a factor fixing the sensitivity of runoff to air temperature, and f_D is an additional correction applied to runoff in response to continental drift. Y is fixed to 0.025 during warm climate modes (before 340 Ma and between 260 and 40 Ma, corresponding to a 2.5% increase in global runoff for a global mean temperature rise of 1 °C, Kothavala et al., 1999), and to 0.045 for other periods corresponding to a 4.5% increase in global runoff for a global mean temperature rise of 1 °C (Hay et al., 1999), a value close to the 4% estimated for the present day world by Labat et al. (2004) from river runoff time series. f_D is taken from the Otto-Bliesner (1995) simulations and is equal to the runoff calculated for each timeslice assuming 1 PAL of CO_2, flat continents and a present-day solar constant divided by the present day runoff.

These two equations are critical. They define how these key parameters of the silicate weathering rate (temperature and runoff) evolve through Phanerozoic times in response to CO_2 and tectonic changes. Being zero-dimensional models, GEOCARB and GEOCARBSULF cannot explicitly account for the role of palaeogeography, despite its potential key role (Marshall et al., 1988; Worsley and Kidder, 1991; Otto-Bliesner, 1995). To overcome this critical limitation, the GEOCARB family of models includes several parameters derived from climate evolution studies (such as Otto-Bliesner, 1995), in such a way that the role palaeogeography is somehow included (Γ, *geog*, f_D, and Y to some extent). The benefit of the use of these parameters to calculate temperature and runoff instead of physically resolving the role of palaeogeography is the gain in time-computation. But the risk of introducing inconsistencies, or overestimating or underestimating the role of palaeogeography cannot be neglected.

4.2. Sensitivity of the GEOCARB family of models to palaeogeography

Most of the other published models calculating past CO_2 levels use the same formalism for the impact of palaeogeography on climate (Wallmann, 2001, 2004) or simply neglect the potential effect of continental drift (Bergman et al., 2004).

What is the contribution of palaeogeography to the Phanerozoic CO_2 signal calculated by the GEOCARB type of models? To answer this question, we built a simplified version of the GEOCARB model (see Appendix A). When running the reference simulation for 21 time slices spanning the Phanerozoic, our simplified model version reproduces the general features of the GEOCARB family of models (Fig. 1): high CO_2 levels in the early Paleozoic, then a rapid decrease starting at 400 Ma. Low levels are predicted between 350 and 260 Ma. Then CO_2 rises again up to 10 times the present day values around 100 Ma. Finally, the late Cretaceous and Cenozoic are characterized by an overall CO_2 decrease towards the present day low level. We refer to this Phanerozoic trend as the "double-peak" feature in the following. Slight differences can be observed between this CO_2 curve and the latest GEOCARBSULF output, particularly higher levels around 300 and 100 Ma (Fig. 1). Indeed, we do not account for the role of the sulfur cycle, and silicate weathering laws and apparent activation energies for silicate dissolution are slightly different. Moreover, the temporal evolution of the continental area is taken from reconstructions by Blakey for the Paleozoic, Besse and Fluteau and Sewall for the Mesozoic and Cenozoic and differs thus slightly from the forcing used in GEOCARB. Finally, the time resolution of our simulations is much lower than Berner (2006). Anyway, our objective is not to reproduce precisely the GEOCARBSULF output, but rather to explore the contribution of the palaeogeographical setting to the "double-peak" evolution of atmospheric CO_2.

Then, we run our version of GEOCARB by fixing successively all parameters to their present day value except the parameters depending on the palaeogeography. At the end of this procedure (GLOBAL#4 simulation), only *geog*, f_D, Γ, and Y are allowed to fluctuate over the Phanerozoic. Solid Earth degassing rate is held constant and the organic carbon subcycle is assumed at steady state, which means that it does not impact the CO_2 level. A linear rise of the solar constant with time is still assumed. By doing so, we find that the double peak feature is mainly due to: (1) the impact of land plant evolution on continental weathering; (2) the variable volcanism; and (3) the fluctuations in the organic carbon cycle. When accounting only for the palaeogeographical parameters and the solar constant evolution, the major features of the GEOCARB CO_2 curve disappeared. The CO_2 displays now a general declining trend from about 6 PAL in the Cambrian to 1 PAL at present day, mainly forced by the rise in the solar constant. A sharp decrease around 460 Ma is predicted. This decline is related to the prediction of very high continental temperatures at 458 Ma in the simulations of Otto-Bliesner (1995), increasing sharply the *geog* factor, promoting silicate weathering, and thus forcing the predicted CO_2 to decrease to maintain the balance between silicate weathering and volcanic degassing. This warm climate is the result of the mean low latitude of the continental blocks during this period (Otto-Bliesner, 1995), and has been confirmed by more recent simulations (Nardin et al., 2011).

Corresponding calculated air temperatures are almost constant over the whole Phanerozoic, close to 14 °C (Fig. 2, GLOBAL#4 simulation), while runoff is predicted to be always larger than at present day, except around 250 Ma where it is very close to the present day value (Fig. 3, GLOBAL#4 simulation).

Overall, the sensitivity of the GEOCARB family of models to palaeogeography is low. The double-peak feature, which is the most visible feature of the CO_2 curve, is thus weakly dependent on the palaeogeographical setting.

4.3. The GEOCLIM model and the palaeogeography

4.3.1. Previous investigations with GEOCLIM

A new step in the carbon-climate modelling is achieved with Donnadieu et al. (2004) who introduce a new method to calculate the atmospheric CO_2 in the specific context of a supercontinent breakup at the end of the Proterozoic. The model they used, the first seed of the GEOCLIM model, couples a global carbon–alkalinity cycle to a climate model of intermediate complexity with a coarse spatial resolution (50°long × 10°lat). Continental weathering rates are resolved spatially, allowing to account explicitly for the continental configuration. Donnadieu et al. (2004) show that the Rodinia super continent,

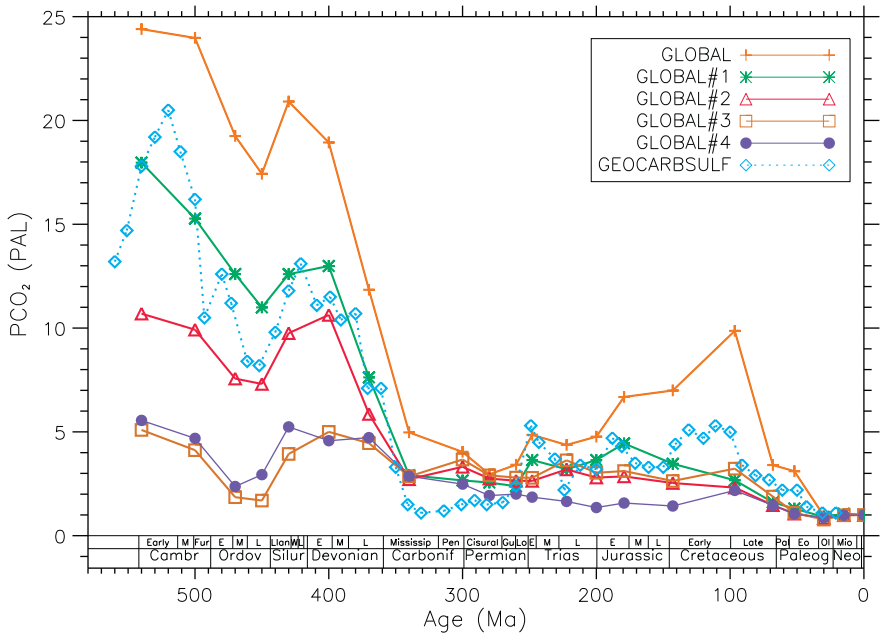

Fig. 1. Evolution of atmospheric CO_2 calculated by zero-dimensional models of the GEOCARB type. The curve labelled GEOCARBSULF is taken from Berner (2006). GLOBAL is the simplified version of the GEOCARB model built for the present purpose. The GLOBAL label reminds that this model includes a zero-dimensional description of the global climate (only global air temperature and runoff are calculated). GLOBAL#1 is the same simulation where the solid Earth degassing is held constant. GLOBAL#2 is the same as GLOBAL#1, but with the organic carbon subcycle always assumed at steady-state. GLOBAL#3 further assumes a constant impact of land plants on weathering (same as today). Finally GLOBAL#4 is the same than GLOBAL#3 but lithology and erosion rates are kept at their present day values. The only forcing functions of GLOBAL#4 are thus the rising solar constant and the palaeogeographical changes.

although located close to the equator, was characterized by low runoff, low weathering rates and hence high CO_2 (1800 ppmv). This is the result of the intense continentality, a finding in agreement with Gibbs et al. (1999). The subsequent breakup of the super continent into small pieces along the equator promotes the weatherability. The steady-state CO_2 level required for weathering to balance the solid Earth degassing equals about 500 ppmv in the dispersed continental configuration, corresponding to the onset of much colder climatic conditions compared to the super continent configuration (8 °C global cooling). When the weathering of freshly erupted basalts is accounted for, the breakup of the Rodinia might even be the ultimate cause for the onset of the Neoproterozoic snowball glaciations (Donnadieu et al., 2004).

The Donnadieu et al. (2004) model was a first 'low-resolution' synthesis of the ideas developed by Marshall et al. (1988) and Gibbs et al. (1999). Evolving from this first model, GEOCLIM is a numerical model of the next generation able to calculate the past geological CO_2 levels (Fig. 4). It couples an 11-box model of the carbon–alkalinity–phosphorus–oxygen cycles (Goddéris and Joachimski, 2004) to the 3-dimensional climate model FOAM (Jacob, 1997). At each time step of the calculation and for any CO_2 level, the output of the FOAM general circulation model is used to estimate the coeval air temperature and

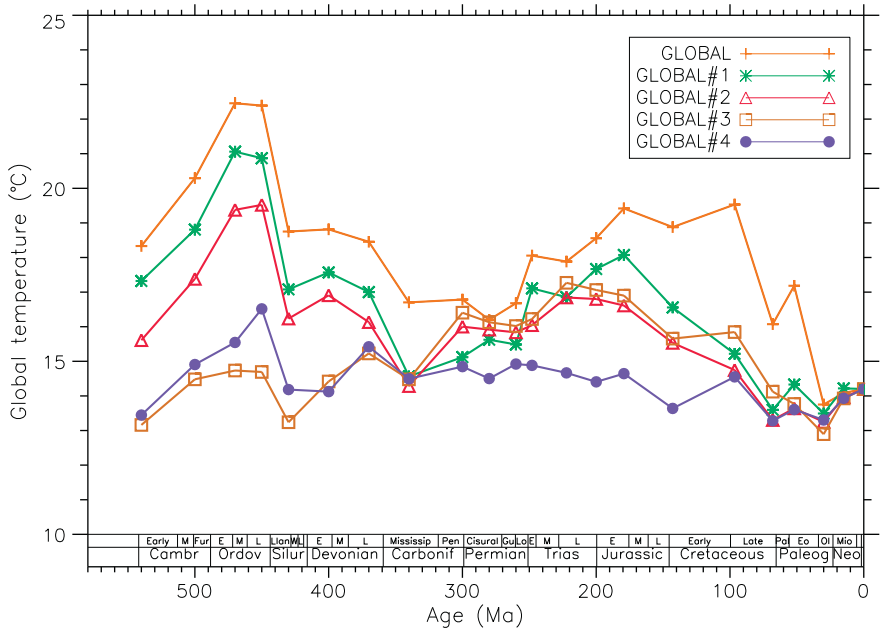

Fig. 2. Globally averaged surface temperature calculated in the various GEOCARB-type simulations described in Fig. 1. The curve GLOBAL#4 stands for the temperature change induced by the rising solar constant and the palaeogeographical changes solely.

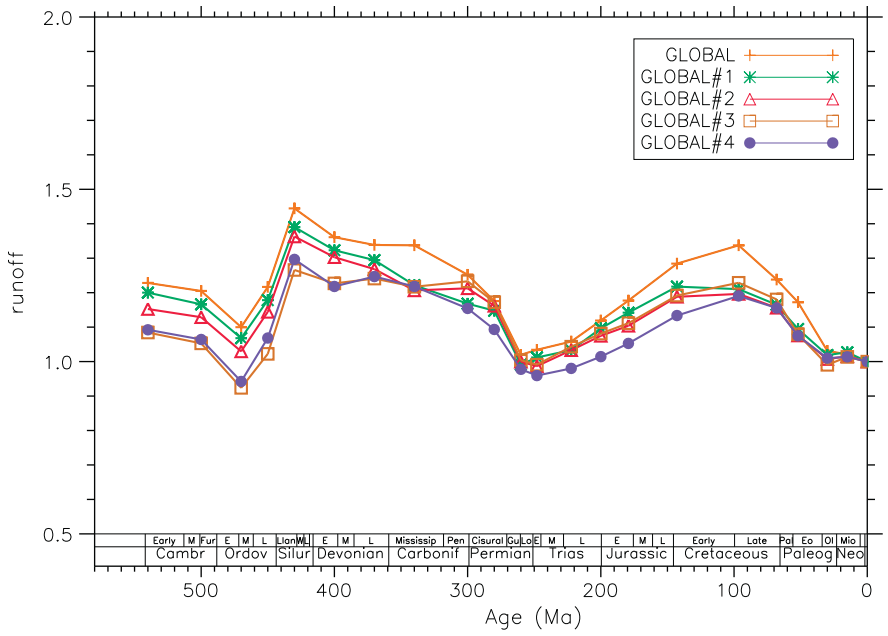

Fig. 3. Globally averaged continental runoff (normalized to present day) calculated in the various GEOCARB-type simulations described in Fig. 1. The curve GLOBAL#4 stands for the runoff change induced by the rising solar constant and the palaeogeographical changes solely.

continental runoff with a spatial resolution of 7.5°long × 4.5°lat. While GEOCARB is a zero-dimensional model (only able to calculate global averages) in which corrective factors have been introduced from several offline GCM simulations (Otto-Bliesner, 1995), GEOCLIM explicitly resolve the impact of palaeogeography coevally with the calculation of the atmospheric CO_2 level. It is important to note that the two methods (GEOCARB vs GEOCLIM) are fundamentally different. In GEOCLIM, temperature, runoff, and more generally the hydrologic cycle, are resolved physically by the GCM (conservation of mass and energy in the atmospheric system) in GEOCLIM while GEOCARB relies on parametric laws. Furthermore, in GEOCARB, *Y* and *geog* are fixed assuming a priori the timing of warm and cold climatic modes. In GEOCLIM, the sensitivity of runoff to temperature and of temperature to CO_2 is a function of the continental configuration, and fluctuates over the Phanerozoic. Furthermore, GEOCLIM allows the discrimination between continental and global temperatures.

In the following discussion, the continental runoff and its dependency on the continental configuration will be a key parameter. The mean global runoff calculated by the FOAM GCM for the present day configuration equals 330 mm/yr, in close agreement with the observations (313 mm/yr, UNH/GRDC database). Furthermore, the FOAM GCM is able to reproduce the observed spatial distribution of the continental

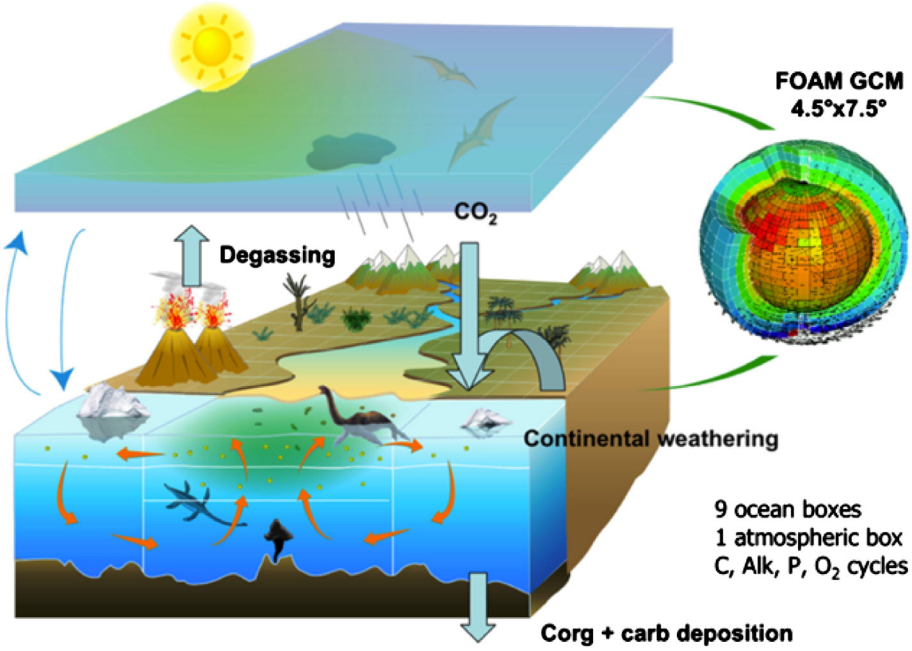

Fig. 4. Schematic description of the GEOCLIM model. A box model describing the geological cycles of carbon and alkalinity is coupled to the 3D FOAM climate model. Temperature and runoff calculated by the climate model are used to estimate the continental weathering fluxes, including the CO_2 consumption by silicate weathering at each time step with a spatial resolution of 7.5° long × 4.5° lat. For each continental configuration spanning the whole Phanerozoic, the GEOCLIM model is run until a steady-state is reached. Each continental configuration can thus be associated to a calculated CO_2 level, depending on other parameters such as the solid Earth degassing rate.

runoff, the main discrepancy between the model and the data being a slight underestimation of the runoff for the northern part of South America by the model (Fig. 5). Anyway, in terms of runoff predictions, the GEOCLIM model appears to be quite robust.

Several studies have been undergone with the GEOCLIM model, keeping all parameters constant but the continental configuration and the slowly rising solar constant. Nardin et al. (2011) demonstrate that the drifting of the Baltica, Laurentia, and Siberia across the equatorial belt promotes continental weathering. As a consequence, CO_2 goes down since the Middle Ordovician from about 5600 ppmv to 2800 ppmv to maintain the balance between silicate weathering and the solid Earth degassing. About 70% of this CO_2 drop is fully related to the drifting of continents, confirming the key role played by palaeogeography. The remaining 30% are due to enhanced young volcanic rock weathering (Nardin et al., 2011). The lowest CO_2 level is reached at the end of the Ordovician/beginning of the Silurian. Then CO_2 rises again in excess of 6000 ppmv in the Early Devonian because of the accretion of the Baltica and Laurentia. The continental configuration thus promotes the onset of colder climatic conditions from the Middle Ordovician to the Early Silurian, in agreement with many geological indicators (Nardin et al., 2011).

Still using the GEOCLIM model, Donnadieu et al. (2006) and Goddéris et al. (2008a) have shown that a <10° northward drift of the Pangea supercontinent from the Carnian to the Rhetian induces a drastic decrease in atmospheric CO_2 from about 3000 ppmv down to 800 ppmv in the late Triassic. This cooling was related to the specific shape of Pangea and does not involve any continental break up process. The continental surface located in the tropical humid zone is almost doubled when Pangea drifts 10° north. Silicate weathering is promoted and CO_2 goes down to maintain the carbon balance. This is in agreement with sedimentary $\delta^{18}O$ data which predicts a global cooling of 3.7 °C, closely matching the 3.3 °C calculated by GEOCLIM. When accounting for the continental drift, what matters is not only the latitudinal location of the continents, but also their size and our ability to reconstruct accurately the past water cycle.

An improvement of the GEOCLIM model is the coupling with a global dynamic vegetation model. Vegetation, which responds to the continental drift, can change the albedo of the continental surfaces, the cycling of water through enhanced evapotranspiration, and the roughness of the continents. All these factors may change the temperature and precipitation patterns, and hence the weathering rates and the calculated CO_2 level. Le Hir et al. (2011) and Donnadieu et al. (2009) have both demonstrated that the key climatic effect of land plants with land plants is to modify the surface albedo. For instance, in the Devonian, the colonization of continents by plants decreases the albedo, resulting in a global warming trend. This global warming promotes CO_2 consumption by continental weathering, and CO_2 is forced to decline to maintain the carbon cycle balance (Le Hir et al., 2011).

4.3.2. Exploring the impact of palaeogeography on the Phanerozoic CO_2 level

GEOCLIM is run for the 21 time slices covering the Phanerozoic. The model is run until steady-state is reached, meaning that continental silicate weathering matches the prescribed solid Earth degassing. We calculate the corresponding atmospheric CO_2 and climate for each of the 21 time slices. The simulations account for dynamic vegetation by coupling the FOAM GCM to the LPJ biospheric model (Sitch et al., 2003; Donnadieu et al., 2009). The FOAM GCM is used in mixed-layer mode, i.e., the atmospheric model is linked to a 50-metre mixed-layer ocean, which parameterizes heat transport through diffusion. Ocean surface temperatures are thus calculated, but not the oceanic circulation. A

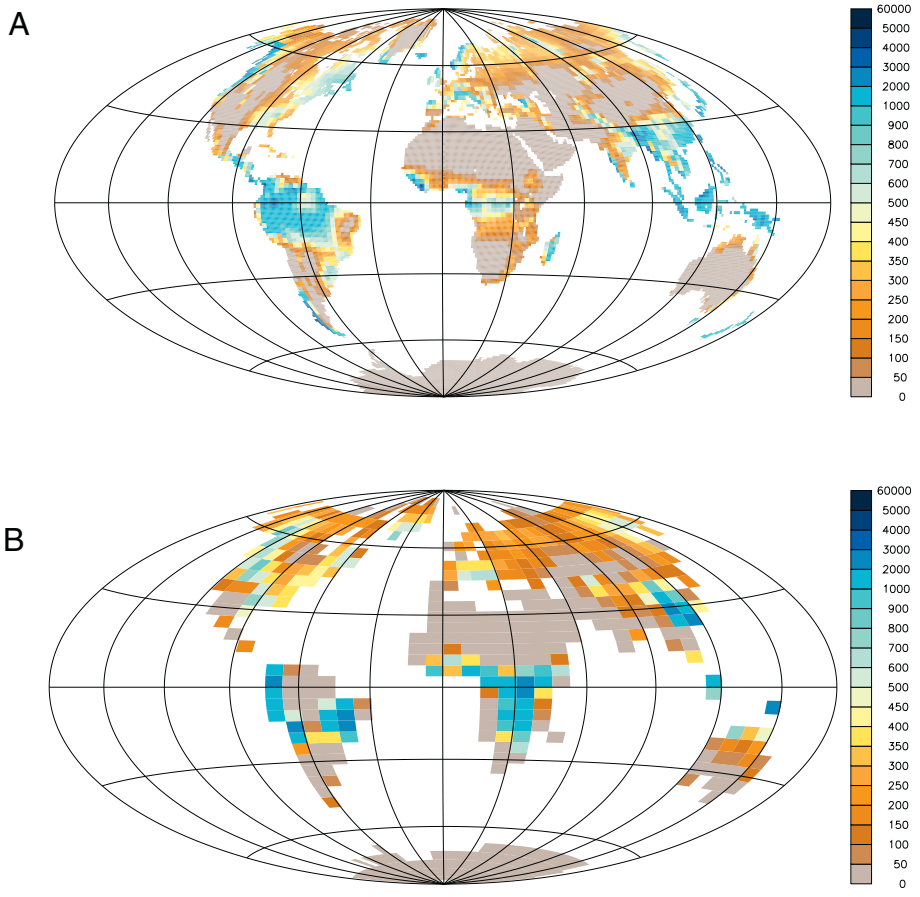

Fig. 5. (A) Present day observed distribution of the mean annual continental runoff (mm/yr) (UNH/GRDC: Composite runoff fields V1, 0.5°lat × 0.5°long). (B) Present day distribution of the mean annual runoff (mm/yr) calculated by the FOAM GCM under 280 ppmv CO_2.

first set of simulations is run assuming the palaeogeography and the increase in the solar constant as the unique forcing functions (GEOCLIMtec simulations). The second set of simulations accounts additionally for the role of land plants on weathering, for a variable degassing, and for imbalances in the organic carbon subcycles, all these forcing functions coming from the GEOCARB model and added in GEOCLIM (GEOCLIM simulations).

Accounting only for palaeogeography and the linear rise in the solar constant, the GEOCLIM CO_2 curve (GEOCLIMtec, Fig. 6) differs considerably from the CO_2 history produced by the GEOCARB family of models. A huge drop in CO_2 is predicted during the Ordovician and an ample CO_2 peak is calculated between 280–220 Ma. CO_2 levels are much higher before the mid-Cretaceous. Very low CO_2 levels dominate after 130 Ma (Fig. 6). The palaeogeographical imprint on the CO_2 history is major, contrasting with the GEOCARB-type simulation in which the palaeogeography has only a second order impact on the CO_2 level. High CO_2 levels at the beginning of the Phanerozoic are forced by the polar location of most of the continents. As identified by Nardin et al. (2011), atmospheric CO_2 then decreases due to the northward drift of Laurentia, Baltica and Siberia. This period of change is followed by a period of relatively constant CO_2 levels, suggesting that the palaeogeographical configuration has played a little role in the onset of the Permo-Carboniferous glacial episode. The end Permian to middle Triassic period is characterized by very high CO_2 levels, promoted by the assembly of Pangea resulting in a dry continental climate. CO_2 abruptly declines in the latest Triassic in response to a northward drift of Pangea (Donnadieu et al., 2006; Goddéris et al., 2008b). A striking feature is the persistent low CO_2 levels predicted for the Jurassic and Cretaceous. If palaeogeography is the only forcing factor, the post-Triassic dispersed continental configuration should favour the onset of a globally cold climatic mode since the Jurassic. The end-Cretaceous and beginning of the Cenozoic are even marked by CO_2 levels below the present day value.

Part of the GEOCLIM CO_2 signal is forced by the response of runoff to palaeogeography. The amplitude of change in runoff over the Phanerozoic is larger in GEOCLIM (both for GEOCLIM and GEOCLIMtec simulations) and in the simulations performed by Gibbs et al. (1999) compared to the simulations of Otto-Bliesner (1995) (Fig. 7). Furthermore, in Otto-Bliesner (1995), the runoff is generally higher than at present day, except for the Permo-Triassic period where it is close to the present day value. This explains partly why the CO_2 levels calculated by GEOCARB (GLOBAL#4 run, only solar constant and palaeogeography changing) are much lower than in the GEOCLIM run (GEOCLIM run) (Fig. 8). Consistently with Gibbs et al. (1999), the GEOCLIM runoff is conversely generally lower than at present day, at least before the mid-Cretaceous. Consequently, the GEOCLIM CO_2 is higher, because weathering is partly inhibited. The dry peak of the Permo-Triassic is also much more ample in more recent GCM simulations than in Otto-Bliesner (1995), explaining the existence of a calculated CO_2 peak (global runoff is below 60% of the present day value).

It is not easy to identify a unique cause for the calculated CO_2 features by GEOCLIM. Considering the GEOCLIMtec simulation, where continental drift is the sole forcing function, a plot of the calculated atmospheric CO_2 versus the total continental surface allows us to identify at least three groups of points (Fig. 9A). The first group has a standard behaviour ("standard" pool): atmospheric CO_2 decreases gently with the continental surface. More continental surface implies more silicate weathering, and hence less CO_2. Then the second group displays a range of high CO_2 values despite a roughly constant continental surface. This is the case for the 260–220 Ma time window and for the early Phanerozoic. These points define the "warm" Phanerozoic pool. Finally, a last group displays very low CO_2 levels whatever the total continental size. This group is identified here as the "cold" pool and covers the end of the Phanerozoic, starting from the middle Cretaceous.

The existence of a "warm" pool is linked to the aridity developing during the assembly of the Pangea super continent (Fig. 9B), but not only. This "warm" pool is also the consequence of a weak fraction of emerged continents in the warm and humid equatorial zone (10°S–10°N), where modelled weathering fluxes are maximized (Fig. 9C). This is the case during the Pangea phase and also during the early Phanerozoic. Consequently, the global weathering rates are inhibited and CO_2 rises. The existence

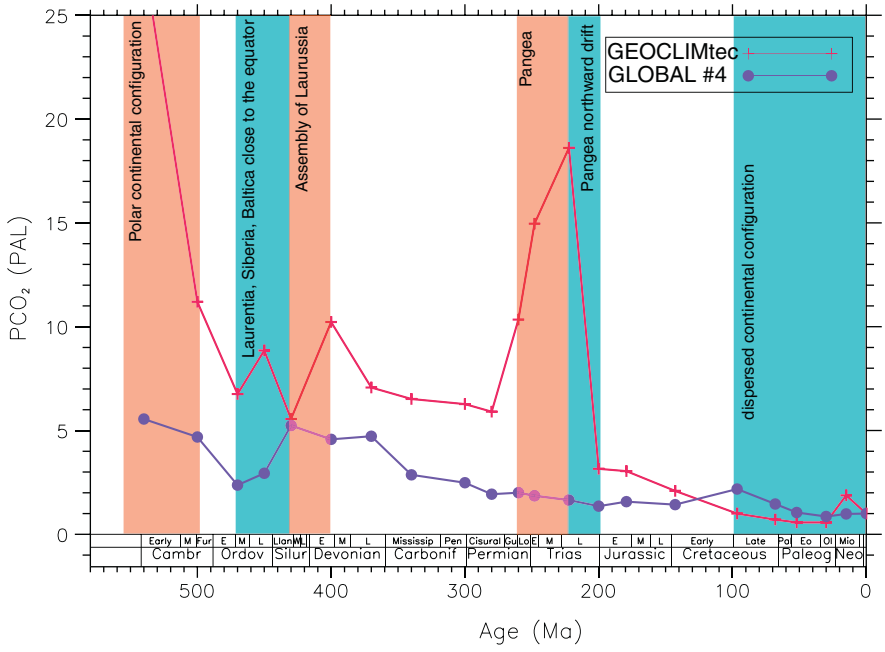

Fig. 6. Calculated evolution of the atmospheric CO_2 level over the Phanerozoic. The curve GLOBAL#4 stands for the CO_2 evolution induced by the rising solar constant and the palaeogeographical changes solely in a GEOCARB-type simulation. Similarly, the GEOCLIMtec curve is the output of the GEOCLIM model when the only forcings are the solar constant and the palaeogeographical changes. Accounting for the spatial distribution of the rainfall and temperature (and hence of weathering) in GEOCLIM impacts strongly on the calculated CO_2 history, suggesting that the palaeogeographical setting is a first order forcing function of the Phanerozoic climatic evolution. Red boxes figurate periods where the palaeogeography acts as a warming forcing function, promoting high CO_2 levels. Conversely, blue boxes stand for period where the continental configuration acts as a cooling forcing function. The ultimate causes for these trends are written in each box.

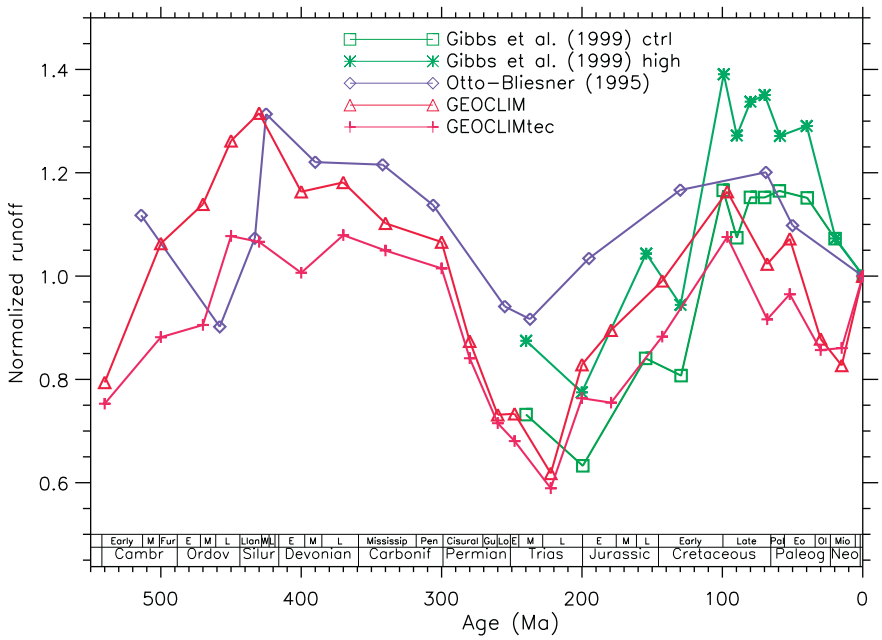

Fig. 7. Time evolution of the global runoff calculated by 3D climate models. The Gibbs et al. (1999) ctrl simulation has been performed assuming a constant 340 ppm of CO_2 and moving continents. The Gibbs et al. (1999) high simulation was performed assuming variable CO_2 taken from GEOCARB. The Otto-Bliesner (1995) simulation was performed assuming 280 ppm of CO_2. Finally, GEOCLIM and GEOCLIMtec are respectively the output of the full GEOCLIM simulation, and of a GEOCLIM simulation where the only forcings are the rising solar constant and the palaeogeography.

of a "cold" pool since the middle Cretaceous is linked to the ability of the Earth system to sustain an intense runoff over large continental surfaces (Fig. 9B). This is true even if the continental surface in the equatorial area stays generally below the mean Phanerozoic value. Runoff is no more dependent on the emerged continental size and stays at a high value. Since about 90 Ma, the continental configuration (highly dispersed continents, with only small polar continents) maintains high runoff and hence high CO_2 consumption by silicate weathering, forcing the Earth system into a cold state.

Consistently with Otto-Bliesner (1995), we found a dependence of runoff on the averaged latitudinal location of the continents (Pearson correlation coefficient 0.60 in the GEOCLIMtec simulation) (Fig. 10A). The highest runoff rates coincide with the highest averaged latitudinal location. At first glance, this result is in agreement with previous calculations performed with generic continental configurations in which an equatorial "ring" world (extending from 17°S to 17°N) was characterized by low global runoff (Hay et al., 1990). Indeed, large continental surfaces located along the equator may inhibit the evaporation in the tropical convergence zone, decreasing the global runoff. However, in our simulations, the increase in global runoff with the mean latitude of the continents can be explained by simple "geometric" consideration. Whatever the considered period, runoff is always minimal between

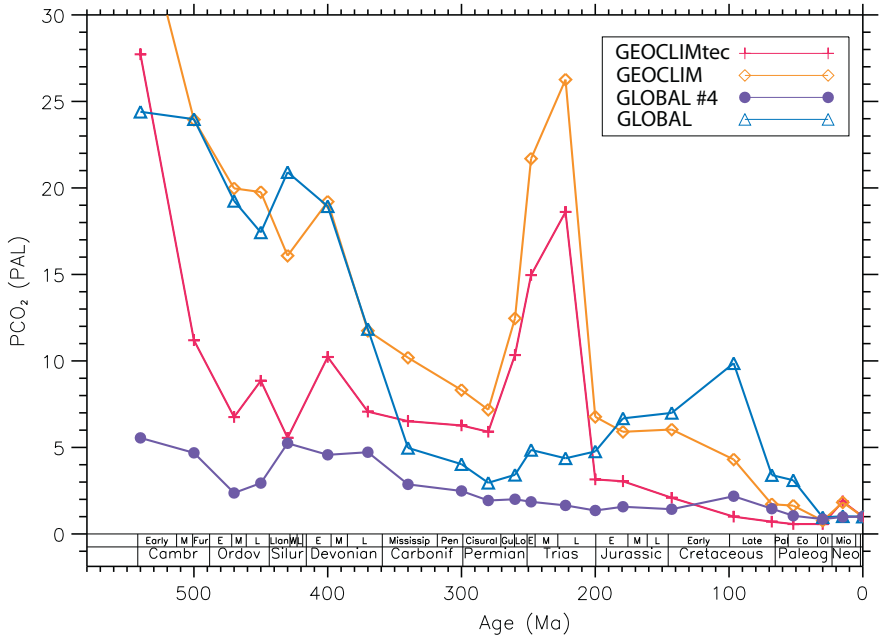

Fig. 8. Phanerozoic CO_2 history calculated by the zero-dimensional GEOCARB-type model and by the three-dimensional GEOCLIM model. GLOBAL#4 and GEOCLIMtec are simulations where the only forcings are the rising solar constant and the palaeogeography.

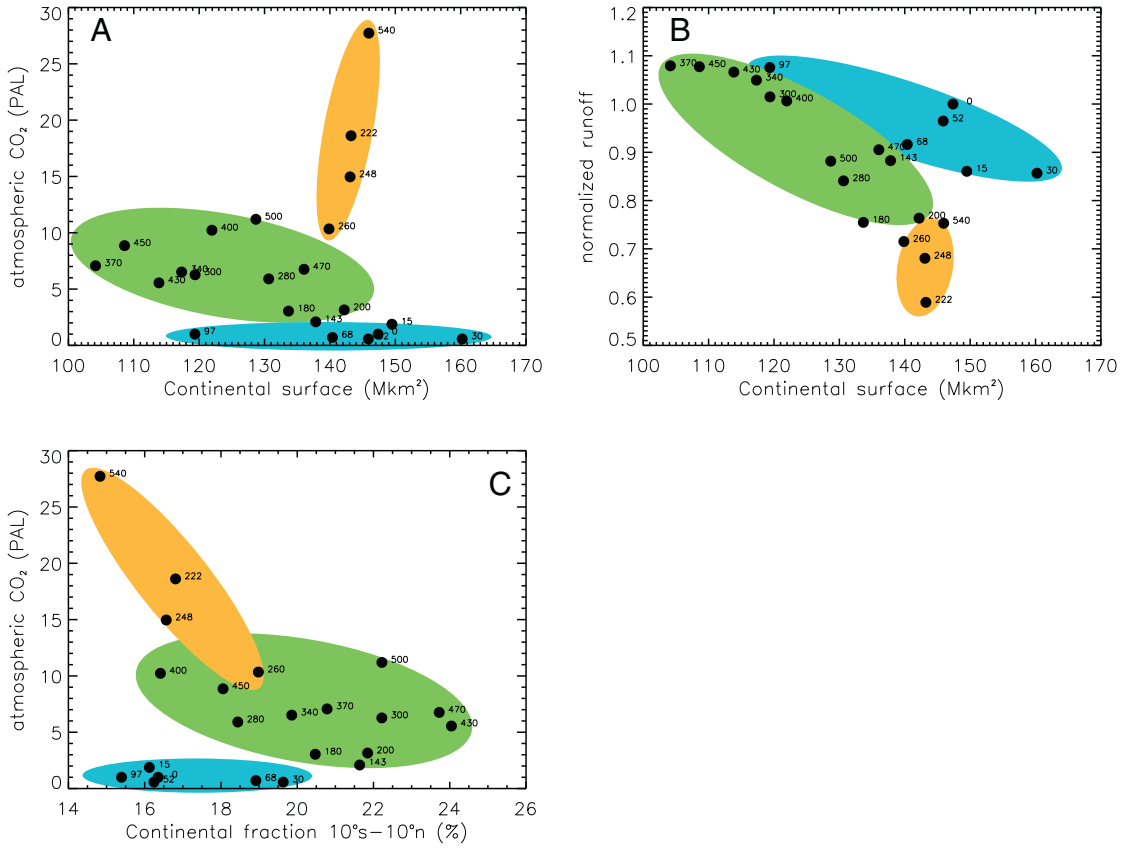

Fig. 9. (A) Atmospheric CO_2 versus the total emerged continental surface in the GEOCLIMtec simulation. The black numbers stand for the age of each dot, in million years. (B) Global continental runoff normalized to its present day value versus the total emerged continental surface in the GEOCLIMtec simulation. (C) Atmospheric CO_2 versus the percentage of the total continental surface located in the 10°S–10°N latitude band in the GEOCLIMtec simulation. The orange envelope represents the "warm" pool, the blue envelop the "cold" pool and the green envelop the "standard" pool. Each of these pools is exclusively forced by the palaeogeographical forcing.

roughly 15° and 35° latitude, because this zone coincides with the subsidence of the Hadley cell. The width of this low rainfall/high evaporation area is somehow dependent on the continental configuration, but not critically. As a consequence, when the continental fraction increases in the 15°–35° zone, we might expect that the global runoff will decrease simply because the continental area exposed to very low rainfall increases. This "geometric" effect is illustrated on Fig. 10B, where the global runoff is negatively correlated to the continental fraction in the 15°–35° latitude band (Pearson correlation coefficient −0.84). The positive correlation between the averaged latitudinal position of the continents and the runoff arises from the "fortuite" existence of a negative correlation between the averaged latitudinal location of the continents and the continental fraction between 15°–35° latitude (Fig. 10C).

It is worth mentioning that both model (GEOCLIM and GEOCARB) have a rather different behaviour with respect to the Permo-Triassic dry event. Although less pronounced than in GEOCLIMtec, the runoff calculated in GLOBAL#4 simulation also displays a decrease around 250 Ma (both GEOCLIM and GEOCARB-style simulations being performed with the palaeogeographical forcing only). Despite this runoff decrease by a about 30% from the Carboniferous to the Permo-Triassic, calculated atmospheric CO_2 in GLOBAL#4 does not display any rise in CO_2 at the same time, while GEOCLIMtec peaks at almost 20 times the present day level with a 40% decrease in runoff (Fig. 6). The reason for these distinctive behaviours is rooted in the parametric expression of silicate weathering as a function of runoff. In GEOCLIMtec, silicate weathering is linearly dependent on runoff, as suggested by recent compilations of field studies of silicate weathering (Dessert et al., 2003; Oliva et al., 2003). In GLOBAL#4, silicate weathering linearly increases with the runoff to the power 0.65, to account for dilution effects (Berner, 1994, 2004). This dilution effect is introduced to fit the database of Dunne (1978) for Kenyan rivers and of Peters (1984) for rivers of the United States. As a result, the response of weathering to runoff changes is seriously damped in GLOBAL#4, explaining why there is no CO_2 peak during the Permo-Triassic low runoff interval. This illustrates that the superposition of numerous parametric laws of various origin to describe the climate/carbon system, may finally hide the role of the palaeogeography on the atmospheric CO_2 level. This result also stresses that runoff and its impact on the CO_2 consumption by rock weathering must be modelled accurately. The use of a GCM to simulate the water cycle in GEOCLIM is a major improvement compared to zero-dimensional models, but we are still dependent on the reliability of parametric laws to describe silicate weathering. Because these parametric laws are fitting functions of the field data (for instance, HCO_3^- fluxes at the watershed outlet versus mean annual runoff, Dessert et al., 2003), the most complete databases must be used. Both the Oliva et al. (2003) and Dessert et al. (2003) databases cover a wide variety of climatic environments. But the spreading of their data points, particularly important for granitic environments, still questions the reliability of parametric laws. This is an inherent limitation of the method.

4.3.3. Role of small continents

The drastic decrease in atmospheric CO_2 in the Rhetian stage of the Triassic is mainly linked to the Northward drift of Pangea (Goddéris et al., 2008a). But there is an additional contributor to this sharp cooling trend. South China is located in the humid tropical area at the same time. In the simulation where the continental configuration is the only forcing (GEOCLIMtec), silicate weathering in South China is accounting for 17% of the global CO_2 consumption by weathering (Fig. 11). If CO_2 consumption by silicate weathering in South China during the Rhetian is removed from the simulation, atmospheric CO_2 would rise from

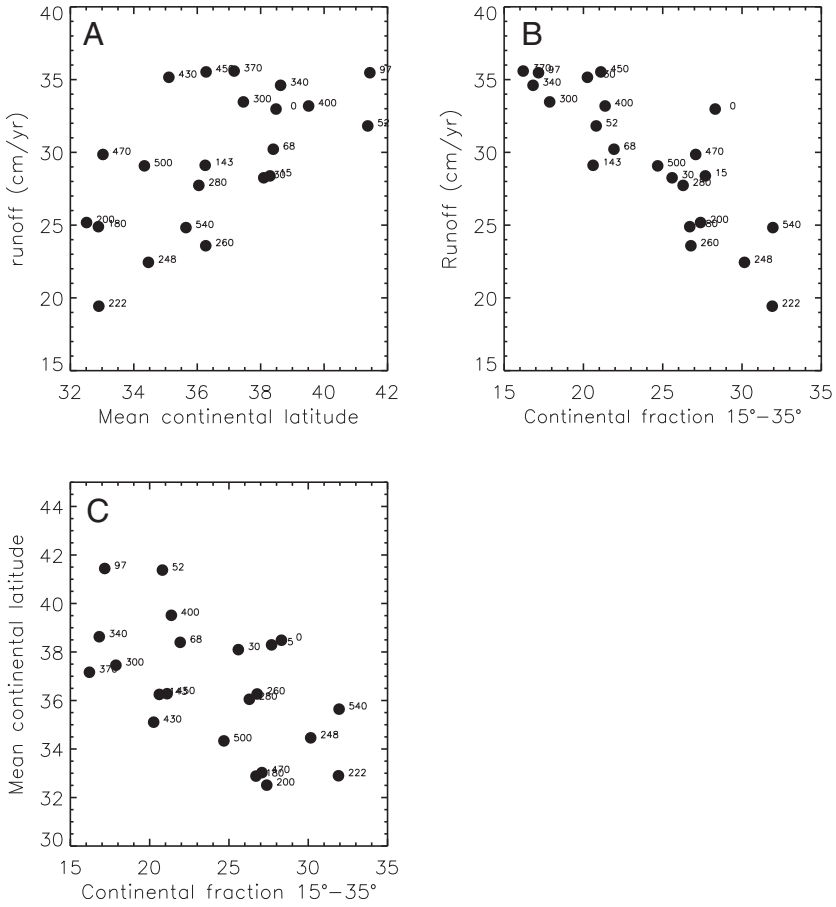

Fig. 10. (A) Global runoff as a function of the averaged latitudinal positions of the continents. (B) Global runoff as a function of the continental fraction within the latitude band extending from 15° to 35° latitude, in both hemisphere. (C) Averaged continental latitude of the continents as a function the continental fraction within the latitude band extending from 15° to 35° latitude, in both hemisphere. Runoff output from the GEOCLIMtec simulation. The black numbers stand for the age of each dot, in million years.

3.15 PAL (880 ppmv) to 5 PAL (1400 ppmv). Because of the logarithmic dependence of temperature on CO_2, the subsequent global warming of the Rhetian stage is significant (3 °C continental warming). This sensitivity test emphasized the potential key role played by small continents on the global carbon cycle, especially when they are located in the humid tropical belt (Oglesby and Park, 1989). This result somehow contradicts Otto-Bliesner (1995), who found that small continental blocks located in the tropical area might be characterized by low runoff, because evapotranspiration exceeds rainfall. If this was the case, small continental blocks should have only a minor effect on the long-term climate evolution. Conversely, our simulations show that small tropical continents might contribute significantly to the global CO_2 sink by weathering.

4.3.4. Climate sensitivity and palaeogeographical configuration

In the recent years, geological climate reconstructions have been used to assess the climate sensitivity to atmospheric CO_2 changes (Berner and Kothavala, 2001; Lunt et al., 2010; Park and Royer, 2011).

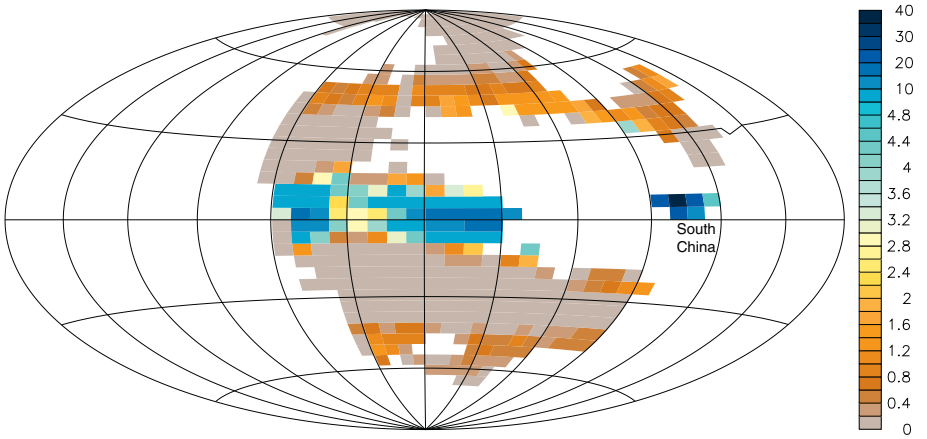

Fig. 11. CO_2 consumption by silicate weathering (10^{10} mol CO_2/yr) calculated for the Rhetian stage of the Triassic in the GEOCLIMtec simulation ($pCO_2 = 5040$ ppmv). South China crosses the equatorial humid belt and consumes 17% of the total CO_2 consumption.

We show here that climate sensitivity is substantially dependent on the palaeogeographical setting. Sensitivity is maximum during the Early Cambrian and during the Early to Middle Triassic period, exceeding 4 °C for a CO_2 doubling (Fig. 12). Except for this two particular geological period, the sensitivity is more less constant oscillating around 2.8 °C with a minimum at 2.4 °C at 90 Ma. What make the Early Cambrian and the Early to Middle Triassic so sensitive to a CO_2 doubling is not straightforward at first. It is important to note that these calculations of the climatic sensitivity account for fast and slow climatic feedbacks, excepting the role of the cryosphere, which is not modelled.

Climate sensitivity seems to respond partly to fluctuations in the continental surface as a function of latitude (Fig. 12). It roughly follows the evolution of the continental fraction between 60° and 30° latitude. Sensitivity increases when mid-latitudinal continental fraction rises, as it is the case in the Early Cambrian and during the Pangean period. But in details, things are trickier. The rapid increase in climate sensitivity from about 2.8 °C to more than 4 °C around 240 Ma is correlated to a strong decrease in the polar continental fraction. Also during the end Mesozoic and the Cenozoic, climate sensitivity decreases while the mid-latitude continental fraction stays roughly constant.

Runoff dependence on global temperature is also modulated by the palaeogeographical evolution. During most of the Paleozoic, from the Ordovician to the Mississippian, the runoff sensitivity to temperature is around 1.5 cm yr^{-1} K^{-1} (Fig. 13). Then it rapidly decreases with the assembly of Pangea, reaching 0.6 cm yr^{-1} K^{-1}. The Mesozoic is then characterized by a slow increase in runoff sensibility. Finally a major rise is predicted in the Miocene, where sensitivity goes back to Paleozoic values.

4.3.5. GEOCLIM output and proxy data

The objective of this contribution is to emphasize the key role played by the palaeogeographical configuration on the carbon cycle and on the climate evolution. At this stage, it is not easy to compare the GEOCLIM outputs with proxy data, because GEOCLIM has been designed to model mechanistically the role of palaeogeography, and does not aim at being a model of the complete carbon cycle. The other processes, including the role of the organic carbon cycle, of the vegetation on weathering, are either not modelled (GEOCLIMtec simulation), or modelled using simple parametric laws (GEOCLIM simulation). Nevertheless, some conclusions can be drawn from the comparison between proxies and model output.

Regarding the CO_2 level, the agreement between the GEOCLIM outputs and the CO_2 proxies is acceptable only for the last 200 Ma of the Earth's history, considering the large uncertainties inherent to the reconstructions (Fig. 14A). Between 200 and 400 Ma, GEOCLIM tends to overestimate the past CO_2 levels. This overestimation is particularly striking in the Triassic, where the supercontinental configuration forces GEOCLIM to very high CO_2 values. These high values are not recorded in the CO_2 proxies. Then, the 250–350 Ma period is characterized by very low proxy-based CO_2 values, around 500 ppmv, while GEOCLIM predicts values in excess of 1000 ppmv.

We also compare the mean annual sea surface temperature (SST) calculated by GEOCLIM within the 30°S–30°N latitudinal band to the temperature reconstructed using the tropical $\delta^{18}O$ data compiled by Prokoph et al. (2008) (Fig. 14B). To translate $\delta^{18}O$ into SST, we follow the method described in Veizer et al. (2000). $\delta^{18}O$ data have been detrended, using a root mean square linear fit. The detrending is applied to avoid unrealistically high temperatures mainly before 100 Ma. Then a running average has been calculated (20 Myr time window), including the calculation of the range containing 68% of the data points. Finally, we set the seawater $\delta^{18}O$ to −0.7 permil in the Cenomanian (a period where continental ice is assumed to be absent), and to 1 permil for the coldest stage of the Phanerozoic (most positive $\delta^{18}O$ detrended value). Because this represents a significant handling of the data, we express the result in terms of relative changes to the present day instead of absolute temperatures. Furthermore, the detrending procedure may hide real long-term climatic trends in the oxygen record. This is particularly critical for the last 100 Ma of Earth history, where the $\delta^{18}O$ signal provides a realistic temperature signal even without detrending (Donnadieu et al., 2009). For that reason, we also display on Fig. 14B the temperature calculated for the last 100 Ma without detrending of the oxygen isotopic data.

The spreading of the temperature values is quite large. The most striking feature is the existence of a warm peak in the Late-Permian/Early Triassic, in agreement with the GEOCLIM output (Goddéris et al., 2008a). A recent study has evidenced the

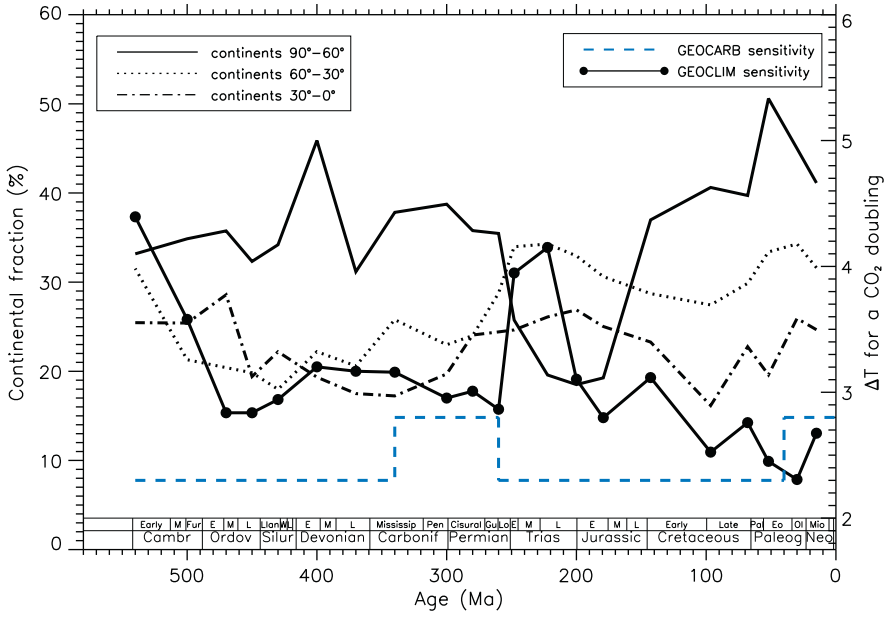

Fig. 12. Mean global temperature change for a CO_2 doubling as a function of age, calculated by the GEOCLIM model (solid line, scale on the right). The dotted blue line stands for the climate sensitivity prescribed in the GEOCARB model. Superimposed is the fraction of continents in various latitude bands (scale on the left).

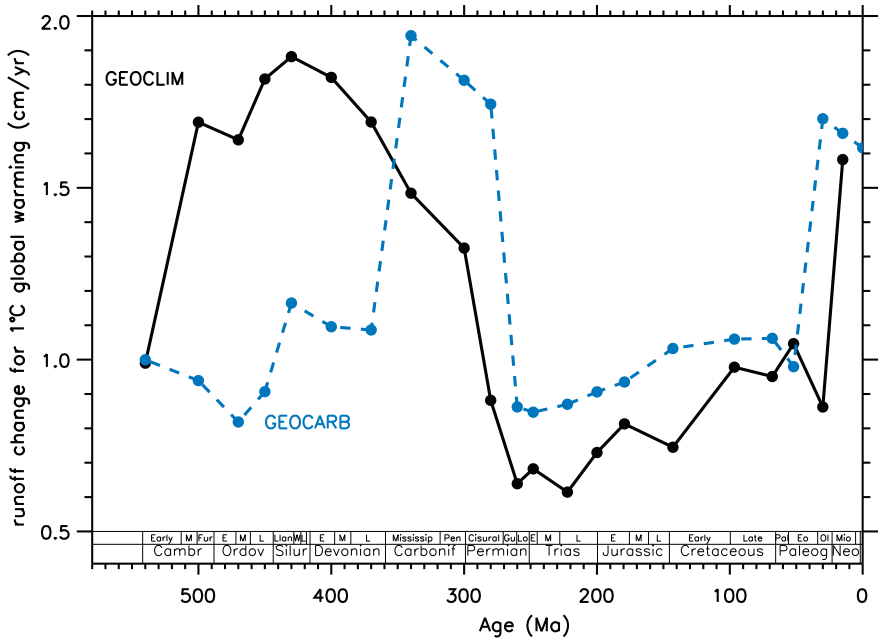

Fig. 13. Runoff change in cm/yr for an increase of 1 °C in the global temperature, calculated by the GEOCLIM model using a three-dimensional calculation of the water budget (solid line). The dotted blue line is the same calculated by the zero-dimensional GEOCARB model, which includes a parametric description of the water cycle.

persistence of very high temperatures in the tropical ocean over the whole Early Triassic, in excess of 35 °C (from conodont apatite $\delta^{18}O$) (Sun et al., 2012). As noted by the authors themselves, high temperatures for the 5 Myr of the Early Triassic require strong and persistent greenhouse conditions. These high temperature conditions may have lasted until the end of the Carnian stage, as inferred from brachiopod $\delta^{18}O$ (Korte et al., 2005). In the GEOCLIM simulations as well as in the Gibbs et al.'s (1999) study, these long lasting warm conditions can be sustained by the developing aridity, limiting the efficiency of continental weathering and promoting high CO_2 levels for millions of years. Conversely, the major temperature decrease occurring after 100 Ma and predicted by the model is not observed in the Prokoph et al. (2008) database when the oxygen isotopic data are detrended. But a cooling of about 5 °C in the tropical SST is reconstructed between 100 and 0 Ma when the oxygen isotopic data are not detrended, in close agreement with the model output (Donnadieu et al., 2009).

Several conclusions can be drawn. (1) When considering the early Triassic warm event, there is a clear disagreement between CO_2 proxy data and temperature data that we already note in a previous contribution (Goddéris et al., 2008a). A warm event seems to be associated to low CO_2 values. A coupled carbon-climate model like GEOCLIM, and even GEOCARB, cannot calculate at the same time high temperatures and low CO_2 levels. This apparent discrepancy between proxy-based temperatures and proxy-based CO_2 levels might be linked to the pretty large uncertainties inherent to the reconstruction methods, but this is beyond the scope of this study. (2) It appears that the palaeogeographical forcing is not responsible for the Permo-Carboniferous cool mode. (3) Reconstructing $\delta^{18}O$-based temperature curves for the whole Phanerozoic is not an easy task. However such composite regional or latitudinal curves would greatly help at validating spatially resolved numerical models. The various available databases are not really self-consistent. They mix phosphate and carbonate signals, the mathematical relationship between $\delta^{18}O$ and temperature fluctuates from one study to the other, and the data reflects the temperatures at various depths, depending on the organisms. Furthermore, the role of diagenesis is still not fully understood. Most of the geochemists now rely preferentially on phosphatic data for periods older than the Jurassic (Trotter et al., 2008; Joachimski et al., 2009), because phosphatic materials are much less sensitive to diagenesis than pre-Jurassic carbonates. But the question of the phosphate–water fractionation equation is still debated (Longinelli, 2013; Pucéat et al., 2013) and the question of the seawater $\delta^{18}O$ value is still critical. (4) Non-quantitative data should not be neglected when using spatially resolved models. Indeed, the GEOCLIM predictions of a very warm early Triassic are in agreement with sedimentological evidence for the deposition of redbeds and massive evaporites. The calculated sharp cooling during the latest Triassic coincides with major climatic changes impacting various regions of the world. Pedogenic and clay mineral data (smectite-rich redbeds) indicate a switch from arid/semi-arid conditions to year-round humid environments, a switch reproduced in our simulations (see Goddéris et al., 2008a, for references and more details). (5) The aim of the modelling efforts described in this work is not really to improve the results in terms of past atmospheric CO_2, but rather to improve the method by introducing physics in the numerical reconstructions of the past climate and carbon cycle. The GEOCARB model paved the way of the quantitative reconstructions of the Phanerozoic carbon cycle. The method used was mostly parametric. Now, recent studies relying on complex coupled climate-carbon numerical models have shown that the palaeogeographical factors have been underestimated. This review demonstrates that we now understand how and to what extent the palaeogeography really impacts the past carbon cycle and climate. This is a good starting point for revisiting the other processes at play, such as the links between weathering and land plants, between weathering and relief, among other parameters.

5. Conclusions

Two modelling pathways have been followed in the recent years for reconstructing the geological atmospheric CO_2 content. Zero-dimensional models (the so-called GEOCARB model family in this contribution) have been developed with the objective of accounting for as much processes as possible, such as the role of land plants or physical erosion on the weathering fluxes. Such models also include a simple parametric description of the climate response to the CO_2 content, the solar constant rise or the continental configuration on a global basis.

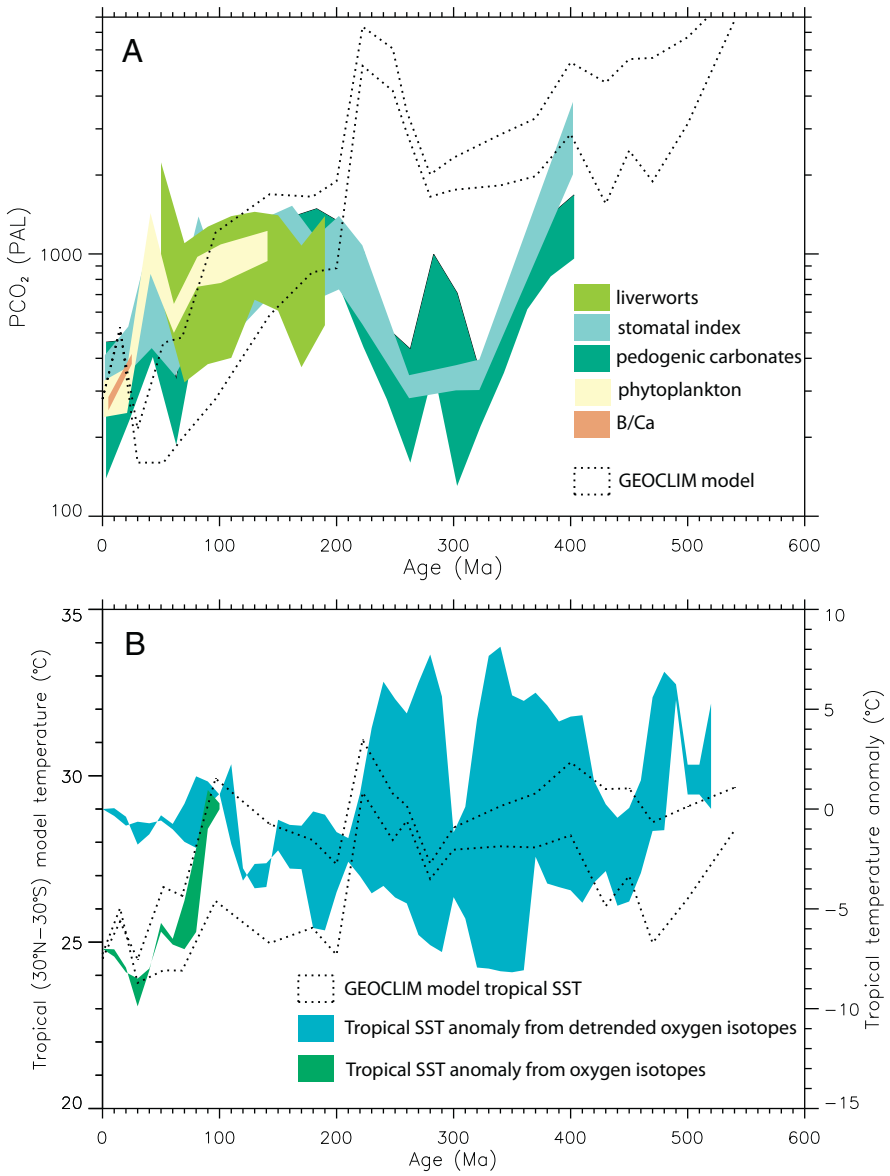

Fig. 14. (A) Comparison between the atmospheric CO_2 level calculated by the GEOCLIM model (dashed lines, the upper curve is the GEOCLIM simulation, the lower curve is the GEOCLIMtec simulation) and the CO_2 levels from various proxies (20 Myr moving averages). (B) The tropical sea surface temperature (averaged 30°S–30°N latitude) calculated by the GEOCLIM model (dashed lines, the upper curve is the GEOCLIM simulation, the lower curve is the GEOCLIMtec simulation, scale on the left). Also shown is the temperature anomaly for the same zonal area estimated from sedimentary carbonate $\delta^{18}O$ (scale on the right). See text for more details.

Those models gather information from other model runs or from field data and include those as parametric laws. Mixing several parametric descriptions from various origins is always at risk of losing the inherent physical behaviour of a complex system such as the Earth system. Nevertheless, these zero-dimensional models have the advantage of being integrative (many processes are considered), and fast in terms of computation time. They also generate past CO_2 reconstruction that can be compared to available data because they aim at accounting for all the factors controlling the evolution of the global carbon cycle.

Since the end of the 80s, physically-based models have also been developed to describe specifically the impact of the continental configuration of the global carbon cycle and climate geological evolution. Such models all include a spatially-resolved description of the climate system. This is the minimum requirement to consider physically the role of the palaeogeography on the global carbon cycle. Those models, one to three-dimensional, proceed from a different philosophy than the zero-dimensional method. The objective is no more to calculate a time evolution of the atmospheric CO_2 than can be compared readily to data, but to explore the sensitivity of the Earth system to one parameter, here the palaeogeographical configuration. These studies come to four major findings:

(1) The palaeogeography is a key controlling factor of the geological evolution of the atmospheric CO_2. By modulating runoff and air temperature above the continental surface, it strongly controls the CO_2 consumption by silicate rock weathering. Supercontinent and polar configurations favour the onset of very high CO_2 pressure in the atmosphere. Conversely, since about the mid-Cretaceous, the palaeogeography promotes the onset of low CO_2 and cold climatic conditions. The role of the palaeogeography has been largely underestimated in zero-dimensional models.

(2) Some of the key features of the Phanerozoic climate can be explained by the modulation of the carbon cycle by continental drift. This is the case for the early Paleozoic (Cambrian to early Silurian) global cooling, the warm and arid early Triassic, and the cold trend of the Cenozoic.
(3) Small continental blocks may contribute significantly to the total CO_2 consumption by weathering when entering the sub-tropical warm and humid zone.
(4) Climate sensitivity is substantially dependent on the continental configuration. As such, though the past might be the key to estimate the amplitude of the future climatic changes, it is important to understand the processes linked to the palaeogeography that have modulated the Earth climatic sensitivity in the past.

Instead of using parametric relationships to estimate global runoff and temperature, the models described in this review (Otto-Bliesner, 1995; Gibbs et al., 1999; Donnadieu et al., 2004, 2006; Goddéris et al., 2008b; Nardin et al., 2011; Lefebvre et al., 2013) resolve spatially the climatic conditions using process-based climate models. Such models implement the energy budget of the Earth atmosphere and oceans and a physical description of the water cycle. Those models are not yet able to propose a CO_2 history that can be compared to data. Indeed, despite a major improvement in the physical basis of the climate compared to parametric models, one major constraint remains the mathematical expression for CO_2 consumption by continental weathering. In Gibbs et al. (1999) and in the GEOCLIM model, continental weathering is calculated on each grid cell assuming runoff (and temperature) dependencies. But weathering is a complex process. It also depends on physical erosion, vegetation cover, soil thickness, and lithology. Regarding the vegetation cover, a few studies try to explore physically the climatic (Donnadieu et al., 2009; Le Hir et al., 2011) and geochemical (Taylor et al., 2012) impacts of land plants within the framework of a three-dimensional climate and geochemical modelling. All these studies show the critical role played by the land plant distribution on the weathering fluxes, and hence on the global carbon cycle. Regarding the thickness of the soil cover, protecting the bedrock from weathering when it becomes too thick, Goddéris et al. (2008b) have shown, using the GEOCLIM model that this effect has modulated the CO_2 levels. But the role of large mountain ranges on the global carbon cycle is still to be included in those spatially-resolved numerical model. Finally, although Gibbs et al. (1999) suggest that spatial variations in lithology account only for small fluctuations in the total chemical erosion rates, this was not the conclusion of Taylor et al. (2011, 2012), Nardin et al. (2011) and Kent and Muttoni (2013). Indeed these authors found that the bulk of weathering may come from basaltic hotspots.

In summary, it appears that we are slowly moving from simple parametric representations of the geological Earth system towards more comprehensive and physically-based descriptions. What we have learnt in the recent years is that the overall picture we had of the carbon cycle and climate evolution may drastically change when more complex models are used. Further works are clearly needed to account for a better representation of the weathering rates for instance, but they should include, as far as possible, a description of the physics at play.

Acknowledgements

Funding for this work has been provided by the CNRS-INSU Eclipse and Syster programs, and by the ACCRO-Earth (ANR-06-BLAN-0347), COLORS (ANR-09-JCJC-0105), TERRES (ANR-10-BLAN-0607) and Anox-Sea (ANR-12-BS06-0011) ANR projects. We thank Jeffrey Park and Lee Kump for their constructive and fruitful reviews of this contribution.

Appendix A

Basically, the calculation of the Phanerozoic atmospheric CO_2 pressure by the GEOCARB family of models relies upon a set of equations. Although the complete GEOCARB model is more complex (Berner, 2004), we only show here the key equations. The objective is to emphasize the role played by the palaeogeography on the climate evolution of the Earth, and not to reconstruct strictly the GEOCARB model.

(1) The carbon balance: given the short residence time of carbon in the ocean/atmosphere system compared to the geological timescale, the exospheric carbon cycle is assumed to evolve through a succession of steady states:

$$F_{vol} + F_{MOR} + F_{cw} + F_{ow} = F_{cd} + F_{od} \tag{A1}$$

where F_{vol} is the supply of CO_2 by subaerial volcanism, F_{MOR} is the degassing flux of CO_2 at mid-oceanic ridges, F_{cw} is the carbon flux released by continental carbonate rock dissolution, and F_{ow} is the carbon flux released to the river system by the oxidation of reduced sedimentary rocks. The sink side corresponds to the storage of carbon on the seafloor either by carbonate sedimentation (F_{cd}) or by organic carbon burial into the sediment (F_{od}).

(2) The alkalinity balance:

$$F_{swo} + F_{swy} + F_{cw} = F_{cd} \tag{A2}$$

F_{swo} and F_{swy} are respectively half of the alkalinity flux created during the weathering of continental old cratonic silicate rocks and of young volcanic rocks. These two terms can be written as follows:

$$F_{swo} = \left(1-\sigma_y\right) F_{sw} \tag{A3}$$

$$F_{swy} = \sigma_y F_{sw} \tag{A4}$$

where F_{sw} equals half of the total alkalinity flux created during the weathering of continental silicate rocks. σ_y is the fraction of the silicate rock outcrop occupied by young volcanic rocks.

Altogether, these two Eqs. (A1) and (A2) can be written as follows, stating that all sources of exospheric carbon by solid Earth degassing is compensated by the continental silicate weathering and the net sink of organic carbon (organic carbon burial minus the oxidation of reduced sedimentary carbon exposed at the Earth surface).

$$F_{vol} + F_{MOR} = F_{swo} + F_{swy} + (F_{od} - F_{ow}) \tag{A5}$$

(3) The organic carbon disequilibrium ($F_{od} - F_{ow}$) can be constrained by considering the carbon isotopic balance.

$$\delta_{vol} F_{vol} + \delta_{MOR} F_{MOR} + \delta_{CW} F_{CW} + \delta_{OW} F_{OW} = \delta_{oc} F_{cd} + \left(\delta_{oc} - \varepsilon_p\right) F_{od} \tag{A6}$$

where δ_{vol} is the averaged volcanic gas $\delta^{13}C$ signature, and δ_{MOR} is the mantle carbon isotopic composition. δ_{cw} and δ_{ow} are the averaged $\delta^{13}C$ of continental carbonated and reduced sedimentary rocks. δ_{oc} is the measured seawater $\delta^{13}C$ (Veizer et al., 1999) and ε_P is the photosynthetic carbon isotopic fractionation (Hayes et al., 1999).

(4) The strontium isotopic budget can be used to constrain the relative importance of young volcanic rocks versus older silicate rocks (Berner, 2004). Given the residence time of strontium in seawater (1.5 to 2 Ma) and the time resolution

of the model simulations (at least several tens of million years), we assume this budget to be close to steady state:

$$\frac{r_{MOR}-r_{OC}}{9.43+r_{MOR}}F^{Sr}_{MOR}+\frac{r_{CW}-r_{OC}}{9.43+r_{CW}}F^{Sr}_{cw}+\frac{r_{swy}-r_{OC}}{9.43+r_{swy}}F^{Sr}_{swy}+\frac{r_{swo}-r_{OC}}{9.43+r_{swo}}F^{Sr}_{swo}=0 \quad (A7)$$

where r_{MOR}, r_{cw}, r_{swy}, and r_{swo} are the $^{87}Sr/^{86}Sr$ ratio of the mantle, carbonates, young volcanics and old cratonic rocks. These are set to 0.703, 0.708, 0.703 and 0.718 respectively. r_{OC} is the measured $^{87}Sr/^{86}Sr$ ratio of seawater recorded in sedimentary carbonates (Veizer et al., 1999). The superscript *Sr* to the flux *F* means that we are considering the strontium fluxes associated to the carbon and alkalinity fluxes.

(5) Lastly, three additional equations describe the dependence of silicate (F_{swy} and F_{swo}) and carbonate weathering (F_{cw}) on atmospheric CO_2, through their dependencies on runoff and air temperature. In GEOCARB-style models, only global runoff and mean average global temperature are calculated as a function of CO_2 (Eqs. (1) and (2)), and then used to calculate mean global weathering fluxes. In GEOCLIM, a physically-based 3D climate model is used to calculate the spatial distribution of runoff and temperature as a function of CO_2, which are subsequently used to reconstruct spatially-distributed weathering fluxes.

If the solid Earth degassing rate is known (F_{vol} and F_{MOR}), the 9 Eqs. ((A1), (A2), (A4), (A5), (A6), (A7) + the three climatic dependences) can be solved for F_{cw}, F_{ow}, F_{sw}, F_{swy}, F_{swo}, σ_y, F_{cd}, F_{od}, and atmospheric CO_2 (9 unknowns).

References

Barron, E.J., Washington, W.M., 1982. Cretaceous climate: a comparison of atmospheric simulations with the geologic record. Palaeogeogr. Palaeoclimatol. Palaeoecol. 40, 103–133.

Barron, E.J., Hay, W.W., Thompson, S., 1989. The hydrologic cycle: a major variable during Earth history. Global Planet. Chang. 75, 157–174.

Barron, E.J., Fawcett, P.J., Pollard, D., Thompson, S., 1993. Model simulations of Cretaceous climates — the role of geography and carbon-dioxide. Philos. Trans. R. Soc. Lond. B Biol. Sci. 341, 307–315.

Bergman, N.M., Lenton, T.M., Watson, A.J., 2004. COPSE: a new model of biogeochemical cycling over Phanerozoic time. Am. J. Sci. 304, 397–437.

Berner, R.A., 1991. A model for atmospheric CO_2 over Phanerozoic time. Am. J. Sci. 291, 339–376.

Berner, R.A., 1994. 3GEOCARB II: a revised model of atmospheric CO_2 over Phanerozoic time. Am. J. Sci. 294, 56–91.

Berner, R.A., 2004. The Phanerozoic Carbon Cycle. Oxford University Press (150 pp.).

Berner, R.A., 2006. GEOCARBSULF: a combined model for Phanerozoic atmospheric O_2 and CO_2. Geochim. Cosmochim. Acta 70, 5653–5664.

Berner, R.A., Caldeira, K., 1997. The need for mass balance and feedback in the geochemical carbon cycle. Geology 25, 955–956.

Berner, R.A., Kothavala, Z., 2001. GEOCARB III: a revised model of atmospheric CO_2 over Phanerozoic time. Am. J. Sci. 301, 182–204.

Bluth, G.J.S., Kump, L.R., 1991. Phanerozoic paleogeology. Am. J. Sci. 291, 284–308.

Craggs, H.J., Valdes, P.J., Widdowson, M., 2012. Climate model predictions for the latest Cretaceous: an evaluation using climatically sensitive sediments as proxy indicators. Palaeogeogr. Palaeoclimatol. Palaeoecol. 315–316, 12–23.

Crowley, T.J., Baum, S.K., 1991. Modelling late Paleozoic glaciation. Geology 20, 507–510.

Crowley, T.J., Baum, S.K., 1995. Reconciling Late Ordovician (440 Ma) glaciation with very high (14×) CO_2 levels. J. Geophys. Res. 100, 1093–1101.

Dessert, C., Dupré, B., Gaillardet, J., François, L.M., Allègre, C.J., 2003. Basalt weathering laws and the impact of basalt weathering on the global carbon cycle. Chem. Geol. 202, 267–273.

Donnadieu, Y., Goddéris, Y., Ramstein, G., Nédélec, A., Meert, J., 2004. A 'snowball Earth' climate triggered by continental break-up through changes in runoff. Nature 428, 303–306.

Donnadieu, Y., Pierrehumbert, R., Jacob, R., Fluteau, F., 2006. Modelling the primary control of paleogeography on Cretaceous climate. Earth Planet. Sci. Lett. 248, 426–437.

Donnadieu, Y., Goddéris, Y., Bouttes, N., 2009. Exploring the climatic impact of the continental vegetation on the Mesozoic atmospheric CO_2 and climate history. Clim. Past 5, 85–96.

Dunne, T., 1978. Rate of chemical denudation of silicate rocks in tropical catchments. Nature 274, 244–246.

François, L.M., Goddéris, Y., 1998. Isotopic constraints on the Cenozoic evolution of the carbon cycle. Chem. Geol. 145, 177–212.

François, L.M., Walker, J.C.G., 1992. Modelling the Phanerozoic carbon cycle and climate: constraints from the $^{87}Sr/^{86}Sr$ isotopic ratio of seawater. Am. J. Sci. 292, 81–135.

Gibbs, M.T., Kump, L.R., 1994. Global chemical erosion during the last glacial maximum and the present: sensitivity to changes in lithology and hydrology. Paleoceanography 9, 529–543.

Gibbs, M.T., Barron, E.J., Kump, L.R., 1997. An atmospheric pCO_2 threshold for glaciation in the Late Ordovician. Geology 25, 447–450.

Gibbs, M.T., Bluth, G.J.S., Fawcett, P.J., Kump, L.R., 1999. Global chemical erosion over the last 250 My: variations due to changes in paleogeography, paleoclimate, and paleoecology. Am. J. Sci. 299, 611–651.

Goddéris, Y., François, L.M., 1995. The Cenozoic evolution of the strontium and carbon cycles: relative importance of continental erosion and mantle exchanges. Chem. Geol. 126, 169–190.

Goddéris, Y., Joachimski, M.M., 2004. Global change in the Late Devonian: modelling the Frasnian–Famennian short-term carbon isotope excursions. Palaeogeogr. Palaeoclimatol. Palaeoecol. 202, 309–329.

Goddéris, Y., Donnadieu, Y., de Vargas, C., Pierrehumbert, R.T., Dromart, G., van de Schootbrugge, B., 2008a. Causal or casual link between the rise of nannoplankton calcification and a tectonically-driven massive decrease in Late Triassic atmospheric CO_2 ? Earth Planet Sci. Lett. 267, 247–255.

Goddéris, Y., Donnadieu, Y., Tombozafy, M., Dessert, C., 2008b. Shield effect on continental weathering: implication for climatic evolution of the Earth at the geological timescale. Geoderma 145, 439–448.

Gyllenhaal, E.D., Engberts, C.J., Markwick, P.J., Smith, L.H., Patzkowsky, M.E., 1991. The Fujita–Ziegler model: a new semi-quantitative technique for estimating paleoclimate from paleogeographic maps. Palaeogeogr. Palaeoclimatol. Palaeoecol. 86, 41–66.

Hay, W.W., Barron, E.J., Thompson, S.L., 1990. Global atmospheric circulation experiments on an Earth with polar and tropical continents. J. Geol. Soc. London 147, 749–757.

Hay, W.W., DeConto, R.M., Wold, C.N., Wilson, K.M., Voight, S., Schulz, M., Wold-Rossby, A., Dullo, W.-C., Ronov, A.B., Balukhovsky, A.N., Soding, E., 1999. Alternative global Cretaceous paleogeography. In: Barrera, E., Johnson, C.C. (Eds.), Evolution of the Cretaceous ocean–climate system. Boulder, Colorado, Geological Society of America Special Paper, 332, pp. 1–48.

Hayes, J.M., Strauss, H., Kaufman, A.J., 1999. The abundance of ^{13}C in marine organic matter and isotopic fractionation in the global biogeochemical cycle of carbon during the past 800 Ma. Chem. Geol. 161, 103–125.

Herrmann, A.D., Patzkowsky, M.E., Pollard, D., 2004. The impact of paleogeography, pCO_2, poleward ocean heat transport and sea level change on global cooling during the Late Ordovician: a climate model analysis. Palaeogeogr. Palaeoclimatol. Palaeoecol. 206, 59–74.

Horton, D.E., Poulsen, C.J., Pollard, D., 2010. Influence of high-latitude vegetation feedbacks on late Palaeozoic glacial cycles. Nat. Geosci. 3, 572–577.

Horton, D.E., Poulsen, C.J., Montañez, I.P., DiMichele, W.A., 2012. Eccentricity-paced late Paleozoic climate change. Palaeogeogr. Palaeoclim. Palaeoecol. 331–332, 150–161.

Hyde, W.T., Crowley, T.J., Tarasov, L., Peltier, W.R., 1999. The Pangean ice age: studies with a coupled climate–ice sheet model. Clim. Dyn. 15, 619–629.

Jacob, R., 1997. Low Frequency Variability in a Simulated Atmosphere Ocean System. Ph.D. Thesis University of Wisconsin, Madison, USA.

Joachimski, M.M., Breisig, S., Buggisch, W., Talent, J.A., Mawson, R., Gereke, M., Morrow, J.R., Day, J., Weddige, K., 2009. Devonian climate and reef evolution: insights from oxygen isotopes in apatite. Earth Planet. Sci. Lett. 284, 599–609.

Kennett, J.P., 1977. Cenozoic evolution of Antarctic glaciation, the circum-Antarctic Ocean, and their impact on global paleoceanography. J. Geophys. Res. 82 (27), 3843–3860.

Kent, D.V., Muttoni, G., 2013. Modulation of Late Cretaceous and Cenozoic climate by variable drawdown of atmospheric pCO_2 from weathering of basaltic provinces on continents drifting through the equatorial humid belt. Clim. Past 9, 525–546.

Köppen, W., Wegener, A., 1924. Die Klimate der geologischen Vorzeit. Gebrüder Bornträger, Berlin.

Korte, C., Kozur, H.W., Veizer, J., 2005. $\delta^{13}C$ and $\delta^{18}O$ values of Triassic brachiopods and carbonate rocks as proxies for coeval seawater and palaeotemperature. Palaeogeogr. Palaeoclimatol. Palaeoecol. 226, 287–306.

Kothavala, Z., Oglesby, R.J., Saltzman, B., 1999. Sensitivity of equilibrium surface temperature of CCM3 to systematic changes in atmospheric CO_2. Geophys. Res. Lett. 26, 209–212.

Kutzbach, J.E., Gallimore, R.G., 1989. Pangaean climates: megamonsoons of the megacontinent. J. Geophys. Res. 94, 3341–3357.

Labat, D., Goddéris, Y., Probst, J.-L., Guyot, J.-L., 2004. Evidence for global runoff increase related to climate warming. Adv. Water Resour. 27, 631–642.

Lagabrielle, Y., Goddéris, Y., Donnadieu, Y., Malavieille, J., Suarez, M., 2009. The tectonic history of Drake Passage and its possible impacts on global climate. Earth Planet. Sci. Lett. 279, 197–211.

Le Hir, G., Donnadieu, Y., Goddéris, Y., Meyer-Berthaud, B., Ramstein, G., Blakey, R.C., 2011. The climate change caused by the land plants invasion in the Devonian. Earth Planet. Sci. Lett. 310, 203–212.

Lefebvre, V., Donnadieu, Y., Sepulchre, P., Swingedouw, D., Zhang, Z.-S., 2012. Deciphering the role of southern gateways and carbon dioxide on the onset of the Antarctic Circumpolar Current. Paleoceanography 27. http://dx.doi.org/10.1029/2012PA002345.

Lefebvre, V., Donnadieu, Y., Goddéris, Y., Fluteau, F., Hubert-Théou, L., 2013. Was the Antarctic glaciation delayed by a high degassing rate during the early Cenozoic? Earth Planet. Sci. Lett. 371–372, 203–211.

Longinelli, A., 2013. Comment on work by Pucéat et al. (2010) on a revised phosphate–water fractionation equation. Earth Planet. Sci. Lett. 377–378, 378–379.

Lunt, D.J., Haywood, A.M., Schmidt, G.A., Salzmann, U., Valdes, P.J., Dowsett, H.J., 2010. Earth system sensitivity inferred from Pliocene modelling and data. Nat. Geosci. 3, 60–64.

Lyell, C., 1830. Principles of Geology, Being an Attempt to Explain the Former Changes of the Earth's Surface by Reference to Causes Now in Operation. , Vol. 1. John Murray, London.
Marshall, H.G., Walker, J.C.G., Khun, W.R., 1988. Long-term climate change and the geochemical cycle of carbon. J. Geophys. Res. 93, 791–801.
Nardin, E., Goddéris, Y., Donnadieu, Y., Le Hir, G., Blakey, R.C., Pucéat, E., Aretz, M., 2011. Modelling the early Paleozoic long-term climatic trend. Geol. Soc. Am. Bull. 123, 1181–1192.
Oglesby, R., Park, J., 1989. The effect of precessional insolation changes on Cretaceous climate and cyclic sedimentation. J. Geophys. Res. 94, 14793–14816.
Oliva, P., Viers, J., Dupré, B., 2003. Chemical weathering in granitic environments. Chem. Geol. 202, 255–256.
Otto-Bliesner, B.L., 1995. Continental drift, runoff, and weathering feedbacks: implications from climate model experiments. J. Geophys. Res. 100, 11537–11548.
Park, J., Royer, D.L., 2011. Geologic constraints on the glacial amplification of Phanerozoic climate sensitivity. Am. J. Sci. 311, 1–26.
Peters, N.E., 1984. Evaluation of Environmental Factors Affecting Yields of Major Dissolved Ions of Streams in the United States. , 2228. U.S. Geological Survey Water Supply Paper (39 pp.).
Prokoph, A., Shields, G.A., Veizer, J., 2008. Compilation and time-series analysis of a marine carbonate $\delta^{18}O$, $\delta^{13}C$, $^{87}Sr/^{86}Sr$ and $\delta^{34}S$ database through Earth history. Earth Sci. Rev. 87, 113–133.
Pucéat, E., Joachimski, M.M., Bouilloux, A., Monna, F., Bonin, A., Motreuil, S., Morinière, P., Hénard, S., Mourin, J., Dera, G., Quesne, D., 2013. Reply on comment by Longinelli (2013) on a revised phosphate–water fractionation equation. Earth Planet. Sci. Lett. 377–378, 380–382.
Raymo, M.E., 1991. Geochemical evidence supporting T.C. Chamberlin's theory of glaciation. Geology 19, 344–347.
Raymo, M.E., Ruddiman, W.F., Froelich, P.N., 1988. Influence of late Cenozoic mountain building on ocean geochemical cycles. Geology 16, 649–653.
Sitch, S., Smith, B., Prentice, I.C., Arneth, A., Bondeau, A., Cramer, W., Kaplan, J.O., Levis, S., Lucht, W., Sykes, M.T., Thonicke, K., Venevsky, S., 2003. Evaluation of ecosystem dynamics, plant geography and terrestrial carbon cycling in the LPJ dynamic global vegetation model. Glob. Chang. Biol. 9, 161–185.
Spicer, R.A., Ahlberg, A., Herman, A.B., Hofmann, C.-C., Raikevich, M., Valdes, P.J., Markwick, P.J., 2008. The Late Cretaceous continental interior of Siberia: a challenge for climate models. Earth Planet. Sci. Lett. 267, 228–235.
Sun, Y., Joachimski, M.M., Wignall, P.B., Yan, C., Chen, Y., Jiang, H., Wang, L., Lai, X., 2012. Lethally hot temperatures during the Early Triassic greenhouse. Science 338, 366–370.
Tajika, E., 2007. Long-term stability of climate and global glaciations throughout the evolution of the Earth. Earth Planets Space 59, 293–299.
Taylor, L.L., Banwart, S.A., Leake, J.R., Beerling, D.J., 2011. Modelling the evolutionary rise of the ectomycorrhiza on subsurface weathering environments and the geochemical carbon cycle. Am. J. Sci. 311, 369–403.
Taylor, L.L., Banwart, S.A., Valdes, P.J., Leake, J.R., Beerling, D.J., 2012. Evaluating the effects of terrestrial ecosystems, climate and carbon dioxide on weathering over geological time: a global-scale process-based approach. Phil. Trans. R. Soc. B 367, 565–582.
Trotter, J.A., Williams, I.S., Barnes, C.R., Lécuyer, C., Nicoll, R.S., 2008. Did cooling oceans trigger the Ordovician biodiversification? Evidence from conodont thermometry. Science 321, 550–554.
Veizer, J., Ala, D., Azmy, K., Bruckschen, P., Buhl, D., Bruhn, F., Carden, G.A.F., Diener, A., Ebneth, S., Goddéris, Y., Jasper, T., Korte, C., Pawellek, F., Podlaha, O.G., Strauss, H., 1999. $^{87}Sr/^{86}Sr$, $\delta^{13}C$ and $\delta^{18}O$ evolution of Phanerozoic seawater. Chem. Geol. 161, 59–88.
Veizer, J., Goddéris, Y., François, L.M., 2000. Evidence for decoupling of atmospheric CO_2 and global climate during the Phanerozoic eon. Nature 408, 698–701.
Von der Heydt, A., Dijkstra, H.A., 2006. Effect of ocean gateways on the global ocean circulation in the late Oligocene and early Miocene. Paleoceanography 21. http://dx.doi.org/10.1029/2005PA001149.
Walker, J.C.G., Hays, P.B., Kasting, J.F., 1981. A negative feedback mechanism for the long-term stabilization of Earth's surface temperature. J. Geophys. Res. 86, 9776–9782.
Wallmann, K., 2001. Controls on the Cretaceous and Cenozoic evolution of seawater composition, atmospheric CO_2 and climate. Geochim. Cosmochim. Acta 65, 3005–3025.
Wallmann, K., 2004. Impact of atmospheric CO_2 and galactic cosmic radiation on Phanerozoic climate change and the marine $\delta^{18}O$ record. Geochem. Geophys. Geosyst. 5, Q06004.
Wegener, A., 1912. Die Entstehung der Kontinente. Geol. Rundsch. 3, 276–292.
Worsley, T.R., Kidder, D.L., 1991. First-order coupling of paleogeography and CO_2, with global surface temperature and its latitudinal contrast. Geology 19, 1161–1164.
Zhang, X., Prange, M., Steph, S., Butzin, M., Krebs, U., Lunt, D.J., Nisancioglu, K.H., Park, W., Schmitter, A., Schneider, B., Schulz, M., 2012. Changes in equatorial Pacific thermocline depth in response to Panamanian seaway closure: insights from a multi-model proxy. Earth Planet. Sci. Lett. 317–318, 76–84.

nature geoscience

LETTERS

PUBLISHED ONLINE: 24 AUGUST 2015 | DOI: 10.1038/NGEO2502

Orbitally forced ice sheet fluctuations during the Marinoan Snowball Earth glaciation

Douglas I. Benn[1,2]*, Guillaume Le Hir[3], Huiming Bao[4], Yannick Donnadieu[5], Christophe Dumas[5], Edward J. Fleming[1,6†], Michael J. Hambrey[7], Emily A. McMillan[6], Michael S. Petronis[8], Gilles Ramstein[5], Carl T. E. Stevenson[6], Peter M. Wynn[9] and Ian J. Fairchild[6]

Two global glaciations occurred during the Neoproterozoic. Snowball Earth theory posits that these were terminated after millions of years of frigidity when initial warming from rising atmospheric CO_2 concentrations was amplified by the reduction of ice cover and hence a reduction in planetary albedo[1,2]. This scenario implies that most of the geological record of ice cover was deposited in a brief period of melt-back[3]. However, deposits in low palaeo-latitudes show evidence of glacial–interglacial cycles[4–6]. Here we analyse the sedimentology and oxygen and sulphur isotopic signatures of Marinoan Snowball glaciation deposits from Svalbard, in the Norwegian High Arctic. The deposits preserve a record of oscillations in glacier extent and hydrologic conditions under uniformly high atmospheric CO_2 concentrations. We use simulations from a coupled three-dimensional ice sheet and atmospheric general circulation model to show that such oscillations can be explained by orbital forcing in the late stages of a Snowball glaciation. The simulations suggest that while atmospheric CO_2 concentrations were rising, but not yet at the threshold required for complete melt-back, the ice sheets would have been sensitive to orbital forcing. We conclude that a similar dynamic can potentially explain the complex successions observed at other localities.

The Wilsonbreen Formation in northeast Svalbard contains a detailed record of environmental change during the Marinoan, the second of the major Cryogenian glaciations (650–635 Ma; refs 7,8). At this time, Svalbard was located in the Tropics on the eastern side of Rodinia[9,10]. The <180 m thick Wilsonbreen Formation was deposited within a long-lived intracratonic sedimentary basin[11]. It is subdivided into three members (W1, W2 and W3) based on the relative abundance of diamictite and carbonate beds[7,8] (Fig. 1 and Supplementary Figs 1 and 2). The occurrence throughout the succession of lacustrine sediments containing both precipitated carbonate and ice-rafted detritus, and intermittent evaporative carbonates and fluvial deposits, indicates that the basin remained isolated from the sea, consistent with eustatic sea-level fall of several hundred metres and limited local isostatic depression (Supplementary Information; ref. 12). This makes it ideal for investigating environmental change within a Neoproterozoic panglaciation, as it provides direct evidence of subaerial environments and climatic conditions.

We made detailed sedimentary logs at ten known and new localities extending over 60 km of strike (Fig. 1 and Supplementary Fig. 1; see Methods). Seven sediment facies associations were identified, recording distinct depositional environments that varied in spatial extent through time (Supplementary Fig. 3 and Supplementary Information). These are: FA1: subglacial, recording direct presence of glacier ice; FA2: fluvial channels; FA3: dolomitic floodplain, recording episodic flooding, evaporation and microbial communities; FA4: carbonate lake margin, including evidence of wave action; FA5: carbonate lacustrine, including annual rhythmites and intermittent ice-rafted debris; FA6: glacilacustrine, consisting of ice-proximal grounding-line fans (FA6-G) and ice-distal rainout deposits (FA6-D); and FA7: periglacial, recording cold, non-glacial conditions. Further descriptions are provided in the Supplementary Information. The vertical and horizontal distribution of these facies associations (Fig. 1) allows the sequence of environmental changes to be reconstructed in detail:

(1) The base of the Wilsonbreen Formation is a well-marked periglacially weathered horizon with thin wind-blown sands (Supplementary Fig. 4a,b). This surface records very limited sediment cycling in cold, arid conditions.
(2) At all localities, the weathering horizon is overlain by fluvial channel facies (FA2) and mudstones, marking the appearance of flowing water in the basin and implying positive air temperatures for at least part of the time (Supplementary Fig. 5a).
(3) Glacilacustrine deposits (FA6-D) record flooding of the basin and delivery of sediment by ice rafting (Supplementary Fig. 4c,d). Far-travelled clasts are common, indicating transport by a large, continental ice sheet.
(4) Warm-based, active ice advanced into the basin, indicated by traction tills and glacitectonic shearing (FA1; Supplementary Fig. 4e–g). (1–4 make up Member W1).
(5) Ice retreat is recorded by a second periglacial weathering surface (FA7). This is overlain by fluvial channel, floodplain, lake-margin and carbonate lacustrine sediments of W2 (FA2-5; Supplementary Fig. 5), recording a shifting mosaic of playa lakes and ephemeral streams. Lakes and river channels supported microbial communities. Millimetre-scale carbonate-siliciclastic rhythmites indicate seasonal cycles of

[1]Department of Geology, The University Centre in Svalbard (UNIS), N-9171 Longyearbyen, Norway. [2]School of Geography and Geosciences, University of St Andrews, St Andrews KY16 8YA, UK. [3]Institut de Physique du Globe de Paris, 75238 Paris, France. [4]Department of Geology and Geophysics, E235 Howe-Russell Complex, Louisiana State University, Baton Rouge, Louisiana 70803, USA. [5]Laboratoire des Sciences du Climat et de l'Environnement, CNRS-CEA, 91190 Gif-sur-Yvette, France. [6]School of Geography, Earth and Environmental Sciences, University of Birmingham, Birmingham B15 2TT, UK. [7]Institute of Geography and Earth Sciences, Aberystwyth University, Aberystwyth SY23 3DB, UK. [8]Natural Resource Management, Environmental Geology, New Mexico Highlands University, Las Vegas, New Mexico 87701, USA. [9]Lancaster Environment Centre, University of Lancaster, Lancaster LA1 4YQ, UK. †Present address: CASP, West Building, 181A Huntingdon Road, Cambridge CB3 0DH, UK. *e-mail: Doug.Benn@unis.no

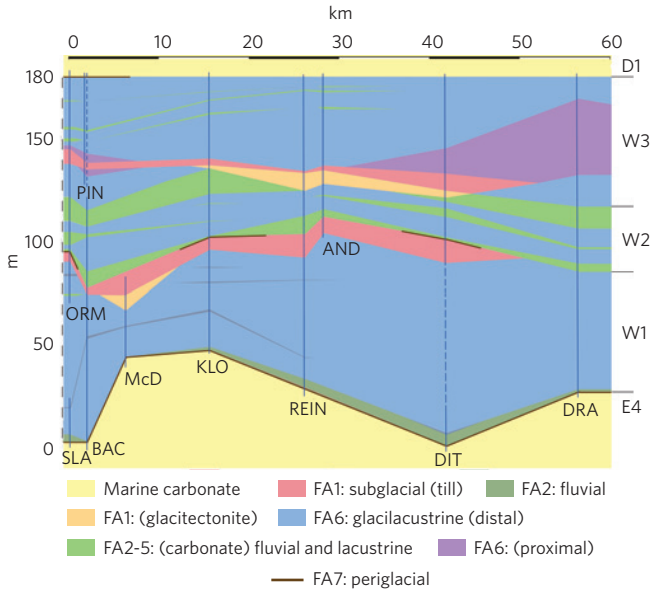

Figure 1 | Sedimentary architecture and palaeoenvironments of the Wilsonbreen Formation. Regional correlation of facies associations and members W1, W2 and W3 across northeast Svalbard. From north to south, study locations are: DRA, Dracoisen; DIT, Ditlovtoppen; AND, East Andromedafjellet; REIN, Reinsryggen (informal name); KLO, Klofjellet; McD, MacDonaldryggen; BAC, Backlundtoppen–Kvitfjellet ridge; PIN, Pinnsvinryggen (informal name); SLA, Slangen and ORM, Ormen.

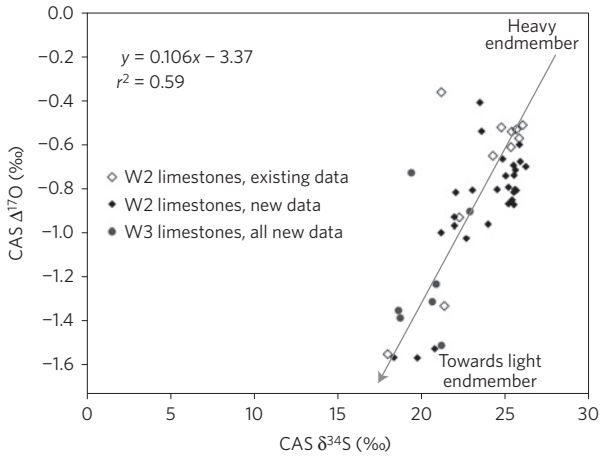

Figure 2 | Co-variation of $\Delta^{17}O$ and $\delta^{34}S$ from carbonate-associated sulphate in W2 and W3. 'Existing data' (ref. 16) and new data define a mixing line between pre-glacial sulphate (top) and an isotopically light sulphate formed by oxidation of pyrite including incorporation of a light-$\Delta^{17}O$ signature from a CO_2-enriched atmosphere. Data from W2 and W3 lie on closely similar trend lines, indicating no detectable change in p_{CO_2} between deposition of the two members.

photosynthesis. The environment seems to have been closely similar to that of the present-day McMurdo Dry Valleys in Antarctica, although with less extreme seasonality owing to its low latitude[13].

(6) Water levels and glacier extent underwent a series of oscillations, recorded by switches between glacilacustrine diamictite (FA6-D) and fluvial, lacustrine and lake-margin sediments (FA2-5) in W2. Sedimentation rates inferred from annual rhythmites in W2 suggest that each retreat phase may have lasted $\sim 10^4$ years.

(7) A second major ice advance marks the base of W3, with widespread deposition of subglacial tills and glacitectonism of underlying sediments. Basal tills are absent from the northernmost locality, but close proximity of glacier ice is recorded by grounding-line fans (FA6-G; Supplementary Fig. 4h,i).

(8) Ice retreated while the basin remained flooded and glacigenic sediment continued to be delivered to the lake by ice rafting. Thin laminated carbonates (FA5) in W3 indicate periods of reduced glacigenic sedimentation, indicative of minor climatic fluctuations over timescales of $\sim 10^3$ years (Supplementary Fig. 5g).

(9) A sharp contact with overlying laminated 'cap' carbonate (Supplementary Fig. 2) records the transition to post-glacial conditions. At some localities, basal conglomerates provide evidence of subaerial exposure, followed by marine transgression. The cap carbonate closely resembles basal Ediacaran carbonates elsewhere, and marks global deglaciation, eustatic sea-level rise and connection of the basin to the sea[1,12,14].

Environmental and atmospheric conditions during deposition of W2 and W3 can be further elucidated by isotopic data from carbonate-associated sulphate in lacustrine limestones (Fig. 2 and Supplementary Fig. 6). These exhibit negative to extremely negative $\Delta^{17}O$ values, with consistent linear co-variation with $\delta^{34}S$, indicating mixing of pre-glacial sulphate and isotopically light sulphate formed in a CO_2-enriched atmosphere[15,16]. The observed values could reflect non-unique combinations of p_{CO_2}, p_{O_2}, O_2 residence time and other factors, but a box model[17] indicates p_{CO_2} was most likely ~10 to 100 mbar (1 mbar = 1,000 ppmv).

These values are far too high to permit formation of low-latitude ice sheets in the Neoproterozoic, but they are consistent with a late-stage Snowball Earth. For an ice-free Neoproterozoic Earth, model studies indicate mean terrestrial temperatures in the range 30–50 °C for $p_{CO_2} = 10$ to 100 mbar (ref. 18). Formation of low-latitude ice sheets requires much lower p_{CO_2}, on the order of 0.1–1 mbar (refs 2,19,20). Once formed, however, ice sheets can persist despite rising CO_2 from volcanic outgassing, as a result of a high planetary albedo. This hysteresis in the relationship between p_{CO_2} and planetary temperature is a key element of Snowball Earth theory. It implies that W2 and W3 were deposited relatively late in the Marinoan, after volcanic outgassing had raised p_{CO_2} from 0.1 or 1 mbar to 10 or 100 mbar. Modelled silicate weathering and volcanic outgassing rates indicate that this would require 10^6 to 10^7 years[21].

The consistent co-variation of $\Delta^{17}O$ and $\delta^{34}S$ in lacustrine limestones in both W2 and W3 suggests no detectable rise in atmospheric p_{CO_2}, as this would alter the slope of the mixing line (Fig. 2). This implies that the glacier oscillations recorded in W2 and W3 occurred during a relatively short time interval ($<10^5$ years[21]) towards the end of the Marinoan. In turn, this implies that the remainder of the Wilsonbreen Formation (including the basal weathering horizon) represents many millions of years, during which p_{CO_2} built up from the low values necessary for inception of low-latitude glaciation to those indicated by the geochemical evidence. The weathering horizon provides direct evidence of cold, arid conditions during this interval, before the appearance of fluvial and glacilacustrine sediments in the basin.

The evidence for ice sheet advance/retreat cycles at low latitudes in a CO_2-enriched atmosphere motivated a series of numerical simulations to test the hypothesis that these cycles were linked to Milankovitch orbital variations. We employed asynchronous coupling of a three-dimensional ice sheet model and an atmospheric general circulation model using the continental configuration of ref. 22. We first ran simulations with a modern orbital configuration to examine ice sheet behaviour through a large range of p_{CO_2} values from 0.1 to 100 mbar (ref. 23; Supplementary Figs 7–10). Consistently with previous results[2,20], at low p_{CO_2} (0.1 mbar), global ice volume reaches 170×10^6 km^3, but substantial tropical land

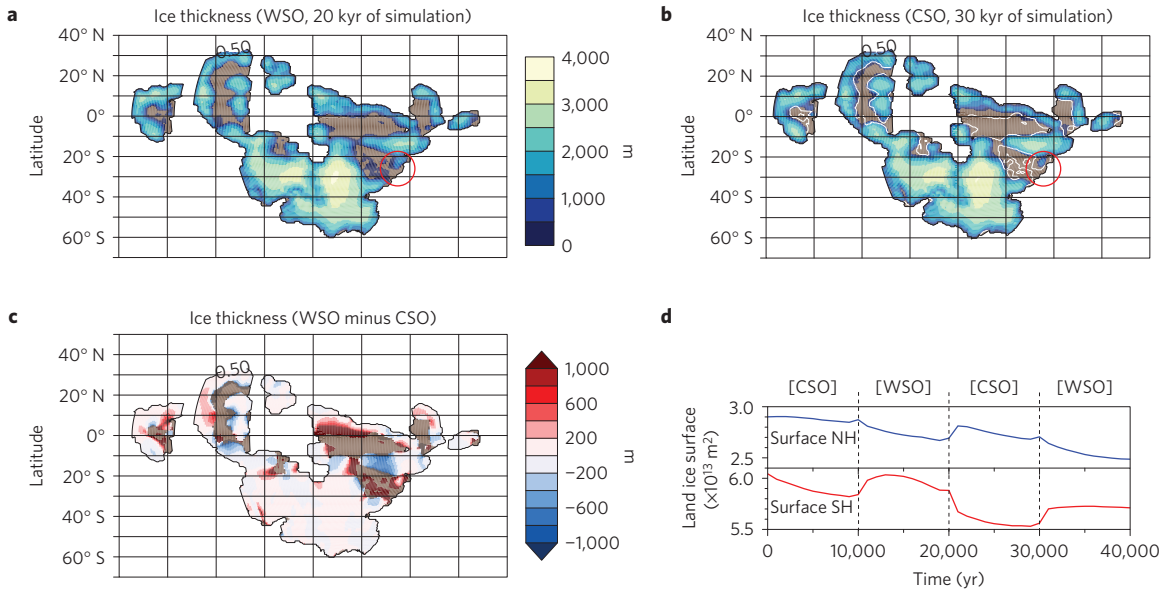

Figure 3 | Modelled ice sheet oscillations in response to orbital forcing. a,**b**, Shaded contours show land ice thickness obtained with 20 mbar of carbon dioxide in response to changes of orbital forcing (WSO (**a**)) and CSO (**b**), warm/cold summer orbit for the northern hemisphere) over the course of two precession cycles (40 kyr of simulation). In the light brown continental areas without ice, the white line is used to represent the old ice sheet extension (WSO case). The Svalbard area is indicated by a red circle. **c**, Ice thickness variation in 10 kyr (WSO case after 20 kyr minus CSO case after 30 kyr of simulation). In **a**–**c** the continental outline is shown by the 0.5 m elevation contour. **d**, Surface of hemisphere covered by ice (m^2) through time ([WSO] and [CSO] indicate which orbital configuration is used).

areas remain ice free as a result of sublimation exceeding snowfall (Supplementary Fig. 10a). Ice volume remains relatively constant for $p_{CO_2} = 0.1$ to 20 mbar (Supplementary Fig. 10b), owing to an increase in accumulation that compensates for higher ablation rates (Supplementary Fig. 13). In contrast, above 20 mbar, ice extent in the eastern Tropics significantly decreases (Supplementary Fig. 10c). At $p_{CO_2} = 100$ mbar, most of the continental ice cover disappears, except for remnants over mountain ranges (Supplementary Fig. 10d).

To test the sensitivity of the tropical ice sheets to Milankovitch forcing, experiments with changing orbital parameters were initialized using the steady-state ice sheets for $p_{CO_2} = 20$ mbar. Although obliquity has been invoked as a possible cause of Neoproterozoic glaciations[24], this mechanism remains problematical and cannot account for significant climatic oscillations at low latitudes[25,26]. We therefore focused on precession as a possible driver, and used two opposite orbital configurations, favouring cold and warm summers, respectively, over the northern tropics (CSO: cold summer orbit and WSO: warm summer orbit; Supplementary Fig. 14). Switching between these configurations causes tropical ice sheets to advance/retreat over several hundred kilometres in 10 kyr (Supplementary Movie 1), with strong asymmetry between hemispheres (Fig. 3). Shifting from WSO to CSO causes ice retreat in the Southern Hemisphere and ice sheet expansion in the Northern Hemisphere (Supplementary Fig. 14c,d). Significant ice volume changes occur between 30° N and S, but are less apparent at higher latitudes. This reflects higher ablation rates in the warmer low latitudes (Supplementary Fig. 14e,h), and higher ice sheet sensitivity to shifting patterns of melt. Larger greenhouse forcing at the end of the Snowball event implies increasing ice sheet sensitivity to subtle insolation changes. Given a strong diurnal cycle[23], our simulations also predict a significant number of days above 0 °C in the tropics (Supplementary Fig. 15), consistent with geological evidence for ice rafting, liquid water in lakes and rivers, and photosynthetic microbial communities.

Our results show that geological evidence for glacial–interglacial cycles[5–7] is consistent with an enriched Snowball Earth theory. Termination of the Marinoan panglaciation was not a simple switch from icehouse to greenhouse states, but was characterized by a climate transition during which glacial cycles could be forced by Milankovitch orbital variations. The geochemical evidence presented here implies that at least the upper 60–70% of the Wilsonbreen Formation was deposited in ~10^5 years, on the assumption that a trend in p_{CO_2} would be evident over longer timescales[21]. Rates of CO_2 build-up, however, may have slowed in the later stages of Snowball Earth owing to silicate weathering of exposed land surfaces, so it is possible that the oscillatory phase was more prolonged.

Initiation of low-latitude glaciation in the Neoproterozoic requires low p_{CO_2} (0.1–1 mbar; refs 2,19,20), implying that the oscillatory phase was preceded by a prolonged colder period (~10^6 to 10^7 years) during which p_{CO_2} increased gradually as a result of volcanic outgassing[21]. This timescale is in agreement with recent dates indicating the Marinoan lasted ~15 million years[27]. The basal weathering horizon is consistent with a period of low temperatures and limited hydrologic cycle before the oscillatory phase[2,19].

Further work is needed to refine the upper and lower limits of p_{CO_2} conducive to climate and ice sheet oscillations in Snowball Earth. Factors not included in the present model, such as supraglacial dust or areas of ice-free tropical ocean[28–30], can be expected to make the Earth system more sensitive to orbital forcing. While many details remain to be investigated, our overall conclusions remain robust.

The Neoproterozoic Snowball Earth was nuanced, varied and rich. We anticipate that detailed studies of the rock record in other parts of the world, in conjunction with numerical modelling studies, will continue to yield insight into the temporal and regional diversity of this pivotal period in Earth history.

Methods

Methods and any associated references are available in the online version of the paper.

Received 17 February 2015; accepted 8 July 2015;
published online 24 August 2015

References

1. Hoffman, P. F. & Schrag, D. P. The Snowball Earth hypothesis: Testing the limits of global change. *Terra Nova* **14,** 129–155 (2002).
2. Donnadieu, Y., Goddéris, Y. & Le Hir, G. *Treatise on Geochemistry* 2nd edn, Vol. 6, 217–229 (Elsevier, 2014).
3. Hoffman, P. F. Strange bedfellows: Glacial diamictite and cap carbonate from the Marinoan (635 Ma) glaciation in Namibia. *Sedimentology* **58,** 57–119 (2011).
4. Allen, P. A. & Etienne, J. L. Sedimentary challenge to Snowball Earth. *Nature Geosci.* **1,** 817–825 (2008).
5. Rieu, R., Allen, P. A., Plötze, M. & Pettke, T. Climatic cycles during a Neoproterozoic "snowball" glacial epoch. *Geology* **35,** 299–302 (2007).
6. Le Heron, D. P., Busfield, M. E. & Kamona, F. An interglacial on snowball Earth? Dynamic ice behaviour revealed in the Chuos Formation, Namibia. *Sedimentology* **60,** 411–427 (2013).
7. Fairchild, I. J. & Hambrey, M. J. Vendian basin evolution in East Greenland and NE Svalbard. *Precambrian Res.* **73,** 217–233 (1995).
8. Halverson, G. P. in *Neoproterozoic Geobiology and Paleobiology* (eds Xiao, S. & Kaufman, A. J.) 231–271 (Springer, 2006).
9. Li, X.-X., Evans, D. A. & Halverson, G. P. Neoproterozoic glaciations in a revised global palaeogeography from the breakup of Rodinia to the assembly of Gondwanaland. *Sedim. Geol.* **294,** 219–232 (2013).
10. Petronis, M. S. *et al.* in *AGU Fall Meeting 2013* Abstract #GP41A-1107 (American Geophysical Union, 2013).
11. Harland, W. B. *The Geology of Svalbard* (Geological Society, 1997).
12. Creveling, J. R. & Mitrovica, J. X. The sea-level fingerprint of a Snowball Earth deglaciation. *Earth Planet. Sci. Lett.* **399,** 74–85 (2014).
13. Lyons, W. B. *et al.* The McMurdo Dry Valleys long-term ecological research program: New understanding of the biogeochemistry of the Dry Valley lakes: A review. *Polar Geogr.* **25,** 202–217 (2001).
14. Hoffman, P. *et al.* Are basal Ediacaran (635 Ma) basal 'cap dolostones' diachronous? *Earth Planet. Sci. Lett.* **258,** 114–131 (2007).
15. Fairchild, I. J., Hambrey, M. J., Spiro, B. & Jefferson, T. H. Late Proterozoic glacial carbonates in northeast Spitsbergen: New insights into the carbonate-tillite association. *Geol. Mag.* **126,** 469–490 (1989).
16. Bao, H., Fairchild, I. J., Wynn, P. M. & Spötl, C. Stretching the envelope of past surface environments: Neoproterozoic glacial lakes from Svalbard. *Science* **323,** 119–122 (2009).
17. Cao, X. & Bao, H. Dynamic model constraints on oxygen-17 depletion in atmospheric O_2 after a snowball Earth. *Proc. Natl Acad. Sci. USA* **110,** 14546–14550 (2013).
18. Le Hir, G. *et al.* The snowball Earth aftermath: Exploring the limits of continental weathering processes. *Earth Planet. Sci. Lett.* **277,** 453–463 (2009).
19. Pierrehumbert, R., Abbot, D. S., Voigt, A. & Koll, D. Climate of the Neoproterozoic. *Ann. Rev. Earth Planet. Sci.* **39,** 417–460 (2011).
20. Pollard, D. & Kasting, J. F. in *The Extreme Proterozoic: Geology, Geochemistry, and Climate* (eds Jenkins, G. S., McMenamin, M. A. S., McKay, C. P. & Sohl, L.) 91–105 (Geophysical Monograph Series 146, American Geophysical Union, 2004).
21. Le Hir, G., Ramstein, G., Donnadiieu, Y. & Goddéris, Y. Scenario for the evolution of atmospheric p_{CO_2} during a snowball Earth. *Geology* **36,** 47–50 (2008).
22. Hoffman, P. F. & Li, Z. X. A palaeogeographic context for Neoproterozoic glaciation. *Palaeogeogr. Palaeoclimatol. Palaeoecol.* **277,** 158–172 (2009).
23. Pierrehumbert, R. T. Climate dynamics of a hard Snowball Earth. *J. Geophys. Res.* **110,** D01111 (2005).
24. Spiegl, T. C., Paeth, H. & Frimmel, H. E. Evaluating key parameters for the initiation of a Neoproterozoic Snowball Earth with a single Earth System Model of intermediate complexity. *Earth Planet. Sci. Lett.* **415,** 100–110 (2015).
25. Donnadieu, Y., Ramstein, G., Fluteau, F., Besse, J. & Meert, J. Is high obliquity a plausible cause for Neoproterozoic glaciations? *Geophys. Res. Lett.* **29,** 2127 (2002).
26. Paillard, D. Quaternary glaciations: From observations to theories. *Quat. Sci. Rev.* **107,** 11–24 (2015).
27. Rooney, A. D. *et al.* A Cryogenican chronology: Two long-lasting synchronous Neoproterozoic glaciations. *Geology* **43,** 459–462 (2015).
28. Abbot, D. S. & Pierrehumbert, R. T. Mudball: Surface dust and Snowball Earth deglaciation. *J. Geophys. Res.* **115,** D03104 (2010).
29. Abbot, D. S., Voigt, S. & Koll, D. The Jormungand global climate state and implications for Neoproterozoic glaciations. *J. Geophys. Res.* **116,** D18103 (2011).
30. Rose, B. E. J. Stable "Waterbelt" climates controlled by tropical ocean heat transport: A nonlinear coupled climate mechanism of relevance to Snowball Earth. *J. Geophys. Res.* **120,** 1404–1423 (2015).

Acknowledgements

This work was supported by the NERC-funded project GR3/ NE/H004963/1 Glacial Activity in Neoproterozoic Svalbard (GAINS). Logistical support was provided by the University Centre in Svalbard. This work was granted access to the HPC resources of CCRT under allocation 2014-017013 made by GENCI (Grand Equipement National de Calcul Intensif). We also thank D. Paillard and P. Hoffman for stimulating discussions and valuable insights.

Author contributions

Field data were collected and analysed by I.J.F., D.I.B., E.J.F., M.J.H., E.A.McM., M.S.P., P.M.W. and C.T.E.S. Geochemical analyses were conducted by H.B. and P.M.W. Model experiments were designed and conducted by G.L.H., Y.D., C.D. and G.R. The manuscript and figures were drafted by D.I.B., I.J.F. and G.L.H., with contributions from the other authors.

Additional information

Supplementary information is available in the online version of the paper. Reprints and permissions information is available online at www.nature.com/reprints. Correspondence and requests for materials should be addressed to D.I.B.

Competing financial interests

The authors declare no competing financial interests.

Methods

Sedimentology. Lithofacies were classified based on grain size, internal sedimentary structures and deformation structures, and bounding surfaces. Detailed stratigraphic logs were made in the field, supplemented by drawings and photographs of key features. Samples were taken for polishing and thin sectioning, to allow detailed examination of microstructures in the laboratory. In addition, data were collected on clast lithology, shape, surface features and fabric. Diamictites of the Wilsonbreen Formation are commonly very friable, allowing included clasts to be removed intact from the surrounding matrix, allowing measurement of both clast morphology and orientation, using methods developed for unlithified sediments. Clast morphology (shape, roundness and surface texture) was measured for samples of 50 clasts to determine transport pathways. Clast fabric analysis was performed by measuring a-axis orientations of samples of 50 clasts with a compass-clinometer, and data were summarized using the eigenvalue or orientation tensor method. Oriented samples for measurement of anisotropy of magnetic susceptibility (AMS) were collected using a combination of field-drilling and block sampling. AMS was measured using an AGICO KLY-3 Kappabridge operating at 875 Hz with a 300 A m^{-1} applied field at the University of Birmingham and an AGICO MFK-1A Kappabridge operating at 976 Hz with a 200 A m^{-1} applied field at New Mexico Highlands University.

Geochemistry. Laboratory procedures for extracting, purifying and measuring the triple oxygen ($\delta^{18}O$ and $\Delta^{17}O$) and sulphur ($\delta^{34}S$) isotope composition of carbonate associated sulphate (CAS) in bulk carbonates are detailed in ref. 16. Briefly, fresh carbonate-bearing rock chips were crushed into fine grains and powders using mortar and pestle. Rinsing the fines with 18 MΩ water revealed little water-leachable sulphate in any of the Wilsonbreen carbonates. Subsequently, about 10 to 30 g carbonates were slowly digested in 1–3 M HCl solutions. The solution was then centrifuged, filtered through a 0.2 μm filter, and acidified before saturated $BaCl_2$ droplets were added. $BaSO_4$ precipitates were collected after >12 h and purified using the DDARP method (see Supplementary Information). The purified $BaSO_4$ was then analysed for three different isotope parameters: $\Delta^{17}O$, by converting to O_2 using a CO_2-laser fluorination method; $\delta^{18}O$, by converting to CO through a Thermal Conversion Elemental Analyzer (TCEA) at 1,450 °C; and $\delta^{34}S$, by converting to SO_2 by combustion in tin capsules in the presence of V_2O_5 through an Elementar Pyrocube elemental analyser at 1,050 °C. The $\Delta^{17}O$ was run in dual-inlet mode, whereas the $\delta^{18}O$ and $\delta^{34}S$ were run in continuous-flow mode. Both the $\Delta^{17}O$ and $\delta^{18}O$ were run on a MAT 253 at Louisiana State University, whereas the $\delta^{34}S$ was determined on an Isoprime 100 continuous-flow mass spectrometer at the University of Lancaster, UK. The $\Delta^{17}O$ was calculated as $\Delta^{17}O \equiv \delta'^{17}O - 0.52 \times \delta'^{18}O$ in which $\delta' \equiv 1{,}000\ln(R_{sample}/R_{standard})$ and R is the molar ratio of $^{18}O/^{16}O$ or $^{17}O/^{16}O$. All δ values are in Vienna Standard Mean Ocean Water VSMOW and Vienna Canyon Diablo Troilite (VCDT) for sulphate oxygen and sulphur, respectively. The analytical standard deviation (1σ) for replicate analysis associated with the $\Delta^{17}O$, $\delta^{18}O$ and $\delta^{34}S$ are ±0.05‰, ±0.5‰ and ±0.2‰, respectively. As the CAS is heterogeneous in hand specimens, the standard deviation is for laboratory procedures. $\delta^{34}S$ values were corrected against VCDT using within-run analyses of international standard NBS-127 (assuming $\delta^{34}S$ values of +21.1‰). Within-run standard replication (1 s.d.) was <0.3‰. All geochemical data are included in Supplementary Table 1.

Numerical modelling. Model runs were conducted with a coupled atmospheric general circulation model (LMDz) and ice sheet model (GRISLI: GRenoble Ice Shelf and Land Ice model). LMDz (spatial resolution 4° in latitude × 5° in longitude with 38 vertical levels) was run with prescribed continental ice to climatic equilibrium. GRISLI has a 40 km grid size and is driven with downscaled climatic fields of surface air temperature, precipitation and evaporation. To capture ice sheet–climate feedbacks, LMDz is rerun using the new ice sheet distribution and topography. This procedure was repeated each 10 kyr to investigate orbital forcing.

Surface mass balance (accumulation minus sublimation and melting) was computed from monthly mean temperature, precipitation and evaporation rate. Melt rate is calculated using the positive-degree-day method.

No sea ice dynamics treatment is specified, the sea ice cover is prescribed and a thickness of 10 m is imposed. Ice albedo is fixed at 0.6, whereas snow albedo varies from 0.9 from 0.55 as a function of the zenith and ageing process. Land ice/snow free surface has the characteristic of a bare soil (rocky regolith) with an albedo of 0.3.

Code availability. Code for the GCM LMDz can be accessed at: http://lmdz.lmd.jussieu.fr. Code for the ISM GRISLI (GRenoble Ice Shelf and Land Ice model) is not available.

Further details of the methods and modelling procedures are provided in the Supplementary Information in the online version of the paper.

AGU PUBLICATIONS

Paleoceanography

RESEARCH ARTICLE
10.1002/2016PA002928

Glacial onset predated Late Ordovician climate cooling

Alexandre Pohl[1], Yannick Donnadieu[1], Guillaume Le Hir[2], Jean-Baptiste Ladant[1], Christophe Dumas[1], Jorge Alvarez-Solas[3], and Thijs R. A. Vandenbroucke[4,5]

[1]Laboratoire des Sciences du Climat et de l'Environnement, LSCE/IPSL, CEA-CNRS-UVSQ, Université Paris-Saclay, Gif-sur-Yvette, France, [2]Institut de Physique du Globe de Paris, Université Paris7-Denis Diderot, 1 rue Jussieu, Paris, France, [3]Departamento Astrofísica y Ciencias de la Atmósfera, Universidad Complutense de Madrid, Madrid, Spain, [4]Department of Geology, Ghent University, Krijgslaan, Belgium, [5]Evo-Eco-Paléo UMR 8198, Université de Lille, Villeneuve d'Ascq CEDEX, France

Abstract The Ordovician glaciation represents the acme of one of only three major icehouse periods in Earth's Phanerozoic history and is notorious for setting the scene for one of the "big five" mass extinction events. Nevertheless, the mechanisms that drove ice sheet growth remain poorly understood and the final extent of the ice sheet crudely constrained. Here using an Earth system model with an innovative coupling method between ocean, atmosphere, and land ice accounting for climate and ice sheet feedback processes, we report simulations portraying for the first time the detailed evolution of the Ordovician ice sheet. We show that the emergence of the ice sheet happened in two discrete phases. In a counterintuitive sequence of events, the continental ice sheet appeared suddenly in a warm climate. Only during the second act, and set against a background of decreasing atmospheric CO_2, followed steeply dropping temperatures and extending sea ice. The comparison with abundant sedimentological, geochemical, and micropaleontological data suggests that glacial onset may have occurred as early as the Middle Ordovician Darriwilian, in agreement with recent studies reporting third-order glacioeustatic cycles during the same period. The second step in ice sheet growth, typified by a sudden drop in tropical sea surface temperatures by ~8°C and the further extension of a single, continental-scale ice sheet over Gondwana, marked the onset of the Hirnantian glacial maximum. By suggesting the presence of an ice sheet over Gondwana throughout most of the Middle and Late Ordovician, our models embrace the emerging paradigm of an "early Paleozoic Ice Age."

Key Points:
- Earth system model providing the first detailed simulation of Middle to Late Ordovician land ice growth
- Model/data comparison suggests a Darriwilian age for glacial onset
- A single ice sheet of large extent covered Gondwana during the Hirnantian glacial maximum

Supporting Information:
- Supporting Information S1
- Supporting Information S2
- Figure S1

Correspondence to:
A. Pohl,
pohl.alexandre@gmail.com

Citation:
Pohl, A., Y. Donnadieu, G. Le Hir, J.-B. Ladant, C. Dumas, J. Alvarez-Solas, and T. R. A.Vandenbroucke (2016), Glacial onset predated Late Ordovician climate cooling, *Paleoceanography*, *31*, doi:10.1002/2016PA002928.

Received 20 JAN 2016
Accepted 21 MAY 2016
Accepted article online 28 MAY 2016

1. Introduction

The Middle to Late Ordovician (470–444 Ma) has long been considered an enigmatic and unique period in Earth's history. Much of this mystery revolved around our inability to explain how a glacial pulse [*Finnegan et al.*, 2011], high pCO_2 levels potentially exceeding 20 times the preindustrial atmospheric level [*Berner*, 1990; *Yapp and Poths*, 1996] (PAL, 1 PAL = 280 ppm), a global biodiversity crisis [*Sheehan*, 2001], and major perturbations of the carbon cycle [*Brenchley et al.*, 1994] could have coincided. Over the last few years, however, evidence has accumulated that some of these apparent conflicts may have resulted from erroneous interpretations of the relatively poorly preserved and incomplete Ordovician sedimentary record [*Ghienne et al.*, 2014]. Recent studies suggest that the atmospheric CO_2 content was probably much lower than had been previously proposed [*Rothman*, 2002; *Herrmann et al.*, 2004; *Berner*, 2006; *Vandenbroucke et al.*, 2010a; *Pancost et al.*, 2013] and that ocean temperatures reached modern-like values as early as the Middle Ordovician, distinctly contrasting with earlier visions of a perennial Ordovician supergreenhouse [*Trotter et al.*, 2008; *Vandenbroucke et al.*, 2009]. Despite a more comprehensive analysis of the physical evidence, major uncertainties persist about the mechanisms that drove ice sheet growth and about its final extent. Rooted in the disperse nature of the Late Ordovician glacial sedimentary records in North Africa [*Ghienne et al.*, 2007], South Africa, and South America [*Díaz-Martínez and Grahn*, 2007], one of the major questions remains whether those glacial outcrops are indicative of a single, large ice sheet that developed from North Africa (then at a polar latitude) to South Africa (at tropical latitudes in latest reconstructions) [*Torsvik and Cocks*, 2013] or if independent ice sheets of smaller extent coexisted over the South Pole and in the tropics [*Ghienne et al.*, 2007; *Le Heron and Dowdeswell*, 2009].

It is also still unclear how glacial onset could have possibly occurred in the midst of a prolonged period of hot climate. Evidence for warm shallow seas in the tropics (up to 37°C) [*Finnegan et al.*, 2011], as suggested by most recent Ordovician geochemical data [*Trotter et al.*, 2008; *Finnegan et al.*, 2011], is in apparent contradiction with Middle to Upper Ordovician deposits where glacioeustatic events are identified [*Loi et al.*, 2010; *Turner et al.*, 2012; *Elrick et al.*, 2013; *Dabard et al.*, 2015; *Rasmussen et al.*, 2016] or suggested [*Nielsen*, 2004] (see discussion in *Amberg et al.* [2016]). These eustatic cycles support the presence of ice sheets since the Middle Ordovician Darriwilian (467 Ma) rather than a sudden emplacement of a massive ice sheet restricted to the Hirnantian stage (445–444 Ma).

To investigate how these apparently contradictive interpretations can be reconciled, we employ an Earth system model to propose the first realistic simulations of Middle to Late Ordovician ice sheet growth. The last modeling attempts of this kind date back to two papers published by *Herrmann et al.* [2003, 2004]. Building on the seminal studies of *Crowley and Baum* [1991, 1995], they provided major insights into the climatic conditions required to trigger Late Ordovician glacial onset. However, they are more than 10 years old, and the experimental setup that is available to us has significantly advanced. *Herrmann et al.*'s [2003, 2004] models notably did not resolve ice sheet feedbacks on global climate. The simulated ice sheet did not extend beyond 60°S and therefore poorly compared to the Ordovician glacial sedimentary record [e.g., *Ghienne et al.*, 2007]. More recently, *Lowry et al.* [2014] asynchronously coupled a slab mixed-layer ocean-atmosphere general circulation model (GENESIS) with an ice sheet model to investigate the impact of the changes in continental configuration on the potential for glacial inception throughout the Paleozoic. However, they did not use specific Ordovician boundary conditions in their coupled simulations—in terms of topography, solar luminosity, and CO_2 level in particular—which resulted in significant discrepancies between Ordovician geological data and modeled ice sheet extent and flow. The flat topography led to an unexpected ice sheet geometry with the maximum ice sheet height simulated along the coasts of Gondwana at 440 Ma. The resulting ice sheet flowed from the coast to the continent interior (*Lowry et al.* [2014]; see their discussion section), at odds with the sedimentary record of the Hirnantian glaciation [e.g., *Ghienne et al.*, 2007]. They ran additional experiments considering the evolution of the solar luminosity value throughout the Paleozoic, but they did not account for the feedbacks of the ice sheet on global climate in these simulations. To capture processes leading to glacial onset and ensure both reliable ice sheet growth mechanisms and robust steady state ice sheet extent, we here use suitable boundary conditions together with an innovative modeling procedure that for the first time in the Ordovician considers ocean-atmosphere-ice sheet interplays as well as a fully dynamic ocean component. Our model accounts for Ordovician orbital variations and for the wide range of suggested CO_2 levels, i.e., 3–24 PAL (see section 2.2.2).

We compare our modeling results with abundant geochemical, sedimentological, and paleontological data, which provides additional insights into both the extent and duration of the glaciation. However, current ice sheet models exhibit severe issues of hysteresis, making land ice too stable and requiring unreasonably high atmospheric CO_2 levels to cause continental-scale ice sheet retreats [*Pollard and DeConto*, 2005; *Horton and Poulsen*, 2009]. Therefore, we did not attempt the simulation of the Late Ordovician deglaciation but identify this as a target for the future. We are confident that ongoing advances in modeling of the cryosphere [*Ganopolski et al.*, 2010; *Pollard et al.*, 2015; *Gasson et al.*, 2016] will help resolve this issue in the years to come.

2. Methods

2.1. Asynchronous Coupling Design

The deep-time Earth system model used throughout the study is described below. Our aim is to simulate ice sheet-climate equilibria under decreasing pCO_2, representative of the well-established Ordovician cooling trend [*Trotter et al.*, 2008]. This requires coupling an ocean-atmosphere general circulation model with an ice sheet model. The most straightforward way to couple an ocean-atmosphere climate model to an ice sheet model is the purely synchronous coupling method, which would account for exchanges between the ocean, atmosphere, and land ice components at each model time step. The long computational time required by an ocean-atmosphere general circulation model (GCM), however, forbids the use of synchronous coupling to solve deep-time issues, which usually require long ice sheet runs lasting hundreds of thousands of model years [e.g., *Ladant et al.*, 2014]. Several alternative methods have therefore been proposed [*Pollard*, 2010], including asynchronous coupling with a GCM lookup table, which remains the only solution applicable on very long

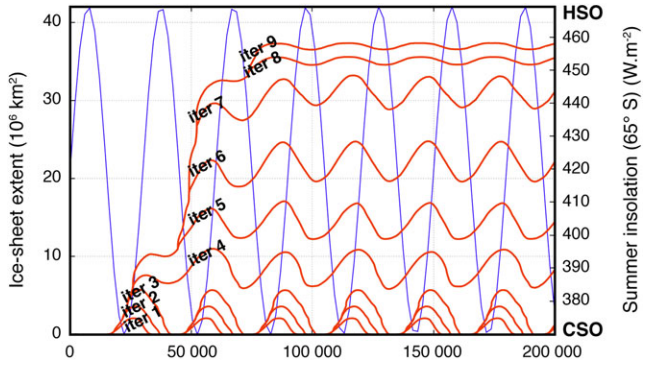

Figure 1. Ice sheet results obtained at 12 PAL, with our Earth system model accounting for orbital variations and ice sheet feedbacks on climate, throughout the successive asynchronous coupling steps. Red curves represent the evolution of the land ice cover through ice sheet model integration time (200 kyr per iteration). The thin blue line stands for the 30 kyr obliquity forcing used to interpolate between the CSO and the HSO. The associated right *y* axis gives the Southern Hemisphere mean summer insolation received at 65°S. The ice sheet model (GRISLI) is first run for 200 kyr from its initial, ice-free state (iter 1), by linearly interpolating between the CSO and HSO temperature and precipitation forcing fields according to the 30 kyr Ordovician obliquity period. Then, the largest ice sheet simulated during this first iteration is returned as a boundary condition to the climate models. New climatic forcing fields are simulated, which therefore take the ice-albedo local radiative effect into account. The latter climatic snapshots are added to the "ice cover" dimension of the GCM lookup table, providing new climatic fields to interpolate with. GRISLI is once again run for 200 kyr from its ice-free state (iter 2), and the ice sheet model climatic forcing fields are interpolated as a function of time both between the CSO and the HSO and between the ice-free state and the glaciated state predicted from previous iteration. The largest ice sheet simulated is used to force the third iteration (new climatic snapshots are added to the GCM lookup table), and the loop is repeated until the ice sheet is in equilibrium with global climate (iter 4 to iter 9), i.e., an additional iteration does not induce a much larger ice sheet extent (compare iter 8 and iter 9).

time scales [e.g., *Ladant et al.*, 2014]. In this method, GCM snapshots are gathered into a multidimensional matrix. Each dimension of the matrix corresponds to a given external forcing (e.g., the orbital configuration or the pCO_2) and contains surface temperature and precipitation fields simulated for several values of this forcing, which provide the entire information required during the subsequent ice sheet model integration. Then, at any point in the long-term ice sheet model run, the surface mass balance of the ice sheet is calculated based on mean monthly temperature and precipitation fields interpolated between the appropriate cells of the matrix [*Pollard*, 2010]. In the present case study, the GCM snapshots are collected in a matrix with three dimensions, i.e., the Earth's orbital parameters, the ice sheet size, and the pCO_2, following the methodology successfully applied to the Antarctic ice sheet onset at the Eocene-Oligocene transition [*Ladant et al.*, 2014]. However, unlike the Antarctic ice sheet, which has limited spatial extent, the maximum ice sheet extent over the vast Gondwana paleocontinent is virtually unlimited, and as such, there is no reason to preconceive any maximum ice sheet extent prior to the buildup of the 3-D matrix. Here the ice sheet sizes are not prescribed, hence evolving freely, instead of imposing successive ice sheet extents for the interpolation. As a consequence we build the matrix step by step.

1. Climatic snapshots representative of ice-free conditions are first obtained: for a given pCO_2 (first dimension of the matrix), two climate states are computed by the GCM with an ice-free bedrock topography (second dimension), for two opposed orbital configurations (third dimension) yielding either a cold or a warm summer over the southern high latitudes (cold and hot summer orbits—CSO and HSO, respectively—see section 2.2.2).
2. A first ice sheet is modeled: the ice sheet model is run, for the same pCO_2 level, using a sinusoidal forcing in obliquity weighted between the two opposite climates from step 1 (iter 1 in Figure 1). The period of the sinusoidal variation in obliquity is set to 30 kyr, based on spectral analysis of Ordovician halite deposits [*Williams*, 1991]. Orbital variations are known as a major driver of Pleistocene glacial cycles [e.g., *Paillard*, 1998], and they have been shown to significantly impact the growth of the ice sheet during the Ordovician as well [*Herrmann et al.*, 2003; *Ghienne et al.*, 2014; *Dabard et al.*, 2015].
3. An ice sheet of larger extent is simulated, provided that climate is favorable to ice sheet growth: in order to account for the feedbacks of the ice sheet on climate, the largest ice sheet simulated previously is reintroduced as a boundary condition into the climate model (still keeping the CO_2 constant). Two additional glacial climatic states are simulated, one for each of the two opposite orbital configurations (CSO and HSO). The climatic snapshots are gathered into the matrix of climatic states, each snapshot corresponding to a specific land ice mask and orbital configuration (i.e., a CSO snapshot and a HSO snapshot for each ice sheet extent, including the ice-free state). The ice sheet model is then run, starting from an ice-free state, forced in temperature and precipitation using climatic fields interpolated, throughout model integration time,

between the climatic snapshots of the matrix as a function of both the orbital forcing and the extent of the ice sheet (iter 2 in Figure 1).

4. Step 3 is repeated until steady state is reached between land ice and global climate: a new member is thus added to the "ice sheet extent" dimension of the matrix as many times as necessary, and the resulting ice sheet is neither limited to a given geometry nor artificially pulled toward a maximal extent, which might have been the case with prescribed ice sheets (iter 3 to iter 9 in Figure 1).
5. The whole procedure is repeated for the other CO_2 values.

Climatic snapshots are obtained using successively the ocean-atmosphere general circulation model FOAM (as a sea surface temperature generator) and the state-of-the-art atmospheric model LMDZ, with the same boundary conditions. The model FOAM is first integrated until deep-ocean equilibrium is reached (≥2000 years). Given that the atmospheric fields of temperature and precipitation simulated with FOAM are not sufficiently well resolved to directly force the ice sheet model GRISLI, the sea surface temperatures simulated with FOAM are subsequently used to force the atmospheric model LMDZ, the outputs of which are in turn used to force GRISLI. The alternate use of FOAM and LMDZ has been shown to perform well, as testified by previously published paleoclimate studies [*Ladant et al.*, 2014; *Licht et al.*, 2014].

2.2. Model Setup

2.2.1. Model Details

FOAM (Fast Ocean Atmosphere Model) version 1.5 is a fully coupled mixed-resolution ocean-atmosphere general circulation model with no flux corrections [*Jacob*, 1997]. Its quick turnaround time allows for long millennium-scale integrations. FOAM is consequently well designed for paleoclimate studies, for which purpose it has been routinely used in the past, including for the Ordovician [*Nardin et al.*, 2011; *Pohl et al.*, 2014, 2015]. The atmospheric component of the model is the National Center for Atmospheric Research's (NCAR) Community Climate Model version 2 (CCM2) benefitting from the upgraded radiative and hydrologic physics from CCM3 version 3.2. It is run at a R15 spectral resolution (4.5° × 7.5°) with 18 vertical levels (14 in the troposphere). The ocean module is the Ocean Model version 3 (OM3). It is a finite difference, 24-level *z* coordinate ocean general circulation model providing a higher resolution than the atmospheric module (1.4° × 2.8°) on a rectangular grid. Sea ice is simulated using the thermodynamics of the NCAR's Climate System Model 1.4 sea ice module, which is based on the *Semtner* [1976] three-layer thermodynamic snow/ice model.

The LMDZ (Laboratoire de Météorologie Dynamique Zoom) model is an IPCC-class (Intergovernmental Panel on Climate Change) atmospheric general circulation model benefitting, as the atmospheric component of the state-of-the-art IPSL (Institut Pierre-Simon Laplace) Earth system model, from the latest physical and dynamical refinements [*Hourdin et al.*, 2013]. A midresolution version of the model is used in this study, providing a resolution of 1.9° × 3.75° with 39 vertical levels (21 in the troposphere) on a rectangular grid.

GRISLI (GRenoble Ice-Shelf and Land Ice) is a three-dimensional ice sheet model accounting for thermodynamical coupling between ice velocities and temperatures [*Ritz et al.*, 2001]. GRISLI runs at 40 km × 40 km resolution and simulates both grounded and floating ice, by considering three types of ice flow: ice sheets, ice streams, and ice shelves. At each time step, the model determines the areas where each type of ice flow applies. Ice shelves are large floating ice plates fed by inland ice. Their location is determined based on a flotation criterion, and ice velocities in these grid points are computed using the shallow-shelf approximation with a basal stress set to zero. The FOAM model does not have the resolution needed to simulate oceanic melting under the ice shelves. This requires specific experimental setups, involving high-resolution (regional) climate models accounting for ocean temperature and circulation patterns under the shelves [e.g., *Heimbach and Losch*, 2012]. In this study, we therefore used a parameterization considering a basic dependence of the melt rate on the ocean bathymetry. We imposed a melt rate of 0.2 m yr^{-1} on the continental shelf (water depth ≤600 m) and 2 m yr^{-1} in open ocean conditions (water depth >600 m). These values are well within the range defined in previous studies on Antarctica [*Pollard and DeConto*, 2012, their Figure 4b]. Calving occurs when the thickness of the ice shelf drops below 150 m. All areas that are not ice shelves are grounded ice, including ice sheets and ice stream zones. Ice sheets are regions of grounded ice where ice flow is mainly due to deformation, basal sliding occurring only where the base is at the pressure melting point. Inland ice velocity fields are computed using the shallow-ice approximation. Because the latter is inaccurate to simulate fast-flowing ice [*Bueler and Brown*, 2009], such regions—the ice stream zones—are specifically treated by the model. Ice streams are corridors of fast flow with widths of a few kilometers, usually smaller than the

model grid size. It is not possible to simulate them individually. Their effect is parameterized in the model by treating areas which have the large-scale characteristics of ice streams independently. Ice stream zones are defined based on both the local slope of the terrain and the effective water pressure below the ice sheet, the latter as a function of the subglacial water depth. Ice flow in these ice stream zones is computed using both the shallow-ice and the shallow-shelf approximations. Contrary to what is prescribed for ice shelves, basal stress is not set to zero. GRISLI simulates the evolution of ice sheets in response to climatic forcing. The model calculates the surface mass balance of the ice sheet as the sum of accumulation minus ablation, using mean monthly surface temperature and precipitation. Ablation is in turn computed with the positive degree day (PDD) method, using a surface melt refreezing rate of 60% and a standard deviation (σ) of 5°C to represent the air temperature variability over the month [*Reeh*, 1991]. The PDD model is based on an empirical relation between air temperature and melting rate, assuming that the near-surface temperature transmits the majority of the climatic forcing to the ice sheet. Despite its simplicity, this ablation scheme has been shown to perform well [e.g., *Ladant et al.*, 2014], although some recent studies suggest that explicitly accounting for the melt contribution from insolation may significantly impact the calculation of surface melt [e.g., *Robinson and Goelzer*, 2014]. GRISLI also accounts for the isostatic adjustment of the bedrock in response to ice load. The common "elastic lithosphere/relaxing asthenosphere" (ELRA) model is used. In this parameterization, the bed underneath the ice sheet is described as a thin, elastic lithosphere governing the spatial shape of the deflection by allowing a regional response to the ice load. The underlying, viscous asthenosphere governs the time-dependent characteristics of the deformation through a standard relaxation time of 3 kyr. GRISLI was initially developed for and validated over Antarctica by *Ritz et al.* [2001]. It has since then been successfully applied to study the mechanisms that drove Heinrich events (last 80 ka) [*Alvarez-Solas et al.*, 2011, 2013], the inception of the Fennoscandian ice sheet during the last glacial period (90 ka) [*Peyaud et al.*, 2007], the partial melt of the Greenland ice sheet during the last interglacial period (130–115 ka) [*Quiquet et al.*, 2013], and the continental-scale initiation of the Antarctic ice sheet at the Eocene-Oligocene boundary (34 Ma) [*Ladant et al.*, 2014].

2.2.2. Boundary Conditions

We use the Late Ordovician (450 Ma) continental configuration from *Blakey* [2016]. Given that continental vegetation was restricted to nonvascular plants during the Ordovician [*Steemans et al.*, 2009; *Rubinstein et al.*, 2010]—the coverage of which is difficult to estimate—we follow previous studies about Ordovician climate [*Nardin et al.*, 2011; *Pohl et al.*, 2014, 2015] in imposing a bare soil (rocky desert) on every continental grid point. Five realistic topographic classes are used, ranging from the deep ocean (−4000 m) to the Caledonian orogen (3000 m) [*Pohl et al.*, 2014]. Simulations are conducted for two end-member orbital configurations (CSO and HSO), respectively, extremely favorable and unfavorable to south polar ice sheet growth. The HSO (CSO) is defined with an obliquity of 24.5° (22.5°), an eccentricity of 0.05 (0.05), and a longitude of perihelion of 90° (270°) [*DeConto and Pollard*, 2003]. Following the models of solar physics [*Gough*, 1981] and previous studies about Ordovician climate [*Pohl et al.*, 2014, 2015], the solar constant is decreased by 3.5% compared to its present value. The values for Ordovician pCO_2 remain a major uncertainty. They were necessarily higher than today, compensating for a weaker insolation, but climatic proxies [*Yapp and Poths*, 1992; *Rothman*, 2002; *Tobin and Bergström*, 2002; *Tobin et al.*, 2005; *Vandenbroucke et al.*, 2010a; *Pancost et al.*, 2013], climate models [*Herrmann et al.*, 2003, 2004], and long-term carbon cycle models [*Berner*, 1990; *François et al.*, 2005; *Berner*, 2006; *Young et al.*, 2009; *Nardin et al.*, 2011; *Goddéris et al.*, 2014] give scattered values ranging from less than 5 PAL to more than 20 PAL. In order to cover this wide spectrum, experiments are conducted for pCO_2 values between 3 PAL and 24 PAL.

2.3. Sensitivity Tests

2.3.1. One-Way Coupling Versus Asynchronous Coupling Method

Most experiments discussed in this study are conducted with the Earth system model described previously (i.e., the asynchronous coupling method; see section 2.1). Additional experiments are conducted with a simpler experimental design to allow comparison with previously published work and to test the sensitivity of our results to various parameters. Similar to previous studies [*Herrmann et al.*, 2003, 2004], we unidirectionally force the ice sheet model (GRISLI) with atmospheric outputs representative of ice-free conditions. As in the asynchronous coupling method, GRISLI updates its surface temperature and precipitation fields as a function of ice sheet height, through an adiabatic lapse rate for the temperature (5 K km^{-1}) and an exponential law for the precipitation (Clausius Clapeyron dependency), thus capturing the effect of the ice sheet on local climate. The one-way forcing method, however, differs from our asynchronously coupled model by lacking

ice sheet feedbacks on regional and global climates. The ice sheet model is not able to account, by itself, i.e., without being provided with additional climatic forcing fields, for larger-scale effects such as the impact of the ice sheet on the atmospheric circulation. It also significantly underestimates the regional cooling induced by the ice sheet by neglecting the strong ice-albedo positive feedback. For these one-way simulations, climatic forcing fields are computed using the method described previously (FOAM and then LMDZ). We use the cold summer orbital configuration (CSO), which is particularly favorable to Southern Hemisphere ice sheet growth. The resulting steady state ice sheets therefore represent the maximum land ice extent and volume that can be reached without considering land ice feedbacks on global climate.

2.3.2. Response of Ice Dynamics to Continental Topography

Published continental reconstructions do not necessarily concur with each other regarding the location of Ordovician highlands over Gondwana [e.g., *Blakey*, 2016; *Scotese*, 2016], and none of them provide numerical values for the altitude of these mountainous areas. In our baseline runs, we define mountainous areas based on *Blakey*'s [2016] Late Ordovician reconstruction (section 2.2.2), and we assign constant altitude of 2000 m to these highlands. To estimate the dependence of our modeling results on the large uncertainties in Ordovician topographic reconstructions, we run two additional sets of experiments involving a flat Gondwana supercontinent over the South Pole (constant altitude of 300 m) and a lowered topography where mountainous areas are set to 600 m altitude. For each of these tests, the one-way forcing method is used. LMDZ is run for each pCO_2 in a cold summer orbital configuration, using the appropriate topography, but keeping the sea surface temperatures previously simulated in our one-way baseline runs (section 2.3.1). GRISLI is subsequently forced using the LMDZ climatic fields. Using fixed sea surface temperatures allows to specifically investigate the impact of mountainous areas on the atmospheric circulation and thus on the patterns of the precipitation and temperature forcing fields provided to GRISLI, by avoiding ocean dynamics complex responses to changing topography.

2.3.3. Response of Ice Dynamics to Glacier/Bedrock Coupling

In spite of their limited spatial extent, ice streams today represent the most dynamic components of ice sheets, notably accounting for more than 90% of all the ice and sediment discharged by the Antarctic ice sheet [*Bennett*, 2003]. Ice streams consequently constitute a central component of the dynamic behavior of present ice sheets. In the model GRISLI, they are simulated using the shallow-shelf approximation (see section 2.2.1). In this context, the driving term for the ice flow computation is the basal sliding, which is computed as a function of basal shear stress and effective pressure, the latter as a function of the subglacial water pressure. Because shear stress and effective pressure are highly dependent on the geology of the subglacial environment, a sediment map is usually provided as a boundary condition to the model. However, the nature of the Ordovician continental surface is unknown over virtually the entire Gondwana supercontinent, challenging the accurate reconstruction of sediment thickness. The strength of the glacier/bed coupling therefore remains a major uncertainty in our deep-time modeling study, potentially biasing the modeled land ice volume and extent. In order to quantify the amplitude of this possible bias, we conduct a sensitivity test of the glacier/bed coupling strength by varying the basal dragging in the model. The basal dragging is the force generated by the friction between the flowing ice sheet and its bedrock, which hampers ice motion. In the model, the direction of basal dragging is opposite to that of basal velocity [*Ritz et al.*, 2001], and its value is a function of the latter [*Alvarez-Solas et al.*, 2011]:

$$\tau_b = -v^2 N U_b \tag{1}$$

where τ_b is the basal dragging, U_b is the basal velocity, N represents the effective pressure, and v^2 is an empirical parameter representing the basal friction coefficient in ice streams, the value of which will be varied. For these tests, the climatic forcing fields used in GRISLI are the same in all the experiments: we use the one-way forcing method, the cold summer orbit, and Blakey's topography [2016] with mountainous areas set to 2000 m.

3. Results

3.1. One-Way Experiments

To facilitate the comparison of our results with previous modeling studies [*Herrmann et al.*, 2003, 2004; *Lowry et al.*, 2014], we first conduct experiments that account neither for ice sheet feedback processes nor for orbital variations (see section 2.3.1). As expected, ice sheets of various extent and height are simulated, depending on the pCO_2 (Figure 2). The lower the pCO_2, the larger the ice sheet. The relationship between pCO_2 and land

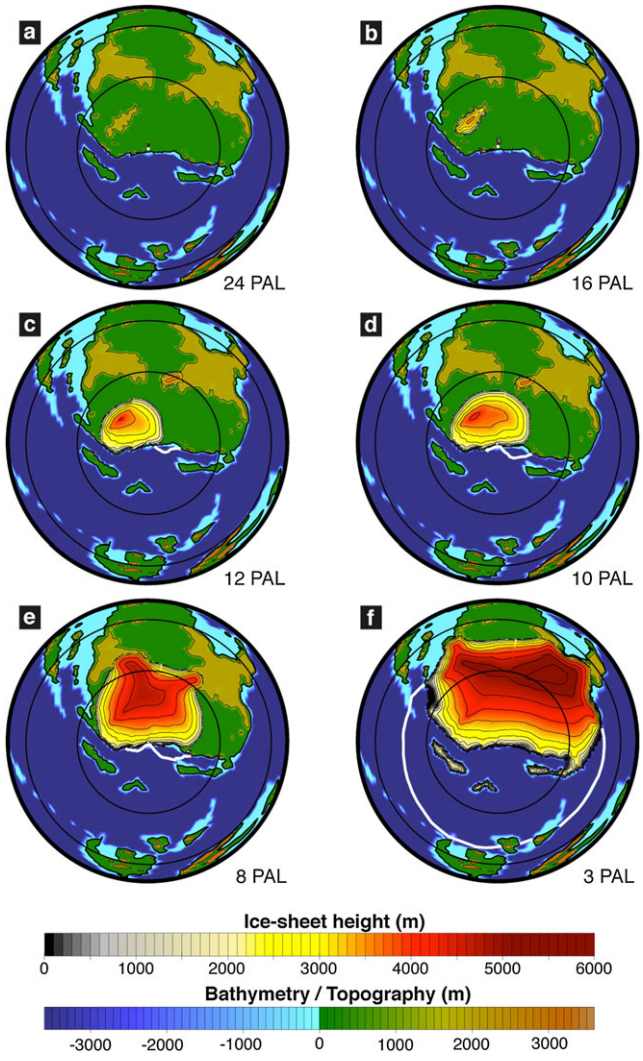

Figure 2. South polar projection maps of Late Ordovician steady state ice sheet heights (m) simulated at various CO_2 levels with the "one-way" forcing method, i.e., with no land ice feedbacks on global climate. For these simulations, the cold summer orbit is used. The thick white line corresponds to a mean annual sea ice fraction equal to 50%. Background shading is topography/bathymetry. Latitude is shown at 30° intervals.

ice volume is linear in a log-axis graph (Figure 3a, blue line). *Herrmann et al.* [2004] employed a similar experimental setup to run simulations on two Late Ordovician continental configurations from *Scotese and McKerrow* [1991]. They investigated the impact of several factors on glacial onset, i.e., pCO_2, sea level, and heat transport. Their set of experiments including a low sea level and a "normal" (versus "decreased") oceanic heat transport was typified by boundary conditions very close to the ones used in this study. As summarized in their Table 2, their simulation conducted at 15 PAL did not lead to glacial onset, whereas a continental-scale ice sheet was simulated at 8 PAL. Figure 2 reveals that in our models, (i) an ice sheet of limited spatial extent develops on polar highlands at 16 PAL, apparently indicating a glacial onset at higher CO_2 levels than *Herrmann et al.* [2004]. *Herrmann et al.* [2004], however, prescribed a flat continent, with altitudes set to 250 m on coastal grid points and 500 m everywhere else, compared to 2000 m for ancient orogens and 300 m elsewhere in our case. Interestingly, additional simulations with mountainous areas lowered to 600 m (see section 3.3.1) are typified by a glacial onset occurring at 8 PAL in our models, eventually providing a CO_2 threshold for glacial onset very comparable to the one proposed by *Herrmann et al.* [2004]; (ii) The ice sheet simulated at 8 PAL extends to ~60°S (Figure 2), which is in reasonable agreement with the extent simulated by *Herrmann et al.* [2004] for the same pCO_2 on their latest Ordovician reconstruction (see their Figure 6).

The experimental setup used by *Lowry et al.* [2014] was very comparable to the one of *Herrmann et al.* [2004]. Similar to *Herrmann et al.* [2004], climatic forcing fields were simulated using the GENESIS model on a flat topography under a cold Southern Hemisphere summer orbital configuration. In their simulations using a solar constant set to −2.5 % below present, *Lowry et al.* [2014] obtained a threshold CO_2 level for glacial inception below 3 PAL. Further accounting for early Paleozoic solar luminosity values raised the pCO_2 threshold to 4 PAL. Land ice growth did not occur at 8 PAL. This discrepancy between the results of *Herrmann et al.* [2004] and ours, on the one hand, and the ones of *Lowry et al.* [2014], on the other hand, may at least partly result from the choice of the vegetation cover. Here we use a barren soil, the albedo of which corresponds to a rocky desert (section 2.2.2). *Herrmann et al.* [2004] used no vegetation and intermediate soil color values. *Lowry et al.* [2014], on the contrary, coupled GENESIS to BIOME4, an equilibrium terrestrial vegetation model simulating the changing distribution of 28 modern biome types in response to climatic forcing. Sensitivity tests demonstrated that ice sheet initiation was sensitive to vegetation (supporting information of *Lowry et al.* [2014]).

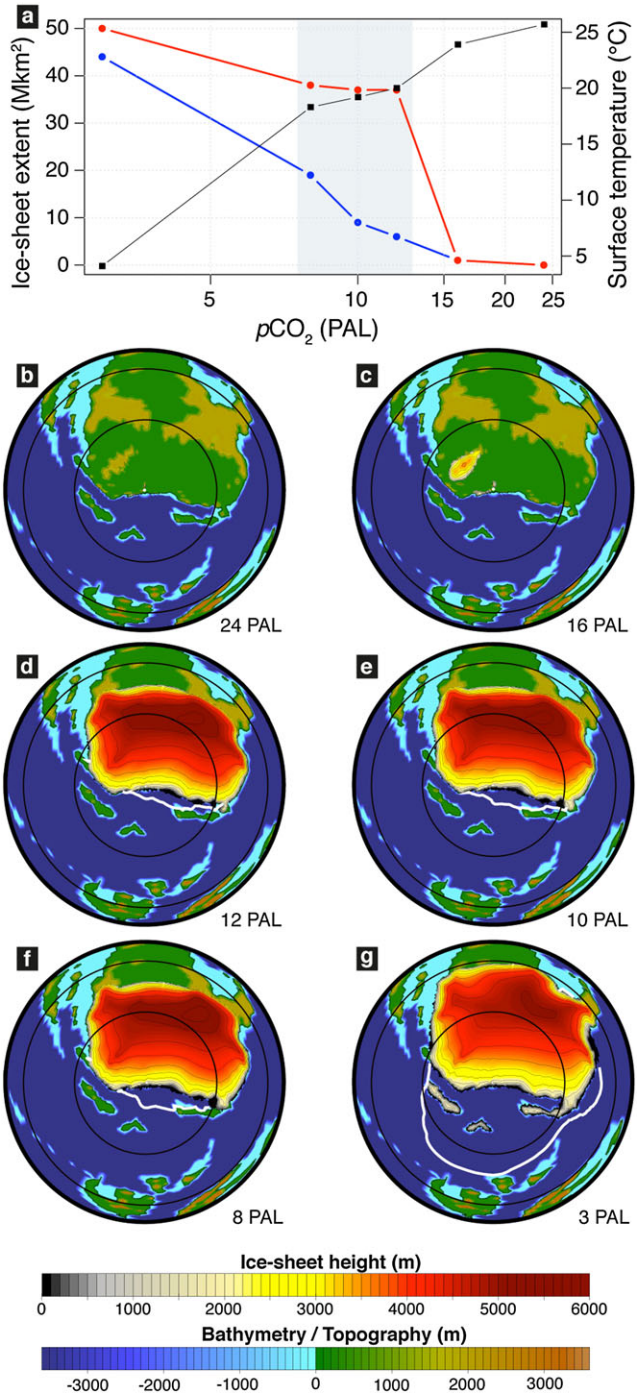

Figure 3. Ice sheet results at various CO_2 levels. (a) Ice sheet extent simulated under a cold summer orbit without taking ice sheet feedbacks on climate into account (one way, blue line) and with our asynchronous coupling procedure accounting for orbital variations and ice sheet feedbacks (red line). Global mean annual surface air temperature (black line, right *y* axis) is displayed for the asynchronous coupling method only, once the ice sheet obtained steady state with global climate. (b–g) South Pole projection maps of Late Ordovician equilibrium ice sheet heights (m) simulated at each CO_2 level, using the asynchronous coupling method accounting for orbital variations and ice sheet feedbacks. Background shading is topography/bathymetry. The thick white line corresponds to a mean annual sea ice fraction equal to 50%. Latitude is given at 30° intervals. See Figure 8 for a time series of land ice growth. The grey rectangle in Figure 3a indicates the domain where ice sheets sustain in an otherwise relatively warm climate; see section 4.2.

The use of a bare ground induced larger ice volumes and surface area. In some time slices of the Phanerozoic, a barren soil raised the CO_2 threshold for glaciation.

It is more difficult to directly compare our results with the work from *Herrmann et al.* [2003], who conducted their experiments for a narrower pCO_2 range (8–12 PAL) and focused on the sensitivity of the modeled ice sheet volume to the obliquity forcing. Orbital variations are not considered in our one-way experiments, though they are in our asynchronously coupled runs (see section 2.1).

It appears that using the one-way forcing method, our models compare relatively well with the results of *Herrmann et al.* [2004]. In the simulations of *Lowry et al.* [2014], glacial onset occurs for slightly lower CO_2 levels, possibly due to their modern vegetation cover.

3.2. Accounting for Ice Sheet Feedback Processes

Simulations are run with the same models and boundary conditions, using the asynchronous coupling method accounting for orbital variations and, for the first time, for the feedbacks of the ice sheet on global climate. Changes in ice surface elevation and extent affect surface air temperatures and atmospheric circulation and vice versa (see section 2.1). Figure 3a displays the equilibrium surface air temperature (black line) and ice sheet extent (red line) simulated at various pCO_2 levels. At 24 PAL, the climate is warm (global, mean annual surface air temperature of ~25.7°C, Figure 3a) and no land ice is observed over the South Pole (Figure 3b). When CO_2 is decreased to 16 PAL, the climate cools slightly (by 1.8°C) and small ice caps appear on the polar highlands (Figure 3c). When CO_2 is lowered to 12 PAL, an ice sheet suddenly expands to the midlatitudes (~45°S, Figure 3d) and global temperature decreases by 3.9°C (from 23.9 at 16 PAL to 20.0°C at 12 PAL, Figure 3a). After this first step of sudden ice sheet growth, the position of the ice front stabilizes and ice sheets of similar size and volume are simulated at 12, 10, and 8 PAL (Figures 3a, 3d–3f). When CO_2 is further lowered to 3 PAL, global temperature suddenly plummets by ~14°C (Figure 3a) inducing a second-step latitudinal expansion of the land ice by a further 15° (Figures 3a and 3g), whereby the continental ice sheet reaches the tropical realm (30°S). Sea ice—previously confined to higher paleolatitudes—expands to 45°S (Figure 3g).

During the first step, global climate suddenly shifts from a greenhouse (pCO_2 > 12 PAL) to an icehouse mode with the land ice front resting at the midlatitudes (12–8 PAL, Figures 3d–3f). Despite the continental configuration favoring a strong continentality over the southern high latitudes, analysis of the mechanisms of incipient glaciation reveals that accumulation is never the limiting factor for land ice growth (Figure 4). The latter is, on the contrary, driven by lack of ablation (Figure 4), as reported for the Laurentide ice sheet during the Last Glacial Maximum [*Bonelli et al.*, 2009]. The Ordovician ice sheet nucleates near the South Pole on highlands where freezing persists during the austral summer season, i.e., where ablation is virtually zero throughout the year. Once the ice cover is sufficiently large, the ice-albedo and height mass balance feedbacks amplify the extension of the zero-ablation zone (Figure 4). The ice sheet expands equatorward until it reaches the midlatitudes, where it stabilizes from 12 to 8 PAL (Figures 3d–3f). This apparent contradiction between pCO_2 decrease and unchanged land ice extent, between 12 PAL and 8 PAL (grey domain in Figure 3a), is caused by higher ablation rates in the warmer midlatitudes (supporting information), limiting the ice line close to 45°S. The nonlinear extension of the land ice simulated in this first step is comparable, to some extent, to the Pleistocene glacial cycles, during which interstadials (when only Greenland was covered by ice) were succeeded by stadials when the Laurentide ice sheet suddenly extended to 40°N [*Ehlers and Gibbard*, 2007]. The ice sheet extension of the second step, simulated at 3 PAL, relies on a specific mechanism. *Pohl et al.* [2014, 2015] showed that there is a threshold CO_2 value, below which Ordovician climate abruptly shifts from a warm climatic equilibrium with no sea ice in the Northern Hemisphere to a much colder state with sea ice extending down to the midlatitudes. They attributed this climatic instability to the particular ocean dynamics developing in the mainly oceanic Ordovician Northern Hemisphere. At 3 PAL, the sudden spread of sea ice to the midlatitudes (Figure 3g), associated with the crossing of this climatic tipping point, induces a global climate cooling by 14°C (Figure 3a). This abrupt cooling leads in turn to the advance of the continental ice front to the tropical latitudes (Figure 3g).

The quasi-absence of ice shelves in our model runs (Figure 3) results from the very strong ablation outside the grounded ice sheet on the one hand (Figure 4h) and from the poorly constrained Ordovician bathymetry on the other hand. The South Pole, in particular, is the single area typified by lower ablation rates (Figure 4h). There, however, open ocean conditions suddenly succeed to the Gondwana peneplain continent in our

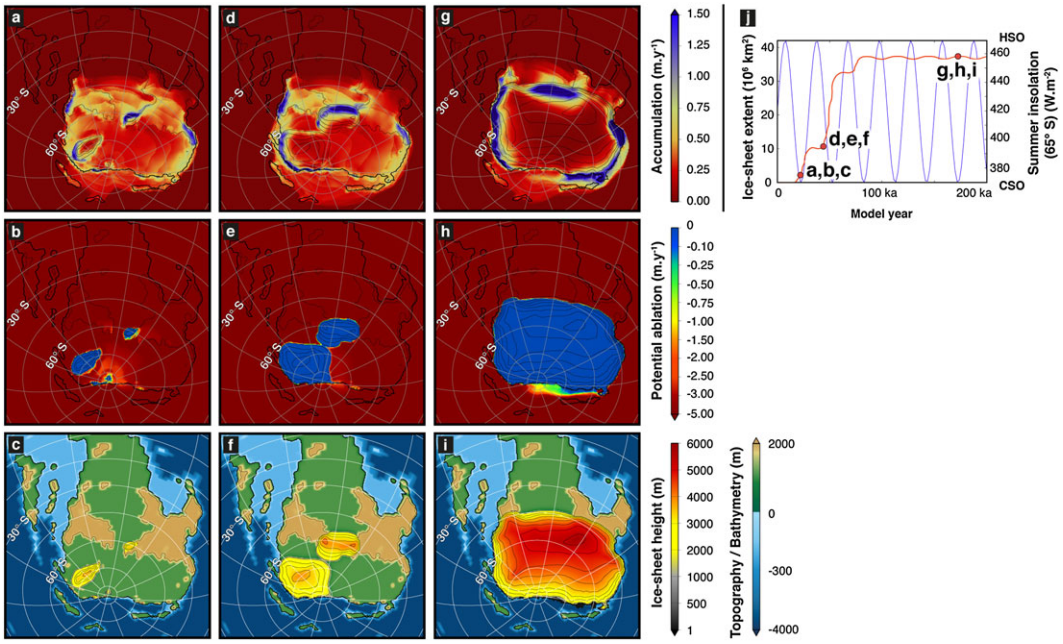

Figure 4. Respective contributions of accumulation and ablation to the growth of the Ordovician ice sheet, illustrated by three snapshots taken from the simulation conducted with ice sheet feedbacks and orbital variations at 12 PAL, at (a–c) 22 ka, (d–f) 44 ka, and (g–i) 173 ka. Latitude is shown at 15° intervals, and land ice cover is systematically displayed through ice sheet height isolines. (j) The three snapshots (22, 44, and 173 ka) are placed on the time series of ice sheet growth (similar to iter 9 in Figure 1), where the red curve represents the increasing extent of the ice sheet through the ice sheet model integration time (200 ka) and the blue curve the oscillations of the orbital forcing between the CSO and HSO end-members (see section 2.2.2). Comparing the three plots provided for each selected model year reveals that accumulation is never the limiting factor for ice growth, because the positive accumulation zone always exceeds the ice sheet extent (Figures 4a, 4d, and 4g). On the contrary, potential ablation is very strong outside of the ice sheet edges, thus limiting further ice sheet extension. The enlargement of the zero-ablation zone (Figures 4b, 4e, and 4h)—driven by local cooling due to the ice-albedo and height mass balance positive feedbacks—allows the ice sheet to develop through the elapsing simulation (Figures 4c, 4f, and 4i).

bathymetric reconstruction, with no fine-scale slope in between (see Figure 4c), which implies strong oceanic melt rates under the shelves in the model (see section 2.2.1). Moreover, there are very few embayments to favor the development of ice shelves. Given that floating ice does not contribute to sea level variations when it forms or breaks up, uncertainties regarding the extent of simulated ice shelves do not alter our estimates of the glacioeustatic fall discussed in section 4.4.

3.3. Sensitivity Analysis

We here quantify the impact of the basal dragging and of the bedrock topography on the geometry of the simulated ice sheet. Because running our asynchronously coupled model for each of these additional experiments would be time consuming and expensive, we here use the one-way forcing method and we conduct simple, first-order sensitivity tests under the cold summer orbital configuration. We previously demonstrated that using the one-way method, a very low CO_2 level (3 PAL) is required to simulate a continental-scale ice sheet similar to the ice sheet modeled with our more sophisticated setup (compare Figure 2f with Figures 3d–3f). We therefore conduct most of our sensitivity tests at 3 PAL, in order to ensure that the results of these tests are instructive regarding the geometry of such a continental-scale ice sheet.

3.3.1. Sensitivity to Topography

The most straightforward effect of a mountainous area is to allow the continental surface to intercept the 0°C isotherm, where a flat topography would not, thus making the nucleation of ice centers easier. Conversely, considering lowered relief is expected to shift the threshold for glacial onset toward lower pCO_2 values. With the default topography used in our baseline runs, glacial onset takes place at 12 PAL (Figure 2). When mountains are lowered to 600 m, the threshold pCO_2 value for glaciation is effectively shifted to 8 PAL. With a flat topography, land ice nucleates only at 3 PAL over Gondwana.

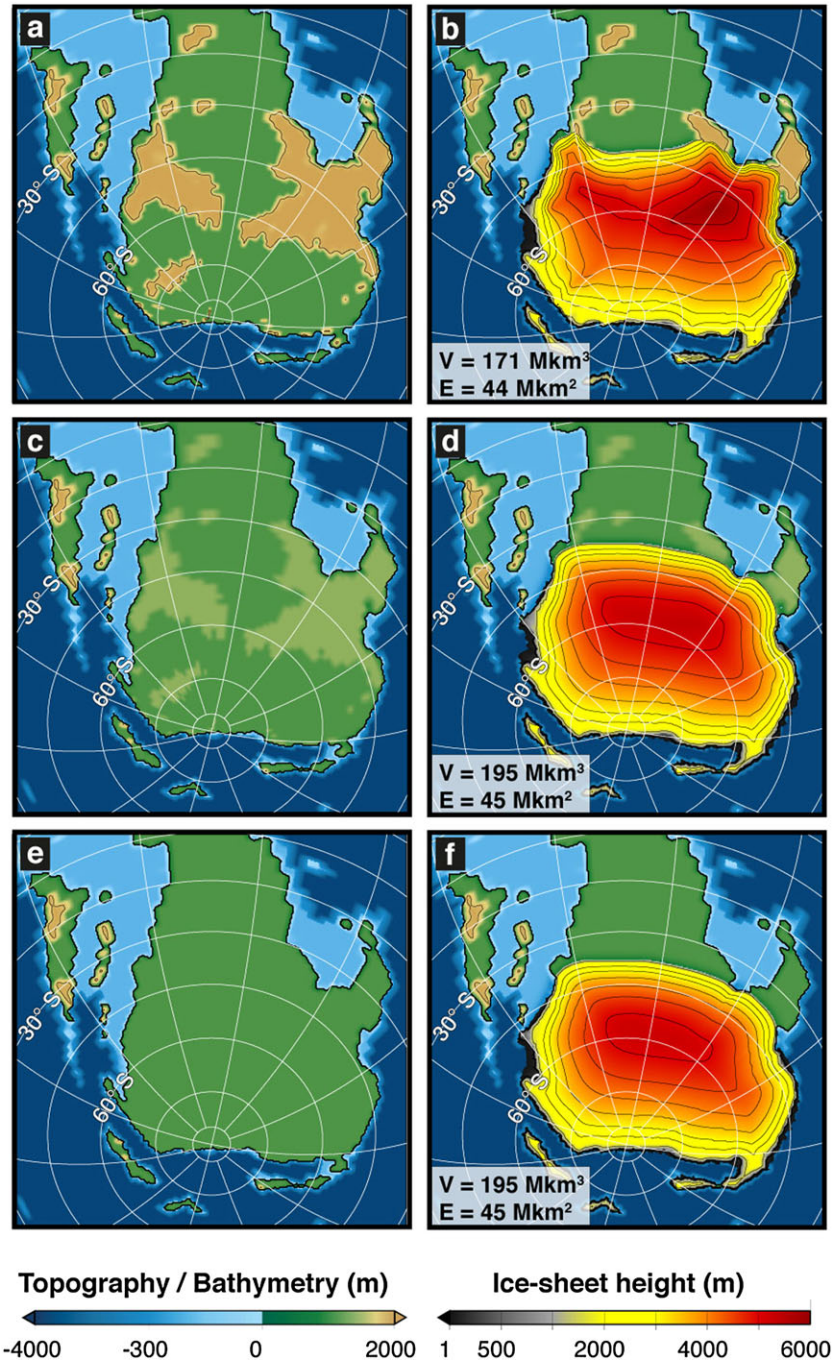

Figure 5. Sensitivity of simulated ice sheet height and extent to topography. Each row corresponds to an experiment. (a, c, and e) The topography used in the model. (b, d, and f) The ice sheet height simulated at equilibrium together with simulated ice sheet volume (V, 1 $Mkm^3 = 10^6\ km^3$) and extent (E, 1 $Mkm^2 = 10^6\ km^2$). For these simulations, we use the one-way forcing method and the cold summer orbital configuration.

Figure 5 compares equilibrium ice sheets simulated at 3 PAL, using each topography. Although topography significantly impacts the ice sheet geometry, equilibrium ice sheet extent is almost insensitive to topography. Lowered mountains (Figures 5c and 5d), or even a flat Gondwana supercontinent (Figures 5e and 5f), alter the modeled land ice area by no more than 4.5%. The maximum latitudinal extent of the ice sheet, in particular, is remarkably stable. The regional advance of the ice front toward lower latitudes in the center of Gondwana, when topography is flattened (compare Figure 5b with Figures 5d and 5f), results from the changing atmospheric circulation when highlands are removed. Zonal winds are not hampered by relief any more, and they

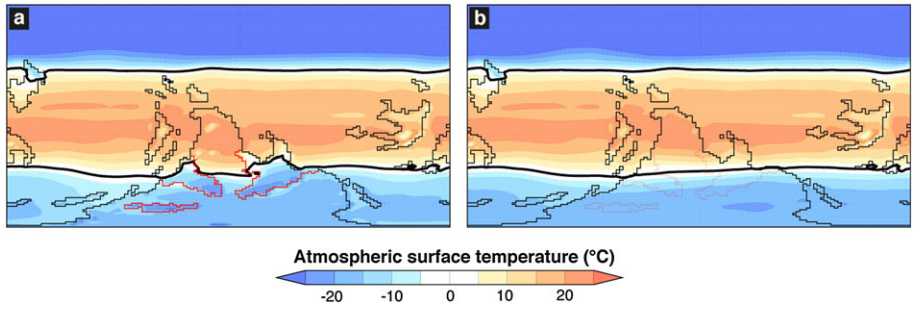

Figure 6. Austral summer (December, January, and February average) surface air temperature simulated using the one-way forcing method under CSO, land ice-free conditions using (a) the default topography reconstructed from Blakey (2000 m) and (b) the flat topography. Continental mass outlines are shown with the black, stepped, thin black lines. In Figure 6a, main mountains typifying the topography used over Gondwana during the simulation are shown with red, stepped lines. In Figure 6b, the topography is set to 300 m everywhere over Gondwana during the simulation but the location of former relief is mapped in order to facilitate the comparison with Figure 6a. In both cases, the thick black line stands for the 0°C isotherm.

allow the austral summer 0°C isotherm to advance toward the tropics (Figure 6). There is, however, quasi-cancelation between this regional extension of the ice sheet and the retreat of the ice sheet from surrounding mountainous areas due to the warming effect of the lapse rate for lowering topography (Figures 5b, 5d, and 5f). As a result, the extent of the ice sheet only slightly increases (+1 Mkm^2, Figures 5b, 5d, and 5f) and the land ice volume follows (+24 Mkm^3, Figures 5b, 5d, and 5f).

3.3.2. Sensitivity to Basal Dragging

Land ice thickness simulated in our baseline runs reaches 6000 m over extensive areas, and the ice sheet systematically displays very steep flanks (Figure 7a). These characteristics are comparable with the results from *Herrmann et al.* [2004] (see their Figure 6), but they are not realistic when compared to present-day Antarctic [e.g., *Fretwell et al.*, 2013] or LGM Laurentide [e.g., *Heinemann et al.*, 2014] ice sheets. Furthermore, the model simulates virtually no ice stream zones over the entire Gondwana supercontinent (Figure 7b), which is at odds with the sedimentary record of the Ordovician glaciation [e.g., *Denis et al.*, 2007; *Ghienne et al.*, 2007]. These discrepancies arise from weakly dynamic ice sheet, notably resulting from the absence of topographic undulations in our poorly constrained Ordovician topographic reconstruction. The latter includes topographic classes with constant elevation, with no valleys to promote fast-flowing ice streams (see section 2.2.1). In order to quantify this bias, we conduct additional experiments using the basal dragging parameterization developed by *Alvarez-Solas et al.* [2011] to account for the ice sheet instability. This basal dragging code was successfully applied to study the Heinrich event 1 [*Alvarez-Solas et al.*, 2011]. It uses, in the ice stream zones, a basal dragging coefficient v^2 (see section 2.3.3) that is lower than the one used in our baseline runs. It is also less restrictive regarding the conditions required to generate ice stream zones. In contrast to the basal dragging parameterization used in our baseline runs, it uses a sediment map and allows ice streams to develop over areas with very limited basal water content if the bedrock is covered by sediments. For the Ordovician, no detailed lithologic maps of Gondwana are available, but some areas were undoubtedly covered by sediments [*Denis et al.*, 2007]. In the absence of better constraints, we here impose a uniform sediment cover over the supercontinent, and we set the basal friction coefficient for ice streams to $v^2 = 2 \times 10^{-5}$ (dimensionless), following *Alvarez-Solas et al.* [2011]. Results obtained with this setup are displayed in Figures 7c and 7d.

Ice sheet geometry simulated at 3 PAL with the *Alvarez-Solas et al.*'s [2011] parameterization shows large differences with our baseline simulation (Figures 7a and 7c). The equilibrium ice sheet extent does not change, but the ice sheet flattens and simulated ice volume decreases from 171 Mkm^2 to 99 Mkm^2, eventually representing only 58% of the volume simulated in the baseline experiment (Figures 7a and 7c). The constant ice sheet extent, on the one hand, is due to the unchanged climatic forcing. Decreased ice volume, on the other hand, results from high land ice velocities over extensive ice stream zones (Figures 7b and 7d). Figure 7e (black points) shows the results from additional experiments with various values of the basal dragging coefficient v^2. It confirms that the strength of the glacier/bedrock coupling impacts the simulated ice volume but not the ice sheet extent. These results are in agreement with the studies of *Clark and Pollard* [1998] and *Tabor and Poulsen* [2016], who simulated similar Laurentide ice sheet extents, but different volumes, as sediment cover changed across the middle Pleistocene transition (~ 0.9 Ma). We also conduct an experiment featuring a

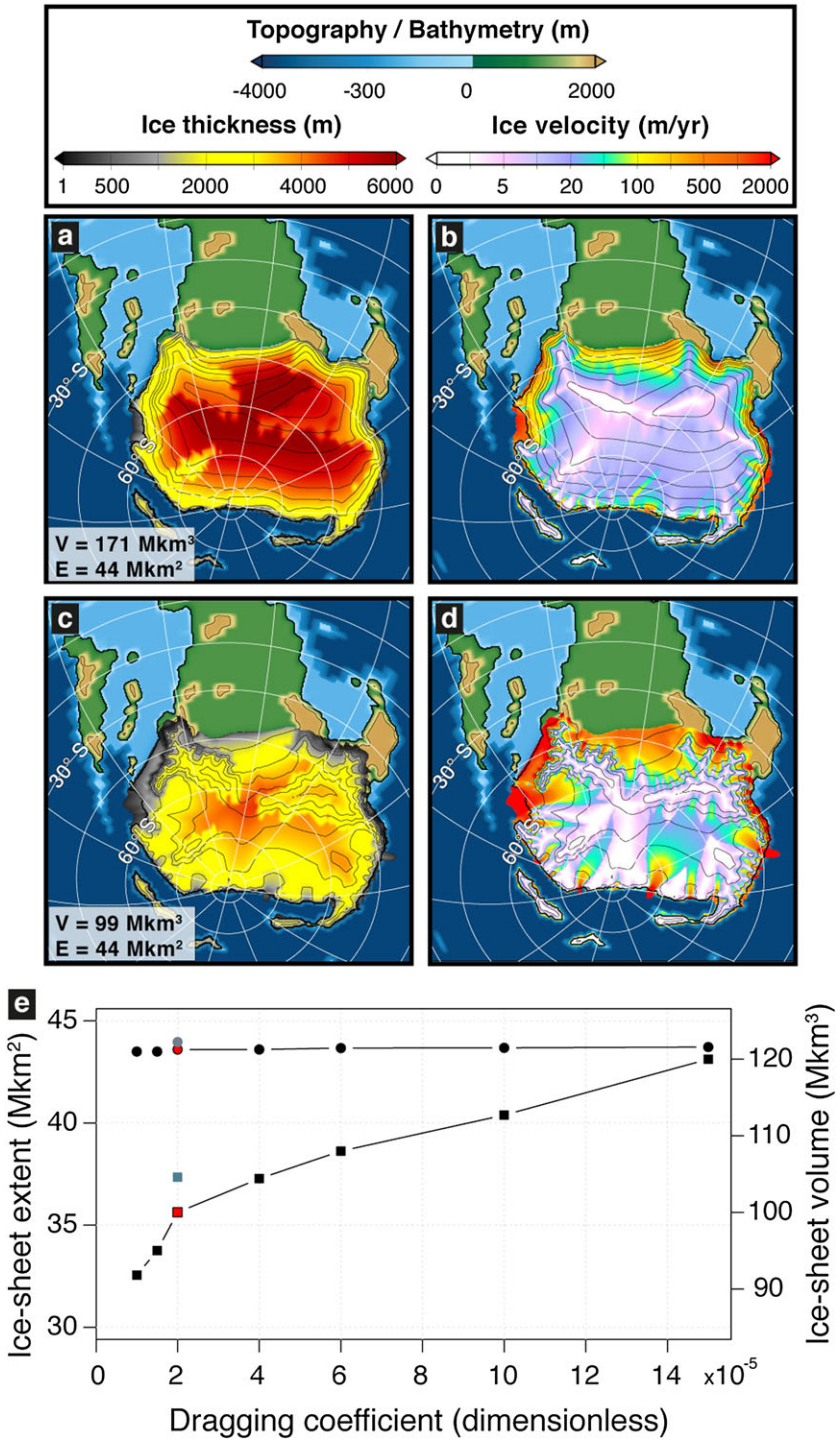

Figure 7. Sensitivity of simulated land ice thickness and extent to basal dragging coefficient. These simulations are conducted using the one-way forcing method and a cold summer orbit. (a, b) Results from our baseline experiments. (c, d) Results obtained using the basal dragging parameterization developed by *Alvarez-Solas et al.* [2011] with the standard basal dragging coefficient: $v^2 = 2 \times 10^{-5}$. Isolines correspond to ice sheet height. They are displayed every 500 m. (e) The dependence of simulated ice sheet extent (circles) and volume (squares, right *y* axis) on the basal dragging coefficient, using the parameterization from *Alvarez-Solas et al.* [2011]. Red circles and squares show the values obtained with the standard basal dragging coefficient of 2×10^{-5}, which results are displayed in Figures 7c and 7d. Grey circles and squares stand for the simulation using the same coefficient and a sediment map in addition. Black symbols stand for simulations where the value of the basal dragging coefficient is varied (*x* axis), with no sediment map.

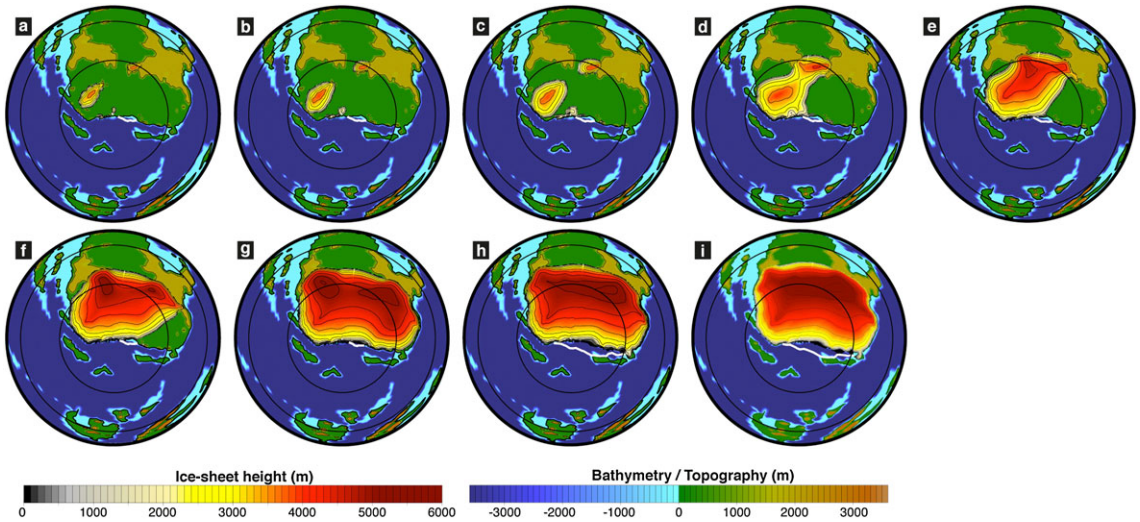

Figure 8. Ice sheet height simulated at 12 PAL, under varying orbital forcing, throughout the successive asynchronous coupling steps (south polar projection maps). (a–i) The largest ice sheet simulated during each one of the successive iterations, which is subsequently returned as a boundary condition in the climate models to simulate the next ice sheet extent (see section 2.1). Background shading is topography/bathymetry. Latitude is shown at 30° intervals.

partial sediment cover. This is a first-order test with sediments present everywhere in topographic lows (i.e., a peneplain continent) but absent where the elevation of the terrain is above 300 m. Highlands are considered as rocky bedrock, and they are characterized by the very strong glacier/bedrock coupling typifying inland ice in GRISLI. This spatialization of the basal dragging strength induces differential sliding over Gondwana. Results (Figure 7e, grey points) show that including a sediment map does not critically impact our results.

In summary, sensitivity tests show that uncertainties in topographic reconstructions impact the threshold CO_2 value for glacial onset. Accounting for ice streams—fast-moving ice regions, demonstrated to have been present from the Upper Ordovician record [*Moreau et al.*, 2005; *Denis et al.*, 2007; *Le Heron et al.*, 2007; *Ghienne et al.*, 2007; *Denis et al.*, 2010; *Ravier et al.*, 2015]—further demonstrates that the land ice volume simulated in our baseline runs has to be considered with caution. The two opposite and relatively extreme parameterizations tested here, leading to a weakly dynamic (in our baseline simulations) and especially dynamic (using the basal dragging dependence on sediments from *Alvarez-Solas et al.* [2011]) ice sheet, provide, respectively, maximum and minimum estimates for the volume of the Ordovician ice sheet. Irrespective of the topography and basal dragging parameterization, the modeled ice sheet extent, by contrast, turns out to be remarkably stable and thus reliable.

4. Discussion

4.1. Constraining Ice Sheet Extent

When accounting for the ice sheet feedbacks on Ordovician climate, the ice sheet expands to the low latitudes rather than being restricted in the polar area ($\geq$ 60°S). This is an important result compared to the earlier models that omitted ocean-atmosphere-ice sheet interplays, such as those of *Herrmann et al.* [2003, 2004]. In our advanced models, a single ice sheet of large extent covers Gondwana from the South Pole to the middle-to-tropical paleolatitudes (Figure 3). The time series of ice sheet growth at 12 PAL, shown in Figure 8, reveals that highlands facilitate independent glacial centers to simultaneously nucleate over the Pole and at 60°S during the primary stages of glacial growth (Figures 8a–8c). However, such glacial centers are not initiated at middle-to-tropical paleolatitudes, where South Africa and South America were situated 445 Ma ago [*Torsvik and Cocks*, 2013], in any of our simulations. Furthermore, results from our Earth system model accounting for ice sheet feedback processes reveal that the local cooling associated with the growth of these glacial centers rapidly induces their coalescence into a single, continental-scale ice sheet (Figures 8c, 8d, and Figure 3). In our simulations, the persistence of independent ice sheets over Gondwana is not a sustainable land ice state. This result contradicts the hypothesized configuration that features multiple, individual ice sheets in North Africa, South Africa, and South America [e.g., *Le Heron and Dowdeswell*, 2009]. The sensitivity analysis we conducted (section 3.3) further reveals that the simulated ice sheet extent is a robust

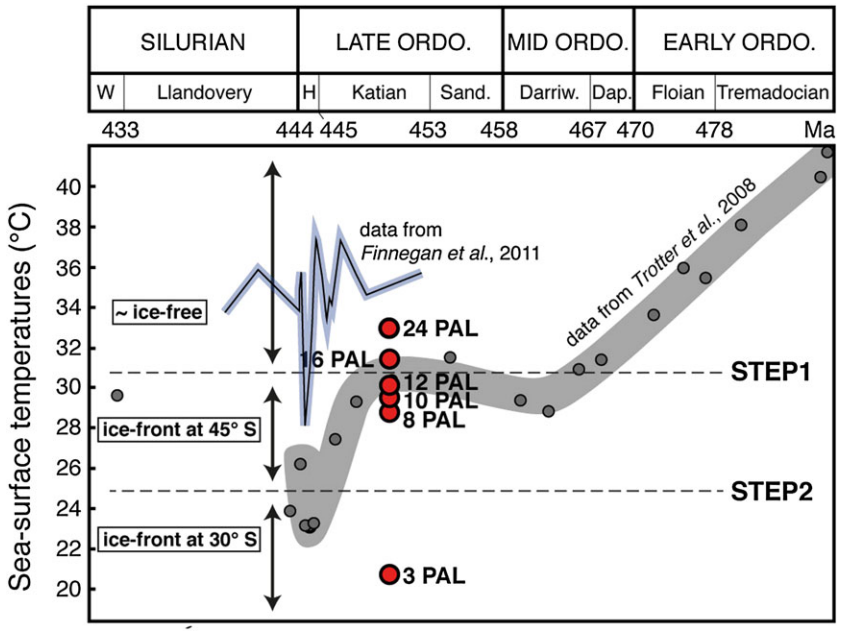

Figure 9. Comparison of tropical sea surface temperatures (SSTs) reconstructed based on $\delta^{18}O$ [*Trotter et al.*, 2008] and $\Delta^{47}CO_2$ [*Finnegan et al.*, 2011] data with annual mean tropical (30°S–30°N) SSTs simulated for the Late Ordovician once ice sheets in steady state (red circles), using our asynchronous coupling method accounting for ice sheet feedback processes and for orbital variations. Modified after *Trotter et al.* [2008] and *Finnegan et al.* [2011]. *Dap.*: *Dapingian*; *Darriw.*: *Darriwilian*; *Sand.*: *Sandbian*; *H*: *Hirnantian*; *W*: *Wenlock*.

feature that is critically dependent neither on the topographic reconstruction nor on a specific basal dragging parameterization. Our results are also supported by the study of *Lowry et al.* [2014], who simulate a single ice sheet over Gondwana with a different asynchronous coupling method and other climate and ice sheet models.

4.2. Glacial Onset in a Warm Climate

The buildup of the ice sheet, in response to a decrease in atmospheric forcing, is not linear. Between 16 PAL and 12 PAL, the ice sheet suddenly extends from the South Pole to the midlatitudes (Figure 3a), whereas tropical sea surface temperatures decrease by no more than 1.3°C (Figure 9). This nonlinear response suggests that the development of a large-scale ice sheet during the Ordovician could have occurred in conjunction with a moderate tropical sea surface temperatures signal, the amplitude of which would be within the error bars of routine geochemical analyses [e.g., *Finnegan et al.*, 2011] and thus potentially below the detection limits. This further implies that warm tropical Ordovician seas [*Trotter et al.*, 2008; *Finnegan et al.*, 2011] and geological evidence for glacioeustatic events [*Loi et al.*, 2010; *Turner et al.*, 2012; *Dabard et al.*, 2015; *Rasmussen et al.*, 2016] are not mutually exclusive (30.3°C at 12 PAL, Figure 9). Interestingly, experiments using a lowered topography (section 3.3.1) are typified by a glacial onset occurring at 8 PAL (instead of 12 PAL). They show that the unexpected glacial inception in a warm climate does not result from the high relief characterization of our baseline runs.

4.3. Toward an "Early Paleozoic Ice Age"

Trotter et al. [2008] demonstrated that tropical SSTs steadily cooled through the Early Ordovician, reaching present-day levels that were subsequently sustained during the Middle and Late Ordovician, followed by a sudden cooling by ~7°C during the latest Ordovician (Figure 9). Several arguments support the validity of these data. *Nardin et al.* [2011] in particular, using a coupled climate-carbon model, showed that changes in Ordovician paleogeography, along with variations in the surface area of outcropping fresh volcanic rocks, induce a long-term decrease in atmospheric CO_2. This provides a potential mechanism for the cooling pattern demonstrated by *Trotter et al.* [2008]. *Trotter et al.*'s [2008] data are also in good agreement with other published geochemical data for the Late Ordovician and for the Silurian, respectively, from *Buggisch et al.* [2010] and *Wenzel et al.* [2000]. Moreover, recent clumped-isotope data from tropical latitudes

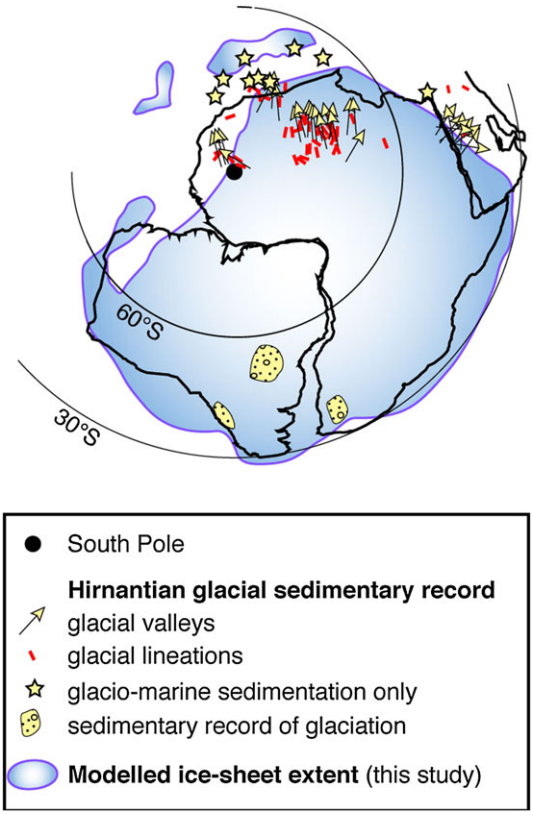

Figure 10. Comparison of the Hirnantian glacial sedimentary record with the ice sheet extent simulated at 3 PAL using our coupling method accounting for ice sheet feedbacks on global climate and for orbital variations. Data from North Africa are from *Ghienne et al.* [2007], and data from South America and South Africa are from *Díaz-Martínez and Grahn* [2007]. Continent outlines are taken from *Torsvik and Cocks* [2009].

[*Finnegan et al.*, 2011], although they are differently calibrated against the absolute temperature scale, display a similar temperature drop of 5 to 7°C during the latest Ordovician Hirnantian (Figure 9).

Figure 9 shows that the absolute values of tropical SSTs reconstructed by *Finnegan et al.* [2011] are systematically higher than those modeled in this study; this applies for our entire pCO_2 range, except for the Hirnantian where modeled and proxy-based SSTs align and correspond to a pCO_2 drop to 8 PAL in the model. Nonetheless, the generally unaligned SSTs (Figure 9) constitute a major discrepancy between *Finnegan et al.*'s [2011] data and our model runs. *Finnegan et al.* [2011] suggest the presence of large land ice volumes well before the Hirnantian, during the Katian, whereas the comparison between their SSTs and our simulations implies CO_2 levels that would have remained above 24 PAL and thus associated with ice-free conditions until the latest Ordovician, i.e., the Hirnantian. The modeled "Step 2" glaciation never occurred, based on these data. Simulated tropical SSTs are, however, in much better agreement with the range of absolute values presented by *Trotter et al.* [2008]. Comparison with Trotter's data suggests that ice sheet growth may have occurred as early as the Middle Ordovician (Figure 9). Taken at face value, our results, combined with these data, indicate a Darriwilian age for the glacial onset (between 16 and 12 PAL, *step 1* in Figure 9). The second step in ice sheet expansion would then correspond to the Hirnantian glacial maximum (3 PAL, *step 2* in Figure 9). Our modeled results are also in agreement with the amplitude of drop in SSTs during the Hirnantian that is suggested in both of these proxy data studies [*Trotter et al.*, 2008; *Finnegan et al.*, 2011], when we decrease CO_2 from 8 PAL to 3 PAL.

Such a straight model-data comparison has to be interpreted cautiously. In addition to potential bias in the data (e.g., dating or preservation issues), simulated absolute values are highly model dependent and may also be biased due to large uncertainties in Ordovician boundary conditions (see section 3.3). Comparing our modeling results with the long-term Ordovician climatic trend proposed by *Trotter et al.* [2008] is nevertheless instructive, as it suggests a Darriwilian glacial onset, which agrees with recently published studies that report glacioeustatic signals in the Darriwilian rock record [*Turner et al.*, 2012; *Dabard et al.*, 2015; *Rasmussen et al.*, 2016] and with paleontological studies that suggest pre-Sandbian cooling [*Vandenbroucke et al.*, 2009], and it provides physical mechanisms for the latest Ordovician glacial maximum and associated sudden climate cooling [*Trotter et al.*, 2008; *Finnegan et al.*, 2011]. Besides this interesting match with geochemically inferred tropical SSTs, our Katian estimates (8–12 PAL, Figure 9) match relatively well the ~8 PAL pCO_2 proposed by *Pancost et al.* [2013] based on the analysis of isotope fractionation between organic and inorganic carbon during photosynthesis (ϵ_p). Furthermore, the modeled spatial ice sheet extent at 3 PAL is overall consistent with the Hirnantian glacial sedimentary record (Figure 10). Discrepancies with shallow-shelf deposits from Turkey can be explained, as glacioeustatic emersion in such environments is not accounted for in our modeling procedure. In addition, using micropaleontological assemblage data to reconstruct climatic belts, *Vandenbroucke et al.* [2010a, 2010b] demonstrated that the Polar Front shifted in latitude from the Sandbian (460 Ma) to the Hirnantian (~440 Ma), reaching 40°S during the latest Ordovician. Comparing these Hirnantian data with the modeled climatic belts (Figure 11) reveals that again, the models best fit the data at 3 PAL. Taken

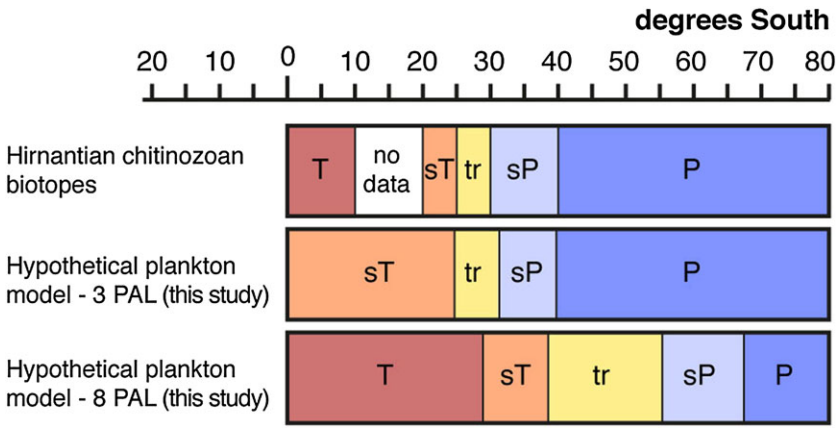

Figure 11. Comparison of Ordovician proxy-derived climatic estimates with values simulated with our asynchronous coupling method once the ice sheet reached steady state with global climate. Southern Hemisphere climatic belts reconstructed based on Hirnantian chitinozoan marine zooplankton data [*Vandenbroucke et al.*, 2010a, 2010b] are compared with climatic belts inferred from modeled SSTs. Abbreviations are plankton province names: *P*: *polar*; *sP*: *subpolar*; *tr*: *transitional*; *sT*: *subtropical*, and *T*: *tropical*. In our model predictions, the boundary between two plankton provinces is defined as the latitude at which the mean annual, latitudinally averaged SSTs simulated in the Southern Hemisphere reach the temperature threshold separating the two provinces in the present-day ocean. The reader is referred to *Vandenbroucke et al.* [2010a] for more details about the methods (see their Figure 1).

as a whole, our results suggest a protracted glaciation beginning as early as the Middle Ordovician Darriwilian and featuring a glacial maximum during the Hirnantian. By supporting the existence an ice sheet over the supercontinent Gondwana during most of the Middle and Late Ordovician, our results support the emerging paradigm of a protracted "Early Paleozoic Ice Age" [*Page et al.*, 2007].

4.4. Ice Volume Analysis

We calculate the glacioeustatic sea level fall associated with growing ice sheets using the methods employed by *Horton et al.* [2007] and *Horton and Poulsen* [2009]. First, the equivalent volume of water is estimated by multiplying modeled volume of ice above the flotation level by the ice density value (0.917). Then, we convert the water equivalent to an isostatically adjusted sea level equivalent (IASLE), by dividing the water equivalent by the Late Ordovician ocean surface area (~413 Mkm^2 at 450 Ma) and subsequently correcting the result for the response of the oceanic lithosphere to seawater loading/unloading. To that end, we multiply the result by $(1 - k)$, where k is the ratio of seawater density to oceanic lithosphere density ($k = 0.284$). Using results from our baseline runs, this simple calculation provides estimates of ~220 m between 12 and 8 PAL (step 1, Middle Ordovician) and ~250 m at 3 PAL (step 2, latest Ordovician Hirnantian). The sensitivity tests conducted in section 3.3.2 reveal that these values constitute uppermost estimates. The calculated minimum estimates are, respectively, 125 and 145 m.

Loi et al. [2010], using a backstripping procedure on the margin of Gondwana (Bou Ingarf section, Anti-Atlas, Southern Morocco), estimated an upper Hirnantian sea level fall of ~70 m. However, they explain that this sea level fall does not correctly represent the total ice volume stored over Gondwana during the latest Ordovician Hirnantian. It does not account for land ice stored over Gondwana before the Hirnantian climax. *Loi et al.* [2010] therefore estimate that the amplitude of the sea level fall would have reached nearly 150 m relative to the preglaciation (late Katian) datum [see also *Haq and Schutter*, 2008], and they note that this is a lower end estimate due to the incompleteness of the glacial sedimentary record. Moreover, recent studies [*Raymo et al.*, 2011; *Stocchi et al.*, 2013] demonstrated that the relationship between ice sheet growth and relative sea level fall is less linear than thought previously. Results obtained by *Stocchi et al.* [2013] on the onset of the Antarctic glaciation at the Eocene-Oligocene transition notably suggest that the near-field sea level change accompanying the growth of a continental-scale ice sheet is expected to strongly deviate from the global eustatic signal. Due to crustal deformation and gravitational perturbations, relative sea level around Antarctica *rose* in response to the buildup of the ice sheet. In the same way, the sea level fall documented by *Loi et al.* [2010] along the margin of Gondwana (150 m) may significantly underestimate Late Ordovician eustatic variations and should be considered as a lower end-member. Furthermore, recent clumped-isotope data from *Finnegan et al.* [2011] suggest that the Hirnantian ice volume may have reached twice that of the LGM, potentially

representing a water volume stored on land equivalent to 240 m sea level fall. It appears that our simulation run at 3 PAL eventually provides a total ice volume equivalent to 145 to 250 m sea level fall relative to ice-free conditions during the Hirnantian, thus in the same order of magnitude as most recent estimates inferred from sedimentological and geochemical data.

Ice volumes modeled between 12 and 8 PAL (125 to 220 m), on the contrary, are clearly much higher than the Middle Ordovician estimates reported by *Dabard et al.* [2015] using a backstripping procedure in the Armorican Massif in France: 50 to 80 m. The latter values seem relatively robust. They confirm previous estimates of 15–50 m (from Jordan, *Turner et al.* [2012]) and are in the same order of magnitude as the eustatic variations documented by *Haq and Schutter* [2008] during the same period of time, though somewhat smaller than the value ~150 m recently reported by *Rasmussen et al.* [2016] based on facies analysis of outcrop sections from Baltica. These discrepancies, i.e., our simulated land ice volume that is too high relative to the geological data, even when considering a slippery bed for the ice sheet (see section 3.3.2), are probably best explained by a significant overestimation of the modeled ice sheet extent. Studies on the last glaciation provide interesting insights into this issue. During the LGM, the Laurentide ice sheet suddenly extended to 40°N [*Ehlers and Gibbard*, 2007], similarly to the Gondwana ice sheet during the first step of Ordovician ice sheet growth. Simultaneously, an ice sheet developed in northern Europe. Northern Asia, on the other side, mysteriously remained ice free at the same latitudes. *Krinner et al.* [2006] suggested that high deposition rates of mineral dust in Asia, due to climate aridity under glacial conditions combined with the proximity to dust sources such as the Gobi desert, prohibited any perennial land ice cover over almost the entire Asian continent during the LGM. The deposition of dust may have similarly restricted the extension of the ice sheet over some regions of Gondwana. An additional cause for the overestimation may be found in our simplified modeling procedure, which imposes a steady pCO_2 forcing until ice sheet-climate equilibrium is reached. *Heinemann et al.* [2014] forced a coupled climate-ice sheet model with realistic orbital and greenhouse gas variations to simulate the Earth system evolution from 78 ka to 0 ka. They successfully simulated, in their transient runs, the Laurentide and Fennoscandian ice sheets evolution over this period of time and also the land ice extent that typifies the LGM. They subsequently ran a simulation by maintaining the LGM orbital configuration and pCO_2 for 90 kyr in order to reach climate-ice sheet equilibrium. Under these conditions, ice sheets extended down to the midlatitudes over both North America and the Eurasian continent, where it was previously restricted to Scandinavia. In the same way, it is reasonable to suppose that the Darriwilian ice sheet never reached full equilibrium due to orbital and/or pCO_2 variations. Such a smaller pre-Hirnantian ice sheet would be consistent with all the existing geological data. It is noteworthy that similar caveats were also suggested by *Horton et al.* [2007] in their simulation of the Late Paleozoic Ice Age. Last but not the least, strong uncertainties remain in paleogeographical and paleoenvironmental reconstructions in deep time [e.g., *Lees et al.*, 2002], and the base maps used in this study might, for instance, overestimate the continental surface situated between the South Pole and 45°S. This would lead to an overestimation of the area available for ice sheet growth and thus of the extent of the ice sheet developing over these latitudes.

4.5. Challenges

Modeling climate and land ice during the early Paleozoic involves numerous processes, which are sometimes difficult to constrain.

Recent studies demonstrated that orbital [*Ghienne et al.*, 2014] and greenhouse gas concentration [*Young et al.*, 2010] variations drove Late Ordovician ice sheet waxing and waning and also Middle Ordovician glacial inceptions [*Turner et al.*, 2012; *Dabard et al.*, 2015]. These phenomena have been shown to control Pleistocene glacial cycles as well [e.g., *Paillard*, 1998], but they cannot yet be precisely reconstructed for the Ordovician (e.g., *Laskar et al.* [2004] for orbital variations). Lack of constraints on these critical boundary conditions has been demonstrated (in the previous section) to significantly impact simulated ice sheet extent during the Middle Ordovician Darriwilian. This also prevents us to capture the high-frequency glacioeustatic variations recently reported in the Middle [*Turner et al.*, 2012; *Dabard et al.*, 2015] and Late [*Ghienne et al.*, 2014] Ordovician. In addition, the simulated ice sheet shows very little sensitivity to orbital and atmospheric forcing once it gets relatively large (Figure 1). Such a behavior was also demonstrated by *Herrmann et al.* [2003] during the Ordovician—although in a lesser extent due to the smaller land ice volume in play in their study—and by *Horton and Poulsen* [2009] in a study about the Late Paleozoic Ice Age. More generally, this strong hysteresis is a major issue in coupled ice sheet-climate studies [e.g., *Huybrechts*, 1993; *Pollard and DeConto*, 2005]. Numerous studies suggest that current ice sheet models may not be sensitive enough to correctly respond to climatic forcing. Melting Last Glacial Maximum ice sheets, for instance, sometimes requires

ad hoc processes, such as input of mineral dust [*Peltier and Marshall*, 1995; *Bonelli et al.*, 2009] or tuning of the PDD coefficients [*Charbit et al.*, 2013]. *Ganopolski et al.* [2010] and *Robinson and Goelzer* [2014] further demonstrated a significant contribution of insolation in surface melt processes, suggesting that the usual PDD melt scheme may constitute a major limitation to simulate the waning of paleo ice sheets. Moreover, recent studies suggest that critical mechanisms may be missing in the building of current ice sheet models, preventing them to simulate correctly the response of land ice to climate changes. The studies recently published by *Pollard et al.* [2015] and *Gasson et al.* [2016], in particular, show that supplementary ice sheet instability mechanisms, such as ice cliff failure and hydrofracturing, are required to correctly simulate the periodic melting of the East and West Antarctic ice sheets during the last ~25 million years. *Austermann et al.* [2015] even suggest that vertical deflections of the continental crust by mantle convective flow, i.e., dynamic topography, may have played a significant role in the Antarctic ice sheet fluctuations during the mid-Pliocene (~3 Ma). *Horton et al.* [2010], in a study about the Late Paleozoic Ice Age, demonstrate that the simulation of glacial-interglacial fluctuations is possible only when they include terrestrial vegetation feedbacks from high-latitude ecosystem changes. They show that changes in vegetation cover amplify the orbitally driven temperature variations. The latter mechanism, however, is not tenable in the Ordovician, when only lichens and mosses covered the land surface [*Steemans et al.*, 2009; *Rubinstein et al.*, 2010].

Beyond the difficulties to simulate the high-frequency temporal evolution of land ice, caveats in modeling the whole deep-time Earth system may induce important errors in continental ice cover numerical reconstruction. Our setup, in particular, does not account for the eustatic sea level fall associated with the growing Gondwana ice sheet, which requires up-to-date bathymetric reconstructions allowing to flood continental areas according to eustatic variations. Such reconstructions exist today [e.g., *Vérard et al.*, 2015], but generally, they are not publicly available.

In summary, the up-to-date deep-time Earth system model employed in this study constitutes an important step forward in modeling Paleozoic climate and ice sheets. Our models notably provide relatively reliable first-order estimates of the temporal and spatial distribution of Ordovician land ice. Uncertainties in the boundary conditions, along with caveats in current ice sheet models, however, prohibit numerical investigation of the high-resolution patterns recently reported based on the Ordovician sedimentary record.

5. Conclusions

In this study, we employed a pioneering deep-time Earth system model to investigate the mechanisms driving Middle to Late Ordovician ice sheet growth, along with the equilibrium ice sheet extent and geometry. Using methods more advanced than earlier reconstructions, our model accounts for ice sheet feedback processes and for orbital variations at the Ordovician obliquity frequency (30 kyr). It was run across the wide spectrum of suggested Ordovician pCO_2 values, 24–3 PAL, resulting in the first simulation portraying the detailed evolution of Middle to Late Ordovician ice sheet growth. Forcing the well-established Ordovician cooling trend with decreasing pCO_2, the emergence of the ice sheet occurs in two steps. In a counterintuitive sequence of events, the vast continental ice sheet appears first and suddenly, covering Gondwana from the South Pole to the midpaleolatitudes. Only during the second act, temperatures drop steeply and sea ice extends. Our models therefore suggest that a single ice sheet extended from the South Pole (North Africa) to the tropics (South Africa) during the latest Ordovician. Scenarios with individual, separate ice centers are not stable and are rejected.

In spite of the particular Ordovician continental configuration potentially inducing a strong continentality over the South Pole, land ice growth is controlled by ablation rather than accumulation. Lack of constraints on Gondwana-wide surface lithology patterns and sediment cover leads to significant uncertainties in modeled land ice volumes. Sensitivity tests demonstrate that the simulated ice sheet spatial extent, however, is reliable and overly dependent neither on the topographic reconstruction nor on the basal dragging parameterization in use.

The sequence of events that we model indicates that glacial onset predated Late Ordovician climate cooling. The comparison with abundant sedimentological, geochemical, and micropaleontological data suggests that the first step in ice sheet growth possibly occurred as early as the Middle Ordovician Darriwilian, in agreement with recent studies reporting third-order eustatic cycles during the same period. Orbital and greenhouse gas variations would have prohibited the ice sheet from reaching long-term equilibrium at this time, explaining the moderate amplitude of reported glacioeustatic variations. The second step in ice sheet growth

is typified by an abrupt global climate cooling by ~14°C, leading to the further extension of the ice sheet into the tropical realm (30°S) during the Hirnantian glacial maximum. By demonstrating that the onset of a pre-Hirnantian continental-scale ice sheet over Gondwana requires no sudden climate cooling, our modeling results supply physical mechanisms for the previously enigmatic Late Ordovician stepped clumped-isotope data, which first display changes in ice volume and only later a drop in tropical sea surface temperatures. Our findings eventually support recent visions of a land ice cover over the supercontinent Gondwana throughout most of the Middle and Late Ordovician, embracing the emerging paradigm of an "Early Paleozoic Ice Age".

This study constitutes a major increment over previously published work that did not account for ice sheet feedback processes. Still, major shortcomings inherent to deep-time studies prevent us from capturing the high-frequency waxing and waning of the ice sheet. Better constrained Ordovician boundary conditions and extensive advances in modeling the cryosphere now constitute a prerequisite for further investigation.

Acknowledgments
We thank David Pollard and an anonymous reviewer for careful and helpful reviews and Heiko Pälike for editorial handling. A.P. also thanks J.-F. Buoncristiani for fruitful discussions and valuable inputs. This work was granted access to the HPC resources of TGCC under the allocation 2014-012212 made by GENCI. T.R.A.V. acknowledges ANR support through grant ANR-12-BS06-0014-SeqStrat-Ice. This research was funded by a CEA PhD grant CFR. This is a contribution to IGCP 591. The code of the FOAM model is available here http://www.mcs.anl.gov/research/projects/foam/index.html. LMDZ can be downloaded from the dedicated website as well http://lmdz.lmd.jussieu.fr/utilisateurs/distribution-du-modele. The code of the GRISLI model is available on request to Catherine Ritz (LGGE, Grenoble). Requests for the model output can be sent to A.P. (alexandre.pohl@lsce.ipsl.fr) or Y.D. (yannick.donnadieu@lsce.ipsl.fr).

References

Alvarez-Solas, J., M. Montoya, C. Ritz, G. Ramstein, S. Charbit, C. Dumas, K. Nisancioglu, T. Dokken, and A. Ganopolski (2011), Heinrich event 1: An example of dynamical ice-sheet reaction to oceanic changes, *Clim. Past*, *7*(4), 1297–1306.

Alvarez-Solas, J., A. Robinson, M. Montoya, and C. Ritz (2013), Iceberg discharges of the last glacial period driven by oceanic circulation changes, *Proc. Natl. Acad. Sci. U.S.A.*, *110*(41), 16350–16354.

Amberg, C. E. A., T. Collart, W. Salenbien, L. M. Egger, A. Munnecke, A. T. Nielsen, C. Monnet, Ø. Hammer, and T. R. A. Vandenbroucke (2016), The nature of Ordovician limestone-marl alternations in the Oslo-Asker District (Norway): Witnesses of primary glacio-eustasy or diagenetic rhythms?, *Sci. Rep.*, *6*, 18787.

Austermann, J., D. Pollard, J. X. Mitrovica, R. Moucha, A. M. Forte, R. M. DeConto, D. B. Rowley, and M. E. Raymo (2015), The impact of dynamic topography change on Antarctic ice sheet stability during the mid-Pliocene warm period, *Geology*, *43*(10), 927–930.

Bennett, M. R. (2003), Ice streams as the arteries of an ice sheet: Their mechanics, stability and significance, *Earth-Sci. Rev.*, *61*(3–4), 309–339.

Berner, R. A. (1990), Atmospheric carbon dioxide levels over Phanerozoic time, *Science*, *249*(4975), 1382–1386.

Berner, R. A. (2006), GEOCARBSULF: A combined model for Phanerozoic atmospheric O_2 and CO_2, *Geochim. Cosmochim. Acta*, *70*(23), 5653–5664.

Blakey, R. C. (2016), Colorado Plateau Geosystems. [Available at http://cpgeosystems.com.]

Bonelli, S., S. Charbit, M. Kageyama, M. N. Woillez, G. Ramstein, C. Dumas, and A. Quiquet (2009), Investigating the evolution of major Northern Hemisphere ice sheets during the last glacial-interglacial cycle, *Clim. Past*, *5*(3), 329–345.

Brenchley, P. J., J. D. Marshall, G. Carden, D. Robertson, D. Long, T. Meidla, L. Hints, and T. F. Anderson (1994), Bathymetric and isotopic evidence for a short-lived Late Ordovician glaciation in a greenhouse period, *Geology*, *22*(4), 295–298.

Bueler, E., and J. Brown (2009), Shallow shelf approximation as a "sliding law" in a thermomechanically coupled ice sheet model, *J. Geophys. Res.*, *114*, F03008, doi:10.1029/2008JF001179.

Buggisch, W., M. M. Joachimski, O. Lehnert, S. M. Bergström, J. E. Repetski, and G. F. Webers (2010), Did intense volcanism trigger the first Late Ordovician icehouse?, *Geology*, *38*(4), 327–330.

Charbit, S., C. Dumas, M. Kageyama, D. M. Roche, and C. Ritz (2013), Influence of ablation-related processes in the build-up of simulated Northern Hemisphere ice sheets during the last glacial cycle, *Cryosphere*, *7*(2), 681–698.

Clark, P. U., and D. Pollard (1998), Origin of the middle Pleistocene transition by ice sheet erosion of regolith, *Paleoceanography*, *13*(1), 1–9.

Crowley, T. J., and S. K. Baum (1991), Toward reconciliation of Late Ordovician (~440 Ma) glaciation with very high CO_2 levels, *J. Geophys. Res.*, *96*(D12), 22,597–22,610.

Crowley, T. J., and S. K. Baum (1995), Reconciling Late Ordovician (440 Ma) glaciation with very high (14X) CO_2 levels, *J. Geophys. Res.*, *100*(D1), 1093–1101.

Dabard, M. P., A. Loi, F. Paris, J.-F. Ghienne, M. Pistis, and M. Vidal (2015), Sea-level curve for the Middle to early Late Ordovician in the Armorican Massif (western France): Icehouse third-order glacio-eustatic cycles, *Palaeogeogr. Palaeoclimatol. Palaeoecol.*, *436*, 96–111.

DeConto, R. M., and D. Pollard (2003), Rapid Cenozoic glaciation of Antarctica induced by declining atmospheric CO_2, *Nature*, *421*(6920), 245–249.

Denis, M., J.-F. Buoncristiani, M. Konaté, J.-F. Ghienne, and M. Guiraud (2007), Hirnantian glacial and deglacial record in SW Djado Basin (NE Niger), *Geodin. Acta*, *20*(3), 177–195.

Denis, M., M. Guiraud, M. Konaté, and J. F. Buoncristiani (2010), Subglacial deformation and water-pressure cycles as a key for understanding ice stream dynamics: Evidence from the Late Ordovician succession of the Djado Basin (Niger), *Int. J. Earth Sci.*, *99*(6), 1399–1425.

Díaz-Martínez, E., and Y. Grahn (2007), Early Silurian glaciation along the western margin of Gondwana (Peru, Bolivia and northern Argentina): Palaeogeographic and geodynamic setting, *Palaeogeogr. Palaeoclimatol. Palaeoecol.*, *245*(1), 62–81.

Ehlers, J., and P. L. Gibbard (2007), The extent and chronology of Cenozoic global glaciation, *Quat. Int.*, *164–165*, 6–20.

Elrick, M., D. Reardon, W. Labor, J. Martin, A. Desrochers, and M. Pope (2013), Orbital-scale climate change and glacioeustasy during the early Late Ordovician (pre-Hirnantian) determined from $\delta^{18}O$ values in marine apatite, *Geology*, *41*(7), 775–778.

Finnegan, S., K. Bergmann, J. M. Eiler, D. S. Jones, D. A. Fike, I. Eisenman, N. C. Hughes, A. K. Tripati, and W. W. Fischer (2011), The magnitude and duration of Late Ordovician-Early Silurian glaciation, *Science*, *331*(6019), 903–906.

François, L., A. Grard, and Y. Goddéris (2005), Modelling atmospheric CO_2 changes at geological time scales, in *Pre-Cambrian to Palaeozoic Palaeopalynology and Palaeobotany*, edited by P. Steemans and E. Javaux, Carnets de Géologie/Notebooks on Geology, Memoir 2005/02, Brest, France.

Fretwell, P., et al. (2013), Bedmap2: Improved ice bed, surface and thickness datasets for Antarctica, *Cryosphere*, *7*(1), 375–393.

Ganopolski, A., R. Calov, and M. Claussen (2010), Simulation of the last glacial cycle with a coupled climate ice-sheet model of intermediate complexity, *Clim. Past*, *6*, 229–244.

Gasson, E., R. M. DeConto, D. Pollard, and R. H. Levy (2016), Dynamic Antarctic ice sheet during the early to mid-Miocene, *Proc. Natl. Acad. Sci. U.S.A.*, *113*(13), 3459–3464, doi:10.1073/pnas.1516130113.

Ghienne, J.-F., D. P. Le Heron, J. Moreau, M. Denis, and M. Deynoux (2007), The Late Ordovician glacial sedimentary system of the North Gondwana platform, in *Glacial Sedimentary Processes and Products, Spec. Publ. Int. Assoc. of Sedimentologists*, edited by M. Hambrey et al., pp. 295–319, Blackwells, Oxford, U. K.

Ghienne, J.-F., et al. (2014), A Cenozoic-style scenario for the end-Ordovician glaciation, *Nat. Commun.*, *5*, 4485.
Goddéris, Y., Y. Donnadieu, G. Le Hir, V. Lefebvre, and E. Nardin (2014), The role of palaeogeography in the Phanerozoic history of atmospheric CO_2 and climate, *Earth Sci. Rev.*, *128*, 122–138.
Gough, D. O. (1981), Solar interior structure and luminosity variations, *Sol. Phys.*, *74*, 21–34.
Haq, B. U., and S. R. Schutter (2008), A chronology of paleozoic sea-level changes, *Science*, *322*(5898), 64–68.
Heimbach, P., and M. Losch (2012), Adjoint sensitivities of sub-ice-shelf melt rates to ocean circulation under the Pine Island Ice Shelf, West Antarctica, *Ann. Glaciol.*, *53*(60), 59–69.
Heinemann, M., A. Timmermann, O. Elison Timm, F. Saito, and A. Abe-Ouchi (2014), Deglacial ice sheet meltdown: Orbital pacemaking and CO_2 effects, *Clim. Past*, *10*(4), 1567–579.
Herrmann, A. D., M. E. Patzkowsky, and D. Pollard (2003), Obliquity forcing with 8–12 times preindustrial levels of atmospheric pCO_2 during the Late Ordovician glaciation, *Geology*, *31*(6), 485–488.
Herrmann, A. D., M. E. Patzkowsky, and D. Pollard (2004), The impact of paleogeography, pCO_2, poleward ocean heat transport and sea level change on global cooling during the Late Ordovician, *Palaeogeogr. Palaeoclimatol. Palaeoecol.*, *206*(1), 59–74.
Horton, D. E., and C. J. Poulsen (2009), Paradox of late Paleozoic glacioeustasy, *Geology*, *37*(8), 715–718.
Horton, D. E., C. J. Poulsen, and D. Pollard (2007), Orbital and CO_2 forcing of late Paleozoic continental ice sheets, *Geophys. Res. Lett.*, *34*, L19708, doi:10.1029/2007GL031188.
Horton, D. E., C. J. Poulsen, and D. Pollard (2010), Influence of high-latitude vegetation feedbacks on late Palaeozoic glacial cycles, *Nat. Geosci.*, *3*(8), 572–577.
Hourdin, F., et al. (2013), Impact of the LMDZ atmospheric grid configuration on the climate and sensitivity of the IPSL-CM5A coupled model, *Clim. Dyn.*, *40*, 2167–2192.
Huybrechts, P. (1993), Glaciological modelling of the Late Cenozoic East Antarctic ice sheet: Stability or dynamism?, *Geogr. Ann.*, *75*(A), 221–238.
Jacob, R. L. (1997), Low frequency variability in a simulated atmosphere ocean system, PhD thesis, Univ. of Wisconsin-Madison, Madison, Wisconsin.
Krinner, G., O. Boucher, and Y. Balkanski (2006), Ice-free glacial northern Asia due to dust deposition on snow, *Clim. Dyn.*, *27*(6), 613–625.
Ladant, J. B., Y. Donnadieu, V. Lefebvre, and C. Dumas (2014), The respective role of atmospheric carbon dioxide and orbital parameters on ice sheet evolution at the Eocene-Oligocene transition, *Paleoceanography*, *29*, 810–823, doi:10.1002/2013PA002593.
Laskar, J., P. Robutel, F. Joutel, M. Gastineau, A. Correia, and B. Levrard (2004), A long-term numerical solution for the insolation quantities of the Earth, *Astron. Astrophys.*, *428*(1), 261–285.
Le Heron, D. P., and J. A. Dowdeswell (2009), Calculating ice volumes and ice flux to constrain the dimensions of a 440 Ma North African ice sheet, *J. Geol. Soc.*, *166*(2), 277–281.
Le Heron, D. P., J.-F. Ghienne, M. El Houicha, Y. Khoukhi, and J.-L. Rubino (2007), Maximum extent of ice sheets in Morocco during the Late Ordovician glaciation, *Palaeogeogr. Palaeoclimatol. Palaeoecol.*, *245*(1–2), 200–226.
Lees, D. C., R. A. Fortey, and L. R. M. Cocks (2002), Quantifying paleogeography using biogeography: A test case for the Ordovician and Silurian of Avalonia based on brachiopods and trilobites, *Paleobiology*, *28*(3), 343–363.
Licht, A., et al. (2014), Asian monsoons in a late Eocene greenhouse world, *Nature*, *513*(7519), 501–506.
Lowry, D. P., C. J. Poulsen, D. E. Horton, T. H. Torsvik, and D. Pollard (2014), Thresholds for Paleozoic ice sheet initiation, *Geology*, *42*(7), 627–630.
Loi, A., et al. (2010), The Late Ordovician glacio-eustatic record from a high-latitude storm-dominated shelf succession: The Bou Ingarf section (Anti-Atlas, Southern Morocco), *Palaeogeogr. Palaeoclimatol. Palaeoecol.*, *296*(3–4), 332–358.
Moreau, J., J.-F. Ghienne, D. P. L. Heron, J.-L. Rubino, and M. Deynoux (2005), 440 Ma ice stream in North Africa, *Geology*, *33*(9), 753–756.
Nardin, E., Y. Goddéris, Y. Donnadieu, G. Le Hir, R. C. Blakey, E. Pucéat, and M. Aretz (2011), Modeling the early Paleozoic long-term climatic trend, *Geol. Soc. Am. Bull.*, *123*(5–6), 1181–1192.
Nielsen, A. T. (2004), Ordovician sea-level changes: A Baltoscandian perspective, in *The Great Ordovician Biodiversification Event*, edited by B. D. Webby et al., pp. 84–93, Columbia Univ. Press, New York.
Page, A., J. A. Zalasiewicz, M. Williams, and L. E. Popov (2007), Were transgressive black shales a negative feedback modulating glacioeustasy in the Early Palaeozoic Icehouse?, in *Deep-Time Perspectives on Climate Change: Marrying the Signal from Computer Models and Biological Proxies*, edited by M. Williams et al., pp. 123–156, The Micropalaeontological Soc., Spec. Publ., The Geolog. Soc., London, U. K.
Paillard, D. (1998), The timing of Pleistocene glaciations from a simple multiple-state climate model, *Nature*, *391*, 378–381.
Pancost, R. D., K. H. Freeman, A. D. Herrmann, M. E. Patzkowsky, L. Ainsaar, and T. Martma (2013), Reconstructing Late Ordovician carbon cycle variations, *Geochim. Cosmochim. Acta*, *105*, 433–454.
Peltier, W. R., and S. Marshall (1995), Coupled energy-balance/ice-sheet model simulations of the glacial cycle: A possible connection between terminations and terrigenous dust, *J. Geophys. Res.*, *100*(D7), 14,269–14,289.
Peyaud, V., C. Ritz, and G. Krinner (2007), Modelling the Early Weichselian Eurasian Ice Sheets: Role of ice shelves and influence of ice-dammed lakes, *Clim. Past*, *3*, 375–386.
Pohl, A., Y. Donnadieu, G. Le Hir, J. F. Buoncristiani, and E. Vennin (2014), Effect of the Ordovician paleogeography on the (in)stability of the climate, *Clim. Past*, *10*(6), 2053–2066.
Pohl, A., E. Nardin, T. Vandenbroucke, and Y. Donnadieu (2015), High dependence of Ordovician ocean surface circulation on atmospheric CO_2 levels, *Palaeogeogr. Palaeoclimatol. Palaeoecol.*, doi:10.1016/j.palaeo.2015.09.036, in press.
Pollard, D. (2010), A retrospective look at coupled ice sheet-climate modeling, *Clim. Change*, *100*(1), 173–194.
Pollard, D., and R. M. DeConto (2005), Hysteresis in Cenozoic Antarctic ice-sheet variations, *Global Planet. Change*, *45*(1–3), 9–21.
Pollard, D., and R. M. DeConto (2012), Description of a hybrid ice sheet-shelf model, and application to Antarctica, *Geosci. Model Dev.*, *5*, 1273–1275.
Pollard, D., R. M. DeConto, and R. B. Alley (2015), Potential Antarctic Ice Sheet retreat driven by hydrofracturing and ice cliff failure, *Earth Planet. Sci. Lett.*, *412*, 112–121.
Quiquet, A., C. Ritz, H. J. Punge, and D. Salas y Mélia (2013), Greenland ice sheet contribution to sea level rise during the last interglacial period: A modelling study driven and constrained by ice core data, *Clim. Past*, *9*(1), 353–366.
Rasmussen, C. M. Ø., et al. (2016), Onset of main Phanerozoic marine radiation sparked by emerging Mid Ordovician icehouse, *Sci. Rep.*, *6*, 18884.
Ravier, E., J. F. Buoncristiani, J. Menzies, M. Guiraud, S. Clerc, and E. Portier (2015), Does porewater or meltwater control tunnel valley genesis? Case studies from the Hirnantian of Morocco, *Palaeogeogr. Palaeoclimatol. Palaeoecol.*, *418*, 359–376.
Raymo, M. E., J. X. Mitrovica, M. J. O'Leary, R. M. DeConto, and P. J. Hearty (2011), Departures from eustasy in Pliocene sea-level records, *Nat. Geosci.*, *4*(5), 328–332.

Reeh, N. (1991), Parameterization of melt rate and surface temperature on the Greenland ice sheet, *Polarforschung*, *59*(1), 113–128.
Ritz, C., V. Rommelaere, and C. Dumas (2001), Modeling the evolution of Antarctic ice sheet over the last 420,000 years—Implications for altitude changes in the Vostok region, *J. Geophys. Res.*, *106*(D23), 31,943–31,964.
Robinson, A., and H. Goelzer (2014), The importance of insolation changes for paleo ice sheet modeling, *Cryosphere*, *8*(4), 1419–1428.
Rothman, D. H. (2002), Atmospheric carbon dioxide levels for the last 500 million years, *Proc. Natl. Acad. Sci. U.S.A.*, *99*(7), 4167–4171.
Rubinstein, C. V., P. Gerrienne, G. S. de la Puente, R. A. Astini, and P. Steemans (2010), Early Middle Ordovician evidence for land plants in Argentina (eastern Gondwana), *New Phytol.*, *188*(2), 365–369.
Scotese, C. R. (2016), PALEOMAP Project. [Availble at http://www.scotese.com.]
Scotese, C. R., and W. S. McKerrow (1991), Ordovician plate tectonic reconstructions, in *Advances in Ordovician Geology*, edited by C. R. Scotese and W. S. McKerrow, pp. 271–282, Geol. Surv. of Canada, Ottawa, Ontario.
Semtner, A. J. (1976), A model for the thermodynamic growth of sea ice in numerical investigations of climate, *J. Phys. Oceanogr.*, *6*(3), 379–389.
Sheehan, P. M. (2001), The late Ordovician mass extinction, *Annu. Rev. Earth Planet. Sci.*, *29*(1), 331–364.
Steemans, P., A. Le Herissé, J. Melvin, M. A. Miller, F. Paris, J. Verniers, and C. H. Wellman (2009), Origin and radiation of the earliest vascular land plants, *Science*, *324*(5925), 353–353.
Stocchi, P., C. Escutia, A. J. P. Houben, B. L. A. Vermeersen, P. K. Bijl, H. Brinkhuis, R. M. DeConto, S. Galeotti, S. Passchier, and D. Pollard (2013), Relative sea-level rise around East Antarctica during Oligocene glaciation, *Nat. Geosci.*, *6*(5), 380–384.
Tabor, C. R., and C. J. Poulsen (2016), Simulating the mid-Pleistocene transition through regolith removal, *Earth Planet. Sci. Lett.*, *434*(C), 231–240.
Tobin, K. J., and S. M. Bergström (2002), Implications of Ordovician (460 Myr) marine cement for constraining seawater temperature and atmospheric pCO_2, *Palaeogeogr. Palaeoclimatol. Palaeoecol.*, *181*(4), 399–417.
Tobin, K. J., S. M. Bergström, and P. De La Garza (2005), A mid-Caradocian (453 Ma) drawdown in atmospheric pCO_2 without ice sheet development?, *Palaeogeogr. Palaeoclimatol. Palaeoecol.*, *226*(3–4), 187–204.
Torsvik, T. H., and L. R. M. Cocks (2009), BugPlates: Linking biogeography and palaeogeography, software manual. [Available at http://www.geodynamics.no.]
Torsvik, T. H., and L. R. M. Cocks (2013), New global palaeogeographical reconstructions for the Early Palaeozoic and their generation, in *Early Palaeozoic Biogeography and Palaeogeography, Geol. Soc. of London Memoirs*, edited by D. A. T. Harper and T. Servais, pp. 5–24, The Geol. Soc., London, U. K.
Trotter, J. A., I. S. Williams, C. R. Barnes, C. Lécuyer, and R. S. Nicoll (2008), Did cooling oceans trigger Ordovician biodiversification? Evidence from conodont thermometry, *Science*, *321*, 550–554.
Turner, B. R., H. A. Armstrong, C. R. Wilson, and I. M. Makhlouf (2012), High frequency eustatic sea-level changes during the Middle to early Late Ordovician of southern Jordan: Indirect evidence for a Darriwilian Ice Age in Gondwana, *Sediment. Geol.*, *251*, 34–48.
Vandenbroucke, T. R. A., H. A. Armstrong, M. Williams, J. A. Zalasiewicz, and K. Sabbe (2009), Ground-truthing Late Ordovician climate models using the paleobiogeography of graptolites, *Paleoceanography*, *24*, PA4202, doi:10.1029/2008PA001720.
Vandenbroucke, T. R. A., H. A. Armstrong, M. Williams, F. Paris, J. A. Zalasiewicz, K. Sabbe, J. Nølvak, T. J. Challands, J. Verniers, and T. Servais (2010a), Polar front shift and atmospheric CO_2 during the glacial maximum of the Early Paleozoic Icehouse, *Proc. Natl. Acad. Sci. U.S.A.*, *107*(34), 14,983–14,986.
Vandenbroucke, T. R. A., H. A. Armstrong, M. Williams, F. Paris, K. Sabbe, J. A. Zalasiewicz, J. Nølvak, and J. Verniers (2010b), Epipelagic chitinozoan biotopes map a steep latitudinal temperature gradient for earliest Late Ordovician seas: Implications for a cooling Late Ordovician climate, *Palaeogeogr. Palaeoclimatol. Palaeoecol.*, *294*(3–4), 202–219.
Vérard, C., C. Hochard, P. O. Baumgartner, G. M. Stampfli, and M. Liu (2015), 3D palaeogeographic reconstructions of the Phanerozoic versus sea, *J. Palaeogeogr.*, *4*(1), 64–84.
Wenzel, B., C. Lécuyer, and M. M. Joachimski (2000), Comparing oxygen isotope records of Silurian calcite and phosphate—$\delta^{18}O$ compositions of brachiopods and conodonts, *Geochim. Cosmochim. Acta*, *64*(11), 1859–1872.
Williams, G. E. (1991), Milankovitch-band cyclicity in bedded halite deposits contemporaneous with Late Ordovician-Early Silurian glaciation, Canning Basin, Western Australia, *Earth Planet. Sci. Lett.*, *103*(1), 143–155.
Yapp, C. J., and H. Poths (1992), Ancient atmospheric CO_2 pressures inferred from natural goethites, *Nature*, *355*, 342–344.
Yapp, C. J., and H. Poths (1996), Carbon isotopes in continental weathering environments and variations in ancient atmospheric CO_2 pressure, *Earth Planet. Sci. Lett.*, *137*(1), 71–82.
Young, S. A., M. R. Saltzman, K. A. Foland, J. S. Linder, and L. R. Kump (2009), A major drop in seawater $^{87}Sr/^{86}Sr$ during the Middle Ordovician (Darriwilian): Links to volcanism and climate?, *Geology*, *37*(10), 951–954.
Young, S. A., M. R. Saltzman, W. I. Ausich, A. Desrochers, and D. Kaljo (2010), Did changes in atmospheric CO_2 coincide with latest Ordovician glacial–interglacial cycles?, *Palaeogeogr. Palaeoclimatol. Palaeoecol.*, *296*(3–4), 376–388.

A warm or a cold early Earth? New insights from a 3-D climate-carbon model

Benjamin Charnay[a,b], Guillaume Le Hir[c], Frédéric Fluteau[c], François Forget[d], David C. Catling[b,e]

[a]*LESIA, Observatoire de Paris, PSL Research University, CNRS, Sorbonne Universités, UPMC Univ. Paris 06, Univ. Paris Diderot, Sorbonne Paris Cité, 5 Place Jules Janssen, 92195 Meudon, France*
[b]*Virtual Planetary Laboratory, University of Washington, Seattle, WA 98125, USA.*
[c]*Institut de Physique du Globe de Paris, Sorbonne Paris Cit, Universit Paris Diderot, 75238 Paris cedex 05, France*
[d]*Laboratoire de Météorologie Dynamique, IPSL/CNRS/UPMC, Paris 75005, France.*
[e]*Department of Earth and Space Science, University of Washington, Seattle, WA 98125, USA.*

Abstract

Oxygen isotopes in marine cherts have been used to infer hot oceans during the Archean with temperatures between 60°C (333 K) and 80°C (353 K). Such climates are challenging for the early Earth warmed by the faint young Sun. The interpretation of the data has therefore been controversial. 1D climate modeling inferred that such hot climates would require very high levels of CO_2 (2-6 bars). Previous carbon cycle modeling concluded that such stable hot climates were impossible and that the carbon cycle should lead to cold climates during the Hadean and the Archean. Here, we revisit the climate and carbon cycle of the early Earth at 3.8 Ga using a 3D climate-carbon model. We find that CO_2 partial pressures of around 1 bar could have produced hot climates given a low land fraction and cloud feedback effects. However, such high CO_2 partial pressures should not have been stable because of the weathering of terrestrial and oceanic basalts, producing an efficient stabilizing feedback. Moreover, the weathering of impact ejecta during the Late Heavy Bombardment (LHB) would have strongly reduced the CO_2 partial pressure leading to cold climates and potentially snowball Earth events after large impacts. Our results therefore favor cold or temperate climates with global mean temperatures between around 8°C (281 K) and 30°C (303 K) and with 0.1-0.36 bar of CO_2 for the late Hadean and early Archean. Finally, our model suggests that the carbon cycle was efficient for preserving clement conditions on the early Earth without necessarily requiring any other greenhouse gas or warming process.

Keywords: early Earth, climate, carbon cycle, Hadean, Archean, Late Heavy Bombardment

.

1. Introduction

Life likely emerged on Earth before 3.5 Ga, during the Hadean or the early Archean [*Buick et al.*, 1981; *Nisbet and Sleep*, 2001; *Bell et al.*, 2015]. Studying the atmosphere and the climates of the Earth during its first billion year is critical for understanding the environment in which life emerged and developed. Oxygen isotopic ratio of Archean marine cherts have been interpreted to suggest hot oceans with temperatures between 60°C (333 K) and 80°C (353 K) [*Knauth and Lowe*, 2003; *Robert and Chaussidon*, 2006], compatible with the thermophiles inferred from evolutionary models of the ancient life [*Gaucher et al.*, 2008] and possibly with the indications for a low ocean water viscosity [*Fralick and Carter*, 2011]. However, such an interpretation has been strongly debated [*Kasting and Howard*, 2006; *van den Boorn et al.*, 2007; *Marin-Carbonne et al.*, 2014; *Tartese et al.*, 2016] and other analyses suggest temperate oceans with temperatures lower than 40°C [*Hren et al.*, 2009; *Blake et al.*, 2010]. Moreover, at 3.5 Ga, the presence of glacial rocks at 20-40° latitude implies temperatures below 20°C [*de Wit and Furnes*, 2016], at least episodically.

In addition, previous modeling of the carbon cycle on the early Earth by *Sleep and Zahnle* [2001] and *Zahnle and Sleep* [2002] suggested that the Archean was cold unless another strong greenhouse gas was present. They also suggested that the Hadean was likely very cold because of the weathering of impact ejecta, particularly during the Late Heavy Bombardment (LHB). Therefore, the temperature of the early oceans remains an open question.

Here, we use a 3D climate-carbon model with pCO_2 ranging from 0.01 to 1 bar in order to determine physically plausible climates of the late Hadean and early Archean Earth. In section 2, we describe the climate simulations. In

section 3 and 4, we analyze the carbon cycle and the effect of the LHB with respect to carbon cycle responses. We finish with a conclusion in section 5.

2. Climate modeling

2.1. Description of the model

We simulated the atmosphere of the early Earth using the Generic LMDZ GCM (Global Climate Model). This model solves the primitive hydrostatic equations of meteorology using a finite difference dynamical core on an Arakawa C grid. It uses robust and general parameterizations in order to simulate planets very different from the present-day Earth. The Generic LMDZ GCM has already been used for studying the temperate and cold climates of the Archean Earth [*Charnay et al.*, 2013], the climates of early Mars with high CO_2 pressures [*Forget et al.*, 2013], and the runaway greenhouse effect on terrestrial planets with high amounts of water vapor [*Leconte et al.*, 2013]. It is thus adapted for simulating the early Earth with high amounts of CO_2 and potentially hot and moist climates.

The radiative scheme is based on the correlated-k method. At a given pressure and temperature, correlated-k coefficients in the GCM are interpolated from a matrix of coefficients stored in a 7×9 temperature and log-pressure grid: T=100, 150, 200, 250, 300, 350, 400 K, $p = 10^{-1}$, 10^0, 10^1, ..., 10^7 Pa. We used 36 spectral bands in the thermal infrared and 38 at solar wavelengths. Sixteen points were used for the g-space integration, where g is the cumulative distribution function of the absorption data for each band.

Simulations were performed with a horizontal resolution of 64×48 (corresponding to resolutions of 3.75° latitude by 5.625° longitude) and with 25 vertical layers with the lowest midlayer level at 5 m and the top level at 0.5 hPa. For the cloud microphysics, we either fixed the radii of water cloud particles (e.g. 12 μm for liquid droplets and 35 μm for icy particles for present-day Earth) or we fixed the density of cloud condensation nuclei (CCN) by mass of air (e.g. 5×10^6 particles/kg for liquid droplets and 2×10^4particles/kg for icy clouds for present-day Earth). As in *Charnay et al.* [2013], the oceanic transport and the sea ice formation were computed with the 2-layer oceanic model from *Codron* [2012].

To investigate the early Earth at 3.8 Ga, we used a solar constant of 1024 W/m^2 corresponding to 75% of the present value (1361 W/m^2). We ran simulations with no land. This hypothesis is valid for small continental surface fractions (e.g. <30% of the present-day fraction or <10% of the total Earth's surface) as we assumed at this time [*Flament et al.*, 2008] (see also section 3.1), although the land fraction is a matter of dispute [*Viehmann et al.*, 2014]. Such small continental fraction should indeed have a negligible direct impact on the global climate. We also assumed that Earth's rotation period was 14h. We used an atmospheric composition with 1 bar of nitrogen, a partial pressure of CO_2 (pCO_2) from 0.01 to 1 bar, and either no CH_4 or 2 mbar of CH_4, spanning the range of plausible methane concentrations estimated by a model for early ecosystems [*Kharecha et al.*, 2005]. *Wordsworth et al.* [2017] showed that CO_2-CH_4 collision-induced absorption could have produced a strong warming on early Mars if the CH_4 mixing ratio was higher than 1%. With our CH_4 mixing ratio of 0.1-0.2 %, CO_2-CH_4 CIA produce a warming lower than 0.1 K with the 1D version of the model. We thus neglected CO_2-CH_4 CIA in our 3D simulations.

2.2. Results

Figure 1 shows the global mean and zonal mean surface temperatures obtained with the GCM for present-day properties of clouds (Global mean values are gathered in table 1). Using 3.8 Ga conditions, the Earth falls into a full glaciation for the present-day pCO_2 (see *Charnay et al.* [2013]), but it is never fully ice-covered with at least 0.01 bar of CO_2. For this case with no methane, the mean surface temperature is -11.8°C, well below the freezing point, but there is still a cold ice-free equatorial belt between -37°N and +37°N. With 0.1 bar of CO_2, the climate is temperate (global mean surface temperature around 7.4°C without CH_4 and 21.3°C with CH_4). Ice-free conditions are obtained for pCO_2 higher than around 0.3 bar without methane or slightly higher than 0.1 bar with methane, corresponding to a mean surface temperature higher than around 23°C. Our model has a climate sensitivity with pCO_2 very similar to the GCM from *Wolf and Toon* [2013] going up to 0.3 bar. With 0.5 bar of CO_2, the climate becomes warm (mean surface temperature around 34.7°C without CH_4 and 49.9°C with CH_4). With 1 bar of CO_2, the mean surface temperature is around 59.5°C without CH_4 and around 67.5°C with CH_4.

Ozak et al. [2016] showed that CO_2 collisional line mixing reduces the atmospheric opacity between 400 and 550 cm^{-1} producing a significant cooling (~10°C) for a 1 bar CO_2 atmosphere for early Mars. Since we do not include

pCO_2 (bar)	pCH_4 (mbar)	Tsurf (°C)	Planetary albedo	Precipitation (mm/day)	SW forcing (W/m^2)	LW forcing (W/m^2)
0.01	0	-11.8	0.4	1.8	-38.3	+24.5
0.01	2	2.7	0.33	2.2	-42.0	+20.2
0.1	0	7.4	0.34	2.8	-47.1	+24.9
0.1	2	21.3	0.28	3.5	-39.8	+18.1
0.3	0	22.1	0.31	3.6	-42.4	+20.8
0.3	2	34.7	0.26	4.4	-32.6	+13.8
0.5	0	34.7	0.27	4.6	-30.4	+16.0
0.5	2	49.9	0.23	5.1	-22.8	+12.3
1.0	0	59.5	0.24	5.7	-19.4	+14.2
1.0	2	67.5	0.23	6.1	-20.3	+14.0

Table 1: Global mean values from the GCM. Columns from left to rights are: pCO_2 (in bar), pCH_4 (in mbar), the mean surface temperature (in °C), the mean planetary albedo, the mean precipitation rate (in mm/day), the shortwave cloud forcing (in W/m^2) and the longwave cloud forcing (in W/m^2).

collisional line mixing, our model might overestimate temperatures for high pCO_2. However, for the early Earth with a 1 bar CO_2 atmosphere, the peak of thermal emission from the surface would be around 1110 cm^{-1} (compared to around 730 cm^{-1} for early Mars), so quite far from the 400-550 cm^{-1} spectral region. We therefore expect a weaker cooling effect by CO_2 collisional line mixing for the early Earth than for early Mars.

Fundamental changes to cloud properties on early Earth have been proposed as alternative solutions to the faint young Sun paradox. In particular, it has been proposed that cloud particles were larger on the early Earth because of less cloud condensation nuclei from biological sources [*Rosing et al.*, 2010]. In figure 2, we tested the impact of larger liquid cloud particles (17 μm versus 12 μm). Larger particles warm the planet by decreasing the planetary albedo [*Charnay et al.*, 2013]. This effect is particularly strong for temperate climate with a warming of around 8°C for pCO_2=0.1 bar. However, it becomes weak for warmer climates. We also simulated the climates with a fixed amount of CCN and varying cloud radii (black line in left panel in figure 2). The mean surface temperature is almost identical to the case with 12 μm particles.

The right panel in figure 2 shows the shortwave (albedo cooling effect) and longwave (greenhouse warming effect) radiative forcing by clouds depending on pCO_2 for the different particle size parametrizations. The trends are similar for all particles size parametrizations. The net cloud radiative forcing is higher for cold climates (e.g. pCO_2=0.01 bar) than for temperate climates (e.g. pCO_2=0.1 bar). This is due to the lower albedo cooling of clouds over sea ice and to a reduction of the cloud cover over the cold equatorial ocean, particularly close to the freezing line (see *Charnay et al.* [2013]). The net cloud radiative forcing increases with pCO_2 when pCO_2 exceeds 0.1 bar. The albedo cooling effect decreases because of a reduction of lower clouds (see right panel in figure 3). At the same time, the greenhouse warming effect decreases. This is mostly due to the gaseous infrared emission level (the altitude where most of the thermal emission is emitted) going up with more CO_2, which reduces the greenhouse effect of clouds. The cloud albedo cooling decreases faster than the cloud greenhouse warming, which leads to a net forcing increasing with pCO_2. Clouds therefore produce a destabilizing feedback on the climate. For hot climates, they tend to have a small net radiative effect (their cooling effect being reduced by around 30 W/m^2), which depends little on the radii of cloud particles.

In response to clouds properties, our GCM predicts that hot climates can be obtained with 1 bar or less of CO_2 at 3.8 Ga. This required amount of CO_2 is significantly lower than previous 1D estimations by *Kasting and Howard* [2006]. They found that if there were no methane, around 3 bars of CO_2 would be required for getting a mean surface temperature of 60°C at 3.3 Ga. This discrepancy is due to cloud feedbacks, not simulated in the 1D model, and to a few other differences in the climate modeling. In particular, they used the present-day land cover while we assumed no continent, and we used more recent opacity data, likely increasing the visible and infrared gaseous absorption. From a purely climate modeling point of view (i.e., ignoring long-term geochemical feedbacks), a warm early Earth with temperature of 60-70°C is possible with sufficient CO_2 if there is no land or almost no land.

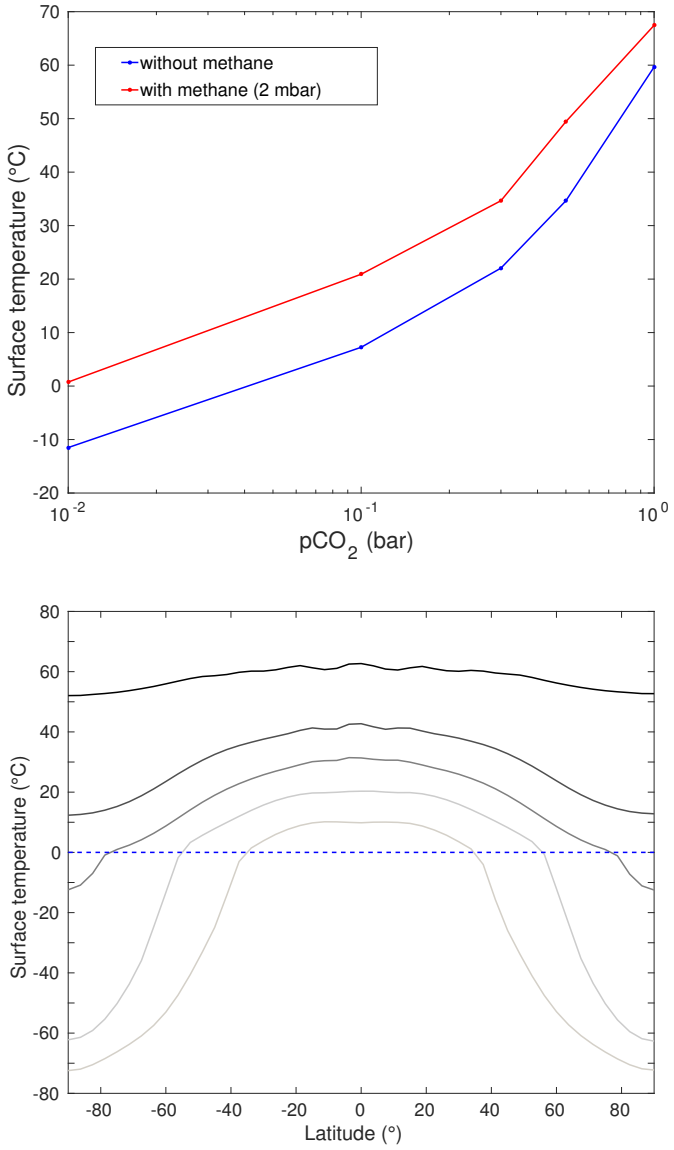

Figure 1: Top panel: global mean surface temperature without methane (blue line) and with 2 mbars of methane (red line). Bottom panel: zonal mean surface temperature for an atmosphere with no methane and with 0.01, 0.1, 0.3, 0.5 and 1 bar of CO_2 for lines from light gray to black respectively. The blue dashed line is the freezing temperature of water.

3. Carbon cycle modeling

3.1. Model set-up and boundary conditions

In order to quantify the carbon cycle equilibrium response to simulated climate, we used the model from *Le Hir et al.* [2008a, b]. We generally assumed a classical plate tectonic regime as in *Sleep and Zahnle* [2001] (see Fig. 1 in Appendix A), although there is debate about when a modern style of plate tectonics began [*Stern*, 2007]. CO_2 reservoirs are 1) the atmosphere, 2) the surface/deep ocean, 3) the mantle, 4) carbonates on continental platforms and 5) calcite precipitation in the oceanic crust resulting from seafloor weathering. The inventory of carbon between

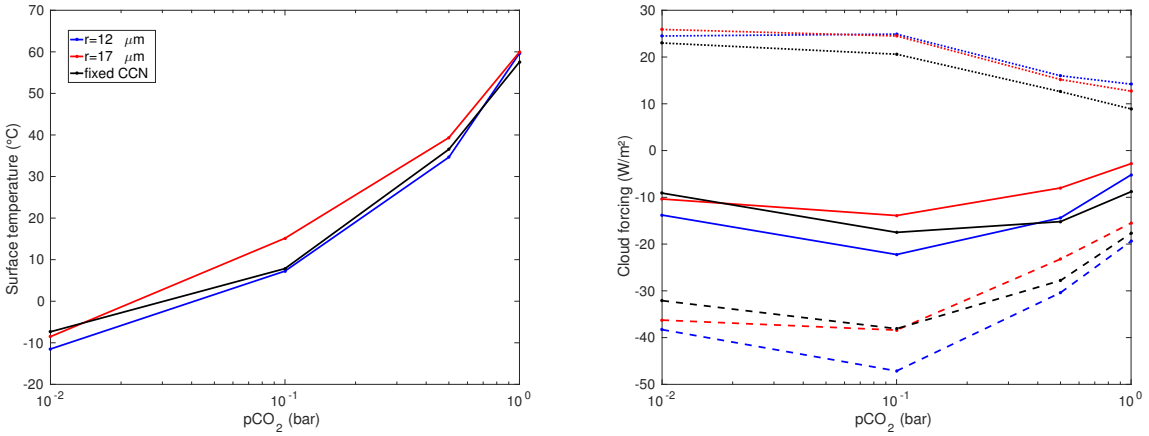

Figure 2: Left panel: global mean surface temperature with no methane with 12 μm liquid cloud droplets (blue), 17 μm liquid cloud droplets (red) and varying cloud droplet radii with a fixed CCN concentration (black line). Right: shortwave cloud forcing (dotted lines), longwave cloud forcing (dashed lines) and net cloud forcing (solid lines). The colors correspond to the same cases as the left panel.

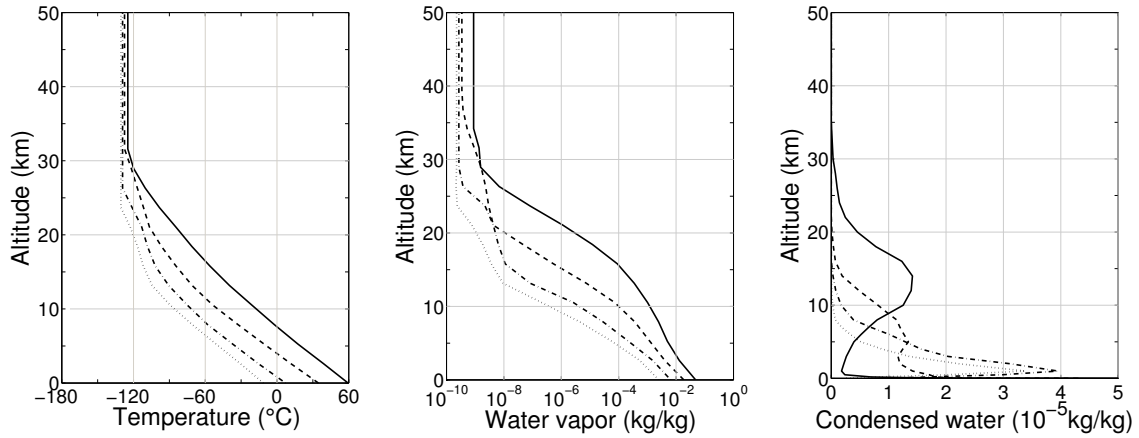

Figure 3: Left panel: vertical profile of global mean temperature. Middle panel: vertical profile of global mean water vapor mixing ratio (in kg/kg). Right panel: vertical profile of global mean condensed water mixing ratio (in 10^{-5} kg/kg). For the three panels, pCO_2 is 0.01 (dotted line), 0.1 (dashed-dotted line), 0.5 (dashed line) and 1 (solid line) bar and there is no methane.

these six reservoirs evolves through CO_2 outgassing by mid oceanic ridges and arc volcanoes, continental and seafloor weathering, carbonate formation/dissolution, subduction and recycling. The part of subducted carbon released by arc volcanoes depends on the recycling factor. Based on a steady state assumption, we considered an instantaneous carbon recycling in subduction zones. The model parametrizations for these processes are described in Appendix A.

We simulated the carbon cycle using the surface temperatures and precipitation-evaporation rates (P-E) from the GCM. In the absence of constraints about geography, we assumed that emerged continents are homogeneously spread over all the Earth as small continents (each grid cell has its own fraction of continents). That tends to maximize the continental weathering. We interpolated GCM temperatures and Precipitation-Evaporation (P-E) between pCO_2 values at each grid point. We parametrized the seafloor weathering with a dependence on the deep ocean temperature (see *Coogan and Gillis* [2013] for geological evidence and *Krissansen-Totton and Catling* [2017] for application for the last 100 Ma), assumed to be equal to sea surface temperature at 60° latitude. Most of the weathering occuring in the upper part of the oceanic crust (<1km), the seafloor weathering is explicitly described between 0 and 500 m by 6

layers with an ambient temperature increasing with depth (116°C/km). We assumed that the potential temperature of the mantle was around 1550°C at 3.8 Ga compared to 1330°C today. Formulas from *Flament et al.* [2008] (with an activation energy for the mantle viscosity of ~350-400 kJ/mol) lead to a oceanic crust mass production rate ~11 times higher at 3.8 Ga than today. This value is consistent with the estimation by *Ohta et al.* [1996] of a 10 times higher oceanic crust production rate during the Archean.

We assumed that the CO_2 flux outgassed by oceanic ridges is proportional to the oceanic crust mass production rate while the seafloor weathering, limited to the first km of the oceanic crust, is proportional to the spreading rate. For a fixed oceanic crust mass production rate, a thicker crust has no impact on the outgassed CO_2 flux but reduces the seafloor weathering in our model, leading to an enhancement of pCO_2. It is generally accepted that the oceanic crust was thicker during the Archean (~18 km versus 6 km in average) [*Bickle*, 1986; *Ohta et al.*, 1996; *Flament et al.*, 2008]. If we assume that the early oceanic crust was 3 times thicker at the mid-oceanic ridge, the spreading rate (SR) must have been 3.8 times higher than today, according to our estimation of the oceanic crust mass production rate. Since the oceanic crust thickness and the associated spreading rate during the Archean are highly uncertain [*Bickle*, 1986], we therefore tested cases with the present-day oceanic crust thickness (6 km) and SR=11.3.

For a warmer mantle and a higher spreading rate on the early Earth, the younger oceanic lithosphere was warmer and melted more easily when subducted. If arc volcanoes, associated with subduction zones, provide a quick return of materials to the surface, the direct melting of oceanic crust may increase the amount of fluid released, suggesting a recycling of suducted carbon higher than today. According to this assumption, the decarbonation efficiency may exceed Cenozoic values used as reference [*Hoareau et al.*, 2015]. We thus explored the effect of the recycling (R) using the Cenozoic value as reference (R=0.1, corresponding to a recycling efficiency of 10%) and values 3 times higher (R=0.3, a recycling efficiency of 30%).

The fraction of emerged land during the Hadean/Archean is still debated [*Roberts and Spencer*, 2015]. We made the assumption that this fraction was low (<30% of the present-day fraction) during the early Archean as suggested by some geochemical data (e.g. [*Dhuime et al.*, 2012]), some evidence for a more voluminous ocean during the Archean [*Pope et al.*, 2012] and some models (e.g. [*Flament et al.*, 2008]). This hypothesis allows us to use the outputs from the 3D land-free simulations for the carbon cycle model. We explored the effect of the emerged continental fraction considering four cases:

- 1) an aquaplanet (no land)
- 2) a very low emerged land fraction (1% of the present-day land fraction)
- 3) a moderate continental fraction (12% of the present-day land fraction)
- 4) a relatively high continental fraction (26% of the present-day fraction)

Although there is clear evidence of emerged land at 3.7-3.8 Ga [*Nutman et al.*, 2015], an aquaplanet model is an idealized case, which is very useful for understanding the effect of seafloor weathering.

3.2. Results and discussion

We ran the climate-carbon model for the four land fractions (0, 0.01, 0.12 and 0.26 times present-day fraction), with a recycling factor R equal to 1 (present-day) or 3, with or without 2 mbars of atmospheric methane and with the present-day oceanic crust thickness (H=6 km, SR=11.3) or a 3 times thicker oceanic crust (H=18 km, SR=3.8). The equilibrium points span a temperature range from 8.5°C to 31.5°C and a pCO_2 range from 0.12 bar to 0.36 bar (see figure 4 and table 1). Ice-free or partly ice-free oceans are obtained in any cases.

3.2.1. Cases with no land

If there is no emerged land, the carbon cycle is controlled by the seafloor weathering and volcanic/mid-oceanic ridge outgassing. At equilibrium, the seafloor weathering is simply given by $F_{sfw} = \frac{F_{mor}+F_{deep}}{1-R}$ (F_{mor} and F_{deep} are the CO_2 fluxes from midocean ridges and mantle, respectively, see Appendix A) and depends on R. Because the carbon species partitioning between ocean and atmosphere is controlled by temperature, sea surface temperature (SST) implicitly determines the seawater pH and pCO_2 for a fixed value of seafloor weathering rate. Light blue and purple curves in figure 4 reveal the CO_2 partial pressure for a given SST with our model. They are computed

assuming no CO_2 climate feedback and thus represent the intrinsic response of the carbon model for Earth's climate in the absence of continents. The light blue curves (6 km thick crust) reveal a maximum pCO_2 of 0.14 bar for R=0.1 (left panel) and 0.26 bar for R=0.3 (right panel). The CO_2 solubility in the ocean decreases with temperature. At temperatures lower than 15°C, this feedback dominates and pCO_2 increases with temperature. When the temperature becomes higher than 15°C, the temperature dependance of the seafloor weathering dominates and pCO_2 decreases with temperature. The combination of both effects (solubility and seafloor weathering) leads to an upper limit for pCO_2 for the thin oceanic crust case. The reduced seafloor accretion rate associated to a thicker oceanic crust scenario combined with cold water strongly limits carbon consumption by seafloor weathering, hence the purple curves (18 km thick crust) do not show a maximum pCO_2 below 1 bar. For these cases without land, the equilibrium point of the climate-carbon model corresponds to the crossing between the intrinsic response of the carbon model (i.e. the light blue and purple curves) and the GCM curves showing the global mean surface temperature as a function of pCO_2 (i.e. the blue and red curves). For instance, the equilibrium point for a methane-free atmosphere with R=0.1 and a thick crust corresponds to a mean SST of 22.3°C and pCO_2=304 mbar.

3.2.2. Effects of land cover

According to our model, land cover has only a limited impact on the carbon cycle and the global climate for the early Earth (temperature change of ~1°C between the four land distributions). Indeed, while the carbon cycle was mostly controlled by continental weathering during the Proterozoic and the Phanerozoic (e.g. *Krissansen-Totton and Catling* [2017]), it was mostly controlled by seafloor weathering on the early Earth. That difference is mainly due to the higher spreading rate (high accretion rate provides a sufficient quantity of weatherable materials which enhances the seafloor weathering) and to the assumed lower land fraction on the early Earth. Under such circumstances, our assumption about the land distribution (i.e. small continents distributed homogeneously) is therefore of minor importance for the results. We also notice that the feedback produced by land does not have the same sign with a 6 or 18 km thick oceanic crust. With a 6 km oceanic crust, the seafloor weathering is slightly stronger than the continental weathering per unit of surface. In that case, the global mean surface temperature and pCO_2 are higher with a higher land fraction. In contrast, with a 18 km thick oceanic crust, the continental weathering is stronger than the seafloor weathering per unit of surface (as today) and a higher land fraction leads to lower pCO_2. The coldest case with our assumptions (mean SST of 8.5°C) is thus obtained with no land, a methane-free atmosphere, R=0.1 and a thin crust. The warmest case (mean SST of 31.5°C) is obtained with no land, a methane-rich atmosphere, R=0.3 and a thick oceanic crust, as shown by the blue point in Figure 4b.

3.2.3. Effects of methane, oceanic crust thickness and recycling rate

A thicker oceanic crust or a higher recycling efficiency always leads to an increase of pCO_2 and so to an increase of temperature. In contrast, adding methane in the atmosphere reduces pCO_2 but still increases the global mean surface temperature. If we use as a reference, the case with a moderate land cover, a 6 km thick crust, no methane and R=0.1 (mean surface temperature=8.5°C), adding 2 mbar of methane produces a 11.7°C warming, a 18 km crust produces a 12.9°C warming, and a 3 times higher recycling rate produces a 8.8°C warming. These three parameters therefore produce significant temperature and pCO_2 changes. In particular, the thicker oceanic crust is generally expected for the early Earth, with an effect on pCO_2. A thicker oceanic crust would have had a large impact, allowing warmer climate for the early Earth than today. The combination of a thicker crust, a high recycling rate, and the presence of methane leads to global mean surface temperatures around 30°C for the three land distributions. That temperature change (~20°C) is much lower than the sum of individual warming (~33°C), mostly because of the non-linear dependence of the seafloor weathering with the deep ocean temperature.

3.2.4. Absence of plate tectonic: the heat-pipe scenario

The onset time of plate tectonic is unknown but most geological and isotopic data suggest that subduction started during the Hadean or early Archean [*Sleep*, 2007; *Tang et al.*, 2016]. *Moore and Webb* [2013] suggested that before the onset of plate tectonic, Earth was in a heat-pipe regime in which volcanism dominated surface heat transport. We tested the consequences of this possible early regime for the carbon cycle with our model. We considered that all the heat flux is released by volcanism, that the spreading rate is null and that submarine basalt flows are weathered as seafloor basalts. In our simulation of the heat-pipe Earth, we assumed a very low land fraction (1% of the present-day land cover). The volcanic outgassing becomes around 4 times as high as with the plate tectonic regime, or 10 times as

Boundary conditions						Results							
Land fraction	Oceanic crust (km)	SR	Recyling	CH_4	rdeg	pCO_2 (mbar)	Tsurf (°C)	pH	DIC	F_{mor}	F_{arc}	F_{con}	F_{sfw}
1	6	1	0.1	no	1	0.285	14.9	8.4	2.4	1.6	7.7	-10.5	-1.1
0.0	6	11.3	0.1	no	2.5	118	8.5	6.70	32.2	18	11.2	0.0	-29.2
0.0	6	11.3	0.3	no	2.5	225	16.5	6.60	39.8	18	19.5	0.0	-37.5
0.0	18	3.8	0.1	no	2.5	304	22.3	6.56	48.9	18	11.2	0.0	-29.2
0.0	18	3.8	0.1	yes	2.5	190	27.0	6.66	35.4	18	11.2	0.0	-29.2
0.0	18	3.8	0.3	no	2.5	359	25.8	6.53	52.4	18	19.5	0.0	-37.5
0.0	18	3.8	0.3	yes	2.5	243	30.6	6.61	39.6	18	19.5	0.0	-37.5
0.01	6	11.3	0.1	no	2.5	118	8.5	6.70	32.21	18	11.2	-0.05	-29.2
0.01	6	11.3	0.3	no	2.5	231	16.9	6.65	45.10	18			
0.01	18	3.8	0.1	no	2.5	303	22.3	6.56	49.51	18			
0.01	18	3.8	0.1	yes	2.5	186	26.8	6.67	35.39	18			
0.01	18	3.8	0.3	no	2.5	358	25.8	6.53	52.73	18			
0.01	18	3.8	0.3	yes	2.5	240	30.5	6.62	39.64	18			
0.12	6	11.3	0.1	no	2.5	117	8.5	6.70	32.06	18	11.6	-0.4	-29.2
0.12	6	11.3	0.1	yes	2.5	97	20.2	6.80	25.52	18			
0.12	6	11.3	0.3	no	2.5	235	17.3	6.66	46.69	18	23.7	-3.1	-38.7
0.12	6	11.3	0.3	yes	2.5	135	23.3	6.75	31.47	18			
0.12	18	3.8	0.1	no	2.5	292	21.4	6.59	50.13	18	12.6	-4.1	-26.5
0.12	18	3.8	0.1	yes	2.5	163	25.2	6.71	34.38	18			
0.12	18	3.8	0.3	no	2.5	356	25.6	6.57	56.31	18			
0.12	18	3.8	0.3	yes	2.5	219	29.0	6.69	41.89	18			
0.26	6	11.3	0.1	no	2.5	121	8.8	6.70	32.50	18	12.1	-0.64	-29.5
0.26	6	11.3	0.3	no	2.5	245	18.0	6.66	48.47	18			
0.12	6	0	0	no	10	257	18.8	6.60	45.75	31.9	1.1	-0.9	-32.1

Table 2: Equilibrium states from the carbon model coupled to the GCM. Columns from left to right are: the land fraction, the oceanic crust thickness (in km), the spreading rate, the recycling rate, the presence (2 mbar) or absence of methane, the outgassing rate, pCO_2 (in mbar), the mean surface temperature (in $^{\circ}C$), the mean oceanic pH, the mean dissolved inorganic carbon (in mol/m^3), the CO_2 flux outgassed from mid-oceanic ridges and from arc volcanoes, and the CO_2 sink by continental weathering and seafloor weathering (all fluxes in 1e12 mol/yrs). The first case, with land fraction equal to 1, is the present-day Earth. The last case, with SR=0, is the heat-pipe scenario with no plate tectonics.

high as the present volcanic outgassing. At equilibrium, pCO_2 is 0.26 bar and the mean surface temperature is around 18.8°C. A heat-pipe regime would thus have led to a temperate early Earth.

3.2.5. Discussion

Our climate-carbon model never reaches warm climates for the early Earth because of the strong temperature feedback by the seafloor weathering. It predicts global mean surface temperatures around 8.5-30.5°C, with pCO_2 around 0.1-0.36 bar. This temperature range is compatible with the most recent measurements by *Hren et al.* [2009] and *Blake et al.* [2010], and also with the evolutionary model from *Bousseau et al.* [2008] for a mesophilic last universal common ancestor (LUCA). Thermophily near the roots of the tree of life may reflect local warm environments (like hydrothermal vents) or survival after hot climates produced just after large impacts [*Bousseau et al.*, 2008; *Abramov and Mojzsis*, 2009]. The pCO_2 range of 0.1-0.35 bar is generally higher than the upper limits initially derived from the stability of different minerals from Archean samples [*Rye et al.*, 1995; *Sheldon*, 2006; *Rosing et al.*, 2010; *Driese et al.*, 2011]. These constraints globally suggest a pCO_2 lower than 30 mbars. However, they are not all compatible together and were essentially obtained for the late Archean. Recent work by *Kanzaki and Murakami* [2015] gives an upper limit for pCO_2 of 0.14-0.7 bar at 2.77-2.46 Ga, compatible with our results.

4. Climate and carbon cycle during the Late Heavy Bombardment

4.1. Impact modeling

The Earth was likely struck by numerous of impactors during the Late Heavy Bombardment (LHB), which would have occurred between around 4.1 and 3.8 Ga [*Gomes et al.*, 2005; *Bottke and Norman*, 2017]. These impactors may have been a sink of CO_2 by producing large amounts of ejecta, which can be easily weathered [*Sleep and Zahnle*, 2001]. They may also have been a source of CO_2 by vaporizing carbonates from the oceanic crust. For instance,

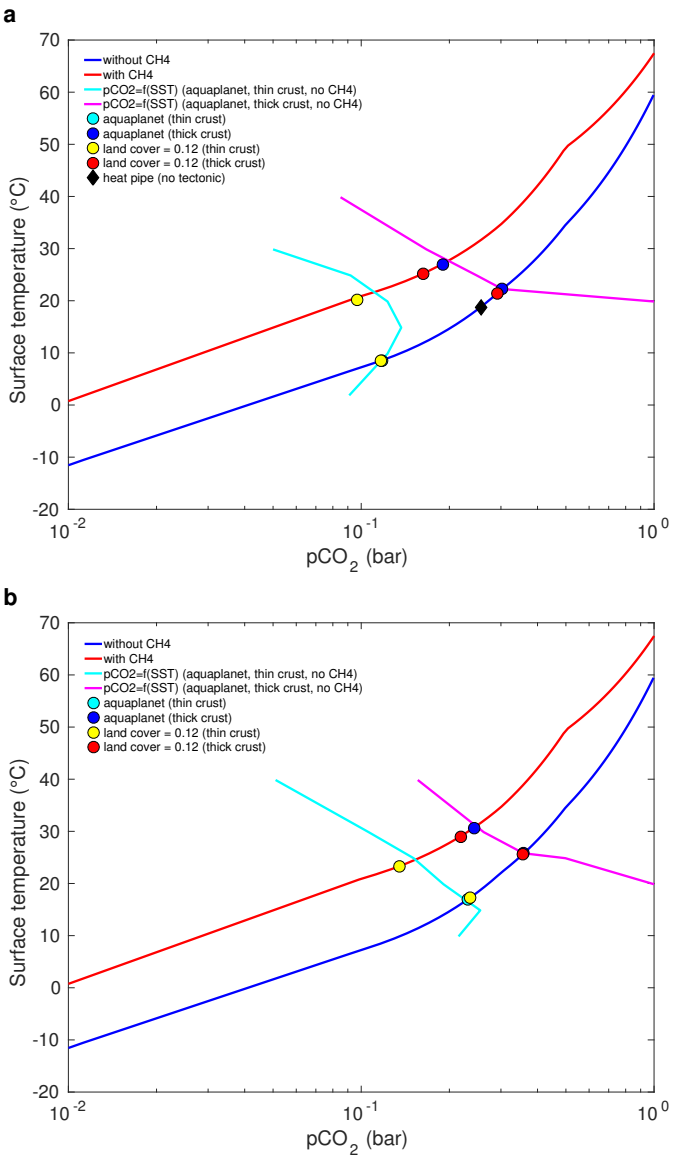

Figure 4: Global mean surface temperature as figure 1 but including the equilibrium points of the carbon model assuming a land fraction of 0.01 (light blue and blue circles) and 0.12 (yellow and red circles) compared to the present-day land fraction. Panel a) shows equilibrium points for the present-day recycling (R=0.1). Light blue and yellow circles are for the present-day oceanic crust thickness while blue and red circles for a 3 times thicker oceanic crust. The black diamond corresponds to the heat pipe scenario with no plate tectonic on an aquaplanet. Panel b) is similar to panel a) but with a 3 times higher recycling (R=0.3). The light blue and the purple curves are the intrinsic response of the carbon cycle model. They are obtained by changing the surface temperature from 10°C to 40°C with no feedback of pCO_2 on the temperature, with no land, for the present-day oceanic crust (light blue) and for a 3 times thicker oceanic crust (purple).

Chixulub impact may have outgassed 350-3500 Gt of CO_2 [*Pierazzo et al.*, 1998], or the equivalent of 0.06-0.6 mbar of CO_2. We investigated the long term effects of impacts on the carbon cycle to understand their consequences for the mean climate during the LHB, in particular if they had a global net warming or cooling effect.

We assumed that the frequency of impact follows a scaling law given in *Anbar et al.* [2001] and *Sleep and Zahnle* [2001]:

$$f(\geq m) = f_0 \times \left(\frac{m}{m_{max}}\right)^{-b} \quad (1)$$

where f is the frequency of impactors having a mass higher than m. For the LHB, we chose b = 0.7 [*Anbar et al.*, 2001]. We considered that the maximal mass was m_{max} = 10^{19} kg (i.e. diameter around 190 km). This upper limit is constrained by the largest crater observed on the Moon. We neglected impacts with a mass lower than 10^{13}kg (i.e. diameter lower than around 1.8 km), which produce little ejecta because of the strong deceleration by the ocean. We fixed $f_0 = 2.9\times10^{-8}$ impacts/year in order to have a cumulative impactor mass equal to 2×10^{20} kg for the 300 millions of years of the LHB. That corresponds to an impact flux of 6.7×10^{11} kg/year.

As *Sleep and Zahnle* [2001] and *Zahnle and Sleep* [2002], we computed the weathering of ejecta, which provides a source of cations, precipitating as carbonates in the ocean. We assumed that the mass distribution of ejecta is given by $N(\geq m) \propto m^{-\gamma}$, where γ=0.87 (derived from scaling laws of *Collins et al.* [2005]). *Zahnle and Sleep* [2002] used a similar law with γ=0.9-0.95. We considered that the diameter of each particle decreases of 1 mm in 167 kyrs [*Crovisier et al.*, 1987] and that cations are present at 0.005 mol/g. With the oceanic crust lifetime for the early Earth, ejecta with a diameter larger than 100 m contribute little to the weathering compared to smaller ejecta.

We included CO_2 delivered by the impactors as done by *de Niem et al.* [2012]. We assumed that the mass fraction of CO_2 is 1% in asteroids and 20% in comets. For comparison, Rosetta measurements of Comet 67P / Churyumov-Gerasimenko indicate a mass ratio of CO_2 to H_2O around 40% [*Marty et al.*, 2016] for a mass fraction of H_2O to dust around 20%, implying a mass fraction of CO_2 around 8%. If all impactors were comets, the LHB would have provided the equivalent of 3.8 bar of CO_2 (taking into account the escaping mass of impactors). The fraction of comets during the LHB is not known and *Bottke et al.* [2012] suggest that comets were a minor player. We did simulations using fractions of comets of 0 and 100%. We also included the CO_2 outgassed by oceanic carbonates and lithosphere melting after impact. We considered that the oceanic crust is covered by a 40 m layer of carbonate, which outgassed CO_2 when shocked at a high pressure (above 60 GPa). We assumed that the lithosphere below the carbonate layer (considered as pure calcite) contains 100 ppmv of CO_2 and outgasses all CO_2 when melted. The complete assumptions for the ejecta weathering and CO_2 outgassing are described in Appendix B.

Figure 5 shows the amount of CO_2 outgassed from impactor/crust and consumed by ejecta as a function of impactor mass for asteroids (density=3000 kg/m^2 and initial velocity=21 km/s) and comets (density=1000 kg/m^2 and initial velocity=30 km/s). The solid red lines show the maximal amount of CO_2 that can be consumed by ejecta. The solid red line show the amount of CO_2 consumed by ejecta in 15 Ma (the lifetime of the oceanic crust in our model). With our size distribution for ejecta, most of ejecta are weathered during the lifetime of the oceanic crust. In all cases, impacts produce a net sink of CO_2 by ejecta weathering.

4.2. Results and discussion for the LHB

To simulate the effect of impacts during the LHB, we computed sequences of 10 millions of years with stochastic impacts following the statistical distribution described above. For simplicity, we assumed that impacts never overlap and that they all fall into the ocean. This assumption is valid because we consider small continental fractions and because the total surface of transient craters (diameter D_{tc} in Appendix B) accumulated in 10 million years only represents 0.6 % of the Earth's surface. These sequences provide a time-dependent CO_2 outgassing rate and alkaline source, which are used in the carbon cycle model to computed the climate and pCO_2 evolution. The top panel in figure 6 shows the cumulated CO_2 outgassed by impacts and consumed by ejecta during a typical 10 million year sequence with stochastic impacts. In this sequence, one 143 km impactor strikes the Earth at 7 Ma and dominates CO_2 fluxes. On average, the weathering of ejecta produces a cations flux of 16 $\times10^{12}$ mol/yr (compared to 300 $\times10^{12}$ mol/yr in *Sleep and Zahnle* [2001]), around half the CO_2 flux from mid oceanic ridges and arc volcanoes (around 30×10^{12}mol/year). The vaporization of carbonates produces a CO_2 flux of 0.05×10^{12}mol/year, negligible on the long term compared to the other fluxes. The bottom panel in figure 6 shows the evolution of pCO_2 during this sequence for the 0.01 land fraction, no methane, R=0.1, a thin or thick oceanic crust and with asteroids or comets. The giant impact at 7 Ma produces a strong decrease of pCO_2 by ejecta weathering triggering a full glaciation for thin oceanic crust cases and a very cold climate with a global mean surface temperature of -10°C for the thick oceanic crust case. Before this impact, the carbon cycle is stabilized with pCO_2 around 50 mbar for the thin crust and around 250 mbar

for the thick crust. As in *Sleep and Zahnle* [2001] and *Zahnle and Sleep* [2002], we thus find a strong cooling by ejecta weathering leading to cold climates, but not always completely ice covered. In particular, cases with a thick crust, methane and R=0.3 should remain temperate or at least partially ice-free most of the time during the LHB.

To better understand the role of each parameter, we derived a simple analytical expression of pCO_2. If we assume a case with no land, a recycling R_0 and an oceanic crust thickness H_0, the equilibrium of the carbon cycle can be expressed for a reference state with no impact as:

$$F^0_{mor} + F^0_{arc} + F^0_{sfw} = 0 \tag{2}$$

where F^0_{mor}, F^0_{arc} and F^0_{sfw} are the CO_2 fluxes from mid-oceanic ridges, arc volcanoes and seafloor weathering from the (crust+mantle) to the (ocean+atmosphere). For a new state with other values of R and spreading rate and with impacts, the equilibrium is given by:

$$F_{mor} + F_{arc} + F_{sfw} + F_{ej} = 0 \tag{3}$$

with $F_{mor} = F^0_{mor}$ and $F_{arc} = F_{deep} - R \times (F_{sfw} + F_{ej})$ (see appendix A). We make the assumption that the seafloor weathering does not depend on oceanic temperature, what is valid for cold climates. By using the simple expression: $F_{sfw} = F^0_{sfw} \left(\frac{pCO_2}{pCO^0_2}\right)^{\alpha} \left(\frac{SR}{SR_0}\right)$ with α=0.5 [*Haqq-Misra et al.*, 2016], we obtain an expression for pCO_2:

$$pCO_2 = pCO^0_2 \times \left(\frac{SR_0}{SR}\right)^{1/\alpha} \left(\frac{1-R_0}{1-R}\right)^{1/\alpha} \left(1 - \frac{(1-R) \times F_{ej}}{F_{mor} + F_{deep}}\right)^{1/\alpha} \tag{4}$$

The term $\frac{(1-R) \times F_{ej}}{F_{mor} + F_{deep}}$ simply corresponds to the ratio of the amount of CO_2 lost in the mantle (due to ejecta weathering) by the amount of CO_2 outgassed directly from the mantle (e.g. without taking into account recycling). When this ratio is higher than 1, there is a net sink of CO_2 toward the mantle and the Earth necessary falls into a full snowball Earth. That occurs for $F_{ej} \leqslant$ -29×12 mol/yr for R=0.1 and $F_{ej} \leqslant$ -37×12 mol/yr for R= 0.3 with our model values. With our impact distribution, the ejecta cations flux (16×10^{12} mol/yr) is below these limits, and the Earth should have avoided a permanent full glaciation during the LHB. Because of the large uncertainties on the carbon cycle parameters and the duration and intensity of the LHB, it is not possible to be definitive on that point. We conclude that the LHB likely had a strong impact on the carbon cycle and climate with potentially snowball Earth events after large impacts.

Large impactors were also frequent during all the Archean [*Bottke et al.*, 2012; *Johnson and Melosh*, 2012; *Bottke and Norman*, 2017] but much less than during the LHB. According to the dynamical model from *Bottke et al.* [2012], the impact frequency was an order of magnitude lower at 3.7 Ga than at the peak of the LHB. Therefore, impacts probably had only a limited effect on the long term carbon cycle and climate during most of the Archean. However, our LHB impact sequence reveals that individual giant impacts could trigger episodic glaciations. *Johnson and Melosh* [2012] evaluated the diameters of ancient large impactors from spherule layers during the Archean and the Proterozoic. A few of them with diameters higher than around 50 km could have been large enough to trigger glaciations.

The existence of the Late Heavy Bombardment is still debated by some authors. For instance, *Boehnke and Harrison* [2016] suggest that the LHB could be an artifact of monotonically decreasing impact flux combined with episodic crust formation. If it did not occur, the impact flux at the end of the Hadean would have been too small to affect the climate on the long term, but strong cooling after episodic large impacts may still have been possible.

5. Conclusions

Our 3D climate simulations (taken in isolation) reveal that warm climates, with mean surface temperatures around 60°C, could have been obtained during the late Hadean/early Archean with around 1 bar of CO_2. However, our carbon model suggests that such states would not have been stable. Indeed, we found that warm climates can be maintained

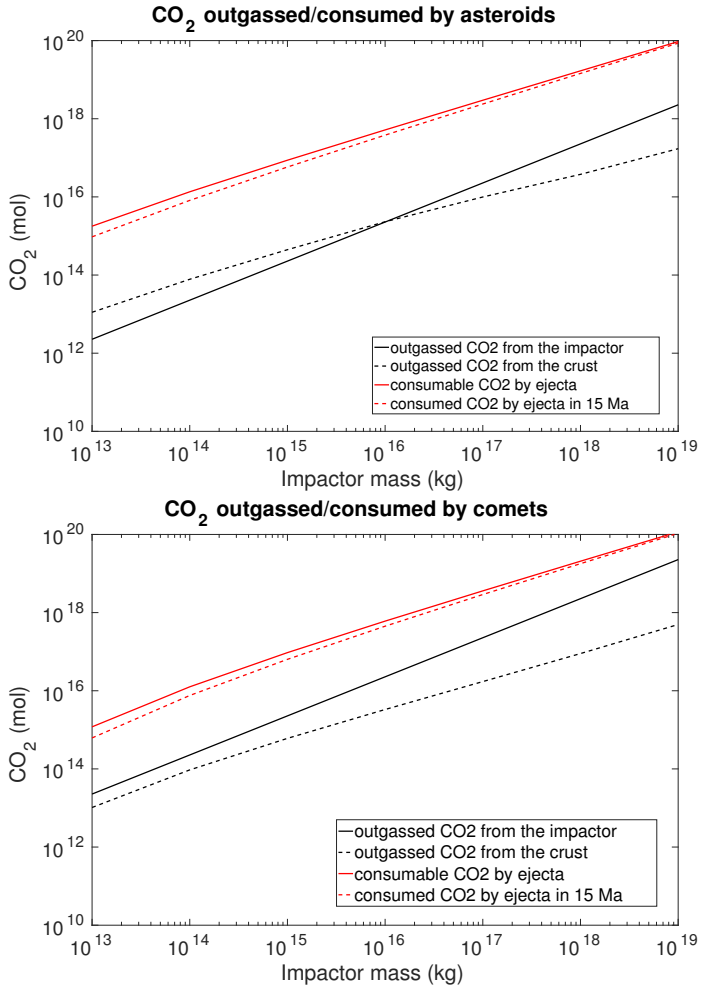

Figure 5: Effect of an individual impact on atmospheric CO_2. Amount of CO_2 outgassed from impactor (black solid lines) and from the crust (black dashed lines) or consumed by ejecta weathering as a function of impactor mass for asteroids (top panel) and comets (bottom panel). The red solid line is the maximal amount of CO_2 that can be consumed by ejecta weathering, while the red dashed line is the amount of $CO2_2$ consumed during 15 Ma (approximately the lifetime of the Archean oceanic crust).

only if the seafloor weathering is assumed independent of temperature. Such an assumption is inconsistent with recent measurements indicating a higher weathering during the late Mesozoic, when the deep ocean was around 10°C warmer [*Coogan and Gillis*, 2013]. Stable very warm climates with a N_2-CO_2-CH_4-H_2O early atmosphere are therefore excluded.

Our results favor instead temperate climates with global mean surface temperatures around 8.5-30.5°C and with pCO_2 around 0.1-0.36 bar. With the increasing solar luminosity over the Archean, the carbon cycle would have led to a reduction of pCO_2. In parallel, with the emergence of land and the slowing seafloor spreading rate during the Archean, the carbon cycle would have progressively become controlled by continental weathering while initially controlled by seafloor weathering. However, a better understanding of the data from O isotopes in ancient cherts together with better constraints on pCO_2 are required to validate our conclusions about the long-debated climate of early Earth.

During the Late Heavy Bombardment, the weathering of ejecta would have dramatically decreased the partial pressure of CO_2 leading to cold climates but not necessary to a snowball Earth during all that period. We predict that large impactors (i.e. with diameters higher than around 50 km) could have trigger extreme glaciations during the Hadean and the Archean.

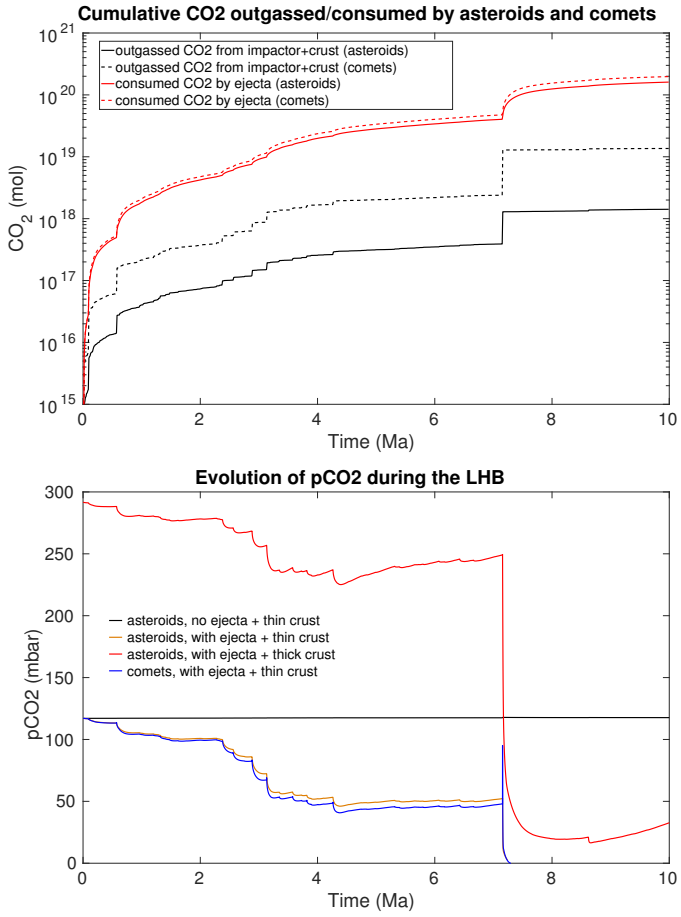

Figure 6: Effect of impacts on pCO_2. Top panel: impact scenario expressed in cumulative mol of CO_2 outgassed by impacts (black line) and consumed by ejecta (red line) with asteroids (solid lines) or comets (dotted lines). Bottom panel: evolution of pCO_2 for the impact scenario, assuming a low land fraction, R=0.1 and no methane. Yellow line is a case with a thin oceanic crust, asteroids and ejecta weathering. Black line is as yellow line but without ejecta weathering. Blue line is as yellow line but with comets. Red line is as yellow line but with a thick oceanic crust.

Finally, our modeling work suggests that the CO_2-dependent carbon cycle could have maintained temperate climates on the early Earth, without requiring any additional greenhouse gas or warming process. This work also highlights the importance of the seafloor weathering, which can dominate the continental weathering. Under such circumstances, the climate becomes relatively insensitive to the presence of land. The strong temperature dependence expected for the seafloor weathering also has implications for the habitability of exoplanets, allowing in particular a stabilizing climate-weathering feedback on waterworlds. Waterworlds might therefore not be much more subject to water loss by moist greenhouse than partially ocean-covered Earth-like planets, as suggested by *Abbot et al.* [2012].

Acknowledgments:. B.C. acknowledges support from Paris Sciences et Lettres and from an appointment to the NASA Postdoctoral Program, administered by USRA. This work was performed as part of the NASA Astrobiology Institute's Virtual Planetary Laboratory, supported by NASA under Cooperative Agreement No. NNA13AA93A. DC also acknowledges support from NASA Exobiology Program grant NNX15AL23G. We thank J. Kasting and an anonymous reviewer for helpful comments.

Appendix A. Carbon cycle modeling

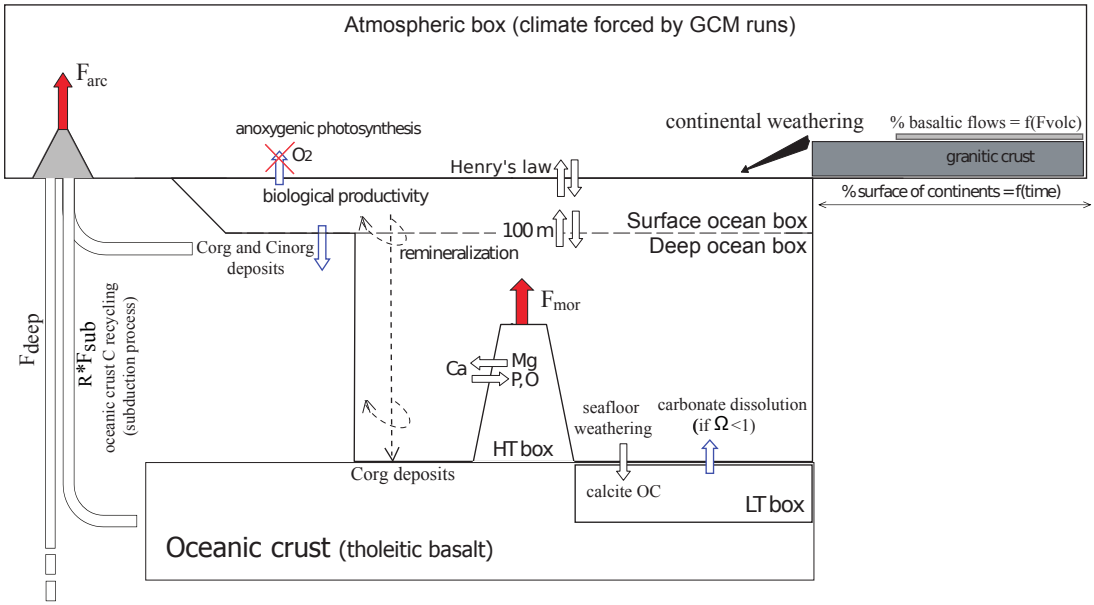

Figure A.7: Representation of the carbon model used for the Hadean Earth.

The carbon cycle model has been previously used for the Proterozoic and the Phanerozoic [*Goddéris et al.*, 2006; *Le Hir et al.*, 2008a, b]. Figure A.7 shows the different processes included in the model. The parametrizations for the different CO_2 flux are briefly described below.

CO_2 outgassing by oceanic ridges and arc volcanoes

We considered that the CO_2 flux from mid oceanic ridges F_{mor} is proportional to the production of oceanic crust:

$$F_{\mathrm{mor}} = F_{\mathrm{mor}_0} \times \frac{SR}{SR_0} \times \frac{H}{H_0} \tag{A.1}$$

where F_{mor_0},= 1.8×10^{12} mol/yr, SR is the spreading rate and H is the oceanic crust thickness (H_0 = 6 km).

We assumed that the flux from arc volcanoes (F_{arc}) is the total degassing flux due to carbonate recycling at subduction zones and mantle outgassing (with the exception of mid-oceanic ridge). Degassing over geologic times being assumed proportional to the heat flux from the interior of the Earth, the mantle outgassing rate is adjusted, as appropriate, using a forcing factor, rdeg=2.5 at 3.8 Ga [*Goddéris and Veizer*, 2000]):

$$F_{\mathrm{arc}} = F_{\mathrm{sub}} \times R + F_{deep} \tag{A.2}$$

where R is the recycling rate and $F_{deep} = C^0_{\mathrm{deep}} \times rdeg$ with $C^0_{deep} = 3.3 \times 10^{12}$ mol/yr. For the heat-pipe case, we

considered that $SR = 0$, $F_{\rm sub} = 0$ and $rdeg$ =10. Indeed, according to *Moore and Webb* [2013], the heat flux had to be around 10 times higher than today to be in the heat-pipe regime.

Continental weathering

Weathering depends on rocks available for reactions (basalt vs. granite) and fraction of continents deduced from crustal growth models. The weathering rate of continental granites and basalts is given by:

$$F_{\rm con} = f_{\rm Ca}^{bas} + f_{\rm Ca}^{gra} + f_{\rm Mg}^{bas} + f_{\rm Mg}^{gra} \tag{A.3}$$

with:

$$f_{\rm Ca}^{bas} = 20.94 \times 10^{12} \times e^{fbas} \times runoff \times \frac{srf_{\rm bas}}{srf_{\rm cont}} \times \frac{srf_{\rm cont}}{srf_{\rm cont0}} \tag{A.4}$$

$$f_{\rm Ca}^{gra} = 3.49 \times 10^{12} \times e^{fgra} \times runoff \times \left(1 - \frac{srf_{\rm bas}}{srf_{\rm cont}}\right) \times \frac{srf_{\rm cont}}{srf_{\rm cont0}} \tag{A.5}$$

$$f_{\rm Mg}^{bas} = 19.86 \times 10^{12} \times e^{fbas} \times runoff \times \frac{srf_{\rm bas}}{srf_{\rm cont}} \times \frac{srf_{\rm cont}}{srf_{\rm cont0}} \tag{A.6}$$

$$f_{\rm Mg}^{gra} = 3.31 \times 10^{12} \times e^{fgra} \times runoff \times \left(1 - \frac{srf_{\rm bas}}{srf_{\rm cont}}\right) \times \frac{srf_{\rm cont}}{srf_{\rm cont0}} \tag{A.7}$$

with $fgra = \frac{-48200}{8.314}\left(\frac{1}{T} - \frac{1}{T_0}\right)$, $fbas = \frac{-42300}{8.314}\left(\frac{1}{T} - \frac{1}{T_0}\right)$ and where $\frac{srf_{\rm cont}}{srf_{\rm cont0}}$ is the fraction of emerged continental area. We used pCO_2^0 = 285 ppm. These values give a present-day flux of 3.49×10^{12} mol/yr for Ca^{2+} and 3.31×10^{12} mol/yr for Mg^{2+}.

To represent the presence of very active volcanoes and potential extent of basaltic flows over small continents, rocks available for weathering is assumed proportional to volcanism ($F_{\rm arc}$). Based on the extent of basalt outcrops of the Cenozoic era, the equilibrium between basaltic flows / volcanism is prescribed as follow:

$$srf_{\rm bas} = \frac{F_{\rm arc}}{F_{\rm arc0}} \times \frac{srf_{\rm cont}}{srf_{\rm cont0}} \times srf_{\rm bas0} \tag{A.8}$$

with $F_{\rm arc0} = 6.8 \times 10^{12}$ mol/yr [*Gaillardet et al.*, 1999], $srf_{cont0} = 146 \times 10^6$ km^2 and $srf_{bas0} = 7.3 \times 10^6$ km^2 [*Dessert et al.*, 2003].

Using this assumption, our model predicts that early Archean continents were mostly mafic, composed 65-70% of basalts and 35-30% of granite, consistent with analysis of Sb/Sr, Ni/Co and Cr/Zn ratios by *Dhuime et al.* [2015]; *Tang et al.* [2016].

The runoff and the surface temperature depend on the latitude and are properly computed by the GCM. We assumed that lands are homogenously distributed over all the Earth. Then, we computed the global continental weathering flux by summing the contribution of each latitudinal band from the GCM.

Seafloor weathering

Contrary to *Caldeira* [1995], we assume that the seafloor weathering does not occur in solutions at steady state with carbonate minerals, but when oceanic water enters in contact with fresh basaltic rock, it evolves along its downward path towards saturation with calcite, which is the ultimate state of the reaction. Our percolating reservoir stands for water during the early stages of seafloor weathering, when all cations are produced. The seafloor weathering rate is given by [*Goddéris et al.*, 2006; *Le Hir et al.*, 2008a, b]:

$$f_{sfw} = \frac{SR}{SR_0} \times \sum_i d_i exp\left(\frac{-E_i}{RT_p}\right) C_i^n \tag{A.9}$$

where SR is the spreading rate. The sum extends up to all the dissolving species (H^+, OH and H_2O), while the index i stands for the dissolving species. E_i and d_i are, respectively, the activation energy and dissolution constant for each mineral depending on the species i promoted dissolution. T_p is the temperature of the percolating waters into the oceanic crust at which dissolution occurs. We divided the oceanic crust in 6 layers from the seafloor to a depth of 500 m in the crust. We assumed that the percolating water has the temperature of surrounding crust fixed with the present-day temperature gradient (around 116 K/km). For the first layer, the deep ocean temperature is assumed to be equal to the sea surface temperature at 60° N/S (see idealized simulations by *Manabe and Bryan* [1985]; *Enderton and Marshall* [2009]). We scaled the seafloor weathering to its present-day value. C_i are the concentration in the species i, while n_i is the order of the dissolution reaction. We considered that the seafloor weathering occurs only in the first 500 m of the oceanic crust. A change of oceanic crust thickness thus does not impact the seafloor weathering, which remains proportional to the spreading rate.

Experimental studies and measurements of carbonate mineral in the oceanic crust reveal that the seafloor weathering strongly depend on the bottom ocean temperature and was around 5 times higher during the late Mesozoic [*Brady and Gíslason*, 1997; *Coogan and Gillis*, 2013], when the deep ocean temperature was around ∼10 K higher. It is therefore expected to play a significant role on the early Earth with a lower land cover and a faster spreading rate. Our model predict a 2-3 times higher seafloor weathering during the late Mesozoic for 4 times the present-day pCO_2. However, the volcanic outgassing may have been higher and continental weathering may have been less efficient at that time, what would have increased the seafloor weathering closer to the measured rates. Because of these uncertainties, we consider that our values remain acceptable but we may underestimate the temperature sensitivity of the seafloor weathering.

Precipitation of carbonates

In the absence of pelagic producers, carbonates are assumed to be precipitated on continental margins (at a depth of less than 100 m) through:

$$f_{cd} = k_{cd}(\Omega - 1)^{1.7} \tag{A.10}$$

where $k_{cd} = 0.172$ mol/yr/m^2 and Ω is the saturation ratio of calcite: $\Omega = \frac{[Ca^{2+}][CO_3^{2-}]}{K_s}$ where K_s is the solubility constant depending on the temperature and the salinity (expression given in *Sacramento and Gruber* [2006]).

Ocean-atmosphere interface

The CO_2 exchange flux between the atmosphere and the oceanis given by:

$$f_{atm-ocean} = \alpha(pCO_2^{atm} - pCO_2^{ocean}) \tag{A.11}$$

where $\alpha = 16$ mol/m^2/PAL and pCO_2^{ocean} is the CO_2 partial pressure computed with Henry's law for the concentration of dissolved CO_2.

Seafloor spreading rate

We computed the seafloor spreading rate SR considering it evolves with the potential temperature of the mantle T_p as Rayleigh-Bénard convection [*Flament et al.*, 2008]:

$$SR = SR_* \times \left(\frac{T_p - T_0}{T_p^* - T_0}\frac{\eta(T_p^*)}{\eta(T_p)}\right)^{2/3} \tag{A.12}$$

where T_0 is the deep ocean temperature (we assumed $T_0 = 0$°C, but the value has a very small impact on SR), $\eta(T_p) = \eta_0\left(\frac{E}{RT_p}\right)$ is the viscosity of the mantle with $E = 380$ kJ and $R = 8.31$ J/K/mol. Assuming T_p^*=1330°C for the present-day Earth and T_p=1550°C for the early Earth then gives $u/u_* = 11$. If the oceanic crust thickness is increased by a factor 3, then the spreading rate becomes 3 times lower while the crust production rate and the heat flux remain constant. A spreading rate 11 times higher than today gives a lifetime of the oceanic crust of around 15 Ma.

Appendix B. Effects of impacts during the Late Heavy Bombardment

Ejecta weathering

We computed the effect of ejecta weathering following *Sleep and Zahnle* [2001]. Impacts produce a global layer of particles with diameters typically from 1 mm to 100 m. Ejecta constitute a source of cations that precipitate with carbonate ions. The mass of ejecta was determined using the scaling laws from *Collins et al.* [2005]. We took into account the deceleration caused by the atmosphere and the ocean but we neglected the breakup in the atmosphere and the mass loss by sublimation. These assumptions are valid for large impactors. We also included the escaping mass of impactor after the impact according to the hydrodynamic simulations from *Shuvalov* [2009].

We assumed that impactor have a velocity v_0 of 21 km/s for asteroids and 30 km/s for comets, a diameter L, an impact angle θ of 45° and a density ρ_i = 3000 kg /m^3 for asteroids and ρ_i = 1000 kg /m^3 for comets. The Earth is supposed covered by a 2700 m deep global ocean. We chose a density ρ_c = 2700 kg/m^3 for the crust.
The mass of ejecta is computed according to *Collins et al.* [2005]:

$$m_{ej} = \frac{\pi D_{tc}^3 \rho_c}{16\sqrt{2}} \tag{B.1}$$

where the transient crater D_{tc} (in m) is given by [*Collins et al.*, 2005]:

$$D_{tc} = 1.161 \left(\frac{\rho_i}{\rho_c}\right)^{1/3} L^{0.78} v_i^{0.44} g_E^{-0.22} sin^{1/3}\theta \tag{B.2}$$

where g_E is Earth gravity and v_i is the impactor velocity at the seafloor.
Taking into account the deceleration by the atmosphere and the ocean, the impactor velocity at the seafloor is [*Collins et al.*, 2005]:

$$v_i = v_0 exp\left(-\frac{3(C_{Datm}\rho_{air}H_{atm} + C_{Docean}\rho_{water}H_{ocean})}{4\rho_i L sin\theta}\right) \tag{B.3}$$

where C_D is the drag coefficient, taken equal to 2 for the atmosphere and 0.877 for the ocean, H_{atm} is the atmospheric scale height, and H_{ocean} is the ocean depth. For a 10 km diameter impactor, the atmosphere reduces the velocity by just 0.1% but the ocean reduces it by around 8%.

Collins et al. [2005] suggest that the mean diameter of ejecta decreases with distance from the crater center r as $d \propto r^{-\alpha}$, where α=2.65 and that the thickness of the ejecta layer decreases as $h \propto r^{-3}$. By integrating these relations, the mass distribution of ejecta is given by $N(\geq m) \propto m^{-\gamma}$, where γ=0.87. *Zahnle and Sleep* [2002] use the same law with γ=0.9-0.95. We assumed that the diameter of each particle decreases of 1 mm in 167 kyrs [*Crovisier et al.*, 1987] and that cations are present at 0.005 mol/g.

With the impact statistics that we use, the impact flux is around 6.7×10^{11} kg/yr and the ejecta production rate is around 3.2×10^{12} kg/yr, corresponding to a cation flux of 1.6×10^{13} mol/yr (compared to 3×10^{14} mol/yr in *Sleep and Zahnle* [2001]). In our carbon cycle model, these cations precipitate if the saturation ratio of calcite is higher than 1 (see Appendix A).

CO_2 outgassing by impacts

We assumed that the early oceanic crust is covered by a 40 m thick carbonate layer (ρ_{carb} = 1500 kg/m^3). We therefore assumed the equivalent of 4 bars of CO_2 (4.8×10^{20} moles of CO_2) are in this layer and can be released during impacts. This amount is lower than the total quantity of CO_2 currently stored in the oceanic crust (around 1.2×10^{21} moles of CO_2 [*Sleep and Zahnle*, 2001]). The shock wave produced by an impact can lead to decarbonation of carbonates. For calcite, the reaction is $CaCO_3 \Rightarrow CaO + CO_2$. This process starts when the pressure is higher than 20 GPa and is total when the pressure is higher than 60 GPa [*Agrinier et al.*, 2001]. However, the amount of outgassed CO_2 is reduced

by recombination through the back reaction. The percentage of CO_2 back reacted is between 37 and 66 % [*Agrinier et al.*, 2001]. For simplicity, we assumed that CO_2 outgassing occurs only at pressures higher than 60 GPa with an efficiency of 50 % due to the reverse reaction. For each impact, we computed the area where the shock pressure is higher than 60 GPa, assuming that it evolves with the distance r to the impact center as $\propto r^{-1.5}$.

We also took into account CO_2 outgassed by melting lithosphere, assuming that its volume V_m is [*Collins et al.*, 2005]:

$$V_m = 8.9 \times 10^{-12} E \sin\theta \tag{B.4}$$

where E is the impactor kinetic energy and θ=45° is the impact angle. We assumed that the lithosphere below the carbonate layer contains 100 ppmv of CO_2 and outgasses all CO_2 when melted.

References

Abbot, D. S., N. B. Cowan, and F. J. Ciesla, Indication of Insensitivity of Planetary Weathering Behavior and Habitable Zone to Surface Land Fraction, *Astrophysical Journal*, *756*, 178, doi:10.1088/0004-637X/756/2/178, 2012.

Abramov, O., and S. J. Mojzsis, Microbial habitability of the Hadean Earth during the late heavy bombardment, *Nature*, *459*, 419–422, doi:10.1038/nature08015, 2009.

Agrinier, P., A. Deutsch, U. Schärer, and I. Martinez, Fast back-reactions of shock-released CO_2 from carbonates: an experimental approach, *Geochimica et Cosmochimica Acta*, *65*, 2615–2632, doi:10.1016/S0016-7037(01)00617-2, 2001.

Anbar, A. D., K. J. Zahnle, G. L. Arnold, and S. J. Mojzsis, Extraterrestrial iridium, sediment accumulation and the habitability of the early earth's surface, *Journal of Geophysical Research*, *106*, 3219–3236, doi:10.1029/2000JE001272, 2001.

Bell, E., P. Boehnke, T. M. Harrison, and W. L. Mao, Potentially biogenic carbon preserved in a 4.1 billion-year-old zircon, *Proceedings of the National Academy of Sciences*, *112*(47), 14,518–14,521, doi:10.1073/pnas.1517557112, 2015.

Bickle, M. J., Implications of melting for stabilisation of the lithosphere and heat loss in the Archaean, *Earth and Planetary Science Letters*, *80*, 314–324, doi:10.1016/10.1016/0012-821X(86)90113-5, 1986.

Blake, R. E., S. J. Chang, and A. Lepland, Phosphate oxygen isotopic evidence for a temperate and biologically active Archaean ocean, *Nature*, *464*, 1029–1032, doi:10.1038/nature08952, 2010.

Boehnke, P., and T. M. Harrison, Illusory Late Heavy Bombardments, *Proceedings of the National Academy of Science*, *113*, 10,802–10,806, doi:10.1073/pnas.1611535113, 2016.

Bottke, W. F., and M. D. Norman, The Late Heavy Bombardment, *Annual Reviews of Earth and Planetary Sciences*, *45*, doi:10.1146/annurev-earth-063016-020131, 2017.

Bottke, W. F., D. Vokrouhlický, D. Minton, D. Nesvorný, A. Morbidelli, R. Brasser, B. Simonson, and H. F. Levison, An Archaean heavy bombardment from a destabilized extension of the asteroid belt, *Nature*, *485*, 78–81, doi:10.1038/nature10967, 2012.

Bousseau, B., S. Blanquart, A. Necsulea, N. Lartillot, and G. Manolo, Parallel adaptations to high temperatures in the Archaean eon, *Nature*, *456*, 942–945, doi:10.1038/nature07393, 2008.

Brady, P. V., and S. R. Gíslason, Seafloor weathering controls on atmospheric CO_2 and global climate, *Geochimica et Cosmochimica Acta*, *61*, 965–973, doi:10.1016/S0016-7037(96)00385-7, 1997.

Buick, R., J. Dunlop, and D. Groves, Stromatolite recognition in ancient rocks: an appraisal of irregularly laminated structures in an early archaean chert-barite unit from north pole, western australia, *Alcheringa: An Australasian Journal of Palaeontology*, *5*(3), 161–181, doi:10.1080/03115518108566999, 1981.

Caldeira, K., Long-term control of atmospheric carbon dioxide: Low-temperature seafloor alteration or terrestrial silicate-rock weathering?, *American Jounral of Science*, *295*, 1077–1114, doi:10.2475/ajs.295.9.1077, 1995.

Charnay, B., F. Forget, R. Wordsworth, J. Leconte, E. Millour, F. Codron, and A. Spiga, Exploring the faint young Sun problem and the possible climates of the Archean Earth with a 3-D GCM, *Journal of Geophysical Research*, *118*, 10,414, doi:10.1002/jgrd.50808, 2013.

Codron, F., Ekman heat transport for slab oceans, *Climate Dynamics*, *38*, 379–389, doi:10.1007/s00382-011-1031-3, 2012.

Collins, G. S., H. J. Melosh, and R. A. Marcus, Earth Impact Effects Program: A Web-based computer program for calculating the regional environmental consequences of a meteoroid impact on Earth, *Meteoritics and Planetary Science*, *40*, 817, doi:10.1111/j.1945-5100.2005.tb00157.x, 2005.

Coogan, L. A., and K. M. Gillis, Evidence that low-temperature oceanic hydrothermal systems play an important role in the silicate-carbonate weathering cycle and long-term climate regulation, *Geochemistry, Geophysics, Geosystems*, *14*, 1771–1786, doi:10.1002/ggge.20113, 2013.

Crovisier, J. L., J. Honnorez, and J. P. Eberhart, Dissolution of basaltic glass in seawater: Mechanism and rate, *Geochimica et Cosmochimica Acta*, *51*, 2977–2990, doi:10.1016/0016-7037(87)90371-1, 1987.

de Niem, D., E. Kührt, A. Morbidelli, and U. Motschmann, Atmospheric erosion and replenishment induced by impacts upon the Earth and Mars during a heavy bombardment, *Icarus*, *221*, 495–507, doi:10.1016/j.icarus.2012.07.032, 2012.

de Wit, M. J., and H. Furnes, 3.5-ga hydrothermal fields and diamictites in the barberton greenstone belt—paleoarchean crust in cold environments, *Science Advances*, *2*(2), doi:10.1126/sciadv.1500368, 2016.

Dessert, B., C.and Dupré, J. Gaillardet, F. L., and A. C., Basalt weathering laws and the impact of basalt weathering on the global carbon cycle, *Chem. Geol*, *202*, 257–273, 2003.

Dhuime, B., C. J. Hawkesworth, P. A. Cawood, and C. D. Storey, A Change in the Geodynamics of Continental Growth 3 Billion Years Ago, *Science*, *335*, 1334–, doi:10.1126/science.1216066, 2012.

Dhuime, B., A. Wuestefeld, and C. J. Hawkesworth, Emergence of modern continental crust about 3 billion years ago, *Nature Geoscience*, *8*, 552–555, doi:10.1038/ngeo2466, 2015.

Driese, S., M. Jirsa, M. Ren, S. Brantley, N. Sheldon, D. Parker, and M. Schmitz, Neoarchean paleoweathering of tonalite and metabasalt: Implications for reconstructions of 2.69 ga early terrestrial ecosystems and paleoatmospheric chemistry, *Precambrian Research*, *189*, 1–17, doi:10.1016/j.precamres.2011.04.003, 2011.

Enderton, D., and J. Marshall, Explorations of Atmosphere-Ocean-Ice Climates on an Aquaplanet and Their Meridional Energy Transports, *Journal of Atmospheric Sciences*, *66*, 1593–1611, doi:10.1175/2008JAS2680.1, 2009.

Flament, N., N. Coltice, and P. F. Rey, A case for late-Archaean continental emergence from thermal evolution models and hypsometry, *Earth and Planetary Science Letters*, *275*, 326–336, doi:10.1016/j.epsl.2008.08.029, 2008.

Forget, F., R. Wordsworth, E. Millour, J. B. Madeleine, L. Kerber, J. Leconte, E. Marcq, and R. M. Haberle, 3D modelling of the early martian climate under a denser CO2 atmosphere: Temperatures and CO2 ice clouds, *Icarus*, *222*(1), 81–99, doi:10.1016/j.icarus.2012.10.019, 2013.

Fralick, P., and J. Carter, Neoarchean deep marine paleotemperature: Evidence from turbidite successions, *Precambrian Research*, *191*, 78–84, doi:10.1016/j.precamres.2011.09.004, 2011.

Gaillardet, J., B. Dupré, L. P., and A. C. J., Global silicate weathering of silicates estimated from large river geochemistry, *Chem. Geol., Special issue Carbon Cycle*, *7159*, 3–30, 1999.

Gaucher, E. A., S. Govindarajan, and O. K. Ganesh, Palaeotemperature trend for Precambrian life inferred from resurrected proteins, *Nature*, *452*, 704–707, doi:10.1038/nature06510, 2008.

Goddéris, Y., and J. Veizer, Tectonic control of chemical and isotopic composition of ancient oceans; the impact of continental growth, *American Journal of Sciences*, *300*, 434–461, doi:doi:10.2475/ajs.300.5.434, 2000.

Goddéris, Y., L. M. François, A. Probst, J. Schott, D. Moncoulon, D. Labat, and D. Viville, Modelling weathering processes at the catchment scale: The WITCH numerical model, *Geochimica et Cosmochimica Acta*, *70*, 1128–1147, doi:10.1016/j.gca.2005.11.018, 2006.

Gomes, R., H. F. Levison, K. Tsiganis, and A. Morbidelli, Origin of the cataclysmic Late Heavy Bombardment period of the terrestrial planets, *Nature*, *435*, 466–469, doi:10.1038/nature03676, 2005.

Haqq-Misra, J., R. K. Kopparapu, N. E. Batalha, C. E. Harman, and J. F. Kasting, Limit Cycles Can Reduce the Width of the Habitable Zone, *Astrophys. J.*, *827*, 120, doi:10.3847/0004-637X/827/2/120, 2016.

Hoareau, G., B. Bomou, D. J. J. van Hinsbergen, N. Carry, D. Marquer, Y. Donnadieu, G. Le Hir, B. Vrielynck, and A.-V. Walter-Simonnet, Did high Neo-Tethys subduction rates contribute to early Cenozoic warming?, *Climate of the Past*, *11*, 1751–1767, doi:10.5194/cp-11-1751-2015, 2015.

Hren, M. T., M. M. Tice, and C. P. Chamberlain, Oxygen and hydrogen isotope evidence for a temperate climate 3.42 billion years ago, *Nature*, *462*, 205ł208, doi:10.1038/nature08518, 2009.

Johnson, B. C., and H. J. Melosh, Impact spherules as a record of an ancient heavy bombardment of Earth, *Nature*, *485*, 75–77, doi:10.1038/nature10982, 2012.

Kanzaki, Y., and T. Murakami, Estimates of atmospheric CO_2 in the Neoarchean-Paleoproterozoic from paleosols, *Geochimica et Cosmochimica Acta*, *159*, 190–219, doi:10.1016/j.gca.2015.03.011, 2015.

Kasting, J. F., and T. M. Howard, Atmospheric composition and climate on the early Earth , *Phil. Trans. R. Soc.*, *361*, 1733–1742, doi:10.1098/rstb.2006.1902, 2006.

Kharecha, P., J. Kasting, and J. Siefert, A coupled atmosphere-ecosystem model of the early archean earth, *Geobiology*, *3*(2), 53–76, doi:10.1111/j.1472-4669.2005.00049.x, 2005.

Knauth, L. P., and D. R. Lowe, High Archean climatic temperature inferred from oxygen isotope geochemistry of cherts in the 3.5 Ga Swaziland Supergroup, South Africa, *Geological Society of America Bulletin*, *115*, 566–580, doi:10.1130/0016-7606(2003)115⟨0566:HACTIF⟩2.0.CO;2, 2003.

Krissansen-Totton, J., and D. C. Catling, Constraining climate sensitivity and continental versus seafloor weathering with an inverse geological carbon cycle model, *Nature Communications*, *8*, doi:10.1038/ncomms15423, 2017.

Le Hir, G., Y. Goddéris, Y. Donnadieu, and G. Ramstein, A geochemical modelling study of the evolution of the chemical composition of seawater linked to a "snowball" glaciation, *Biogeosciences*, *5*, 253–267, 2008a.

Le Hir, G., G. Ramstein, Y. Donnadieu, and Y. Goddéris, Scenario for the evolution of atmospheric pCO_2 during a snowball Earth, *Geology*, *36*, 47–50, 2008b.

Leconte, J., F. Forget, B. Charnay, R. Wordsworth, and A. Pottier, Increased insolation threshold for runaway greenhouse processes on Earth-like planets, *Nature*, *504*, 268–271, doi:10.1038/nature12827, 2013.

Manabe, S., and K. Bryan, Jr., CO2-induced change in a coupled ocean-atmosphere model and its paleoclimatic implications, *Journal of Geophysical Research*, *90*, 11, doi:10.1029/JC090iC06p11689, 1985.

Marin-Carbonne, J., M. Chaussidon, and F. Robert, The silicon and oxygen isotope compositions of Precambrian cherts: A record of oceanic paleo-temperatures?, *Precambrian Research*, *247*, 223–234, doi:10.1016/j.precamres.2014.03.016, 2014.

Marty, B., G. Avice, Y. Sano, K. Altwegg, H. Balsiger, M. Hässig, A. Morbidelli, O. Mousis, and M. Rubin, Origins of volatile elements (H, C, N, noble gases) on Earth and Mars in light of recent results from the ROSETTA cometary mission, *Earth and Planetary Science Letters*, *441*, 91–102, doi:10.1016/j.epsl.2016.02.031, 2016.

Moore, W. B., and A. G. Webb, Heat-pipe Earth, *Nature*, *501*, 501–505, doi:doi:10.1038/nature12473, 2013.

Nisbet, E. G., and N. H. Sleep, The habitat and nature of early life, *Nature*, *409*, 1083–1091, 2001.

Nutman, A. P., V. C. Bennett, and C. R. L. Friend, The emergence of the Eoarchaean proto-arc: evolution of a c. 3700 Ma convergent plate boundary at Isua, southern West Greenland, *Geological Society of London Special Publications*, *389*, 113–133, doi:10.1144/SP389.5, 2015.

Ohta, H., S. Maruyama, E. Takahashi, Y. Watanabe, and Y. Kato, Field occurrence, geochemistry and petrogenesis of the Archean Mid-Oceanic Ridge Basalts (AMORBs) of the Cleaverville area, Pilbara Craton, Western Australia, *Lithos*, *37*, 199–221, doi:10.1016/0024-4937(95)00037-2, 1996.

Ozak, N., O. Aharonson, and I. Halevy, Radiative transfer in co2-rich atmospheres: 1. collisional line mixing implies a colder early mars, *Journal of Geophysical Research: Planets*, *121*(6), 965–985, doi:10.1002/2015JE004871, 2015JE004871, 2016.

Pierazzo, E., D. A. Kring, and H. J. Melosh, Hydrocode simulation of the Chicxulub impact event and the production of climatically active gases, *Journal of Geophysical Research*, *103*, 28,607–28,625, doi:10.1029/98JE02496, 1998.

Pope, E. C., D. K. Bird, and M. T. Rosing, Isotope composition and volume of Earths early oceans, *Proceedings of the National Academy of Sciences*, *109*(12), 4371–4376, doi:10.1073/pnas.1115705109, 2012.

Robert, F., and M. Chaussidon, A palaeotemperature curve for the Precambrian oceans based on silicon isotopes in cherts, *Nature*, *443*, 969–972, 2006.

Roberts, N., and C. Spencer, The zircon archive of continent formation through time, *Geological Society, London, Special Publications*, *389*, 197225, 2015.

Rosing, M. T., D. K. Bird, N. H. Sleep, and C. J. Bjerrum, No climate paradox under the faint early Sun, *Nature*, *464*(7289), 744–747, doi:10.1038/nature08955, 2010.

Rye, R., P. H. Kuo, and H. D. Holland, Atmospheric carbon dioxide concentrations before 2.2 billion years ago, *Nature*, *378*, 603–605, doi:10.1038/378603a0, 1995.

Sacramento, J., and N. Gruber, *OCEAN BIOGEOCHEMICAL DYNAMICS*, 2006.

Sheldon, N., Precambrian paleosols and atmospheric CO2 levels, *Precambrian Research*, *147*, 148–155, doi:10.1016/j.precamres.2006.02.004, 2006.

Shuvalov, V., Atmospheric erosion induced by oblique impacts, *Meteoritics and Planetary Science*, *44*, 1095–1105, doi:10.1111/j.1945-5100.2009.tb01209.x, 2009.

Sleep, N. H., Plate Tectonics through Time, *Treatise on Geophysics,*, *9*, 145–169, 2007.

Sleep, N. H., and K. Zahnle, Carbon dioxide cycling and implications for climate on ancient Earth, *Journal of Geophysical Research*, *106*, 1373–1400, doi:10.1029/2000JE001247, 2001.

Stern, R. J., When and how did plate tectonics begin? Theoretical and empirical considerations, *Chinese Sci. Bull.*, *52*, 578–591, 2007.

Tang, M., K. Chen, and R. L. Rudnick, Archean upper crust transition from mafic to felsic marks the onset of plate tectonics, *Science*, *351*, 372–375, doi:10.1126/science.aad5513, 2016.

Tartese, R., C. M., A. Gurenko, F. Delarue, and F. Robert, Warm Archean oceans reconstructed from oxygen isotope composition of early-life remnants, *Geochemical Perspective letters*, *3*, 55–65, doi:10.1126/science.aad5513, 2016.

van den Boorn, S., M. van Bergen, W. Nijman, and P. Vroon, Dual role of seawater and hydrothermal fluids in Early Archean chert formation: Evidence from silicon isotopes, *Geology*, *35*, 939, doi:10.1130$\%$2FG24096A.1, 2007.

Viehmann, S., J. E. Hoffmann, C. Munker, and M. Bau, Decoupled Hf-Nd isotopes in Neoarchean seawater reveal weathering of emerged continents, *Geology*, *42*, 115–118, doi:10.1130/G35014.1, 2014.

Wolf, E. T., and O. B. Toon, Hospitable Archean Climates Simulated by a General Circulation Model, *Astrobiology*, *13*, 656–673, doi:10.1089/ast.2012.0936, 2013.

Wordsworth, R., Y. Kalugina, S. Lokshtanov, A. Vigasin, B. Ehlmann, J. Head, C. Sanders, and H. Wang, Transient reducing greenhouse warming on early Mars, *Geophysical Research Letters*, *44*, 665–671, doi:10.1002/2016GL071766, 2017.

Zahnle, K., and N. H. Sleep, Carbon dioxide cycling through the mantle and implications for the climate of ancient Earth, *Geological Society of London Special Publications*, *199*, 231–257, doi:10.1144/GSL.SP.2002.199.01.12, 2002.

Amplifying Factors Leading to the Collapse of Primary Producers during the Chicxulub Impact and Deccan Traps

by Le Hir G., Fluteau F., Sucheras B. and Goddéris Y.

Abstract

The latest Cretaceous (K; Maastrichtian) through earliest Paleogene (Pg; Danian) interval is a time marked by one of five major mass extinctions in the Earth's history. The synthesis of published data permits the temporal correlation of the K-Pg boundary crisis with two major geological events: 1) the Chicxulub impact discovered in the Yucatán peninsula (Mexico) and 2) the Deccan Traps located on the west-central India plateau. In this paper, environmental and biological consequences from the Chicxulub impact and the Deccan continental flood basalts have been explored using a climate-carbon-biodiversity coupled model called the ECO-GEOCLIM model. The novelty of this study is to investigate how abiotic factors (temperature, pH, and calcite saturation state) act on various marine organisms to determine the primary productivity and biodiversity changes in response to a drastic environmental change. This study shows that the combination of the Deccan volcanism with a 10-km impact led to global warming (3.5°C) caused by rising carbon dioxide (CO_2) concentration (+470 ppmv), interrupted by a succession of short-term cooling events, provided by a 'shielding effect' due to the formation of sulphate aerosols. The consequences related to these climate changes are the decrease of the surface ocean pH by 0.2 (from 8.0 to 7.8), while the deep ocean pH dropped by 0.4 (from 7.8 to 7.4). Without requiring any additional perturbations, these environmental disturbances led to a drastic decrease of the biomass of calcifying species and their biodiversity by about 80%, while the biodiversity of noncalcifying species was reduced by about 60%. We also suggest that the short-lived acidification caused by the Chicxulub impact, when combined with the Deccan traps, may explain the severity of the extinction among pelagic calcifying species.

1. Introduction

The Cretaceous-Paleogene (K–Pg) boundary is the best-documented mass extinction event, and calcified pelagic plankton provides the most striking example of biotic loss. Among the 131 Late Maastrichtian species of calcareous nannoplankton (i.e., photosynthetic algae producing minute 1–20 μm calcite platelets), only 10 to 12 survived into the Danian period (Bown, 2005; Bown et al., 2004), corresponding to a turnover of ~93% (Bown, 2005). The planktic foraminifera also underwent an important turnover of 70% to 80% (Macleod et al., 1997; Molina et al., 1998). The severity of extinction among pelagic calcifying species compared to non-calcareous taxa (~50% siliceous diatoms; Macleod et al., 1997) or noncalcifying phytoplankton suggests that a massive acidification of the oceans occurred at the K-Pg boundary (Keller, 2014; Tyrrell et al., 2015).

Prinn and Fegley (1987) were the first to advocate the assumption of a wide dispersal of acid rain (HNO_3) having a large effect, whereas, using estimates of SO_2 released by the K-Pg impact, D'Hondt et al. (1994) were the first to propose that sulphur dioxide (SO_2)-induced seawater acidification was an efficient killing mechanism (Sigurdsson et al., 1991, 1992; Pope et al., 1993; Pierazzo et al., 2003). Ohno et al. (2014) simulated an intense and short-lived acidification to reduce the calcite saturation state of the surface ocean, assuming a rapid scavenging of sulphuric acid aerosols (acid rain). A few months later, Tyrrell et al. (2015) contested this finding, demonstrating that a 10-km impactor was too small to repeat the expected decrease in pH.

The bolide scenario was widely accepted in the 1990s when research advances in radiometric dating of large igneous provinces revealed a close temporal relationship between the emplacement of continental flood basalts and oceanic plateaus with the mass extinctions over the last 380 Ma (Courtillot and Renne, 2003). This close temporal match suggests the existence of a cause-and-effect link between the emplacement of the Deccan Traps and the K-Pg mass extinction (Chenet et al., 2009; Courtillot et al., 1986; Courtillot and Renne, 2003; Wignall, 2001), a result challenging the bolide scenario. With an estimated ~2×10^6 km^3 of extruded lava, it has been

proposed that Deccan eruptions have injected massive quantities of gases into the atmosphere over a period not exceeding 700 kyrs (Schoene et al., 2015), spanning the K-Pg boundary.

To assess the consequences of the Deccan Traps on the inorganic carbon cycle, Dessert et al. (2001) used a biogeochemical model and were the first to highlight a significant pH decrease in seawater (ΔpH = 0.3) associated with the rise of the partial pressure of carbon dioxide (pCO_2; ΔpCO_2 = +1000 ppmv). The assumptions proposed by Dessert et al. (2001) about the Deccan Traps: 1) the volcanism dynamics (linear and continuous degassing), 2) duration of emplacement (100 or 1000 kyrs), and 3) mass of released gases (70,000 $GtCO_2$) are become obsolete with research updates. In addition, recent findings have demonstrated the importance of SO_2 in the Earth's climate during the Deccan Trap emplacements (Mussard et al., 2014; Schmidt et al., 2016). Considering for the first time the combination of 4090 $GtCO_2$ and 3200 $GtSO_2$, Henehan et al. (2016) found a decline of surface seawater pH close 0.2. They demonstrated that the efficiency of weathering accompanying the induced warming rapidly balances (50 kyrs) the acidification of seawater. Based on this finding, they concluded that the initial environmental perturbation caused by direct gas releases was too weak to explain the major disorders observed in the carbonate record at the K-Pg boundary.

Following the conclusions made by Henehan et al. (2016), this study explores the feedback on inorganic climatic interplays between SO_2 and CO_2 and organic tolerance of marine primary producers to amplify this initial perturbation. Consequently, a climate-carbon model has been developed, including carbon and sulphur cycles coupled with a biodiversity model describing the behaviour of marine ecosystems. Instead of a standard approach where the primary producers are only represented as a single pool of organic carbon driven by the amount of nutrients available in the ocean (Dessert et al., 2001; Henehan et al., 2016; Petersen et al., 2016; Schmidt et al., 2016; Tobin et al., 2017; Tyrrell et al., 2015), here the biodiversity model splits the oceanic biosphere into n species (n = 50, see SI), each characterised by biological factors (such as death and reproduction

rates) combined with the sensitivity to abiotic factors (seawater temperature, pH, and calcite saturation state).

This paper presents the influence of the Chicxulub asteroid and Deccan Traps at the K-Pg boundary using a carbon-climate-biodiversity model (ECO-GEOCLIM). The key points addressed in this study include the quantification of environmental changes provided by the Chicxulub asteroid and Deccan Traps and their respective effects on the marine biodiversity, highlighting the amplifying response to an initial perturbation caused by inorganic and organic carbon cycles.

The paper is structured as follows. Section 2 describes the modelling approach and the novelty compared to previous modelling studies. Section 3 presents the results of the scenario combining Deccan Traps and/or the bolide impact to identify explanations for the marine fauna turnover at the K-Pg boundary. Subsequently, a comparison is made between the experiment findings and available data and the previous modelling results in Section 4. Finally, the model limitations are discussed in Section 5, before a summary of the key findings is presented in Section 6.

2. Methods

2.1 Model Description

In this paper, by coupling GEOCLIM and a biodiversity model, a new climate-carbon-biodiversity coupled model (ECO-GEOCLIM) is presented and tested. GEOCLIM (Donnadieu et al., 2006) is a comprehensive climate-carbon model coupling a general circulation model called the fast ocean atmospheric model 1.5 (FOAM 1.5; Jacob, 1997) with a model of the main biogeochemical cycles called COMBINE (Goddéris and Joachimski, 2004). The atmospheric component of FOAM is a parallel version of the National Center for Atmospheric Research's Community Climate Model 2 (CCM2) with upgraded radiative and hydrologic physics incorporated in CCM3 v.3.2 (Jacob, 1997). All simulations have been performed with R15 spectral resolution (4.5° × 7.5°) and 18 vertical levels. In addition, FOAM is used in mixed-layer mode, meaning the atmospheric model is linked

to a 50 m mixed-layer ocean with heat transport parameterised through diffusion. The sea ice module uses the thermodynamic component of the CSM1.4 sea ice model, which is based on the Semtner three-layer thermodynamic snow/ice model (Semtner, 1976). No land ice component was included. It is noteworthy that FOAM does not include an interactive chemistry module; all sulphate reactions and climate forcing are computed in COMBINE (for extended details, see Mussard et al., 2014).

COMBINE is a box model that describes the biogeochemical cycles for carbon, phosphorus, alkalinity, oxygen, and sulphates (fig.1 electronic supplementary material). The present version was updated to include the seafloor weathering process as an additional long-term carbon sink (Brady and Gíslason, 1997; Coogan and Dosso, 2015; Krissansen-Totton and Catling, 2017). We divided the oceanic crust into six layers from the seafloor to a depth of 500 m in the crust, according to a formalism developed by Charnay et al. (2017). Deep water percolating into the oceanic crust follows the present-day temperature gradient (around 116 K/km), starting from the deep ocean temperature at the water-crust interface. To balance the additional carbon consumption from seafloor weathering, the solid Earth degassing rate was increased by 10% compared to its present-day value (i.e. 6.8×10^{12} moles of CO_2/year for aerial volcanoes and 1.8×10^{12} moles of CO_2/year for mid-ocean ridges) in agreement with the fluxes presented by Wallmann (2001).

For the continental carbon sink, field work shows that silicate weathering is linearly dependent on the mean annual continental runoff, combined with a dependence on the mean annual air temperature through Arrhenius formalism (Walker et al. 1981). Continental weathering fluxes are spatially resolved at the FOAM general circulation model resolution (7.5° longitude by 4.5° latitude). The calculated weathering fluxes also depend on continental bedrock lithology (granite vs basalt; Dessert et al., 2001; Oliva et al., 2003). Given the rapid dissolution rate of carbonate rocks, we assume that continental runoff water is at equilibrium with respect to calcite for each continental grid cell under the calculated CO_2 level. Sulphur dioxide reactions are computed in the atmospheric box using the parametric laws developed by Pierazzo et al. (2003) and Miles et al. (2004). The

incoming radiative flux reduction caused by atmospheric aerosols is directly expressed by ΔT, depending on the sulphate aerosols loads (H_2SO_{4liq}) and sea ice thickness (for details, see Mussard et al., 2014). Recent simulations performed by Schmidt et al. (2016) are used to adjust the climate response of the model (see fig.2 electronic supplementary material).

One-third of the atmospheric aerosols are assumed to fall over continents, and the remainder go directly to the surface ocean. Over continents, sulphuric acid aerosols instantaneously react with the available carbonates and alter the weathering process (Donnadieu et al., 2006; Guidry and Mackenzie, 2000). The riverine input flux of sulphate ions into the oceans is calculated as the product of the runoff and ion concentrations. For oceans, H_2SO_{4liq} primarily acts on the alkalinity budget and associated processes (e.g. the carbonate saturation state). Sulphate anions are also transported into the global ocean by ocean mixing within a few thousand years. In the absence of fully coupled simulations, including active oceanic dynamics, oceanic transport processes occurring in the biogeochemical model are represented by exchange fluxes between the ten-box model. These fluxes have been calibrated on present-day conditions and have held constant in all the simulations, given the lack of information about the changes in ocean mixing in the geological past.

To assess the oceanic environmental disturbance, long-term simulations (>100,000 yrs) are required. Since the length of simulations of general circulation models cannot exceed a few thousand years, the coupling procedure between FOAM and COMBINE is done through interpolations of the climate runs. Moreover, FOAM is used to generate an off-line catalogue of continental air temperature (T_{air}) and continental runoff (R) values for a wide range of pCO_2 values. At each time step of the GEOCLIM calculation, and for each corresponding atmospheric pCO_2, T_{air} and R above each continental pixel are calculated through a linear interpolation procedure from the climatic catalogue.

In the GEOCLIM model, the oceanic biosphere is modelled as an organic carbon reservoir in the photic zone in each oceanic basin. Up to now, these reservoirs are fed by a flux of primary productivity, dependent on the input of phosphorus (the only nutrient modelled) inside the surface

ocean by upwelling or continental discharge. Biomass is then lost by decay and transferred to the deep ocean. In the present study, we introduce a highly simplified model for the biodiversity inside the photic zone. A fixed number of planktonic functional types (PFTs) n is prescribed (n = 50 in this study). These PFTs are represented by a mass of carbon (mol of C). Each PFT has its own physiological parameters and can interact with the others (primarily competing for resources; Quere et al., 2005). The growth rate of each PFT, α_i, is a function of the calculated surface temperature and pH according to the following equation:

$$\alpha_i = br_i \cdot a_1^i \cdot \exp\left[\frac{-\left(T - b_1^i\right)^2}{2\left(c_1^i\right)^2}\right] \cdot a_2^i \cdot \exp\left[\frac{-\left(pH - b_2^i\right)^2}{2\left(c_2^i\right)^2}\right] \cdot I_i \cdot F_{in}^P$$

where br_i is the birth rate, and α_i is the maximal growth rate of species i, modulated by two Gaussian functions. The first one is centred on the optimum temperature of growth b_1^i with a tolerance of c_1^i, and the second is centred on the optimum pH of growth b_2^i with a tolerance of c_2^i. Additionally, the GEOCLIM model calculates the surface temperature T and the pH at each time step for each ocean basin. The optimal temperature of growth for each PFT, b_1^i, is fixed at the averaged value of the surface ocean reservoir for the pre-perturbation, with a random noise of ± 5°C. The same procedure is applied to the optimum pH, b_2^i, with the random noise fixed at ± 0.1 pH. The tolerances (standard deviation c_1^i and c_2^i) are randomly set at a value within the interval [-4°C, 4°C] and [-0.3, 0.3] around the optimum temperature and pH.

The factor I_i represents the potential competition for resources among the primary producers. For each species i, the existence of a competitive relationship with all the other species j is randomly fixed (yes or no). If there is no competition, I_i is set to 1. Otherwise, it is calculated as the average of all competitive factors $I_{i,j}$. These factors are calculated as a Michaelis-Menten function of the ratio of the biomass of PFT i and j. The death rate of each species is assumed to be proportional to their global biomass, with the proportionality constant being fixed randomly prior to the simulations. At this stage, we do not account for a trophic chain, including predators, nor the

dynamics of ecosystems (the processes of evolution). All PFTs are thus primary producers. If the present version of the model does not explicitly simulate the biomass and behaviour of grazers, the effect of grazers is lumped into the death term of each producer, F^{p}_{in}, the nutrients flux (phosphorus).

To consider the role of carbonate ion concentration in calcification by marine organisms we used the $CaCO_3$ saturation state (Ω_{CaCO3}). This assumption is based on positive correlation between Ω_{CaCO3} and the calcification rate, This link is defined as follows (Zeebe and Wolf-Gladrow, 2001):

$$\Omega_{CaCO3} = [Ca^{2+}]\,[CO_3^{2-}] / K_{sp} \quad \text{wherein } K_{sp} = [Ca^{2+}]_{sat}\,[CO_3^{2-}]_{sat}$$

$[Ca^{2+}]$ being constant into the ocean over a period not exceeding few millions of years, here ~20 $mmol \cdot kg^{-1}$ (Stanlet and Hardie, 1999), Ω_{CaCO3} is largely determined by $[CO_3^{2-}]$ therefore the seawater pH. Using this property, if the ocean is still saturated ($\Omega>1$) the calcification by marine organisms depends on the saturation state for calcite (see next section for details) or becomes null if ($\Omega<1$). In this latest case the calcifying organisms are supposed extinct (their biomass is fixed to 0).

2.2 Boundary Conditions: The Late Maastrichtian

To quantify the K-Pg oceanic disturbance, the latest Cretaceous boundary conditions are applied to ECO-GEOCLIM. Climatic outputs are extracted from Maastrichtian simulations performed by Donnadieu et al. (2009). The land-ocean configuration (~68 Ma) is based on paleomagnetic data, hotspot tracks, geological constraints (Besse and Courtillot, 2002; Dercourt et al., 1993), the circular orbit of the Earth around the sun (eccentricity = 0), and the Earth's obliquity at 23.5° (this setting leads to an equal annual insolation for both hemispheres). In addition, the solar radiation is reduced by 0.6% (i.e. 1357 W/m^2), according to the stellar evolution models (Gough, 1981). The tested atmospheric CO_2 values range from 160 to 2000 ppmv to cover all plausible atmospheric CO_2 scenarios for the K-Pg boundary (Caldeira and Rampino, 1990; Dessert et al., 2001). The presumed extent and spatial distribution of the Deccan Traps at the K-Pg boundary are based on the work by

Lefebvre et al. (2013). Plant cover is extracted from Donnadieu et al. (2009), where GEOCLIM was coupled to the dynamic vegetation model (LPJ; Lund-Postdam-Jena; Sitch et al., 2003). This coupling ensures constant coherence between climate and vegetation cover, which influences the silicate weathering but only through the runoff and temperature variables. The model does not account for other effects of vegetation on continental weathering (such as enhanced weathering by organic acids or the below ground CO_2 increase). Since FOAM does not consider the atmospheric chemistry of sulphur, land plants are neither affected by acid rains nor short-term cooling.

The Maastrichtian is considered a period of high carbonate production and deposition (Hay, 2004) with extant carbonate platforms and important chalk deposition (Kiessling et al., 2000, 2003). In light of available data on change during the Phanerozoic, the real extent of tropical carbonate indicates that the latest Maastrichtian carbonate platforms (<30° latitudes) occupy ~16×10^6 km² (i.e., the modern areas of shelfal carbonate accumulation are ~0.6×10^6 km²; Walker et al., 2002). Consequently, we updated the computation of the carbonate accumulation in shallow water (freef flux) as follows:

$$freef = akcr * \text{ocean surface} * reefS * (\Omega\text{-}1)^{1,7},$$

where *akcr* represents the most dominant mode of carbonate production for shallow water (low/high value describes a Cretan/Neritan ocean, respectively), with *reefS* (areal extent of the tropical carbonate over the Phanerozoic period) as the constant 16×10^6 km². Thevolume of the coastal ocean is held constant at 4.86×10^6 km³.

In the neritic environment, carbonate production remains globally dominated by skeletal debris, such as large benthic foraminifera, rudists, bivalves, echinoderms, ectoprota, and algae with a small contribution from peloids and ooids (Kiessling et al., 2003; Steuber, 2002), while the open ocean was dominated by planktic foraminifera and calcareous nannoplankton. The ecological success of planktic calcifiers during the Mesozoic (Martin, 1995) induced a transition from a Neritan ocean, where the $CaCO_3$ production is driven by neritic organisms living on shelves, to a Cretan ocean dominated by biogenic pelagic $CaCO_3$ precipitation (Zeebe and Westbroek, 2003).

To represent Cretan and Neritan oceans, we changed the percentage of the primary producers able to calcify in the photic zone. In the case of a Neritan ocean, 33% of the total biomass of the primary producers living on shelves are calcifiers (which corresponds to 17 PFTs as calcifiers and 33 as non-calcifiers; see fig. 3 electronic supplementary material), and 10% are in the open ocean (calcifying PFTs are reduced to five). Conversely, in the case of the Cretan ocean, we assumed that biological innovations have led to increasing the percentage to 33% in the open ocean, while the efficiency of calcifier species living on shelves remains unchanged at 33% (calcifying PFTs = 17, noncalcifying PFTs = 33; see fig. 3 electronic supplementary material).

2.3 The K-Pg Events and Experimental Set-up

Using the Late Maastrichtian boundary conditions, the weathering of silicates and the simultaneous uptake of atmospheric CO_2 leads to stabilising the load of atmospheric carbon at 230 ppmv. This value is the result of elevated weathering rates due to emplacement of a large igneous province combined with the paleogeographic impact. Compared to usual estimates for the Late Cretaceous, 500 ppm < pCO_2 < 1500 ppm, our pre-crisis load of CO_2 appears too low (Royer, 2006). However the last CO_2 compilation shows that the atmospheric CO_2 at 65 Ma was close to 280 ppm, and may even be below that level (Foster et al., 2017)

Moreover, a tropical climate prevails despite this apparently low load of carbon dioxide. Simulated SSTs present an averaged value [50°S-50°N] of 18.6°C, accompanied by a wide latitudinal gradient, <15°C at mid-latitudes to >25°C close to the equator. Since this starting state provided us a description of the Late Cretaceous environment not so far for estimates proposed by proxies (Woelders et al. 2017), we preferred to leave the pCO_2 pre-crisis value unchanged, rather than tune the carbon cycle parameterisation (enhanced degassing and weaker weathering).

By fixing the latest Maastrichtian areas of shelfal carbonate accumulation at 16×10^6 km² (Walker et al., 2002), the alkalinity was depleted compared to present-day conditions; thus, the ocean was less saturated with calcite ($\Omega_{calcite} \sim 2.2$, instead of $4.5 < \Omega_{calcite} < 5$ for the modern ocean).

the lysocline tends to be much shallower than present-day (2,7 instead of 4km) but no region of the surface ocean becomes undersaturated for calcite (Ω_{min} polar regions = 2). This pre-crisis steady state implies that the latest Cretaceous ocean should be more sensitive to any process increasing the dissolved inorganic carbon without adding alkalinity.

To better explore the effect of coupling between environmental disturbances and biodiversity, we tested the effects of the Deccan Traps and/or bolide impact. To assess the effects of biological feedback in response to the Deccan Traps or bolide impact (or a combination of the two), we compared simulations where the primary production does not depend on environmental perturbations ('without biological feedback' experiments, Table 1) with simulations where the physiological parameters of species alter their efficiency in producing organic carbon ('with biological feedback' experiments, Table 1). In the absence of biological feedback, the amount of organic carbon produced is solely controlled by the available nutrients. Most of our runs used the Cretan ocean as the standard condition to fit palaeontological records; however, to highlight the role of pelagic calcifiers as primary producers, we also conducted experiments assuming a Neritan ocean. Table 1 summarises all runs performed in this study.

2.3.1 Eruptive Sequence of the Deccan Traps

The Deccan Traps outcrop over vast areas of west-central India and are currently formed by a 3500 m-thick lava pile. The eruptive sequence established in the Western Ghats, the thickest remnant of the main Deccan province, includes 30 major eruptive events and 41 single lava flows corresponding to a volume of ~253,000 km^3 (Chenet et al., 2009). After scaling to the total volume of the Deccan Traps (~2×10^6 km^3; Chenet et al., 2009), more than 75% of the lava volume is not considered, leading to an underestimation of the number of individual lava flows. Assuming a simple geometry for lava flows and accounting for the estimations of SO_2 and CO_2 concentrations in basalts (Self, 2006), Chenet et al. (2009) proposed that 15,000 to 35,000 Gt of CO_2 and 6800 to 17,000 Gt of SO_2 were released into the atmosphere, primarily during the emplacement of the main

province. We assume that sulphur species have reached the stratosphere due to the pulse-like degassing of the Deccan Traps (Kaminski et al., 2011), as suggested by *akaganéite* minerals (Font et al., 2017).

The emplacement of the Deccan continental flood basalts started with the eruption of the Northern Deccan province (Malwa plateau and Mandla area), a minor event in terms of volume, dated at 67.3 ± 0.3 Ma, lasting about 1.7 Ma (Schöbel et al., 2014). The main province started erupting during the C30n/C29r transition, continued during chron C29r, and finally, ended during chron C29n, straddling the K-Pg boundary (Chenet et al., 2007, 2008). The main province clearly represents the largest volcanic event during which at least 80% of Deccan lavas erupted. Chenet et al. (2009) suggested that the main erupting phase (Phase 2 according to Chenet et al. 2009) would have been as short as 200 kyrs. Recently, using U-Pb ages on zircon from lava flows collected in the Western Ghats (the main province), Schoene et al. (2015) concluded that the duration of emplacement lasted 0.7 Ma. Unfortunately, the absence of U-Pb ages out of the lowest and highest volcanic units did not allow a conclusion regarding the tempo of emplacement, notably the presence of a hiatus within the eruptive sequence. However, according to Schoene et al. 2019, this considered period covers the emplacement Polardpur and Ambenali formations (ie 66.1 to 65.9Ma), two among the most active phases of the Deccan traps. In addition, these two volcanic events encompass the K-Pg boundary (66.04Ma).

By deciding to focus on a shorter period of time of maximum activity (~200 kyrs) instead of studying 700 kyrs of eruption (Schoene et al. 2016, 2019, Sprain et al. 2019), we considered that the most important factor affecting the Earth's environment was the timing of eruption not the total duration of the emplacement of the Deccan traps. Indeed the emplacement of the main province (as all large igneous provinces) consists of individual lava flows and volcanic pulses made of successive flows erupting over a period that is too short to record the magnetic secular variation (< 100 yrs; Chenet et al., 2008, 2009; Courtillot and Fluteau, 2014). This result implies that the volcanic activity is interrupted by periods of quiescence, occasionally evidenced by thick weathered

levels (red bole). Following this evidence, we developed a sequence based on a pulse like activity instead of considering a linear degassing, a scenario appearing much more realistic to describe the large igneous province volcanism.

Based on constraints on time, volume, and fluxes of volatiles, we developed a stochastic model to obtain a pulse-like degassing scenario of CO_2 and SO_2. We fixed the total volume of erupted magma at 2×10^6 km^3, the total emission of CO_2 at 28,000 Gt, and the emission of SO_2 at 6,800 Gt. We assumed that the volume of lava flows and volcanic pulses follow a Gaussian distribution ($m = 0$, $\sigma = 5000$ km^3), meaning that only a few lava flows may exceed 10,000 km^3. We fixed the duration of a single volcanic activity equal to 10 yrs, whatever the volume of erupted magma. The (first) year of eruption was chosen randomly over a 200-kyr period. The pulse-like degassing scenario contained about 500 eruptive events and was used as an input parameter for the biogeochemical model (for details about the eruptive sequence see fig. 4 electronic supplementary material).

2.3.2 Gases Released and Solid Particles Ejected by the Chicxulub Meteorite

The Chicxulub crater (170 km in diameter) in the Yucatán peninsula is due to a collision with an asteroid of about 10 km in diameter. The sea floor at the target site is composed of a 3 km-thick sedimentary sequence of carbonate rocks (~35% dolomite and 30% limestone) and anhydrite (~30%) (Ward et al., 1995). To estimate the amount of CO_2 released into the atmosphere by vaporisation, we used the approach developed by Charnay et al. (2017). We tested three values of bulk density: 3320, 2490, and 1660 $kg{\cdot}m^{-3}$ to cover the entire range of cases (pure dunite with 0%, 25%, and 50% porosity, respectively). Assuming a decarbonation pressure fixed at 60 GPa (Martinez et al., 1995) and a mass fraction of CO_2 of 1% in asteroids (Charnay et al., 2017), the mass of CO_2 released by the impactor ranged from 1955 $GtCO_2$ to 1260 $GtCO_2$. In line with these computations, we considered a mean value of 1400 $GtCO_2$, a value in the range of Pierazzo's

estimate (1998) of ~1471 Gt. Our computational tests performed with the same assumptions predicted higher loads of SO_2 (~180 GtS or 360 $GtSO_2$). However, to be consistent with prior studies, while investigating the Chicxulub impact (Brugger et al., 2017), we prefer to use 100 GtS (or 200 $GtSO_2$) to represent the load of S released by the platform vaporisation. It is notable that additional sources of carbon due to burned biomass and remineralisation of the dying terrestrial vegetation were not considered.

The mass of ejecta produced by the impact, primarily silicates, is calculated using the approach proposed by Collins et al. (2005) and developed by Charnay et al. (2017). Assuming a density of 2490 $kg \cdot m^{-3}$ for the impactor, a total mass of ejecta distributed worldwide reaches 4.42×10^{16} kg (2.95×10^{16} kg with a density of 1660 $kg \cdot m^{-3}$, and 5.86×10^{16} kg with a density of 3320 $kg \cdot m^{-3}$). The weathering of ejecta, a net sink of CO_2, is calculated following Sleep and Zahnle (2001). In the absence of modules devoted to include following complex processes nitrogen oxide formation due to atmospheric shock waves (Tyrrell et al., 2015), ozone depletion, and bedrock contamination (Ganino and Arndt, 2009), for example, were not considered. . Since the residence time of water in the atmosphere, it would not have exceeded a few months; thus, we do not consider its effect further.

2.3.3 Time Coincidence Between Deccan Traps and the Chicxulub Meteorite

Recent high-precision ^{40}Ar-^{39}Ar dating of the K-Pg boundary in Hell Creek (Montana, USA) and of the Chicxulub (Yucatán, Mexico) impact ejecta shows that these two events are time-coincident within ~32,000 yrs precision at ca. 66.04 Ma (Renne et al., 2013). The discovery of the oldest spherules in the vicinity of the Chicxulub astrobleme in layers is attributed to C29r (between C30n and C29n), suggesting that the impact occurred at least 10 kyrs later than the main phase of the Deccan Traps (Keller, 2014).

Nevertheless, the sudden outburst of Deccan eruptions, accounting for more than 70% of the main-phase eruption, occurred within ~100,000 yrs or less of the K-Pg boundary (Renne et al.,

2015), suggesting a longer interval. Without precise time constraints, to enhance asteroid effects on the environment, we assumed that the Chicxulub impact struck the Earth's surface 100 kyrs later than the inception of the Deccan main province volcanism. It is noteworthy that a sensitivity experiment with a different time coincidence (10 kyrs instead of 100 kyrs) presents similar effects (ΔSST~0.1°C, see electronic material fig. 5).

3. Results

3.1 Chicxulub Impact Modelling

Over the five years following the impact, the modelled SST drops by 8°C in the low latitudes despite the rise in CO_2 (ΔpCO_2 = +120 ppmv, Fig. 1) caused by rock vaporisation (especially carbonates). In response to sulphate aerosols (Robock et al., 2009; Schmidt et al., 2016), the cooling trend continues for at least three decades after the impact. Because the S-aerosol particles are progressively washed out from the atmosphere, the cooling effect is progressively outweighed by the warming provided by the pCO_2 due to its longer residence, which causes post-impact warming of ~1.5°C after a century (Fig. 1). Due to the ice-albedo feedback, the warming of polar SST is delayed by about 100 yrs and does not exceed +0.5°C.

The post-impact CO_2 evolution is highly sensitive to biological feedback. Succeeding a brief increase in CO_2, pCO_2 decreases within 1 kyr in the absence of feedback (A-Cretan-2), while several 10 kyrs are needed when feedback is considered (A-Cretan-1). As long as S-aerosol amounts remain high, a transient shutdown of the primary production is simulated when biological feedback is considered (Fig. 2a). The primary productivity briefly increases within the first years after the end of cooling, a phenomenon that could be related to the phosphorus accumulation from previous years. This transient peak can be considered a 'swan song'. After the removal of the excess phosphorus, the primary productivity decreases and reaches its lowest value around a decade after the impact (Fig. 2a). Between 50 and 200 years after the impact, the consumption of nutrients is less

efficient due to environmental changes (Figs. 1 and 3), and the phosphorus content increases (Fig. 2b).

Driven by oceanic disturbances, despite the presence of nutrients (Fig. 2b), primary productivity and oceanic biomass both decline (Fig. 4), especially the calcifying primary producers, due to acidification of the surface ocean (Fig. 3). The recovery of the primary productivity happens over a period of a few centuries (Fig. 2) when pre-impact conditions tend to be restored. In response to the low percentage of residual living biomass (Fig. 4) in the aftermath of the impact, the burial of organic carbon is weakened; thus, only weathering processes efficiently reduce pCO_2. Consequently, by including biological species' inherent properties, environmental perturbations lead to creating a sluggish organic carbon cycle characterised by a delayed response of reducing pCO_2.

Focusing on biogeochemical disturbances, the most severe acidification occurs in surface oceans (ΔpH equals -0.15), while the deep ocean remains weakly affected (< 0.1 pH; Fig. 3a). However, whatever seawater conditions are tested (Cretan or Neritan), the surface ocean remains oversaturated with calcite ($\Omega_{calcite}$ ~ 1.3; Fig. 3c). A puzzling behaviour is observed a few decades after the asteroid impact. Despite the ocean acidification, the model predicts an increase in carbonate precipitation (Fig. 3d), while the surface ocean remains depleted of CO_3^{2-} ($1.3 < \Omega_{calcite} < \sim 1.5$; Fig. 3c), a result that is contradictory to the theoretical view, assuming a strict dependence on carbonate deposition with $\Omega_{calcite}$. In fact, because carbonates are bio-induced (see Section 2.2 for details), marine calcifier organisms benefit because all primary producers of abundant nutrients remain available in the surface ocean. Consequently, during the first century after impact, carbonate deposition is dominated by primary productivity rather than by $\Omega_{calcite}$. With a longer time scale, $\Omega_{calcite}$ drives fluctuations of carbonate precipitation. Coastal seas receive the majority of alkalinity fluxes from carbonate and silicate weathering, and carbonate deposits are quickly restored on continental shelves (~100 yrs) compared to open oceans (~1000 yrs; Figs. 3d–3f).

For a better understanding of how oceanic disturbances lead to extinctions among calcifying and noncalcifying species, we explored variations of living marine organisms in a Cretan ocean before, during, and after the Chicxulub impact. We developed the following relationships for each PFT in the photic zone, where primary producers are abundant (surface boxes). The present relationship is based on specimen abundance (*SA*) for each PFT (full details given in footnote[1]) and provides an apparent extinction pattern (i.e., apparent species extinction or *aSE*).

$$SA = [PFT\ biomass\ (t=0) - PFT\ biomass\ (t)] / PFT\ biomass\ (t=0)$$

$$aSE = 1,\ if\ SA < SAT,$$

$$else = 0\ ME_{ratio} = \Sigma^{1}_{n\ species}\ aSE,$$

where *ME* is the mass extinction ratio and *SAT* is the specimen abundance threshold.

Based on our assemblage of marine PFTs, A-Cretan-1 case illustrates that, if the overall disturbance is sufficient to trigger a biomass reduction of 60% for calcifying organisms (40% for noncalcifying; Fig. 4), this results from the collapse of a few dominant calcifying PFTs that were providing the most biomass. Furthermore, biotic losses for primary producers would not have exceeded 20%, assuming an *SAT* close to 0.1 (i.e., the abundance of living specimens decreases to 10% of the pre-crisis value). Despite these drastic perturbations, this result suggests that no major extinction occurs when we combine an instantaneous release of 1400 $GtCO_2$ with 200 Gt of SO_2. Additional sources of carbon due to burned biomass and remineralisation of the dying terrestrial vegetation may enhance this perturbation however but SO_2 emissions cannot rise above 250Gt – threshold of the reversible cooling (see section 4.1 to see sensitivity experiments).

1 We defined the mass extinction ratio based on specimen abundance. We supposed that each type of organism remains characterised by a body shape and mass held constant through time. Biomass ($t = 0$) and (t) correspond to the initial and computed biomass at time t, respectively. The specimen abundance threshold (SAT) represents an arbitrary value to describe the apparent presence of specimens in the fossil record. In this study, the arbitrary SAT ranges from 0.2 to 0.01. This range is used to represent the complex set of factors distorting the observed extinction record for each species (the Signor-Lipps effect). According to this assumption, when SAT is fixed to 0.01, the extinction occurs when the apparent abundance of living specimens reduces to 1% of the pre-crisis value. Based on these equations, species can reappear later in the geological record if the biomass of the species rises.

3.2 Deccan Traps Modelling

To simulate the effects of the Deccan Traps, we computed a sequence of 200 kyrs with pulses following the stochastic distribution as described in Subsection 2.3.1. The response to a single volcanic pulse presents tendencies similar to those simulated for the Chicxulub impact but with a weaker amplitude. Both cases show an abrupt cooling over several decades, driven by S-aerosols, followed by warming caused by enhanced pCO_2 after aerosol scavenging. However, through time, the load of CO_2 accumulated by degassing by the Deccan Traps overcomes the rise in CO_2 triggered by a 10-km impactor, $+250 < \Delta pCO_2 < +470$ ppmv (instead of +120 ppmv for the Chicxulub impactor; Figs. 5 and fig.1 in electronic supplementary material).

The primary driver controlling the rise of pCO_2 is the degassing itself; however, biological feedback suggests an external mechanism able to amplify the initial perturbation. The mean response obtained with the D-Cretan-1 scenario presents a rise of SST by 3.5°C (~23.5°C) between 50°S and 50°N, whereas the warming does not exceed 2.5°C in the absence of biological feedback (D-Cretan-2). This finding demonstrates that the same eruption scenario generated variable environmental disturbances, depending on the properties of the oceanic ecosystem (Fig. 5). Nevertheless, the style of an eruption has a significant influence as well. Examining the linear degassing case (Fig. 5), volcanic sulphur products are washed without disturbing the long-term warming provided by the CO_2 (the warming is just slightly weaker due to the continuous S-aerosol formation; D-Cretan-linear) whereas the opposite behaviour is found when the eruptive sequence includes a succession of pulses (the long-term warming is interrupted by a succession of cooling events; D-Cretan-1). The slowing of the weathering process caused by the aerosol-induced cooling is highly dependent on the assumed quiescence period between two pulses. For instance, using a quiescence period twice longer D-Cretan-long-degaz), the excess CO_2 is removed from the atmosphere because silicate weathering becomes efficient enough to limit long-term warming (i.e.

480 self-regulation of the Earth's temperature; Walker et al., 1981). Consequently, if the eruptive sequence is intense enough, the long-term warming should be briefly interrupted by cooling events lasting 10 to 100 years. Otherwise, the Earth's climate should be characterised by limited long-term warming due to the efficiency of silicate weathering. Despite the importance of emitted SO_2 (D-Cretan-noSO_2) and aerosol formation in the Earth's climate by limiting silicate weathering
485 (Mussard et al., 2014), the intense build-up of CO_2 caused by biological feedback illustrates that organic carbon more efficiently destabilises the global carbon cycle than inorganic processes over the time scale of a thousand years.

Over the first 100,000 years of volcanic activity, what happens at the surface vastly affects the deep ocean, and both parts present the same tendency, although the shift in deep water towards
490 lower pH is greater than the surface ocean (Fig. 6a). At the opposite end, over the next 100,000 years, the acidification of the surface ocean stops (Fig. 6b), while the pH of the deep ocean still decreases (Fig. 6a). Acidic seawater affects the deep and surface oceans in varying ways. Most of the calcite is dissolved at depth (Fig. 6c), forcing the lysocline to rise close to 1500 m (Fig. 6d). The calcite dissolution leads to an increase in deep ocean alkalinity. This increases the propagation to
495 the rest of the ocean due to water upwelling. A positive alkalinity flux is generated from the deep to the surface layers, inhibiting the acidification of surface waters. Consequently, the saturation state of shallow water increases (Fig. 6c), facilitating carbonate production in whatever the initial states of the ocean are considered (Cretan or Neritan).

These experiments reveal contrasting disturbances of the oceans with two distinct phases. 1)
500 Deccan Trap volcanism reduces carbonates deposition and limits the primary productivity in the whole ocean during the first 100,000 years. Then, 2) the deep ocean acidification (lysocline shallowing) enhances the alkalinity flux from the bottom to the surface of the ocean with the direct effect of limiting the surface acidification. This process restores carbonate deposition on shelf surfaces and favours primary production during the second half of the Deccan Trap emplacement
505 (10^5 to 2.10^5 years).

The results from oceanic disturbances modelled in D-Cretan-1 run is a biomass reduction of about 90% for calcifying organisms and 65% for noncalcifying organisms (Fig. 7). Conversely to the asteroid case (A-Cretan-1), the biomass fall simulated with Deccan Trap volcanism (D-Cretan-1) corresponds to a global collapse, whatever the considered PFTs. Calcifying PFTs are more affected because their primary productivity efficiency is affected by the cumulative effect of abiotic factors varying (ΔSST, ΔpH, and calcite saturation), whereas no calcifiers remain only affected by SST and pH changes. It is noteworthy that most parts of the biomass lost occurred on a time scale ranging from 10,000 to 100,000 years, suggesting that an eruptive sequence that will last longer is not necessarily associated with more drastic environmental changes and biomass crises. If a biomass disturbance seems sufficient to qualify this event as a massive collapse, the patterns of extinction for calcifying and/or noncalcifying PFTs, both ranged from 50% to 80%, suggest a mass extinction event in terms of marine biodiversity as well.

To specifically investigate the effects of seawater pH on calcifying and noncalcifying producers, we conducted an additional run in which pH fluctuations have no effect on the marine biosphere (D-Cretan-3). Compared to standard conditions (D-Cretan-1), after 100,000 years of volcanic activity, the phosphorus content becomes twice lower, while the primary productivity is only reduced by 40% instead of 60% (Fig. 8). However, in two cases, we observed a clear inflexion over the next 100,000 years with the re-increase of primary productivity. This tipping point is crossed when the ΔpH exceeds 0.1. Since most of the marine PFTs appear tolerant to ΔpH of ~0.1 (Fig. 3 SI), the organic carbon cycle will not be destabilised below this threshold of fluctuation. As long as changes in seawater pH do not exceed 0.1, the primary production remain nearly unaffected, and the productivity curves for both experiments look similar through the first 60-70 kyrs.

After this timespan, we observe that the primary production and phosphorus tendencies appear less pronounced for the D-Cretan-3 experiment (only driven by variations of SST). Finally, in response to a sturdier rate of organic carbon burial linked to a more abundant biomass in oceans,

the D-Cretan-3 run presents a lower pCO_2 (ΔpCO_2 = +420 ppmv) compared to standard conditions (ΔpCO_2 = +470 ppmv) at the end of the Deccan Traps.

3.3 The K-Pg Mass Extinction Modelling

We now combine the 200 kyr-long eruptive sequence of the Deccan Traps and the Chicxulub impact, which collided with the Earth 100,000 years after the onset of the degassing of Poladpur (Schone et al. 2019). Compared to the Deccan run (D-Cretan-1 and D-Neritan), the Chicxulub impact leads to an instantaneous, albeit moderate, rise of pCO_2 (+80 ppmv; Fig. 9a), whatever the state of the ocean tested (Cretan or Neritan). Our model simulates global warming reaching 3.5°C due to the rise of atmospheric CO_2 (+470 ppmv) only interrupted by intense and brief cooling events due to S-aerosols derived from SO_2 emissions by volcanism or rock vaporisation (Chicxulub impact). In addition to SST fluctuations, the spread of sea ice (Fig. 10) should inhibit photosynthesis during most of the year at high latitudes (from the pole to 60° latitudes). Forced by our volcanic sequence, the Earth has undergone four to five major climate changes (Fig. 10) on a time scale not exceeding 100,000 years (Fig. 9b), with one being caused by the impact and the other driven by intense phases of volcanism.

In addition to climate changes, atmosphere-ocean exchanges lead to a pH decrease in the global ocean by 0.2 for the surface ocean (from 8.0 to 7.8) while the deep ocean pH drops by 0.4 (from 7.8 to 7.4). Without requiring any additional perturbations, these environmental disturbances lead to a dramatic decrease in calcifier organisms (~90% of their biomass and ~80% of their apparent biodiversity, assuming an *SAT* fixed at 0.1), while noncalcifying organisms appear less affected (biomass and biodiversity are reduced by about 65% and 60%, respectively) . It is noteworthy that mass extinction patterns (Fig. 9e) are affected by the Chicxulub impactor, and the mass extinction ratio of calcifying and noncalcifying species only differs after the impact, suggesting that very rapid marine acidification can be considered an effective trigger for explaining the severity of extinctions among pelagic calcifying species compared to non-calcareous taxa.

4. Discussion

Here, we compare our modelling results with prior studies and geological records to validate the mechanisms described in Section 3.

4.1 Chicxulub Impactor

According to Brugger et al. (2017), the mid-tropical SST underwent a similar cooling (ΔSST = -8°C in this study compared to -6°C), whatever the stratospheric residence time assumed for S-aerosols. Both studies used the same amounts of released gases, but the S-aerosol computation is governed by different processes. In ECO-GEOCLIM, the S-aerosol loads are derived from chemical reactions depending the gas amounts with the effect on the climate predicted using a parameterisation based on that by Schmidt et al. (2016). Conversely, CLIMBER3α follows the assumptions by Pierazzo et al. (2003), but the S-aerosol load is simulated by a reduced solar flux. However, in the absence of direct measurements (high loads of S-aerosols not yet observed), considering the complex interplays of sulphur species in the atmosphere (aerosol size; Timmreck, 2012), the scavenging issue (Ohno et al., 2014), and the altitude of ejection (Kaminski et al., 2011), both estimates of climate change can be considered consistent with the existing data. In addition to these processes, the cooling could be more marked using a mixed-layer oceanic model for computing SST (this study), with the heat transport computation being less accurate than in a fully dynamic ocean model (Brugger et al., 2017).

The reconstructed SST based on TEX_{86} palaeothermometry for sediments deposited within 100 years following the impact (Vellekoop et al., 2014) also shows a sharp drop in tropical coastal seawater temperature (ΔSST_{max} = -7°C). The same section (Brazos River, Texas) also reveals a prolonged warming following the 'impact winter', where the post-impact SST is 1°C to 2°C warmer than the pre-impact values. Compared to our model results for the Chicxulub impact, the best match is observed with the A-Cretan-1 run. Indeed, the data and model results show the same

sequence of events: intense cooling followed by moderate warming. Without excluding some issues in the recording of such short-lived events (reworked materials), palaeothermometry measurements on the Brazos River section also fit well with the AD-cretan-1 run (Table 1), where distinct cooling phases could be potentially associated with volcanic pulses in addition to the Chicxulub impact.

Whatever the scenario considered, our model failed to reproduce massive acidification (Fig. 3) that would be able to create surface waters that are undersaturated with calcite, as defended by Ohno et al. (2014). If the S-aerosol scavenging within a few days may be invoked to solve this issue, this assumption also implies small amounts of stratospheric S-aerosols and a lifespan of S-aerosols that is too short to explain the Earth's cooling (Vellekoop et al., 2014).

Following this conclusion, we explored an alternative solution by carrying out a set of experiments where we test the Earth's system response to massive injections of sulphur (D'Hondt et al., 1994; Ohno et al., 2014; Tyrrell et al., 2015). Holding the mass of CO_2 released by the impact constant, sensitivity tests revealed that surface waters become very briefly (< 1 year) undersaturated for calcite ($\Omega_{calcite} \sim 0.95$), with a modest increase of injected sulphur (175 GtS instead of 100 GtS). Very massive injections can help to extend the length of the surface ocean undersaturation of calcite, but such high fluxes lead to surface cooling of the Earth. For example, the tropical SST [50°S-50°N] declines to 0°C for 1 year in response to an injection of 250 GtS (surface ocean pH = 7.6, $\Omega_{calcite} \sim 0.75$) or 10 years with 770 GtS (surface ocean pH = 7.4, $\Omega_{calcite} < 0.5$). Beyond this amount of sulphur, an irreversible cooling occurs due to sea ice spreading and snow extending. Within a few years, the Earth becomes entirely covered in ice (snowball Earth state). Although climate instability thresholds due to ice-albedo feedback may be model-dependent, the first-order conclusion rejects the existence of very massive injections of sulphur, a conclusion that is in agreement with findings by Tyrrell et al. (2015). Consequently, based on AD-Cretan runs (Fig. 9), we defend that the likely solution will be a combination of long-term acidification provided by CO_2

(Deccan Traps) coupled with short-term acidification resulting from the rainout of sulphate aerosols (Chicxulub).

4.2 Deccan Traps Emplacement

Using $\delta^{18}O$ measured in foraminifera, the Late Maastrichtian (chron C29r – planktic foraminiferal zones CF2, then CF1 – last biozones before the K-Pg boundary) was originally identified as a tropical climate (Li and Keller, 1998). This view was challenged by recent paleoclimate estimates that suggest a succession of warm-cool events rather than a single global warming event (Punekar et al., 2014). These new data lead to a reassessment of the K-Pg boundary, which may be defined as follows (Keller, 2014): the CF2 zone (spanning ~120 kyrs) characterised by an intense warming close to 3°C to 4°C (Li and Keller, 1998), followed by the CF1 zone (~160 kyrs), a warm fluctuating period because the warming trend ends in the middle of the CF1 zone, and the Earth's temperature starts to decline. Despite this complexity, all experiments simulating Deccan Traps emplacement (with or without Chicxulub impact) ~~gather all~~ explain some of the major features presented in the geological record: 1) the combination of warm-cool events, 2) warming duration (150-200 kyrs) fitting with foraminifera biozones, and 3) the SST rise in close agreement with proxies ~3.5°C, which is roughly equivalent to 7°C in high latitudes, according to Tobin et al. (2017). The model-proxy agreement emphasises that the emplacement of Deccan Traps seems to be the main driver causing climate changes over the K-Pg boundary.

Tobin et al. (2017) demonstrated the relevance of pulse-like degassing to explain climatic perturbation and revealed a striking correlation between warming and emitted CO_2. In their attempt to reproduce 3°C to 6°C of global warming (7°C for polar regions) deduced from oxygen isotopes (Barrera and Savin, 1999; Li and Keller, 1998), Tobin et al. postulated that 35,000 Gt CO_2 must be injected over 200 kyrs for rising pCO_2 by ~400 ppmv and that it warms the Earth's surface by ~3°C. These estimates were obtained with a box model describing the biogeochemical cycles (GEOCYC, a model derived from GEOCARB) in which the load of atmospheric CO_2 is solely driven by the

enhancement of silicate weathering in response to Earth's heating, with feedback precluding the accumulation of CO_2 into the atmosphere. Considering the biological and SO_2 feedback, we revised this issue because both mechanisms act as a limiting factor of the carbon consumption. Our model simulates more intense global warming of 3.5°C and +470 ppmv for a lower gas release compared to that found by Tobin et al. (2017) (28,000 $GtCO_2$ and 6800 $GtSO_2$).

4.3 The K-Pg Calcareous Plankton Diversity Conundrum

The simulated biomass of calcifying and noncalcifying plankton (Fig. 9d) clearly captured the palaeontological pattern of a more important turnover of calcareous plankton (calcareous nannoplankton and planktic foraminifera) in comparison to siliceous and organic plankton (diatoms and dinoflagellates; e.g. Macleod et al., 1997). This difference in plankton type response to the environmental perturbation clearly lies in the carbonate system and pH degradation, which is more detrimental for calcifying organisms.

Unfortunately, quantitative and semi-quantitative studies on calcareous nannofossil accumulation rates show no decrease before the K-Pg boundary (Bernaola and Monechi, 2007; Henriksson, 1996; Thibault et al., 2016), suggesting that the calcareous nannoplankton productivity (i.e., organic production by calcareous nannoplankton approximated by the accumulation rate of calcareous nannofossil) was not affected by the environmental changes (pH, $\Omega_{calcite}$, and SST) induced by the onset of Deccan Traps Phase 2. On the other hand, the mass extinction event in relation with the Chicxulub impact clearly decreased the calcareous nannoplankton productivity (Bernaola and Monechi, 2007; Henriksson, 1996; Hull et al., 2011). This singular feature of nannofossils leads the authors to conclude that the Chicxulub impact has a more important influence than the Deccan Traps activity (e.g. Bernaola and Monechi, 2007; Bown, 2005; Gardin, 2002).

This apparent discrepancy between nannoplankton fossils and our model runs may be explainedby Fig.9e. According to these results, the Deccan traps should be responsible of the

collapse of primary producers while the abrupt short-lived acidification caused by the Chicxulub impact may explain the severity of the extinction among pelagic calcifying species.

4.4 The K-Pg Mass Extinction

With the K-Pg mass extinction, a collapse of the organic flux from the surface to the deep sea is described due to the decrease in plankton organic production (Strangelove Ocean Hypothesis; Zachos et al., 1989). More recently, a reduction of export of production to the seafloor by a change in organic matter recycling was proposed (Living Ocean Hypothesis; D'Hondt et al., 1998). Nevertheless, these studies were challenged by recent findings. Indeed, the benthic foraminifera did not suffer significantly from the mass extinction event (Alegret et al., 2012; Kaiho, 1992), whereas the organic abundance of algal steranes and bacterial hopanes alongside the recovery of the $\delta^{13}C_{org}$ and $\delta^{15}N_{org}$ ratio would suggest a brief (less than a century) reduction in the algal primary productivity (Sepúlveda et al., 2009). A primary productivity proxy, the biogenic barium accumulation rates would suggest a more complex pattern: on one hand, a rapid recovery to no effect in the Central Pacific Ocean or neritic regions of the Atlantic Ocean and, on the other hand, a depressed organic flux in the Southern Ocean, Indian Ocean, and northeast and southwest Atlantic Ocean (Hull et al., 2011).

Our simulations propose some plausible explanations for this regional variability. Indeed, the Deccan Traps induced less important disturbances for calcifying organisms living in the neritic zone than for species living in the open ocean, with the bottom water becoming more aggressive towards carbonate sediments. For the organic matter, the increase in the mean concentration of nutrients in the ocean over the course of the Deccan Traps may enhance the spatial pattern of the primary productivity in the surface ocean. In most regions, dramatic disturbances should lead to a collapse in the organic flux, but restricted areas where upwelling carried an abundant supply of

690 nutrients to the surface may remain relatively unaffected, with the load of nutrients overcoming the low efficiency to synthesise organic matter.

Among the biologic oceanic community, the mass extinction event has not affected all the groups the same way (Macleod et al., 1997). The coccolithophores and associated *incertae sedis*, altogether defined as calcareous nannoplankton, were particularly affected by the mass extinction 695 event with a loss of 93% of the diversity (Bown, 2005), corresponding to the most important diversity loss of this group since its first occurrence in the Late Triassic (Bown et al., 2004). The pattern of this turnover is particularly interesting. Although the diversity loss seems instantaneous on the geological scale, before the K-Pg boundary, the species richness and relative abundances fluctuate in relation to climatic changes at the end of the Maastrichtian. Most notably, the episode of 700 warming, lasting ~200 to 250 kyrs before the K-Pg boundary, has induced an increase in relative abundance of warm-water species, extending the latitudinal range of presence of those species, and was marked by a slight decrease in species richness (Thibault et al., 2016; Thibault and Husson, 2016).

This global warming seems to be associated with the beginning of emplacement of Deccan 705 Traps Phase 2 (Petersen et al., 2016; Thibault and Husson, 2016). Nevertheless, as noted by Thibault et al. (2015), those changes in species richness are relatively weak compared to the diversity and absolute decrease in abundance of calcareous nannofossils in the sediment at the K-Pg boundary (Bernaola and Monechi, 2007; Henriksson, 1996; Hull et al., 2011).

Immediately following the mass extinction, the calcareous nannoplankton community is still 710 dominated by the Cretaceous survivor taxa, which is rapidly replaced by the newly evolving Paleogene species (e.g. Bown, 2005). The switch in the community is associated with a decrease in the size of the coccoliths. The broad pattern is the loss of large Cretaceous species, which are replaced by smaller Paleogene species (Herrmann and Thierstein, 2012). Along with the absolute abundance decrease, this exacerbates the decrease in the carbonate accumulation rate. Nevertheless, 715 in detail, this pattern is challenged by the rapid occurrence in the Paleogene of large coccolith

(Bernaola and Monechi, 2007; Bown, 2005).The Cretaceous survivors are supposed to be r-strategist species (opportunistic), which are more frequently in high latitudes and neritic environments (Bown, 2005). Those species were more likely to survive a mass extinction event because of their capacity to live in unstable environments with changes in temperature, nutrient concentration, or even $\Omega_{calcite}$ on a short time scale (days, seasons, or years).

Looking at all of these studies, if some aspects of our results are in accordance with the observed palaeontological pattern, our initial assumptions appear still too simple to capture the complexity of the patterns of K-Pg extinction. Consequently, we highlight in the following section the limitations of this study to present the future improvements.

5. Limitations

Our simulations provide an overview of possible patterns of marine primary productivity and biodiversity collapse in response to climate changes and oceanic acidification during a short window (200 kyrs) of the K-Pg transition (~1 M yrs). Our simulations suggest that emissions of SO_2 and CO_2 are first-order triggers of the K-Pg environmental crisis. Considering that short-term processes reveal that the initial perturbation (gas loads of CO_2 and SO_2) may be amplified by two major factors: 1) the type of eruption over the course of 200 kyrs and 2) the inherent biological parameters of marine organisms. Unfortunately, the time computation has led us to limit the number of factors tested. To advise the reader about implications of these choices, the cautions are briefly presented with respect to the limitations of this study.

To assess the potential effect of the Deccan Traps, we conservatively assume that 3.4 Tg of SO_2 and 14 Tg of CO_2 were degassed for every cubic kilometre of erupted lava. These values are held constant over 200 kyrs. With this approach, we omitted 1 Tg of chlorine per cubic kilometre yield by the Traps (Self et al., 2008). In addition, eruption parameters, such as the effusion rate and tempo, have been considered important to explain environmental effects (Rader et al., 2017). Unfortunately, the lack of information about these parameters has led us to build the eruptive

sequence using a stochastic approach. Despite the development of a pulse-like emission, the absence of a realistic degassing scenario at the K-Pg boundary implies that major environmental features occurring before or after the Deccan Traps cannot be captured (i.e., pre-event warming accompanied by the rise of *M. Murus*; Thibault et al., 2017, the post-Traps overshoot or the absence of a progressive warming 100 kyrs before the K-Pg boundary).

In addition, we addressed sensitivity to climate change by computing inherent parameters with random functions (temperature and pH dependence), without considering a species distribution model or the ocean dynamics. Consequently, the presented results are model-dependent. The primary producer collapse is driven by the set of assessed species. To balance the lack of data to establish the tolerance patterns of species, only simulations including a high number of species (1000 or more) and/or different sets of marine biospheres would be more accurate to capture all patterns recorded in the fossil database. The K-Pg boundary is well known for extinctions of marine species occupying the upper levels of the food chain, such as ammonites, belemnites, or marine reptiles. This study does not include any predator-prey model. In the absence of such links, we cannot explore potential extinctions of consumers due to cascading effects in the food web. This aspect is beyond the scope of this study, but this feedback should be tested in future models to determine why calcareous plankton were more severely affected by the mass extinction event than other calcareous benthic organisms.

The simple model developed here to describe oceanic primary productivity is not yet an ecological model. However, for the first time in a long-term climate-carbon model, it introduces a retroaction between marine biodiversity and the long-term evolution of biogeochemical cycles. This study introduces the development of more complex trophic chains featuring several levels of consumers.

Regarding the Chixculub impact, we do not explicitly consider the change in the light influx (i.e impact winter assumption by blocking out of sunlight) because marine organisms may present tolerance to a decline of light flux by increasing the size of organic structure absorbing photons

(Geider et al. 1997). Consequently, the change of light influx has been considered by computing the primary productivity as a function of SST (see section 2.1). This assumption is based on measurements of photosynthetic rates derived from satellites (Behrenfeld and Falkowski, 1997 - validity range -1 to 29°C).

Finally, we cannot clearly assess the K-Pg transition without more precisely exploring processes occurring over continents. Traces of acidification in lacustrine sediments (Font et al., 2016) and strong weathering related to volcanic pulses (Gertsch et al., 2011) suggest that the neutralisation reaction is not verified everywhere (i.e., sulphuric acid reacting with limestone), as defended by Maruoka and Koeberl (2003) and supported by the very low extinction rate of freshwater vertebrates (Sheehan and Fastovsky, 1992). Consequently, very strong acidification may have occurred in rivers or restricted zones of the coastal ocean. In addition, evidence of very drastic climate changes over continents (Tobin et al., 2014) may also enhance extinction rates in the continental domain. Continental species should disappear more rapidly than marine organisms.

6. Conclusion

Using a coupled biodiversity-climate-carbon numerical model (ECO-GEOCLIM), we explored the triggering mechanisms of extinctions through the K-Pg boundary by quantifying the environmental effects on primary productivity, biomass, and biodiversity. We discovered two plausible pathways responsible for the K-Pg extinction. i) Due to the load of sulfate aerosols formed by the released of sulfur (by the meteorite or by volcanic pulses), the abrupt cooling event decreases the consumption of the atmospheric carbon while the emissions are enhanced. Consequently the accumulation of atmospheric carbon is amplified and all the processes associated to inorganic carbon in the ocean are heavily perturbed (pH, alkalinity budget, calcite saturation...). ii) By the introduction of primary producers dependent on pH and sea surface temperatures, marine biomass declines due to oceanic

disturbances despite the presence of nutrients. In response to the low percentage of residual living biomass, the burial of organic matter is weakened, and the atmospheric carbon dioxide increases.

Assuming a 10-km impactor, oceanic disturbances are characterised by an intense and brief cooling, spanning 10 years, driven by atmospheric S-aerosols. This brief cooling phase leads to a transient shutdown of the primary productivity. Whatever the pre-perturbation oceanic conditions (Cretan or Neritan), surface oceans stay saturated with calcite ($\Omega_{calcite}$ ~ 1.3) despite acidification (ΔpH -0.15) in open or coastal areas. Biotic losses for primary producers do not exceed 20%, while ocean biomass is reduced by 60% (40%) for calcifying (noncalcifying) species. The discrepancy between biodiversity and biomass results from a collapse of a few calcifying species, accounting for most of the biomass.

When the emplacement of the Deccan Traps is considered, the surface ocean pH decreases by 0.2, from 8.0 to 7.8, while the deep ocean pH drops by 0.4 (from 7.8 to 7.4). This marine acidification is caused by the combination of long-term acidification triggered by the CO_2 released by the Deccan Traps, coupled with short-term acidification resulting from the rainout of sulphate aerosols (Chicxulub). Succession of climate changes and marine acidification produces a dramatic decrease of the oceanic biomass of calcifying species. Given the assumed sensitivity of marine organisms to abiotic factors (ΔSST and ΔpH), the biodiversity of calcifying species drops by about 80%, while the biodiversity of noncalcifying species is reduced by about 60%. This simulated mass extinction is supposed to be driven by the eruption of the Deccan Traps and amplified by the combination of CO_2 and SO_2 interplays and a sluggish organic carbon cycle. However, abrupt and short-lived acidification caused by the Chicxulub impact may explain the severity of extinctions among pelagic calcifying species.

These findings may help us understand how an initial perturbation can be amplified, leading to mass extinction, but some cautions should be heeded. Despite a lack of data about sensitivity to abiotic factors of fossil species, all results presented in this study remain model-dependent because only one set of theoretical species has been used, with all of them being primary producers.

Moreover, these short-lived processes, acting as amplifying factors, become efficient only if the degassing is intense enough to overcome the silicate weathering buffering activity. Consequently, in the absence of a degassing scenario running over the whole K-Pg boundary period (~1 Ma), the present study is not able to capture some of the major features recorded before or in the aftermath of the Deccan main phase.

acknowledgment :

CCRT, INSU Tellus SYSTER 2016 to BSM and GlH.

Table 1.

Experimental set-up. Columns from left to right are: i) tested event: A for Asteroid scenario, D for Deccan traps and/or traps (both are defined as CO_2 and SO_2 emitted), ii) ocean state corresponds to carbonate cycle mode assumed (calcifying phytoplankton species versus other primary producer species), iii) biological feed-backs column indicates if species depend (or not) on abiotic environmental factors. D-Cretan-3 experiment presents a case where all other environmental factors remain efficient excepted seawater pH. Eruption parameters for the Deccan traps have been explored. D-Cretan-linear has been performed with a linear degassing – loads of CO_2 and SO_2 held constant. D-Cretan-noSO_2 loads of CO_2 held constant, SO_2 emitted = 0. D-Cretan-longdegaz: load of gases held constant however the temporal spacing of eruptions has been doubled, which means that the length of the simulation is close to 400 kyrs.

It is noteworthy that all runs are performed with late Maastrichtian boundary conditions and a large number of species for primary producers (nveg=50). Reference runs (whatever ocean conditions) correspond to a carbon-climate equilibrium of pCO_2 ~230ppmv.

Run	Tested geological event(s)	Ocean state	biological feed-backs
Ref-Cretan	None	Cretan	yes
Ref-Neritan	None	Neritan	yes
A-Cretan-1	Asteroid (10 km size)	Cretan	yes
A-Cretan-2	Asteroid (10 km size)	Cretan	no
A-Neritan	Asteroid (10 km size)	Neritan	yes
D-Cretan-1	Deccan traps	Cretan	yes
D-Cretan-2	Deccan traps	Cretan	no
D-Cretan-3	Deccan traps	Cretan	*p*H effect cut-off
D-Cretan-linear	Deccan traps (linear degassing)	Cretan	yes
D-Cretan-noSO2	Deccan traps (no SO2 emitted)	Cretan	yes
D-Cretan-longdegaz	Deccan traps (temporal spacing of eruptions has been doubled)	Cretan	yes
D-Neritan	Deccan traps	Neritan	yes
AD-Cretan-1	Asteroid+Deccan traps	Cretan	yes
AD-Cretan-1bis	Asteroid+Deccan traps (time-coincidence = 10 kyrs)	Cretan	yes
AD-Cretan-2	Asteroid+Deccan traps	Cretan	no
AD-Neritan	Asteroid+Deccan traps	Neritan	yes

845 **references :**

Alegret, L., Thomas, E., Lohmann, K.C., 2012. End-Cretaceous marine mass extinction not caused by productivity collapse. Proc. Natl. Acad. Sci. 109, 728–732.

Barrera, E., Savin, S.M., 1999. Evolution of late Campanian-Maastrichtian marine climates and oceans. Spec. Pap.-Geol. Soc. Am. 245–282.

Bernaola, G., Monechi, S., 2007. Calcareous nannofossil extinction and survivorship across the Cretaceous- Paleogene boundary at Walvis Ridge (ODP Hole 1262C, South Atlantic Ocean). Palaeogeogr. Palaeoclimatol. Palaeoecol. 255, 132–156.

Besse, J., Courtillot, V., 2002. Apparent and true polar wander and the geometry of the geomagnetic field over the last 200 Myr. J. Geophys. Res. Solid Earth 107.

Bown, P., 2005. Selective calcareous nannoplankton survivorship at the Cretaceous-Tertiary boundary. Geology 33, 653–656. https://doi.org/10.1130/G21566AR.1

Bown, P.R., Lees, J.A., Young, J.R., 2004. Calcareous nannoplankton evolution and diversity through time, in: Coccolithophores. Springer, Berlin, Heidelberg, pp. 481–508. https://doi.org/10.1007/978-3-662-06278-4_18

Brady, P.V., Gíslason, S.R., 1997. Seafloor weathering controls on atmospheric CO2 and global climate. Geochim. Cosmochim. Acta 61, 965–973. https://doi.org/10.1016/S0016-7037(96)00385-7

Brugger, J., Feulner, G., Petri, S., 2017. Baby, it's cold outside: Climate model simulations of the effects of the asteroid impact at the end of the Cretaceous. Geophys. Res. Lett. 44, 419–427.

Caldeira, K., Rampino, M.R., 1990. Carbon dioxide emissions from Deccan volcanism and a K/T boundary greenhouse effect. Geophys. Res. Lett. 17, 1299–1302.

Charnay, B., Hir, G.L., Fluteau, F., Forget, F., Catling, D.C., 2017. A warm or a cold early Earth? New insights from a 3-D climate-carbon model. Earth Planet. Sci. Lett. 474, 97–109. https://doi.org/10.1016/j.epsl.2017.06.029

Chenet, A.L., Courtillot, V., Fluteau, F., Gérard, M., Quidelleur, X., Khadri, S.F.R., Subbarao, K.V., Thordarson, T., 2009. Determination of rapid Deccan eruptions across the Cretaceous-Tertiary boundary using paleomagnetic secular variation : 2. Constraints from analysis of eight new sections and synthesis for a 3500-m-thick composite section. J. Geophys. Res. - Solid Earth 114. https://doi.org/10.1029/2008jb005644

Chenet, A.-L., Fluteau, F., Courtillot, V., Gérard, M., Subbarao, K.V., 2008. Determination of rapid

Deccan eruptions across the Cretaceous-Tertiary boundary using paleomagnetic secular variation: Results from a 1200-m-thick section in the Mahabaleshwar escarpment. J. Geophys. Res. Solid Earth 113.

Chenet, A.-L., Quidelleur, X., Fluteau, F., Courtillot, V., Bajpai, S., 2007. 40K–40Ar dating of the Main Deccan large igneous province: Further evidence of KTB age and short duration. Earth Planet. Sci. Lett. 263, 1–15.

Collins, G.S., Melosh, H.J., Marcus, R.A., 2005. Earth impact effects program: A web-based computer program for calculating the regional environmental consequences of a meteoroid impact on Earth. Meteorit. Planet. Sci. 40, 817–840.

Coogan, L.A., Dosso, S.E., 2015. Alteration of ocean crust provides a strong temperature dependent feedback on the geological carbon cycle and is a primary driver of the Sr-isotopic composition of seawater. Earth Planet. Sci. Lett. 415, 38–46. https://doi.org/10.1016/j.epsl.2015.01.027

Courtillot, V., Besse, J., Vandamme, D., Montigny, R., Jaeger, J.-J., Cappetta, H., 1986. Deccan flood basalts at the Cretaceous/Tertiary boundary? Earth Planet. Sci. Lett. 80, 361–374. https://doi.org/10.1016/0012-821X(86)90118-4

Courtillot, V., Fluteau, F., 2014. A review of the embedded time scales of flood basalt volcanism with special emphasis on dramatically short magmatic pulses. Geol. Soc. Am. Spec. Pap. 505, SPE505–15.

Courtillot, V.E., Renne, P.R., 2003. On the ages of flood basalt events. Comptes Rendus Geosci. 335, 113–140. https://doi.org/10.1016/S1631-0713(03)00006-3

Dercourt, J., Ricou, L.E., Vrielynck, B., coopération, I. français du pétrole B. d'études industrielles et de, 1993. Atlas Tethys palaeoenvironmental maps. Paris : [Gauthier-Villars] : Diffusion-CCGM.

Dessert, C., Dupré, B., François, L.M., Schott, J., Gaillardet, J., Chakrapani, G., Bajpai, S., 2001. Erosion of Deccan Traps determined by river geochemistry: impact on the global climate and the 87Sr/86Sr ratio of seawater. Earth Planet. Sci. Lett. 188, 459–474. https://doi.org/10.1016/S0012-821X(01)00317-X

D'hondt, S., Donaghay, P., Zachos, J.C., Luttenberg, D., Lindinger, M., 1998. Organic carbon fluxes and ecological recovery from the Cretaceous-Tertiary mass extinction. Science 282, 276–279.

D'Hondt, S., Pilson, M.E.Q., Sigurdsson, H., Hanson, A.K., Carey, S., 1994. Surface-water acidification and extinction at the Cretaceous-Tertiary boundary. Geology 22, 983–986. https://doi.org/10.1130/0091-7613(1994)022<0983:SWAAEA>2.3.CO;2

Donnadieu, Y., Goddéris, Y., Bouttes, N., 2009. Exploring the climatic impact of the continental vegetation on the Mezosoic atmospheric CO2 and climate history. Clim. Past 5, 85–96.

Donnadieu, Y., Goddéris, Y., Pierrehumbert, R., Dromart, G., Fluteau, F., Jacob, R., 2006. A GEOCLIM simulation of climatic and biogeochemical consequences of Pangea breakup. Geochem. Geophys. Geosystems 7, Q11019. https://doi.org/10.1029/2006GC001278

Font, E., Carlut, J., Rémazeilles, C., Mather, T.A., Nédélec, A., Mirão, J., Casale, S., 2017. End-Cretaceous akaganéite as a mineral marker of Deccan volcanism in the sedimentary record. Sci. Rep. 7, 11453. https://doi.org/10.1038/s41598-017-11954-y

Font, E., Ponte, J., Adatte, T., Fantasia, A., Florindo, F., Abrajevitch, A., Mirão, J., 2016. Tracing acidification induced by Deccan Phase 2 volcanism. Palaeogeogr. Palaeoclimatol. Palaeoecol., Impact, Volcanism, Global changes and Mass Extinctions 441, 181–197. https://doi.org/10.1016/j.palaeo.2015.06.033

Foster, G., Royer, D. and Lunt, D., 2017, Future climate forcing potentially without precedent in the last 420 million years, *Nature Communications* volume 8, Article number: 14845

Ganino, C., Arndt, N.T., 2009. Climate changes caused by degassing of sediments during the emplacement of large igneous provinces. Geology 37, 323–326.

Gardin, S., 2002. Late Maastrichtian to early Danian calcareous nannofossils at Elles (Northwest Tunisia). A tale of one million years across the K–T boundary. Palaeogeogr. Palaeoclimatol. Palaeoecol. 178, 211–231.

Geider, R., MacIntyre, H., Kana, T. 1997, Dynamic model of phytoplankton growth and acclimation: Responses of the balanced growth rate and the chlorophyll a:carbon ratio to light, nutrient-limitation and temperature, Marine Ecology Progress Series 148(1-3):187-200 doi: 10.3354/meps148187

Gertsch, B., Keller, G., Adatte, T., Garg, R., Prasad, V., Berner, Z., Fleitmann, D., 2011. Environmental effects of Deccan volcanism across the Cretaceous–Tertiary transition in Meghalaya, India. Earth Planet. Sci. Lett. 310, 272–285. https://doi.org/10.1016/j.epsl.2011.08.015

Goddéris, Y., Joachimski, M.M., 2004. Global change in the Late Devonian: modelling the Frasnian–Famennian short-term carbon isotope excursions. Palaeogeogr. Palaeoclimatol. Palaeoecol. 202, 309–329. https://doi.org/10.1016/S0031-0182(03)00641-2

Gough, D.O., 1981. Solar interior structure and luminosity variations, in: Physics of Solar Variations. Springer, pp. 21–34.

Guidry, M.W., Mackenzie, F.T., 2000. Apatite weathering and the Phanerozoic phosphorus cycle.

Geology 28, 631–634. https://doi.org/10.1130/0091-7613(2000)28<631:AWATPP>2.0.CO;2

Hay, W.W., 2004. Carbonate fluxes and calcareous nannoplankton, in: Coccolithophores. Springer, pp. 509–528.

Henehan, M.J., Hull, P.M., Penman, D.E., Rae, J.W.B., Schmidt, D.N., 2016. Biogeochemical significance of pelagic ecosystem function: an end-Cretaceous case study. Phil Trans R Soc B 371, 20150510. https://doi.org/10.1098/rstb.2015.0510

Henriksson, A.S., 1996. Calcareous nannoplankton productivity and succession across the Cretaceous–Tertiary boundary in the Pacific (DSDP Site 465) and Atlantic (DSDP Site 527) Oceans. Cretac. Res. 17, 451–477.

Herrmann, S., Thierstein, H.R., 2012. Cenozoic coccolith size changes—Evolutionary and/or ecological controls? Palaeogeogr. Palaeoclimatol. Palaeoecol. 333, 92–106.

Hull, P.M., Norris, R.D., Bralower, T.J., Schueth, J.D., 2011. A role for chance in marine recovery from the end-Cretaceous extinction. Nat. Geosci. 4, 856.

Jacob, R.L., 1997. Low frequency variability in a simulated atmosphere-ocean system. PhD Thesis 1698.

Kaiho, K., 1992. A low extinction rate of intermediate-water benthic foraminifera at the Cretaceous/Tertiary boundary. Mar. Micropaleontol. 18, 229–259.

Kaminski, E., Tait, S., Ferrucci, F., Martet, M., Hirn, B., Husson, P., 2011. Estimation of ash injection in the atmosphere by basaltic volcanic plumes: The case of the Eyjafjallajökull 2010 eruption. J. Geophys. Res. Solid Earth 116.

Keller, G., 2014. Deccan volcanism, the Chixculub impact, and the end-Cretaceous mass extinction : Coincidence ? Cause and effect ? Volcanism, Impacts, and Mass Extinctions: Causes and Effects. Geological Society of America, Boulder.

Kiessling, W., Flügel, E., Golonka, J., 2000. Fluctuations in the carbonate production of Phanerozoic reefs. Geol. Soc. Lond. Spec. Publ. 178, 191–215.

Kiessling, W., Flügel, E., Golonka, J.A.N., 2003. Patterns of Phanerozoic carbonate platform sedimentation. Lethaia 36, 195–225.

Krissansen-Totton, J., Catling, D.C., 2017. Constraining climate sensitivity and continental versus seafloor weathering using an inverse geological carbon cycle model. Nat. Commun. 8, 15423. https://doi.org/10.1038/ncomms15423

Lefebvre, V., Donnadieu, Y., Goddéris, Y., Fluteau, F., Hubert-Théou, L., 2013. Was the Antarctic

glaciation delayed by a high degassing rate during the early Cenozoic? Earth Planet. Sci. Lett. 371–372, 203–211. https://doi.org/10.1016/j.epsl.2013.03.049

Li, L., Keller, G., 1998. Abrupt deep-sea warming at the end of the Cretaceous. Geology 26, 995–998.

Macleod, N., Rawson, P.F., Forey, P.L., Banner, F.T., Boudagher-Fadel, M.K., Bown, P.R., Burnett, J.A., Chambers, P., Culver, S., Evans, S.E., Jeffery, C., Kaminski, M.A., Lord, A.R., Milner, A.C., Milner, A.R., Morris, N., Owen, E., Rosen, B.R., Smith, A.B., Taylor, P.D., Urquhart, E., Young, J.R., 1997. The Cretaceous-Tertiary biotic transition. J. Geol. Soc. 154, 265–292. https://doi.org/10.1144/gsjgs.154.2.0265

Martin, R.E., 1995. Cyclic and secular variation in microfossil biomineralization: clues to the biogeochemical evolution of Phanerozoic oceans. Glob. Planet. Change 11, 1–23.

Martinez, I., Deutsch, A., Schärer, U., Ildefonse, P., Guyot, F., Agrinier, P., 1995. Shock recovery experiments on dolomite and thermodynamical calculations of impact induced decarbonation. J. Geophys. Res. Solid Earth 100, 15465–15476.

Maruoka, T., Koeberl, C., 2003. Acid-neutralizing scenario after the Cretaceous-Tertiary impact event. Geology 31, 489–492.

Miles, G.M., Grainger, R.G., Highwood, E.J., 2004. The significance of volcanic eruption strength and frequency for climate. Q. J. R. Meteorol. Soc. 130, 2361–2376.

Molina, E., Arenillas, I., Arz, J.A., 1998. Mass extinction in planktic Foraminifera at the Cretaceous/Tertiary boundary in subtropical and temperate latitudes. Bull. Société Géologique Fr. 169, 351–363.

Mussard, M., Le Hir, G., Fluteau, F., Lefebvre, V. and Goddéris, Y., 2014. Modeling the carbon-sulfate interplays in climate changes related to the emplacement of continental flood basalts, Volcanism, Impacts, and Mass Extinctions: Causes and Effects. Geological Society of America, , pp. 339-352.

Ohno, S., Kadono, T., Kurosawa, K., Hamura, T., Sakaiya, T., Shigemori, K., Hironaka, Y., Sano, T., Watari, T., Otani, K., Matsui, T., Sugita, S., 2014. Production of sulphate-rich vapour during the Chicxulub impact and implications for ocean acidification. Nat. Geosci. 7, 279. https://doi.org/10.1038/ngeo2095

Oliva, P., Viers, J., Dupré, B., 2003. Chemical weathering in granitic environments. Chem. Geol. 202, 225–256.

Petersen, S.V., Dutton, A., Lohmann, K.C., 2016. End-Cretaceous extinction in Antarctica linked to both Deccan volcanism and meteorite impact via climate change. Nat. Commun. 7, 12079. https://doi.org/10.1038/ncomms12079

Pierazzo, E., Hahmann, A.N., Sloan, L.C., 2003. Chicxulub and Climate: Radiative Perturbations of Impact-Produced S-Bearing Gases. Astrobiology 3, 99–118. https://doi.org/10.1089/153110703321632453

Pierazzo, E., Kring, D.A., Melosh, H.J., 1998. Hydrocode simulation of the Chicxulub impact event and the production of climatically active gases. J. Geophys. Res. Planets 103, 28607–28625.

Prinn, R.G and Fegley, B., Bolide impacts, 1987. Acid rain, and biospheric trauams at the Cretaceous-Tertiary boundary. Earth and Planetary Science Letters, 83 (1987) 1 - 15

Punekar, J., Mateo, P., Keller, G., Keller, G., 2014. Effects of Deccan volcanism on paleoenvironment and planktic foraminifera: A global survey. Geol. Soc. Am. Spec. Pap. 505. https://doi.org/10.1130/2014.2505(04)

Quere, C.L., Harrison, S.P., Colin Prentice, I., Buitenhuis, E.T., Aumont, O., Bopp, L., Claustre, H., Cotrim Da Cunha, L., Geider, R., Giraud, X., 2005. Ecosystem dynamics based on plankton functional types for global ocean biogeochemistry models. Glob. Change Biol. 11, 2016–2040.

Renne, P.R., Deino, A.L., Hilgen, F.J., Kuiper, K.F., Mark, D.F., Mitchell, W.S., Morgan, L.E., Mundil, R., Smit, J., 2013. Time scales of critical events around the Cretaceous-Paleogene boundary. Science 339, 684–687.

Renne, P.R., Sprain, C.J., Richards, M.A., Self, S., Vanderkluysen, L., Pande, K., 2015. State shift in Deccan volcanism at the Cretaceous-Paleogene boundary, possibly induced by impact. Science 350, 76–78.

Robock, A., Ammann, C.M., Oman, L., Shindell, D., Levis, S., Stenchikov, G., 2009. Did the Toba volcanic eruption of 74 ka BP produce widespread glaciation? J. Geophys. Res. Atmospheres 114.

Royer D., 2006. CO_2-forced climate thresholds during the Phanerozoic, Geochimica et Cosmochimica Acta, 70(23), 5665-5675 doi.org/10.1016/j.gca.2005.11.031

Schmidt, A., Skeffington, R.A., Thordarson, T., Self, S., Forster, P.M., Rap, A., Ridgwell, A., Fowler, D., Wilson, M., Mann, G.W., Wignall, P.B., Carslaw, K.S., 2016. Selective environmental stress from sulphur emitted by continental flood basalt eruptions. Nat. Geosci. 9, 77. https://doi.org/10.1038/ngeo2588

Schöbel, S., de Wall, H., Ganerød, M., Pandit, M.K., Rolf, C., 2014. Magnetostratigraphy and

40Ar–39Ar geochronology of the Malwa Plateau region (Northern Deccan Traps), central western India: Significance and correlation with the main Deccan Large Igneous Province sequences. J. Asian Earth Sci. 89, 28–45.

Schoene, B., Samperton, K., Eddy, M., Keller, G., Adatte, T., Bowring, S., Khadri, S., GERTSCH, B., 2015. U-Pb geochronology of the Deccan Traps and relation to the end-Cretaceous mass extinction. Science 347, 182–184. https://doi.org/10.1126/science.aaa0118

Schoene, B., Eddy, M., Samperton, K., Keller,B., Keller, G., Adatte,T., Khadri, S. 2019, U-Pb constraints on pulsed eruption of the Deccan Traps across the end-Cretaceous mass extinction. *Science* 363, doi: 10.1126/science.aau2422

Self, S., 2006. The effects and consequences of very large explosive volcanic eruptions. Philos. Trans. R. Soc. Lond. Math. Phys. Eng. Sci. 364, 2073–2097.

Self, S., Blake, B., Sharma, K., Widdowson, M, Sephton, S. 2008, Sulfur and Chlorine in Late Cretaceous Deccan Magmas and Eruptive Gas Release, Sciences, 3195870):1654-7 doi :10.1126/science.1152830

Semtner, A.J., 1976. A Model for the Thermodynamic Growth of Sea Ice in Numerical Investigations of Climate. J. Phys. Oceanogr. 6, 379–389. https://doi.org/10.1175/1520-0485(1976)006<0379:AMFTTG>2.0.CO;2

Sepúlveda, J., Wendler, J.E., Summons, R.E., Hinrichs, K.-U., 2009. Rapid resurgence of marine productivity after the Cretaceous-Paleogene mass extinction. Science 326, 129–132.

Sheehan, P.M., Fastovsky, D.E., 1992. Major extinctions of land-dwelling vertebrates at the Cretaceous-Tertiary boundary, eastern Montana. Geology 20, 556–560.

Sitch, S., Smith, B., Prentice, I.C., Arneth, A., Bondeau, A., Cramer, W., Kaplan, J.O., Levis, S., Lucht, W., Sykes, M.T., 2003. Evaluation of ecosystem dynamics, plant geography and terrestrial carbon cycling in the LPJ dynamic global vegetation model. Glob. Change Biol. 9, 161–185.

Sprain, C., Renne, P., Vanderkluysen, L., Pande, K., Self, S., Mittal, T. 2019, The eruptive tempo of Deccan volcanism in relation to the Cretaceous-Paleogene boundary. *Science* 363, 866. doi: 10.1126/science.aav1446

Stanley, S.M., Hardie, L.A., 1998. Secular oscillations in the carbonate mineralogy of reef-building and sediment-producing organisms driven by tectonically forced shifts in seawater chemistry. Palaeogeogr. Palaeoclimatol. Palaeoecol. 144, 3–19.

Steuber, T., 2002. Plate tectonic control on the evolution of Cretaceous platform-carbonate

production. Geology 30, 259–262.

Thibault, N., Galbrun, B., Gardin, S., Minoletti, F., Le Callonnec, L., 2016. The end-Cretaceous in the southwestern Tethys (Elles, Tunisia): orbital calibration of paleoenvironmental events before the mass extinction. Int. J. Earth Sci. 105, 771–795.

Thibault, N., Husson, D., 2016. Climatic fluctuations and sea-surface water circulation patterns at the end of the Cretaceous era: Calcareous nannofossil evidence. Palaeogeogr. Palaeoclimatol. Palaeoecol. 441, 152–164.

Timmreck, C., 2012. Modeling the climatic effects of large explosive volcanic eruptions. Wiley Interdiscip. Rev. Clim. Change 3, 545–564.

Tobin, T.S., Bitz, C.M., Archer, D., 2017. Modeling climatic effects of carbon dioxide emissions from Deccan Traps volcanic eruptions around the Cretaceous–Paleogene boundary. Palaeogeogr. Palaeoclimatol. Palaeoecol., Mass Extinction Causality: Records of Anoxia, Acidification, and Global Warming during Earth's Greatest Crises 478, 139–148. https://doi.org/10.1016/j.palaeo.2016.05.028

Tobin, T.S., Wilson, G.P., Eiler, J.M., Hartman, J.H., 2014. Environmental change across a terrestrial Cretaceous-Paleogene boundary section in eastern Montana, USA, constrained by carbonate clumped isotope paleothermometry. Geology 42, 351–354.

Tyrrell, T., Merico, A., McKay, D.I.A., 2015. Severity of ocean acidification following the end-Cretaceous asteroid impact. Proc. Natl. Acad. Sci. 112, 6556–6561. https://doi.org/10.1073/pnas.1418604112

Vellekoop, J., Sluijs, A., Smit, J., Schouten, S., Weijers, J.W., Damsté, J.S.S., Brinkhuis, H., 2014. Rapid short-term cooling following the Chicxulub impact at the Cretaceous–Paleogene boundary. Proc. Natl. Acad. Sci. 111, 7537–7541.

Walker, L., Wilkinson, B.H., and Ivany, L.C. 2002.Continental Drift and Phanerozoic Carbonate Accumulation in Shallow-Shelf and Deep-Marine Settings. Journal of Geology 110(75-87), doi : 10.1086/324318

Wallmann, K., 2001. Controls on the cretaceous and cenozoic evolution of seawater composition, atmospheric CO2 and climate. Geochim. Cosmochim. Acta 65, 3005–3025. https://doi.org/10.1016/S0016-7037(01)00638-X

Ward, W.C., Keller, G., Stinnesbeck, W., Adatte, T., 1995. Yucatán subsurface stratigraphy: Implications and constraints for the Chicxulub impact. Geology 23, 873–876.

Wignall, P.B., 2001. Large igneous provinces and mass extinctions. Earth-Sci. Rev. 53, 1–33. https://doi.org/10.1016/S0012-8252(00)00037-4

Woelders, L., Vellekoop, J., Kroon, D., Smit, J., Casadío, S., Prámparo, M. B., Speijer, R. P. (2017). Latest Cretaceous climatic and environmental change in the South Atlantic region. Paleoceanography, 32(5), 466-483. doi: 10.1002/2016PA003007

Zachos, J.C., Arthur, M.A., Dean, W.E., 1989. Geochemical evidence for suppression of pelagic marine productivity at the Cretaceous/Tertiary boundary. Nature 337, 61.

Zeebe, R.E., Westbroek, P., 2003. A simple model for the CaCO3 saturation state of the ocean: The "Strangelove," the "Neritan," and the "Cretan" Ocean. Geochem. Geophys. Geosystems 4

Figure 1. Atmospheric carbon dioxide and surface seawater changes caused by Chicxulub impact.
Red curves are attributed to A-Cretan-1 case, black ones to A-Cretan-2.
Both simulations start from identical initial conditions : Ref-Cretan (pCO2 init ~230ppmv).

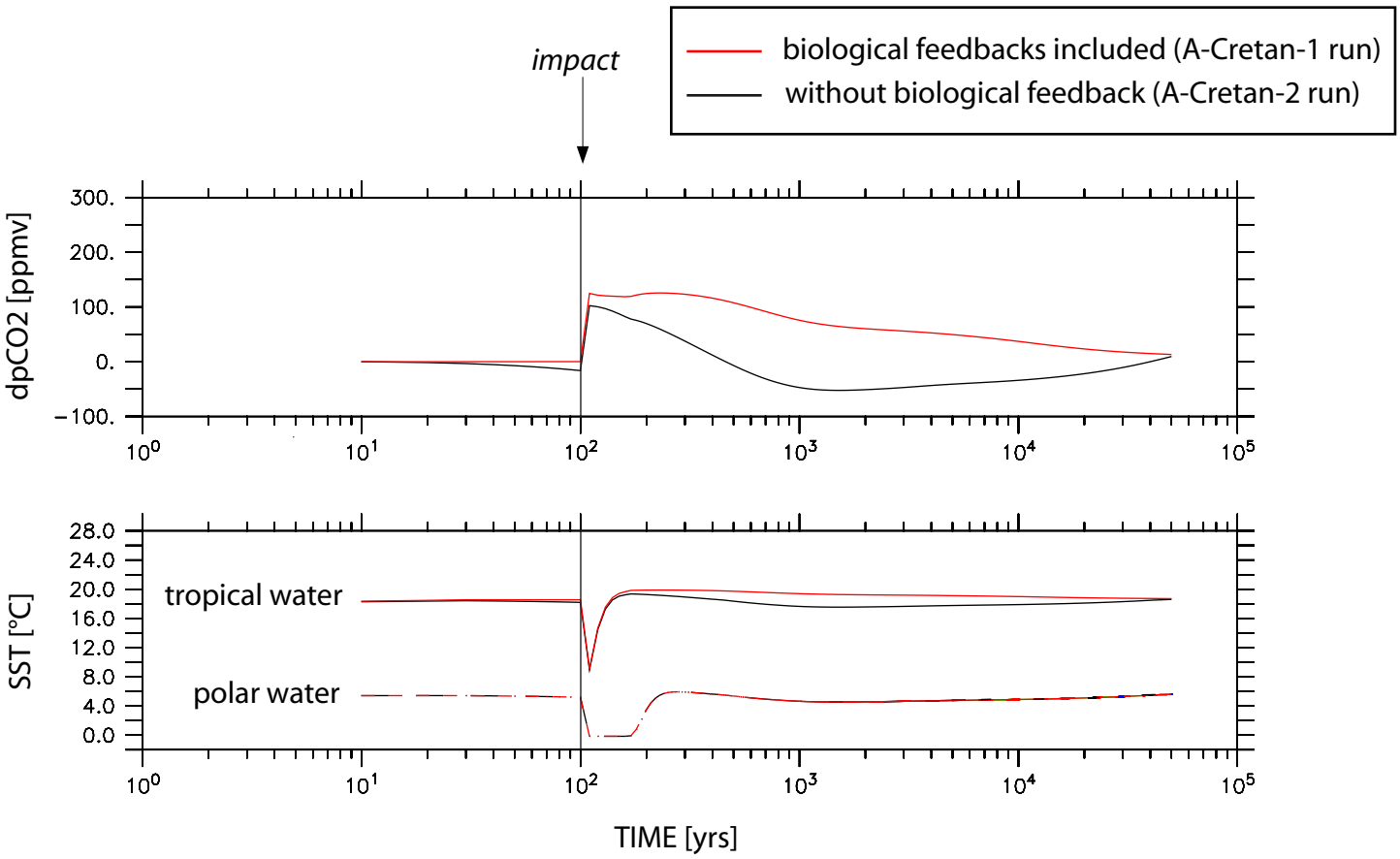

Figure 2. a) world wide primary productivity and b) phophorus content (surface ocean) simulated for the Chicxulub impact

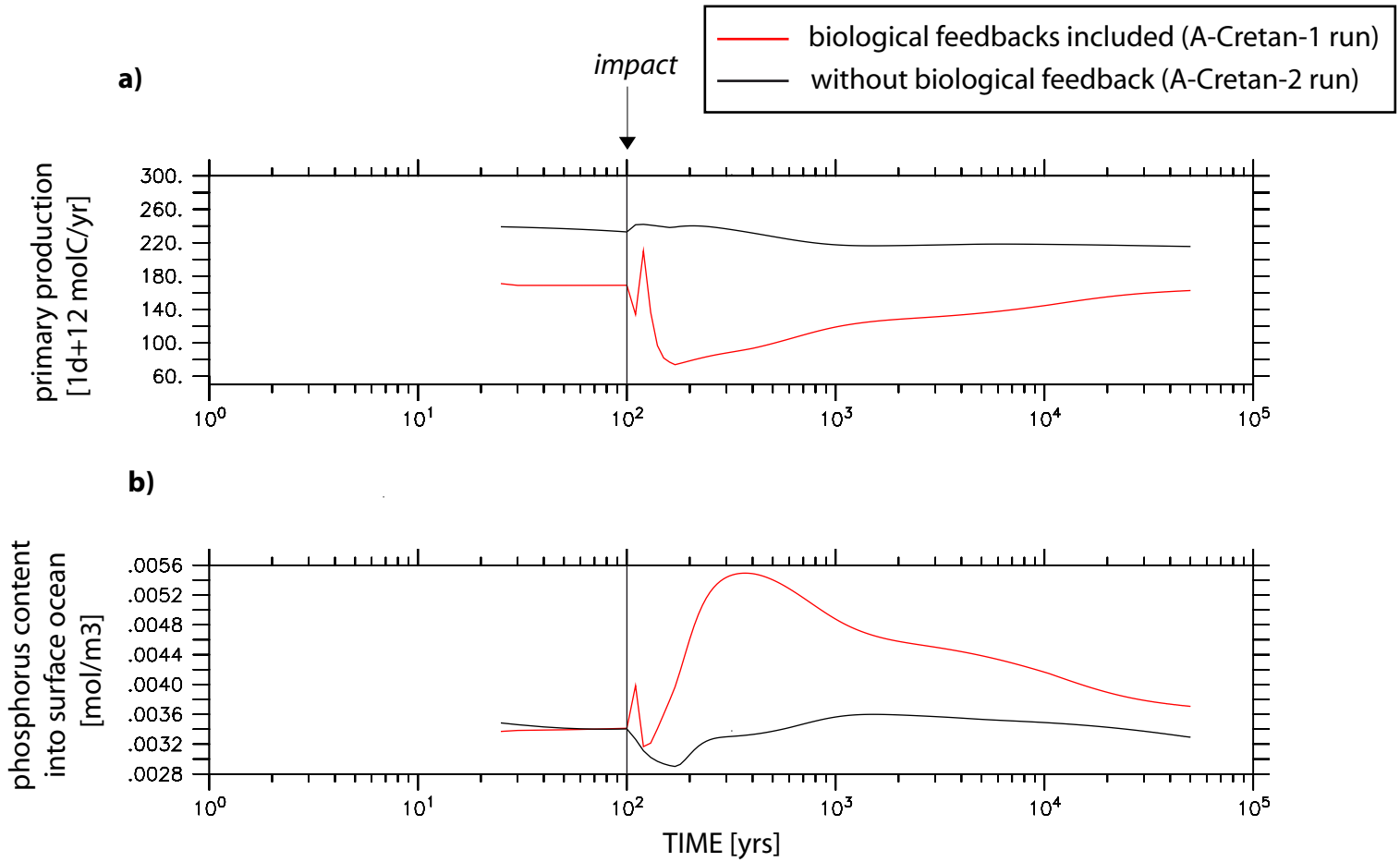

Figure 3: ocean perturbations induced by the Chicxulub impact.
2 states of ocean : Neritan (blue lines) versus Cretan (red lines), are considered.
*p*H evolutions simulated for **a)** surface versus deep ocean, **b)** open versus coastal ocean.
c) calcite saturation state for surface ocean compared to deep ocean.
d) carbonates precipitation changes for pelagic versus nereitic environment.
e) global alkalinity of the ocean compared to the coastal tropical ocean.

a) surface ocean (continous line) vs deep ocean (dashed line)

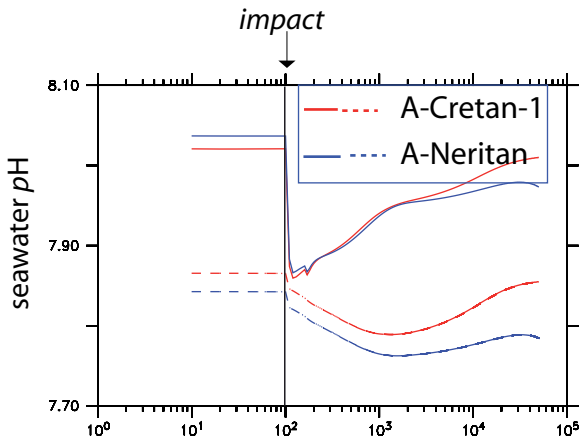

d) pelagic (thick line) vs neritic (thin line)

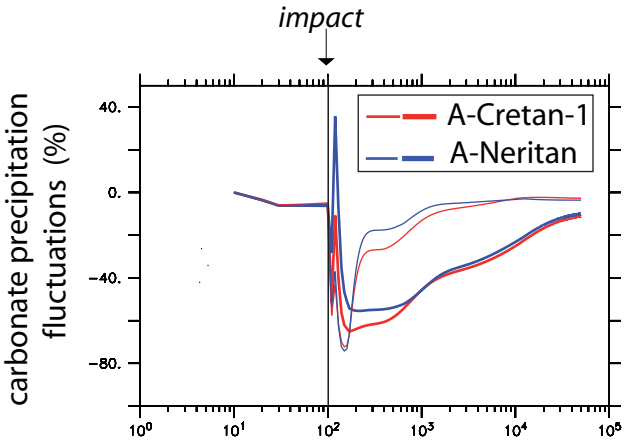

b) open ocean (continous line)
vs coastal ocean (dashed line)

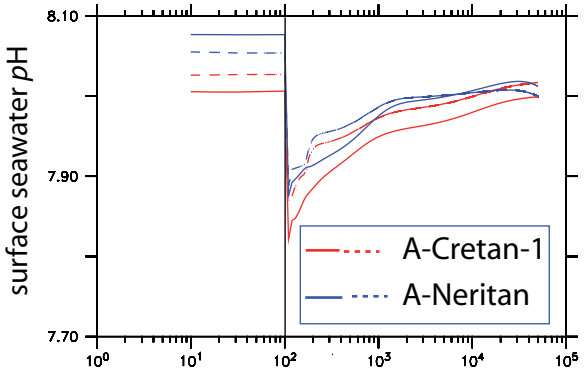

e) global alkalinity (black curve)
vs coastal ocean (red)

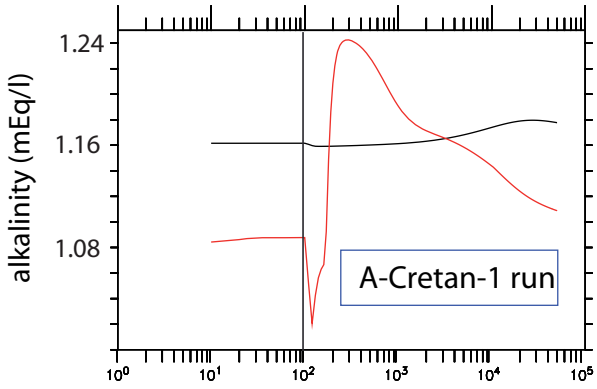

c) surface ocean (continous line)
vs deep water (dashed line)

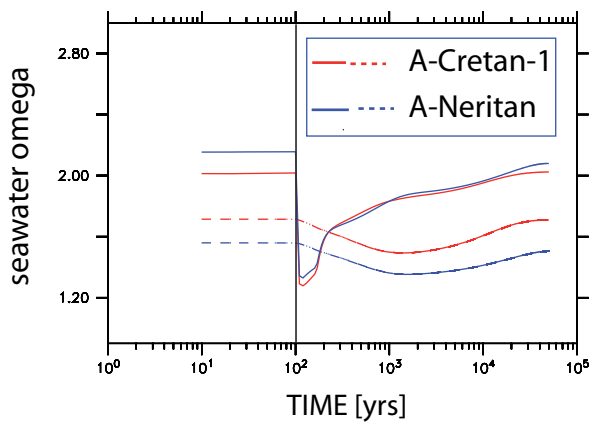

f) carbonates weathered (cw_0 =2.0 10^{12} molC/yr)
vs silicates (sw_0 = 5.3 10^{12} molC/yr)

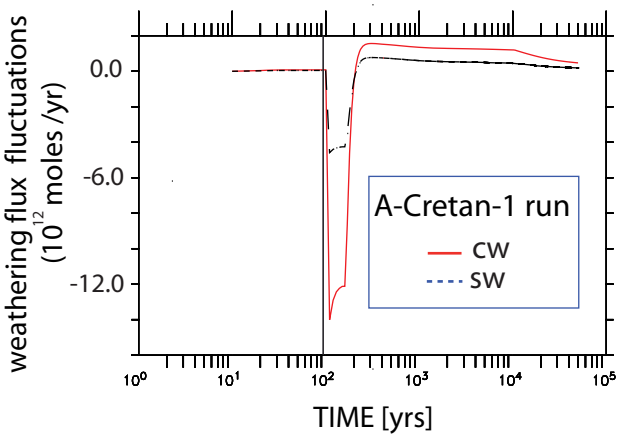

Figure 4. Biomass and mass extinction ratio(ME ratio) induced by the Chicxulub impact
a) for noncalcifying (upper panels) - coloured lines represent PFTs
b) calcifying primary producers (lower panels).

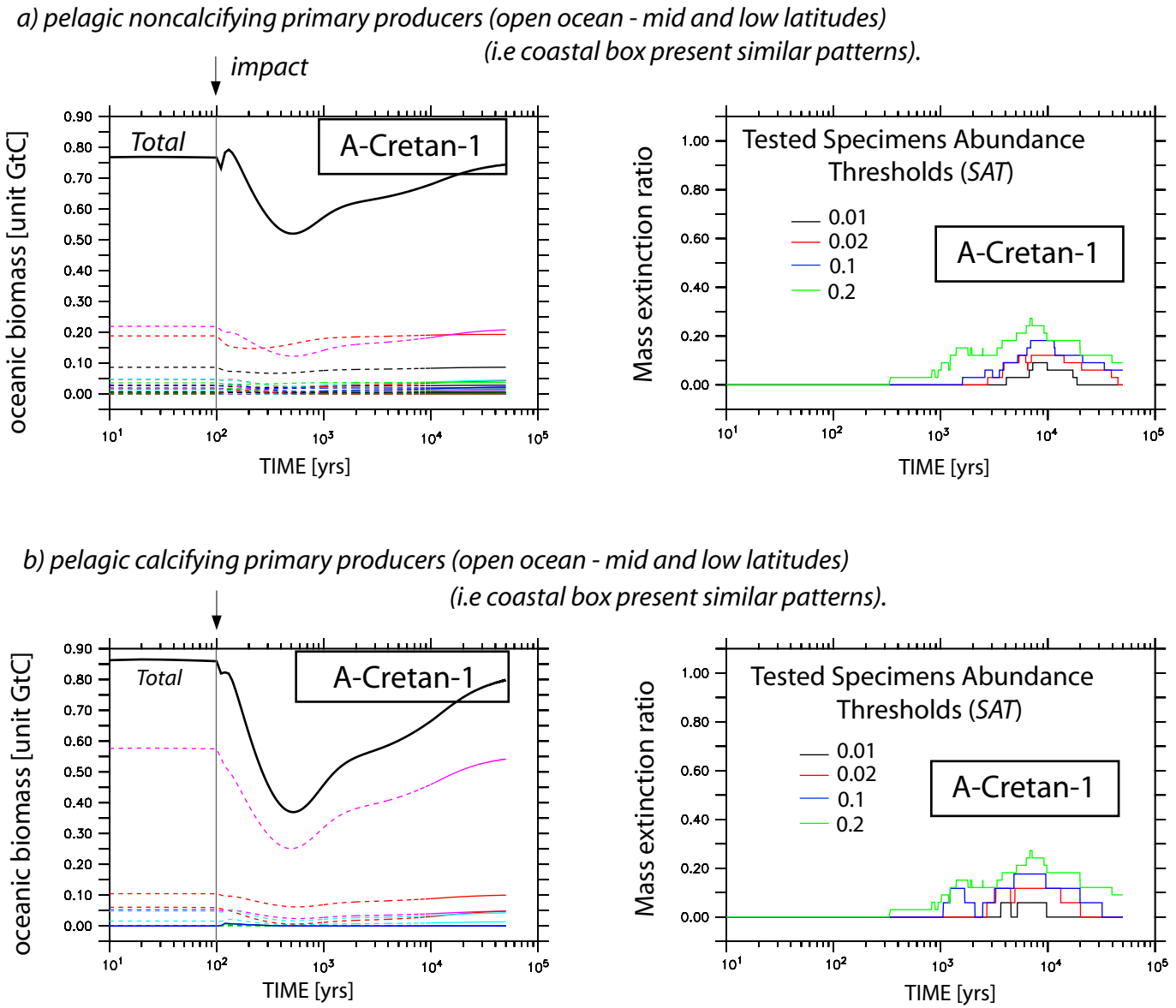

Figure 5 : Rise of atmospheric carbon dioxide and the corresponding dSST. dSST are presented at different time-scale for showing long-term warming interrupted by short-lived cooling events. Grey band represents the deccan traps (main phase)

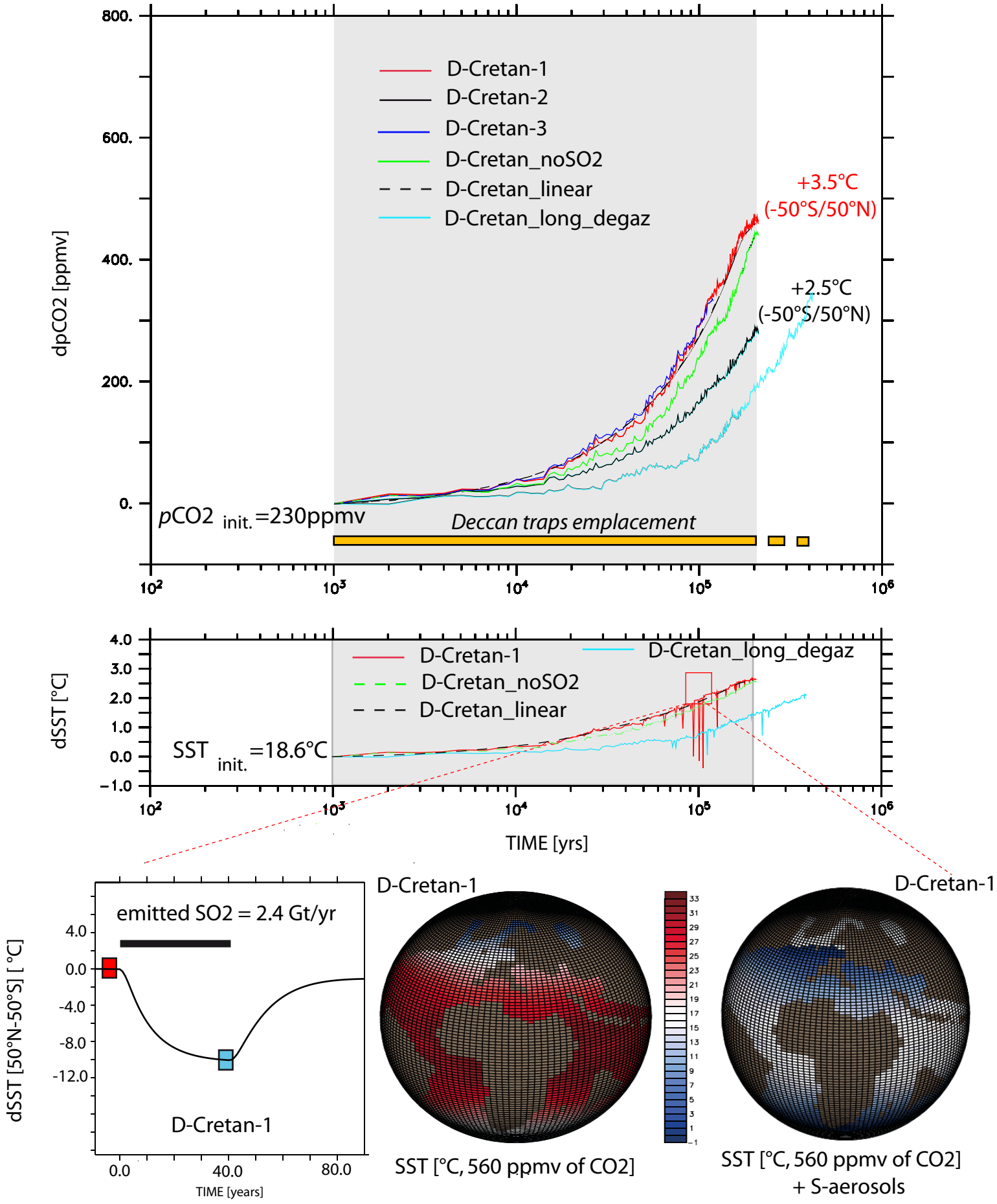

Figure 6: ocean perturbations induced by Deccan traps emplacement.
2 states of ocean : Neritan (blue lines) versus Cretan (red lines), are considered.
*p*H evolutions simulated for **a)** surface versus deep ocean, **b)** open versus coastal ocean.
c) calcite saturation state for surface ocean compared to deep ocean, and **d)** lysocline depth evolution.

a) surface ocean (contineous line) vs deep water (dashed line)

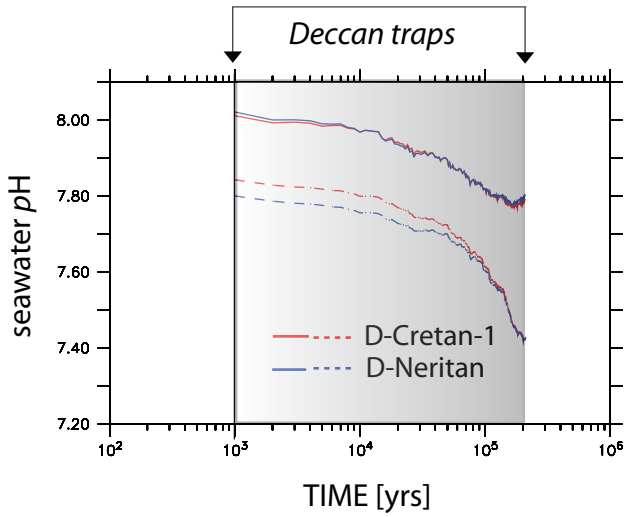

b) open ocean (contineous line) vs coastal ocean (dashed line)

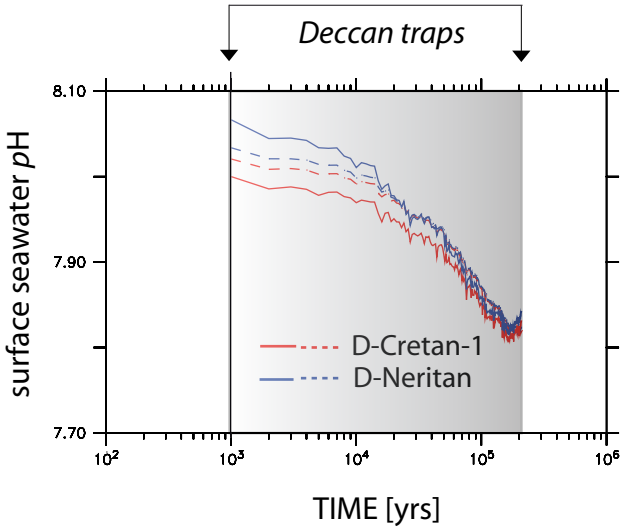

c) surface ocean (contineous line) vs deep water (dashed line)

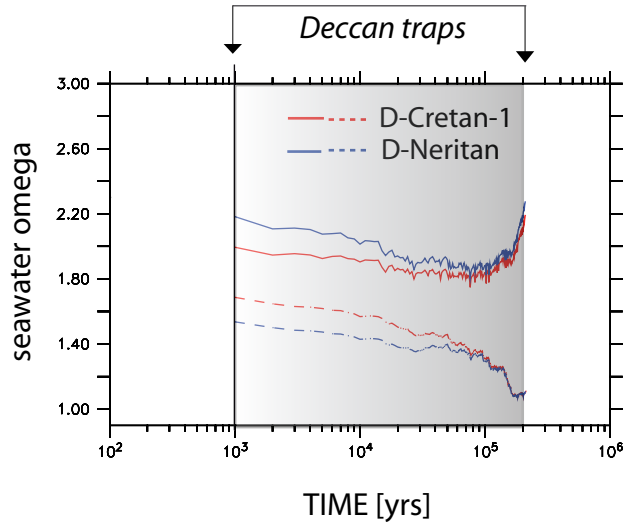

d) lysocline depth evolution

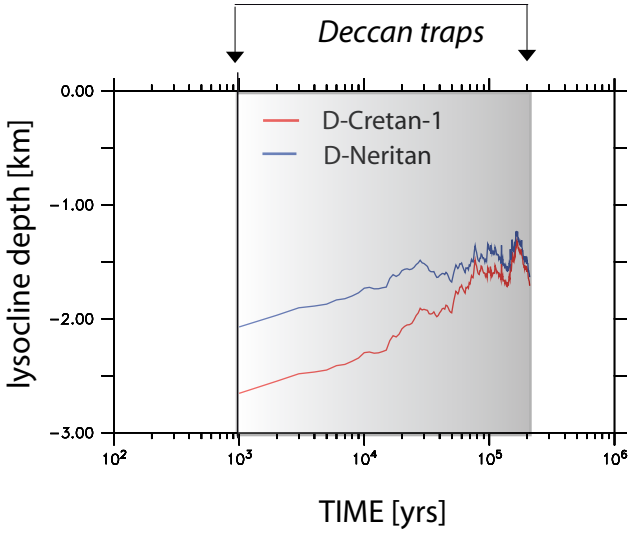

Figure 7. Biomass and mass extinction ratio(ME ratio) induced by Deccan traps
a) for noncalcifying (upper panels) - coloured lines represent PFTs
b) calcifying primary producers (lower panels).

a) *pelagic noncalcifying primary producers (open ocean - mid and low latitudes) coastal boxes present similar patterns.*

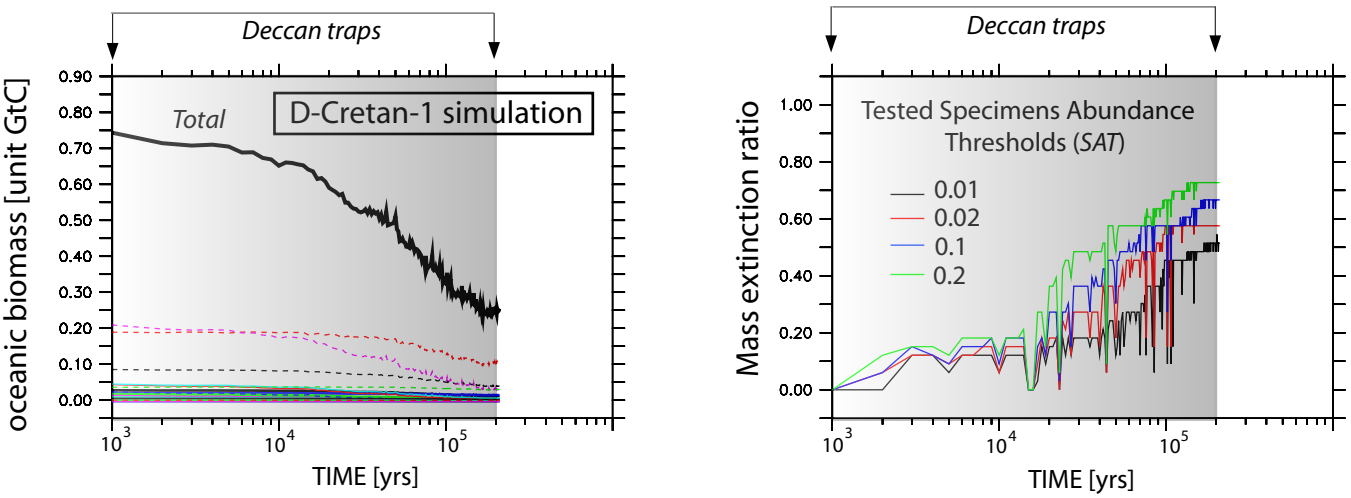

b) *pelagic calcifying primary producers (open ocean - mid and low latitudes) coastal boxes present similar patterns.*

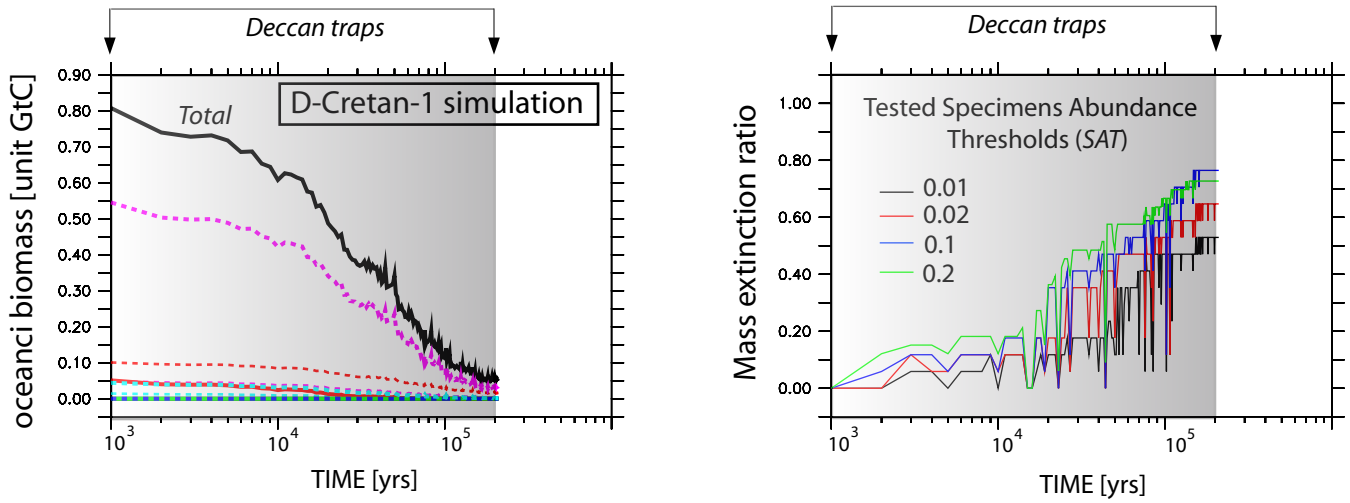

figure 8. Relative changes for **a)** world wilde primary productivity and **b)** phophorus content (upper ocean) simulated for Deccan traps

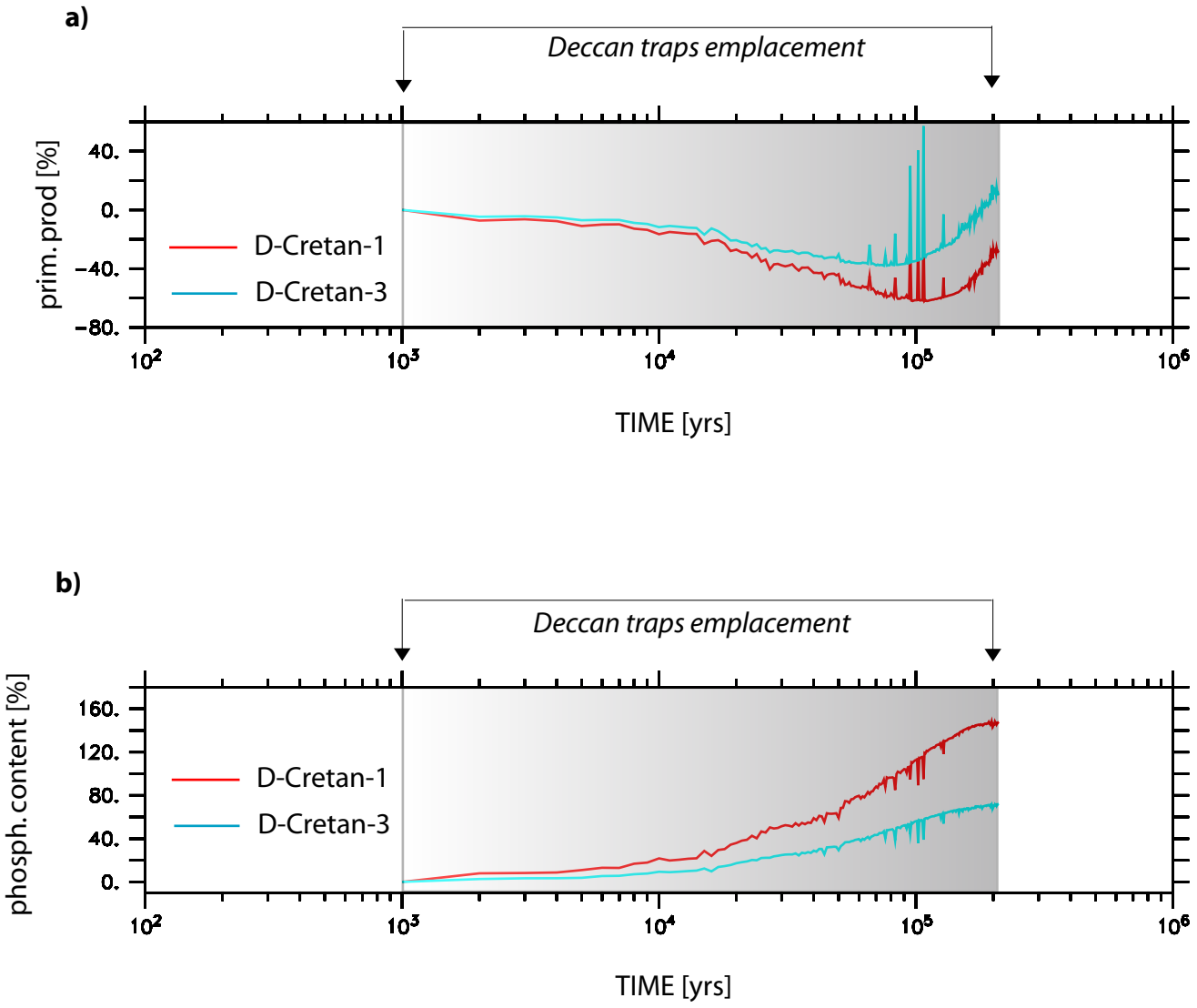

Figure 9. from **a) to c)** AD-Cretan-1 simulation compared to AD-Neritan, contineous line (surface o
vs dashed line (deep water). Panels **d) and e)** presents calcifying/noncalcifying perturbati
for AD-Cretan-1 run.

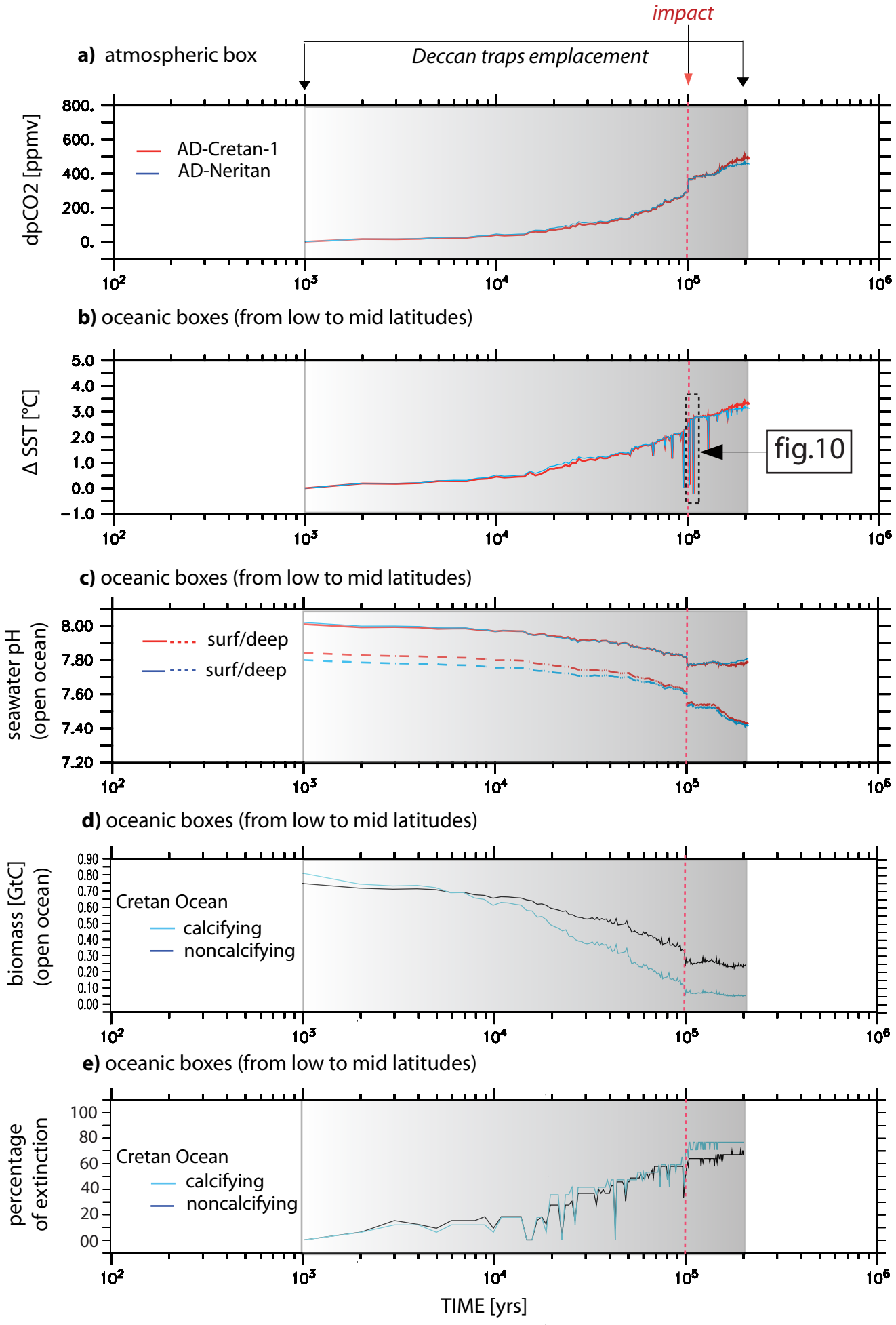

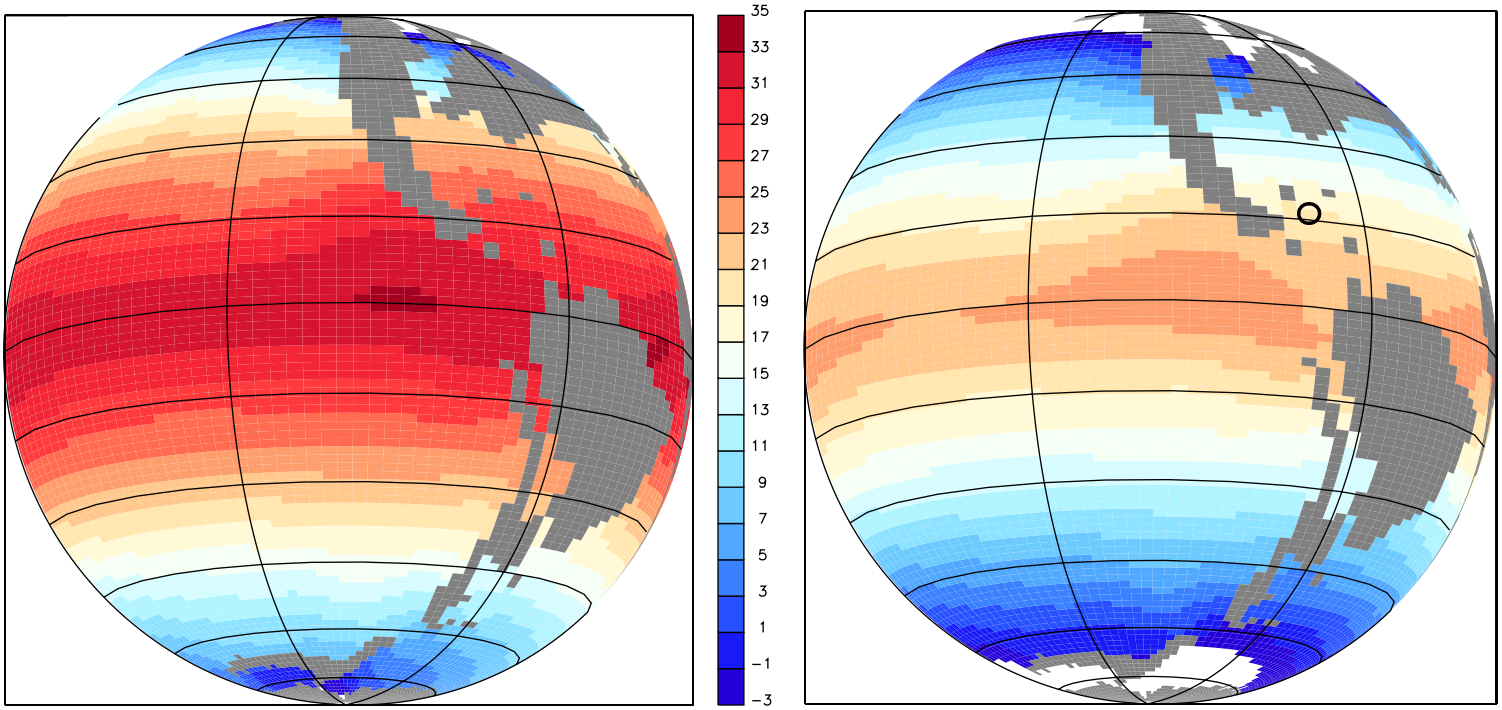

Figure 10:
SST patterns after 100 kyrs of emission (degassing fluxes available in electronic supplementary materials - fig.4). According to the AD-Cretan 1 experiment, the time coincidence between the traps of the impact of Chicxulub is fixed in half of the Deccan traps.
The left/right panel presents SST before/after the asteroid fell in Yucatan Peninsula (black circle). Corresponding oceanic disturbances are detailed in the fig.9